METAL-LIGAND COOPERATION IN TRANSITION METAL-CATALYZED HYDROBORATION OF POLAR UNSATURATED ORGANIC GROUPS

Saeed Ataie

Thesis Submitted to the University of Ottawa

in Partial Fulfilment of the Requirements for

the Degree of Doctor of Philosophy

in Chemistry

Department of Chemistry and Biomolecular Sciences

Faculty of Science

University of Ottawa

ABSTRACT

Metal-Ligand Cooperation (MLC) has been under study over the past two decades as a powerful tool for small molecule activation and functionalization. However, more mechanistic details are needed in order to understand the detailed steps that are enabled by the bifunctional cooperation between ligand and metal. In this regard, the hydroboration reaction offers a useful platform through which to assess the details of bifunctional reaction pathways and catalyst speciation. This dissertation focuses on the synthesis, characterization, and catalytic activity of base-metal complexes with cooperative N-, S-, and O-donor ligands to explore reaction pathways that are a consequence of diverging from traditional phosphine-based ligands.

In Chapter 1 concepts and examples of MLC, especially as applied to hydroboration catalysis, are presented. In Chapter 2, three new Zn(II)-(κ^2-SNS)$_2$ complexes were synthesized to directly compare the bifunctional catalytic activity rendered by amido and thiolate SNS ligands. Although all three complexes catalyzed carbonyl hydroboration, a detailed catalyst speciation study showed that the Zn amido complex reacts with pinacolborane (HBpin) to generate Zn–H and an unbound borylamido ligand. Subsequent substrate-derived zinc alkoxide formation followed by a second equiv of HBpin generates the product, regenerating the Zn hydride catalyst. In contrast, the Zn thiolate complex adds HBpin to the ligand imine unit, followed by aldehyde deoxygenation to give a benzothiazoline heterocycle and [Zn](OBpin). Reaction of the latter with HBpin then gives pinBOBpin and Zn–H, leading to the same active catalyst as that derived from the Zn amido precatalyst! For these systems, then, the bifunctional N- and S-donors serve to *activate* the catalyst rather than participating in a bifunctional catalytic cycle.

Dissociation of the borylamido SNS ligand in Chapter 2 led us to reinvestigate a previously reported Cu(I) amido complex Cu[(κ^2-SNS)(IPr) that was proposed to hydroborate carbonyls via

an outer sphere process [IPr = bis(2,6-diisopropylphenyl)imidazol-2-ylidene]. Indeed, we showed that this complex also undergoes ligand borylation-dissociation to form the active catalyst $[CuH(IPr)]_2$ which had been reported previously as a carbonyl hydrosilylation catalyst. To compare these complexes with their heavier Group 10 analogue, we prepared and structurally characterized the silver amido SNS complex. Interestingly, this complex was not able to serve as a carbonyl hydroboration catalyst.

Then we sought to use the MLC catalyst activation strategy to prepare an especially active Zn hydride hydroboration catalyst. Using a bidentate amine-pyrollide ligand with an aryl ether side-group, the 5-coordinate Zn complex, $Zn(\kappa^2\text{-ONN})_2(DDI)$ (**2.11$_{Zn}$**) was prepared and structurally characterized (DDI = 4,5-dichloro-1,3-dimethylimidazol-2-ylidene). On treatment with excess HBpin, formation of $ONN(Bpin)_2$ [**(Bpin)$_2$-L3**] gave rise to the reactive NHC-stabilized ZnH_2 catalyst that effected the rapid hydroboration of nitriles and quinoline derivatives under ambient conditions with only 0.01 and 0.05 mol% catalyst loading, respectively.

In Chapter 3, in an attempt to prepare a cobalt complex containing both amido and thiolate SNS ligands, we obtained instead the Co(II) dithiolate complex, $Co(\kappa^3\text{-SNS})(DDI)$ (**3.2$_{Co}$**). This complex showed a unique selectivity for aldehyde hydroboration, over other functional groups such as ketones, cyanides, nitriles and olefins. A DFT study, in collaboration with Prof. Erin Johnson from Dalhousie University, showed that **3.2$_{Co}$** bifunctionally assembles the HBpin and aldehyde substrates, with Co binding the aldehyde oxygen and sulfur binding the boron of HBpin. With aromatic aldehyde substrates, interesting aromatic-aromatic dispersion effects led to catalyst inhibition which could be reversed by simply rinsing off the product with hexane. These effects were not observed for catalytic hydroboration of aliphatic aldehydes.

In Chapter 4 we focused on expanding our MLC investigation to include additional donors beyond N and S. First, a dimeric Zn(II)-(κ^4-NSNO) complex (**4.1$_{Zn}$**) was synthesized and evaluated as a catalyst for nitrile dihydroboration to compare aryloxide and amido donors for B–H bond activation. In fact, **4.1$_{Zn}$** successfully catalyzed dihydroboration of a range of different aromatic and aliphatic nitriles under neat condition. Mechanistic studies determined that the aryloxide donor activates the B–H bond in the first step and the mechanism then likely proceeds through an inner-sphere insertion. As detected by our kinetic study, at high turnovers the catalyst decomposes when Bpin also binds to the amido donor.

To compare the potential of other donors for B–H bond activation, a series of divalent $Ni^{II}X(\kappa^3$-NNN) complexes were synthesized, with X = bromide (**4.3$_{Ni}$**), phenoxide (**4.4$_{Ni}$**), thiophenoxide (**4.5$_{Ni}$**), 2,5-dimethylpyrrolide (**4.6$_{Ni}$**), diphenylphosphide (**4.7$_{Ni}$**), and phenyl (**4.8$_{Ni}$**), and employed as precatalysts for nitrile dihydroboration. Superior activity of the phenoxy derivative (*vs.* thiophenoxy or phenyl) suggests that B–H bond activation occurs at the Ni–X (*vs.* ligand Ni-$N_{pyrrolide}$) bond. Furthermore, stoichiometric treatment of **4.3$_{Ni}$-4.8$_{Ni}$** with a nitrile showed no reaction, whereas stoichiometric reactions of **4.3$_{Ni}$-4.8$_{Ni}$** with pinacolborane (HBpin) afforded the same Ni–H complex for **4.3$_{Ni}$**, **4.4$_{Ni}$** and **4.6$_{Ni}$**. Considering that only **4.3$_{Ni}$**, **4.4$_{Ni}$** and **4.6$_{Ni}$** successfully catalyzed nitrile dihydroboration reaction, we suggest that the catalytic cycle involves a conventional inner sphere pathway initiated by substrate insertion into Ni–H.

In summary, our investigations confirm the importance of mechanistic studies and catalyst speciation for studies involving potential bifunctional catalysis. In Chapter 5 we summarize the findings of this thesis, placing them in the context of the current state of the art and speculating on future investigations they may enable.

ACKNOWLEDGEMENTS

Before any word, I want to express my deepest gratitude to professor Baker, who believed in me and provided me with everything a tired student needed to get going again. Your support made me finish the 4-year work (even longer) in 3 years. I know you want to say that my hard work paved the way for me, but we both know very well that this was a two-sided mission that could never be completed unilaterally, and it was you who made my ambitions a reality. Although this is just the beginning of my adventures, I will always be grateful to you for this beginning. I wish the best moments for both of us in B.C.

Profs. Richeson and Fogg - thank you both so much for your constructive comments on my work and presentations, and also the recommendation letters that you provided me with every time I needed them. Profs. Mehrkhodavandi, Murugesu and Rowley– thank you for serving as my thesis examiners. I would like to thank Prof. Erin Johnson for unhesitating cooperation on her DFT study of one of my projects. I also want to thank Dr. Jeffrey Ovens for training me to learn how to work with the X-ray crystallography instruments and solve my structures. Another thanks to all staff, technicians, and administration at uOttawa, especially Annik St-Jean, Peter Pallister, and Chloé Lagacé.

Thank you to the Baker group - especially Dr. Behnaz Ghaffari; you have been a very supportive friend to me. Thank you Loïc for the DFT study on my last project, and also being helpful always. Thank you Luana and Atousa for being such heartwarming friends.

My dear parents, even though there are thousands of miles between us, you never hesitated to give me energy and you cared about me like all the moments of my life. Those morning calls that we had every day on the way to lab were enough to make my day and give me endless energy. Hoping to spend all the seconds together again - I miss you very much!

I thank the undergraduate students who I mentored, Seth, Samantha and Maxwell. You guys made enjoyable moments in my life. For all the days we discussed mystical and scientific issues together and played instruments together. Seth, you will be a wonderful teacher undoubtedly. For all the days we talked about the future plans, Samantha, and I'm glad you made it to the University of Toronto. For all the days that we trained together in the gym, Max, especially the biceps days, which were our favorites. Of course, I received the email requesting a

recommendation letter from UBC. I put in good words for you. I hope you can make it so we can go to gym together again. I will miss you guys.

My lovely wife, Faezeh. Words fail me, so I would like to dedicate our favorite poem to you:

Tear is a mystery,
Smile is a mystery,
Love is a mystery.

The tear in that night was my love's smile.
I am not a story you can tell
Not a melody you can sing
Not a voice you can hear
Or something you can see
Or you can know
I am the common pain, scream me!

The tree has a word with the forest,
The grass with the plain,
The star with the galaxy;
and I speak with you.

Tell me your name,
give me your hand.
Tell me your word,
give me your heart.

I have understood your roots;
With your lips, I have spoken to all the lips,
and your hands are familiar with mine.
In the bright solitude, I have wept with you for the alive;
And in the dark cemetery, I have sung with you
the most beautiful songs of all;
Because the dead of that year, were in love more than anyone alive....

Give me your hands;
your hands are familiar with me.
Sigh the late-found, I speak with you
Like the cloud with the storm,
Like the grass with the plain,
Like the rain with the sea,
Like the bird with the spring,
Like the tree speaks with the forest.

For, I have understood your roots,
Because my voice is familiar with yours.

"**Ahmad Shamlou**"

And after all, I would like to dedicate my favorite poem to all the readers of this dissertation:

Before I take the last breath,
Before the curtain falls,
Before the last flower wilts,

I intend to live,
I intend to love,
I intend to be.

In this dark world,
In this era steeped in disasters,
In this world filled with hatred.

To those who need me,
Those who I need,
Those who are praiseworthy.

So that I can discover,
be amazed,
and understand anew,
All that I am,
All that I can be,
All that I want to be.

So that the days do not remain fruitless,
The hours revive,
And the moments gain significance.

When I laugh,
When I cry,
When I am silent,
in my journey towards you,
Towards myself,
Towards God.

That it is an unknown path,
Full of thorns,
And uneven.

A path that I step in,

That I have already stepped in,
And do not intend to return,
without me having seen the blossoming of the flowers,
without me having heard the rivers roar,
without me having been awed by the beauty of life…

Now death can come,
Now I can set out,
Now I can say that I have lived.

"Margot Bickel"

Table of Contents

LIST OF ABBREVIATIONS/SYMBOLS

α	alpha position, or angle label (X-ray crystallography)
Å	Ångström
ADC	alcohol dehydrogenative coupling
AH	asymmetric hydrogenation
Al	aluminum
Anal.	analysis
Ar	aryl
ATH	asymmetric transfer hydrogenation
aq.	aqueous workup
av	average
B	boron
Br	bromine
β	beta position, or angle label (X-ray crystallography)
br	broad (NMR spectroscopy)
cm^{-1}	wavenumbers
^{13}C	carbon-13
Cat	catecholate
RCN	nitrile
C_6D_6	benzene-d_6
CD_3CN	acetonitrile-d_3
δ	chemical shift
Δ	delta (difference between variables)
‡	double dagger (transition state)
D	deuterium, ^2H
d	doublet (NMR spectroscopy)
dd	doublet of doublets (NMR spectroscopy)

DDI	4,5-dichloro-1,3-dimethylimidazol-2-ylidene
deg (or °)	degrees
DFT	density functional theory
e^-	electron
E	element
EA	elemental analysis
EI-MS	electron impact mass spectroscopy
ESI-MS	electron spray ionization mass spectroscopy
equiv	equivalents
F	structure factors (X-ray crystallography)
FW	formula weight
γ	gamma, angle label (X-ray crystallography)
g	gram
GOF	goodness of fit
ΔG	Gibbs free energy
$\Delta G^{\ddagger}$	Gibbs free energy of activation
η^n	n–Hapticity
h	hour(s)
HBpin	pinacolborane
HRMS	high-resolution mass spectroscopy
^1H	proton
$\{^1H\}$	proton-decoupled
Hz	Hertz
ΔH	enthalpy
$\Delta H^{\ddagger}$	enthalpy of activation
IPr	1,3-bis(2,6-diisopropylphenyl)imidazol-2-ylidene
J	Joules

$^{n}J_{AB}$	n-bond scalar coupling constant between nuclei A and B (NMR spectroscopy)
k	rate constant
K	Kelvin
kcal	kilocalorie
kJ	kilojoules
λ	wavelength
L	neutral ligand donor
μ	bridging ligand or absorption coefficient (X-ray crystallography)
M	central metal atom (or molar when referring to concentration)
M^{+}	parent ion (mass spectrometry)
m	multiplet
Me	methyl, $–CH_3$
mg	milligram
MHz	megahertz
min	minutes
mL	milliliter
MLC	metal-ligand cooperation/cooperativity
mmol	millimoles
mol	moles
MW	molecular weight
Np	naphthalene
NHC	N–heterocyclic carbene
NMR	nuclear magnetic resonance
No.	number
OMe	methoxy group, $–OCH_3$
ORTEP	Oak Ridge Thermal Ellipsoid Plot Program
π	pi-bonding or orbital

p	pentet
Ph	phenyl group, $–C_6H_6$
^{i}Pr	isopropyl group, $–CH(CH_3)_2$
ppm	parts per million
%	percent
Θ	theta diffraction/Bragg angle (X-ray crystallography)
q	quartet (NMR spectroscopy)
R	alkyl group
R	reliability factor (X-ray crystallography)
Reflns	reflections (X-ray crystallography)
σ	estimated standard deviation (X-ray crystallography), type of bonding or orbital
s	singlet (NMR spectroscopy)
tr	triplet (NMR spectroscopy)
T	temperature in Kelvin or degrees
THF	tetrahydrofuran
TMS	tetramethylsilane
TOF	turnover frequency
TON	turnover number
TS	transition state
V	unit cell volume
$W_{1/2}$	width at half height
X	halide substituent (or anionic ligand donor)
Z	number of formula units per unit cell (X-ray crystallography)

LIST OF SCHEMES

LIST OF FIGURES

LIST OF TABLES

LIST OF NEW COMPOUNDS

Label	Complex	Label	Complex	Label	Complex
2.1_{Zn}	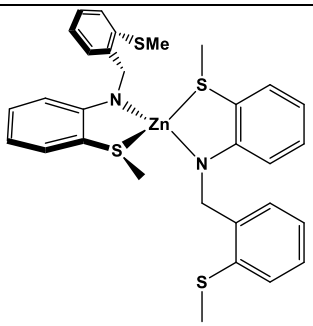	**2.2_{Zn}**	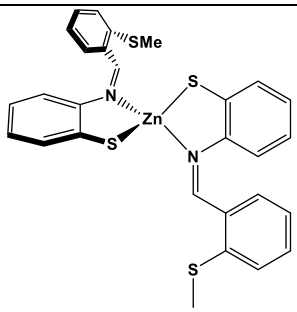	**2.4_{Zn}**	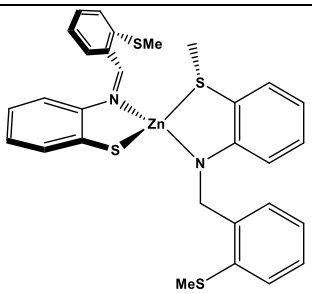
Bpin-L^1	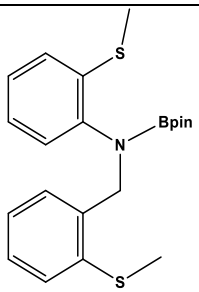	**S-P1**	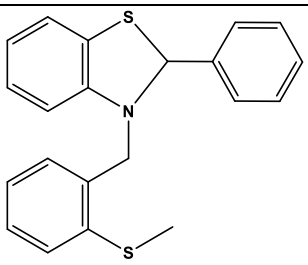	**2.7_{Ag}**	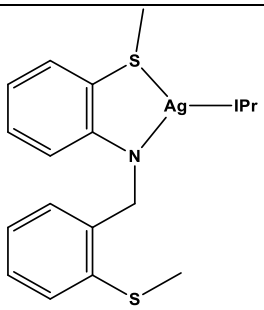
H_2L^3	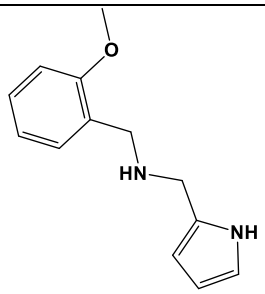	**2.8_{Zn}**	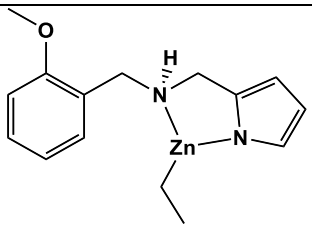	**2.9_{Zn}**	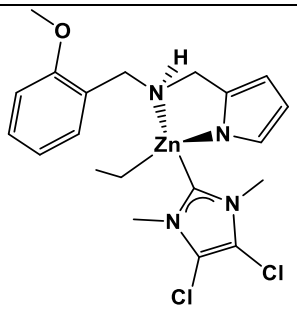
2.10_{Zn}	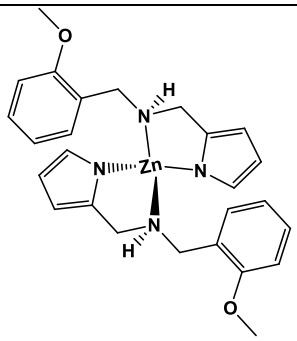	**2.11_{Zn}**	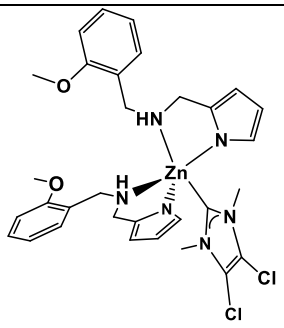	**$(Bpin)_2$ -L^3**	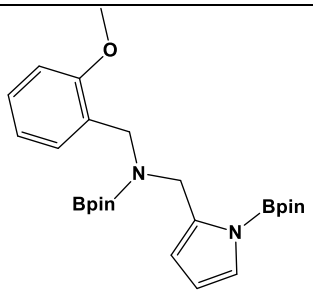

2.12$_{Zn}$	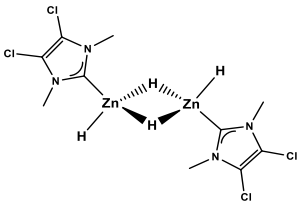	**3.2$_{Co}$**	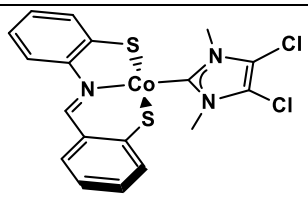	**3.3$_{Co}$**	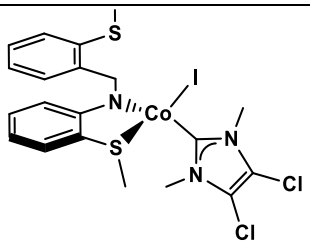
3.4$_{Co}$	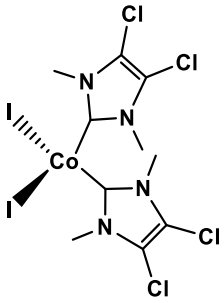	**H_2L^4**	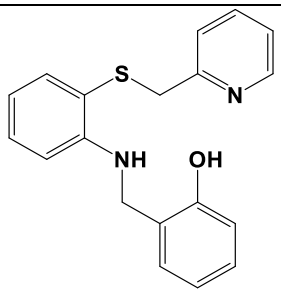	**4.1$_{Zn}$**	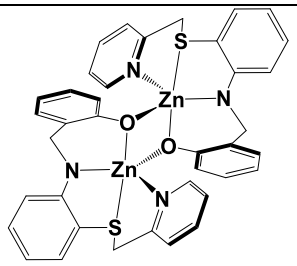
Bpin-HL^4	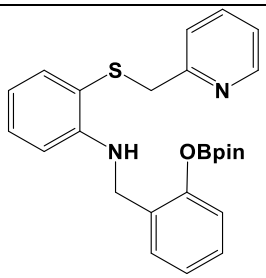	**4.2$_{Ni}$**	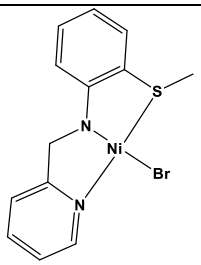	**4.3$_{Ni}$**	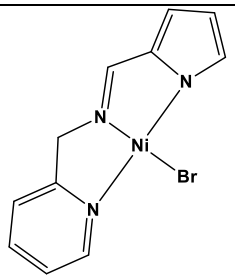
4.4$_{Ni}$	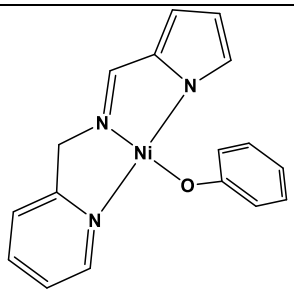	**4.5$_{Ni}$**	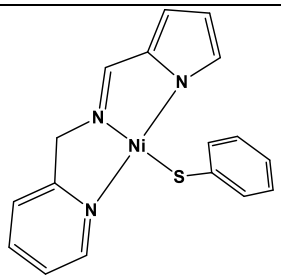	**4.6$_{Ni}$**	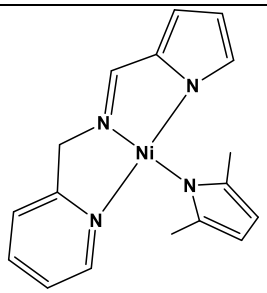
4.7$_{Ni}$	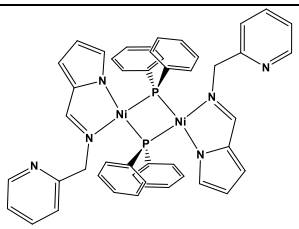	**4.8$_{Ni}$**	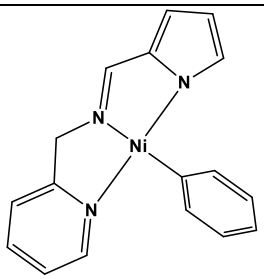	**Bpin-L^5**	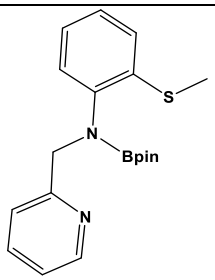

DECLARATION OF CO-AUTHORSHIP AND PREVIOUS PUBLICATIONS

I. Declaration of Co-Authorship and Previous Publications

I hereby declare that this dissertation incorporates material that is a result of joint research as follows: this dissertation contains five chapters. Chapters 2-4 include six projects, three of which have been published in peer-reviewed journals and three that are submitted or under revision. All work contained herein was performed in consultation with my supervisor, Prof. R. Tom Baker. Nearly all experimental work was carried out by me; however, some work was performed by expert collaborators. Density functional theory (DFT) calculations presented in Chapter 3 pertaining to reaction profiles of a cobalt catalyst were performed by Prof. Erin Johnson from Dalhousie University, Canada. Mr. Seth Hogeterp, Ms. Samantha Dudra and Mr. Maxwell Lohoar, undergraduate students under my supervision, contributed to experimental parts presented in Chapters 2-4. Dr. Jeffrey S. Ovens collected a portion of the X-ray crystallography data presented in Chapters 2 and 4.

Chapter 2 contains results from the communication, "SNS ligand-assisted catalyst activation in Zn-catalysed carbonyl hydroboration." Ataie, S.; Hogeterp, S.; Ovens, J. S.; Baker, R. T. *Chem. Commun*. **2022**, *58*, 3795–3798, the communication, "Correction and addition: Cu(I)–SNS complexes for outer-sphere hydroboration and hydrosilylation of carbonyls. Consequences of catalyst speciation." Ataie, S.; Lohoar, M. I.; Elsby, M. R.; Baker, R. T. *Chem. Commun*. **2022**, submitted, and the full article, "Bifunctional Activation in Zinc Dihydride-Catalyzed Quinoline Hydroboration and Nitrile Dihydroboration Reactions." Ataie, S.; Baker, R. T. *Inorg. Chem.* **2022**, submitted.

Chapter 3 contains results from the full article, "Selective Cobalt(II)-SNS Dithiolate Complex-Catalyzed Bifunctional Hydroboration of Aldehydes: Kinetics and Mechanistic Studies." Ataie, S.; Dudra, S. L.; Johnson, E. R.; Baker, R. T. *ACS Catal.* **2022**, submitted.

Chapter 4 contains results from the communication, "Solvent-free Zn (NSNO) complex-catalysed dihydroboration of nitriles." Ataie, S.; Ovens, J. S.; Baker, R. T. *Chem. Commun*. **2022**, *58*, 8266–8269, and the full article, "Comparing B–H Bond Activation in $Ni^{II}X$(NNN)-Catalyzed

Nitrile Dihydroboration (X = anionic N-, C-, O-, S- or P-donor).” Ataie. S.; Baker, R. T. *Inorg. Chem.* **2022**, In press.

I acknowledge my supervisor as a co-author in this work as he made a significant contribution to the editing and preparation of these manuscripts. I acknowledge that other listed authors on the manuscripts contributed through raw data acquisition and interpretation of results.

I declare that this is a true copy of my thesis, including any final revisions, as approved by my thesis advisory committee and the Graduate Studies office.

II. Published Contributions

All thesis publications with contributions from Saeed Ataie from the period of **2019-2022** appear below and are enumerated by date.

(7) **S. Ataie**, L. P. F. Mangin, M. I. Lohoar, R. T. Baker* “Ligand Exchange Through Pre-Protonation in Iron(II)- and Cobalt(II)-SNS Bis-Amido Complexes.” *Organometallics*, **2023**, submitted.

(6) **S. Ataie**, S. L. Dudra, E. R. Johnson,* R. T. Baker* “Selective Cobalt(II)-SNS Dithiolate Complex-Catalyzed Bifunctional Hydroboration of Aldehydes: Kinetics and Mechanistic Studies.” *ACS Catalysis,* **2022**, submitted.

(5) **S. Ataie**, R. T. Baker* “Bifunctional Activation Leading to Zinc Pre-Catalyst in Zinc dihydride Catalyzed Quinoline Hydroboration and Nitrile Di–Hydroboration Reactions.” *Inorg. Chem.* **2022**, submitted.

(4) **S. Ataie**, M. I. Lohoar, M. R. Elsby, R. T. Baker* “Correction and addition to *Cu(I)–SNS complexes for outer-sphere hydroboration and hydrosilylation of carbonyls*. Consequences of catalyst speciation.” *Chem. Commun*. **2022**, submitted.

(3) **S. Ataie**, R. T. Baker* “Comparing B–H Bond Activation in $Ni^{II}X$(NNN)-Catalyzed Nitrile Dihydroboration (X = anionic N-, C-, O-, S- or P-donor).” *Inorg. Chem.* **2022**, in press.

(2) **S. Ataie**, J. S. Ovens, R. T. Baker* “Solvent-free Zn (NSNO) complex-catalysed dihydroboration of nitriles.” *Chem. Commun*. **2022**, *58,* 8266–8269.

(1) **S. Ataie**, S. Hogeterp, J. S. Ovens, R. T. Baker* “SNS ligand-assisted catalyst activation in Zn-catalysed carbonyl hydroboration.” *Chem. Commun*. **2022**, *58*, 3795–3798.

CHAPTER 1

METAL-LIGAND COOPERATIVITY USING LATE FIRST-ROW METAL COMPLEXES IN CATALYTIC HYDROBORATION REACTIONS

1.1 General Introduction

This dissertation is primarily focused on the synthesis, characterization, and catalytic study of late first-row metal complexes (M = Co, Ni, Cu, Zn) supported by pincer ligands that can undergo bifunctional B–H bond activation in hydroboration reactions. Herein, the term bifunctional refers to a ligand which not only serves to stabilize the metal center, but also participates in chemical reactions in concert with the metal. This strategy was introduced as metal-ligand cooperation (MLC) by Hansjörg Grützmacher[1] in 2008 and has been explored extensively over the last two decades. The work in this thesis is focused on the detailed mechanisms of catalytic reaction pathways and associated catalyst speciation. As such, this chapter includes a brief overview of metal-ligand cooperation and potentially bifunctional Lewis-base ligands used in molecular catalysis.

1.2 Metal-Ligand Cooperation

When Ryoji Noyori won the Nobel prize in 2001 for the asymmetric catalytic systems he discovered for ketone hydrogenation (**Scheme 1.1**),[2] increased attention was concentrated on the mechanistic details.

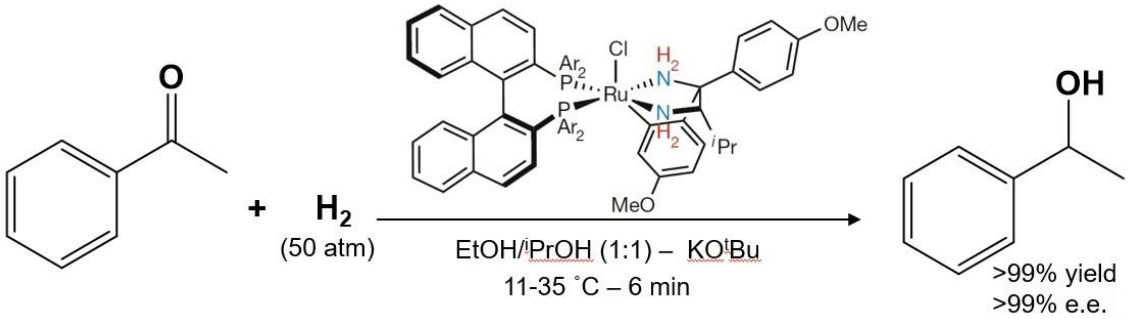

Scheme 1.1. Noyori's catalytic system for asymmetric hydrogenation of ketones.

The first computational investigation using density functional theory (DFT) showed a cooperation between amine and ruthenium in which the Ru hydride and amine proton transfer to the carbonyl substrate through an outer-sphere mechanism (**Scheme 1.2**).[3]

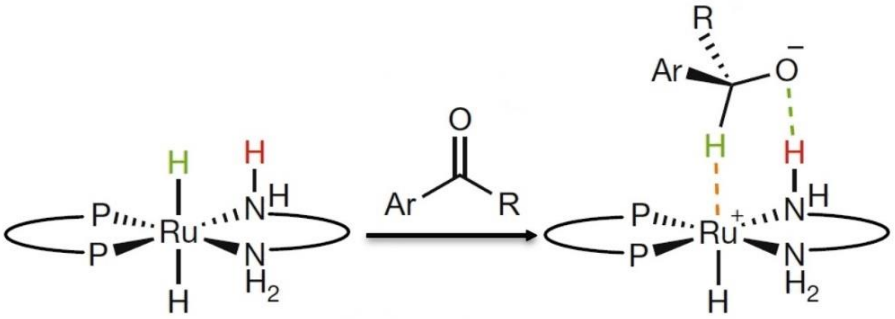

Scheme 1.2. Proposed mechanism for Noyori's catalytic system in gas phase.

Canadian chemists Morris and Bergens made significant experimental contributions especially in the role played by the alkoxide base.[4-9] More recently, a study by Dub and Gordon showed that inclusion of solvent in their DFT calculations disfavored the concerted outer-sphere mechanism.[10] The lowest energy pathway involves two steps in which the Ru hydride is first transferred to the carbonyl that is activated by interaction of its O with the amine proton or N-M^I in which M^I is Na^+ or K^+ (from added tert-butoxide base). In the second step the resulting alkoxide anion is protonated by the polarized Ru dihydrogen ligand, not the amine proton as originally proposed (**Scheme 1.3**).

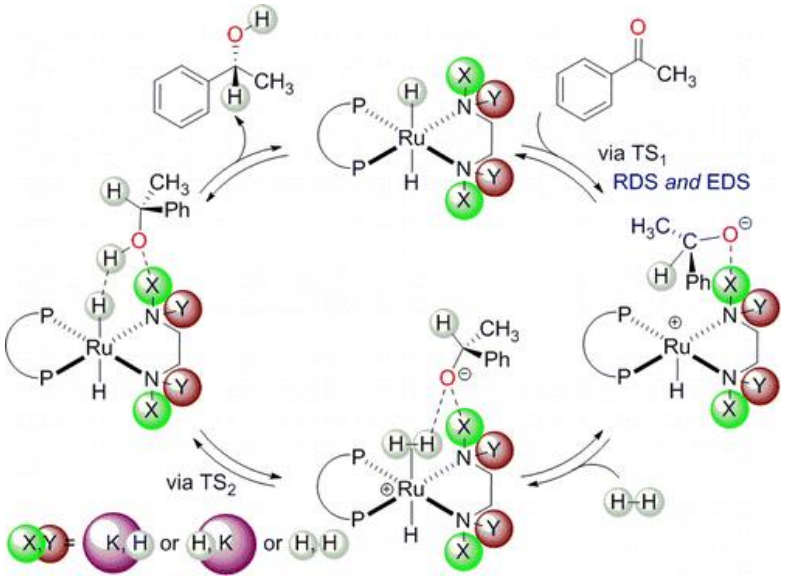

Scheme 1.3. Proposed mechanism for Noyori's catalytic system in solution.

Further discovery of MLC in natural enzymes such as [FeFe]–hydrogenase (**1.1**)[11] that catalyzes reversible formation of dihydrogen from protons and electrons [$2H^+ + 2e^- \rightleftharpoons H_2$],

revealed that the metal's oxidation state undergoes no change in this mechanism (**Scheme 1.4**). These results opened new doors for researchers to include first row transition metals and main group metals in MLC[12] and to further investigate the roles of metal and ligand. These metals are relatively more environmentally and biologically (such as zinc) friendly, and are also naturally more abundant compared to their heavier congeners, which makes them more economically accessible. As a result, this area has experienced a renaissance over the past decade as a powerful mechanistic strategy in homogeneous catalysis, particularly with the base metals.[13,14]

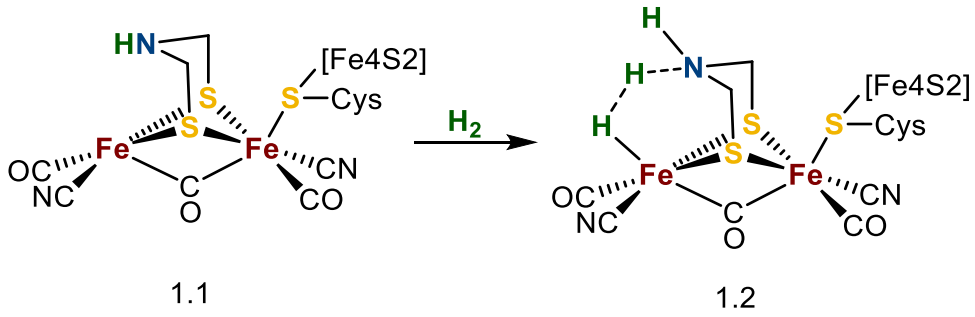

1.1 1.2

Scheme 1.4. Proposed activation of H_2 by [FeFe]–Hydrogenase.

1.3 Bifunctional Ligands for Metal-Ligand Cooperative Catalysis

A cooperative ligand has been defined as one that actively participates in substrate activation to facilitate catalysis with a metal ion in a synergistic fashion.[13] The chemical structure of the ligand may either remain intact during the reaction or undergo a reversible transformation (i.e., protonation/deprotonation). In some cases, the ligand may only participate in catalyst activation. This scenario has mostly been observed in hydroboration and hydrosilylation reactions, in which bifunctional activation of the E–H bond (E = B or Si) by the M–X bond affords the M–H catalyst and E–X with the latter unit (i.e. borylamido) not involved in the ensuing catalytic cycle.[15,16]

1.3.1 Ligand acts as a Lewis base

The most prominent class of cooperative ligands are those which utilize an X donor with more than one lone pair, often in a multidentate framework. The X donor then uses one lone pair to bind the Lewis acidic metal center and another one to participate in bifunctional catalysis with the metal. Electron-rich transition metal complexes with amido ligands are particularly well suited for this application due to high N-centered basicity.[17] The mutual behavior of the Lewis basic ligand and Lewis acidic metal enables their participation in several different mechanisms, including: outer-

sphere reduction (A), inner-sphere insertion (B), and inner-sphere hydride transfer (C),[18] as depicted in **Figure 1.1** for ketone hydroboration. Note that mechanisms A and C rely on MLC for every turnover whereas the formed alkoxide in mechanism B could react with another equivalent of B–H to give the product and regenerate M–H in an example of bifunctional catalyst *activation*.

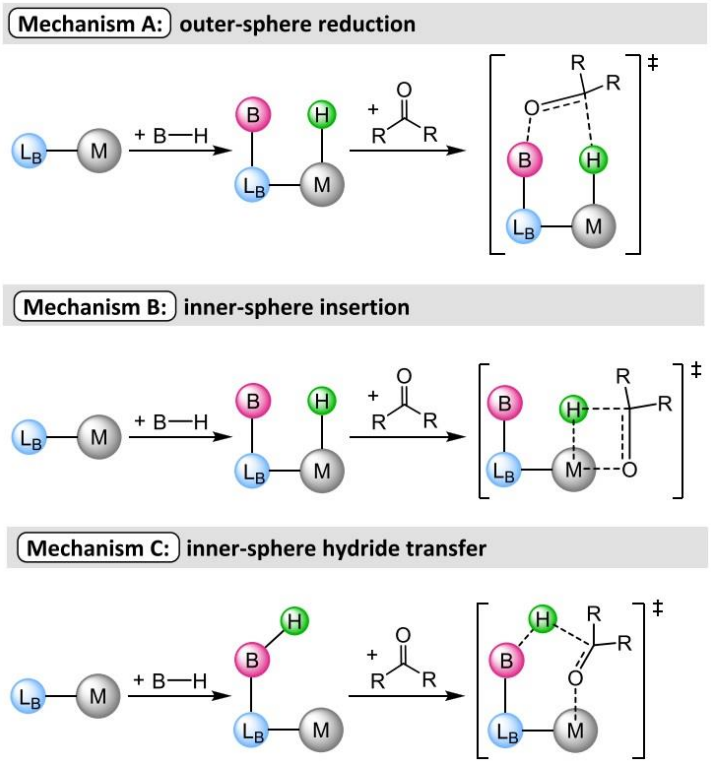

Figure 1.1. Different modes of metal-ligand cooperativity originated from Lewis basic ligand and Lewis acidic metal in carbonyl hydroboration.

Different studies have shown that nitrogen-, sulfur-, and oxygen-donor ligands have the potential to function in MLC.[19] In the following, we summarize examples in hydroboration reactions.

1.3.1.1 Nitrogen-based ligands

Although the polarity of R_2B–H bonds in dialkylboranes (Pauling electronegativity for B = 2.04 and H = 2.2)[20,21] can be reduced by substitution with R = alkoxide or amido groups, the B–H bond (389 kJ/mol) is comparatively weaker than H–H bond (432 kJ/mol), facilitating cleavage of the former by catalysts utilizing MLC.[22,23] In a recent example, Thomas et al. successfully isolated and characterized the double HBpin addition product (**1.4**) to both Fe–N bonds in an Fe complex

(**1.3**) ligated by a tetradentate bis(phosphine)-bis(amido) PNNP donor (**Scheme 1.5**).[24] Note, however, that the B–H bond has not been completely cleaved in this product.

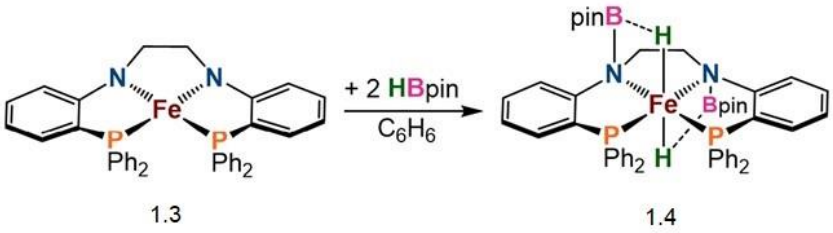

Scheme 1.5. Double B–H bond activation across Fe–N bond.

Leitner *et al.* isolated and characterized a similar key intermediate in their report of hydroboration of difficult carbonyl substrates (amides, esters, CO_2) catalyzed by manganese complex **1.5** supported by a PNP pincer ligand (**Scheme 1.6**).[25] Stoichiometric amount of base generates **1.6** that is armed with an amido donor that adds HBpin. to give key intermediate **1.7** which was crystallographically characterized. Mild heating of **1.7** leads to cleavage of the B–H bond to give Mn–H complex **1.7a.** The authors suggested that interaction of the carbonyl oxygen with the boron in **1.7a** allows for facile reduction by the Mn–H.

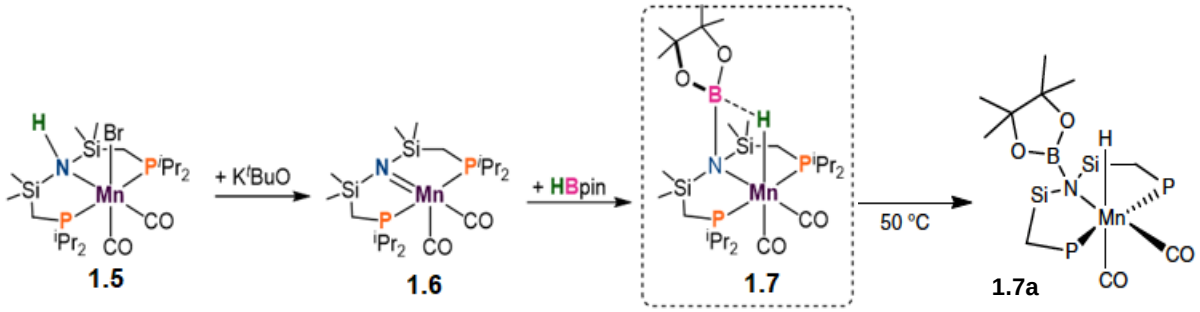

Scheme 1.6. Isolation of Mn–H intermediate from bifunctional B–H activation.

Wang's group isolated another intermediate in a study on Co-catalyzed hydroboration of olefins.[26] While treatment of **1.8** with olefin gave no product, **1.8** facilitates B–H bond cleavage to afford isolable intermediate **1.9**, a Co(II) hydride complex in which the Bpin is bound to the uncoordinated nitrogen atom of the ligand (**Scheme 1.7**). The existence of a heteroatom (N or O) on the olefin potentially accelerates the reaction and subsequent 1,2-insertion of the olefin into the Co–H forms **1.11**. Wang proposed two possible pathways for formation of the hydroborated

product. No evidence was provided for Path 1 which regenerates complex **1.8**, while Path 2 proceeds through a σ-bond metathesis step with a second equivalent of HBpin, affording product and reforming **1.9**. While MLC may thus be confined to catalyst activation, the authors' catalyst demonstrated excellent activity for olefin hydroboration under mild conditions and relatively low catalyst loading.

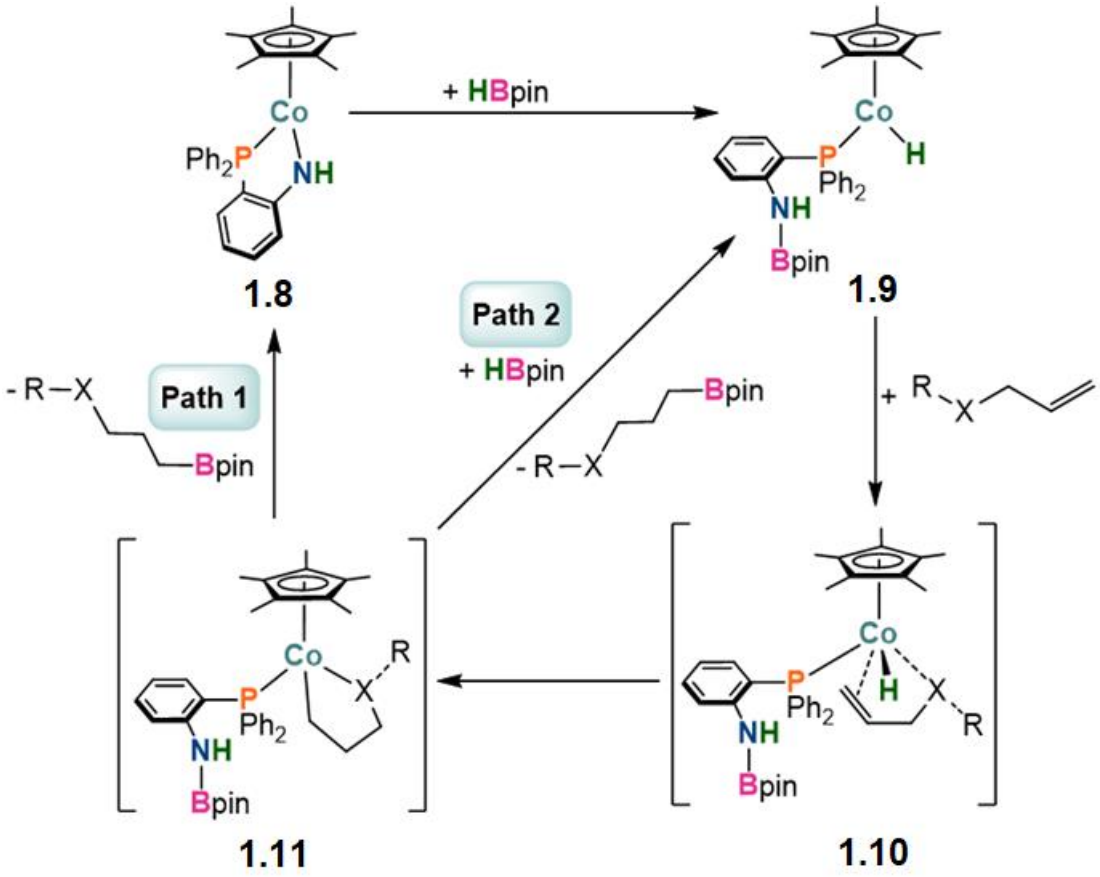

Scheme 1.7. Proposed catalyst activation mechanism for HBpin addition to Co-amido complex.

In a study of Co-catalyzed nitrile dihydroboration, the Trovitch and Baik groups identified a low energy pathway involving transfer of the Bpin group from the amido N in intermediate **1.18** to the substrate derived imino-cobalt N through 4-membered transition state **1.19** (**Scheme 1.8**).[27] Since the monoborylated product was not observed throughout catalysis, the authors proposed that the borylimine directly enters the second reduction cycle. While stoichiometric treatment of **1.12** and nitrile showed no reaction, **1.12** reacts with 2.2 equiv of HBpin to give a Co complex containing both amido-boryl and Co-boryl groups (**Scheme 1.9**). Although this was found to be

an off-cycle product, a previous report on Co-catalyzed nitrile hydroboration considered that as oxidative addition of borane to form a metal hydride in a key activation step.[28]

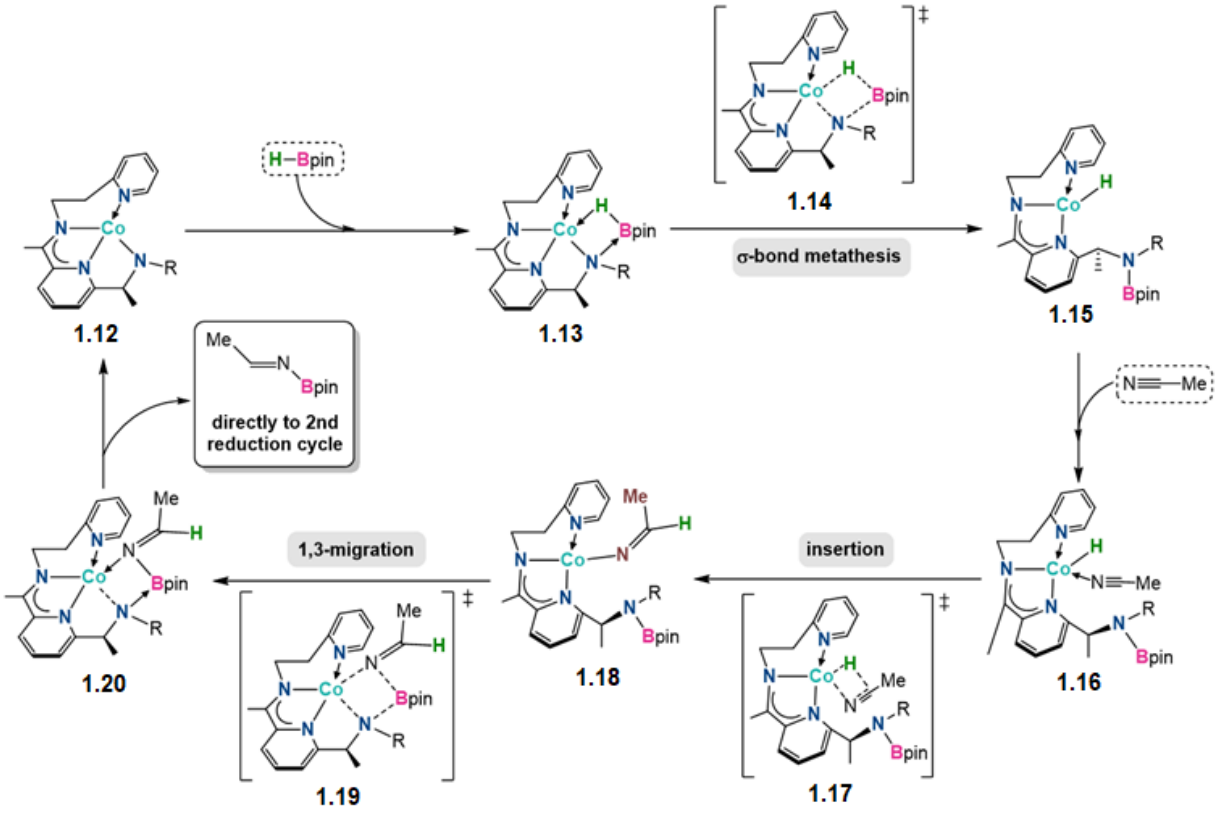

Scheme 1.8. Proposed mechanism for dihydroboration of nitriles by Co-complex.

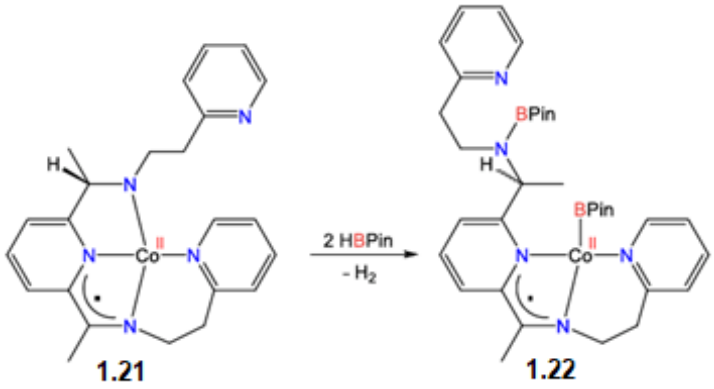

Scheme 1.9. Formation of off-cycle Co-boryl product

In two reports by Panda et al. on Group 4 metal complex-catalyzed hydroboration of aldehydes and dihydroboration of nitriles, the ligand again only participates in catalyst activation by cleaving the B–H bond and generating the M–H catalyst.[15,16] As depicted in **Scheme 1.10**, the formed

Me_2NBpin molecule dissociates from the Ti center.[15] In the next step, benzaldehyde binds to the titanium center **1.25**, followed by hydride transfer to give titanium alkoxide **1.27**. In the last step addition of a second equivalent affords the product and regenerates Ti–H **1.24** via transition state **1.28**.

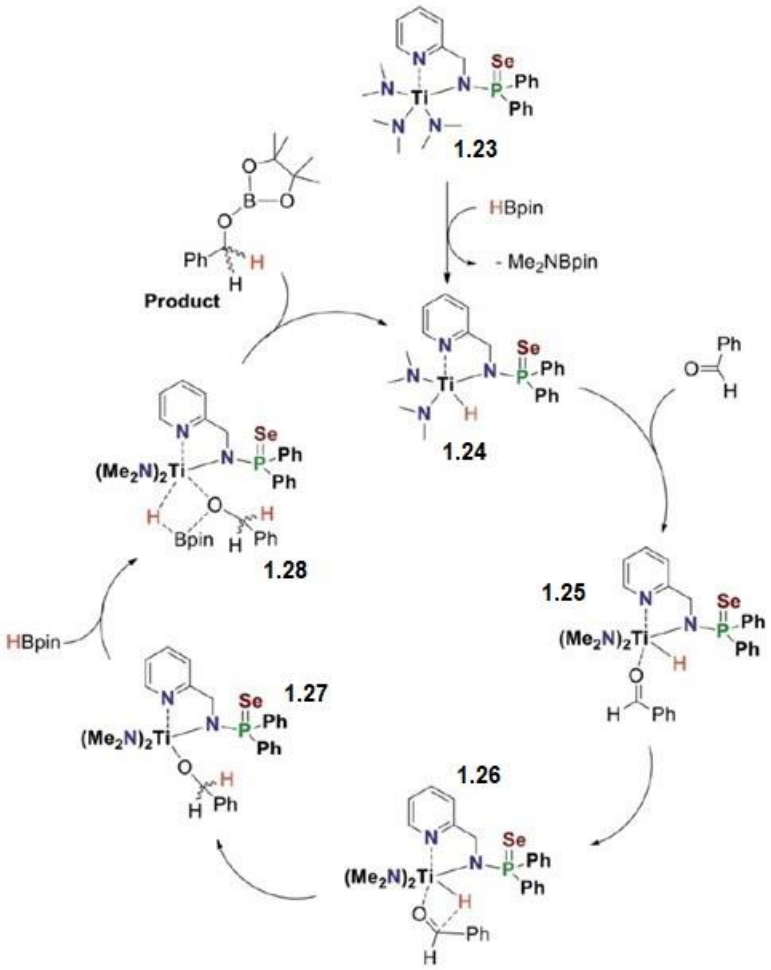

Scheme 1.10. Hydroboration of aldehydes by activated Titanium hydride through inner-sphere insertion mechanism.

1.3.1.2 Sulfur-based ligands

The majority of MLC examples in catalysis are limited to complexes composed of polar-metal-nitrogen bonds (amido ligands), while transition metal catalysts incorporating metal-sulfur bonds that function as Lewis basic reactive sites are underdeveloped.

Metal-sulfur bonds are crucial features in living systems. They play key roles in biological processes such as dihydrogen activation by hydrogenases.[29,30] To shed light on mechanisms of

various enzymatic processes utilizing metal-sulfur bonds, extensive work has been performed.[31,32] Therefore, the study of sulfur donors that are capable of acting bifunctionally in MLC catalysis, may potentially provide insight into biological mechanisms and help propel homogeneous catalysis in line with greener biomimetic systems. It has been shown that sulfur donors, better donate their lone pair electrons as a Lewis base as thiolates (RS^-),[33,34] and exhibit bifunctional behaviour in MLC mechanisms, while other types of sulfur X-donors have not yet shown such behaviour. In the following, some important examples of thiolate ligands in MLC are summarized.

In one of the earliest studies Bergman and Anderson reported Si–H bond cleavage by MLC using a titanocene sulfide complex.[35] In 2017, Hillhouse, Cundari and Jordan reported the cleavage of E–H bonds in their study of a dinuclear nickel complex with bridging sulfides.[36] Treatment of **1.29** with dihydrogen yielded the bis thiolate-bridged Ni complex **1.31a**. Kinetic and computational studies showed that **1.31a** formation proceeds via H_2 cleavage across a cooperative Ni–S bond (**Scheme 1.11**). Subsequent *cis*/*trans* isomerization at Ni followed by H atom migration from Ni to S forms **1.30a**. Similar reactivity was observed with HBpin to afford **1.31b,** showing the utility of metal-sulfur systems for more generalized E–H bond activations.

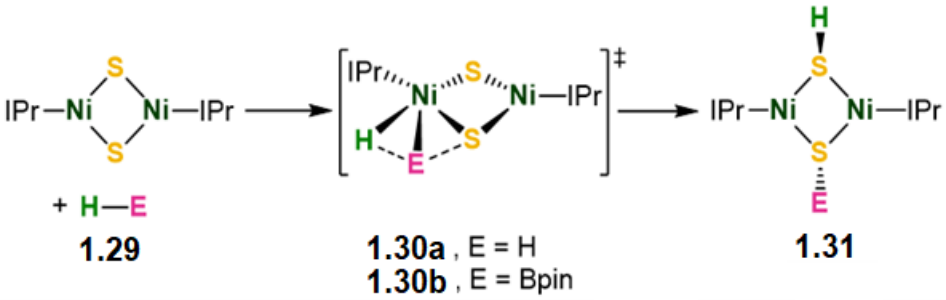

Scheme 1.11. Heterolytic cleavage of H–H and B–H bonds across a Ni–S bond.

The Wang group has extended the capabilities of base-metal thiolate complexes for MLC in catalysis. In 2017, Wang et al., reported a regioselective hydroboration of aryl epoxides by iron thiolate pre-catalyst **1.32** that converts to active catalyst **1.33** by loss of acetonitrile ligand (**Scheme 1.12**).[37] Interestingly and unexpectedly, in the first step of the cycle direct addition of the epoxide across the Fe–S bond is notable rather than initial B–H bond activation. Although reaction of **1.32** with Lewis acidic boranes such as H_3B•THF and 9–H-BBN resulted in iron-borane adducts featuring Fe B–H interactions, DFT studies found that HBpin addition across the iron-thiolate bond is endergonic by 12.9 $kcalmol^{-1}$ (BBN = borabicyclo[3.3.1]nonane). Stoichiometric treatment of

1.32 with *trans*-2,3-diphenyloxirane yielded the 5-membered cyclic Fe alkoxide complex **1.34**. Then, epoxide ring-opening through Fe–S cooperativity afforded **1.33.** After that, electrophilic addition of HBpin afforded **1.35** followed by S–C bond cleavage/H transfer through **1.36** ending up with the final hydroborated product and **1.33** regeneration. The mechanistic pathway presented in this work shows that direct addition of HBpin is thermodynamically unfavourable, providing potentially valuable insight for future studies on MLC in catalytic systems.

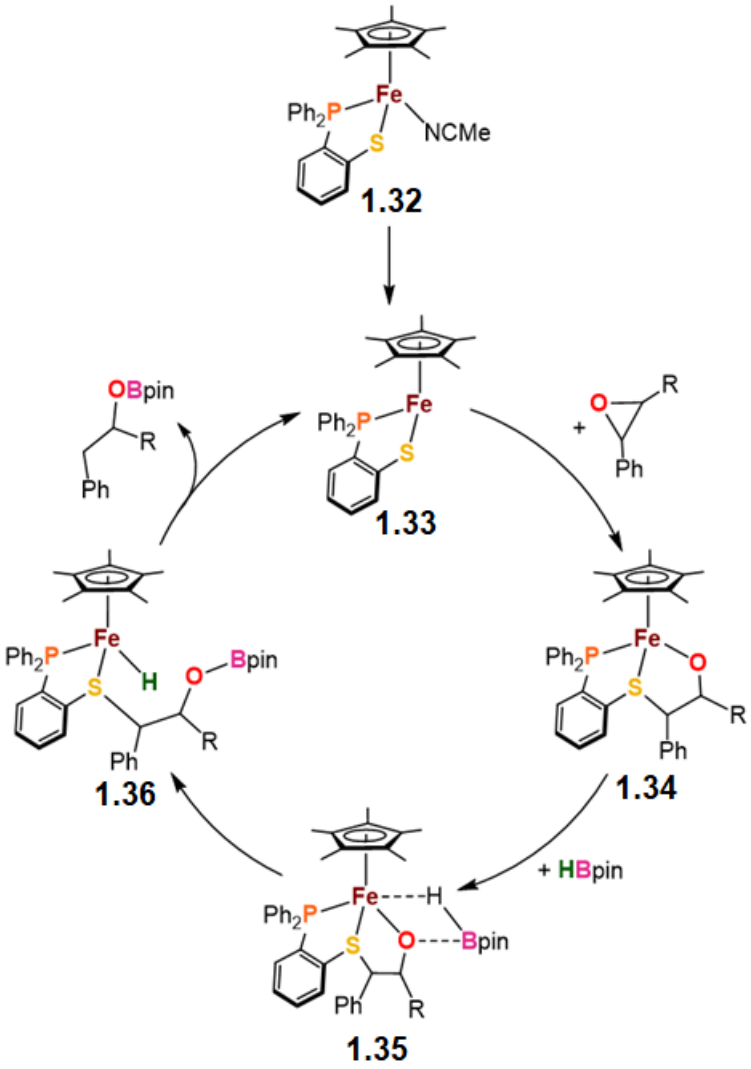

Scheme 1.12. Proposed mechanism for Fe thiolate complex-catalyzed hydroboration of aryl epoxides.

In another study, The Wang group extended metal-thiolate cooperation to hydroboration of heteroarenes. Using N_2-bridged diiron complex **1.37** as pre-catalyst, *N*-borylated 1,2-reduced products were obtained with low catalyst loadings (1 mol%) and excellent regioselectivity.[38] Stoichiometric studies suggested that the initial activation step includes displacement of N_2 by the

N–Heteroarene yielding mononuclear **1.38**, rather than B–H bond cleavage (**Scheme 1.13**), as HBpin did not react readily with **1.37**. Subsequent thiolate-facilitated hydride transfer from HBpin to C_2 (passing through **1.39**) forms **1.40**. Then, the Bpin group transfers from S to the reduced heterocycle giving the hydroborated product and reforming **1.33**.

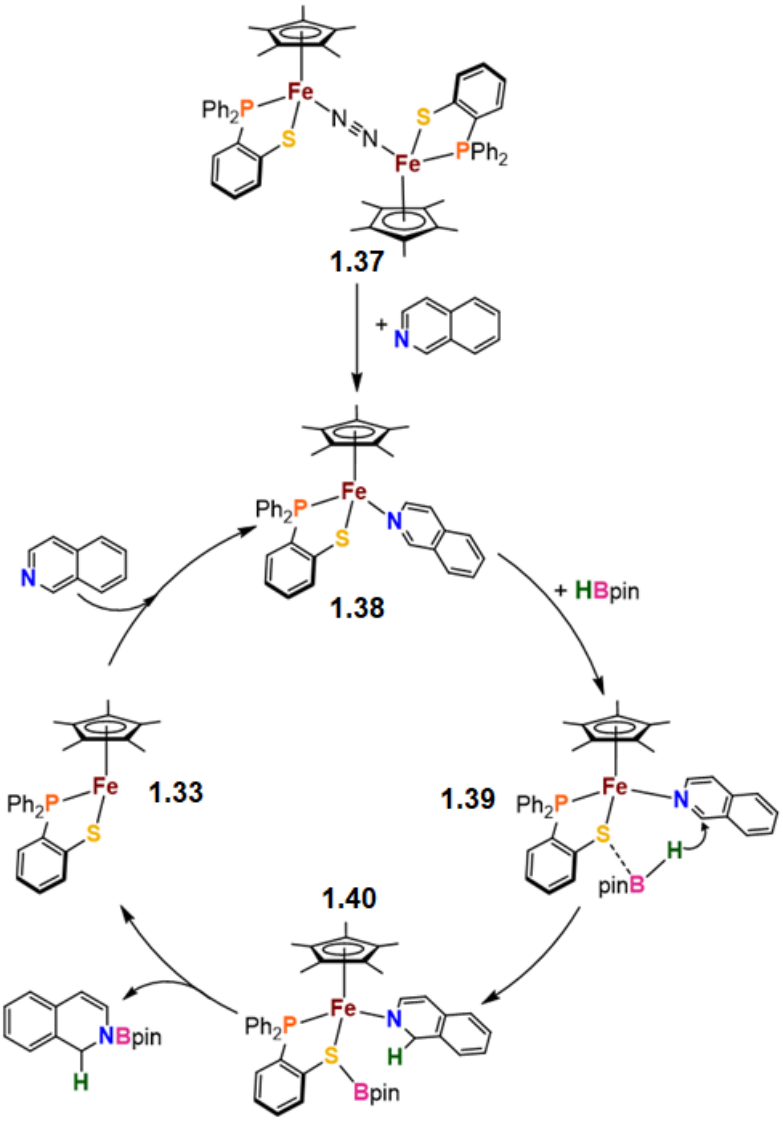

Scheme 1.13. Proposed mechanism for Fe-catalyzed hydroboration of *N*–Heteroarenes.

In the most recent study on Metal-Sulfur cooperation, Baker et. al., reported a Mn(I) complex, $Mn(\kappa^3\text{-}S^{Me}NS)(CO)_3$ that catalyzed nitrile dihydroboration at room temperature with 1 mol% catalyst loading. Through a combined experimental and computational mechanistic study, the authors revealed that catalysis requires the presence of UV light to enter and remain in the catalytic

cycle by loss of two CO ligands. Stoichiometric reactions showed that HBpin reduces the imine N=C of the ligand backbone in the absence of nitrile, forming an inactive off-cycle by-product. DFT calculations showed that the bifunctional thiolate donor activates HBpin without breaking B–H bond and the reaction proceeds through an inner-sphere hydride transfer (**Scheme 1.14**).[39]

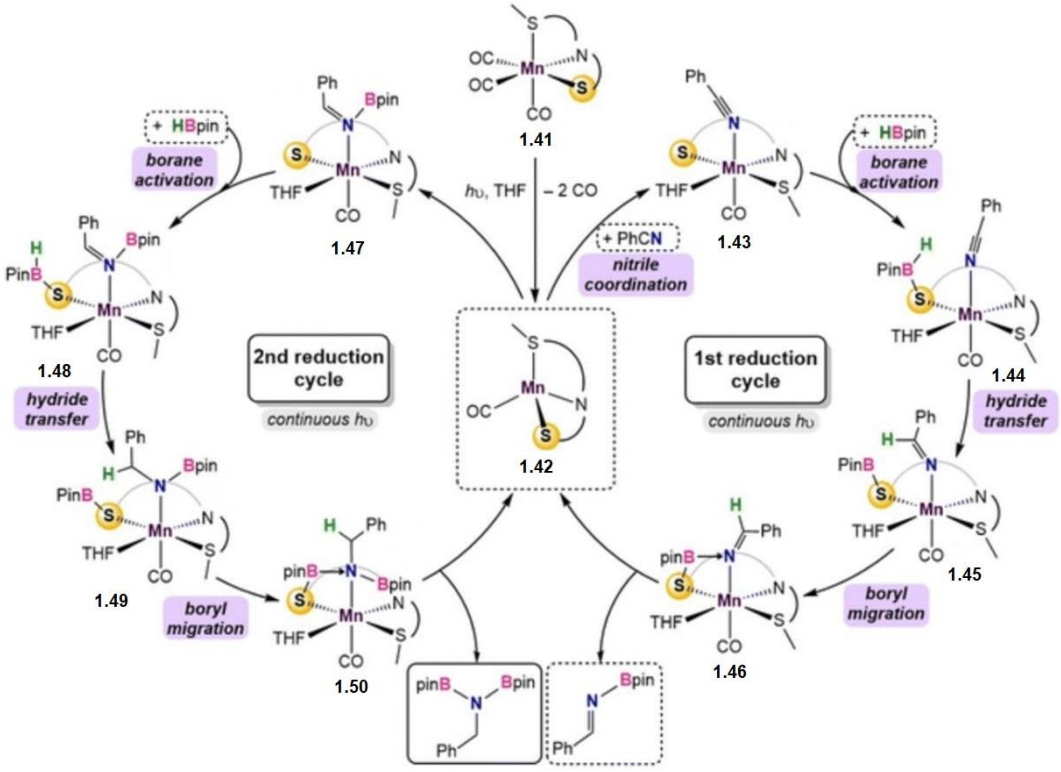

Scheme 1.14. Proposed mechanism for Mn-catalyzed dihydroboration of nitriles.

These recent studies highlight the potential utility of thiolate donors in MLC although further investigation is required to obtain more insight on their potential reactivity scope as base metal biomimetic catalysts.

1.3.1.3 Oxygen-based ligands

Although the role of oxygen in several hydrogenase enzymes has been revealed,[40-42] weak-field oxygen donors such as alkoxides have seen limited study in MLC systems for E–H bond activation. In addition, reduced Lewis basicity of coordinated alkoxides (vs amido) and higher lability of alcohols versus amines, limit utility of oxygen donors in bond activation. Therefore, there are few reports of metal-oxygen cooperation for bond activation.

In one of the earliest reports on metal-oxygen MLC, the Adolfsson group, in a study on catalytic hydrosilylation of carbonyls, showed that a mixture of iron acetate and hydroxyethyl-imidazolium salts constitutes an efficient and selective catalyst system.[43] Although their efforts to isolate or characterize any Fe intermediates were unsuccessful, they proposed bidentate alkoxide-NHC coordination and showed no conversion using the O-tosyl analogue.

In 2015, Rauchfuss *et al*. used bis(phosphine)-dialkoxide Fe(II) complex **1.51** to demonstrate Si–H bond activation through metal-oxygen cooperation that resulted in fully characterized Fe–H complex **1.52** (**Scheme 1.15**).[44] Although **1.52** was not an active hydrosilylation catalyst, substitution of one CO ligand by PMe_3 or NCMe afforded precursors which catalyzed hydrosilylation of benzaldehyde, acetophenone, and even styrene with relatively low catalyst loading (1 mol%).

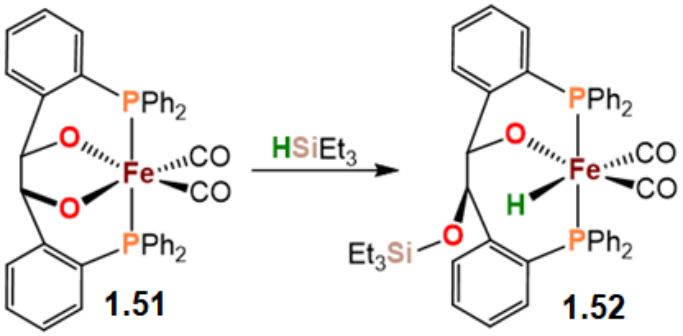

Scheme 1.15. Fe-alkoxide-assisted Si–H bond activation.

Wang and co-workers recently employed their previous half-sandwich framework to construct a Ni(II) complex bound to a phosphino-phenoxide ligand for catalytic hydroboration of pyridine and other *N*–*H*eteroarenes.[45] Complex **1.53** successfully catalyzed the reaction with 2 mol% loading at room temperature. The necessity of the bifunctional ligand became evident when nickel–Hydride complex Cp*Ni(H)(PPh_3) showed no catalytic activity. The reaction initiates by Ni-phenoxide-assisted B–H bond cleavage, affording fully characterized 18e- intermediate **1.54** which features a B-O moiety (**Scheme 1.16**). DFT calculations showed that the heteroatom of the substrate coordinates to boron, and subsequent hydride transfer from Ni to the pyridine ortho-carbon through intermediate **1.55** affords **1.56**. Finally, B–O bond cleavage led to the 1,2-reduced pyridine and regeneration of **1.53**. Hydride transfer to the *ortho*-site was also supported by deuterium labelling. DFT studies also showed another possible pathway in which **1.55** can be converted to a radical pair intermediate, **1.55a** by dissociation of the C_6H_5N–Bpin moiety from the

phosphinophenolato oxygen, and the 1,2-product converts to the 1,4-product. This report suggests a crucial role for the oxygen donor in both generating Ni–H and supporting in-cycle catalytic intermediates.

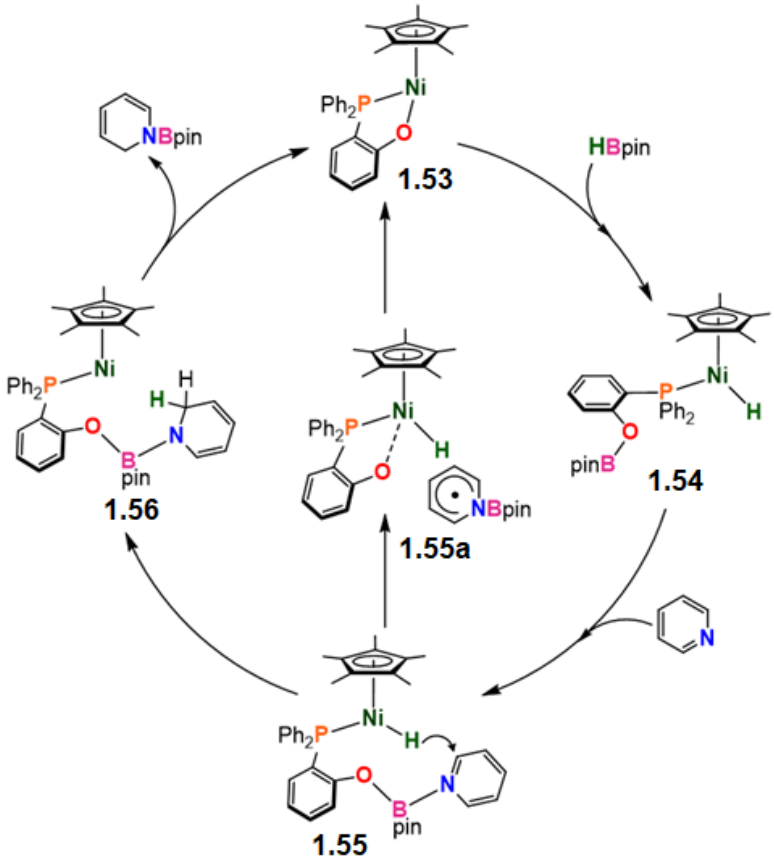

Scheme 1.16. Proposed mechanism for Ni-catalyzed hydroboration of *N*–Heteroarenes.

While the number of designed ligand metal-alkoxide cooperation studies in E–H bond activation is still quite limited, we note that reaction of metal alkoxide with HBpin to give M–H and carbonyl hydroboration product is a common step in simple metal hydride-catalyzed reactions.

1.3.1.4 Carbon-based ligands

Recently, carbenes have attracted specific interest as amphoteric platforms for cooperative bond activation.[46] As the carbene center has both a lone pair and an empty orbital, both protic and hydridic E–H bonds have been activated across the M=C unit. In contrast to the X-donors described above, when a substrate is added across the M=C bond, a transition-metal alkyl complex

is formed. To date, carbene ligands cooperating with late transition metals have made the most successful cases for MLC although the only reports with base metals are with nickel.

The Piers group, utilizing a rigid $PC_{sp2}P$ pincer ligand for stabilizing the carbene, has reported several Ni-carbene complexes that proved to be effective for cooperative bond activation. Addition of E–H substrates such as H_2, H_2O, NH_3 and HC≡CPh, to **1.57** led to rapid Ni=C bond cleavage, forming species such as **1.58** with concurrent loss of PPh_3 (**Scheme 1.17 A**).[47]

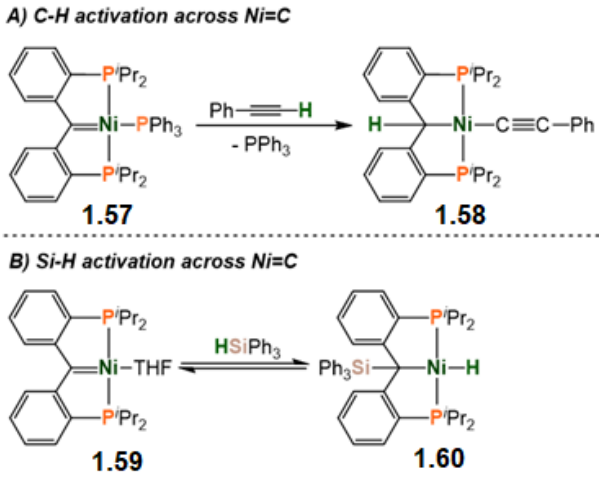

Scheme 1.17. Cooperative activation of A) C–H and B) Si–H bonds across a nickel-carbene.

In another study, **1.59** was investigated for the reversible activation of tertiary and secondary phenyl-silanes affording **1.60** (**Scheme 1.17 B**).[48] An isotope labelling study showed E–H addition across the Ni=C bond, as seen for metal–amido/thiolate bonds; these results were also supported by kinetic studies.

In a catalytic application, Hall used DFT calculations to suggest that Baker's Ni NHC catalysts[49] for ammonia-borane dehydrogenation operate via carbene ligand MLC (**Scheme 1.18**).[50]

1.4 Hydroboration

The hydroboration reaction can be defined as addition of a boron–hydrogen bond to different unsaturated organic groups. The first report of hydroboration was by H. C. Brown in 1956.[51] Brown's work on organoborane chemistry earned him the Nobel Prize in 1979. The incredible synthetic versatility of organoboranes has made the hydroboration reaction of great importance. in

fact, transformation of organoboranes into several other functionalities can be readily achieved in high yields (**Scheme 1.19**).[52]

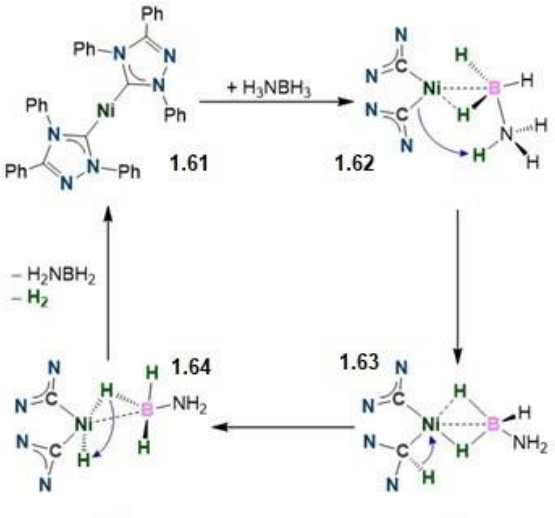

Scheme 1.18 Proposed reaction pathway for Ni-catalyzed ammonia-borane dehydrogenation.

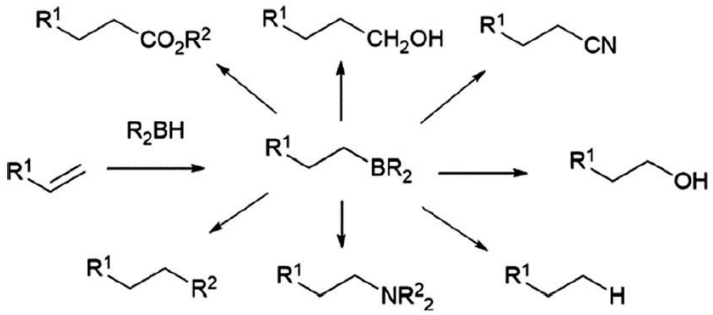

Scheme 1.19. Derivatization of organoboranes.

While the earliest efforts were concentrated on oxidation of organoboranes to the corresponding alcohols, the development of additional transformations (particularly C–C bond formation using the Suzuki–Miyaura cross-coupling reaction) has further enhanced the importance of organoboranes in organic synthesis.[52] The first report of transition metal-catalyzed hydroboration involved addition of 2-butyne to pentaborane, B_5H_9, employing the bimetallic alkyne-bridged dimer, dimethylacetylene dicobalthexacarbonyl. The importance of this catalyzed reaction was evident as the uncatalyzed reaction required higher temperatures that resulted in cage fragmentation and other undesired products (**Scheme 1.20**).[53] Moreover, flash thermolysis of the

alkenyl-boron product afforded a mixture of novel 6-vertex monocarboranes. Nonetheless, the yield and turnover number of this catalytic reaction (10 mol% cat loading at 75 ˚C) were low.

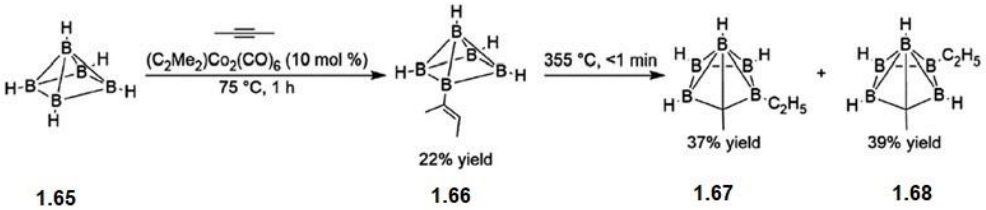

Scheme 1.20. Hydroboration of dimethylacetylene using a polyhedral borane.

Since then, many studies have been reported on catalytic hydroboration reactions, first using catecholborane and then other boron reagents having heteroatom-substituted (N, O, S) ancillary groups.[54-59] Amongst these boron reagents, pinacolborane (HBpin)[60] has become the most popular due to the enhanced water stability of its products and its potential for offering complementary regioselectivity to catecholborane. Overall, the continuous attention given to transition metal-catalyzed hydroboration over the last three decades originates from higher selectivity of the products obtained by this method vs uncatalyzed hydroboration.

In the following, we summarize the highlights of three hydroboration reactions of relevance to this thesis: carbonyl compounds, nitriles, and N–Heterocycles.

1.4.1 Carbonyl hydroboration

The catalytic hydroboration of carbonyl substrates using HBpin is an efficient methodology for the synthesis of borate esters that are widely utilized as intermediates to synthesize alcohols and other derivatives.[61-63] More recently, the design of sustainable homogeneous catalysts with inexpensive, earth-abundant, environmentally friendly, and cheaper metals has been a popular research topic.

In the beginning days of catalytic hydroboration, aldehyde substrates did not attract much interest as the uncatalyzed reaction at moderate temperatures generally sufficed. Recent reports, however, identified complexes that were able to selectively catalyze aldehyde hydroboration *vs.* ketones.[64,65] On the other hand, as uncatalyzed ketone hydroboration requires higher temperatures, ketones are more challenging substrates than aldehydes. Furthermore, the potential of ketones for asymmetric catalysis earned them much attraction.[66-70]

1.4.2 Nitrile dihydroboration

Reductive transformations are important synthetic tools for accessing nitrogen-containing essential chemicals.[71] Easy transformation to the corresponding primary amines has made N,N-diborylamines very important chemical building blocks, as direct nitrile hydrogenation usually needs harsh conditions including elevated pressure and temperatures, Lewis acid additives, and precious metal catalysts.[72,73] Another challenge of nitrile hydrogenation is the low selectivity, due to competing formation of primary, secondary and tertiary amines and imines.[74,75]

Nikonov and Khalimon et al. reported the first example of transition-metal-catalyzed nitrile dihydroboration in 2012.[76] They used a tetravalent molybdenum imido hydride complex, $MoHCl(NDipp)(PMe_3)_3$ (**1**; **Scheme 1.21A**; Dipp = 2,6-$^{i}Pr_2C_6H_3$), which was previously used as a hydrosilylation catalyst.[77] In the first step of the reaction, nitrile insertion is followed by HBCat addition across the Mo−N bond of the resulting metallo-imine intermediate (**Scheme 1.21B**). Later in 2015, a similar pathway through a NB−H···Mo transient intermediate was proposed for hydroboration of RCN (R=Me, Ph, ^{t}Bu) using the similar catalysts $MoH_2(NDipp)(PMe_3)_3$ (**2**) and $MoH_2(PMe_3)_3[\eta^3$-(Dipp)N-BHCat] (**3**; **Scheme 1.21A**).[78]

Besides the reduction, another interesting aspect of nitrile hydroboration is exploring the chemistry of borylamines (**Scheme 1.22**).[79-81] In 2012 Khalimon and Nikonov[71,73] synthesized *N*-benzylidenebenzylamine by treating $PhCH_2N(BCat)_2$ (Cat=catechol) with benzaldehyde. Although the same studies showed that this reaction requires more forcing conditions (18 h at 150 °C) when using Bpin, in 2020 Khalimon presented an advanced cobalt-based catalytic system that catalyzed the reaction under much milder condition (5 h at 50 °C).[82]

In 2019, N,N-diborylamines were used in N-arylation reactions with aryl bromides in the presence of a palladium catalyst.[83] In the same year, a study reported synthesis of secondary carboxamides through treatment of N,N-diborylamines with aromatic carboxylic acids.[84]

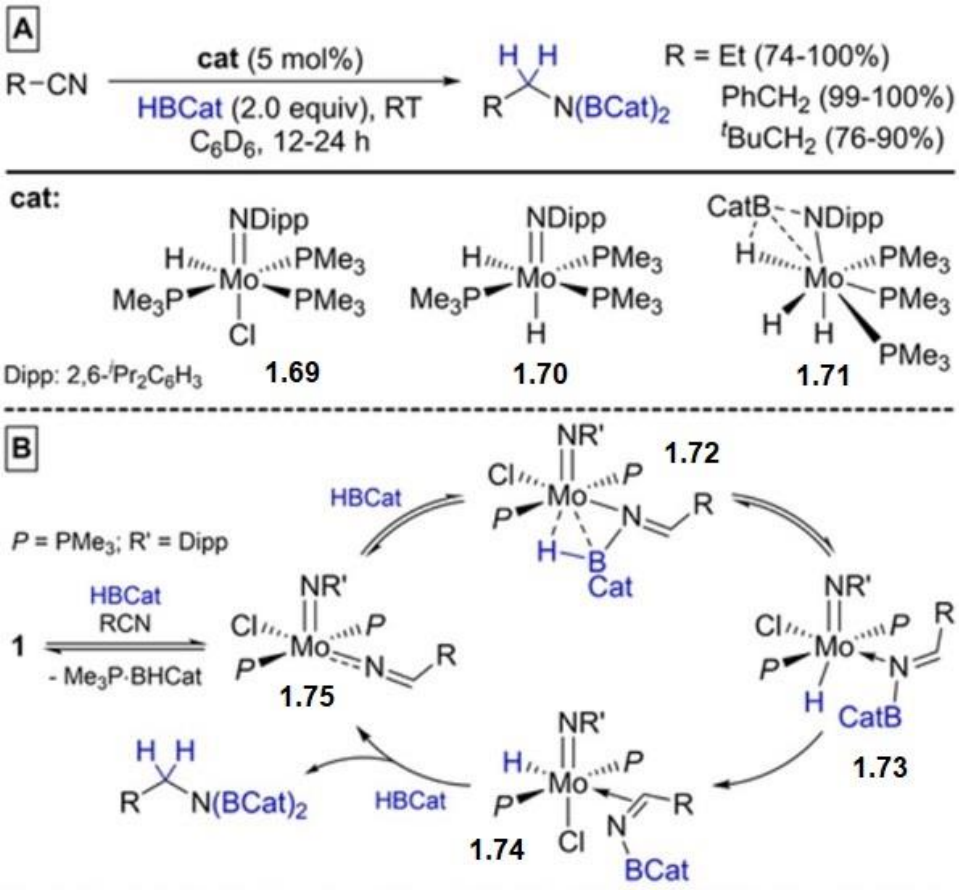

Scheme 1.21. (A) hydroboration of RCN (R=Me, Ph, *t*Bu) with HBCat catalyzed by molybdenum hydrides 1–3. (B) Proposed mechanism for 1-catalyzed hydroboration of nitriles.

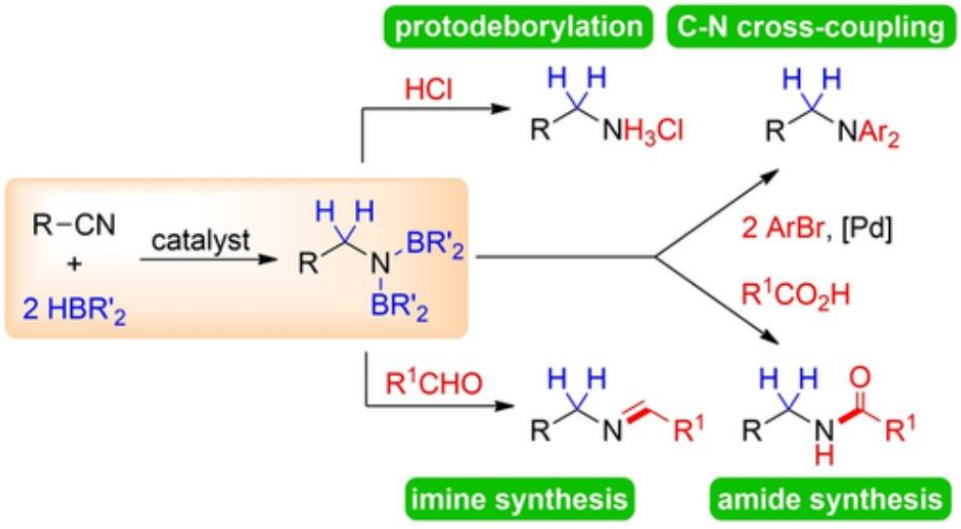

Scheme 1.22. Dihydroboration of nitriles and further transformations of N,N-diborylamines.

1.4.3 N–Heterocycle hydroboration

As a practical route to obtain useful structural motifs that have determinative roles in bioactive products and synthetic building units, dearomatization of heteroarenes has attracted significant attention.[85,86] Particularly, partially reduced 1,2- or 1,4-dihydro-N–Heteroarenes can efficiently serve as versatile precursors in synthesizing azacyclic molecules.[87-92] Additionally, they have been widely used as organic reducing agents.[93] Therefore, exploration of different methodologies to access dearomatized heterocycles using hydroboranes and hydrosilanes as convenient hydride sources, has been the focus of many studies.[94] In this context, a suitable catalytic system and reducing agent can result in better control of regioselectivity (**Scheme 1.23**).[95-101]

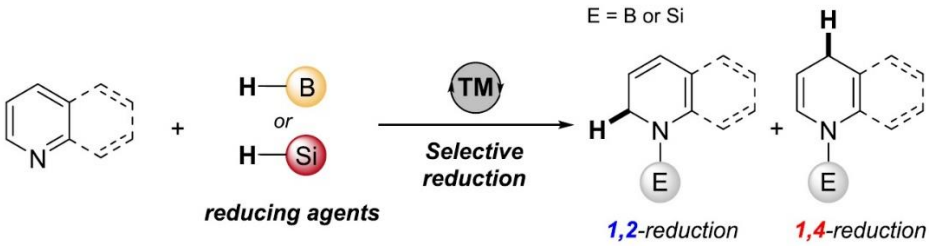

Scheme 1.23. Regioselective Reduction of N–Heteroarenes.

While pyridine selective reduction, using transition metal catalysts, has been widely studied,[199,102-104] there are only few reports on transition metal-catalyzed selective reduction of quinolines,[96,99,105,106] even though tetrahydroquinolines are a common synthetic motif in many pharmaceutical compounds and bioactive natural products (**Scheme 1.24**).[107,108]

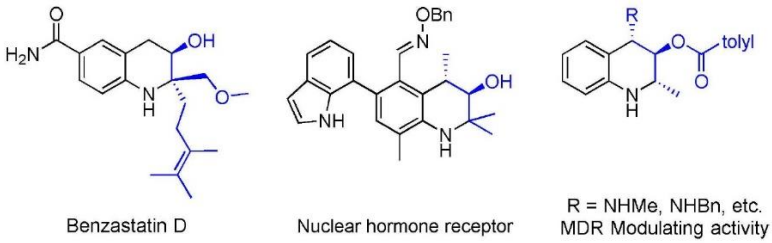

Scheme 1.24. Tetrahydroquinoline derivatives in pharmaceuticals.

Hydrogenation is not only the most straightforward but also the most atom-economic method to access tetrahydroquinolines.[109-111] However, the substrates reduced by this method have inferior functional group tolerance, resulting in limited molecular diversity in the reduced N–

Heterocyclic products for serving as synthetic intermediates. In this regard, N–Heteroaromatic reduction with hydroboranes can be an attractive alternative[112] as stoichiometric amounts of reductants can be precisely applied.

1.5 Scope of the Thesis

There are four additional chapters in this dissertation which expand upon the MLC reactivity of N-, O-, C-, P- and S-donor ligands in late transition metal complexes. All new complexes are characterized and their functions are investigated as bifunctional catalysts. Each complex that proved to be an active catalyst or precatalyst, is thoroughly investigated to gain insight into its mechanism. Chapter 2 details the synthesis of three new zinc complexes of the type Zn(κ^2-**SNS**)$_2$, in order to directly compare the bifunctional reactivity of amido and thiolate donors as hard and soft Lewis base donors, respectively. Also, using zinc as a redox-inactive metal lets us investigate bifunctional behavior of the ligands more clearly. Furthermore, this is the first example using just the amido (**L1**) and thiolate (**L2**) ligands in the same complex. These precatalysts undergo bifunctional activation, generating the same active catalyst in all three systems. The results of this study led us to reinvestigate the mechanism of the previously reported copper amido complex Cu(κ^2-**L1)(**IPr).[12] We show that the outer-sphere mechanism proposed for this catalytic system is not actually correct, as the complex converts to the IPr copper hydride dimer upon treatment with HBpin and release of **Bpin-L1**. This reinvestigation demonstrates that the mechanism is more likely an inner-sphere carbonyl insertion into Cu–H.

Following the same line of study, a new amido ligand (**L3 =** $O^{Me}N^{H}N^{pyrrolide}$) is used in a zinc complex (**2.8$_{Zn}$**) to compare aliphatic and aromatic amido donors. Although the aliphatic amine donor was not deprotonated, reaction of **2.8$_{Zn}$** with HBpin gives $L^3(Bpin)_2$ in which both ligand nitrogens are borylated. This observation generated a new plan in which bifunctional catalyst activation could access a reactive Zn dihydride catalyst bearing a small NHC ligand, 4,5-dichloro-1,3-dimethylimidazol-2-ylidene (DDI). Indeed, precatalyst Zn(κ^2-ONN)$_2$(DDI) (**2.11$_{Zn}$**) proves to exhibit unprecedented activity for hydroboration of nitriles and quinoline heterocycles.

Chapter 3 details the synthesis of a new bifunctional Co dithiolate complex, Co(κ^3-SNS)(DDI) that selectively catalyzes aldehyde hydroboration. The initial goal was to investigate the amido and thiolate ligands in the same cobalt complex to directly compare their functions. In fact, S-Me

activation of the thiolate ligand by the amido ligand afforded a dithiolate complex which serves as a selective aldehyde hydroboration catalyst through a hydride-free pathway.

In Chapter 4 comparison of Lewis base donors for bifunctional B–H bond activation is expanded to include O-, S-, P- and C- donors. First, using a dimeric zinc complex featuring a tetradentate amido-aryloxide donor ligand, $[Zn(\kappa^4\text{-NSNO})]_2$, we show the aryloxide to be the dominant B–H bond activator through MLC, while the catalyst deactivates when the amido participates. However, this complex catalyzes nitrile dihydroboration efficiently in the absence of added solvent. Next, for the most comprehensive comparison yet, we prepare and test a series of NiX(NNN) complexes both in stoichiometric B-H bond activation and as catalysts for nitrile dihydroboration (X = anionic N-, C-, O-, S- or P-donor). The results again point to the superiority of the phenoxide donor, presumably due to formation of the strong B-O bond.

Finally, Chapter 5 summarizes the findings of this thesis, placing them in the context of the current state of the art and speculating on what future investigations they will enable.

1.6 References

(1) Grützmacher, H. Cooperating ligands in catalysis. *Angew. Chem. Int. Ed.* **2008**, *47*, 1814-1818.

(2) Ohkuma, T.; Ooka, H.; Hashiguchi, S.; Ikariya, T.; Noyori, R. Practical Enantioselective Hydrogenation of Aromatic Ketones. *J. Am. Chem. Soc.* **1995**, *117*, 2675–2676.

(3) Sandoval, C. A.; Ohkuma, T.; Muñiz, K.; Noyori, R. Mechanism of Asymmetric Hydrogenation of Ketones Catalyzed by BINAP/1,2-Diamine–Ruthenium(II) Complexes. *J. Am. Chem. Soc.* **2003**, *125*, 13490–13503.

(4) Hamilton, R. J.; Bergens, S. H. An unexpected possible role of base in asymmetric catalytic hydrogenations of ketones. Synthesis and characterization of several key catalytic intermediates. *J. Am. Chem. Soc.* **2006**, *128*, 13700–13701.

(5) Hamilton, R. J.; Bergens, S. H. Direct Observations of the Metal–Ligand Bifunctional Addition Step in an Enantioselective Ketone Hydrogenation. *J. Am. Chem. Soc.* **2008**, *130*, 11979–11987.

(6) Morris, R. H. in *Handbook of Homogeneous Hydrogenation*; de Vries, J. G.; Elsevier, C. J., Eds.; Wiley-VCH: Weinheim, **2007**; Vol. 1, p 45.

(7) Kai Y. Wan, Molly M. H. Sung, Alan J. Lough, and Robert H. Morris. Half-Sandwich Ruthenium Catalyst Bearing an Enantiopure Primary Amine Tethered to an N–Heterocyclic Carbene for Ketone Hydrogenation. *ACS Catal.* **2017,** *7*, 6827-6842.

(8) Morris, R. H. Exploiting Metal–Ligand Bifunctional Reactions in the Design of Iron Asymmetric Hydrogenation Catalysts. *Acc. Chem. Res.* **2015**, *48*, 1494–1502.

(9) Clapham, S. E.; Hadzovic, A.; Morris, R. H. Mechanisms of the H_2–Hydrogenation and Transfer Hydrogenation of Polar Bonds Catalyzed by Ruthenium Hydride Complexes. *Coord. Chem. Rev.* **2004**, *248*, 2201–2237.

(10) Dub, P. A.; Henson, N. J.; Martin, R. L.; Gordon, J. C. Unravelling the Mechanism of the Asymmetric Hydrogenation of Acetophenone by [RuX_2(diphosphine)(1,2-diamine)] Catalysts. *J. Am. Chem. Soc.* **2014**, *136*, 3505–3521.

(11) Kubas, G. J. Fundamentals of H_2 binding and reactivity on transition metals underlying hydrogenase function and H_2 production and storage. *Chem. Rev.* **2007**, *107*, 4152–4205.

(12) Van der Vlugt, J. I. Cooperative Catalysis with First-Row Late Transition Metals. *Eur. J. Inorg. Chem.* **2012**, *2012*, 363–375.

(13) Khusnutdinova, J. R.; Milstein, D. Metal–Ligand Cooperation. *Angew.Chem. Int. Ed.* **2015**, *54*, 12236–12273.

(14) Fritz, M.; Schneider, S. in *The Periodic Table II: Catalytic, Materials, Biological and Medical Applications*, Ed. Mingos, D. M. P. Springer, **2019**, vol. 182.

(15) Harinath, A.; Bhattacharjee, J.; Gorantla, K. R.; Mallik, B. S.; Panda, T. K. Hydroboration, Cyanosilylation, and Sequential Cyanosilylation and Hydroboration of Carbonyl Compounds in the Presence of a Ti^{IV} Amido Complex as an Efficient Catalyst. *Eur. J. Org. Chem.* **2018**, 3180–3192.

(16) Bhattacharjee, J.; Harinath, A.; Bano, K.; Panda, T. K. Highly Chemoselective Hydroboration of Alkynes and Nitriles Catalyzed by Group 4 Metal Amidophosphine-Borane Complexes. *ACS Omega* **2020**, *5* (3), 1595–1606.

(17) Rauch, M.; Kar, S.; Kumar, A.; Avram, L.; Shimon, L. J. W.; Milstein, D. Metal-Ligand Cooperation Facilitates Bond Activation and Catalytic Hydrogenation with Zinc Pincer Complexes. *J. Am. Chem. Soc.* **2020**, *142*, 14513–14521.

(18) Elsby, M. R.; Son, M.; Oh, C.; Martin, J.; Baik, M.–H.; Baker, R. T. Mechanistic Study of Metal–Ligand Cooperativity in Mn(II)-Catalyzed Hydroborations: Hemilabile SNS Ligand Enables Metal Hydride-Free Reaction Pathway. *ACS Catal.* **2021**, *11*, 9043–9051.

(19) Elsby, M. R.; Baker, R. T. Strategies and mechanisms of metal–ligand cooperativity in first-row transition metal complex catalysts. *Chem. Soc. Rev.* **2020**, *49*, 8933–8987.

(20) Pauling, L. *The Nature of the Chemical Bond, Third Edition*, Cornell University Press, Ithaca, New York, **1960**.

(21) Pauling, L. *The Chemical Bond*, Cornell University Press, Ithaca, New York, **1967**.

(22) Forster, F.; Oestreich, M. Metal–ligand cooperative Si─H bond activation, in *Organosilicon Chemistry: Novel Approaches and Reactions*, Hiyama, T.; Oestreich, M., Eds., Wiley-VCH, Weinheim, **2020**, pp 115-130.

(23) Palacios, A. A.; Alemany, P.; Alvarez, S. Electronic Structure and Bonding in Tricoordinate Amido Complexes of Transition Metals, *Inorg. Chem.* **1999**, *38*, 707−715.

(24) Hatzis, G. P.; Thomas, C. M. Metal-ligand cooperativity across two sites of a square planar iron (II) complex ligated by a tetradentate PNNP ligand. *Chem. Commun.* **2020**, *56*, 8611-8614.

(25) Erken, C.; Kaithal, A.; Sen, S.; Weyhermüller, T.; Hölscher, M.; Werlé, C.; Leitner, W. Manganese-catalyzed hydroboration of carbon dioxide and other challenging carbonyl groups. *Nat. Commun.* **2018**, *9*, 1-9.

(26) Pang, M.; Wu, C.; Zhuang, X.; Zhang, F.; Su, M.; Tong, Q.; Tung, C.–H.; Wang, W. Addition of a B–H bond across an amido–cobalt bond: Co^{II}–H-catalyzed hydroboration of olefins. *Organometallics* **2018**, *37*, 1462-1467.

(27) Ghosh, C.; Kim, S.; Mena, M. R.; Kim, J.–H.; Pal, R.; Rock, C. L.; Groy, T. L.; Baik, M.–H.; Trovitch, R. J. Efficient cobalt catalyst for ambient-temperature nitrile dihydroboration, the elucidation of a chelate-assisted borylation mechanism, and a new synthetic route to amides. *J. Am. Chem. Soc.* **2019**, *141*, 15327-15337.

(28) Ben-Daat, H.; Rock, C. L.; Flores, M.; Groy, T. L.; Bowman, A. C.; Trovitch, R. J. Hydroboration of alkynes and nitriles using an α-diimine cobalt hydride catalyst. *Chem. Commun.* **2017**, *53*, 7333-7336.

(29) Gordon, J. C.; Kubas, G. J. Perspectives on How Nature Employs the Principles of Organometallic Chemistry in Dihydrogen Activation in Hydrogenases. *Organometallics* **2010**, *29*, 4682–4701.

(30) Evans, D. J.; Pickett, C. J. Chemistry and the hydrogenases. *Chem. Soc. Rev.* **2003**, *32*, 268−275.

(31) Sellmann, D.; Sutter, J. In Quest of Competitive Catalysts for Nitrogenases and Other Metal Sulfur Enzymes. *Acc. Chem. Res.* **1997**, *30*, 460.

(32) Gennari, M.; Duboc, C. Bio-Inspired, Multifunctional Metal-Thiolate Motif: From Electron Transfer to Sulfur Reactivity and Small-Molecule Activation. *Acc. Chem. Res.* **2020**, *53*, 2753–2761.

(33) Dilworth, J. R. Thiolates — Intriguing and Versatile Ligands for Transition Metals. *Studies Inorg. Chem.* **1984**, *5*, 141-165.

(34) Saha, K.; Kaur, U.; Raghavendra, B.; Ghosh**,** S. Role of Metals and Thiolate Ligands in the Structures and Electronic Properties of Group 5 Bimetallic–Thiolate Complexes. *Inorg. Chem.* **2020**, *59*, 12494–12503.

(35) Sweeney, Z. K.; Polse, J. L.; Bergman, R. G.; Andersen, R. A. Dihydrogen activation by titanium sulfide complexes. *Organometallics* **1999**, *18*, 5502-5510.

(36) Olechnowicz, F.; Hillhouse, G. L.; Cundari, T. R.; Jordan, R. F. Heterolytic H–H and H–B bond cleavage reactions of $\{(IPr)Ni(\mu\text{-}S)\}_2$. *Inorg. Chem.* **2017**, *56*, 9922-9930.

(37) Song, H.; Ye, K.; Geng, P.; Han, X.; Liao, R.; Tung, C.–H.; Wang, W. Activation of epoxides by a cooperative iron–thiolate catalyst: Intermediacy of ferrous alkoxides in catalytic hydroboration. *ACS Catal.* **2017**, *7*, 7709-7717.

(38) Zhang, F.; Song, H.; Zhuang, X.; Tung, C.–H.; Wang, W. Iron-catalyzed 1,2-selective hydroboration of N–Heteroarenes. *J. Am. Chem. Soc.* **2017**, *139*, 17775-17778.

(39) Elsby, M. R.; Oh, C.; Son, M.; Kim, S. Y. H.; Baik, M.–H.; Baker, R. T. Spin-state Crossover in Photo-catalyzed Nitrile Dihydroboration via Mn-thiolate Cooperation. *Chem. Sci.* **2022**, 13, 12550-12559.

(40) Ahmed, M. E.; Dey, S.; Darensbourg, M. Y.; Dey, A. Oxygen-Tolerant H_2 Production by [FeFe]–H_2ase Active Site Mimics Aided by Second Sphere Proton Shuttle. *J. Am. Chem. Soc.* **2018**, *140* (39), 12457–12468.

(41) Simmons, T. R.; Berggren, G.; Bacchi, M.; Fontecave, M.; Artero, V. Mimicking hydrogenases: From biomimetics to artificial enzymes. *Coord. Chem. Rev.* **2014**, *270–271*, 127–150.

(42) Darensbourg, M. Y.; Weigand, W. Sulfoxygenation of Active Site Models of [NiFe] and [FeFe] Hydrogenases – A Commentary on Possible Chemical Models of Hydrogenase Enzyme Oxygen Sensitivity. *Eur. J. Inorg. Chem.* **2011**, *2011*, 994–1004.

(43) Buitrago, E.; Tinnis, F.; Adolfsson, H. Efficient and selective hydrosilylation of carbonyl compounds catalyzed by iron acetate and N-hydroxyethylimidazolium salts. *Adv. Synth. Catal.* **2012**, *354*, 217-222.

(44) Chu, W.-Y.; Zhou, X.; Rauchfuss, T. B. Cooperative metal–ligand reactivity and catalysis in low-spin ferrous alkoxides. *Organometallics* **2015**, *34*, 1619-1626.

(45) Liu, J.; Chen, J.-Y.; Jia, M.; Ming, B.; Jia, J.; Liao, R.-Z.; Tung, C.–H.; Wang, W. Ni–O Cooperation versus nickel(II) hydride in catalytic hydroboration of N–Heteroarenes. *ACS Catal.* **2019**, *9*, 3849-3857.

(46) Feichtner, K.-S.; Gessner, V. H. Cooperative bond activation reactions with carbene complexes. *Chem. Commun.* **2018**, *54*, 6540-6553.

(47) Gutsulyak, D. V.; Piers, W. E.; Borau-Garcia, J.; Parvez, M. Activation of water, ammonia, and other small molecules by $PC_{carbene}P$ nickel pincer complexes. *J. Am. Chem. Soc.* **2013**, *135*, 11776-11779.

(48) LaPierre, E. A.; Piers, W. E.; Spasyuk, D. M.; Bi, D. W. Activation of Si–H bonds across the nickel carbene bond in electron rich nickel $PC_{carbene}P$ pincer complexes. *Chem. Commun.* **2016**, *52*, 1361-1364.

(49) Keaton, R. J.; Blacquiere, J. M.; Baker, R. T. Base metal catalyzed dehydrogenation of ammonia-borane for chemical hydrogen storage. *J. Am. Chem. Soc.* **2007**, *129*, 1844–1845.

(50) Yang, X.; Hall, M. B. The Catalytic Dehydrogenation of Ammonia-Borane Involving an Unexpected Hydrogen Transfer to Ligated Carbene and Subsequent Carbon–Hydrogen Activation. *J. Am. Chem. Soc.* **2008**, *130*, 1798–1799.

(51) Brown, H. C. *Hydroboration*, W. A. Benjamin: New York, **1962**.

(52) Geier, S. J.; Vogels, C. M., Melanson, J. A.; Westcott, S. A. The transition metal-catalysed hydroboration reaction. *Chem. Soc. Rev.*, **2022**, https://doi.org/10.1039/D2CS00344A.

(53) Wilczynski, R.; Sneddon, L. G. Transition metal catalyzed reactions of alkynes and boron hydrides: synthesis of 2-(cis-2-butenyl)pentaborane(9) and its conversion into monocarbon carboranes. *J. Am. Chem. Soc.*, **1980**, *102*, 2857–2858.

(54) Lang, A.; Nöth, H.; Thomann-Albach, M. Contributions of the Chemistry of Boron, 236. In Quest of New and Stable Bis(organyloxy)boranes $(RO)_2BH$ for Catalytic Hydroboration. *Chem. Ber./Recueil*. **1997**, *130*, 363−369.

(55) Fritschi, C. B.; Wernitz, S. M.; Vogels, C. M.; Shaver, M. P.; Decken, A.; Bell, A.; Westcott, S. A. 4,4,5,5-Tetraphenyl-1,3,2-dioxaborolane: A Bulky Borane for the Transition Metal Catalysed Hydroboration of Alkenes. *Eur. J. Inorg. Chem.* **2008**, *5*, 779-785.

(56) Hadebe, S. W.; Robinson, R. S. Rhodium-catalyzed hydroboration reactions with sulfur and nitrogen analogues of catecholborane. *Eur. J. Org. Chem.* **2006**, *21*, 4898-4904.

(57) Motry, D. H.; Brazil, A. G.; Smith, M. R. Significance of Borane Tuning in Titanium-Catalyzed Borylation Chemistry. *J. Am. Chem. Soc.* **1997**, *119*, 2743–2744.

(58) Yoshida, H.; Kimura, M.; Tanaka, H.; Murashige, Y.; Kageyuki, I.; Osaka, I. An anthranilamide-substituted borane [H–B(aam)]: its stability and application to iridium-catalyzed stereoselective hydroboration of alkynes. *Chem. Commun.* **2019**, *55*, 5420–5422.

(59) Iwadate, N.; Suginome, M. Synthesis of B-Protected beta-Styrylboronic Acids via Iridium-Catalyzed Hydroboration of Alkynes with 1,8-Naphthalenediaminatoborane Leading to Iterative Synthesis of Oligo(phenylenevinylene)s. *Org. Lett.* **2009**, *11*, 1899–1902.

(60) Tucker, C. E.; Davidson, J.; Knochel, P. Mild and stereoselective hydroborations of functionalized alkynes and alkenes using pinacolborane. *J. Org. Chem.* **1992**, *57*, 3482–3485.

(61) Shegavi, M. L.; Bose, S. K. Recent advances in the catalytic hydroboration of carbonyl compounds. *Catal. Sci. Technol.* **2019**, *9*, 3307–3336.

(62) Chong, C. C.; Kinjo, R. Catalytic Hydroboration of Carbonyl Derivatives, Imines, and Carbon Dioxide. *ACS Catal.* **2015**, *5*, 3238–3259.

(63) Tamang, S. R.; Findlater, M. Emergence and Applications of Base Metals (Fe, Co, and Ni) in Hydroboration and Hydrosilylation. *Molecules* **2019**, *24*, 3194.

(64) Kaithal, A.; Chatterjee, B.; Gunanathan, C. Ruthenium Catalyzed Selective Hydroboration of Carbonyl Compounds. *Org. Lett.* **2015**, *17*, 4790–4793.

(65) Das, U. K.; Higman, C. S.; Gabidullin, B.; Hein, J. E.; Baker, R. T. Efficient and Selective Iron-Complex-Catalyzed Hydroboration of Aldehydes. *ACS Catal.* **2018**, *8*, 1076–1081.

(66) Liu, W.; Guo, J.; Xing, S.; Lu, Z. Highly Enantioselective Cobalt-Catalyzed Hydroboration of Diaryl Ketones. *Org. Lett.* **2020**, *22*, 2532–2536.

(67) Lebedev, Y.; Polishchuk, I.; Maity, B.; Dinis Veloso Guerreiro, M.; Cavallo, L.; Rueping, M. Asymmetric Hydroboration of Heteroaryl Ketones by Aluminum Catalysis. *J. Am. Chem. Soc.* **2019**, *141*, 19415–19423.

(68) Guo, J.; Chen, J.; Lu, Z. Cobalt-catalyzed asymmetric hydroboration of aryl ketones with pinacolborane. *Chem. Commun.* **2015**, *51*, 5725–5727.

(69) Wang, R.; Park, S. Recent Advances in Metal-Catalyzed Asymmetric Hydroboration of Ketones. *ChemCatChem.* **2021**, *13*, 1898–1919.

(70) Heitkämper, J.; Herrmann, J.; Titze, M.; Bauch, S. M.; Peters, R.; Kästner, J. Asymmetric Hydroboration of Ketones by Cooperative Lewis Acid− Onium Salt Catalysis: A Quantum Chemical and Microkinetic Study to Combine Theory and Experiment. *ACS Catal.* **2022**, *12*, 1497−1507.

(71) Hayes, K. S. Industrial Processes for Manufacturing Amines. *Appl. Catal., A* **2001**, *221*, 187–195.

(72) Bagal, D. B.; Bhanage, B. M. Recent Advances in Transition Metal-Catalyzed Hydrogenation of Nitriles. *Adv. Synth. Catal.* **2015**, *357*, 883–900.

(73) Werkmeister, S.; Junge, K.; Beller, M. Catalytic Hydrogenation of Carboxylic Acid Esters, Amides, and Nitriles with Homogeneous Catalysts. *Org. Process Res. Dev.* **2014**, *18*, 289–302.

(74) Gomez, S.; Peters, J. A.; Maschmeyer, T. The reductive amination of aldehydes and ketones and the hydrogenation of nitriles: mechanistic aspects and selectivity control. *Adv. Synth. Catal.* **2002**, *344*, 1037–1057.

(75) de Bellefon, C.; Fouilloux, P.; Homogeneous and Heterogeneous Hydrogenation of Nitriles in a Liquid Phase: Chemical, Mechanistic, and Catalytic Aspects. *Catal. Rev.* **1994**, *36*, 459–506.

(76) Khalimon, A. Y.; Farha, P.; Kuzmina, L. G.; Nikonov, G. I. Catalytic Hydroboration by an Imido–Hydrido Complex of Mo(IV). *Chem. Commun.* **2012**, *48*, 455–457.

(77) Peterson, E.; Khalimon, A. Y.; Simionescu, R.; Kuzmina, L. G.; Howard, J. A. K.; Nikonov, G. I. Diversity of Catalysis by an Imido–Hydrido Complex of Molybdenum.

Mechanism of Carbonyl Hydrosilylation and Silane Alcoholysis. *J. Am. Chem. Soc.* **2009**, *131*, 908–909.

(78) Khalimon, A. Y.; Farha, P.; Nikonov, G. I. Imido–hydrido complexes of Mo(IV): Catalysis and mechanistic aspects of hydroboration reactions. *Dalton Trans* **2015**, *44*, 18945–18956.

(79) Hayrapetyan, D.; Khalimon, A. Y. Catalytic Nitrile Hydroboration: A Route to N,N-Diborylamines and Uses Thereof. *Chem. - Asian J.* **2020**, *15*, 2575–2587.

(80) Itazaki, M.; Nakazawa, H. Selective Double Addition Reaction of an E–H Bond (E = Si, B) to a C≡N Triple Bond of Organonitriles. *Molecules*, **2018**, *23*, 2769.

(81) Liu, H.; Eisen, M. S. Organo-*f*-Complexes for Efficient and Selective Hydroborations. *Synthesis*, **2020**, *52*, 629–644.

(82) Gudun, K. A.; Slamova, A.; Hayrapetyan, D.; Khalimon, A. Y. Efficient Co-Catalyzed Double Hydroboration of Nitriles: Application to One-Pot Conversion of Nitriles to Aldimines. *Chem. - Eur. J.* **2020**, *26*, 4963–4968.

(83) Kitano, T.; Komuro, T.; Tobita, H. Double and Single Hydroboration of Nitriles Catalyzed by a Ruthenium–Bis(silyl)xanthene Complex: Application to One-Pot Synthesis of Diarylamines and *N*-Arylimines. *Organometallics* **2019**, *38*, 1417–1420.

(84) Ghosh, C.; Kim, S.; Mena, M. R.; Kim, J.–H.; Pal, R.; Rock, C. L.; Groy, T. L.; Baik, M.–H.; Trovitch, R. J. Efficient Cobalt Catalyst for Ambient-Temperature Nitrile Dihydroboration, the Elucidation of a Chelate-Assisted Borylation Mechanism, and a New Synthetic Route to Amides. *J. Am. Chem. Soc.* **2019**, *141*, 15327–15337.

(85) Roche, S. P.; Porco, J. A. Dearomatization Strategies in the Synthesis of Complex Natural Products. *Angew. Chem., Int. Ed.* **2011**, *50*, 4068−4093.

(86) Oshima, K.; Ohmura, T.; Suginome, M. Palladium-Catalyzed Regioselective Silaboration of Pyridines Leading to the Synthesis of Silylated Dihydropyridines. *J. Am. Chem. Soc.* **2011**, *133*, 7324−7327.

(87) Muthukrishnan, I.; Sridharan, V.; Menéndez, J. C. Progress in the Chemistry of Tetrahydroquinolines. *Chem. Rev*. **2019**, *119*, 5057−5191.

(88) Shao, M.; Wu, Y.; Feng, Z.; Gu, X.; Wang, S. Synthesis of Polysubstituted 1,2-Dihydroquinolines and Indoles via Cascade Reactions of Arylamines and Propargylic Alcohols Catalyzed by $FeCl_3 \cdot 6H_2O$. *Org. Biomol. Chem*. **2016**, *14*, 2515−2521.

(89) Mizoguchi, H.; Oikawa, H.; Oguri, H. Biogenetically Inspired Synthesis and Skeletal Diversification of Indole Alkaloids. *Nat. Chem*. **2014**, *6*, 57−64.

(90) Mistry, S. N.; Valant, C.; Sexton, P. M.; Capuano, B.; Christopoulos, A.; Scammells, P. J. Synthesis and Pharmacological Profiling of Analogues of Benzyl Quinolone Carboxylic Acid (BQCA) as Allosteric Modulators of the M1Muscarinic Receptor. *J. Med. Chem*. **2013**, *56*, 5151−5172.

(91) Liu, X.-Y.; Ding, P.; Huang, J.-S.; Che, C.-M. Synthesis of Substituted 1,2-Dihydroquinolines and Quinolines from Aromatic Amines and Alkynes by Gold(I)-Catalyzed Tandem Hydroamination–Hydroarylation under Microwave-Assisted Conditions. *Org. Lett*. **2007**, *9*, 2645−2648.

(92) Stout, D. M.; Meyers, A. I. Recent Advances in the Chemistry of Dihydropyridines. *Chem. Rev.* **1982**, *82*, 223−243.

(93) Murakami, Y.; Kikuchi, J-.i.; Hisaeda, Y.; Hayashida, O. Artificial Enzymes. *Chem. Rev*. **1996**, *96*, 721−758.

(94) For a comprehensive review for the catalytic dearomatization of N–heteroarenes: Park, S.; Chang, S. Catalytic Dearomatization of N-Heteroarenes with Silicon and Boron Compounds. *Angew. Chem., Int. Ed*. **2017**, *56*, 7720−7738.

(95) Oshima, K.; Ohmura, T.; Suginome, M. Regioselective Synthesis of 1,2-Dihydropyridines by Rhodium-Catalyzed Hydroboration of Pyridines. *J. Am. Chem. Soc*. **2012**, *134*, 3699−3702.

(96) Dudnik, A. S.; Weidner, V. L.; Motta, A.; Delferro, M.; Marks, T. J. Atom-Efficient Regioselective 1,2-Dearomatization of Functionalized Pyridines by an Earth-Abundant Organolanthanide Catalyst. *Nat. Chem*. **2014**, *6*, 1100−1107.

(97) Zhang, F.; Song, H.; Zhuang, X.; Tung, C.- H.; Wang, W. Iron-Catalyzed 1,2-Selective Hydroboration of N–Heteroarenes. *J. Am. Chem. Soc*. **2017**, *139*, 17775−17778.

(98) Lortie, J. L.; Dudding, T.; Gabidullin, B. M.; Nikonov, G. I. Zinc-Catalyzed Hydrosilylation and Hydroboration of N–Heterocycles. *ACS Catal*. **2017**, *7*, 8454−8459.

(99) Liu, H.; Khononov, M.; Eisen, M. S. Catalytic 1,2-Regioselective Dearomatization of N-heteroaromatics via Hydroboration. *ACS Catal*. **2018**, *8*, 3673−3677.

(100) Kaithal, A.; Chatterjee, B.; Gunanathan, C. Ruthenium-Catalyzed Regioselective 1,4–Hydroboration of Pyridines. *Org. Lett*. **2016**, *18*, 3402−3405.

(101) Ji, P.; Feng, X.; Veroneau, S. S.; Song, Y.; Lin, W. Trivalent Zirconium and Hafnium Metal−Organic Frameworks for Catalytic 1,4-Dearomative Additions of Pyridines and Quinolines. *J. Am. Chem. Soc*. **2017**, *139*, 15600−15603.

(102) Intemann, J.; Lutz, M.; Harder, S. Multinuclear Magnesium Hydride Clusters: Selective Reduction and Catalytic Hydroboration of Pyridines. *Organometallics* **2014**, *33*, 5722–5729.

(103) Rao, B.; Chong, C. C.; Kinjo, R. Metal-Free Regio- and Chemoselective Hydroboration of Pyridines Catalyzed by 1,3,2-Diazaphosphenium Triflate. *J. Am. Chem. Soc.* **2018**, *140*, 652–656.

(104) Hynes, T.; Welsh, E. N.; McDonald, R.; Ferguson, M. J.; Speed, A. W. H. Pyridine Hydroboration with a Diazaphospholene Precatalyst. *Organometallics* **2018**, *37*, 841–844.

(105) Jeong, J.; Park, S.; Chang, S. Iridium-Catalyzed Selective 1,2–Hydrosilylation of N–Heterocycles. *Chem. Sci*. **2016**, *7*, 5362−5370.

(106) Konigs, C. D. F.; Klare, H. F. T.; Oestreich, M. Catalytic 1,4-Selective Hydrosilylation of Pyridines and Benzannulated Congeners. *Angew. Chem., Int. Ed*. **2013**, *52*, 10076−10079.

(107) Sridharan, V.; Suryavanshi, P. A.; Menéndez, J. C. Advances in the Chemistry of Tetrahydroquinolines. *Chem. Rev.* **2011**, *111*, 7157–7259.

(108) Scott, J. D.; Williams, R. M. Chemistry and Biology of the Tetrahydroisoquinoline Antitumor Antibiotics. *Chem. Rev.* **2002**, *102*, 1669–1730.

(109) Wang, D.-S.; Chen, Q.-A.; Lu, S.-M.; Zhou, Y.-G. Asymmetric Hydrogenation of Heteroarenes and Arenes. *Chem. Rev.* **2012**, *112*, 2557–2590.

(110) Glorius, F. Asymmetric hydrogenation of aromatic compounds. *Org. Biomol. Chem.* **2005**, 3, 4171–4175.

(111) Eisenberger, P.; Bestvater, B. P.; Keske, E. C.; Crudden, C. M. Hydrogenations at Room Temperature and Atmospheric Pressure with Mesoionic Carbene-Stabilized Borenium Catalysts. *Angew. Chem. Int. Ed.* **2015**, *54*, 2467‑2471.

(112) Troegel, D.; Stohrer, J. Recent advances and actual challenges in late transition metal catalyzed hydrosilylation of olefins from an industrial point of view. *Coord. Chem. Rev.* **2011**, *255*, 1440–1459.

CHAPTER 2

LIGAND-ASSISTED CATALYST ACTIVATION IN Zn-CATALYZED HYDROBORATION REACTIONS

2.1 Introduction

Over the last two decades metal–ligand cooperativity (MLC) has allowed first row metals to emerge as uniquely active and selective catalysts,[1-3] complementing their more well-studied 2nd- and 3rd-row congeners.[4-6] As ligands that include an additional Lewis base function upon metal coordination are most widely employed for MLC, the Baker group has been comparing first row metal bifunctional catalysts containing biomimetic SNS ligands which contain a hard N donor (amido)[7,8] vs. a soft S donor (thiolate)[9,10] in hydroboration and hydrosilylation catalysis.[11,12] Building on previous mechanistic investigations,[12-14] they recently identified a new metal hydride-free bifunctional mechanism in which the carbonyl substrate is activated by coordination to the metal and the B–H bond by coordination to the ligand N donor.[13] In a more recent study on nitrile hydroboration, they showed that a spin state change of the monovalent Mn center also plays a role in enabling a low-energy catalytic reaction pathway.[14] As MLC using main group metals has been less extensively investigated,[15] we now extend these studies to zinc-based carbonyl hydroboration catalysis. Previous examples of zinc complex-catalyzed carbonyl hydroboration function via Lewis acid substrate activation or metal hydride generation and subsequent substrate insertion.[16,17] In an attempt to extend these mechanisms to include MLC with a 'redox-innocent' metal, we prepared and assessed both bis(amido) and bis(thiolate) Zn complexes, **2.1**$_{\mathbf{Zn}}$ and **2.2**$_{\mathbf{Zn}}$ respectively. Detailed investigations of the catalyst speciation revealed a heretofore underappreciated role for MLC in precatalyst activation. Determination of the reaction pathway for **2.1**$_{\mathbf{Zn}}$ prompted us to revisit the previously proposed carbonyl hydroboration pathway for Cu(**L1**)(IPr) (**2.6**$_{\mathbf{Cu}}$),[12] and more closely investigate its catalyst speciation. In addition, we sought to compare the reactivity of the copper complex with its silver analogue.

To further exploit ligand-assisted catalyst activation, we prepared a different zinc bis(amido) complex supported by a small NHC, Zn(κ^2-ONN)$_2$(DDI) (**2.11**$_{\mathbf{Zn}}$; DDI = 4,5-dichloro-1,3-dimethylimidazol-2-ylidene). As zinc dihydrides have been shown to be active hydroboration catalysts,[18] this complex was purposefully treated with HBpin to generate a very active zinc

dihydride catalyst *in-situ*. Indeed, both nitriles and quinolines are easily reduced under ambient conditions using 0.01 and 0.05 mol%, respectively of **2.11$_{Zn}$.** We also used Variable Time Normalization Analysis (VTNA) to study the kinetics of the catalytic reactions. This technique grew out of Blackmond's Reaction Progress Kinetic Analysis (RPKA) in which analysis of the reaction time course mitigated the need for excess of one reagent commonly used in pseudo-first order kinetic techniques.[19] RPKA can also provide insight regarding induction periods, catalyst deactivation, or changes in mechanism. VTNA employs a graphical interrogation of kinetic data, which takes advantage of the human visual capacity to easily, quickly, and accurately identify tendencies and patterns.[20] For the present catalytic system, VTNA revealed a first order dependence on quinoline, HBpin and **2.11$_{Zn}$** and no evidence of catalyst deactivation.

2.2 Results and Discussion for Zinc SNS Amido and Thiolate Complex Precatalysts

2.2.1 Synthesis of Complexes 2.1$_{Zn}$ and 2.2$_{Zn}$

Zn bis(amido) **(2.1$_{Zn}$)** and bis(thiolate) **(2.2$_{Zn}$)** SNS complexes were obtained from reaction of $ZnCl_2$ with 2 equiv. of the SNS proligand and LiHMDS base (HMDS = hexamethyldisilazide); (**Scheme 2.1**). Both complexes include a distorted tetrahedral Zn centre (t'_4 = 0.70, 0.78)[21] and κ^2-SNS ligands with uncoordinated thioethers. A comparison of the Zn–S and Zn–N bond distances shows ca. 8% decrease for the anionic thiolate or amido vs. neutral thioether or imine donor. The imine C–H bonds in **2.2$_{Zn}$** appear at δ 9.06 in the ^{1}H NMR spectrum and the benzylic C–Hs in **2.2$_{Zn}$** at δ 6.34 ppm. The $^{13}C\{^1H\}$ NMR spectra for the two complexes are unremarkable.

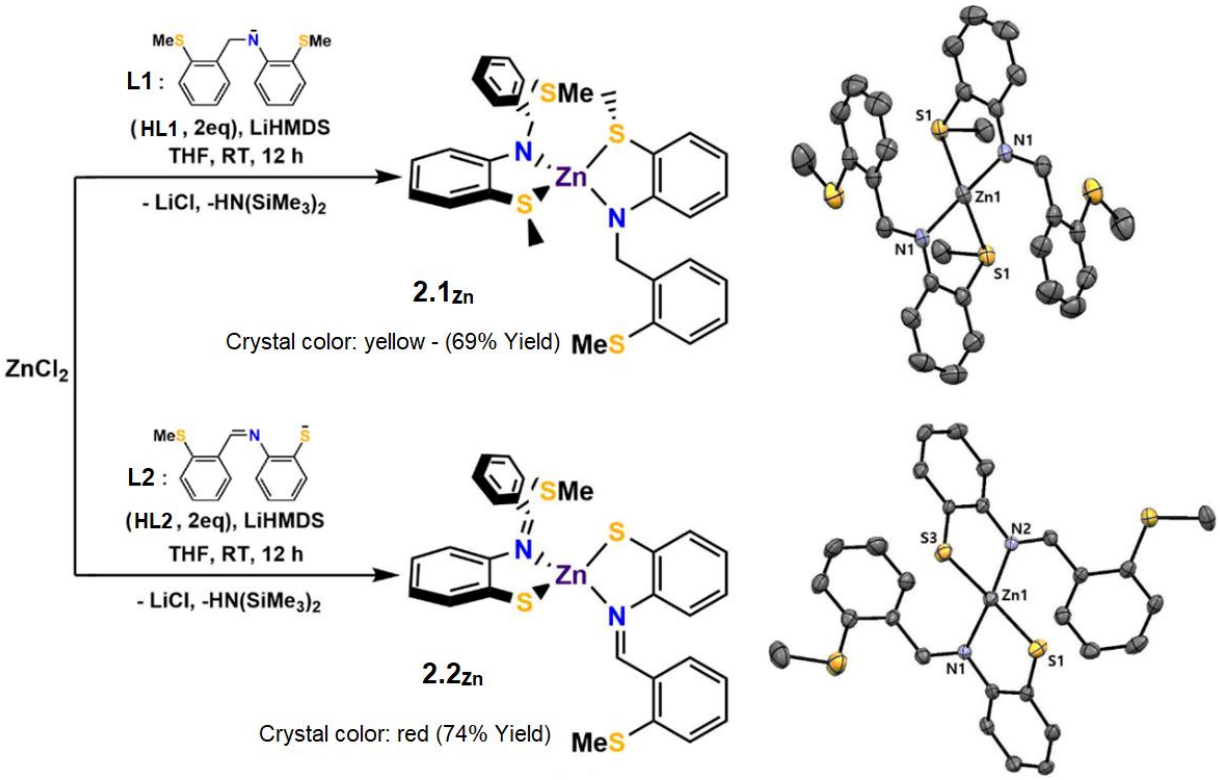

Scheme 2.1. Synthesis and molecular structures of **2.1$_{Zn}$** and **2.2$_{Zn}$** with 50% probability thermal ellipsoids and hydrogen atoms omitted for clarity. Selected bond distances (Å) and angles (deg) for **2.1$_{Zn}$**: Zn-S1 2.466(1), Zn-N1 1.925(2), S1-Zn-N1 85.22, S1-Zn-S1' 107.62, S1-Zn-N1' 123.17, N1-Zn-N1' 133.75. For **2.2$_{Zn}$**: Zn-S1 2.273(1), Zn-S3 2.246(1), Zn-N1 2.085(2), Zn-N2 2.109(2), S1-Zn-N1 88.03(7), S1-Zn-N2 124.87(7), S1-Zn-S3 124.48(4), S3-Zn-N2 88.98(7), S3-Zn-N1 119.37(7), N1-Zn-N2 114.05(9).

2.2.2 Catalytic Reactivity of 2.1$_{Zn}$ and 2.2$_{Zn}$

Both complexes successfully catalyzed hydroboration of aldehydes in 2–5 min and ketones in 10–25 min, giving quantitative yields using pinacolborane (HBpin) with 1 mol% catalyst loading at room temperature (**Table 2.1**). The carbonyl moiety was reduced selectively (vs. alkene) in both cinnamaldehyde and 5-Hexene-2-one and overall, **2.1$_{Zn}$** was the more active pre-catalyst. The color of the reaction solutions both changed (from pale-yellow for **2.1$_{Zn}$** and red for **2.2$_{Zn}$** to colorless during catalysis, indicative of structural changes.

Table 2.1. Hydroboration of carbonyls catalyzed by **2.1$_{Zn}$** and **2.2$_{Zn}$**.

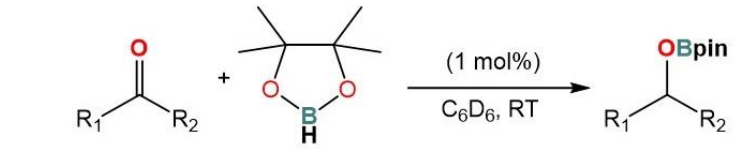

Substrate	Product	Time (min) 2.1_{Zn} /2.2_{Zn}	Yield (%)[b][c] 2.1_{Zn} /2.2_{Zn}
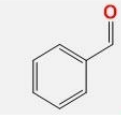	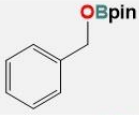	3 / 5	>98 / >98
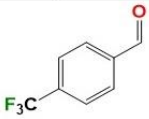	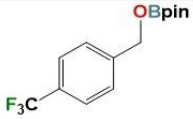	2 / 5	>98 / >98
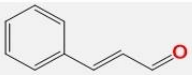	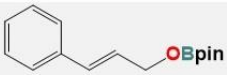	5 / 9	>98 / >98
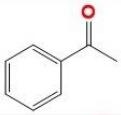	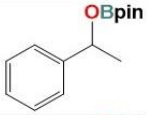	10 / 21	>98 / >98
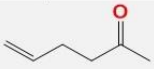	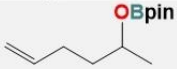	11 / 20	>98 / >98
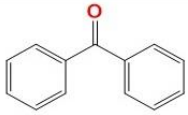	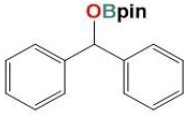	12 / 25	>98 / >98
	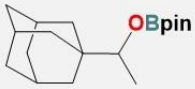	10 / 23	>98 / >98

Reaction conditions: Substrate (1.0 mmol), HBpin (1.0 mmol), **2.1_{Zn}** (6.1 mg, 1 mol%), or **2.2_{Zn}** (5.8 mg, 1 mol%), room temperature, in 1 mL of C_6D_6. [b]Yields were determined by ^{1}H NMR analysis based on substrates. [c]Selectivity in all cases was 100% for the reported products.

2.2.3 Mechanistic Studies of Carbonyl Hydroboration Using 2.1_{Zn} and 2.2_{Zn}

To gain more insight into the catalytic mechanism, stoichiometric reactions of the two Zn complexes with HBpin were performed. Reaction of **2.1_{Zn}** with 2 equiv. of HBpin afforded 2 equiv. of **Bpin-L1**, via bifunctional activation of the B–H bond. The resulting ZnH_2 product was unstable, giving H_2 and Zn metal precipitate. **Bpin-L1** (**Figure 2.1**) was also observed in the catalytic reaction, suggesting bifunctional formation of Zn–H which rapidly inserts the substrate, affording ZnH(alkoxide) and/or Zn(alkoxide)$_2$ which constitute(s) the active catalyst (**Scheme 2.2**).

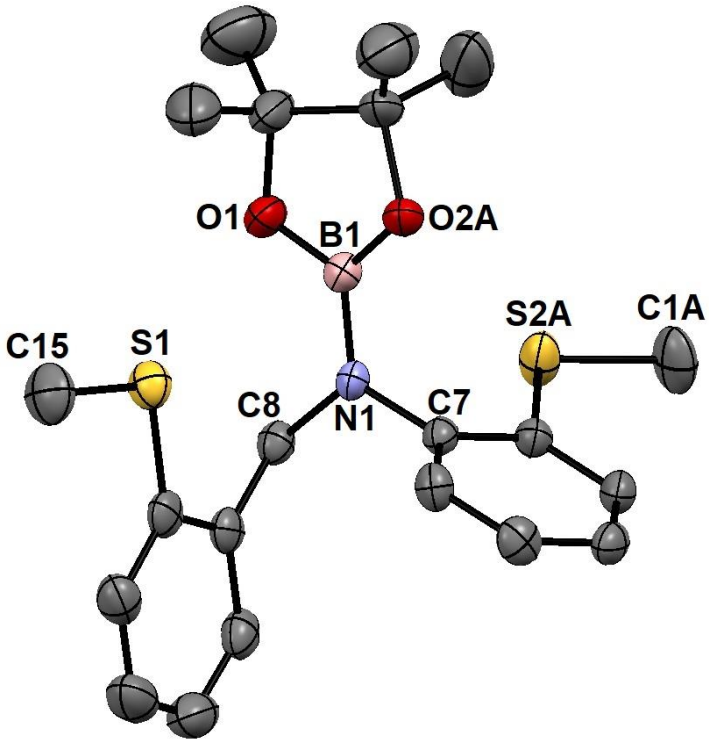

Figure 2.1. Molecular structure of **Bpin-L1** with 50% probability thermal ellipsoids and hydrogen atoms omitted for clarity.

Monitoring the reaction by ^{1}H NMR spectroscopy, we found evidence for formation of both **Bpin-L1** and **HL1** in approximately equal amounts (Fig. A24) with no evidence of a significant Zn alkoxide resting state, suggesting that the detailed catalytic mechanism may be more complicated. An analogous Ti amido complex has been proposed previously to catalyze the hydroboration of carbonyls via a similar mechanism to that shown in **Scheme 2.2**.[22] Complex **2.2$_{Zn}$** also reacted quantitatively with 2 equiv. of HBpin to give **2.3$_{Zn}$** in which the C=N bond in **L2** has been reduced by HBpin. We were unable to fully characterize **2.3$_{Zn}$**; the ^{1}H NMR spectrum indicated a fluxional process (Fig. A9) but the nuclearity of this intermediate has not been determined.

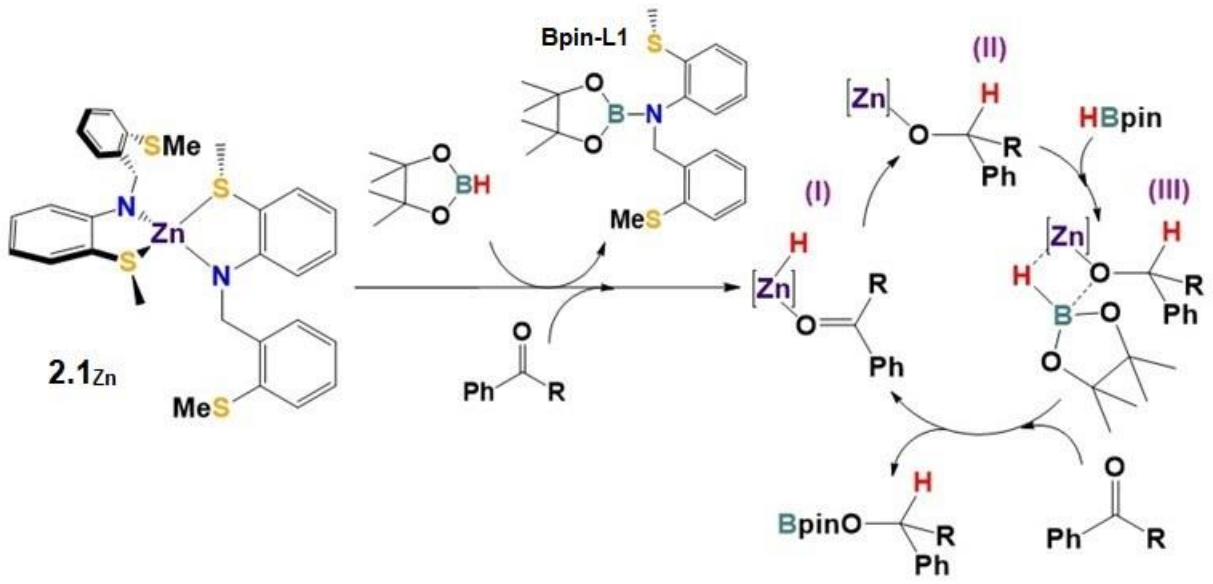

Scheme 2.2. Proposed mechanism for carbonyl hydroboration using HBpin and **2.1$_{Zn}$** precatalyst. On right, one **L1** ligand is omitted for clarity.

Nonetheless, addition of excess benzaldehyde to **2.3$_{Zn}$** afforded benzothiazoline heterocycle **S-P1** (**Figure 2.2**) and presumably $Zn(OBpin)_2$ (**II**), which converts subsequently to $O(Bpin)_2$ and the same substrate-derived Zn alkoxide complex proposed above (**Scheme 2.3**).

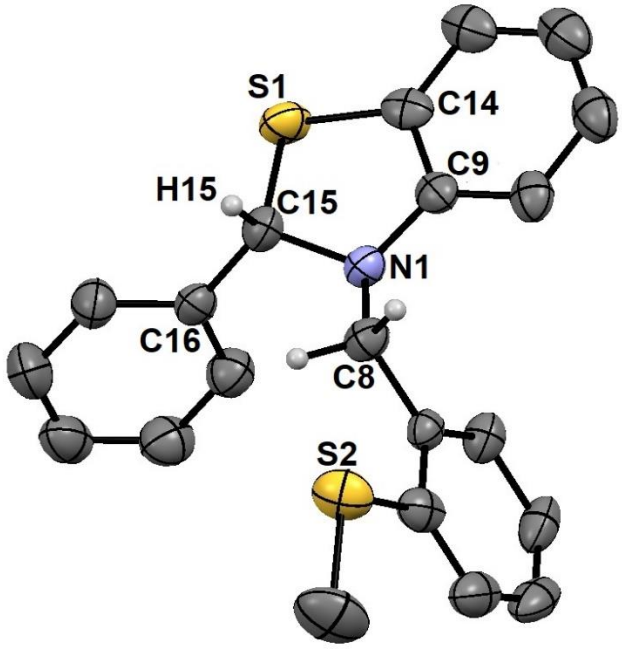

Figure 2.2. Molecular structure of **S-P1** with 50% probability thermal ellipsoids and hydrogen atoms omitted for clarity.

Although an analogous by-product (**S-P2**) was obtained from cinnamaldehyde, reactions of **2.3$_{Zn}$** with acetophenone gave a mixture of products that were not identified further. As depicted in **Schemes 2.2** and **2.3**, bifunctional activation of both precatalysts **2.1$_{Zn}$** and **2.2$_{Zn}$** proceeds presumably through formation of substrate-derived zinc alkoxide catalyst with the multi-step activation process for **2.2$_{Zn}$** requiring longer times.

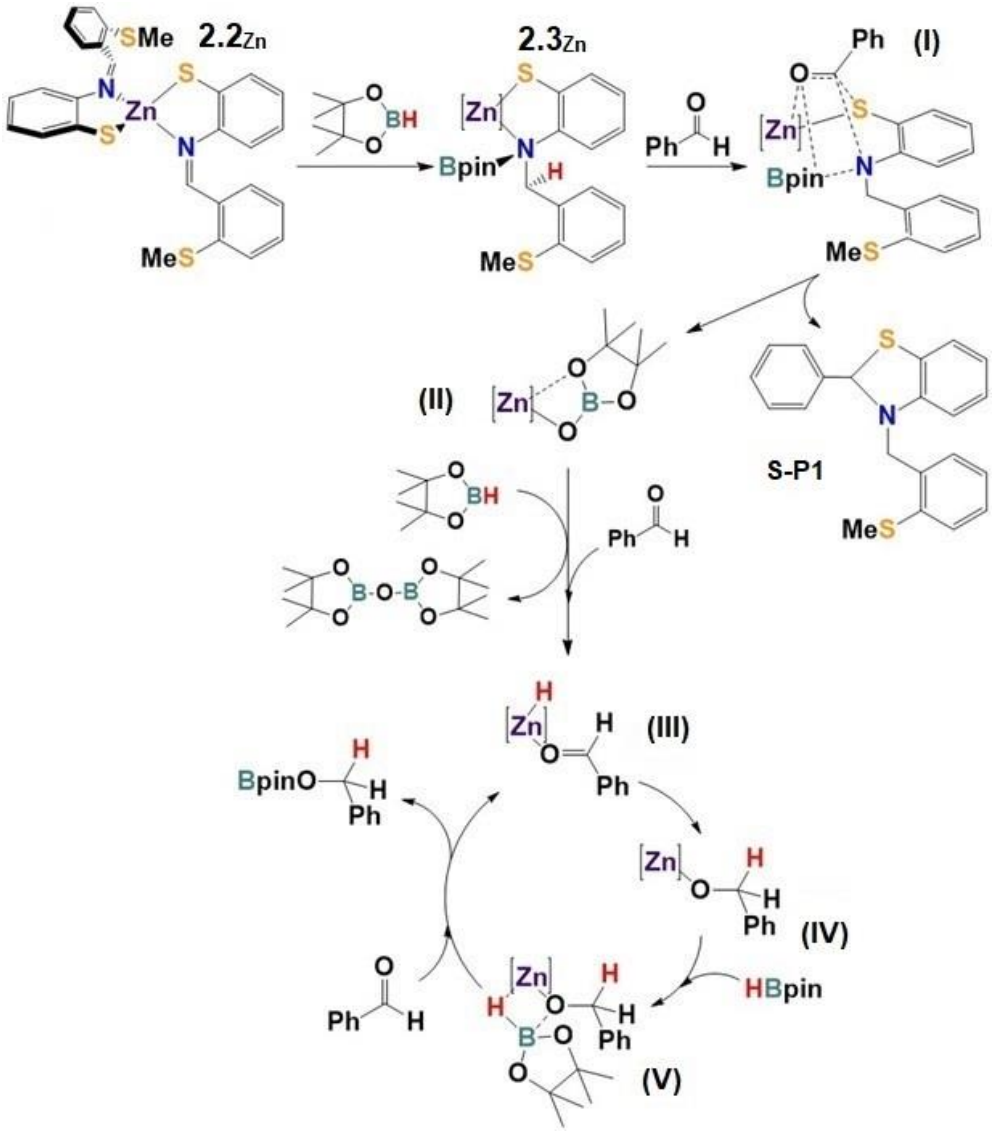

Scheme.2.3 Proposed mechanism for benzaldehyde hydroboration using HBpin and **2.2$_{Zn}$** precatalyst. On right, one **L2** ligand is omitted for clarity.

2.2.4 Synthesis of Complex 2.4_{Zn}

These disparate pre-catalyst activation results encouraged us to investigate the mixed-ligand zinc complex **2.4_{Zn}**, easily prepared by reaction of $ZnCl_2$ with **L1** then **L2** (**Scheme 2.4**). The molecular structure again shows a distorted tetrahedral Zn center (τ'_4 = 0.62) with similar Zn–N and Zn–S bond distances as those for the homoleptic complexes.

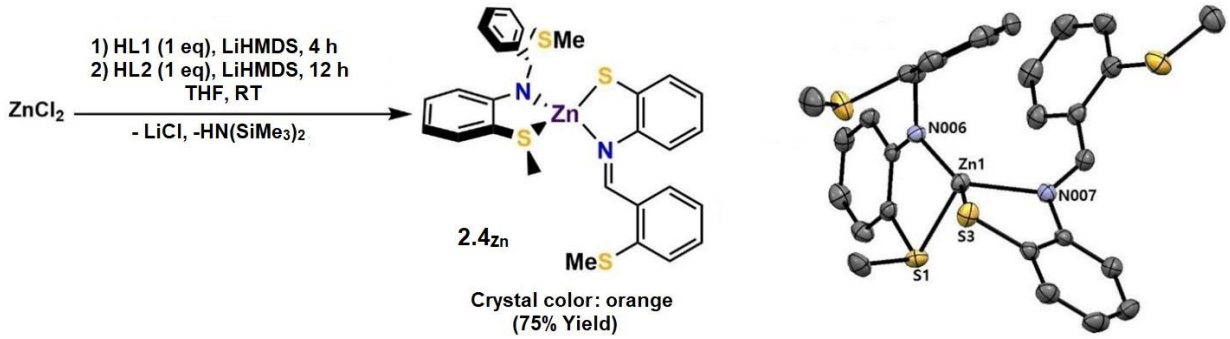

Scheme 2.4. Synthesis and molecular structure of **2.4_{Zn}** with 50% probability thermal ellipsoids and hydrogen atoms omitted for clarity. Selected bond distances (Å) and angles (deg): Zn-S1 2.479(1), Zn-S3 2.256(1), Zn-N006 1.923(3), Zn-N007 2.106(2), S1-Zn-N006 85.34(7), S1-Zn-N007 107.56(7), S1-Zn1-S3 106.17(3), S3-Zn-N007 87.33(7), S3-Zn-N006 140.99(7), N006-Zn-N007 125.33(9).

2.2.5 Catalytic Reactivity of 2.4_{Zn}

Surprisingly, **2.4_{Zn}** catalyzed both aldehyde and ketone hydroboration in less than 15 sec, giving quantitative yield with 1 mol% catalyst loading at room temperature. To monitor the reaction progress, the loading of **2.4_{Zn}** was lowered to 0.1 mol% and the acetophenone reduction took 16 min to complete at room temperature (Fig. A27). The stoichiometric reaction of **2.4_{Zn}** with 2 equiv. of benzaldehyde and 1 equiv. of HBpin, showed both **L1** and **L2** are involved in the same activation process they had shown separately in **2.1_{Zn}** and **2.2_{Zn}**, eventually proceeding through the same substrate-derived zinc alkoxide. Indeed, a catalyst recycle study showed similar rates in the 2nd to 5th cycles for all three catalytic systems (**Table 2.2**).

Table 2.2. Recycle study of **2.1**$_{Zn}$, **2.2**$_{Zn}$, **2.4**$_{Zn}$ and Zn-Alkoxide (**2.5**$_{Zn}$)[a]

Complex	Cycle1	Cycle2	Cycle3	Cycle4	Cycle5
2.1$_{Zn}$	>98% (14 min)	>98%	93%	89%	94%
2.2$_{Zn}$	>98% (21 min)	>98%	98%	92%	93%
2.4$_{Zn}$	>98% (15 sec)	>98%	96%	98%	96%
2.5$_{Zn}$	92% (35 min)	96%	91%	91%	88%

[a] Zinc complex (1 mol%), acetophenone (1.00 mmol), HBpin (1.00 mmol), 0.5 mL C_6D_6, room temperature. Time for 2nd to 5th cycles is 25 min. After each cycle the reaction NMR tube was charged with 1 mmol each of acetophenone and HBpin. **2.5**$_{Zn}$ is Zn[O-(2,6-Ph_2-C_6H_3)]$_2$(THF)$_2$.[23]

2.2.6 Why Does 2.4$_{Zn}$ Show The Highest Activation Rate in Benzene Solvent?

Surmising that oligomerization of the initially formed Zn–alkoxide in **2.1**$_{Zn}$ could slow the activation process vs. **2.4**$_{Zn}$, which would still contain the slower activating thiolate ligand, we performed the reaction in THF which could maintain mononuclear Zn intermediates. Indeed, the activation rate of **2.1**$_{Zn}$ in THF solvent is now much closer to that of **2.4**$_{Zn}$ (**Figure 2.3**).

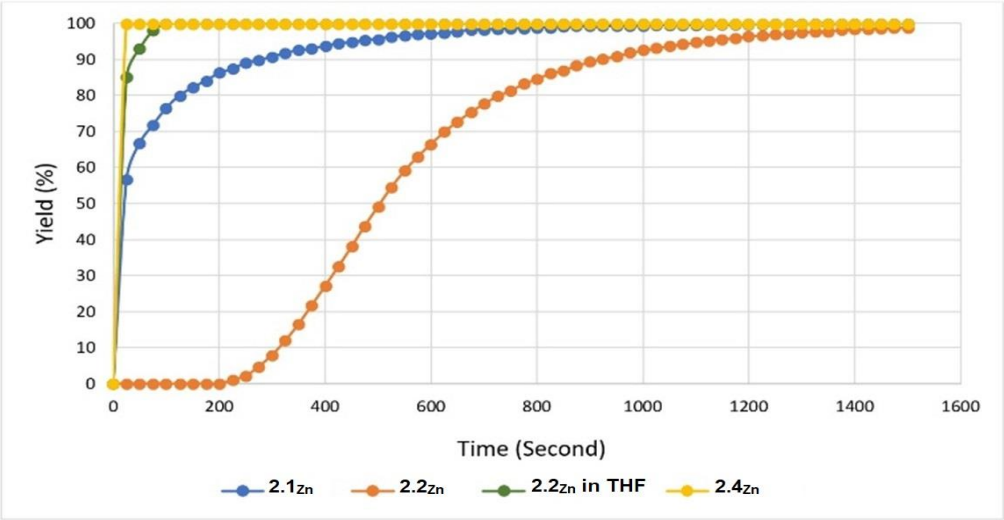

Figure 2.3. Acetophenone hydroboration profiles catalyzed by 1 mol% of **2.1**$_{Zn}$, **2.2**$_{Zn}$, **2.4**$_{Zn}$ in C_6D_6, and **2.1**$_{Zn}$ in THF.

Finally, since all three catalytic systems presumably end up forming substrate-derived zinc alkoxide as the active catalyst, the activity of previously published zinc bis(alkoxide) complex, Zn[O-(2,6-Ph_2-C_6H_3)]$_2$(THF)$_2$ (**2.5**$_{Zn}$),[23] was investigated over 5 cycles for comparison (**Table 2.2**). After the first cycle which includes the activation process, the rate and activity were, as

expected, nearly the same for all four complexes over the next 4 cycles. In addition, these simple substrate-derived zinc bis(alkoxide) complexes proved to be active and robust catalysts for carbonyl hydroboration, similar to ZnR(OAr) catalysts used previously for carbonyl hydrosilylation (R = Me, Et; Ar = substituted phenyl).[24,25] In conclusion, a detailed study of metal complex evolution using bifunctional zinc amido and thiolate SNS precatalysts for carbonyl hydroboration using HBpin revealed disparate ligandassisted activation pathways leading to the substrate-derived Zn alkoxide active catalyst. While HBpin reaction with the SNS amido ligand has precedence in related pincer ligands,[26] this is a rare example involving decoordination of the N-borylated ligand from the metal. Moreover, while the imine-reduced thiolate ligand was also observed in the stoichiometric reaction of Mn(κ^3-SNS^{Me})(CO)$_3$ with HBpin,[14] it was identified as an off cycle by-product that did not affect the complex's ability as a photocatalyst for nitrile dihydroboration. In contrast, when coordinated to Zn, the imine-reduced thiolate ligand undergoes a novel reaction with the aldehyde substrate, affording a benzothiazoline by-product and presumably Zn(OBpin)$_2$, which can further react with HBpin and substrate to generate O(Bpin)$_2$ and the active Zn alkoxide catalyst. As a result, this study highlights the importance of mechanistic studies, and especially catalyst speciation, in advancing our understanding of metal–ligand cooperation in first-row metal catalysis. These finding also helped us revisit and scrutiny the previously proposed reaction pathway of copper amido Cu(**L1**)(IPr) (**2.6$_{Cu}$)** in carbonyl hydroboration,[12] and more closely investigate its catalyst speciation. In addition, we wished to compare the reactivity of **2.6$_{Cu}$** with silver analogue.

2.2.7 Reinvestigation of 2.6$_{Cu}$-catalyzed carbonyl hydroboration mechanism

The Baker group showed previously that the copper amido complex, Cu(**L1**)(IPr) (**2.6$_{Cu}$**), gives rise to an active catalyst for carbonyl hydroboration.[12] Mechanistic studies prompted the authors to propose an outer-sphere activation of the substrate following bifunctional activation of the B–H bond across the copper-amido unit (**Scheme 2.5 A**). As shown above, stoichiometric treatment of **2.1$_{Zn}$** with HBpin afforded free **Bpin-L1** (**Scheme 2.5 B**) which was isolated and characterized.[27] This allowed the direct comparison of its ^{1}H NMR spectrum with the reaction mixture of stoichiometric **2.6$_{Cu}$** and HBpin (**Figure 2.4**). The resulting spectrum confirmed formation of **Bpin-L1** and a copper–hydride dimer, [CuH(IPr)]$_2$, previously reported by the Sadighi group.[28] Taken in context of our work with **2.1$_{Zn}$**, this observation indicates that **2.6$_{Cu}$**

undergoes an analogous activation pathway as **2.1$_{Zn}$** (**Scheme 2.6**). Borylation of **L1** liberates free **Bpin-L1**, generating active species [CuH(IPr)]$_2$, a known carbonyl hydrosilylation catalyst.[28] This observed lability of **Bpin-L1** is in contrast to the protonated analogue **H-L1** that remains κ^3-bound in the Baker group's Fe[11] and Co[29] examples. To further investigate the coordination chemistry of **Bpin-L1**, we sought to prepare the heavier Group 11 analogues of **2.6$_{Cu}$**.

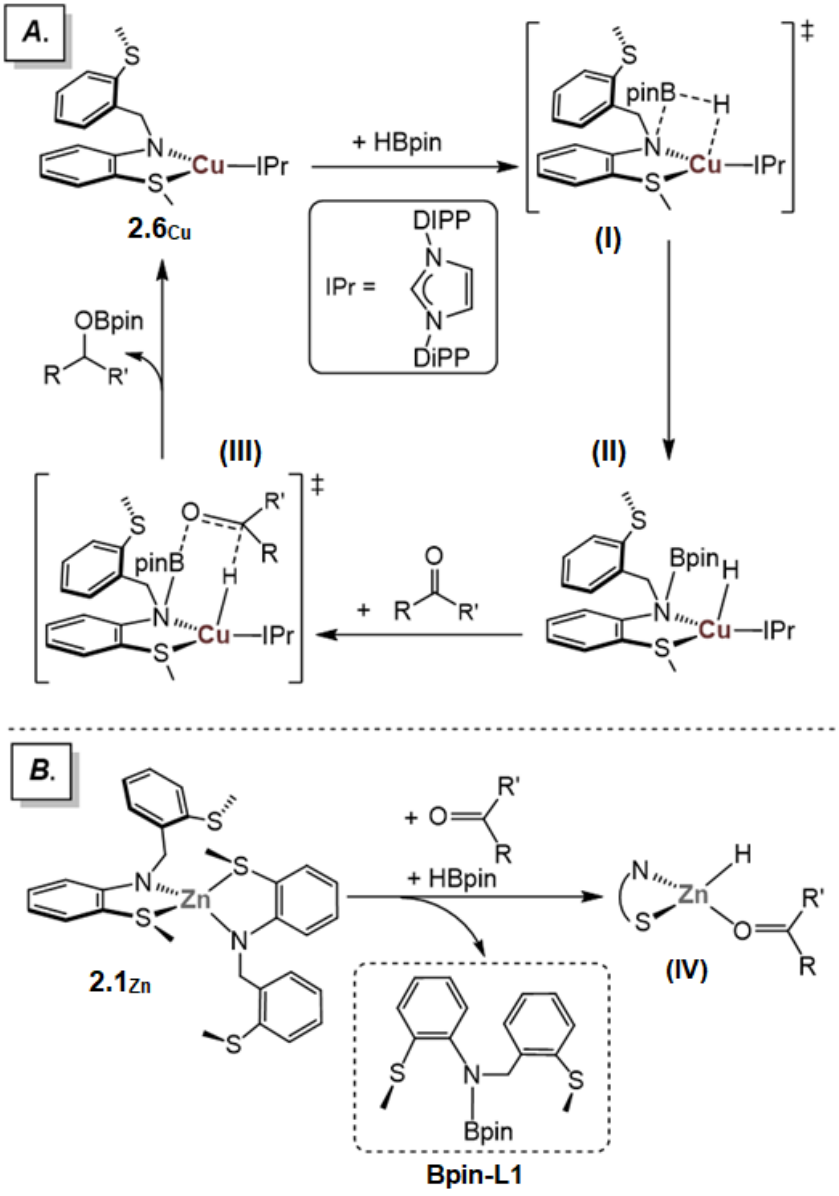

Scheme 2.5. A) Reaction pathway for carbonyl hydroboration by catalyst **2.6$_{Cu}$** proposed in previous work (DiPP = 2,6-diisopropylphenyl); B) Catalyst activation pathway for previously studied **2.1$_{Zn}$** system.

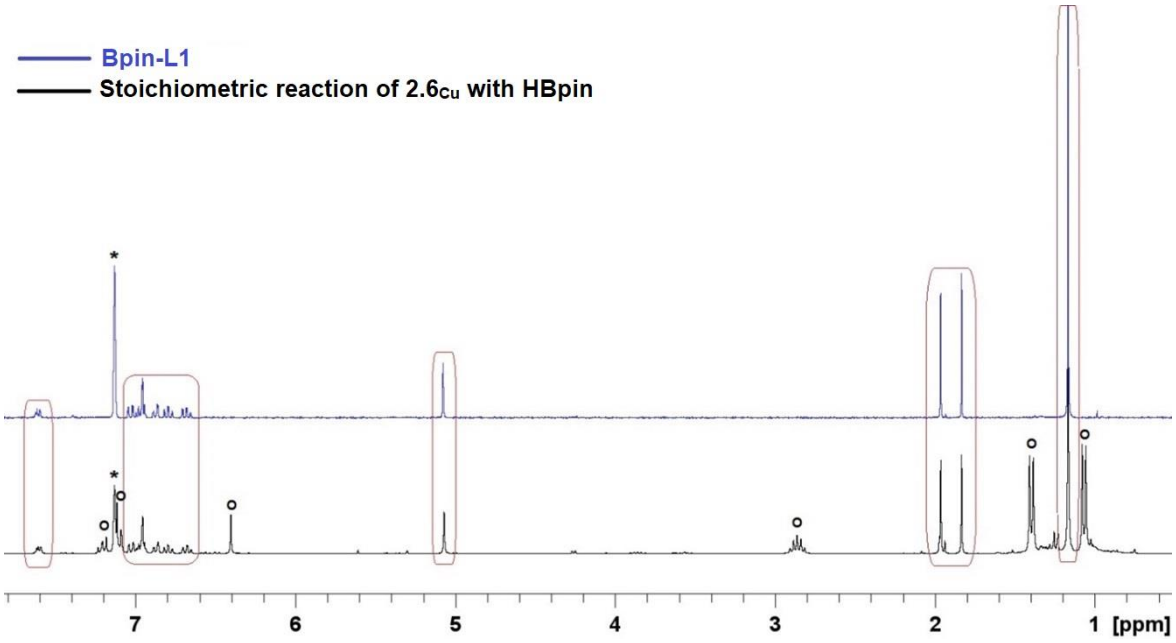

Figure 2.4. Stacked plot of ^{1}H NMR spectra of **Bpin-L1** and reaction mixture of stoichiometric reaction of **2.6$_{Cu}$** with HBpin in C_6D_6. ^{o} indicates $[(IPr)CuH]_2$, and * indicates protic impurity in C_6D_6.

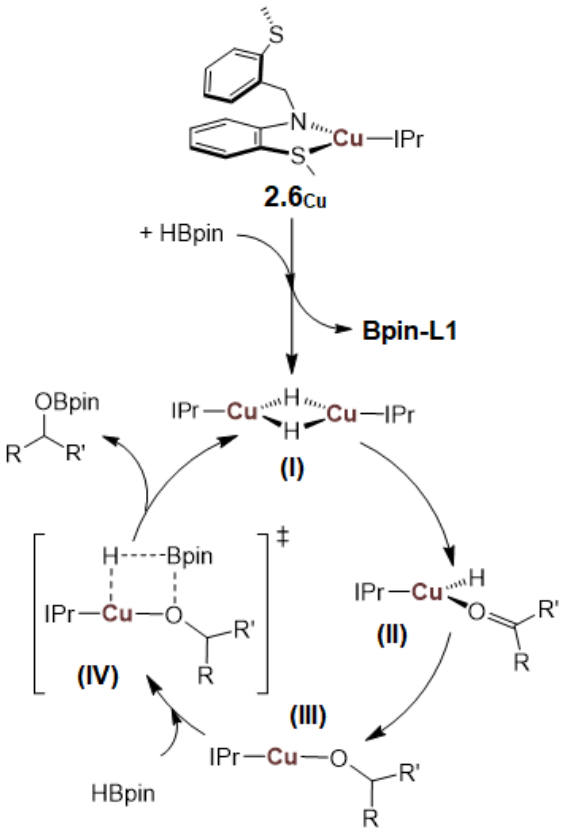

Scheme 2.6. Proposed mechanism for catalytic carbonyl hydroboration by **2.6$_{Cu}$.**

2.2.8 Synthesis and reactivity of $\mathbf{2.7_{Ag}}$

Treatment of AgCl(IPr) with **L1** and NaHMDS afforded Ag(κ^2-$S^{Me}NS^{Me}$)(IPr) ($\mathbf{2.7_{Ag}}$; **Scheme 2.7**). The molecular structure of $\mathbf{2.7_{Ag}}$ shows a strained trigonal planar geometry (S1-Ag1-N1 = 75.83(5)˚; S1-Ag1-C1 = 126.07(6)˚ and N1-Ag1-C1 = 158.10(8)˚), because of the small bite angle of the κ^2-SNS ligand and the long Cu–$S_{thioether}$ bond length (Ag1-S1 2.8032(8) Å) which is significantly longer than that of $\mathbf{2.6_{Cu}}$ (2.482(1) Å), due partly to the larger covalent radius of the silver atom (1.53 vs 1.38 Å for Cu).

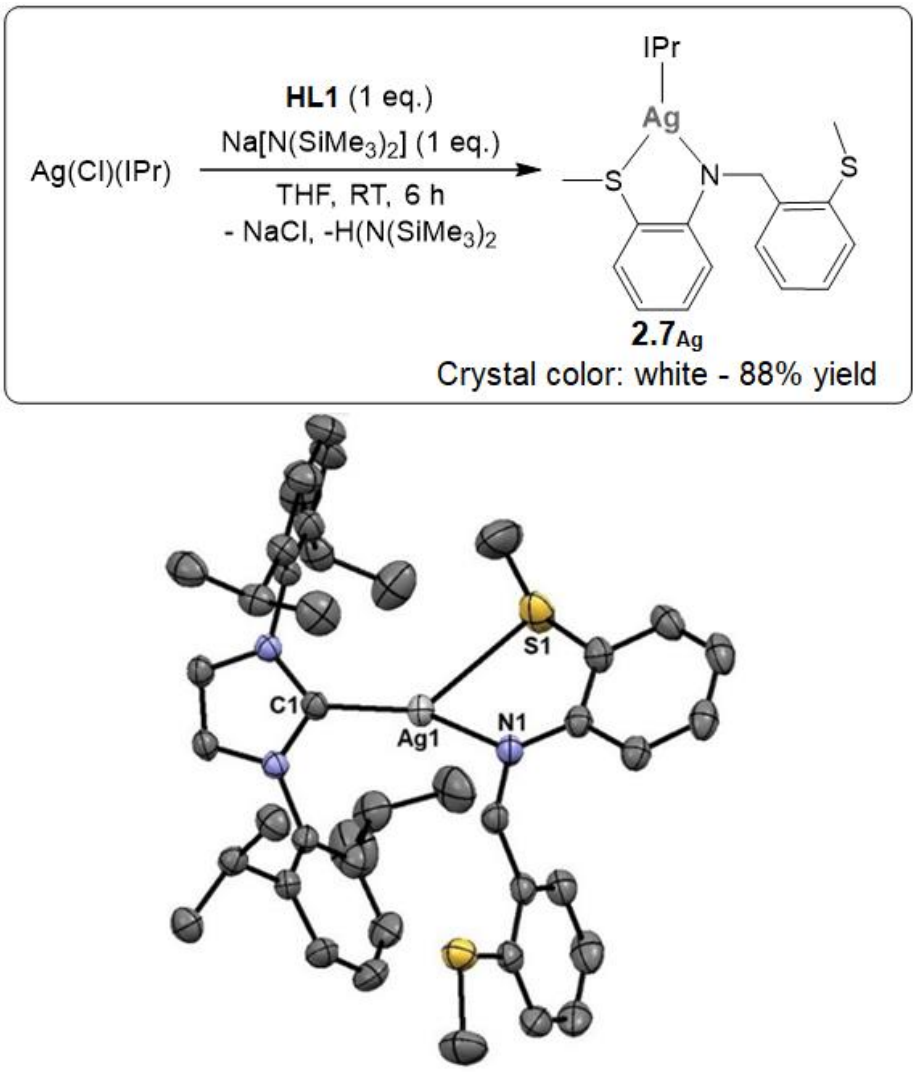

Scheme 2.7. Synthesis and molecular structure of $\mathbf{2.7_{Ag}}$ with 50% probability thermal ellipsoids. Hydrogen atoms and DCM molecule are omitted for clarity. Selected bond distances (Å) and angles (°): Ag1-S1 2.8032(8), Ag1-N1 2.105(2), Ag1-C1 2.070(2), S1-Ag1-N1 75.83(5), S1-Ag1-C1 126.07(6), N1-Ag1-C1 158.10(8).

The ^{1}H NMR spectrum of **2.7$_{Ag}$** showed two doublets at δ 1.25 and 1.31, for the isopropyl methyls, two singlets at δ 2.38 and 2.54 for the two S-methyls, a methine septet at δ 2.57, a singlet at δ 4.47 for N-CH_2-C, and seventeen aromatic protons between δ 6.5-7.6 (Fig. A31). Attempts to use **2.7$_{Ag}$** as a pre-catalyst for carbonyl hydroboration were unsuccessful. Furthermore, stoichiometric reaction of **2.7$_{Ag}$** with HBpin afforded **Bpin-L1** and silver metal as evidenced by the observation of a black precipitate (Fig. A33). This indicates that after B–H bond activation and liberation of **Bpin-L1**, the resulting silver hydride species is unstable and instantly decomposes.

The results of these two studies with zinc and copper showed that amido donors, due to their higher Lewis basicity, are better B–H bond activators than thiolate donors. Also, it was found that when the amido ligand is not incorporated into a strongly chelating multidentate ligand, it can lose its connectivity upon forming the N-B bond. To exploit these findings, a new amido ligand (L = O^{Me}N^{H}N^{pyrrolide}) was used for the synthesis of a series of zinc complexes, **2.8$_{Zn}$-2.11$_{Zn}$**. Upon treatment with HBpin, **2.11$_{Zn}$** generate a very reactive zinc dihydride (**2.12$_{Zn}$**) that proved to be an effieint catalyst for reduction of nitriles and quinolines.

2.3 Results and Discussion for Amino-pyrrolide Complexes, 2.8$_{Zn}$-2.11$_{Zn}$

2.3.1 Synthesis and Characterization of H$_2$L3 and 2.8$_{Zn}$-2.11$_{Zn}$

Reaction of 4-methoxybenzylamine and pyrrole-2-carboxaldehyde, followed by $NaBH_4$, afforded **H$_2$L3** (**Scheme 2.8**). The ^{1}H NMR spectrum of **H$_2$L3** (Fig. A34) showed a broad peak at δ 9.21 for pyrrole NH and another broad peak at δ 2.62 for the other NH, showing successful reduction of the imine, as observed in the molecular structure of **H$_2$L3** determined by X-ray diffraction.

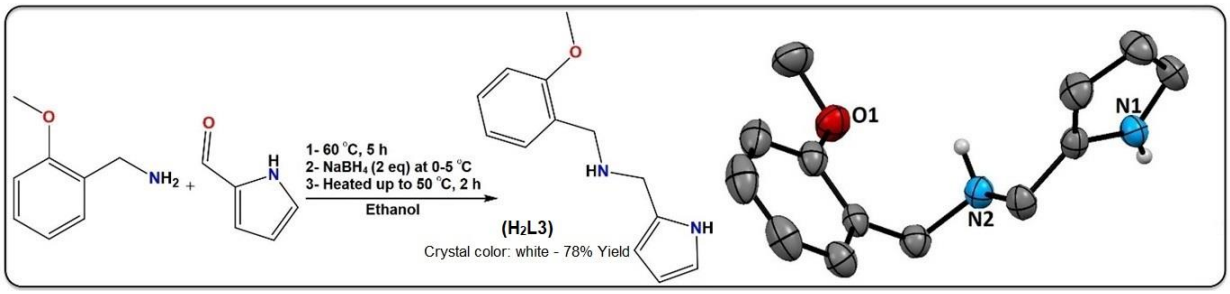

Scheme 2.8. Synthesis and molecular structure of **H$_2$L3** with 50% probability thermal ellipsoids and hydrogen atoms omitted for clarity.

Treatment of **H_2L3** with one equiv of diethyl zinc afforded **2.8$_{Zn}$** (**Scheme 2.9**). The ^{1}H NMR spectrum of **2.8$_{Zn}$** (Fig. A35) showed a singlet at δ 3.93 due to O-CH_3, two doublets at δ 3.87 and 3.67 for N-CH_2-, and a broad resonance at δ 3.12 for the amino NH. Existence of a triplet at δ 1.09 and a quartet at δ 0.22 revealed that one ethyl group remained attached to Zn. The molecular structure of **2.8$_{Zn}$** consists of a three-coordinate zinc center in a distorted trigonal planar geometry [N1-Zn-N2 = 81.3(1), N1-Zn-C1 = 138.3(1)°] and no interaction with the methoxy oxygen. The Zn-$N_{pyrrolide}$ bond distance [1.975(2) Å] is significantly shorter than Zn-N_{amine} [2.191(3) Å] and Zn-C_{ethyl} [1.973(4) Å] is in the typical range for such bonds.[30,31]

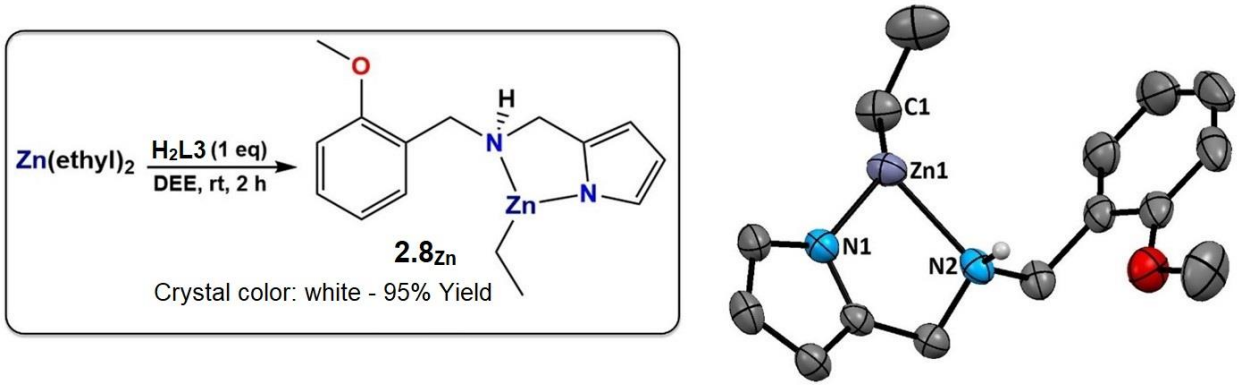

Scheme 2.9. Synthesis and molecular structure of **2.8$_{Zn}$** with 50% probability thermal ellipsoids and hydrogen atoms omitted for clarity. Selected bond distances (Å) and angles (deg): Zn-N1 1.975(2), Zn-N2 2.191(3), Zn-C1 1.973(4), N1-Zn-N2 81.3(1), N1-Zn-C1 138.3(1), N2-Zn-C1 119.3(1).

To assess the reactivity of **2.8$_{Zn}$** with HBpin, 1 equiv of **2.8$_{Zn}$** was treated with two equiv of HBpin and the reaction product was extracted into hexane and analyzed. NMR spectra of the extracted product showed **H_2L3** with two attached Bpin groups [**(Bpin)$_2$-L3**] (Fig. A44). The composition of **(Bpin)$_2$-L3** was confirmed by EI-MS (Fig. A45). This observation showed that both N-donors in **L3** are able to activate the B–H bond of HBpin, one by releasing H_2 and the other by forming Zn–H. Thus, to obtain an active zinc dihydride catalyst, both another **L3** and a strong donor ligand are needed. For this, **2.8$_{Zn}$** was separately treated with one equiv of 4,5-dichloro-1,3-dimethyl-1H-imidazol-3-ium iodide [(H-DDI)I] in one reaction, and with one equiv of **L** in another, affording **2.9$_{Zn}$** (**Scheme 2.10**) and **2.10$_{Zn}$** (**Scheme 2.11**), respectively. The ^{1}H NMR spectrum of **2.9$_{Zn}$** (Fig. A7) contained two peaks at δ 3.89 and 3.66 for N-CH_2-, one at δ 3.76 for O-CH_3, a singlet at δ 3.44 for DDI-CH_3, and a triplet and quartet at δ 1.24 and 0.05 for -CH_3 and -CH_2- of the Zn-Et.

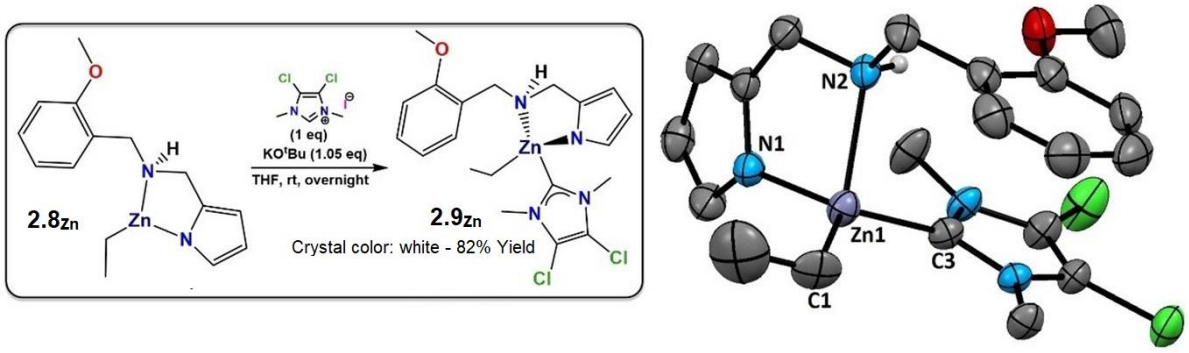

Scheme 2.10. Synthesis and molecular structure of **2.9Zn** with 50% probability thermal ellipsoids and hydrogen atoms omitted for clarity. Selected bond distances (Å) and angles (deg): Zn-N1 2.019(3), Zn-C1 2.049(4), Zn-N2 2.212(3), Zn-C3 2.098(4), N1-Zn-N2 81.1(1), N1-Zn-C1 119.4(2), N1-Zn-C3 107.2(1), N2-Zn-C1 117.4(1), N2-Zn-C3 95.4(1), C1-Zn-C3 125.5(2).

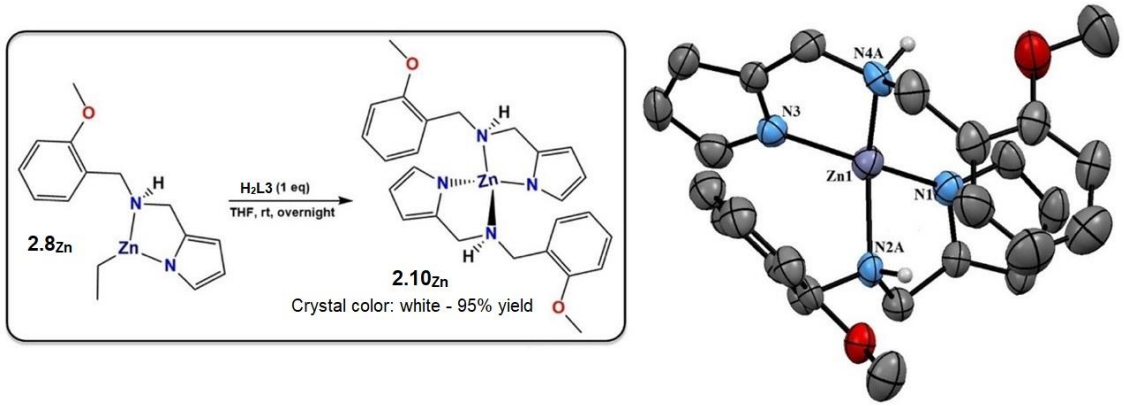

Scheme 2.11. Synthesis and molecular structure of **2.10Zn** with 50% probability thermal ellipsoids and hydrogen atoms omitted for clarity. Selected bond distances (Å) and angles (deg): Zn-N1 1.934(5), Zn-N3 1.949(3), Zn-N2A 2.11(2), Zn-N4A 2.055(6), N1-Zn-N2A 83.5(6), N1-Zn-N3 137.7(2), N1-Zn-N4A 117.7(2), N3-Zn-N2A 111.2(6), N3-Zn-N4A 86.4(2), N2A-Zn-N4A 125.9(6).

The molecular structure of **2.9Zn** displayed a strained tetrahedral geometry [N2-Zn-C3 = 95.4(1), C1-Zn-C3 = 125.5(2)°] with slightly elongated Zn-N bonds vs **2.8Zn**. The ^{1}H NMR spectrum (Fig. A39) of **2.10Zn** displayed a singlet at δ 3.84 due to O-CH_3 and singlets at δ 3.75 and 3.66 for N-CH_2. The molecular structure of **2.10Zn** showed a tetrahedral geometry with distortions resulting from the ca. 85° bite angle of the amino-pyrrolide ligand. Both Zn-N distances (avg 1.94, 2.08 Å) are somewhat shorter than those in **2.8Zn** (1.98, 2.19 Å) and **2.9Zn** (2.02 and 2.21Å).

As illustrated in **Scheme 2.12**, the target zinc complex ligated by two **L3** and one small NHC (**2.11Zn**) could be synthesized through two separate pathways. Using **2.10Zn** as precursor gave **2.11Zn** in higher yield (88%) than when **2.9Zn** was used (63%). The ^{1}H NMR spectrum of

2.11$_{Zn}$ (Fig. A41) showed a singlet at δ 3.84 for O-C*H*$_3$, two singlets at δ 3.78 and 3.76 for N-CH$_2$ a singlet at δ 3.32 for DDI-C*H*$_3$ and a broad N*H* resonance at δ 3.12. The molecular structure of **2.11$_{Zn}$** consists of a distorted trigonal bipyramidal geometry around zinc. While the Zn-N$_{pyrrolide}$ bond distances are similar to those in **2.8$_{Zn}$** and **2.9$_{Zn}$**, the Zn-N$_{amino}$ distances are substantially longer (2.33, 2.54 Å), reflecting the steric hindrance in five-coordinate **2.11$_{Zn}$**.

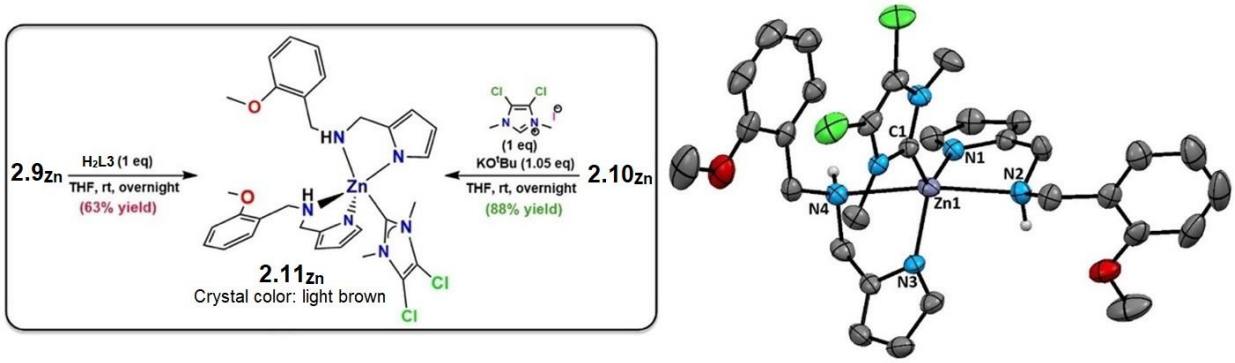

Scheme 2.12. Synthesis and molecular structure of **2.11$_{Zn}$** with 50% probability thermal ellipsoids and hydrogen atoms omitted for clarity. Selected bond distances (Å) and angles (deg): Zn1-N1 2.003(2), Zn1-N2 2.329(2), Zn1-N3 1.975(2), Zn1-N4 2.540(2), Zn1-C1 2.061(2), N1-Zn1-N2 78.76(7), N1-Zn1-N3 123.81(8), N1-Zn1-N4 88.81(7), N1-Zn1-C1 123.14(8), N2-Zn1-N3 96.89(8), N2-Zn1-N4 160.22(7), N2-Zn1-C1 100.94(8), N3-Zn1-N4 77.22(7), N3-Zn1-C1 112.75(8), N4-Zn1-C1 98.73(8).

2.3.2 Catalytic Activity of 2.8$_{Zn}$-2.11$_{Zn}$ in Nitrile Dihydroboration

In the next step, complexes **2.8$_{Zn}$-2.11$_{Zn}$** were evaluated as catalysts for dihydroboration of nitriles (**Table 2.3**). Starting with 1 mol% loading at rt, **2.8$_{Zn}$** and **2.9$_{Zn}$** gave 70% and 92% yield respectively after 14 h (entries 1 and 2), while **2.10$_{Zn}$** and **2.11$_{Zn}$** gave quantitative yields (entries 3 and 4). Lowering the **2.10$_{Zn}$** loading to 0.5 mol% decreased the yield to 81% (entry 5), while lowering the **2.11$_{Zn}$** loading to 0.01 mol% had no effect (entries 6-9). Further decreasing the loading of **2.11$_{Zn}$** to 0.005 mol% dropped the yield to 61 mol% (entry 10). Shortening the reaction time to 40 min kept the yield quantitative (entry 11), but to 30 min gave 93% yield (entry 12).

Table 2.3. Hydroboration of benzonitrile using **2.8$_{Zn}$-2.11$_{Zn}$** as pre-catalysts

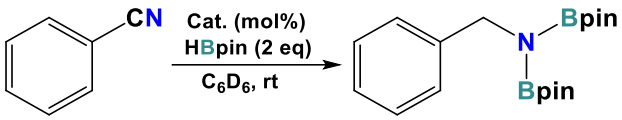

Entry	Cat. (mol%)	Time	Yield* (%)	TON	TOF
1	**2.8$_{Zn}$** (1)	14 (h)	70	70	-
2	**2.9$_{Zn}$** (1)	14 (h)	92	92	-
3	**2.10$_{Zn}$** (1)	14 (h)	>99	99	-
4	**2.11$_{Zn}$** (1)	14 (h)	>99	99	-
5	**2.10$_{Zn}$** (0.5)	14 (h)	81	162	-
6	**2.11$_{Zn}$** (0.5)	14 (h)	>99	198	-
7	**2.11$_{Zn}$** (0.1)	14 (h)	>99	990	-
8	**2.11$_{Zn}$** (0.05)	14 (h)	>99	1980	-
9	**2.11$_{Zn}$** (0.01)	14 (h)	>99	9900	-
10	**2.11$_{Zn}$** (0.005)	14 (h)	61	12200	871
11	**2.11$_{Zn}$** (0.01)	40 (min)	>99	9900	14850
12	**2.11$_{Zn}$** (0.01)	30 (min)	93	9300	18600

Reaction condition: Benzonitrile (0.1 mmol), HBpin (0.2 mmol). Amount of the zinc catalysts were calculated according to the amount of benzonitrile. *Product yields were determined by ^{1}H NMR integration vs substrate.

To test the efficiency of the **2.11$_{Zn}$** catalytic system on different nitriles, a scope study (**Table 2.4**) was performed using 0.01 mol% **2.11$_{Zn}$** at rt, aliphatic nitriles acetonitrile (entry a) and isobutyronitrile (b) were converted quantitatively to their corresponding dihydroborated products in 20 min, which is much faster than the best previous reports.[18,33-35] For ortho-functionalized substrates the chloro derivative (c) was hydroborated faster than the bromo one (d). It is unclear whether this is solely a steric effect, however, as the same trend was observed for the meta-substituted benzonitriles. For the para-substituted derivatives the bromo and methoxy derivatives were hydroborated at nearly the same rate.[21,38] Considering the low loading of **2.11$_{Zn}$** in these catalytic reactions (TON=9900), its performance rivals the most active dihydroboration catalysts.[18,34-36] In fact, using 0.5 mol% of a zinc dihydride complex with a bulkier NHC ligand, dihydroboration of 2-thiophenecarbonitrile gave a 95% yield of the diborylamine after 40 min[18] as compared to a comparable conversion using just 0.01 mol% of **2.11$_{Zn}$** (entry i in Table 2.4).

Table 2.4. Hydroboration of nitriles using **2.11$_{Zn}$** as pre-catalyst*

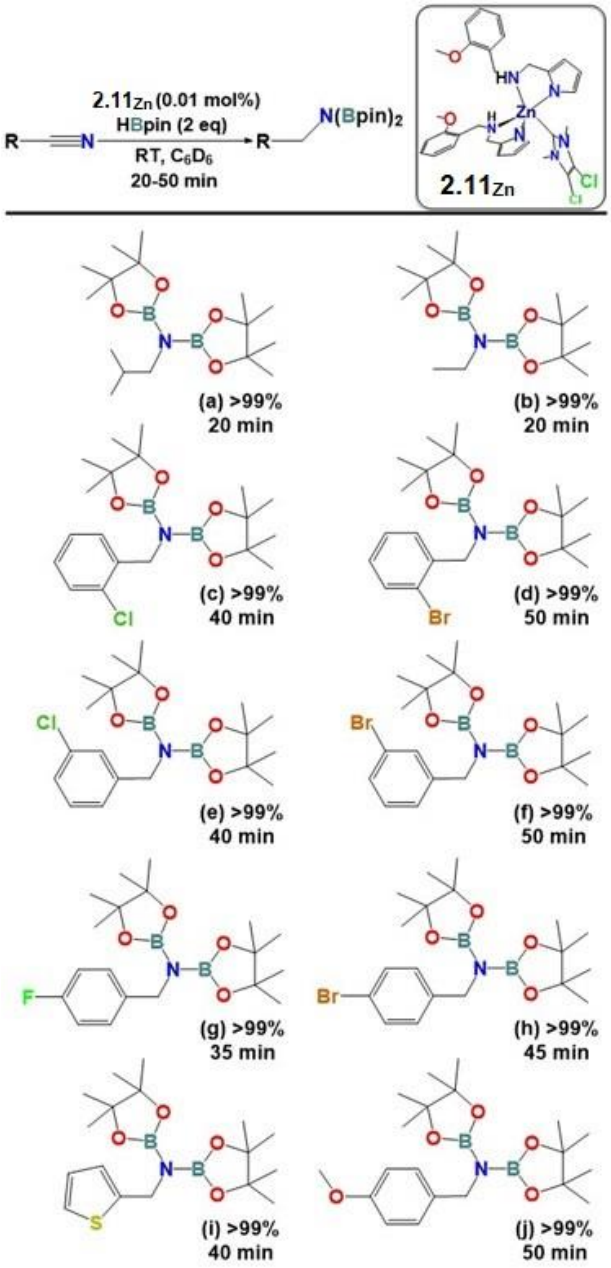

Reaction condition: Nitrile substrate (0.1 mmol), HBpin (0.2 mmol). *Product yields were determined by ^{1}H NMR integration vs substrate. Selectivity in all cases was 100% for the reported products.

2.3.3 Catalytic Activity of 2.8$_{Zn}$-2.11$_{Zn}$ in Quinoline Hydroboration

Complexes **2.8$_{Zn}$-2.11$_{Zn}$** were also assessed as catalysts for quinoline hydroboration (**Table 2.5**). With 5 mol% loading after 24 h at 23 °C, 61 and 88% yields were obtained using **2.8$_{Zn}$** and **2.9$_{Zn}$**, respectively (entries 1 and 2), whereas complete conversion was observed using **2.10$_{Zn}$** and **2.11$_{Zn}$** (3 and 4). Decreasing **2.10$_{Zn}$** to 3 mol% gave 94% yield (5), while **2.11$_{Zn}$** could be lowered

to 0.05 mol% with no yield decrease (6-10); going to 0.01 mol% of **2.11$_{Zn}$** gave a significant drop to 63% yield (11). Decreasing the reaction time to 2.5 h maintained the quantitative yield (12), while a further decrease to 2 h lowered the yield to 88% (13).

Using 0.05 mol% of **2.11$_{Zn}$**, hydroboration of different quinoline derivatives was investigated (**Table 2.6**). Sterically encumbered C2- and C8-substituted quinolines showed no tendency for reduction (entries l and p), in agreement with previous reports.[37-40] For C4-, C5- and C3-substituted derivatives, full reduction was observed after 2.5 h (m-o). Acridine could also be successfully reduced after 4 h (q) and isoquinoline after just 2.5 h (r).

2.3.4 Mechanistic Study of Quinoline Hydroboration Using 2.11$_{Zn}$

To probe the mechanism of quinoline hydroboration using **2.11$_{Zn}$**, a set of reactions was performed (See experimental section, mechanistic study part). First, stoichiometric treatment of **2.11$_{Zn}$** with quinoline showed no change in the ^{1}H NMR spectrum (Fig. A43). Quinoline hydroboration was then performed using 10 mol% of **2.11$_{Zn}$**, so the catalyst could be observed by ^{1}H NMR. As depicted in Fig. S12, in addition to quinoline hydroboration product and **(Bpin)$_2$-L3**, a singlet at δ 3.20 ppm, and some minor broad resonances between δ 3 and 3.6 were evident. This suggests that the resting state of **2.11$_{Zn}$** has no ligand **L3** attached to zinc, as both **L3** were converted to **(Bpin)$_2$-L3**. Then, **2.11$_{Zn}$** was treated with 4 equiv of HBpin and the formed **(Bpin)$_2$-L3** was extracted into hexane. The remaining residue was filtered, dried and characterized by ^{1}H NMR and EI-MS. ^{1}H NMR of this residue again showed a singlet at δ 3.20 ppm, and two small broad peaks at δ 2.98 and 3.40 (Fig. A48). The EI-MS spectrum of the residue showed cations derived from both ZnH_2(DDI) and dimer $[ZnH_2(DDI)]_2$ (**2.12$_{Zn}$**) (Fig. A47). All efforts to grow crystals of **2.12$_{Zn}$**, using different solvents and methods, were unsuccessful as only tiny, twinned needles were obtained which gave no processible X-ray diffractions. Using 0.05 mol% of isolated **2.12$_{Zn}$** as a catalyst for quinoline hydroboration gave the same yield as **2.11$_{Zn}$** (**Table 2.5**, entry 14). When isolated **2.12$_{Zn}$** dimer was treated with 4 equiv of quinoline, half of the used quinoline was converted to a new species and the other half was unreacted (Fig. A48).

Table 2.5. Hydroboration of quinoline using **2.8$_{Zn}$-2.11$_{Zn}$** as pre-catalysts

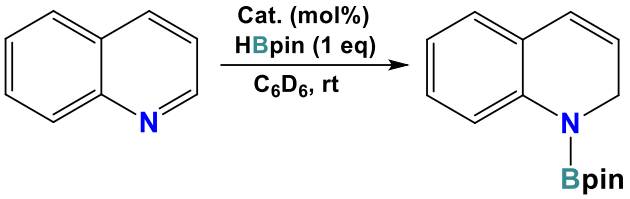

Entry	Cat. (mol%)	Time (h)	Yield* (%)	TON	TOF
1	**2.8$_{Zn}$** (5)	24	61	12	-
2	**2.9$_{Zn}$** (5)	24	88	17	-
3	**2.10$_{Zn}$** (5)	24	>99	19	-
4	**2.11$_{Zn}$** (5)	24	>99	19	-
5	**2.10$_{Zn}$** (3)	24	94	31	-
6	**2.11$_{Zn}$** (3)	24	>99	32	-
7	**2.11$_{Zn}$** (1)	24	>99	99	-
8	**2.11$_{Zn}$** (0.5)	24	>99	198	-
9	**2.11$_{Zn}$** (0.1)	24	>99	990	-
10	**2.11$_{Zn}$** (0.05)	24	>99	1980	-
11	**2.11$_{Zn}$** (0.01)	24	63	6300	262
12	**2.11$_{Zn}$** (0.05)	2.5	>99	1980	792
13	**2.11$_{Zn}$** (0.05)	2	88	1760	880
14	**2.12$_{Zn}$** (0.05)	3	>99	1980	660
15	**2.12$_{Zn}$** (0.05)[a]	3	>99	1980	660

Reaction condition: Quinoline (0.1 mmol), HBpin (0.2 mmol). Amount of the zinc complexes were calculated according to the amount of quinoline. * Product yields were determined by ^{1}H NMR integration vs substrate. [a] After the first run, 1 more equiv each of HBpin and quinoline were added *in-situ* as a second run.

This observation clearly showed that only one of the hydrides is involved in the catalytic cycle. This finding was supported by our VTNA kinetic analysis which showed first-order dependence on the concentrations of quinoline, HBpin and **2.11$_{Zn}$** (**Figure 2.5**). VTNA was also employed to check if the **2.11$_{Zn}$** catalytic system faces a barrier in the catalytic cycle. For this purpose, two reactions were carried out in the presence of **2.11$_{Zn}$**, with one monitoring consumption of quinoline from the beginning, and the second one from the reaction time mid-point. After performing the time adjustment, it was found the catalytic system suffers from neither catalyst deactivation nor product inhibition (Fig. A69).

Table 2.6. Hydroboration of quinoline using **2.11$_{Zn}$** as pre-catalyst*

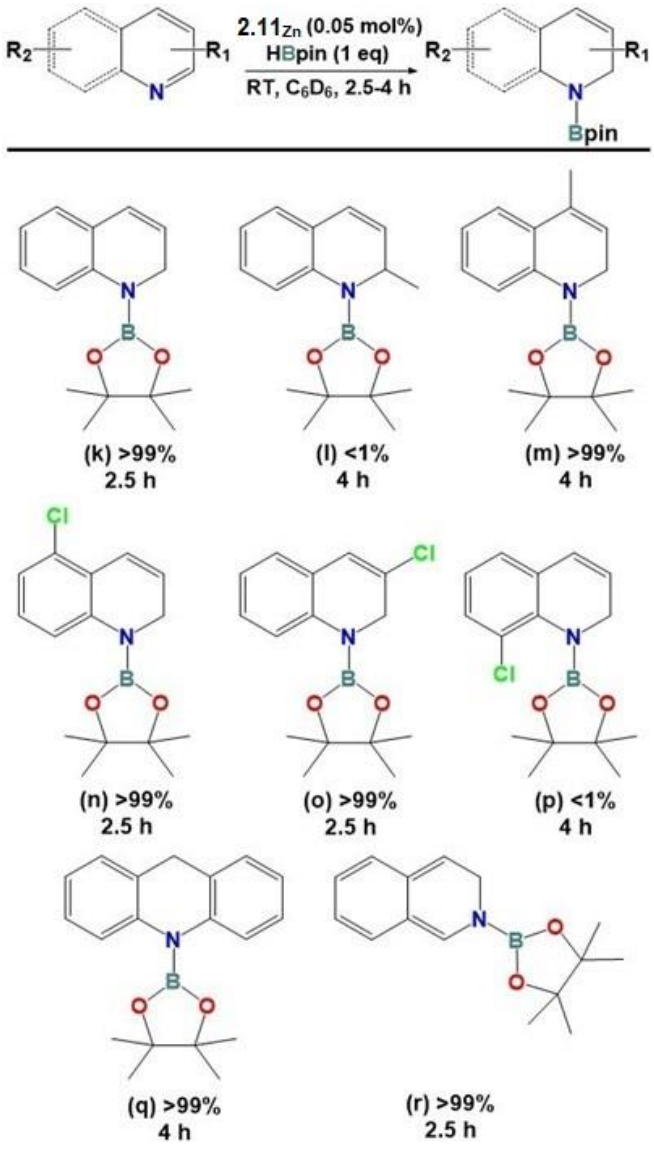

Reaction condition: Quinoline substrate (0.1 mmol), HBpin (0.1 mmol). *Yields were determined by ^{1}H NMR integration vs substrates. Selectivity in all cases was 100% for the reported products.

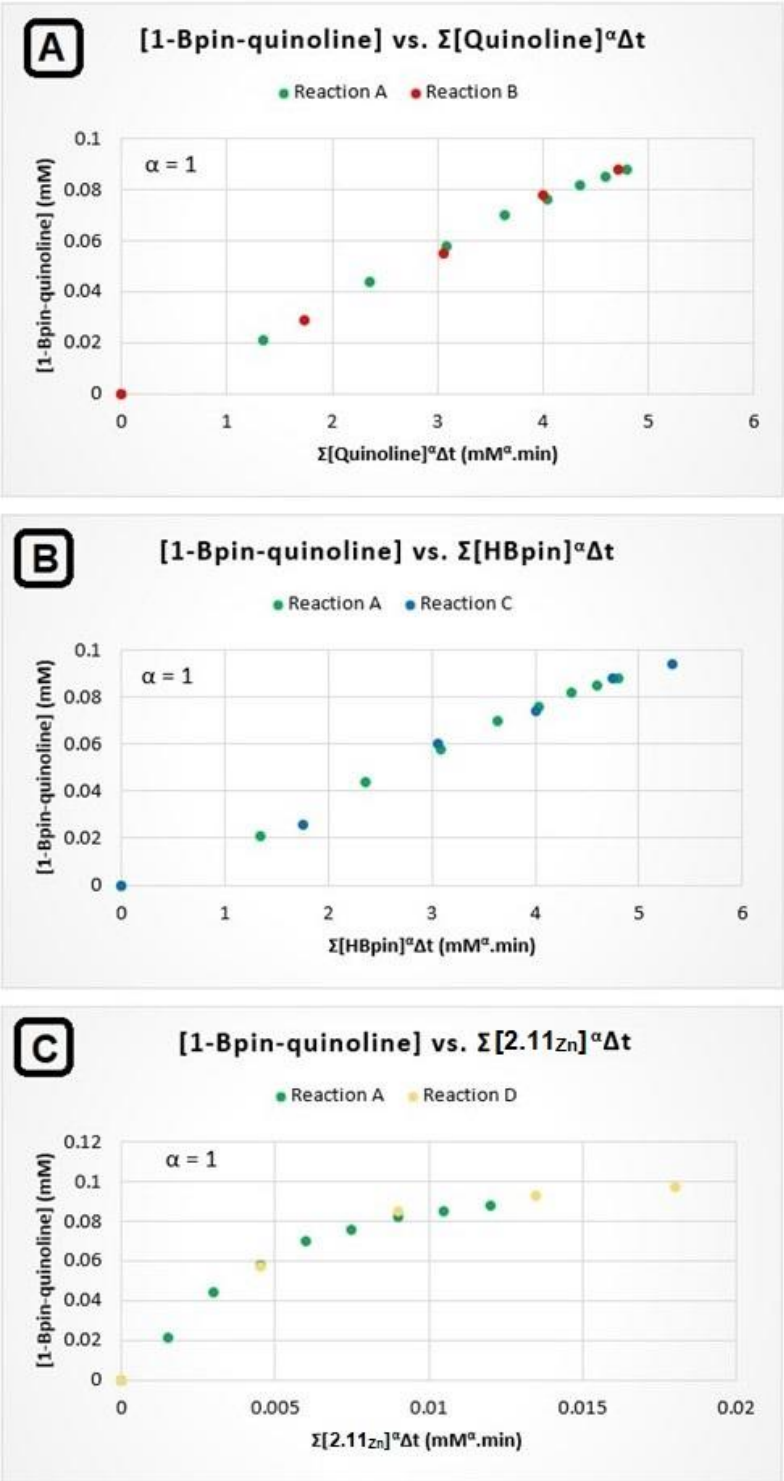

Figure 2.5. $\mathbf{2.11_{Zn}}$-catalyzed quinoline hydroboration kinetic study using VTNA: (A) rate dependence on [quinoline]; (B) rate dependence on [HBpin]; (C) rate dependence on [$\mathbf{2.11_{Zn}}$].

These findings support our experimental results when **2.12$_{Zn}$** was used in a second catalytic run and showed the same efficiency as the first (**Table 2.5**, entry 15). Plotting [1–Bpin-quinoline] vs. the normalized rate components gave k_{obs} = 3325.2 $mM^{-2}min^{-1}$ (Fig. A68).

According to the obtained evidence, a plausible mechanism for quinoline hydroboration using **2.11$_{Zn}$** is shown in **Scheme 2.13**. The first step involves *in-situ* preparation of **2.12$_{Zn}$** (I) through **2.11$_{Zn}$** reacting with 4 equiv of HBpin. Coordination of the quinoline is followed by hydride transfer to C2 forming complex III. After that, another equiv of HBpin adds across the Zn-B bond, affording the product and regenerating the Zn-H catalyst. Although the high catalytic activity of **2.11$_{Zn}$** can be partially attributed to the small size of the DDI ligand, addition of one equiv. of DDI to **2.11$_{Zn}$** still gave an 87% yield of the quinoline hydroboration product after just 3 h with a 0.1 mol% catalyst loading.

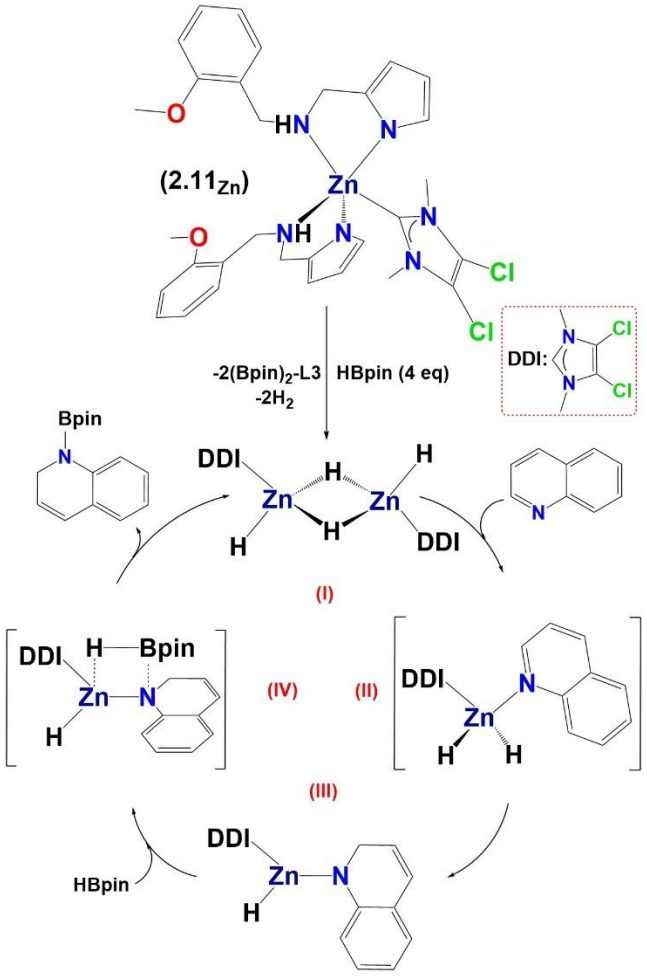

Scheme 2.13. Proposed mechanism for quinoline hydroboration using HBpin and **2.11$_{Zn}$** precatalyst.

2.3.5 Proposed Mechanism of Nitrile Dihydroboration Using 2.11_{Zn}

Based on the above information and a previous report,[18] a plausible inner-sphere mechanism can be proposed for the DDI-zinc dihydride (**2.12_{Zn}**) catalyzed nitrile hydroboration (**Scheme 2.14**).

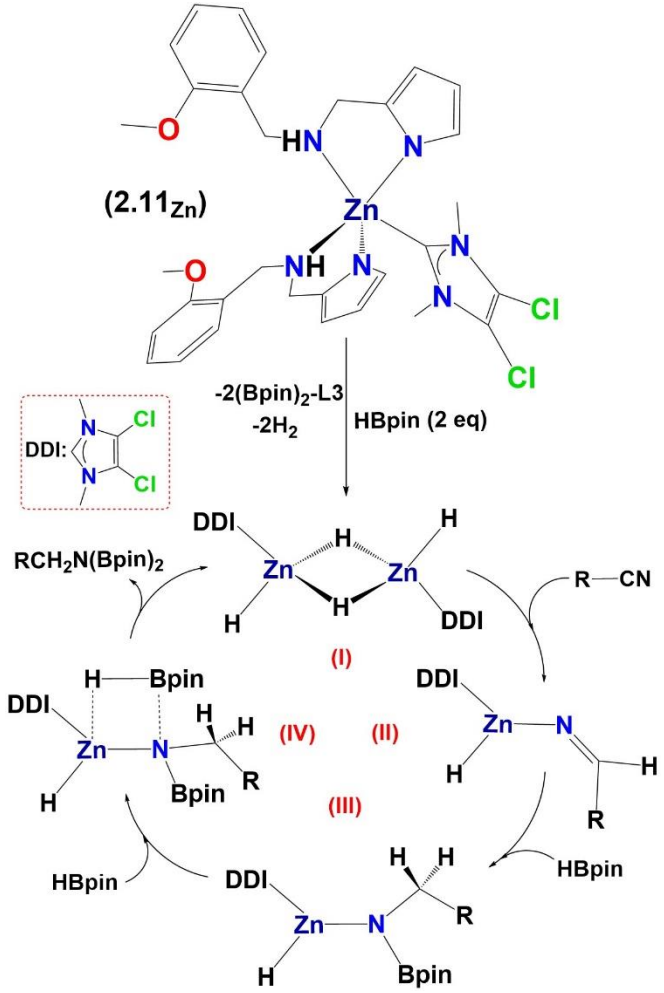

Scheme 2.14. Proposed mechanism for nitrile hydroboration using HBpin and **2.11_{Zn}** precatalyst.

2.4 Conclusions

Zinc dihydride complexes are very active and sustainable catalysts in hydroboration reactions.[18] Our catalyst speciation studies using Zn bis(amido) and -bis(thiolate) SNS complexes (**2.1_{Zn}** and **2.2_{Zn}**) showed that presumed mixtures of ZnH(alkoxide) and Zn(alkoxide)$_2$ are effective catalysts for carbonyl hydroboration as long as there is always substrate present. Depending on the substrate, however, we can imagine that oligomerization of the substrate-derived alkoxide

complexes could also be a liability for the long-term stability of these catalysts. Moreover, our reinvestigation of the Cu amido catalysts, Cu(κ^2-S^{Me}NS^{Me})(IPr) (**2.6$_{Cu}$**) identified an additional liability for the SNS amido ligand which, upon borylation, is no longer an effective bidentate chelating ligand. For the SNS thiolate ligand, hydroboration of the imine backbone was also identified as a source of unwanted reactivity for the Zn bis(thiolate) complex (**2.2$_{Zn}$**). For both Cu and Ag, we have been unable to identify the detailed catalyst speciation using this ligand.

In the last part of this Chapter, we employed bifunctional catalyst activation using an amino-pyrrolide ligand (**L3**) to access a very reactive Zn dihydride catalyst bearing the small DDI NHC ligand that would likely be difficult to prepare directly [vs. formation of $ZnH_2(DDI)_2$ (**2.13$_{Zn}$**)]. Adding the strong donor NHC ligands increases the reactivity of the Zn-H, enabling hydroboration of nitriles and quinolines under ambient conditions at very low catalyst loadings. Moreover, stoichiometric reactions indicated that only one of the two hydrides takes part in the catalytic cycle and our VTNA kinetic studies showed that the **2.11$_{Zn}$** catalytic system faces no challenging deactivation pathways, in accordance with its high activity and reusability. Given the simplicity of the amino-pyrrolide ligand synthesis our MLC catalyst activation strategy may represent a more general strategy by which air-stable metal coordination complexes can access reactive metal hydride catalysts of a variety of E-H functionalization reactions.

2.5 Experimental Section

2.5.1 General Details (2.1$_{Zn}$-2.5$_{Zn}$)

All experiments were carried out under a dry nitrogen atmosphere using Schlenk techniques or an MBraun glovebox unless otherwise stated. Hexane, diethyl ether, and THF were dried on columns of activated alumina using a J. C. Meyer solvent purification system. Benzene-d^6 (C_6D_6) was dried by standing over activated alumina (ca. 10 wt %). All solvents were stored over activated (heated at ca. 250 °C for >10 h under vacuum) 4 Å molecular sieves, except ethanol which was stored over activated 3 Å molecular sieves. Glassware was oven-dried at 160 °C for >1 h. The following chemicals were obtained commercially, as indicated: zinc chloride (Alfa Aesar, 99.98%), Dichloromethane (HPLC grade, ≥99.8%, contains amylene as stabilizer), ethanol (anhydrous, ≤0.005% water) and $LiN[Si(CH_3)_3]_2$ (Sigma Aldrich, 97%). ^{1}H, ^{13}C, ^{11}B, and HSQC NMR spectra were recorded on a 300 MHz Bruker Avance II instrument at room temperature. ^{1}H

and $^{13}C\{^{1}H\}$ NMR spectra were referenced to residual protons and solvent carbons (C_6D_6, δ 7.13, 127.66 ppm; $CDCl_3$, δ 7.26, 77.02 ppm). Proligands (**HL1**)[7] and (**HL2**)[9] and Zn bis(alkoxide) complex **2.5**$_{Zn}$[23] were prepared according to literature procedures. For electron impact (EI), solid samples were prepared by drying products under vacuum, and spectra obtained using a Kratos Concept S1 instrument (Hres 7000−10000). X-ray diffraction data were collected on a Bruker Smart or Kappa diffractometer equipped with an ApexII CCD detector and a sealed-tube Mo K source (λ = 0.71073 Å). EI-MS data were collected using a Kratos Concept S1 instrument.

2.5.2 Synthesis and Characterization

2.5.2.1 Preparation of [Zn(κ^2-S^{Me}NS^{Me})$_2$], (**2.1**$_{Zn}$)

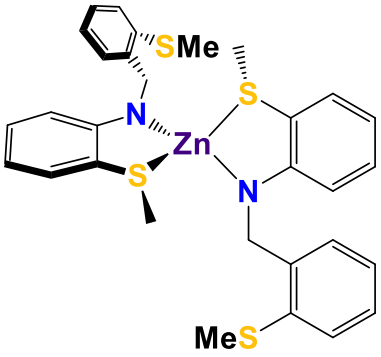

A 42 mL vial was charged with 2-(2-methylthiobenzyl)-methylthioaniline, [S^{Me}N^{H}S^{Me}] (0.201 g, 0.732 mmol), LiN[Si(CH$_3$)$_3$]$_2$ (0.122 g, 0.732 mmol) and 15 mL of THF, and then a solution of $ZnCl_2$ (0.05 g, 0.366 mmol, in 5 mL of THF) was added gradually, which resulted in a yellowish solution. The resulting solution was stirred overnight at room temperature. Afterward, the solution was pumped off under vacuum. The complex was extracted into benzene and then filtered. After removing the benzene under vacuum the resulting precipitate was washed with diethyl ether multiple times and then crystallized from DCM at -35 °C. The crystalline product was then filtered and dried in vacuo. Yield: 0.156 g, 69% based on $ZnCl_2$. Crystals of **2.1**$_{Zn}$ suitable for X-ray crystallography were obtained by layering a DCM solution of **2.1**$_{Zn}$ with hexane.

^{1}H NMR (300 MHz, $CDCl_3$ at 25 °C): δ 2.18 (s, 6H, S−Me), 2.43 (s, 6H, S−Me), 4.19 (s, 4H, N-CH_2), 6.34 (m, 4H, Ar−H), 6.91 (td, 2H, Ar−H), 7.12 (m, 8H, Ar−H), 7.3 (dd, 2H, Ar−H). **^{13}C{^{1}H} NMR (75 MHz, $CDCl_3$, 25 °C,):** δ 15.1 (s, 2C, S–*C*H3); 21.9 (s, 2C, S–*C*H3); 51.4 (s, 2C, N–*C*H2); 111.0 (s, 2C, ArSNS–*C*); 111.7 (s, 2C, ArSNS–*C*); 113.6 (s, 2C, ArSNS–*C*); 124.3 (s, 2C, ArSNS–*C*); 124.5 (s, 2C, ArSNS–*C*); 127.4 (s, 2C, ArSNS–*C*); 128.0 (s, 2C, ArSNS–*C*); 131.9 (s, 2C, ArSNS–*C*); 135.0 (s, 2C, ArSNS–*C*); 137.4 (s, 2C, ArSNS–*C*); 138.7 (s, 2C, ArSNS–*C*); 156.5 ppm (s, 2C, ArSNS–*C*) (Figures A1 and A2).

2.5.2.2 Preparation of [Zn(κ^2-SNS^{Me})$_2$], (**2.2$_{Zn}$**)

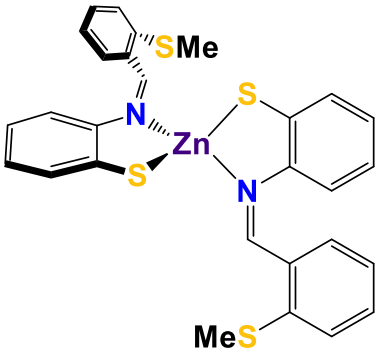

A 42 mL vial was charged with 2-(2-methylthiophenyl)-benzothiazolidine, [S^{H}NS^{Me}] (0.190 g, 0.732 mmol), LiN[Si(CH$_3$)$_3$]$_2$ (0.122 g, 0.732 mmol) and 15 mL of THF, and then a solution of [ZnCl$_2$] (0.05 g, 0.366 mmol, in 5 mL of THF) was added gradually, giving a red solution. The resulting solution was stirred overnight at room temperature, yielding a red precipitate that was filtered, washed with THF (2 times) and diethyl ether (multiple times) and then recrystallized from hot THF. Finally, the recrystallized product was filtered and dried under vacuum. Yield: 0.158 g, 74% based on [ZnCl$_2$]. Crystals of **2.2$_{Zn}$** suitable for X-ray crystallography were obtained by layering a DCM solution of **2.2$_{Zn}$** with hexane.

^{1}H NMR (300 MHz, CDCl$_3$ at 25 °C): δ 2.47 (s, 6H, S−Me), 6.49 (td, 2H, Ar−H), 7.02 (m, 6H, Ar−H), 7.28 (m, 4H, Ar−H), 7.44 (dd, 2H, Ar−H), 7.61 (dd, 2H, Ar−H), 9.06 (s, 2H, N=CH). **^{13}C{^{1}H} NMR (75 MHz, CDCl$_3$, 25 °C):** 17.1 (s, 2C, S–*C*H3); 119.2 (s, 2C, ArSNS–*C*); 122.7 (s, 2C, ArSNS–*C*); 125.4 (s, 2C, ArSNS–*C*); 127.5 (s, 2C, ArSNS–*C*); 128.7 (s, 2C, ArSNS–*C*); 129.5 (s, 2C, ArSNS–*C*); 132.9 (s, 2C, ArSNS–*C*); 133.0 (s, 2C, ArSNS–*C*); 133.7 (s, 2C, ArSNS–*C*); 141.4 (s, 2C, ArSNS–*C*); 144.4 (s, 2C, ArSNS–*C*); 146.4 (s, 2C, ArSNS–*C*); 163.1 ppm (s, 2C, N=*C*) (Figures A3 and A4).

2.5.2.3 Preparation of [Zn(κ^2-S^{Me}N$^-$S^{Me})(κ^2-S$^-$NS^{Me})], **2.4$_{Zn}$**

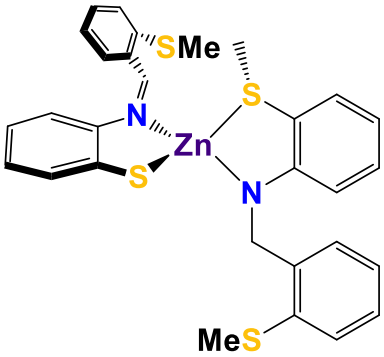

A 42 mL vial was charged with ZnCl$_2$ (0.138 g, 1.016 mmol) in 5 mL of THF and then a solution of 2-(2-methylthiobenzyl)-methylthioaniline, [S^{Me}N^{H}S^{Me}] (0.280 g, 1.016 mmol) and LiN[Si(CH$_3$)$_3$]$_2$ (0.170 g, 1.016 mmol) in 15 mL of THF was added gradually, giving a yellowish solution. The resulting solution was stirred for 3 h at room temperature. Then a solution of 2-(2-methylthiophenyl)benzothiazolidine, [S^{H}NS^{Me}] (0.263 g, 1.016 mmol) and LiN[Si(CH$_3$)$_3$]$_2$ (0.170 g, 1.016 mmol) in 15 mL of THF was added, yielding an orange solution with precipitate

after 1 h. The mixture was stirred for 2 h and t filtered, washed with DEE and dried under vacuum. Yield: 0.458 g, 75% based on $ZnCl_2$. Crystals of **2.4$_{Zn}$** suitable for X-ray crystallography were obtained by layering a DCM solution of **2.4$_{Zn}$** with hexane.

^{1}H NMR (300 MHz, $CDCl_3$, 25 °C): δ 2.27 (s, 3H, S−Me), 2.35 (s, 3H, S−Me), 2.52 (s, 3H, S−Me) 4.06 (dd, 2H, N-CH_2), 6.29 (td, 1H, Ar−H), 6.43 (dd, 1H, Ar−H), 6.84 (td, 1H, Ar−H), 7.02 (m, 7H, Ar−H), 7.16 (dt, 2H, Ar−H), 7.29 (m, 2H, Ar−H), 7.45 (d, 2H, Ar−H). **^{13}C{^{1}H} NMR (75 MHz, $CDCl_3$, 25 °C):** 15.6 (s, 1C, S–*C*H3); 16.9 (s, 1C, S–*C*H3); 22.3 (s, 1C, S–*C*H3); 51.5 (s, 1C, N–*C*H2); 111.4 (s, 1C, ArSNS–*C*); 111.5 (s, 1C, ArSNS–*C*); 114.2 (s, 1C, ArSNS–*C*); 119.0 (s, 1C, ArSNS–*C*); 122.7 (s, 1C, ArSNS–*C*); 124.8 (s, 1C, ArSNS–*C*); 125.4 (s, 1C, ArSNS–*C*); 125.5 (s, 1C, ArSNS–*C*); 126.8 (s, 1C, ArSNS–*C*); 127.8 (s, 1C, ArSNS–*C*); 128.6 (s, 1C, ArSNS–*C*); 129.0 (s, 1C, ArSNS–*C*); 129.5 (s, 1C, ArSNS–*C*); 132.0 (s, 1C, ArSNS–*C*); 132.3 (s, 1C, ArSNS–*C*); 132.8 (s, 1C, ArSNS–*C*); 133.3 (s, 1C, ArSNS–*C*); 135.4 (s, 1C, ArSNS–*C*); 138.2 (s, 1C, ArSNS–*C*); 138.7 (s, 1C, ArSNS–*C*); 141.4 (s, 1C, ArSNS–*C*); 143.4 (s, 1C, ArSNS–*C*); 146.5 (s, 1C, ArSNS–*C*); 156.1 (s, 1C, ArSNS–*C*); 161.8 ppm (s, 1C, N=*C*) (Figures A5 and A6).

2.5.3 Catalysis protocols (2.1$_{Zn}$-2.5$_{Zn}$)

A stock solution of **2.4$_{Zn}$** was prepared by dissolving 5.9 mg **2.4$_{Zn}$** in 5 mL of C_6D_6. A vial containing appropriate amount of catalyst [**2.1$_{Zn}$** (6.1 mg, 1mol%), **2.2$_{Zn}$** (5.8 mg, 1mol%), **2.4$_{Zn}$** (5.9 mg, 1mol%), or 0.5 mL of stock solution of **2.4$_{Zn}$** (0.59 mg, 0.1 mol%)], was charged with 0.5 mL C_6D_6, 1.00 mmol of carbonyl substrate (102 µL of benzaldehyde, 116 µL of acetophenone), and subsequently with 1.00 mmol of pinacolborane (145 µL), resulting in a color change from red **2.2$_{Zn}$**, pale-yellow **2.1$_{Zn}$** or orange **2.4$_{Zn}$** to colorless. The rate of color change for **2.4$_{Zn}$** was extremely fast, for **2.1$_{Zn}$** was relatively fast, and for **2.2$_{Zn}$** was slow. The solution was charged to an NMR tube for further analysis. Reaction times varied slightly from 5-30 minutes. Yield was determined by ^{1}H NMR in reference to internal standard mesitylene.

Hydroboration of benzaldehyde

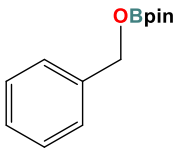

Following the general procedure, benzaldehyde (101.7 µl, 1.00 mmol), pinacolborane (144.5 µL, 1.00 mmol), and either **2.1$_{Zn}$** (6.1 mg, 1 mol%), or **2.2$_{Zn}$** (5.8 mg, 1 mol%), or **2.4$_{Zn}$** (5.9 mg, 1mol%) were used. ^{1}H NMR showed quantitative conversion to hydroboration product after 5 min for **2.1$_{Zn}$** and **2.2$_{Zn}$**, and 15 seconds

for **2.4$_{Zn}$** at room temperature. ^{11}B and ^{1}H NMR shifts matched with literature values.[4] (Figure A17)

Hydroboration of 4-trifluoromethylbenzaldehyde

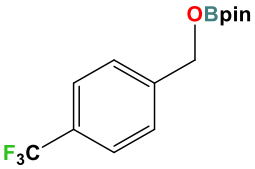

Following the general procedure, 4-Trifluoromethylbenzaldehyde (136.5 µL, 1.00 mmol), pinacolborane (144.5 µl, 1.00 mmol), and either **2.1$_{Zn}$** (6.1 mg, 1 mol%), or **2.2$_{Zn}$** (5.8 mg, 1 mol%) were used. ^{1}H NMR showed quantitative conversion to hydroboration product after 5 min, at room temperature. (Figure A18)

Hydroboration of cinnamaldehyde

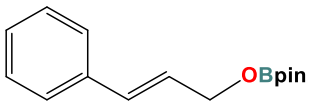

Following the general procedure, cinnamaldehyde (125.8 µl, 1.00 mmol), pinacolborane (144.5 µL, 1.00 mmol), and either **2.1$_{Zn}$** (6.1 mg, 1 mol%), or **2.2$_{Zn}$** (5.8 mg, 1 mol%) were used. ^{1}H NMR showed quantitative conversion to hydroboration product after 5 min at room temperature. (Figure A19)

Hydroboration of acetophenone

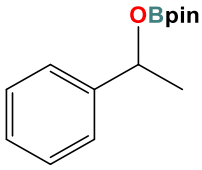

Following the general procedure, acetophenone (116 µL, 1.00 mmol), pinacolborane (144.5 µL, 1.00 mmol), and either **2.1$_{Zn}$** (6.1 mg, 1 mol%), or **2.2$_{Zn}$** (5.8 mg, 1 mol%), or **2.4$_{Zn}$** (5.9 mg, 1mol%), or 0.5 mL of stock solution of **2.4$_{Zn}$** (0.59 mg, 0.1 mol%) were used. ^{1}H NMR showed quantitative conversion to hydroboration product after 25 min for **2.1$_{Zn}$** and **2.2$_{Zn}$**, 15 seconds for **2.4$_{Zn}$** (1 mol%), and 16 min for **2.4$_{Zn}$** (0.1 mol%) at room temperature. ^{11}B and ^{1}H NMR shifts matched with literature values.[4] (Figure A20)

Hydroboration of 5-hexen-2-one

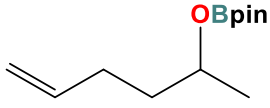

Following the general procedure, 5-hexen-2-one (115.8 µL, 1.00 mmol), pinacolborane (144.5 µL, 1.00 mmol), and either **2.1$_{Zn}$** (6.1 mg, 1 mol%), or **2.2$_{Zn}$** (5.8 mg, 1 mol%) were used. ^{1}H NMR showed quantitative conversion to hydroboration product after 20 min, at room temperature. (Figure A21)

Hydroboration of benzophenone

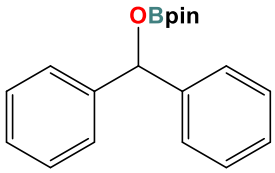

Following the general procedure, benzophenone (182 mg, 1.00 mmol), pinacolborane (144.5 µL, 1.00 mmol), and either **2.1**$_{Zn}$ (6.1 mg, 1 mol%), or **2.2**$_{Zn}$ (5.8 mg, 1 mol%) were used. ^{1}H NMR showed quantitative conversion to hydroboration product after 28 min, at room temperature. (Figure A22)

Hydroboration of 1-adamantyl methyl ketone

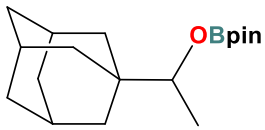

Following the general procedure, cinnamaldehyde (178 mg, 1.00 mmol), pinacolborane (144.5 µL, 1.00 mmol), and either **2.1**$_{Zn}$ (6.1 mg, 1 mol%), or **2.2**$_{Zn}$ (5.8 mg, 1 mol%) were used. ^{1}H NMR showed quantitative conversion to hydroboration product after 25 min, at room temperature. (Figure A23)

2.5.4. Mechanistic Studies

2.5.4.1 Stoichiometric reaction of 2.1$_{Zn}$ with HBpin: Formation of Bpin-L1

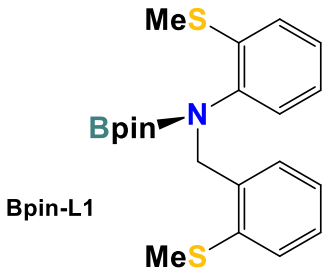

Bpin-L1

A pale-yellow solution of **2.1**$_{Zn}$ (0.05 g, 0.08 mmol) in C_6D_6 was charged with pinacolborane (11.5 µL, 0.08 mmol), resulting in a fast color change to almost colorless. The crude ^{1}H NMR spectrum showed half of **2.1**$_{Zn}$ was consumed into a new compound and half remained as **2.1**$_{Zn}$, and also a light grey precipitate was formed. In another attempt, the ratio of pinacolborane was increased to 2 equiv (23 µL, 0.16 mmol) and full consumption was observed. The light grey precipitate was filtered off and the filtrate evaporated slowly. After 2 days colorless crystals were formed. The ^{1}H and ^{11}B NMR spectra and X-ray diffraction study revealed the product to be **Bpin-L1** (Figures A7 and A8).

^{1}H NMR (300 MHz, C_6D_6 at 25 °C): δ 1.17 (s, 12H, Bpin Me), 1.83 (s, 3H, S−Me), 1.97 (s, 3H, S−Me), 5.07 (s, 2H, N-CH_2), 6.68 (td, 1H, Ar−H), 6.80 (td, 1H, Ar−H), 6.88 (dd, 1H, Ar−H), 6.96 (m, 3H, Ar−H), 7.03 (dd, 1H, Ar−H), 7.62 (m, 1H, Ar−H). **^{11}B{^{1}H} NMR (96 MHz, C_6D_6, 25 °C,):** 24.1 ppm (s).

2.5.4.2 Stoichiometric reaction of 2.2_{Zn} with HBpin: Formation of (2.3_{Zn})

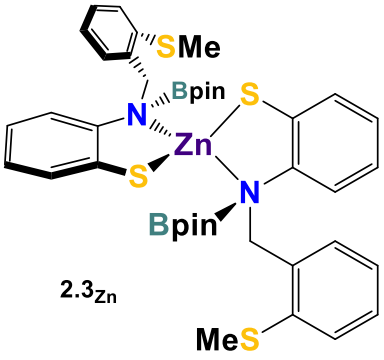

2.3_{Zn}

A red suspension of **2.2_{Zn}** (0.05 g, 0.085 mmol) in C_6D_6 was charged with pinacolborane (12.5 µL, 0.085 mmol), giving a homogeneous light orange solution after 3 h. The crude ^{1}H NMR spectrum showed half of **2.2_{Zn}** was converted into a new species and half remained as **2.2_{Zn}**. In another attempt, the ratio of pinacolborane was increased to 2 equiv (25 µL, 0.17 mmol) giving a very slow color change to colorless, and full consumption of **2.2_{Zn}** was monitored by ^{1}H NMR. After complete conversion, the solvent was removed under vacuum and the residue washed with hexane and filtered. The high temperature ^{1}H NMR of the solution at 50 °C revealed a new species **2.3_{Zn}** (Figure A9). **2.3_{Zn}** was also characterized by ^{13}C and ^{11}B NMR (Figures A10 and A11). All attempts at growing a crystal of **2.3_{Zn}** were unsuccessful.

^{1}H NMR (300 MHz, C_6D_6 at 45 °C): δ 1.24 (s, 24H, Bpin Me), 2.00 (s, 6H, S−Me), 4.91 (s, 4H, N-CH_2), 6.68 (m, 4H, Ar−H), 6.83 (m, 6H, Ar−H), 6.98 (m, 4H, Ar−H), 7.75 (s, 2H, Ar−H). **^{13}C{^{1}H} NMR (75 MHz, C_6D_6, 45 °C):**15.9 (S-Me); 24.3 (Bpin Me); 50.3 (N-CH_2); 82.4 (Bpin); 110.9 (ArSNS–*C*); 118.5 (ArSNS–*C*); 124.5 (ArSNS–*C*); 125.5 (ArSNS–*C*); 127.0 (ArSNS–*C*); 129.9 (ArSNS–*C*); 130.9 (ArSNS–*C*); 134.6 (ArSNS–*C*); 136.1 (ArSNS–*C*); 137.1 (ArSNS–*C*); 144.5 ppm (ArSNS–*C*). **^{11}B{^{1}H} NMR (96 MHz, C_6D_6, 45 °C):** 21.1 ppm. **EI-MS** showed (**Bpin-H-L2**)$^+$ Calc'd for [$C_{21}H_{27}BNO_2S_2$] 387.15, Found 387.2 (Figure A12).

2.5.4.3 Stoichiometric reaction of 2.3_{Zn} with benzaldehyde: Formation of S-P1

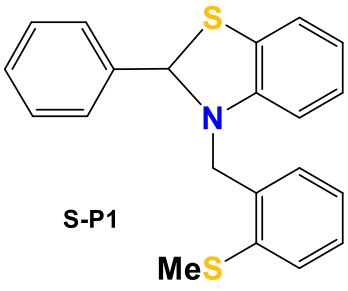

S-P1

After the reaction mentioned in section 4.2 (1 equiv of **2.2_{Zn}** and 2 equiv of pinacolborane in C_6D_6) became colorless and **2.3_{Zn}** was formed, 2 equiv of benzaldehyde (17.2 µL, 0.17 mmol) was added to the reaction mixture, resulting immediately in a pale yellow solution. After 3 h the solvent was evaporated under vacuum and the residue was washed with hexane and filtered. ^{1}H NMR of both solid and filtrate showed no hydroborated product, but the latter showed a new product is formed (**S-P1**). The product was isolated using

column chromatography and characterized by ^{1}H and ^{13}C NMR, and X-ray crystallography (Figures A13 and A14)

^{1}H NMR (300 MHz, $CDCl_3$ at 25 °C): δ 2.45 (s, 3H, S-Me), 4.31 (q, 2H, N-CH_2), 6.24 (s, 1H, N-CHR-S), 6.29 (dd, 1H, Ar−H), 6.73 (td, 1H, Ar−H), 6.96 (td, 1H, Ar−H), 7.11 (m, 2H, Ar−H); 7.30 (m, 6H, Ar−H), 7.48 (m, 2H, Ar−H). **$^{13}C\{^{1}H\}$ NMR (75 MHz, $CDCl_3$, 25 °C):** 15.8 (S-Me); 48.5 (N-CH_2); 74.3 (N-C-S); 107.7 (ArSNS–*C*); 119.1 (ArSNS–*C*); 121.4 (ArSNS–*C*); 125.0 (ArSNS–*C*); 125.5 (ArSNS–*C*); 125.7 (ArSNS–*C*); 125.7 (ArSNS–*C*); 127.2 (ArSNS–*C*); 127.3 (ArSNS–*C*); 127.7 (ArSNS–*C*); 128.7 (ArSNS–*C*); 128.9 (ArSNS–*C*); 134.3 (ArSNS–*C*); 136.9 (ArSNS–*C*); 140.3 (ArSNS–*C*); 147.0 ppm (ArSNS–*C*).

2.5.4.4 Stoichiometric reaction of 2.3$_{Zn}$ with cinnamaldehyde: Formation of S-P2

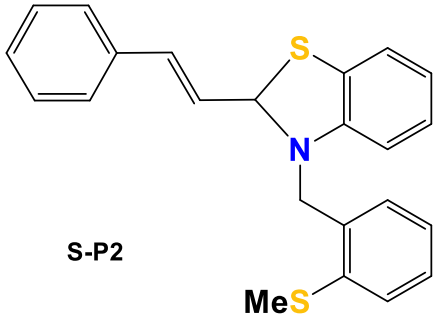

S-P2

After the reaction mentioned in section 4.2 (1 equiv of **2.2$_{Zn}$** and 2 equiv of pinacolborane in C_6D_6) became colorless and **2.3$_{Zn}$** was formed, 2 equiv of cinnamaldehyde (21.4 μL, 0.17 mmol) was added to the reaction mixture, resulting immediately in a very pale yellow solution. After 3 h the solvent was evaporated under vacuum and the residue was washed with hexane and filtered. ^{1}H NMR of both solid and filtrate showed no hydroboration product, but the latter showed a new product is formed (**S-P2**). The product was isolated using column chromatography and characterized by ^{1}H and ^{13}C NMR (Figures A15 and A16).

^{1}H NMR (300 MHz, $CDCl_3$ at 25 °C): δ 2.45 (s, 3H, S-Me), 4.40 (s, 2H, N-CH_2), 5.80 (dd, 1H, N-CHR-S), 6.26 (dd, 1H, Ar−H), 6.44 (m, 2H, Ar−H), 6.68 (td, 1H, Ar−H), 6.91 (td, 1H, Ar−H), 7.07 (dd, 1H, Ar−H), 7.14 (m, 1H, Ar−H), 7.30 (m, 7H, Ar−H). **$^{13}C\{^{1}H\}$ NMR (75 MHz, $CDCl_3$, 25 °C,):** 15.1 (S-Me); 48.5 (N-CH_2); 73.1 (N-C-S); 107.8 (ArSNS–*C*); 118.9 (ArSNS–*C*); 121.8 (ArSNS–*C*); 125.0 (ArSNS–*C*); 125.0 (ArSNS–*C*); 125.6 (ArSNS–*C*); 125.7 (ArSNS–*C*); 126.89 (ArSNS–*C*); 127.0 (ArSNS–*C*); 127.4 (ArSNS–*C*); 127.8 (ArSNS–*C*); 128.2 (ArSNS–*C*); 128.6 (ArSNS–*C*); 129.6 (ArSNS–*C*); 132.3 (ArSNS–*C*); 135.8 (ArSNS–*C*); 137.0 (ArSNS–*C*); 146.8 ppm (ArSNS–*C*).

2.5.4.5 Stoichiometric reaction of 2.4_{Zn} with benzaldehyde and HBpin

In order to find out which one of **L1** and **L2** plays the dominant role in catalysis, an orange suspension of **2.4_{Zn}** (0.01 g, 0.017 mmol) in C_6D_6 was charged with benzaldehyde (3.4 μL, 0.034 mmol), and then pinacolborane (2.5 μL, 0.017 mmol) was added, giving a homogeneous light orange solution after 3-5 min. The crude ^{1}H NMR spectrum showed presence of free benzaldehyde, hydroborated benzaldehyde, **Bpin-L1** and **S-P1**. After addition of the second equivalent of pinacolborane, the ^{1}H-NMR spectrum showed hydroborated benzaldehyde, **Bpin-L1** and **S-P1** (Figure A26).

2.5.4.6 Monitoring Acetophenone Hydroboration Reactions Using Zinc Complexes

To monitor the reaction progress, a vial was charged with acetophenone (116 μL, 1.00 mmol) and either **2.1_{Zn}** (6.1 mg, 1 mol%), **2.2_{Zn}** (5.8 mg, 1 mol%), or **2.4_{Zn}** (5.9 mg, 1 mol%), or 0.5 mL of stock solution of **2.4_{Zn}** (0.59 mg, 0.1 mol%), then 0.3 mL of C_6D_6 was added and the solution transferred to an NMR tube and capped with a rubber septum. Another vial was charged with pinacolborane (144.5 μL, 1.00 mmol) and 0.3 mL C_6D_6, and the solution was transferred to a 1 mL syringe. Then, the syringe was capped by poking into the rubber septum. The NMR tube containing the reaction mixture and the syringe were removed from the glovebox. The HBpin was injected into the NMR tube, shaken quickly, and immediately inserted into the NMR spectrometer. A ^{1}H NMR spectrum was taken every 15-25 sec for 25 min at room temperature. Concentration of the product was calculated based on the characteristic signals of the product and acetophenone.

For the reactions carried out in THF, the conditions and procedures are the same but the solvent was THF intead of C_6D_6, and the concentration of the product was calculated based on the characteristic signals of the product and HBpin by ^{11}B NMR.

2.5.5 X-ray Diffraction Data (2.1_{Zn}, 2.2_{Zn} and 2.4_{Zn})

Crystallographic data were collected from single crystals mounted on MiTeGen dual thickness MicroMounts using Parabar oil. Data were collected on a Bruker Smart ApexII single crystal diffractometer equipped with a graphite monochromator. The instrument was equipped with a sealed tube Mo Kα source ($\lambda = 0.71073$ Å), an ApexII CCD detector and a dry compressed air-cooling system. All samples were cooled to 203(2) K during data collection. Raw data

collection and processing were performed with the Apex3 software package from Bruker.[42] Initial unit cell parameters were determined from 36 data frames from select $\boldsymbol{\omega}$ scans. Semi-empirical absorption corrections based on equivalent reflections were applied.[43] Systematic absences in the diffraction data-set and unit-cell parameters were consistent with the assigned space group. The initial structural solutions were determined using ShelxT direct methods,[44] and refined with full-matrix least-squares procedures based on $\boldsymbol{F^2}$ using ShelXL or ShelXle.[45] Compound **Bpin-L1** exhibited minor positional disorder which was refined in ShelXle. Hydrogen atoms were placed geometrically and refined using a riding model.

2.5.6 General considerations ($\mathbf{2.7_{Ag}}$, $\mathbf{2.8_{Zn}}$-$\mathbf{2.12_{Zn}}$)

All experiments were carried out under dinitrogen, using an MBraun glovebox unless otherwise stated. Diethyl ether, toluene and THF were dried on columns of activated alumina using a J. C. Meyer (formerly Glass Contour) solvent purification system. Anhydrous C_6D_6 were dried with activated alumina (ca. 10 wt %) overnight, followed by filtration. $CDCl_3$ was stored over activated 4 Å molecular sieves (heated at 250 ^oC for 24 h under vacuum). Anhydrous ethanol and DCM were purchased from Aldrich and used as obtained. 4,5-dichloro-1,3-dimethyl-1H-imidazol-3-ium iodide[41] was prepared according to literature procedures. Other chemicals were used as obtained commercially: CuCl(IPr), AgCl(IPr) and AuCl(IPr) (Sigma Aldrich), triethoxysilane (Sigma Aldrich, 95%), pinacolborane (Sigma Aldrich, 97%), $LiN[Si(CH_3)_3]_2$ (Sigma Aldrich, 97%), 2-methoxybenzylamine (Sigma Aldrich, 98%), Pyrrole-2-carboxaldehyde (Alfa Aesar, 99%), Sodium borohydride (Sigma Aldrich, >98%), Potassium tert-butoxide (Sigma Aldrich, >98%) and 1M diethyl zinc (1.0 M in hexane, Sigma Aldrich) and $NaN[Si(CH_3)_3]_2$ (Sigma Aldrich, 95%). ^1H, $^{13}C\{^1H\}$ and ^{11}B NMR spectra were recorded on a 300 MHz Bruker Avance or Avance II instrument at room temperature (21−25 °C). ^1H NMR spectra were referenced respectively to solvent residual protons (C_6D_6, δ 7.15; $CDCl_3$, δ 7.26), ^{13}C to solvent resonances and ^{11}B to external $F_3B{\bullet}OEt_2$ at 0 ppm. Proligand **HL1** was prepared according to literature procedures.[7] Mass spectra were recorded on an AB Sciex Q1MS mass spectrometer with electrospray ionization (ESIMS) in positive mode (ion spray voltage, 5000.0 V; TEM, 400 °C; declustering potential, 11.00 V; focusing potential, 300.0 V) with samples prepared to ca. 0.05 mg/mL in acetonitrile or dichloromethane. For electron impact (EI), solid samples were prepared by drying products under vacuum, and spectra obtained using a Kratos Concept S1 instrument (Hres 7000−10000). X-ray

diffraction data were collected on a Bruker Smart or Kappa diffractometer equipped with an ApexII CCD detector and a sealed-tube Mo K source (λ = 0.71073 Å).

2.5.7 Synthesis of $\mathbf{2.7_{Ag}}$

A 42 mL glass vial was charged with AgCl(IPr) (200 mg, 0.376 mmol) and 5 mL of THF. To this solution was added dropwise a solution containing **HL1** (103 mg, 0.376 mmol) and NaHMDS (69 mg, 0.376 mmol) in 5 mL of THF. The final solution turned colorless immediately and was stirred for 6 h. The solvent was then evaporated under vacuum and the product extracted with DCM (2 × 3 mL). The DCM was evaporated under vacuum and the resulting residue was washed with hexane (3 × 3 mL) and filtered, giving 255 mg of $\mathbf{2.7_{Ag}}$ as a white powder (88%). Crystals suitable for X-ray crystallography were grown by hexane layering of a concentrated DCM solution of $\mathbf{2.7_{Ag}}$ after 3 days. ^{1}H NMR (300 MHz, $CDCl_3$): δ 1.25 (d, 12H, CH(C*H*$_3$)$_2$, $^{3}J_{HH}$ = 6.5 Hz); 1.31 (d, 12H, CH(C*H*$_3$)$_2$, $^{3}J_{HH}$ = 6.5 Hz); 2.38 (s, 3H, SC*H*$_3$); 2.54 (s, 3H, SC*H*$_3$); 2.57 (sept, 4H, C*H*(Me)$_2$, $^{3}J_{HH}$ = 6.5 Hz); 4.47 (s, 2H, N-C*H*$_2$); 6.59 (dd, 1H, Ar–*H*, $^{3}J_{HH}$ = 8 Hz, $^{4}J_{HH}$ = 1 Hz); 6.68 (ddd, 1H, Ar–*H*, $^{3}J_{HH}$ = 7.5, $^{4}J_{HH}$ = 1 Hz); 7.17 (d, 4H, Ar–*H*); 7.24 (dd, 1H, Ar–*H*, $^{3}J_{HH}$ = 1.5 Hz, $^{4}J_{HH}$ = 1 Hz); 7.31 (s, 2H, Ar–*H*); 7.34 (ov mult, 4H, Ar–*H*); 7.45 (dd, 1H, Ar–*H*, $^{3}J_{HH}$ = 7.5, 7.5, $^{4}J_{HH}$ = 1.5 Hz); 7.53 (ov mult, 3H, Ar–*H*, $^{3}J_{HH}$ = 8, 8 Hz). ^{13}C{^{1}H} NMR ($CDCl_3$, 25 °C, 300 MHz): δ 16.0 (s, 1C, S*C*H$_3$); 18.4 (s, 1C, S*C*H$_3$); 24.0 (s, 4C, CH*C*H$_3$); 24.8 (s, 4C, CH*C*H$_3$); 28.8 (s, 4C, *C*HCH$_3$); 45.9 (s, 1C, N*C*H$_2$); 110.5 (s, 1C, Ar–C); 114.4 (s, 1C, Ar–C); 117.2 (s, 1C, Ar–C); 120.0 (s, 2C, H*C*=*C*H); 120.6 (s, 1C, ArC); 123.7 (s, 1C, ArC); 123.8 (s, 1C, ArC); 124.2 (s, 1C, ArC); 125.1 (s, 1C, ArC); 126.0 (s, 1C, ArC); 127.7 (s, 1C, ArC); 127.9 (s, 1C, Ar–C); 129.5 (s, 1C, Ar–C); 130.9 (s, 1C, Ar–C); 134.2 (s, 1C, Ar–C); 134.4 (s, 1C, Ar–C); 145.1 (s, 1C, Ar–C); 157.2 (s, 1C, Cu*C*). EI-MS $[M–H]^+$ 770.3221, Calc'd 770.2760 (Fig. A32).

2.5.8 Stoichiometric Reaction of $\mathbf{2.6_{Cu}}$ with HBpin

A pale-yellow solution of $\mathbf{2.6_{Cu}}$ (0.01 g, 0.014 mmol) in C_6D_6 was charged with pinacolborane (0.002 g, 2 µl, 0.014 mmol), resulting in an immediate color change to deep yellow. The crude ^{1}H NMR spectrum showed complete consumption of $\mathbf{2.6_{Cu}}$ into $[CuH(IPr)]_2$ and **Bpin-L1**.

2.5.9 Stoichiometric Reaction of 2.7_{Ag} with HBpin

A colorless solution of **2.7_{Ag}** (0.01 g, 0.014 mmol) in C_6D_6 was charged with pinacolborane (0.002 g, 2 μl, 0.014 mmol), resulting in an immediate color change to black which became a colorless solution with insoluble black precipitate. The crude ^{1}H NMR spectrum showed complete conversion of **2.7_{Ag}** into **Bpin-L1** and presumably silver metal (Fig. A33).

2.5.10 Synthesis of H_2L3 and 2.8_{Zn}-2.11_{Zn}

2.5.10.1 Synthesis of H_2L3

A 100 mL round bottom flask was charged with 4-methoxybenzylamine (1000 mg, 7.28 mmol), pyrrole-2-carboxaldehyde (690 g, 7.28 mmol), 40 mL ethanol, and a stir bar. The solution was stirred at 60 ˚C for 5 h. Then, the solution was cooled down to room temperature and then to 0-5 ˚C using an ice bath. To this solution, was added $NaBH_4$ (0.55 g, 14.56 mmol) pinch-wise and then the mixture was heated up to 50 ˚C for 2 h, resulting in a color change from pale orange to colorless. Afterward, the solvent was evaporated under vacuum and 50 mL H_2O was added. The product was extracted into dichloromethane (3 × 30 mL) and the organic phase was washed with brine solution (50 mL, 1 M). After that, the solution was concentrated to 5 mL and kept in -5 ˚C overnight, affording big crystals of **H_2L3** (1.24 g, 78%). The crystals were suitable for single X-ray crystallography. ^{1}H NMR (300 MHz, $CDCl_3$) δ 9.21 (b, 1H, Pyrrole-NH), 7.28 (t, 1H, Ar–H), 7.21 (d, 1H, Ar–H), 6.92 (ov mult, 2H, Ar–H), 6.71 (dd, 1H, Ar–H), 6.14 (dd, 1H, Ar–H), 6.03 (d, 1H, Ar–H), 3.84 (s, 3H, O-CH^3), 3.80 (d, 2H, -CH_2-), 3.78 (d, 2H, -CH_2-), 2.62 (b, 1H, -NH-). ^{13}C{^{1}H} NMR (75 MHz, $CDCl_3$) δ 157.7, 130.2, 128.5, 127.5, 120.4, 130.6, 117.3, 110.3, 107.8, 106.3, 55.2 (O-CH_3), 48.6 (-CH_2-), 45.5 (-CH_2-) (Fig. A34).

2.5.10.2 Synthesis of 2.8_{Zn}

A 42 mL vial was charged with 1M diethyl zinc solution in hexane (4 mL, 4 mmol), 5 mL DEE and a stir bar. To this solution, was added a DEE solution of **H_2L3** (865 mg, 4 mmol, in 10 mL of DEE) dropwise at room temperature. After 2 h, a white precipitate was formed. The mixture was stirred for 3 more hours and then the precipitate was filtered, washed by DEE (3 × 2 mL), and dried under vacuum, resulting in **2.8_{Zn}** (1180 mg, 95%). Crystals of **2.8_{Zn}** suitable for X-ray crystallography were obtained from hexane layering of a concentrated DCM solution at room

temperature after 1 day. ^{1}H NMR (300 MHz, $CDCl_3$) δ 7.38 (d, 1H, Ar–H), 7.25 (t, 1H, Ar–H), 7.00 (t, 1H, Ar–H), 6.92 (ov mult, 2H, Ar–H), 6.32 (t, 1H, Ar–H), 6.07 (d, 1H, Ar–H), 3.93 (s, 3H, O-CH_3), 3.87 (d, 2H, -CH_2-), 3.67 (d, 2H, -CH_2-), 3.12 (b, 1H, NH), 1.09 (t, 3H, ethyl's -CH_3), 0.22 (q, 2H, ethyl's -CH_2-). $^{13}C\{^{1}H\}$ NMR (75 MHz, $CDCl_3$) δ 157.6, 131.2, 130.2, 124.8, 121.5, 120.9, 118.5, 111.2, 109.0, 103.0, 55.7 (O-CH_3), 50.4 (-CH_2-), 48.3 (-CH_2-). MS: [M^+] 308.0, Calcd. 308.09 (Fig. A36).

2.5.10.3 Synthesis of $\mathbf{2.9_{Zn}}$

A 42 mL vial was charged with **2.8_{Zn}** (325 mg, 1.05 mmol) in 5 mL THF and a solution of 4,5-dichloro-1,3-dimethyl-1H-imidazol-3-ium iodide (307 mg, 1.05 mmol) and KO^{t}Bu (117 mg, 1.05 mmol) in 10 mL THF was added dropwise. No color change was observed. After stirring overnight at room temperature, the solution was filtered and the solvent was evaporated under vacuum. The residue was washed with hexane (3 × 3 mL) and DEE (3 × 3 mL) and dried under vacuum to give a white powder as **2.9_{Zn} (**410 mg, 82%). Crystals of **2.9_{Zn}** suitable for X-ray crystallography were obtained from hexane layering of a concentrated DCM solution at room temperature after 2 days. ^{1}H NMR (300 MHz, $CDCl_3$) δ 7.28 (t, 1H, Ar–H), 7.13 (d, 1H, Ar–H), 6.93 (t, 1H, Ar–H), 6.80 (ov mult, 2H, Ar–H), 6.24 (t, 1H, Ar–H), 6.06 (d, 1H, Ar–H), 3.89 (s, 2H, -CH_2-), 3.76 (s, 3H, O-CH_3), 3.66 (s, 2H, -CH_2-), 3.44 (s, 6H, -CH_3), 1.24 (t, 3H, ethyl's -CH_3), 0.05 (q, 2H, ethyl's -CH_2-). $^{13}C\{^{1}H\}$ NMR (75 MHz, $CDCl_3$) δ 158.2, 139.5, 136.6, 131.9, 128.2, 128.7, 125.1, 121.0, 112.8, 110.1, 107.5, 102.4, 55.1 (O-CH_3), 51.6 (-CH_2-), 49.9 (-CH_2-), 31.9 (CH_3), 22.9 (ethyl's -CH_3), 14.2 (ethyl's -CH_2-). MS: [M^+] 473.0, Calcd. 473.09 (Fig. A38).

2.5.10.4 Synthesis of $\mathbf{2.10_{Zn}}$

A 42 mL glass vial was charged with **2.8_{Zn}** (325 mg, 1.05 mmol) in 5 mL of THF and a solution of **H_2L3** (227 mg, 1.05 mmol) was added dropwise at room temperature. No color change was observed. After stirring overnight at room temperature, the solution was filtered and the solvent was evaporated under vacuum. The residue was washed with hexane (3 × 3 mL) and dried under vacuum to give a white powder of **2.10_{Zn} (**498 mg, 95%). Crystals of **2.10_{Zn}** suitable for X-ray crystallography were obtained from hexane layering of a concentrated THF solution at room temperature after 6 h. ^{1}H NMR (300 MHz, $CDCl_3$) δ 7.36 (t, 2H, Ar–H), 6.89 (ov mult, 8H, Ar–H), 6.33 (t, 2H, Ar–H), 6.08 (d, 2H, Ar–H), 3.84 (s, 6H, O-CH_3), 3.75 (s, 4H, -CH_2-), 3.66 (s, 4H,

-CH_2-). $^{13}C\{^1H\}$ NMR (75 MHz, $CDCl_3$) δ 157.9, 134.9, 131.4, 130.1, 125.6, 124.3, 121.1, 110.4, 109.0, 103.0, 55.5 (O-CH_3), 50.7 (-CH_2-), 48.6 (-CH_2-). MS: [M^+] 494.2, Calcd. 494.17 (Fig. A40).

2.5.10.5 Synthesis of 2.11$_{Zn}$ from 2.10$_{Zn}$

A 42 mL glass vial was charged with **2.10$_{Zn}$** (520 mg, 1.05 mmol) in 5 mL of THF and a solution of 4,5-dichloro-1,3-dimethyl-1H-imidazol-3-ium iodide (307 mg, 1.05 mmol) and KO^{t}Bu (117 mg, 1.05 mmol) in 10 mL THF was added dropwise. The color changed to light brown from colorless. After stirring overnight at room temperature, the solution was filtered and the solvent was evaporated under vacuum. The residue was washed with hexane (3 × 3 mL) and DEE (3 × 3 mL) and dried under vacuum to give a light brown powder of **2.11$_{Zn}$ (**618 mg, 88%). Crystals of **2.11$_{Zn}$** suitable for X-ray crystallography were obtained from hexane layering of a concentrated DCM solution at room temperature after 1 day. ^1H NMR (300 MHz, $CDCl_3$) δ 7.25 (t, 2H, Ar–H), 6.98 (ov mult, 4H, Ar–H), 6.82 (ov mult, 4H, Ar–H), 6.26 (t, 2H, Ar–H), 6.00 (d, 2H, Ar–H), 3.84 (s, 6H, O-CH_3), 3.78 (s, 4H, -CH_2-), 3.76 (s, 4H, -CH_2-), 3.32 (s, 6H, -CH_3), 3.12 (b, 2H, NH). $^{13}C\{^1H\}$ NMR (75 MHz, $CDCl_3$) δ 157.6, 142.2, 135.3, 131.8, 130.1, 127.2, 122.3, 120.6, 111.8, 110.4, 107.1, 103.2, 55.1 (O-CH_3), 50.8 (-CH_2-), 48.2 (-CH_2-), 31.8 (CH_3). MS: [$(M\text{-}CH_3)^+$] 644.8464, Calcd. 644.1 (Fig. A42).

2.5.10.6 Synthesis of 2.11$_{Zn}$ from 2.9$_{Zn}$

A 42 mL vial was charged with **2.9$_{Zn}$** (499 mg, 1.05 mmol) in 5 mL of THF and a solution of **H_2L3** (227 mg, 1.05 mmol) was added dropwise at room temperature. No immediate color change was observed, but stirring overnight the color changed to light brown from colorless. Then the solution was filtered and the solvent evaporated under vacuum. The residue was washed with hexane (3 × 3 mL) and dried under vacuum to give a light brown powder of **2.11$_{Zn}$ (**441 mg, 63%).

2.5.11 Catalytic Procedures Using 2.11$_{Zn}$

2.5.11.1 Nitrile Dihydroboration

A catalyst stock solution was prepared by dissolving 6 mg (0.01 mmol) of **2.11$_{Zn}$** in 10 mL of C_6D_6. A small vial was charged with 10 µL of the catalyst stock solution (0.006 mg, 0.01 µmol, 0.01 mol%). Then, 0.5 mL of C_6D_6 and nitrile substrate (0.1 mmol: benzonitrile 10 µL, isobutyronitrile 6.9 mg or 8.9 µL, acetonitrile 4.1 mg or 5.2 µL, 2-chlorobenzonitrile 13.7 mg, 2-

bromobenzonitrile 18.2 mg, 3-chlorobenzonitrile 13.7 mg, 3-bromobenzonitrile 18.2 mg, 4-fluorobenzonitrile 12.1 mg, 4-bromobenzonitrile 18.2 mg, 2-thiophenecarbonitrile 10.9 mg or 9.3 µL, 4-methoxybenzonitrile 13.3 mg) were added to the vial and HBpin (29 µL, 0.2 mmol) was added. The vial was capped and after stirring for 2-5 h, the reaction mixture was transferred to an NMR tube and ^{1}H and ^{11}B NMR spectra were recorded at room temperature. Concentration of the dihydroborated products was calculated based on integrals of the characteristic product signal in the reaction mixture and the known [HBpin] as well.

2.5.11.2 Quinoline Hydroboration

A catalyst stock solution was prepared by dissolving 6 mg (0.01 mmol) of **2.11$_{Zn}$** in 10 mL of C_6D_6. A small vial was charged with 50 µL of the catalyst stock solution (0.03 mg, 0.05 µmol, 0.05 mol%). Then, 0.5 mL of C_6D_6 and quinoline substrate (0.1 mmol: quinoline 11.8 µL, 2-methyl-quinoline 13.5 µL, 4-methyl-quinoline 13.2 µL, 5-chloro-quinoline 16 mg, 3-chloroquinoline 16 mg, 8-chloro-quinoline 16 mg, acridine 18 mg, iso-quinoline 11.7 µL) were added to the vial, and HBpin (14.5 µL, 0.1 mmol) was added. The vial was capped for 2.5-4 h and the reaction mixture was transferred to an NMR tube for ^{1}H and ^{11}B NMR analysis. Concentration of the hydroborated products were calculated based on integrals of the characteristic product signal in the reaction mixture and the known [HBpin] as well.

2.5.12 Mechanistic Studies of 2.11$_{Zn}$ Catalytic System

2.5.12.1 Reaction of 2.8$_{Zn}$ with HBpin

A small vial was charged with 1 equiv of **2.8$_{Zn}$** (0.06 mmol, 18.0 mg) and 2 equiv of HBpin (0.12 mmol; 17.4 µL) and 2 mL of benzene. The solution stirred for 2 h and then the solvent was evaporated and the residue was washed extensively with hexane and filtered. The solvent of the filtrate was concentrated to 1 mL under vacuum and kept at -30 ˚C. After one day needle-shaped crystals were grown but were too small to be characterized by X-ray single crystallography; they were characterized by EI-MS and ^{1}H NMR.

2.5.12.2 Reaction of $\mathbf{2.11_{Zn}}$ with quinoline

A small vial was charged with 1 equiv of $\mathbf{2.11_{Zn}}$ (0.015 mmol, 10.0 mg) and 1 equiv of quinoline (0.015 mmol; 1.7 µL) and 0.5 mL of C_6D_6. The solution was stirred for 2 h and then transferred to an NMR tube for further analysis.

2.5.12.3 Reaction of $\mathbf{2.11_{Zn}}$ with HBpin

A small vial was charged with 1 equiv of $\mathbf{2.11_{Zn}}$ (0.06 mmol, 40.0 mg) and 4 equiv of HBpin (0.24 mmol; 34.8 µL) and 2 mL of C_6D_6. The solution was stirred for 2 h and then 0.5 mL of that was transferred to an NMR tube for further analysis. The remaining solvent was evaporated and the residue was washed extensively with hexane and filtered. The residue was dried under vacuum for 5 h, and then analyzed by ^{1}H NMR and EI-MS. The hexane filtrate was concentrated to 1 mL under vacuum and kept at -30 ˚C. After one day needle shaped crystals were grown but were too small for X-ray single crystallography; they were characterized by EI-MS and ^{1}H NMR.

2.5.12.4 Reaction of $\mathbf{2.12_{Zn}}$ with quinoline

A small vial was charged with 1 equiv of $\mathbf{2.12_{Zn}}$ (0.021 mmol, 10.0 mg) and 4 equiv of quinoline (0.084 mmol; 10 µL) and 2 mL of C_6D_6. The solution was stirred for 2 h and then transferred to an NMR tube for further analysis.

2.5.12.5 Control Reaction Using $\mathbf{2.11_{Zn}}$ and In Situ Formed $\mathbf{2.13_{Zn}}$

In a vial containing $\mathbf{2.11_{Zn}}$ (0.075 mmol, 50 mg) and 2 mL of C_6D_6, was added a solution of 4,5-dichloro-1,3-dimethyl-1H-imidazol-3-ium iodide (0.075 mmol, 12 mg in 1 mL of C_6D_6) dropwise and then the vial was capped and the final solution stirred for 8 h. We named this solution "$\mathbf{2.13_{Zn}}$ solution". A separate vial was charged with 0.5 mL C_6D_6, quinoline (0.1 mmol, 11.8 µL) and HBpin (14.5 µL, 0.1 mmol). Then $\mathbf{2.13_{Zn}}$ solution (0.1 µmol, 4 µL, 0.1 mol%) was added and the vial was capped, stirred for 3 h and transferred to an NMR tube for checking the reaction yield, giving 87% yield.

2.5.13 Kinetic Studies of $\mathbf{2.11_{Zn}}$ Catalytic System

(All kinetic reactions were set up in a dinitrogen glovebox and performed the same way with appropriate amounts of $\mathbf{2.11_{Zn}}$, quinoline and HBpin – See **Table 2.7**).

General Procedure for Reaction A

A catalyst stock solution was prepared by dissolving 6 mg (0.01 mmol) of **2.11$_{Zn}$** in 10 mL of C_6D_6. An NMR tube was charged with 100 µL of catalyst stock solution (0.06 mg, 0.1 µmol, 0.1 mol%). Afterward, a vial was charged with C_6D_6 (0.2 mL) and quinoline (0.1 mmol, 11.8 µL) and the solution was transferred to the NMR tube. The vial was rinsed with 0.2 mL of C_6D_6 and transferred to the same NMR tube. The NMR tube was capped with a rubber septum. A 50 µL micro-syringe, pre-charged with HBpin (14.5 µL, 0.1 mmol) was capped by poking into the rubber septum. The NMR tube containing the reaction mixture and the micro-syringe were removed from the glovebox. The HBpin was injected into the NMR tube, shaken quickly, and immediately inserted into the NMR spectrometer. A ^{1}H NMR spectrum was recorded every 15 min for 2 h at room temperature. Concentration of the quinoline hydroborated product was calculated based on integrals of the characteristic product signal in the reaction mixture. All other 4 reactions (B-E) were carried out through the same procedure.

Table 2.7. Concentrations of Reagents for Reactions A-F for VTNA*.

Reaction	[**2.11$_{Zn}$**]	[Quiniline]	[HBpin]
A ●	0.0001	0.10	0.10
B ●	0.0001	0.13	0.10
C ●	0.0001	0.10	0.13
D ●	0.0003	0.10	0.10
E ●	0.0001	0.056	0.056

*All the amounts are in mmol.

2.5.14 X-ray Crystallographic Details (2.7$_{Ag}$, H$_2$L3, 2.8$_{Zn}$-2.11$_{Zn}$)

Crystallographic data were collected from single crystals mounted on MiTeGen dual thickness MicroMounts using Parabar oil. Data were collected on a Bruker Smart (**2.7$_{Ag}$** and **2.10$_{Zn}$**) or Kappa (**H$_2$L3**, **2.8$_{Zn}$**, **2.9$_{Zn}$** and **2.11$_{Zn}$**) ApexII single crystal diffractometer equipped with a graphite monochromator. The instrument was equipped with a sealed tube Mo Kα source ($\lambda = 0.71073$ Å), an ApexII CCD detector and a dry compressed air-cooling system. The samples were cooled to different temperatures during data collection: **2.11$_{Zn}$** at 200, **H$_2$L3** and **2.9$_{Zn}$** at 203, **2.10$_{Zn}$** at 208, and **2.8$_{Zn}$** at 293 K. Raw data collection and processing were performed with the Apex3 software package from Bruker.[42] Initial unit cell parameters were determined from 36 data frames from select ω scans. Semi-empirical absorption corrections based on equivalent reflections were applied.[43] Systematic absences in the diffraction data-set and unit-cell parameters were

consistent with the assigned space group. The initial structural solutions were determined using ShelxT direct methods,[44] and refined with full-matrix least-squares procedures based on F^2 using ShelXL or ShelXle.[45] **2.10$_{Zn}$** exhibited positional disorder which was refined in ShelXle. Hydrogen atoms were placed geometrically and refined using a riding model. Deposition Numbers: 2190706-2190710.

2.6 References

(1) Dub, P. A.; Gordon, J. C. Metal-Ligand Bifunctional Catalysis: The "Accepted" Mechanism, the Issue of Concertedness, and the Function of the Ligand in Catalytic Cycles Involving Hydrogen Atoms. *ACS Catal.* **2017**, *7*, 6635–6655.

(2) Khusnutdinova, J. R.; Milstein, D. Metal-Ligand Cooperation. *Angew. Chem., Int. Ed.* **2015**, *54*, 12236–12273.

(3) Elsby, M. R.; Baker, R. T. Strategies and Mechanisms of Metal–Ligand Cooperativity in First-row Transition Metal Complex Catalysts. *Chem. Soc. Rev.* **2020**, *49*, 8933–8987.

(4) Du, Y.; Pearson, R. M.; Lim, C. H.; Sartor, S. M.; Ryan, M. D.; Yang, H.; Damrauer, N. H.; Miyake, G. M. Strongly Reducing, Visible-light Organic Photoredox Catalysts as Sustainable Alternatives to Precious Metals. *Chem.-Eur. J.* **2017**, *23*, 10962–10968.

(5) Gunanathan, C.; Milstein, D. Metal–Ligand Cooperation by Aromatization-Dearomatization: A New Paradigm in Bond Activation and "Green" Catalysis. *Acc. Chem. Res.* **2011**, *44*, 588–602.

(6) Gruetzmacher, H. Cooperating Ligands in Catalysis. *Angew. Chem., Int. Ed.* **2008**, *47*, 1814–1818.

(7) Das, U. K.; Daifuku, S. L.; Iannuzzi, T. E.; Gorelsky, S. I.; Korobkov, I.; Gabidullin, B.; Neidig, M. L.; Baker, R. T. Iron(II) Complexes of a Hemilabile SNS Amido Ligand: Synthesis, Characterization, and Reactivity. *Inorg. Chem.* **2017**, *56*, 13766–13776.

(8) Elsby, M. R.; Kim, S. Y. H.; Steinmann, S.; Baker, R. T. Same Ligand, Three First-row Metals: Comparing M-amido Bifunctional Reactivity (Mn, Fe, Co). *Dalton Trans.*, **2021**, *50*, 14542-14546.

(9) Das, U. K.; Daifuku, S. L.; Gorelsky, S. I.; Korobkov, I.; Neidig, M. L.; Le Roy, J. J.; Murugesu, M.; Baker, R. T. Mononuclear, Dinuclear, and Trinuclear Iron Complexes Featuring a New Monoanionic SNS Thiolate Ligand. *Inorg. Chem.* **2016**, *55*, 987–997.

(10) Albkuri, Y. M.; Ovens, J. S.; Martin, J.; Baker, R. T. Nickel(II)-SNS Thiolate Complexes: Reactivity and Solution Dynamics. *Inorg. Chem.* **2021**, *60*, 10934–10942.

(11) Das, U. K.; Higman, C. S.; Gabidullin, B.; Hein, J. E.; Baker, R. T. Efficient and Selective Iron-Complex-Catalyzed Hydroboration of Aldehydes. *ACS Catal.* **2018**, *8*, 1076–1081.

(12) Elsby, M. R.; Baker, R. T. Cu(I)-SNS Complexes for Outer-sphere Hydroboration and Hydrosilylation of Carbonyls. *Chem. Commun.* **2019**, *55*, 13574–13577.

(13) Elsby, M. R.; Son, M.; Oh, C.; Martin, J.; Baik, M.–H.; Baker, R. T. Mechanistic Study of Metal–Ligand Cooperativity in Mn(II)-Catalyzed Hydroborations: Hemilabile SNS Ligand Enables Metal Hydride-Free Reaction Pathway. *ACS Catal.* **2021**, *11*, 9043–9051.

(14) Elsby, M. R. PhD thesis, University of Ottawa, **2022**.

(15) Greb, L.; Ebner, F.; Ginzburg, Y.; Sigmund, L. M. Element-Ligand Cooperativity with p-Block Elements. *Eur. J. Inorg. Chem.* **2020**, *2020*, 3030–3047.

(16) Kumar, G. S.; Harinath, A.; Narvariya, R.; Panda, T. K. Homoleptic Zinc-Catalyzed Hydroboration of Aldehydes and Ketones in the Presence of HBpin. *Eur. J. Inorg. Chem.*, **2020**, *2020*, 467-474.

(17) Sahoo, R. K.; Mahato, M.; Jana, A.; Nembenna, S. Zinc Hydride-Catalyzed Hydrofunctionalization of Ketones. *J. Org. Chem.* **2020**, *85*, 11200–11210.

(18) Wang, X.; Xu, X. Hydroboration of Nitriles and Imines by Highly Active Zinc Dihydride Catalysts. *RSC Adv.* **2021**, *11*, 1128–1133.

(19) (a) Blackmond, D. G. Reaction Progress Kinetic Analysis: A Powerful Methodology for Mechanistic Studies of Complex Catalytic Reactions. *Angew. Chem., Int. Ed.* **2005**, *44*, 4302−4320. (b) Blackmond, D. G. Kinetic Profiling of Catalytic Organic Reactions as a Mechanistic Tool. *J. Am. Chem. Soc.* **2015**, *137*, 10852−10866.

(20) (a) Martínez-Carrión, A.; Howlett, M. G.; Alamillo-Ferrer, C.; Clayton, A. D.; Bourne, R. A.; Codina, A.; Vidal-Ferran, A.; Adams, R. W.; Burés, J. Kinetic Treatments for Catalyst Activation and Deactivation Processes based on Variable Time Normalization Analysis. *Angew. Chem., Int. Ed.* **2019**, *58*, 10189–10193. (b) Nielsen, C. D.-T.; Burés, J. Visual Kinetic Analysis. *Chem. Sci.* **2019**, *10*, 348–353.

(21) Okuniewski, A.; Rosiak, D.; Chojnacki, J.; Becker, B. Coordination Polymers and Molecular Structures Among Complexes of Mercury(II) Halides with Selected 1-Benzoylthioureas. *Polyhedron* **2015**, *90*, 47–57.

(22) Harinath, A.; Bhattcharjee, J.; Gorantla, K. R.; Mallik, B. S.; Panda, T. K. Hydroboration, Cyanosilylation, and Sequential Cyanosilylation and Hydroboration of Carbonyl Compounds in the Presence of a Ti^{IV} Amino Complex as an Efficient Catalyst. *Eur. J. Org. Chem.* **2018**, *2018*, 3180–3192.

(23) Darensbourg, D. J.; Holtcamp, M. W.; Struck, G. E.; Zimmer, M. S.; Niezgoda, S. A.; Rainey, P.; Robertson, J. B.; Draper, J. D.; Reibenspies, J. H. Catalytic Activity of a Series of Zn (II) Phenoxides for the Copolymerization of Epoxides and Carbon Dioxide. *J. Am. Chem. Soc.* **1999**, *121*, 107–116.

(24) Li, Y.; Junge, K.; Beller, M. in *Zinc Catalysis*, Enthaler, S.; Wu, X.-F., Eds., Wiley VCH: Weinheim, **2015**, pp. 5-31.

(25) Enthaler, S.; Eckhardt, B.; Inoue, S.; Irran, E.; Driess, M. Facile and Efficient Reduction of Ketones in the Presence of Zinc Catalysts Modified by Phenol Ligands. *Chem. - Asian J.* **2010**, *5*, 2027–2035.

(26) Higashi, T.; Kusumoto, S.; Nozaki, K. Cleavage of Si–H, B–H, and C–H Bonds by Metal–Ligand Cooperation. *Chem. Rev.* **2019**, *119*, 10393–10402.

(27) Ataie, S.; Hogeterp, S.; Ovens, J. A.; Baker, R. T. SNS Ligand-assisted Catalyst Activation in Zn-catalysed Carbonyl Hydroboration .*Chem. Commun.* **2022**, *58*, 3795-3798.

(28) Mankad, N. P.; Laitar, D. S.; Sadighi, J. P. Synthesis, Structure, and Alkyne Reactivity of a Dimeric (Carbene)Copper(I) Hydride. *Organometallics* **2004**, *23*, 3369–3371.

(29) B. Fitchett, University of Ottawa MSc thesis, **2018**.

(30) Bhide, M. A.; Manzi, J. A.; Knapp, C. E.; Carmalt, C. J. Synthetic and Structural Studies of Ethyl Zinc β-Amidoenoates and β-Ketoiminates. *Molecules* **2021**, *26*, 3165.

(31) Bhide, M. A.; Mears, K. L.; Carmalt, C. J.; Knapp, C. E. Synthesis, Solution Dynamics and Chemical Vapour Deposition of Heteroleptic Zinc Complexes via Ethyl and Amide Zinc Thioureides. *Chem. Sci.* **2021**, *12*, 8822–8831.

(32) de Vries, F.; Travieso-Puente, R.; Roewen, P.; Otten, E. Three-Coordinate Zinc Methyl Complexes with Sterically Demanding Formazanate Ligands. *Organometallics* **2021**, *40* (1), 63–71.

(33) Ataie, S.; Ovens, J. S.; Baker, R. T. Solvent-free Zn (NSNO) Complex-catalysed Dihydroboration of Nitriles. *Chem. Commun.* **2022**, *58*, 8266–8269.

(34) Bedi, D.; Brar, A.; Findlater, M. Transition Metal- and Solvent-free Double Hydroboration of Nitriles. *Green Chem.* **2020**, *22*, 1125–1128.

(35) Ghosh, C.; Kim, S.; Mena, M. R.; Kim, J.–H.; Pal, R.; Rock, C. L.; Groy, T. L.; Baik, M.–H.; Trovitch, R. J. Efficient Cobalt Catalyst for Ambient-Temperature Nitrile Dihydroboration, the Elucidation of a Chelate-Assisted Borylation Mechanism, and a New Synthetic Route to Amides. *J. Am. Chem. Soc.* **2019**, *141*, 15327–15337.

(36) Saha, S.; Eisen, M. S. Catalytic Recycling of a Th–H Bond via Single or Double Hydroboration of Inactivated Imines or Nitriles. *ACS Catal.* **2019**, *9*, 5947–5956.

(37) Lortie, J. L.; Dudding, T.; Gabidullin, B. M.; Nikonov, G. I. Zinc-Catalyzed Hydrosilylation and Hydroboration of N–Heterocycles. *ACS Catal.* **2017**, *7*, 8454–8459.

(38) Wang, X.; Zhang, Y.; Yuan, D.; Yao, Y. Regioselective Hydroboration and Hydrosilylation of N–Heteroarenes Catalyzed by a Zinc Alkyl Complex. *Org. Lett.* **2020**, *22*, 5695–5700.

(39) Liu, T.; He, J.; Zhang, Y. Regioselective 1,2–Hydroboration of *N*–Heteroarenes Using a Potassium-based Catalyst. *Org. Chem. Front.* **2019**, *6*, 2749–2755.

(40) Zhang, F.; Song, H.; Zhuang, X.; Tung, C. H.; Wang, W. Iron-Catalyzed 1,2-Selective Hydroboration of *N*–Heteroarenes. *J. Am. Chem. Soc.* **2017**, *139*, 17775–17778.

(41) Westmoreland, D. E.; Lopez-Arteaga, R.; Weiss, E. A. N-Heterocyclic Carbenes as Reversible Exciton-Delocalizing Ligands for Photoluminescent Quantum Dots. *J. Am. Chem. Soc.* **2020**, *142*, 2690.

(42) APEX Softward Suite v 2010 Bruker AXS Inc. Madison Wisconsin USA, **2010**.

(43) Blessing R. H. An Empirical Correction for Absorption Anisotropy**.** *Acta Crystallogr*. **1995**, *A51*, 33–38.

(44) Sheldrick, G. M. A Short History of SHELX. *Acta Crystallogr*. **2008**, *A64*, 112–122.

(45) Hübschle, C. B.; Sheldrick, G. M.; Dittrich, B. *ShelXle*: A Qt Graphical User Interface for *SHELXL*. *J. Appl. Crystallogr.* **2011**, *44*, 1281–1284.

CHAPTER 3

SELECTIVE Co^{II}-SNS DITHIOLATE COMPLEX-CATALYZED BIFUNCTIONAL HYDROBORATION OF ALDEHYDES: KINETICS AND MECHANISTIC STUDIES

3.1 Introduction

The hydroboration reaction, as a potent and direct method for reduction of various unsaturated compounds such as imines, nitriles, carbonyls, alkenes, amides and carbon dioxide, has attracted much attention over the last decade.[1] Carbonyl hydroboration is known as an efficient and selective technique for production of 1º and 2º alcohols, comparing to methods using stoichiometric reduction by $LiAlH_4$ or $NaBH_4$, which also suffer poor functional group tolerance and selectivity (aldehydes *vs* ketones, or over-reduction).[2,3] Cobalt complexes, due to low price and high natural abundance, have been widely employed in hydride transfer reactions such as hydrogenation,[4] hydrosilylation[5] and hydroboration[6] of a variety of unsaturated organic substrates. So far, there have been five molecular cobalt catalysts employed for carbonyl hydroboration[7] (**Scheme 3.1A**), but potential access to multiple oxidation and spin states has hampered detailed mechanistic studies. In most metal-catalyzed hydroborations, B–H bond activation plays a key role.[9] Depending on the nature of the unsaturated group and the potential for metal ligand cooperativity (MLC), three main bifunctional hydroboration pathways have been characterized: outer-sphere reduction via $(BR_2)E$-MH (E = N, O, S), inner-sphere insertion into M–H, and inner-sphere hydride transfer.[10] The Baker group has recently been investigating first-row transition metal complexes containing two different SNS ligands[12] (one with amido as a hard N-donor and the other with thiolate as a soft S-donor) as bifunctional catalysts. Following early studies of Ru-thiolate complexes[13] additional examples of Mo-,[14] Fe-[3b,15] and Ni-thiolate[16] complexes have been applied as hydroboration catalysts. In previous studies on copper-[17] and zinc-catalyzed[18] carbonyl hydroboration, the thiolate donor was less effective for B–H or Si–H activation, compared to its amido analogue.

The work in this chapter began as an effort to prepare a Co complex containing both amido and thiolate SNS ligands. Instead, reaction of the previously reported Co bis(amido) complex,[19] $Co(S^{Me}NS^{Me})_2$ (**3.1_{Co}, Scheme 3.2**) with the deprotonated thiolate ligand afforded a new cobalt complex (**3.2_{Co}**), ligated by a dithiolate SNS ligand and a small NHC ligand (**Scheme 3.1B**).

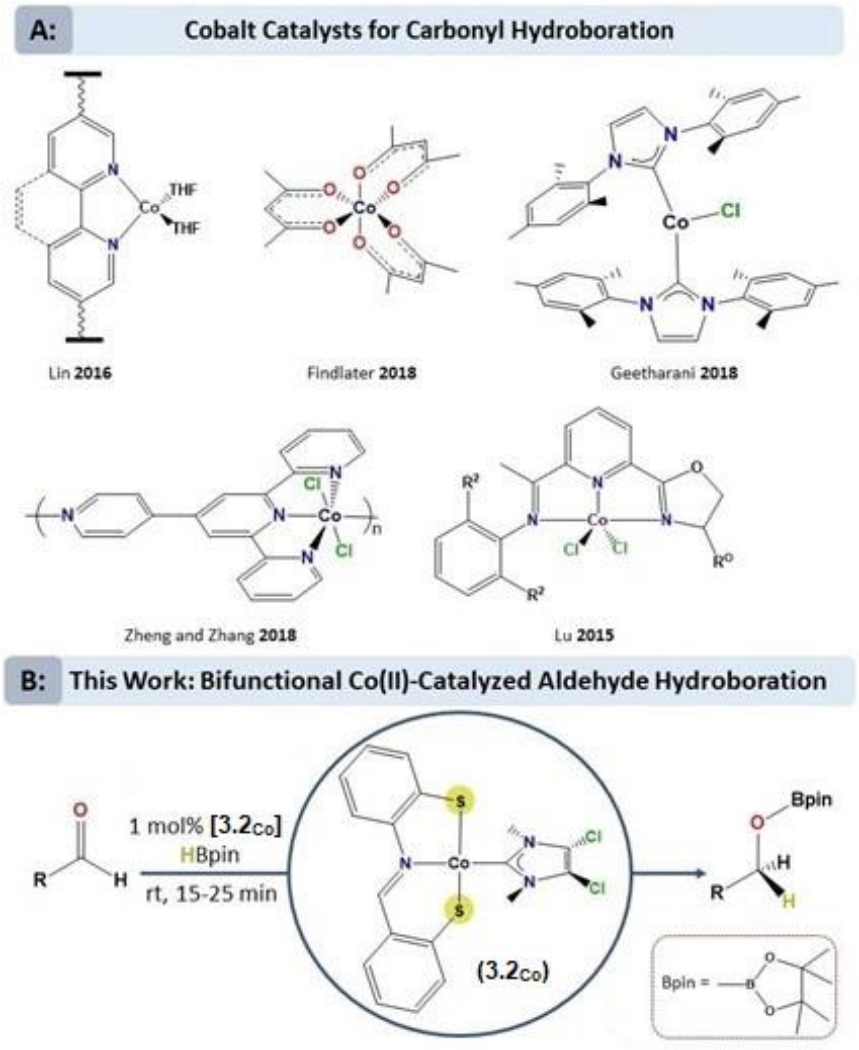

Scheme 3.1. Recently reported Co catalyst for carbonyl hydroboration (A) and our current report on Co-catalyzed hydroboration of aldehydes (B).

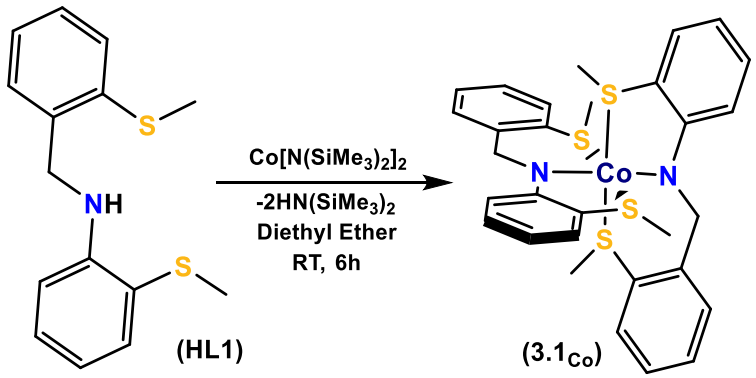

Scheme 3.2. Synthesis of $\mathbf{3.1_{Co}}$.

In addition, we show that **3.2$_{Co}$** is an effective catalyst for selective hydroboration of aldehydes (vs. ketones) as shown by mechanistic, kinetics and DFT studies.

3.2 Results and Discussion

3.2.1 Synthesis and Characterization of 3.2$_{Co}$

To synthesize **3.2$_{Co}$** , 1 equiv of the imidazolium salt, 4,5-dichloro-1,3-dimethyl-1H-imidazol-3-ium iodide [DDI-H)I], was added to Co bis(amido) complex **3.1$_{Co}$** (to protonate one **L1** and install the Co-I bond), yielding a navy-blue solution. To this solution was added a THF solution containing 1 equiv each of benzothiazoline (**HL2**) and NaHMDS, giving a dark grey solution (HMDS = hexamethyldisilazanyl). After stirring for 12 h, the solvent was removed and the residue extracted with CH_2Cl_2, dried, washed with diethyl ether, and dried again, affording Co(κ^2-SNS)((DDI) (**3.2$_{Co}$)** in 62 % yield (**Scheme 3.3**). The paramagnetically-shifted ^{1}H NMR spectrum of **3.2$_{Co}$**showed 10 distinct resonances between δ +36 and -30, including one at δ -5.1 due to the two N-Me groups (Fig. B1). The room temperature isotropic EPR spectrum showed an octet pattern at g = 1.917 [a(^{59}Co) = 29.2 G], which is typical for square-planar low-spin (S = ½) Co(II) complexes.[20,21] Furthermore, density functional theory (DFT) calculations show the low-spin doublet configuration is 2.5 kcal/mol lower in electronic energy and 0.7 kcal/mol lower in free energy than the high-spin quartet; only the low-spin geometry is consistent with the X-ray crystal structure. Hexane layering of a concentrated dichloromethane solution of **3.2$_{Co}$** at room temperature afforded suitable single crystals for X-ray diffraction (**Scheme 3.3**).

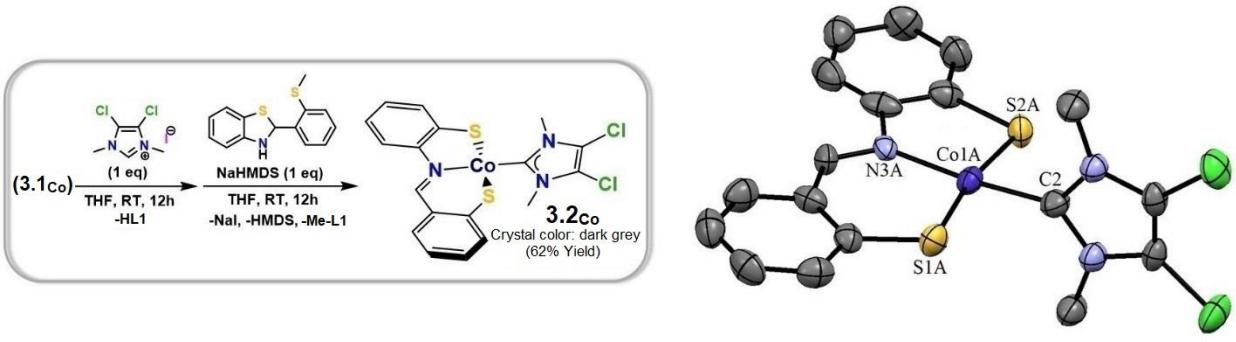

Scheme 3.3. Synthesis and molecular structure of **3.2$_{Co}$** with 50% probability thermal ellipsoids and hydrogen atoms omitted for clarity. Selected bond distances (Å) and angles (deg): Co-S1A 2.160(8), Co-S2A 2.166(6), Co-N 1.921(6), Co-C 1.891(5), S1A-Co-C 83.07(3), S2A-Co-C 87.9(2), S1A-Co1A-N 98.8(3), S2A-Co-N 90.0(2), S1A-Co-S2A 170.5(3), C2-Co-N 174.5(3).

The molecular structure of **3.2$_{Co}$** shows a distorted square-planar geometry with some bending of the S-Co-S angle (170.5(3)°) and minor deviations originating from formation of five- and six-membered metallacycle rings (cf. S1A-Co-N angle = 98.8(3) ° in the latter *vs* S2A-Co-N = 90.0(2)° in the former). The Co-S bond lengths [2.160(8) and 2.166(6)Å] are similar to those reported previously for Co thiolates.[22]

In the workup process of **3.2$_{Co}$**, evaporation of the diethyl ether wash allowed for EI-MS characterization of **Me-L1** (Fig. B9). In a previous study on Ni SNS thiolate complexes,[23] the IPr NHC ligand was shown to demethylate the thioether, affording a similar IPr-Ni-dithiolate complex (IPr = 2,6-diisopropylphenyl-imidazolylidene). Hence, to find out if the smaller NHC ligand used here also activates the S-Me bond of **L2**, complexes **3.3$_{Co}$** and **3.4$_{Co}$** were prepared (**Scheme 3.4**) and characterized (See experimental section for procedures and characterization). Treatment of **3.3$_{Co}$** with 1 equiv of (**L2**)$^-$ successfully afforded **3.2$_{Co}$** and **Me-L1,** while reaction of **3.4$_{Co}$** and (**L2**)$^-$ failed to form **3.2$_{Co}$** , proving that only **L1** activates the S-Me bond of **L2**. An alternate, less likely pathway to produce **3.2$_{Co}$** from **3.3$_{Co}$** is iodide reaction with the S-Me and then the formed iodomethane methylates **L1** to **Me-L1**.

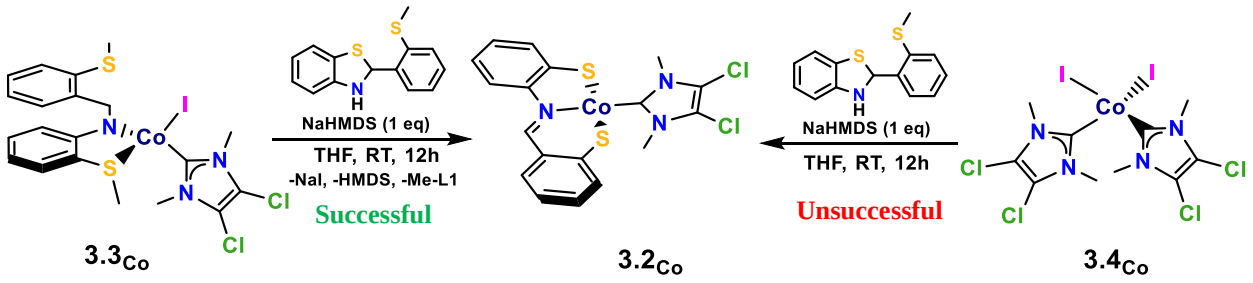

Scheme 3.4. Reactions of **3.3$_{Co}$** and **3.4$_{Co}$** with **L2** for synthesis of **3.2$_{Co}$.**

3.2.2 3.2$_{Co}$-Catalyzed Hydroboration

Our previous study on zinc-catalyzed nitrile dihydroboration, comparing amido and aryloxide donors, showed aryloxide as the primary donor participating in B–H bond activation.[24] On the other hand, our previous Cu work showed the amido donor in **L1** is typically more active for B–H bond activation than the thiolate donor in **L2**. Herein, **3.2$_{Co}$**, ligated to two thiolate donors, demonstrated selective aldehyde hydroboration. To optimize the reaction conditions, we first showed that uncatalyzed benzaldehyde hydroboration gave only 5% yield in the absence of **3.2$_{Co}$** after 2 h at room temperature (**Table 3.1,** entry 1). Increasing the temperature to 60 ˚C raised the

yield to 86% (Entry 2) as reported previously.[25] Adding benzaldehyde and HBpin to 5 mol% of **3.2$_{Co}$** in C_6D_6 at ambient temperature, despite showing no color change, gave quantitative yield in 30 min (Entry 3). Lowering the catalyst loading to 1 mol%, and the time to 15 min kept the yield quantitative (Entry 8). Further decrease in catalyst loading or time (Entries 6 and 9) showed a significant yield drop. *In-situ* addition of HBpin and benzaldehyde to the reaction mixture after the first run, afforded an insignificant amount of product (Entry 10). In contrast, recovery (see experimental section for further details) and reuse of **3.2$_{Co}$** afforded the same catalytic performance (Entry 11). Under the same conditions, using hexanal in place of benzaldehyde gave quantitative yield after 4 min (Entry 12). *In-situ* addition of HBpin and hexanal to the reaction mixture after the first run, resulted in complete yields for second and third runs (Entries 13 and 14).

Table 3.1. Optimization of reaction conditions for **3.2$_{Co}$**-catalyzed aldehyde hydroboration.[a]

Entry	*Cat. (mol%)*	*Time (min)*	*Yield (%)*[b]
1	-	120	<5
2	-	120[c]	86
3	**3.2$_{Co}$** (5)	30	>99
4	**3.2$_{Co}$** (3)	30	>99
5	**3.2$_{Co}$** (1)	30	>99
6	**3.2$_{Co}$** (0.5)	30	74
7	**3.2$_{Co}$** (1)	20	>99
8	**3.2$_{Co}$ (1)**	**15**	**>99**
9	**3.2$_{Co}$** (1)	10	82
10	2nd run-**3.2$_{Co}$** (1)[d]	60	<10
11	R-**3.2$_{Co}$** (1)[e]	15	>99
12	**3.2$_{Co}$** (1)[f]	4	>99
13	**3.2$_{Co}$**[g]	5	>99
14	**3.2$_{Co}$**[h]	5	>99

[a] Reaction conditions: benzaldehyde (0.53 mmol), HBpin (0.53 mmol), C_6D_6 as solvent (0.5 mL), catalyst loading relative to benzaldehyde, at room temperature. [b] Yields were determined by ^{1}H NMR spectroscopy using mesitylene as an internal standard. [c] At 60 °C. [d] *in-situ* addition of benzaldehyde (0.53 mmol) and HBpin (0.53mmol) after the first run. [e] Recovered **3.2$_{Co}$**. [f] hexanal (0.53 mmol), HBpin (0.53 mmol), C_6D_6 as solvent (0.5 mL), catalyst loading relative to hexanal, at room temperature. [g] *in-situ* hexanal (0.53 mmol) and HBpin (0.53 mmol) were added after the first run in entry 12. [h] *in-situ* hexanal (0.53 mmol) and HBpin (0.53 mmol) were added after the second run in entry 13.

In assessing the substrate scope, **3.2$_{Co}$** was found to be efficient in reducing bulky aldehydes (**Table 3.2**, entries b and c), and tolerating functional groups such as N–Heterocycles (entries e and g), olefins (entry f), ketones (entry h), nitriles (entry i), and nitro groups (entry j).

3.2$_{Co}$ was also efficient in reducing aldehydes possessing electron-withdrawing and -donating functional groups in sterically compromising positions (entries k-n and p-s). For all the substrates, full conversion was observed within 4-25 min in the presence of 1 mol% of **3.2$_{Co}$**. As shown in entries h and o, **3.2$_{Co}$** showed no tendency for catalyzing ketone hydroboration, even at 70 ˚C after 14 h. Interestingly, **3.2$_{Co}$** proved to be more efficient in hydroboration of an aliphatic aldehyde in terms of time (entry t).

3.2.3 Mechanistic Studies

In our previous study on selective Fe-catalyzed aldehyde hydroboration, our reaction profile kinetic analysis[26] revealed an unusual rate dependence on the concentrations of HBpin and substrate.[3b] In a later study on Mn(**L1**)$_2$-catalyzed carbonyl hydroboration,[8] using variable time normalization analysis (VTNA),[27] a simpler rate dependence was obtained on concentrations of HBpin, substrate, and catalyst. For **3.2$_{Co}$**, reaction progress was assessed using ^{11}B NMR spectroscopy. Using VTNA, the results were graphically analyzed. Using 1-pyrenecarboxaldehyde as the substrate, first-order rate dependence on [HBpin], [1-pyrenecarboxaldehyde] and [**3.2$_{Co}$**] was obtained (**Figure 3.1**). In addition, plotting [(pyrene)CH_2OBpin] vs. the normalized rate components gave k_{obs} = 2.16 $M^{-2}min^{-1}$ (Fig. B35). Finally, VTNA was also utilized to see if the catalytic system suffers from possible catalyst deactivation or product inhibition.[27] To do so, two catalytic reactions were carried out, with one monitoring consumption of 1-pyrenecarboxaldehyde from the beginning, and the other from the reaction time mid-point. After the time adjustment, it was determined that the catalytic system indeed suffers from either product inhibition or catalyst deactivation (Fig. B36). To distinguish which one, a new pair of reactions was performed - one with less substrate and HBpin compared to the normal reaction, and another with the product present at the beginning. After the time adjustment was applied, it was found that the catalytic system suffers from product inhibition (Fig. B37), which was confirmed by DFT (below).

Table 3.2. Substrate scope for catalytic aldehyde hydroboration using **3.2$_{Co}$**.

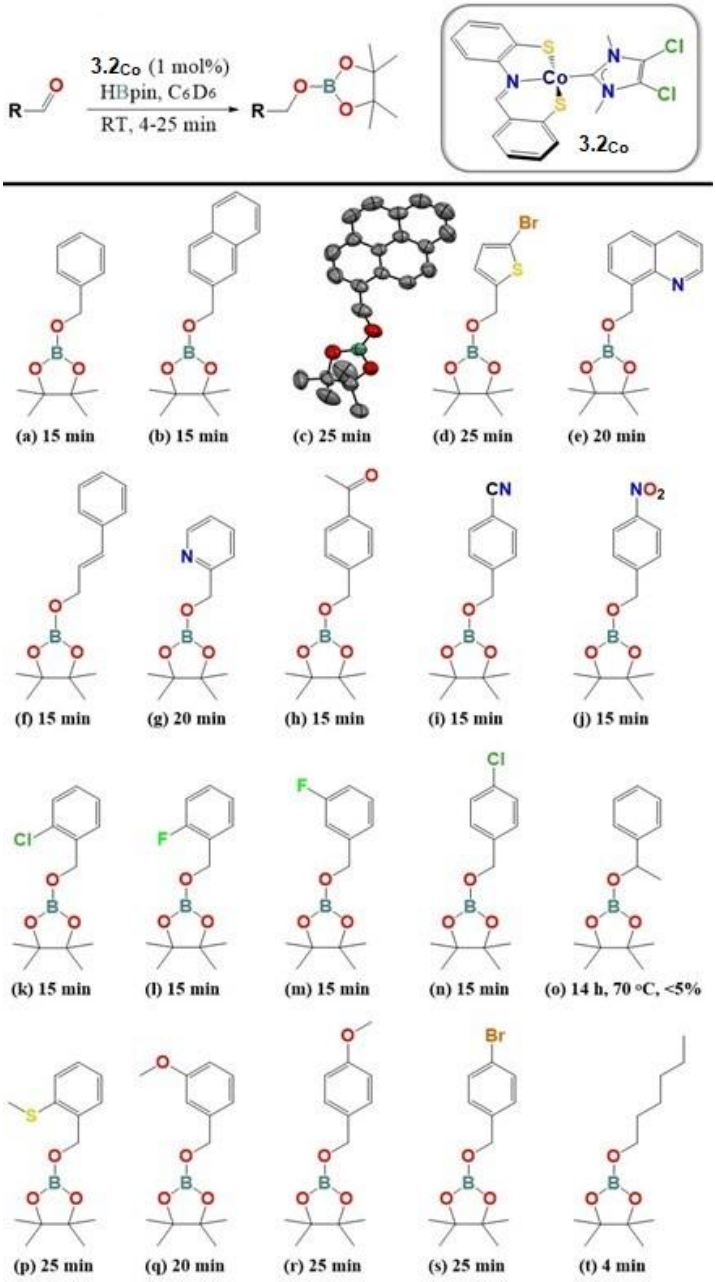

[a]Reaction conditions: Substrate (0.53 mmol), pinacolborane (0.53 mmol), **3.2$_{Co}$** (1 mol%), C_6D_6 (0.5 mL) at room temperature for 4-25 min. Yields were determined from ^{1}H NMR integration relative to mesitylene internal standard.

These results are in agreement with **3.2$_{Co}$** being reusable after recovering and washing the hydroboration product away, as described earlier. Since it was observed that hydroboration of an aliphatic aldehyde proceeds to completion in shorter time than aromatic derivatives, and also *in-situ* addition of extra hexanal and HBpin in the second and third runs shows the same catalytic

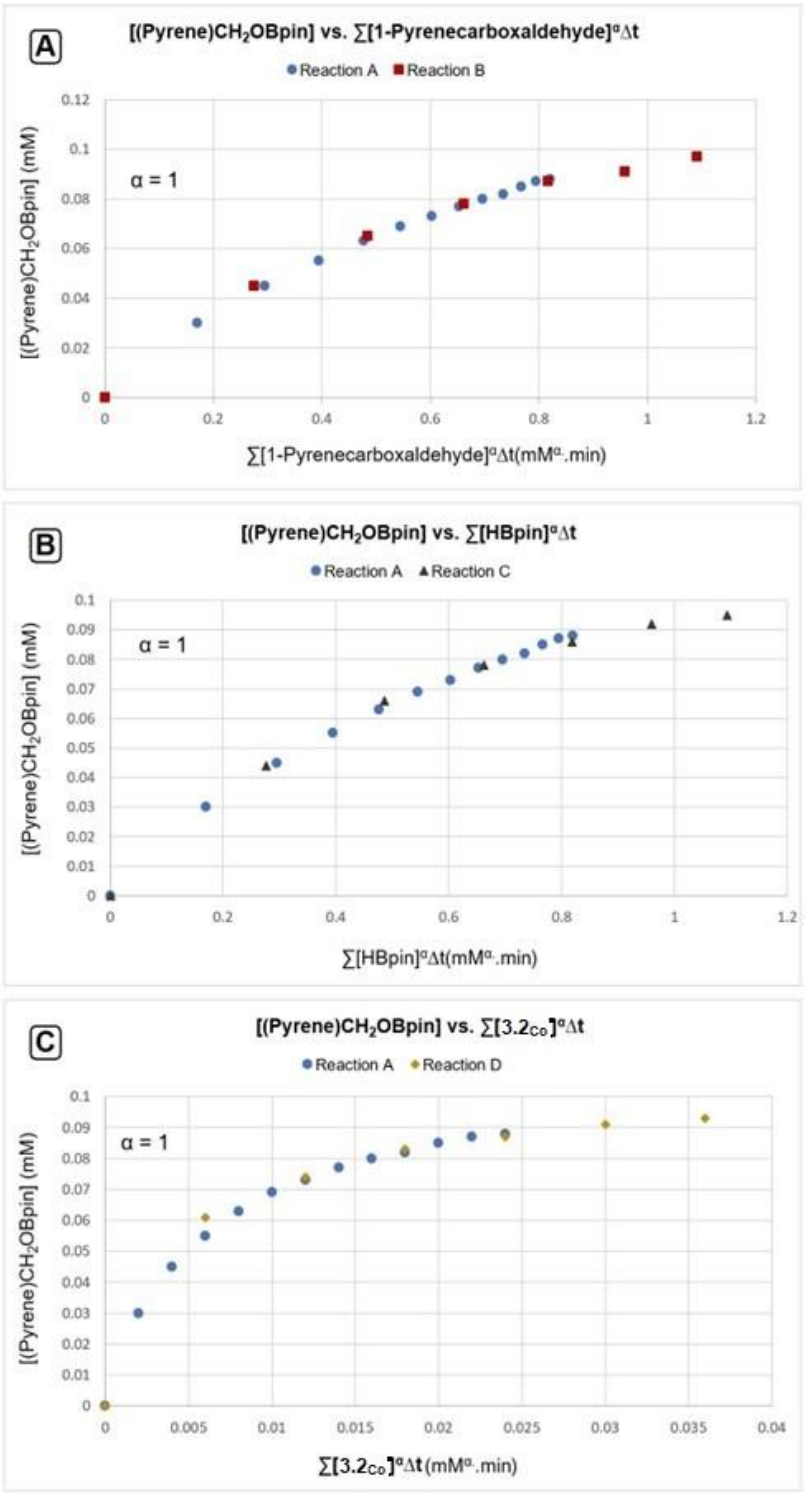

Figure 3.1. VTNA of the kinetics data: (A) rate dependence on [1-pyrenecarboxaldehyde]; (B) rate dependence on [HBpin]; (C) rate dependence on [**3.2**$_{Co}$].

activity for **3.2$_{Co}$**, VTNA was applied using hexanal as the substrate (See experimental section). First order dependence was found for hexanal, HBpin and **3.2$_{Co}$** and no product inhibition or catalyst deactivation was found (Fig. B42), showing the impact of substrate aromatic rings on product inhibition.

To gain further insight into the reaction pathway, stoichiometric reaction of **3.2$_{Co}$** and HBpin in C_6D_6 was monitored by ^{1}H NMR, showing no reaction (**Figure 3.2**). Stoichiometric reaction of **3.2$_{Co}$** and benzaldehyde, however, resulted in two new resonances at δ +14 and +17.8 in the ^{1}H NMR spectrum. This observation suggests some interaction of benzaldehyde with **3.2$_{Co}$** although no other changes or shifts were observed in other resonances assigned to **3.2$_{Co}$** (**Figure 3.2**). Subsequent stoichiometric addition of HBpin to this reaction mixture resulted in disappearance of the two peaks, while those due to **3.2$_{Co}$** remained unchanged (**Figure 3.2**). Furthermore, when aliphatic aldehyde hexanal was treated with one equiv of **3.2$_{Co}$**, no additional resonances were detected (**Figure 3.2**). In addition, the EPR spectrum of the benzaldehyde/**3.2$_{Co}$** reaction mixture was indistinguishable from that of **3.2$_{Co}$** (**Figure 3.3**). In another experiment, a gram-scale catalytic hydroboration of 1-pyrenecarboxaldehyde was performed and the catalyst was recovered and analyzed using EPR (Fig. B11) and ^{1}H NMR (Fig. B12), again showing unchanged **3.2$_{Co}$**. To identify the roles of the two thiolate donors in B–H bond activation and aldehyde reduction, DFT calculations were performed.

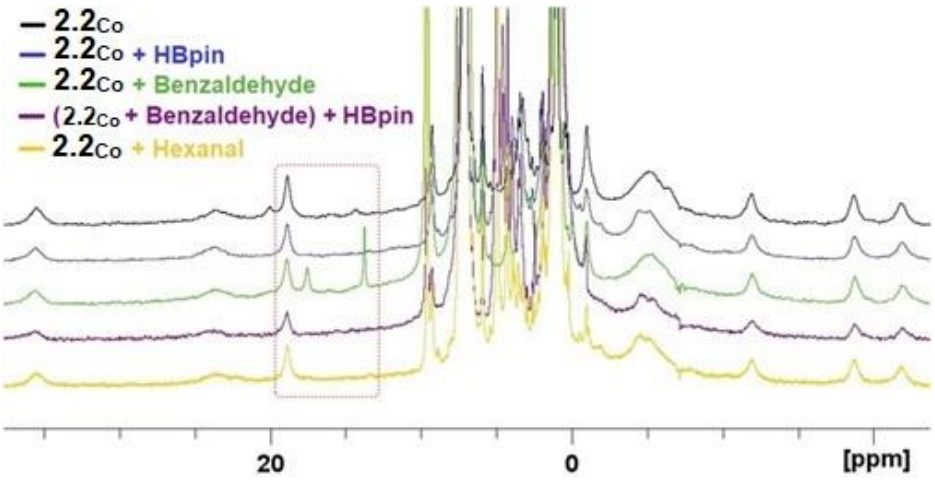

Figure 3.2. Stacked plot of ^{1}H NMR spectra of **3.2$_{Co}$** (black), stoichiometric reactions of **3.2$_{Co}$** with HBpin (blue), **3.2$_{Co}$** with benzaldehyde (green), **3.2$_{Co}$** with benzaldehyde and subsequently HBpin (purple), and **3.2$_{Co}$** with hexanal.

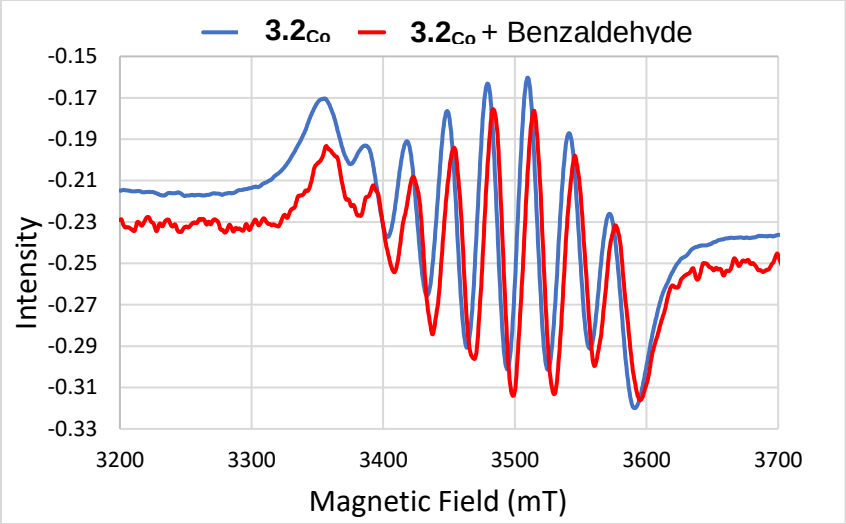

Figure 3.3. EPR spectra of **3.2$_{Co}$** (blue) and reaction mixture of **3.2$_{Co}$** and benzaldehyde (red).

3.2.4 DFT Calculations

DFT calculations using the B3LYP functional[28] and the XDM dispersion correction[29] were performed to evaluate catalysis reaction pathways. The proposed pathways, along with the computed free-energy changes for all steps, are shown in **Figure 3.4**. Two pathways were considered, depending on which of the inequivalent thiolate S atoms initially interacts with HBpin. Calculations predict initial formation of a stable, π-stacked van der Waals complex between benzaldehyde and **3.2$_{Co}$**. HBpin can then approach this complex, yielding a van der Waals ternary complex in an arrangement conducive to reaction. In agreement with the experimental NMR and EPR findings, we were able to identify distinct ternary complexes that allow the inequivalent thiolate S donors to coordinate to B in the downhill step via a cyclic, 6-membered transition state (TS). The **3.2$_{Co}$** catalyst aids B–H bond activation and TS stabilization through formation of both a partial S-B bond (~2.0 Å) involving the HBpin and a partial Co-O bond (~2.2 Å) involving the benzaldehyde. The free energy of activation is slightly lower for the pathway involving the S atom of the 5-membered ring (22.2 kcal/mol) compared to the 6-membered ring (24.2 kcal/mol). However, both pathways give activation free energies that are significantly lower than the value of 39.2 kcal/mol calculated for the uncatalyzed, bimolecular reaction of benzaldehyde and HBpin. Finally, the hydroboration product also forms a fairly strongly bound π-stacked complex with **3.2$_{Co}$**, consistent with the observed product inhibition. The same mechanism was calculated using acetophenone as substrate and the calculated free-energies are displayed in Fig. B43. Overall, the

obtained free-energies are very close to those of benzaldehyde, which is not in agreement with experimental results, as **3.2$_{Co}$** showed no potential for catalyzing hydroboration of acetophenone. Thus we cannot explain the observed lack of reactivity for acetophenone based on transition-state modeling alone. The pre-reaction complexes for the benzaldehyde and acetophenone show that the methyl group of acetophenone does need to move up and out of the way, which would affect the reaction coordinate (**Figure 3.5**).

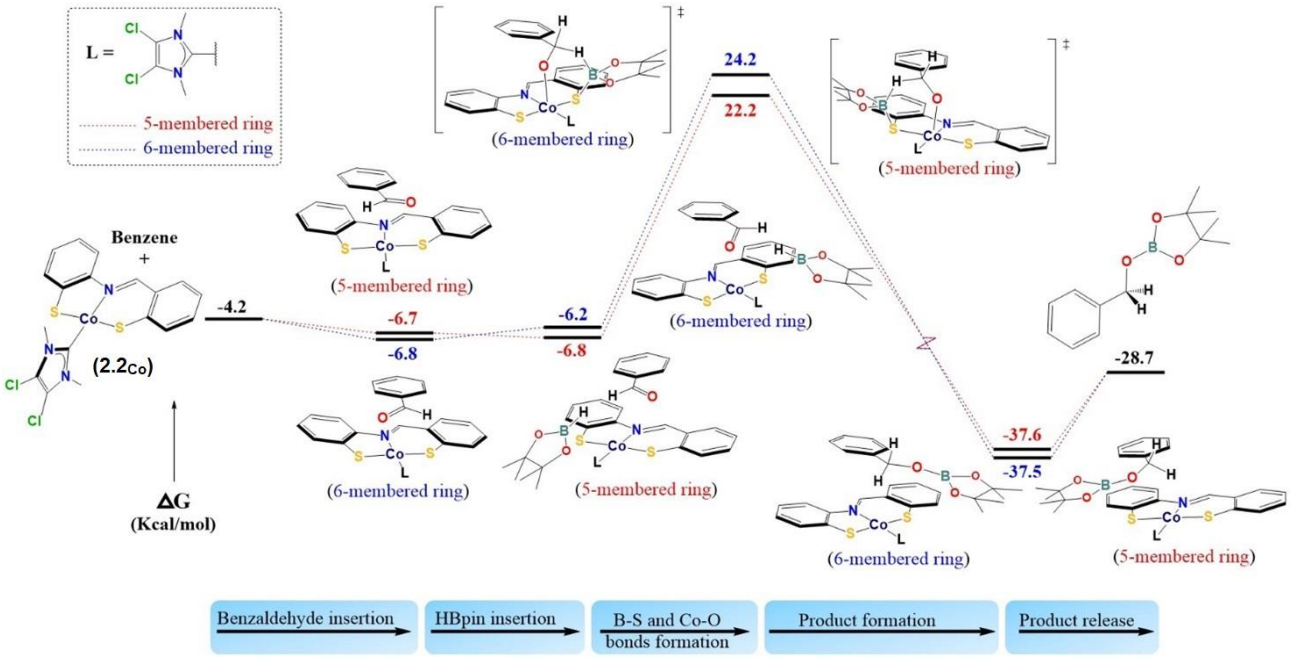

Figure 3.4. DFT calculated energy profile of **3.2$_{Co}$**-catalyzed benzaldehyde hydroboration through 5- and 6-membered metallocycles.

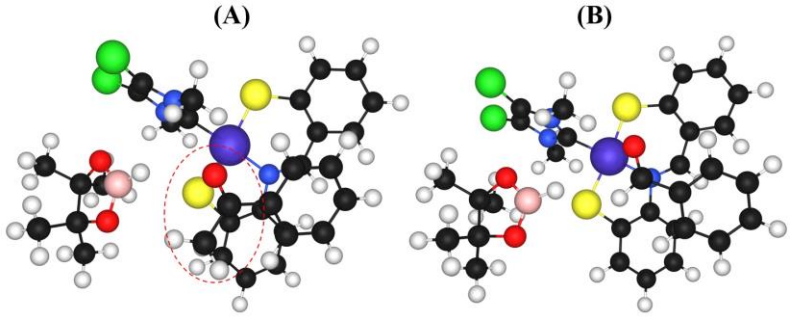

Figure 3.5. Geometries of the pre-reaction ternary complexes of **3.2$_{Co}$** with HBpin and acetophenone (A) benzaldehyde (B).

3.3 Conclusions

The **3.2$_{Co}$** catalytic system showed a remarkable selectivity for aldehyde hydroboration, and also a bifunctional, hydride-free mechanism. DFT study showed two minima of a pi-stacked complex formed by dispersion of benzaldehyde on **3.2$_{Co}$**, which ended up proceeding through the 5-membered metallocycle being 2 kcal/mol more stable in transition state, compared to that of the 6-membered metallocycle. VTNA showed that aromatic aldehydes, unlike aliphatic aldehydes, suffer from product inhibition. These observations were verified by stoichiometric and catalytic reactions. As previously observed[15], first row metal thiolate catalysts tend to prefer a hydride-free mechanism in carbonyl hydroborations.

3.4 Experimental Section

3.4.1 General Considerations

All experiments were carried out under nitrogen, using a Schlenk line or an MBraun glovebox unless otherwise stated. Hexane, diethyl ether, acetonitrile and THF were dried on columns of activated alumina using a J. C. Meyer (formerly Glass Contour) solvent purification system. Anhydrous benzene (Aldrich), C_6D_6 and acetone-d_6 were dried with activated alumina (ca. 10 wt %) overnight, followed by filtration. Dichloromethane (DCM) and $CDCl_3$ were refluxed over calcium hydride under nitrogen, collected by distillation, dried further by passing through activated alumina (ca.10 wt%), and stored over activated 4 Å molecular sieves (heated at 250 ºC for 3 d under vacuum). Ligand precursor 2-(methylthio)-benzaldehyde,[30] 4,5-dichloro-1,3-dimethyl-1H-imidazol-3-ium iodide,[31] $S^{Me}N^{H}S^{Me}$ (**HL1**)[12b] and $SN^{H}S^{Me}$ (**HL2**)[12a] ligands, as well as $Co^{II}(\kappa^3\text{-}S^{Me}NS^{Me})_2$ (**3.1$_{Co}$**)[32] were prepared according to literature procedures. Other chemicals were used as obtained commercially: 2-(methylthio)-aniline (Alfa Aesar, 98%), $CoCl_2$ (Alfa Aesar, 97%), trifluoromethane sulfonimide ($NHTf_2$, Aldrich >95%), 4,5-dichloroimidazole (Alfa Aesar, 98%), iodomethane (Aldrich 99%), potassium carbonate (Aldrich >99%) and sodium bis(trimethylsilyl)amide (Alfa Aesar, 98%). ^{1}H and ^{11}B NMR spectra were recorded on a 300 MHz Bruker Avance or Avance II instrument at room temperature (21−25 °C). ^{1}H NMR spectra were referenced respectively to residual solvent protons (C_6D_6, δ 7.15; $CDCl_3$, δ 7.26; CD_3OD, δ 1.75 and 3.31) and ^{11}B NMR spectra to external BF_3 etherate at 0.0 ppm. EPR spectra were recorded on a Bruker Elexsys E580 X-band spectrometer equipped with nitrogen gas temperature control system. Mass spectra were recorded on an AB Sciex Q1MS mass spectrometer with electrospray

ionization (ESI-MS) in positive mode (ion spray voltage: 5000.0 V, TEM: 400 °C, declustering potential: 11.00 V and focusing potential: 300.0 V) with samples prepared to *ca.* 0.05 mg/mL in acetonitrile. For electron impact (EI), solid samples were prepared by drying products under vacuum, and spectra obtained using a Kratos Concept S1 instrument (Hres 7000−10000). X-ray diffraction data were collected on a Bruker Smart or Kappa diffractometer equipped with an ApexII CCD detector and a sealed-tube Mo K source (λ = 0.71073 Å).

3.4.2 Synthesis of Cobalt Complexes

Synthesis of $Co^{II}(\kappa^3$-SNS)(DII) (3.2_{Co}) (Procedure A)

A 42 mL scintillation vial was charged with **3.1_{Co}** (200 mg, 0.328 mmol) in 15 mL of THF. To this solution, 4,5-dichloro-1,3-dimethyl-1H-imidazol-3-ium iodide (96 mg, 0.328 mmol) in 5 mL THF was added dropwise. The solution was stirred overnight at room temperature, resulting in a navy-blue solution. To this solution was added dropwise a solution containing **HL2** (85 mg, 0.328 mmol) and sodium bis(trimethylsilyl)amide (60 mg, 0.328 mmol) in 10 mL THF. The solution changed to dark grey after being stirred overnight at room temperature. Then the solvent was removed and the residue extracted with DCM, filtered through Celite and the solvent removed. After washing with diethyl ether (3 × 3 mL), the residue was dried under vacuum affording 95 mg of **3.2_{Co}** (62%). Crystals suitable for X-ray diffraction were grown by hexane layering of a concentrated DCM solution at room temperature. ^{1}H NMR (300 MHz, $CDCl_3$): δ -4.46 (br, 6H), -29.50 (s, 1H), -24.54 (s, 1H), -22.43 (s, 1H), -17.33 (s, 1H), -11.68 (s, 1H), 9.62 (s, 1H), 19.73 (s, 1H), 26.55 (br, 1H), 37.55 (br, 1H). EI-MS: Calcd for $C_{18}H_{15}Cl_2CoN_3S_2$ m/z 465.94 ([M^+]). Found m/z 465.9.

Synthesis of $Co^{II}I(\kappa^2$-$S^{Me}NS^{Me}$)(DII) (3.3_{Co})

A 42 mL scintillation vial was charged with **3.1_{Co}** (200 mg, 0.328 mmol) in 15 mL of THF. To this solution, 4,5-dichloro-1,3-dimethyl-1H-imidazol-3-ium iodide (96 mg, 0.328 mmol) in 5 mL THF was added dropwise. The solution turned navy blue after 2 h and was then stirred overnight at room temperature. The solvent was removed under vacuum and the residue was washed with diethyl ether (3 × 3 mL) and dried under vacuum affording 155 mg of **3.3_{Co}** (75%). ^{1}H NMR (300 MHz, $CDCl_3$): δ -4.46 (b, 6H), -29.50 (s, 1H), -24.54 (s, 1H), -22.43 (s, 1H), -17.33

(s, 1H), -11.68 (s, 1H), 9.62 (s, 1H), 19.73 (s, 1H), 26.55 (b, 1H), 37.55 (b, 1H). EI-MS: Calcd for $C_{18}H_{15}Cl_2CoN_3S_2$ m/z 465.94 ([M^+]). Found m/z 465.9.

Synthesis of $\mathbf{3.2_{Co}}$ (Procedure B: from $\mathbf{3.3_{Co}}$)

A 42 mL scintillation vial was charged with **$\mathbf{3.3_{Co}}$** (205 mg, 0.328 mmol) in 15 mL of THF. To this solution was added dropwise a THF solution (5 mL) containing **HL2** (85 mg, 0.328 mmol) and NaHMDS (60 mg, 0.328 mmol). The solution turned dark grey and was stirred overnight at room temperature. Then the solvent was removed under vacuum and the residue was extracted into DCM. DCM was removed under vacuum and the residue was washed with diethyl ether (3 × 3 mL) and dried under vacuum affording 97 mg of **$\mathbf{3.2_{Co}}$** (63%).

Synthesis of $CoI_2(DDI)_2$ ($\mathbf{3.4_{Co}}$)

A 42 mL scintillation vial was charged with **$\mathbf{3.1_{Co}}$** (200 mg, 0.328 mmol) in 15 mL of THF. To this solution, 4,5-dichloro-1,3-dimethyl-1H-imidazol-3-ium iodide (192 mg, 0.656 mmol) in 5 mL THF was added dropwise. The solution turned green from the starting purple and was then stirred overnight at room temperature. The solvent was removed and the residue was washed with diethyl ether (3 × 3 mL), and dried under vacuum affording 182 mg **$\mathbf{3.4_{Co}}$** (86%). Crystals suitable for X-ray diffraction were grown by hexane layering of a concentrated DCM solution at room temperature. ^{1}H NMR (300 MHz, $CDCl_3$): δ -0.07 (br, 6H, DII-CH_3). EI-MS: Calcd for $C_{10}H_{12}Cl_4CoI_2N_4$ m/z 642.72 ([M^+]). Found m/z 642.7.

Synthesis of $\mathbf{3.2_{Co}}$ (Procedure C – unsuccessful)

A 42 mL scintillation vial was charged with **$\mathbf{3.4_{Co}}$** (210 mg, 0.328 mmol) in 15 mL of THF. To this solution, a THF solution (5 mL) containing **HL2** (85 mg, 0.328 mmol) and NaHMDS (60 mg, 0.328 mmol) was added dropwise. The solution turned brown and was stirred overnight at room temperature. Then the solvent was removed under vacuum and the residue was extracted into DCM. The DCM was removed under vacuum and the residue was washed with diethyl ether (3 × 3 mL), and dried under vacuum affording 170 mg product which was not **$\mathbf{3.2_{Co}}$**. Due to the different color of this product and absence of **$\mathbf{3.2_{Co}}$** in the EI-MS of the product, further characterization was not pursued.

3.4.3 Catalysis Protocols

General procedure for hydroboration of aldehydes

A catalyst stock solution was prepared by dissolving **3.2$_{Co}$** (10 mg) in C_6D_6 (4 mL). A vial was charged with the appropriate amount of **3.2$_{Co}$** (2.5 mg, 1 mL, 5.3 μmol, 1 mol%), aldehyde substrate (0.53 mmol), and subsequently pinacolborane (77 μL, 0.53 mmol). Every 5 minutes 2 drops of the reaction mixture were transferred to an NMR tube and diluted with C_6D_6 for further analysis. Reaction times varied from 15-25 min at room temperature. Yield was determined by ^{1}H NMR in reference to internal standard mesitylene. For substrates having another functional group with potential of being hydroborated, ^{11}B NMR was also performed to check the selectivity.

In order to isolate the hydroborated product (4,4,5,5-tetramethyl-2-(pyren-1-ylmethoxy)-1,3,2-dioxaborolane) for the kinetic study, the reaction mixture was evaporated and the residue was dissolved in hexane and filtered. The filtrate was kept at -39 ˚C overnight, affording colorless crystals of the product.

Hydroboration of benzaldehyde

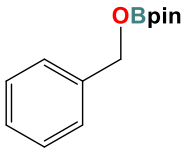

Following the general procedure, benzaldehyde (53.8 μL, 0.53 mmol), pinacolborane (77 μL, 0.53 mmol), and **3.2$_{Co}$** (2.5 mg, 1 mol%) were used. ^{1}H NMR showed quantitative conversion to hydroboration product after 15 min at room temperature.

Hydroboration of 2-naphthaldehyde

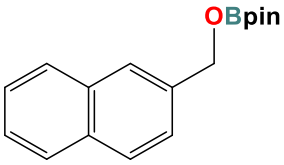

Following the general procedure, 2-naphthaldehyde (82 mg, 0.53 mmol), pinacolborane (77 μL, 0.53 mmol), and **3.2$_{Co}$** (2.5 mg, 1 mol%) were used. ^{1}H NMR showed quantitative conversion to hydroboration product after 15 min at room temperature.

Hydroboration of 1-pyrenecarboxaldehyde

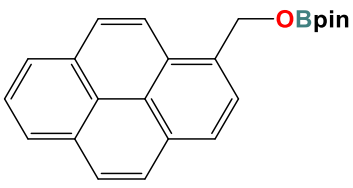

Following the general procedure, 1-pyrenecarboxaldehyde (122 mg, 0.53 mmol), pinacolborane (77 μL, 0.53 mmol), and **3.2$_{Co}$** (2.5 mg, 1 mol%) were used. ^{1}H NMR showed quantitative conversion to hydroboration product after 25 min at room temperature.

Hydroboration of 5-bromo-2-thiophenecarboxaldehyde

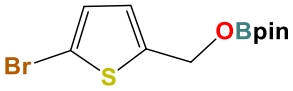

Following the general procedure, 5-bromo-2-thiophenecarboxaldehyde (63 µL, 0.53 mmol), pinacolborane (77 µL, 0.53 mmol), and **3.2**$_{Co}$ (2.5 mg, 1 mol%) were used. ^{1}H NMR showed quantitative conversion to hydroboration product after 25 min at room temperature.

Hydroboration of quinoline-8-carboxaldehyde

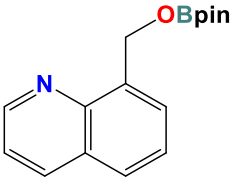

Following the general procedure, quinoline-8-carboxaldehyde (83 mg, 0.53 mmol), pinacolborane (77 µL, 0.53 mmol), and **3.2**$_{Co}$ (2.5 mg, 1 mol%) were used. ^{1}H NMR showed quantitative conversion to hydroboration product after 20 min at room temperature.

Hydroboration of cinnamaldehyde

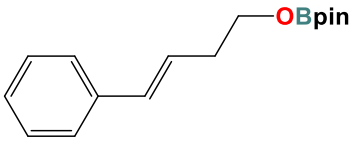

Following the general procedure, cinnamaldehyde (66.7 µL, 0.53 mmol), pinacolborane (77 µL, 0.53 mmol), and **3.2**$_{Co}$ (2.5 mg, 1 mol%) were used. ^{1}H NMR showed quantitative conversion to hydroboration product after 15 min at room temperature.

Hydroboration of pyridine-2-carboxaldehyde

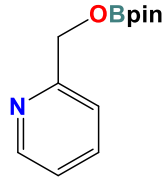

Following the general procedure, pyridine-2-carboxaldehyde (50.4 µL, 0.53 mmol), pinacolborane (77 µL, 0.53 mmol), and **3.2**$_{Co}$ (2.5 mg, 1 mol%) were used. ^{1}H NMR showed quantitative conversion to hydroboration product after 20 min at room temperature.

Hydroboration of 4-acetyl-benzaldehyde

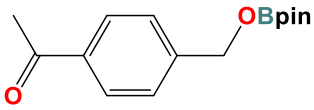

Following the general procedure, 4-acetyl-benzaldehyde (78 mg, 0.53 mmol), pinacolborane (77 µL, 0.53 mmol), and **3.2**$_{Co}$ (2.5 mg, 1 mol%) were used. ^{1}H NMR showed quantitative conversion to hydroboration product after 15 min at room temperature.

Hydroboration of 4-cyano-benzaldehyde

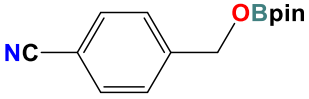

Following the general procedure, 4-cyano-benzaldehyde (69 mg, 0.53 mmol), pinacolborane (77 µL, 0.53 mmol), and **3.2**$_{Co}$ (2.5 mg, 1 mol%) were used. ^{1}H NMR showed quantitative conversion to hydroboration product after 15 min at room temperature.

Hydroboration of 4-nitro-benzaldehyde

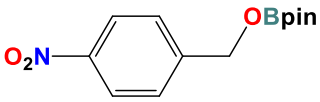

Following the general procedure, 4-nitro-benzaldehyde (80 mg, 0.53 mmol), pinacolborane (77 µL, 0.53 mmol), and **3.2**$_{Co}$ (2.5 mg, 1 mol%) were used. 1H NMR showed quantitative conversion to hydroboration product after 15 min at room temperature.

Hydroboration of 2-chloro-benzaldehyde

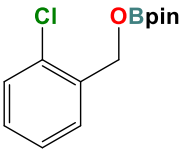

Following the general procedure, 2-chloro-benzaldehyde (59.6 µL, 0.53 mmol), pinacolborane (77 µL, 0.53 mmol), and **3.2**$_{Co}$ (2.5 mg, 1 mol%) were used. ^{1}H NMR showed quantitative conversion to hydroboration product after 15 min at room temperature.

Hydroboration of 2-fluoro-benzaldehyde

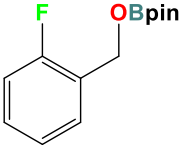

Following the general procedure, 2-fluoro-benzaldehyde (55.8 µL, 0.53 mmol), pinacolborane (77 µL, 0.53 mmol), and **3.2**$_{Co}$ (2.5 mg, 1 mol%) were used. ^{1}H NMR showed quantitative conversion to hydroboration product after 15 min at room temperature.

Hydroboration of 3-fluorobenzaldehyde

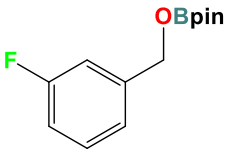

Following the general procedure, 3-fluorobenzaldehyde (56.2 µL, 0.53 mmol), pinacolborane (77 µL, 0.53 mmol), and **3.2**$_{Co}$ (2.5 mg, 1 mol%) were used. ^{1}H NMR showed quantitative conversion to hydroboration product after 15 min at room temperature.

Hydroboration of 4-chloro-benzaldehyde

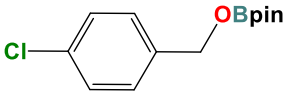

Following the general procedure, 4-chloro-benzaldehyde (74 mg, 0.53 mmol), pinacolborane (77 µL, 0.53 mmol), and **3.2**$_{Co}$ (2.5 mg, 1 mol%) were used. ^{1}H NMR showed quantitative conversion to hydroboration product after 15 min at room temperature.

Hydroboration of 2-(methylthio)-benzaldehyde

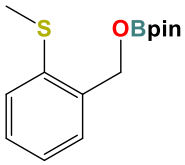

Following the general procedure, 2-(methylthio)-benzaldehyde (68.3 µL, 0.53 mmol), pinacolborane (77 µL, 0.53 mmol), and **3.2**$_{Co}$ (2.5 mg, 1 mol%) were used. ^{1}H NMR showed quantitative conversion to hydroboration product after 25 min at room temperature.

Hydroboration of 3-methoxy-benzaldehyde

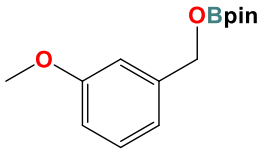

Following the general procedure, 3-methoxy-benzaldehyde (64.6 µL, 0.53 mmol), pinacolborane (77 µL, 0.53 mmol), and **3.2**$_{Co}$ (2.5 mg, 1 mol%) were used. ^{1}H NMR showed quantitative conversion to hydroboration product after 20 min at room temperature.

Hydroboration of 4-methoxy-benzaldehyde

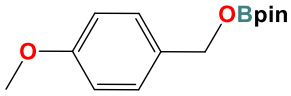

Following the general procedure, 4-methoxy-benzaldehyde (64.4 µL, 0.53 mmol), pinacolborane (77 µL, 0.53 mmol), and **3.2**$_{Co}$ (2.5 mg, 1 mol%) were used. ^{1}H NMR showed quantitative conversion to hydroboration product after 25 min at room temperature.

Hydroboration of 4-bromo-benzaldehyde

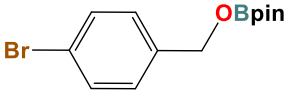

Following the general procedure, 4-bromo-benzaldehyde (98 mg, 0.53 mmol), pinacolborane (77 µL, 0.53 mmol), and **3.2**$_{Co}$ (2.5 mg, 1 mol%) were used. ^{1}H NMR showed quantitative conversion to hydroboration product after 25 min at room temperature.

Hydroboration of hexanal

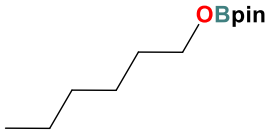

Following the general procedure, hexanal (65 μL, 0.53 mmol), pinacolborane (77 μL, 0.53 mmol), and **3.2$_{Co}$** (2.5 mg, 1 mol%) were used. ^{1}H NMR showed quantitative conversion to hydroboration product after 4 min at room temperature.

3.4.4 Mechanistic studies

3.4.4.1 Stoichiometric reaction of 3.2$_{Co}$ and pinacolborane

To a navy-blue solution of **3.2$_{Co}$** (0.010 g, 0.021 mmol, in 1 mL of C_6D_6) was added pinacolborane (3.00 μL, 0.021 mmol, 1 equiv) and the mixture was stirred for 2 h, but no color changes were observed. Afterwards, the solution was transferred to an NMR tube for further analysis. The ^{1}H NMR spectrum of the mixture showed no changes in **3.2$_{Co}$**.

3.4.4.2 Stoichiometric reaction of 3.2$_{Co}$ and benzaldehyde

To a navy-blue solution of **3.2$_{Co}$** (0.010 g, 0.021 mmol, in 1 mL of C_6D_6) was added benzaldehyde (2.1 μL, 0.021 mmol, 1 equiv.) and the mixture was transferred to an NMR tube. No color changes were noted. The ^{1}H NMR spectrum showed 2 extra peaks in the paramagnetic area, but no significant shifts or changes were observed in **3.2$_{Co}$** related peaks. In addition, the EPR spectrum showed no changes compared to that of **3.2$_{Co}$**.

3.4.4.3 Stepwise stoichiometric hydroboration

To a navy-blue solution of **3.2$_{Co}$** (0.010 g, 0.021 mmol, in 1 mL of C_6D_6) was added benzaldehyde (2.1 μL, 0.021 mmol, 1 equiv.) and then the mixture was transferred to an NMR tube. The two extra peaks mentioned earlier appeared again. To this solution was added pinacolborane (3.00 μL, 0.021 mmol, 1 equiv) and the NMR tube was shaken well. After 30 min, the solution was analyzed by ^{1}H NMR showing hydroboration product, disappearance of the two peaks which showed up after addition of benzaldehyde to **3.2$_{Co}$**, and still no shifts or changes in **3.2$_{Co}$** resonances (Figure B10).

3.4.4.4 Catalyst recovery and reusability

A vial was charged with the appropriate amount of **3.2$_{Co}$** (25 mg, 53 μmol, 1 mol%) and 5 mL of benzene, 1-pyrenecarboxaldehyde (1220 mg, 5.3 mmol), and subsequently pinacolborane (770 μL, 5.3 mmol). The mixture was stirred for 1 h at room temperature. Then the solvent was completely evaporated under vacuum and the residue was washed with hexane (3 x 5 mL) and filtered. The recovered **3.2$_{Co}$** was dried under vacuum and a portion was dissolved in C_6D_6 for ^1H NMR analysis (Fig. B12), another portion was dissolved in DCM for EPR analysis (Fig. B11), and the rest was employed in catalytic benzaldehyde hydroboration reaction for checking the reusability of **3.2$_{Co}$**.

3.4.5 Kinetic Studies

(All kinetic reactions were set up in a dinitrogen glovebox and performed the same way with appropriate amounts of **3.2$_{Co}$**, 1-pyrenecarboxaldehyde, HBpin, and 4,4,5,5-tetramethyl-2-(pyren-1-ylmethoxy)-1,3,2-dioxaborolane – See **Table 3.3**, and Hexanal – See **Table 3.4**).

General Procedure for Reaction A

A catalyst stock solution was prepared by dissolving 0.014 g (0.030 mM) of **3.2$_{Co}$** in 3 mL of C_6D_6. An NMR tube was charged with 100 μL of catalyst stock solution (0.467 mg, 0.001 mM, 1 mol%). Afterward, a vial was charged with 1-pyrenecarboxaldehyde (23 mg, 0.1 mM) and 0.300 mL of C_6D_6 and the solution was transferred to the NMR tube. The vial was rinsed with 0.200 mL of C_6D_6 and transferred to the same NMR tube. The NMR tube was capped with a rubber septum. A 50 μL micro-syringe, pre-charged with HBpin (14.5 μL, 0.1 mM) was capped by poking into the rubber septum. The NMR tube containing the reaction mixture and the micro-syringe were removed from the glovebox. The HBpin was injected into the NMR tube, shaken quickly, and immediately inserted into the NMR spectrometer. A ^{11}B NMR spectrum was taken every 2 min for 25 min at room temperature. Concentration of (pyrene)CH_2OBpin product was calculated based on integrals of the known [HBpin]. All 5 other reactions (B-F) were carried out through the same procedure, but for reaction F, (pyrene)CH_2OBpin (0.010 mg, 0.03 mM) was added to the vial containing 1-pyrenecarboxaldehyde. Through the same procedure, hexanal was used as an aliphatic aldehyde (**Table 3.4**).

Table 3.3. Concentrations of Reagents for Reactions A-F for VTNA*.

Reaction	[**3.2**$_{Co}$]	[1-Pyrenecarboxaldehyde]	[HBpin]	[(Pyrene)CH_2OBpin]
A ●	0.001	0.10	0.10	-
B ■	0.001	0.16	0.10	-
C ▲	0.001	0.10	0.16	-
D ♦	0.003	0.10	0.10	-
E ●	0.001	0.07	0.07	-
F ●	0.001	0.07	0.07	0.03

*All the amounts are in mM.

Table 3.4. Concentrations of Reagents for Reactions G-K for VTNA*.

Reaction	[**3.2**$_{Co}$]	[Hexanal]	[HBpin]
G ●	0.001	0.10	0.10
H ●	0.001	0.16	0.10
I ●	0.001	0.10	0.16
J ●	0.003	0.10	0.10
K ●	0.001	0.07	0.07

*All the amounts are in mM.

3.4.6 Crystallographic Details

Crystallographic data were collected from single crystals mounted on MiTeGen dual thickness MicroMounts using Parabar oil. Data were collected on a Bruker Smart ApexII single crystal diffractometer equipped with a graphite monochromator. The instrument was equipped with a sealed tube Mo K$\boldsymbol{\alpha}$ source ($\boldsymbol{\lambda} = 0.71073$ Å), an ApexII CCD detector and a dry compressed air-cooling system. All samples were cooled to 203(2) (**3.2**$_{Co}$ and **3.4**$_{Co}$) or 293(2) (**C**) K during data collection. Raw data collection and processing were performed with the Apex3 software package from Bruker.[33] Initial unit cell parameters were determined from 36 data frames from select $\boldsymbol{\omega}$ scans. Semi-empirical absorption corrections based on equivalent reflections were applied.[34] Systematic absences in the diffraction data-set and unit-cell parameters were consistent with the assigned space group. The initial structural solutions were determined using ShelxT direct methods,[35] and refined with full-matrix least-squares procedures based on $\boldsymbol{F^2}$ using ShelXL or ShelXle.[36] Compounds **3.2**$_{Co}$ and **C** exhibited positional disorders which were refined in ShelXle.

Hydrogen atoms were placed geometrically and refined using a riding model. Deposition Numbers: 2162426-2162428.

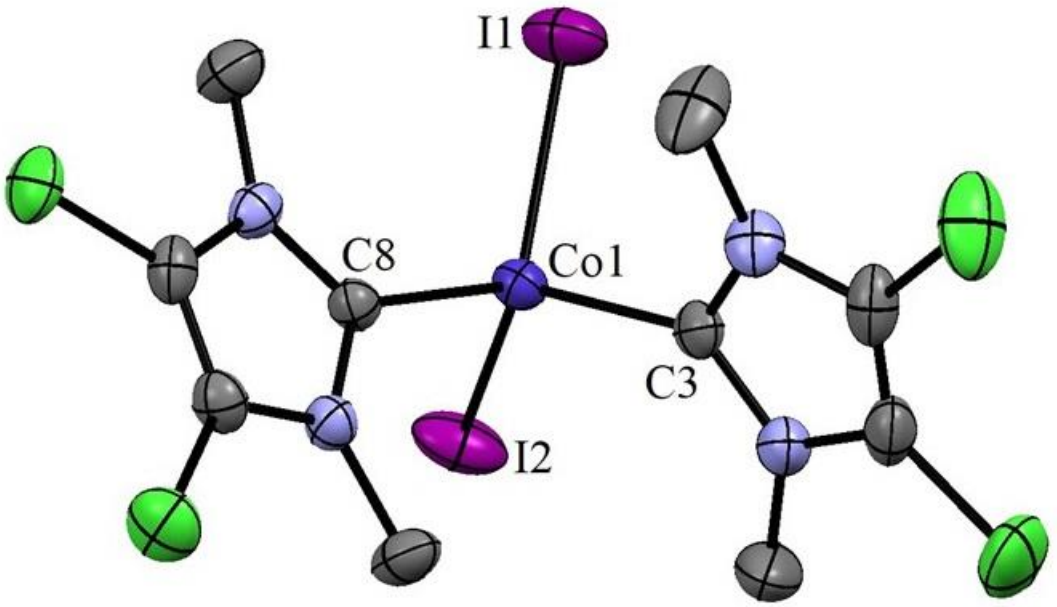

Figure 3.6. Molecular structure of **3.4$_{Co}$** with 50% probability thermal ellipsoids and hydrogen atoms omitted for clarity. Selected bond distances (Å) and angles (deg): Co-I1 2.5917(7), Co-I2 2.5988(8), Co-C3 2.056(4), Co-C8 2.049(4), I1-Co-I2 103.98(2), I1-Co-C3 105.4(1), I1-Co-C8 117.7(1), I2-Co-C3 118.5(1), I2-Co-C8 106.6(1), C3-Co-C8 105.3(2).

3.4.7 Computational Details

All calculations were carried out using the B3LYP functional[28] and the XDM dispersion correction[29] with the Gaussian 09[37] and postg[38] programs. The geometries of all species were optimized using a mixed basis set, in which 6-31G* was assigned to H, B, and C, while 6-31+G* was assigned to N, O, S, Cl, and Co. Frequency calculations with this same mixed basis set were performed to determine the thermal free-energy corrections assuming an ideal gas with a molar volume of 1L and a temperature of 298.15 K. Subsequent single-point energy calculations were performed on the optimized structures using the larger 6-311+G(2d,2p) basis set. The XDM damping parameters were set to a_1=0, a_2=3.7737 A for the geometry optimizations and frequency calculations, and a_1=0.4376, a_2=2.1607 A for the single-point energies. Polarizable continuum models were not used as all reactions were carried out in non-polar, benzene solvent. Initial tests

applying a solvent correction to the uncatalyzed reaction revealed no change in the predicted free energy of activation.

3.5 References

(1) (a) Magre, M.; Szewczyk, M.; Rueping, M. s-Block Metal Catalysts for the Hydroboration of Unsaturated Bonds. *Chem. Rev.* **2022**, *122*, 8261-8312; (b) Rej, S.; Das, A.; Panda, T. K. Overview of Regioselective and Stereoselective Catalytic Hydroboration of Alkynes. *Adv. Synth. Catal.* **2021**, *363*, 4818–4840; (c) Pandey, V. K.; Tiwari, C. S.; Rit, A. Silver-Catalyzed Hydroboration of C−X (X = C, O, N) Multiple Bonds. *Org. Lett.* **2021**, *23*, 1681−1686.

(2) (a) Li, M.; Liu, X.; Cui, D. Catalytic Hydroboration of Carbonyl Derivatives by using Phosphinimino Amide-Ligated Magnesium Complexes. *Dalton Trans.* **2021**, *50*, 13037–13041; (b) Makarov, K.; Kaushansky, A.; Eisen, M. S. Catalytic Hydroboration of Esters by Versatile Thorium and Uranium Amide Complexes. *ACS Catal.* **2022**, *12*, 273−284; (c) Walker, E. R. H. The Functional Group Selectivity of Complex Hydride Reducing Agents. *Chem. Soc. Rev.* **1976**, *5*, 23−50.

(3) (a) Kaithal, A.; Chatterjee, B.; Gunanathan, C. Ruthenium Catalyzed Selective Hydroboration of Carbonyl Compounds. *Org. Lett.* **2015**, *17*, 4790−4793; (b) Das, U. K.; Higman, C. S.; Gabidullin, B.; Hein, J. E.; Baker, R. T. Efficient and Selective Iron-Complex-Catalyzed Hydroboration of Aldehydes. *ACS Catal.* **2018**, *8*, 1076−1081.

(4) (a) Mendelsohn, L. N.; MacNeil, C. S.; Tian, L.; Park, Y.; Scholes, G. D.; Chirik, P. J. Visible-Light-Enhanced Cobalt-Catalyzed Hydrogenation: Switchable Catalysis Enabled by Divergence between Thermal and Photochemical Pathways. *ACS Catal.* **2021**, *11*, 1351−1360; (b) Hu, Y.; Zhang, Z.; Liu, Y.; Zhang, W. Cobalt-Catalyzed Chemo- and Enantioselective Hydrogenation of Conjugated Enynes. *Angew. Chem. Int. Ed.* **2021**, *60*, 16989–16993; (c) Borthakur, I.; Sau, A.; Kundu, S. Cobalt-catalyzed Dehydrogenative Functionalization of Alcohols: Progress and Future Prospects. *Coord. Chem. Rev.* **2022**, *451*, 214257.

(5) (a) You, Y.; Ge, S. Asymmetric Cobalt-Catalyzed Regioselective Hydrosilylation/Cyclization of 1,6-Enynes. *Angew. Chem. Int. Ed.* **2021**, *60*, 12046–12052; (b) Cheng, Z.; Guo, J.; Sun, Y.; Zheng, Y.; Zhou, Z.; Lu, Z. Regio-controllable

Cobalt-catalyzed Sequential Hydrosilylation/Hydroboration of Arylacetylenes. *Angew. Chem. Int. Ed.* **2021**, *60*, 22454–22460; (c) Jin, S.; Liu, K.; Wang, S.; Song, Q. Enantioselective Cobalt-catalyzed Cascade Hydrosilylation and Hydroboration of Alkynes to Access Enantioenriched 1,1-Silylboryl Alkanes. *J. Am. Chem. Soc.* **2021**, *143*, 13124−13134; (d) Lu, W.; Zhao, Y.; Meng, F. Cobalt-catalyzed Sequential Site- and Stereoselective Hydrosilylation of 1,3- and 1,4-Enynes. *J. Am. Chem. Soc.* **2022**, DOI: 10.1021/jacs.2c00288.

(6) (a) Li, C.; Song, S.; Li, Y.; Xu, C.; Luo, Q.; Guo, Y.; Wang, X. Selective Hydroboration of Unsaturated Bonds by an Easily Accessible Heterotopic Cobalt Catalyst. *Nat. Commun.* **2021,** *12*, 3813; (b) Chen, X.; Cheng, Z.; Lu, Z. Cobalt-Catalyzed Asymmetric Markovnikov Hydroboration of Styrenes. *ACS Catal*. **2019**, *9*, 4025−4029; (c) Peng, J.; Docherty, J. H.; Dominey, A. P.; Thomas, S. P. Cobalt-catalysed Markovnikov Selective Hydroboration of Vinylarenes. *Chem. Commun.* **2017**, *53*, 4726—4729; (d) Park, J-W. Cobalt-catalyzed Alkyne Hydrosilylation as a New Frontier to Selectively Access Silyl–Hydrocarbons. *Chem. Commun.* **2022**, *58*, 491–504; (e) Sun, Y.; Guo, J.; Shen, X.; Lu, Z. Ligand Relay Catalysis for Cobalt-catalyzed Sequential Hydrosilylation and Hydrohydrazidation of Terminal Alkynes. *Nat. Commun.* **2022**, *13*, 650.

(7) (a) Wu, J.; Zeng, H.; Cheng, J.; Zheng, S.; Golen, J. A.; Manke, D. R.; Zhang, G. Cobalt(II) Coordination Polymer as a Precatalyst for Selective Hydroboration of Aldehydes, Ketones, and Imines. *J. Org. Chem.* **2018**, *83*, 9442−9448; (b) Tamang, S. R.; Bedi, D.; Shafiei–Haghighi, S.; Smith, C. R.; Crawford, C.; Findlater, M. Cobalt-Catalyzed Hydroboration of Alkenes, Aldehydes, and Ketones. *Org. Lett.* **2018**, *20*, 6695−6700; (c) Verma, P. K.; Sethulekshmi, A. S.; Geetharani, K. Markovnikov-Selective Co(I)-Catalyzed Hydroboration of Vinylarenes and Carbonyl Compounds. *Org. Lett.* **2018**, *20*, 7840−7845; (d) Guo, J.; Chen, J.; Lu, Z. Cobalt-catalyzed Asymmetric Hydroboration of Aryl Ketones with Pinacolborane. *Chem. Commun.* **2015**, *51*, 5725—5727; (e) Zhang, T.; Manna, K.; Lin, W. Metal−Organic Frameworks Stabilize Solution-Inaccessible Cobalt Catalysts for Highly Efficient Broad-scope Organic Transformations. *J. Am. Chem. Soc*. **2016**, *138*, 3241−3249.

(8) Elsby, M. R.; Son, M.; Oh, C.; Martin, J.; Baik, M–H.; Baker, R. T. Mechanistic Study of Metal−Ligand Cooperativity in Mn(II)-catalyzed Hydroborations: Hemilabile SNS Ligand Enables Metal Hydride-Free Reaction Pathway. *ACS Catal.* **2021**, *11*, 9043−9051.

(9) (a) Cao, K.; Xu, T-T.; Wu, J.; Zhang, C-Y.; Wen, X-Y.; Yang, J. The *in situ* NHC-Palladium-catalyzed Selective Activation of B(3)−H or B(6)−H Bonds of o-Carboranes for Hydroboration of Alkynes: An Efficient Approach to Alkenyl-o-carboranes. *Inorg. Chem.* **2021**, *60*, 1080−1085; (b) Devillard, M.; Cordier, M.; Roisnel, T.; Dinoi, C.; Rosal, I. D.; Alcaraz, G. Hydroboration of Vinyl Halides with Mesitylborane: A Direct Access to (Mesityl)(alkyl)haloboranes. *Chem. Commun.* **2022**, *58*, 1589–1592; (c) Skoch, K.; Daniliuc, C. G.; Kehr, G.; Erker, G. Alkyne 1,1–Hydroboration to a Reactive Frustrated P/B–H Lewis Pair. *Angew. Chem. Int. Ed.* **2021**, *60*, 6757–6763.

(10) (a) Elsby, M. R.; Baker, R. T. Strategies and Mechanisms of Metal–ligand Cooperativity in First-row Transition Metal Complex Catalysts. *Chem. Soc. Rev.* **2020**, *49*, 8933-8987; (b) Khusnutdinova, J. R.; Milstein, D. Metal–Ligand Cooperation. *Angew. Chem. Int. Ed.* **2015**, *54*, 12236–12273; (c) Fritz, M.; Schneider, S. in *The Periodic Table II: Catalytic, Materials, Biological and Medical Applications*, D. M. P. Mingos, Ed., Springer, **2019**.

(11) (a) Lata, C. J.; Crudden, C. M. Dramatic Effect of Lewis Acids on the Rhodium-Catalyzed Hydroboration of Olefins. *J. Am. Chem. Soc.* **2010**, *132*, 131–137; (b) Fleige, M.; Mobus, J.; Stein, T. V.; Glorius, F.; Stephan, D. W. Lewis Acid Catalysis: Catalytic Hydroboration of Alkynes Initiated by Piers' Borane. *Chem. Commun.* **2016**, *52*, 10830—10833; (c) Titze, M. Heitkamper, J.; Junge, T.; Kastner, J.; Peters, R. Highly Active Cooperative Lewis Acid—Ammonium Salt Catalyst for the Enantioselective Hydroboration of Ketones. *Angew. Chem. Int. Ed.* **2021**, *60*, 5544–5553.

(12) (a) Das, U. K.; Daifuku, S. L.; Gorelsky, S. I.; Korobkov, I.; Neidig, M. L.; Le Roy, J. J.; Murugesu, M.; Baker, R. T. Mononuclear, Dinuclear, and Trinuclear Iron Complexes Featuring a New Monoanionic SNS Thiolate Ligand. *Inorg. Chem.* **2016**, *55*, 987−997; (b) Das, U. K.; Daifuku, S. L.; Iannuzzi, T. E.; Gorelsky, S. I.; Korobkov, I.; Gabidullin, B.; Neidig, M. L.; Baker, R. T. Iron(II) Complexes of a Hemilabile SNS Amido Ligand: Synthesis, Characterization, and Reactivity. *Inorg. Chem.* **2017**, *56*, 13766−13776.

(13) (a) Bahr, S.; Oestreich, M. A Neutral Ru^{II} Hydride Complex for the Regio- and Chemoselective Reduction of N-Silylpyridinium Ions. *Chem. Eur. J.* **2018**, *24*, 5613–5622; (b) Königs, C. D. F.; Klare, H. F. T.; Oestreich, M. Catalytic 1,4-Selective Hydrosilylation of Pyridines and Benzannulated Congeners. *Angew. Chem. Int. Ed.* **2013**, *52*, 10076 – 10079.

(14) Hou, S-F.; Chen, J-Y.; Xue, M.; Jia, M.; Zhai, X.; Liao, R-Z.; Tung, C–H.; Wang, W. Cooperative Molybdenum-Thiolate Reactivity for Transfer Hydrogenation of Nitriles. *ACS Catal.* **2020**, *10*, 380−390.

(15) (a) Chen, J-Y.; Liao, R-Z. Mechanism and Regioselectivity of the Iron-Catalyzed Hydroboration of N-Heteroarenes: A Computational Study. *Organometallics* **2019**, *38*, 3267−3277; (b) Zhang, F.; Song, H.; Zhuang, X.; Tung, C–H.; Wang, W. Iron-Catalyzed 1,2-Selective Hydroboration of N-Heteroarenes. *J. Am. Chem. Soc.* **2017**, *139*, 17775−17778.

(16) (a) Liu, J.; Chen, J-Y.; Jia, M.; Ming, B.; Jia, J.; Liao, R-Z.; Tung, C–H.; Wang, W. Ni−O Cooperation versus Nickel(II) Hydride in Catalytic Hydroboration of N-Heteroarenes. *ACS Catal.* **2019**, *9*, 3849−3857.

(17) Elsby, M. R.; Baker, R. T. Cu(I)–SNS Complexes for Outer-sphere Hydroboration and Hydrosilylation of Carbonyls. *Chem. Commun.* **2019**, *55*, 13574—13577.

(18) Ataie, S.; Hogeterp, Ovens, J. S.; Baker, R. T. SNS Ligand-assisted Catalyst Activation in Zn-catalysed Carbonyl Hydroboration. *Chem. Commun.* **2022**, *58*, 3795–3798.

(19) Elsby, M. R.; Oh, C.; Son, M.; Kim, S. Y. H.; Baik, M.–H.; Baker, R. T. Spin-state Crossover in Photo-catalyzed Nitrile Dihydroboration via Mn-thiolate Cooperation. *Chem. Sci.* **2022**, 13, 12550-12559.

(20) Fitchett, B.; MSc Thesis, Université d'Ottawa/University of Ottawa, **2018**.

(21) (a) Hoffman, B. M.; Diemente, D. L.; Basolo, F. Electron Paramagnetic Resonance Studies of Some Cobalt (II) Schiff Base Compounds and Their Monomeric Oxygen Adducts. *J. Am. Chem. Soc.* **1970**, *92*, 61–65; (b) Maki, A. H.; Edelstein, N.; Davison, A.; Holm, R. H. Electron Paramagnetic Resonance Studies of the Electronic Structures of Bis(maleonitriledithiolato)copper(II), -nickel(III), -cobalt(II), and -rhodium(II) Complex. *J. Am. Chem. Soc.* **1964**, *86*, 4580–4587.

(22) Mo, Z.; Li, Y.; Lee, H. K.; Deng, L. Square-Planar Cobalt Complexes with Monodentate N–Heterocyclic Carbene Ligation: Synthesis, Structure, and Catalytic Application. *Organometallics* **2011**, *30*, 4687–4694.

(23) (a) Gennari, M.; Gerey, B.; Hall, N.; Pécaut, J.; Vezin, H.; Collomb, M-N.; Orio, M.; Duboc, C. Structural, Spectroscopic and Redox Properties of a Mononuclear Co^{II} Thiolate Complex – the Reactivity Toward S-Alkylation: An Experimental and Theoretical Study. *Dalton Trans.* **2012**, *41*, 12586–12594; (b) Wu, Y-Y.; Hong, J-C.; Tsai, R-F.; Pan, H-R.; Huang, B–H.; Chiang, Y-W.; Lee, G–H.; Cheng, M-J.; Hsu, H-F. Ligand-Based Reactivity of Oxygenation and Alkylation in Cobalt Complexes Binding with (Thiolato)phosphine Derivatives. *Inorg. Chem.* **2020**, *59*, 4650−4660; (c) Orchanian, N. M.; Hong, L. E.; Velazquez, D. A.; Marinescu, S. C. Electrocatalytic Syngas Generation with a Redox Non-innocent Cobalt 2-Phosphinobenzenethiolate Complex. *Dalton Trans.* **2021**, *50*, 10779–10788.

(24) Albkuri, Y. M.; Ovens, J. S.; Martin, J.; Baker, R. T. Ni(II)-SNS Thiolate Complexes: Reactivity and Solution Dynamics. *Inorg. Chem.* **2021**, *60*, 10934-10942.

(25) Ataie, S.; Ovens, J. S.; Baker, R. T. Solvent-Free Zn (NSNO) Complex-Catalysed Dihydroboration of Nitriles. *Chem. Commun.* **2022**, in press.

(26) Nowicki, M.; Kucinski, K.; Hreczycho, G.; Hoffmann, M. Catalytic and Non-Catalytic Hydroboration of Carbonyls: Quantum-chemical Studies. *Org. Biomol. Chem.* **2021**, *19*, 3004-3015.

(27) (a) Blackmond, D. G. Reaction Progress Kinetic Analysis: A Powerful Methodology for Mechanistic Studies of Complex Catalytic Reactions. *Angew. Chem., Int. Ed.* **2005**, *44*, 4302−4320. (b) Blackmond, D. G. Kinetic Profiling of Catalytic Organic Reactions as a Mechanistic Tool. *J. Am. Chem. Soc.* **2015**, *137*, 10852−10866.

(28) (a) Nielsen, C. D.-T.; Burés, J. Visual Kinetic Analysis. *Chem. Sci.* **2019**, *10*, 348-353; (b) Burés, J. Variable Time Normalization Analysis: General Graphical Elucidation of Reaction Orders from Concentration Profiles. *Angew. Chem. Int. Ed.* **2016**, *55*, 16084-16087.

(29) (a) Becke, A. D. Density-functional Thermochemistry. 3. The Role of Exact Exchange. *J. Chem. Phys.* **1993**, *98*, 5648-5652. (b) Lee, C.; Yang, W.; Parr, R. G.

Development of the Colle-Salvetti Correlation-energy Formula into a Functional of the Electron Density. *Phys. Rev. B* **1988**, *37*, 785-789.

(30) (a) Otero de la Roza, A.; Johnson, E. R. Non-Covalent Interactions and Thermochemistry using XDM-Corrected Hybrid and Range-Separated Hybrid Density Functionals. *J. Chem. Phys.* **2013**, *138*, 204109. (b) Johnson, E. R. The Exchange–Hole Dipole Moment Dispersion Model, in Non-Covalent Interactions in Quantum Chemistry and Physics. **2017**, Ch. *5*, 169-194.

(31) Kawamoto, T.; Takeda, K.; Nishiwaki, M.; Aridomi, T.; Konno, T. Square-Planar $N_2S_2Ni^{II}$ Complexes with an Extended π-Conjugated System. *Inorg. Chem.* **2007**, *46*, 4239.

(32) Westmoreland, D. E.; Lopez-Arteaga, R. A.; Weiss, E. N-Heterocyclic Carbenes as Reversible Exciton-Delocalizing Ligands for Photoluminescent Quantum Dots. *J. Am. Chem. Soc.* **2020**, 142, 2690.

(33) R. Elsby, M.; Y. H. Kim, S.; N. Steinmann, S.; Baker, R. T. Same Ligand, Three First-row Metals: Comparing M-amido Bifunctional Reactivity (Mn, Fe, Co). *Dalton Trans.* **2021**, 50, 14542.

(34) APEX Softward Suite v 2010 Bruker AXS Inc. Madison Wisconsin USA, **2010**.

(35) Blessing, R. H. An Empirical Correction for Absorption Anisotropy**,** *Acta Crystallogr.* **1995**, *A51*, 33–38.

(36) Sheldrick G. M. A Short History of SHELX, *Acta Crystallogr.* **2008**, *A64*, 112–122.

(37) Hübschle, C. B.; Sheldrick, G. M.; Dittrich, B. *ShelXle*: A Qt Graphical User Interface for *SHELXL. J. Appl. Crystallogr.* **2011**, *44*, 1281–1284.

(38) Frisch, M. J. et al. Gaussian 09 Revision E.01 Gaussian Inc. Wallingford CT **2013**.

(39) The postG code is available from http://schooner.chem.dal.ca

CHAPTER 4

COMPARATIVE B–H BOND ACTIVATION IN Zn(NSNO)- AND NiX(NNN)-CATALYZED NITRILE DIHYDROBORATION (X= ANIONIC N-, C-, O-, S- OR P-DONOR)

4.1 Introduction

In recent work The Baker group has been employing simple SNS amido and thiolate ligands in mechanistic studies of metal- ligand cooperativity (MLC) ligand using first row metals.[1,2] In Chapter 2, we compared Zn SNS thiolate and amido complexes as efficient catalysts for hydroboration of carbonyls, demonstrating that the MLC role was confined to precatalyst activation. In this Chapter we sought to expand our comparison of Lewis base donor-assisted hydroboration, first comparing amido and aryloxide donors in a tetradentate NSNO ligand with zinc, and then in a series of X donors in Ni(NNN)X complexes (X = Br, phenoxide, thiophenoxide, 2,5-dimethylpyrollide and phenyl).

4.2 Introduction to Zn-NSNO complex-catalyzed nitrile dihydroboration

In spite of its limited functional group tolerance, catalyzed dihydroboration of organonitriles affords products that can serve as valuable intermediates to primary amines (important as building blocks for proteins, drugs, polymers, pigments and agrochemicals)[1] or to build C−N bonds.[2] These notable applications have encouraged a broad focus on nitrile dihydroboration over the past decade with active catalysts including a range of transition, f-element, and main group metals.[3] Zinc, as an abundant and economically accessible first row metal, is one of the most environmentally friendly and biocompatible elements that can be employed in synthetic and catalytic processes.[4] Indeed, various hydroboration reactions of N–heterocycles,[5] carbonyls,[6] isocyanates,[7] carbon dioxide[8] and alkynes[9] have been catalysed using zinc-based systems. Reports to date of zinc complex-catalysed dihydroboration of nitriles both involve dimeric precatalysts (**A**,[10] **B**[11]) with strongly donating ligands (**Scheme 4.1**).

In this work we report the synthesis and characterization of a dimeric Zn complex (**4.1$_{Zn}$**) containing a tetradentate NSNO ligand bearing both amido and aryloxide donors. Mechanistic studies show that the aryloxide is the preferred donor for this first example of

MLC in a catalytic cycle using zinc. Moreover, variable time normalization kinetic analysis (VTNA)[14] indicates a first order rate dependence on the concentrations of zinc, HBpin and nitrile and provides evidence for catalyst deactivation at high conversion.

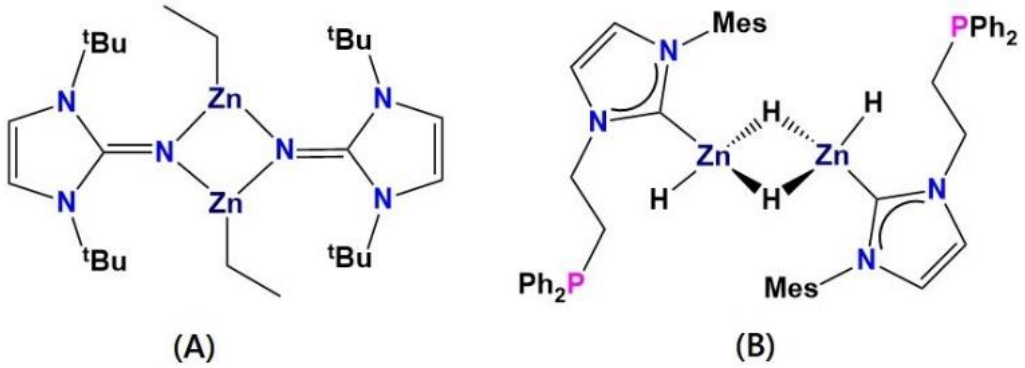

Scheme 4.1. Previous zinc catalysts employed for nitrile dihydroboration

4.3 Results and Discussion

4.3.1 Synthesis and Characterization of H_2L4 and 4.1$_{Zn}$

Reaction of 2-aminobenzenethiol with 2-(chloromethyl)-pyridine in Na/MeOH solution gave the functionalized amine (**1**). Reaction of **1** with salicylaldehyde and subsequent $NaBH_4$ reduction in methanol gave **H_2L4** (**Scheme 4.2**). In addition to the 12 unique aryl hydrogens between δ 6.70 and 8.50, the ^{1}H NMR spectrum of H_2L shows a broad peak at 9.09 for the OH, a triplet at 5.91 for the NH, a doublet at 4.39 for the N-benzylic CH_2 and a singlet at 3.99 for the S-benzylic CH_2 (Fig. C1). In the $^{13}C\{^1H\}$ NMR spectrum the N-C and S-C benzylic carbons appearing at 47.2 and 42.1 ppm are accompanied by seventeen aromatic C resonances (Fig. C2). The molecular structure of single crystals of **H_2L4** confirms the successful synthesis. Reaction of **H_2L4** and 1 equiv of diethylzinc afforded yellow crystals of $[Zn(\kappa^4\text{-NSNO})]_2$ (**4.1$_{Zn}$**) (**Scheme 4.3**).

The ^{1}H NMR spectrum of **4.1$_{Zn}$** confirms the disappearance of the OH and NH resonances and includes diastereotopic N- and S-CH_2 groups due to the reduced symmetry *vs* **H_2L4** (Fig. C3). The $^{13}C\{^1H\}$ NMR spectrum shows shifted N-C and S-C benzylic carbons due to formation of the 5,6-membered bimetallacycle (Fig. C4). The molecular structure of **4.1$_{Zn}$** consists of an

unsymmetrically aryloxide-bridged dinuclear structure [cf. Zn1-O1 =1.964(2) vs Zn1-O1' = 2.059(2) Å] with a distorted trigonal bipyramidal geometry [N1-Zn1-O1' = 133.07(9)°].

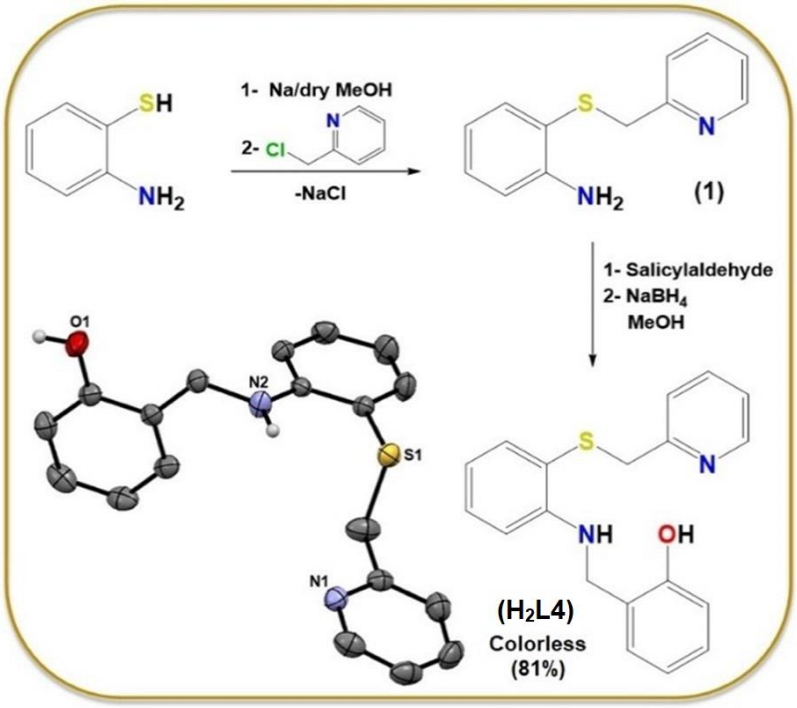

Scheme 4.2. Synthesis and molecular structure of **H_2L4** with 50% probability thermal ellipsoids and hydrogen atoms omitted for clarity.

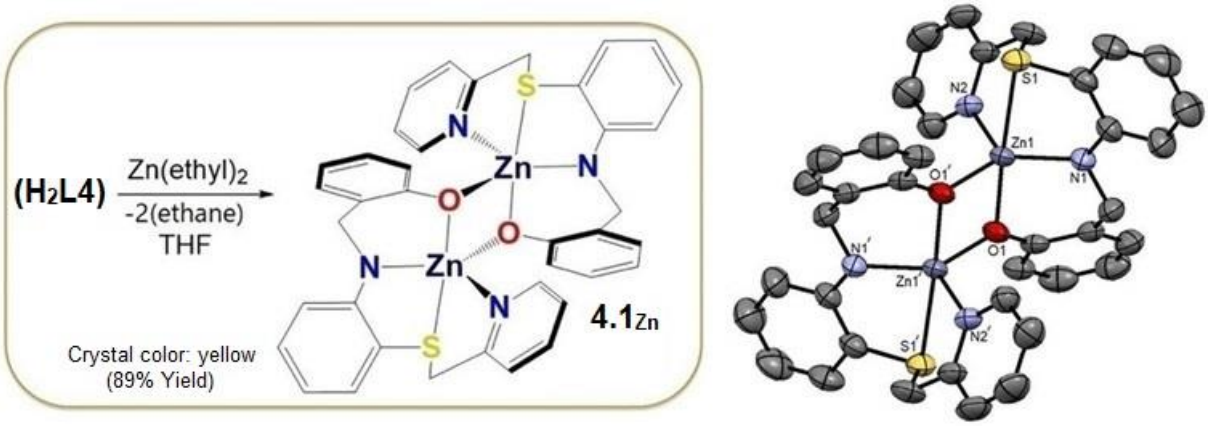

Scheme 4.3. Synthesis and molecular structure of **4.1_{Zn}** with 50% probability thermal ellipsoids and hydrogen atoms and two THF molecules omitted for clarity. Selected bond distances (Å) and angles (deg): Zn1-S1 2.5784(8), Zn1-N1 1.940(2), Zn1-N2 2.056(2), Zn1-O1 1.964(2), Zn1-O1' 2.059(2), N2-Zn1-S1 81.21(6), S1-Zn1-N1 82.49(6), N1-Zn1-O1 94.48(8), N1-Zn1-O1' 133.07(8), N2-Zn1-O1 98.22(8), N2-Zn1-O1' 109.19(8), N1-Zn1-N2 117.74(9), S1-Zn1-O1 176.17(5), S1-Zn1-O1' 105.78(6), O1-Zn1-O1' 78.01(7), Zn1-O1-Zn1' 101.99(8).

4.3.2 Catalytic Reactivity of **4.1$_{Zn}$** in Nitrile Dihydroboration

The catalytic potential of **4.1$_{Zn}$** for dihydroboration of nitriles was investigated using benzonitrile as a model substrate and 2 equiv of HBpin (**Table 4.1**). In the presence of 5 mol% of **4.1$_{Zn}$** in C_6D_6 at 80 °C, 89% of benzonitrile was converted exclusively to the diborylamine after 3 h (entry 1). Moving from 80 °C to room temperature decreased the yield to 32% (entry 2). By omitting the solvent, benzonitrile was quantitatively dihydroborated after 5 h at room temperature (entry 4). Increasing the time to 12 h and stepwise lowering the **4.1$_{Zn}$** loading to 1 mol% maintained the high yield at >99%. A further decrease to 0.5 mol% lowered the yield to 72% after 12 h (entry 8). Under the optimized conditions of 1 mol% **4.1$_{Zn}$** at room temperature with no solvent, several different nitriles were dihydroborated (**Table 4.2**). Aliphatic substrates such as isobutyronitrile and acetonitrile gave full conversion after only 6 h (entries a and b respectively), whereas 9 h was sufficient for most aromatic nitriles with electron-withdrawing groups.

Although treatment of **4.1$_{Zn}$** in C_6D_6 with 2 equiv of 4-fluoro-benzonitrile gave no changes in the ^{1}H or ^{19}F NMR spectra (Fig. C16), resonances were shifted on reaction of **4.1$_{Zn}$** with 2 equiv of HBpin (Fig. C17).

Table 4.1. Optimization table for hydroboration of benzonitrile using **4.1$_{Zn}$** as pre-catalysts

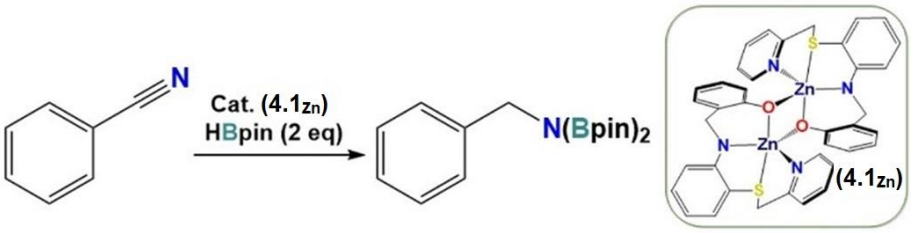

Entry	*Solvent*	***4.1$_{Zn}$*** *(mol%)*	*Time (h)*	*Temp. (˚C)*	*Yield (%)*
1	C_6D_6	5	3	80	89
2	C_6D_6	5	3	RT	32
3	Neat	5	5	80	99
4	Neat	5	5	RT	99
5	Neat	3	12	RT	99
6	Neat	2	12	RT	99
7	Neat	1	12	RT	99
8	Neat	0.5	12	RT	72

Reaction condition: Benzonitrile (0.1 mmol), HBpin (0.2 mmol). The amount of **4.1$_{Zn}$** was calculated according to the amount of benzonitrile. *Yields were calculated by integration of the characteristic ^{1}H NMR product signal in the reaction mixture vs. internal standard. Selectivity in all cases was 100% for the reported product.

Table 4.2. Catalytic dihydroboration of organic nitriles using **4.1$_{Zn}$**.

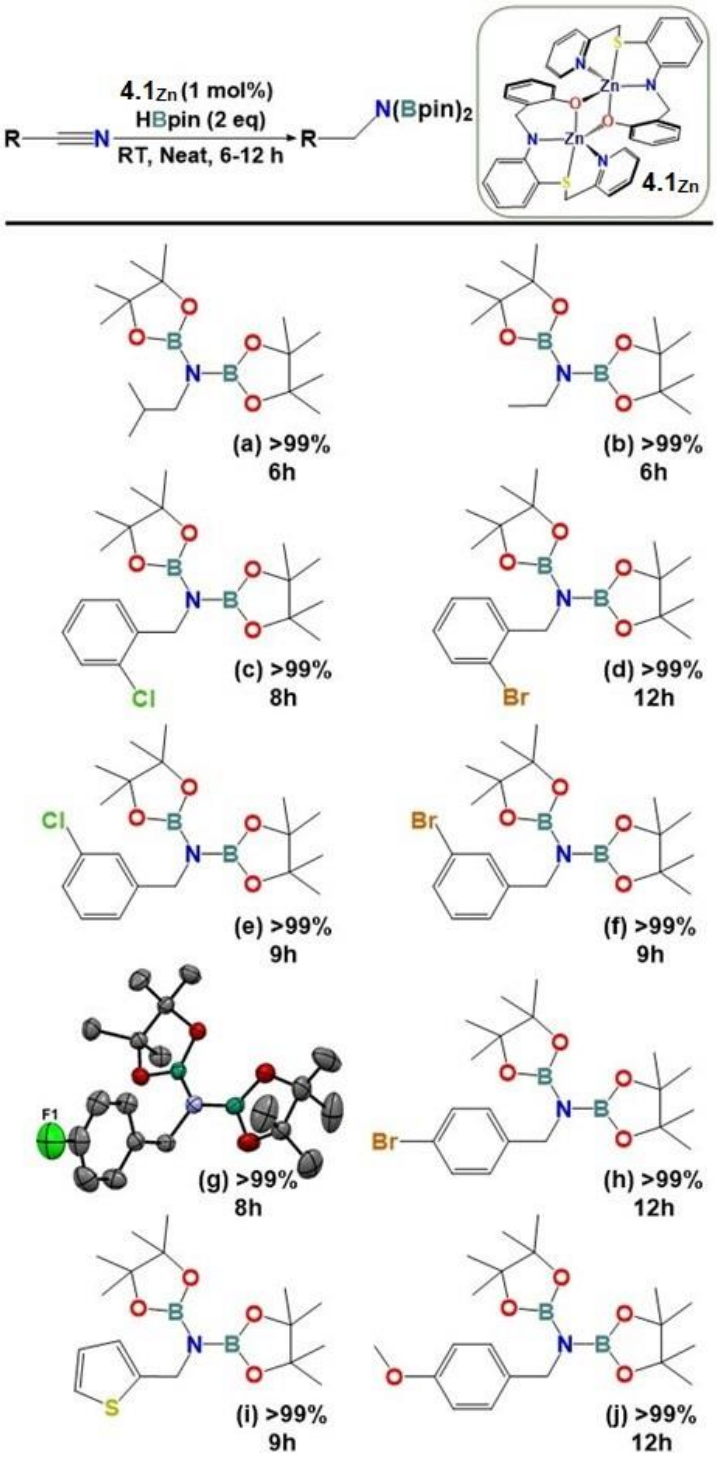

Reaction conditions: **4.1$_{Zn}$** (1 mol%), nitriles (0.1 mmol), HBpin (0.2 mmol), neat conditions at room temperature. Conversion was calculated by ^{1}H and ^{11}B NMR integration of the characteristic product signal in the reaction mixture *vs* substrate and HBpin, respectively. Selectivity for all cases was 100% for the reported product.

Moreover, the benzylic N- and S-CH_2 groups were no longer diastereotopic. Although we were unable to identify a Zn–H resonance in the ^{1}H NMR spectrum, the ^{11}B NMR spectrum showed a new singlet resonance at 21.8 ppm suggesting B-O bond formation[15] (Fig. C18). On subsequent addition of 1 equiv of acetonitrile, the ^{1}H and ^{11}B NMR spectra showed this new species was replaced with diborylamine product resonances (Figs. C17,18).

4.3.3 Mechanistic Studies of $\mathbf{4.1_{Zn}}$ Catalytic System

In order to confirm which of our ligand donors is involved in HBpin activation, we treated **H_2L4** with HBpin. The ^{11}B NMR spectrum of the resulting O-borylated product, **Bpin-HL4**, is superimposable on that due to the **$\mathbf{4.1_{Zn}}$** + 2 HBpin intermediate, confirming that the aryloxide (and not the amido) donor is involved in B–H bond activation. This likely arises from the stronger B-O (vs B-N) bond[16] and is in contrast to H_2 activation in which the M-O bond in metal alkoxide complexes does not react under conditions that the M-N bond does in metal amido complexes in the same catalytic cycle.[17]

Further analysis of catalyst speciation showed that the **$\mathbf{4.1_{Zn}}$** + 2 HBpin intermediate is unstable over time (Fig. C17,18). After 12 h the NMR resonances of this intermediate were identical to those observed after a catalytic reaction using 15 mg of **$\mathbf{4.1_{Zn}}$**. Filtration of the resulting reaction mixture afforded insoluble zinc metal (as evidenced by gas bubble formation on treatment with HCl). Characterization of the resulting filtrate by ESI-MS provided evidence for formation of both **H_2L4** and **Bpin-HL4** as their Na^+ adducts (Fig. C5). As the ^{11}B NMR spectrum of this filtrate provided no evidence for O-borylated **L4**, we suggest that decomposition of **$\mathbf{4.1_{Zn}}$** involves subsequent formation of N-borylated **L4,** which then dissociates from the Zn centre.

To gain deeper insight into the reaction pathway, kinetic studies were performed. The catalytic reactions were monitored by ^{1}H and ^{11}B NMR and the data were analysed graphically employing variable time normalization analysis (VTNA).[14] Using 4-fluorobenzonitrile as the substrate, a first-order rate dependence was found for [HBpin], [substrate], and [**$\mathbf{4.1_{Zn}}$**], assuming a monomeric catalyst resting state for **$\mathbf{4.1_{Zn}}$** after reaction with HBpin (**Figure 4.1**).

Plotting the concentration of the diborylamine product [(4-F-C_6H_4)$CH_2N(Bpin)_2$] *vs* the normalized rate components employing VTNA gives k_{obs} = 13.9 $mM^{-2}min^{-1}$ (Fig. C24). Finally, VTNA was utilized to find out if the catalytic system suffers possible product inhibition or catalyst deactivation. To do so, two catalytic reactions were performed, with one monitoring consumption of 4-fluorobenzonitrile from the beginning, and the other from the reaction time mid-point.

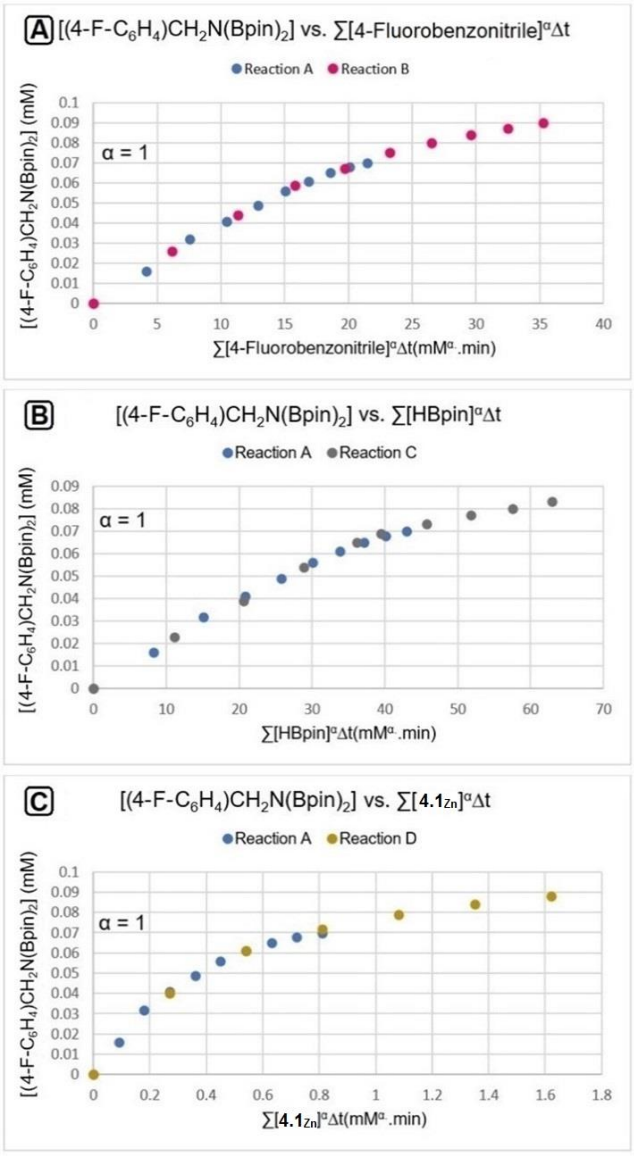

Figure 4.1. VTNA of the kinetics data: (A) rate dependence on [4-fluorobenzonitrile]; (B) rate dependence on [HBpin]; (C) rate dependence on [**4.1$_{Zn}$**] (as monomer).

After the time adjustment, it turned out the catalytic system indeed suffers from either product inhibition or catalyst deactivation (Fig. C25). To determine which one, a new pair of reactions was carried out - one with less substrate and HBpin compared to the normal reaction, and another one with the product present at the beginning. After the time adjustment, it was revealed that the catalytic system suffers from catalyst deactivation (Fig. C26) in agreement with our previous results on catalyst speciation.

Based on the results of the stoichiometric reactions, kinetic studies and evidence regarding the catalyst resting state, a plausible mechanism can be proposed (**Figure 4.2**).

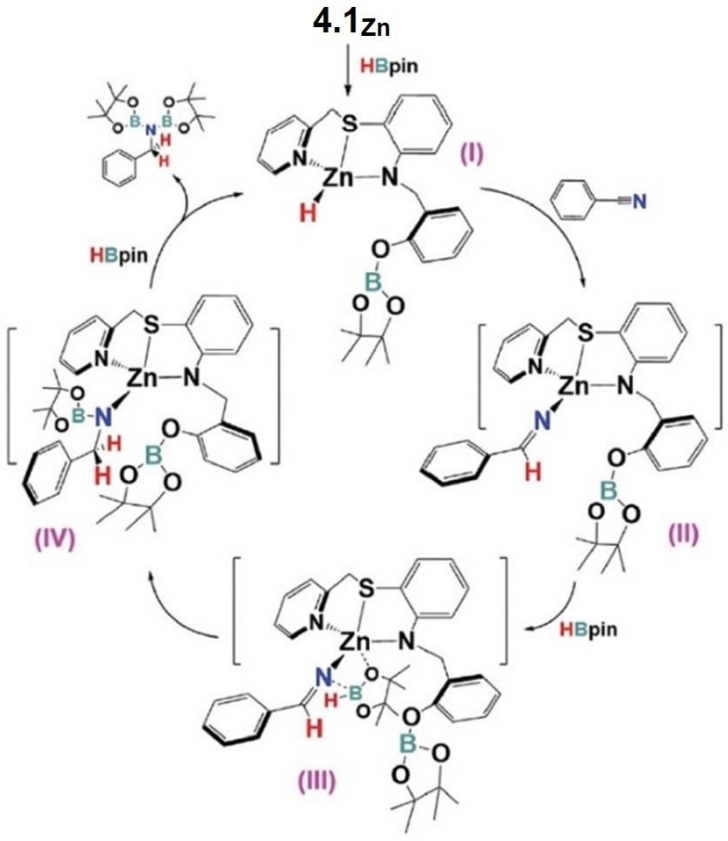

Scheme 4.4. Proposed mechanism for nitrile hydroboration by **4.1$_{Zn}$**.

In the first step, bifunctional activation of HBpin forms the borylated ligand and zinc hydride (I). Then, nitrile insertion gives intermediate (II), external HBpin coordinates to the N atom of the coordinated substrate and, passing through (III), transfers a hydride to the C=N carbon to form (IV). Finally, a third equivalent of HBpin generates the product, reforming zinc hydride (I). As long as sufficient substrate is available the catalytic cycle is unperturbed, but at high

substrate conversion competing catalyst deactivation occurs, proposed to result from borylation of the amido donor and subsequent ligand dissociation from the Zn centre.[6c]

4.4 Conclusion

In summary, **4.1$_{Zn}$** effects the catalytic dihydroboration of nitriles under neat conditions and ambient temperature. Although the reaction rate does not compare to that using catalyst B in Fig. 1, **4.1$_{Zn}$** generates the Zn–H in situ, precluding the need for a very strongly donating ligand. Kinetic studies revealed a simple reaction rate law but detailed examination at high conversion provided evidence for catalyst deactivation. Further detailed mechanistic studies of related zinc complexes and additional catalyzed reductive transformations[18] will continue to elevate this main group metal's status as a versatile source of efficient molecular catalysts.

4.5 Experimental

4.5.1 General considerations

All experiments were carried out under dinitrogen, using a MBraun glovebox unless otherwise stated. Diethyl ether, toluene and THF were dried on columns of activated alumina using a J. C. Meyer (formerly Glass Contour) solvent purification system. Anhydrous C_6D_6 and THF-d_8 were dried with activated alumina (ca. 10 wt %) overnight, followed by filtration. $CDCl_3$ was stored over activated 4 Å molecular sieves (heated at 250 ^oC for 24 h under vacuum). Anhydrous methanol and ethanol were purchased from Aldrich and used as obtained. Other chemicals were used as obtained commercially: 2-chloromethylpyridine (Alfa Aesar), 2-amino benzenethiol (Alfa Aesar), diethylzinc (Aldrich), salicylaldehyde (Aldrich), sodium borohydride (Aldrich). All reagents were purchased from commercial suppliers. ^1H and ^{11}B NMR spectra were recorded on a 300 MHz Bruker Avance or Avance II instrument at room temperature (21−25 °C). ^1H NMR spectra were referenced respectively to solvent residual protons (C_6D_6, δ 7.15; $CDCl_3$, δ 7.26; THF-d_8, δ 1.72 and 3.58). Mass spectra were recorded on an AB Sciex Q1MS mass spectrometer with electrospray ionization (ESIMS) in positive mode (ion spray voltage, 5000.0 V; TEM, 400 °C; declustering potential, 11.00 V; focusing potential, 300.0 V) with samples prepared to ca. 0.05 mg/mL in acetonitrile or dichloromethane. For electron impact (EI), solid samples were prepared by drying products under vacuum, and spectra obtained using a Kratos Concept S1 instrument (Hres 7000−10000). X-ray diffraction data were collected on a Bruker Smart or Kappa

diffractometer equipped with an ApexII CCD detector and a sealed-tube Mo K source (λ = 0.71073 Å).

4.5.2 Synthesis of H_2L^4

Precursor **1** was obtained through the literature procedure.[19] To an ethanolic solution of **1** (2.00 g, 9.24 mmol) was added salicylaldehyde (1.129 g, 9.24 mmol) and the mixture was refluxed for 2 h. Then, the solution was cooled down to 0-5 ˚C and $NaBH_4$ (0.70 g, 18.48 mmol) was added pinch wise and the mixture was heated to 50 ˚C for 2 h. Finally, the solvent was removed under vacuum and **H_2L^4** was extracted with ethyl acetate and kept in the freezer. After 4-6 h, colourless crystals of **H_2L^4** appeared and were filtered and dried (2.41 g, 81%). The same crystal was used for X-ray crystallography. ^{1}H NMR (300 MHz, CDCl3): δ 9.09 (b, 1H, OH), 8.50 (d, 1H, N-adjacent H in pyr ring), 7.62 (t, 1H, aromatic), 7.39 (d, 1H, aromatic), 7.21 (ov mult, 4H, aromatic), 7.12 (d, 1H, aromatic), 6.90 (m, 2H, aromatic), 6.84 (d, 1H, aromatic), 6.70 (t, 1H, aromatic), 5.91 (brt, 1H, NH), 4.39 (d, 2H, N-CH_2), 3.99 (s, 2H, S-CH_2).

4.5.3 Synthesis of 4.1_{Zn}

3 mL of 1 M solution of diethylzinc in hexane (3.00 mmol) was added to a solution of H_2L (0.96 g, 3 mmol in 5 mL of THF) dropwise at RT. The final solution turned yellow after 5 min and 4.1_{Zn} precipitated out after 2 h. The precipitate was filtered, washed with diethyl ether (3 × 3 mL), and dried under vacuum (2.08 g, 89%). Suitable crystals for crystallography were grown by ether layering of a THF solution of **4.1_{Zn}** at RT. ^{1}H NMR (300 MHz, CDCl3): δ 8.80 (d, 1H, N-adjacent H in Py ring), 7.72 (t, 1H, aromatic), 7.64 (d, 1H, aromatic), 7.38 (ov mult, 2H, aromatic), 7.21 (d, 1H, aromatic), 7.02 (ov mult, 2H, aromatic), 6.84 (d, 1H, aromatic), 6.66 (d, 1H, aromatic), 6.58 (t, 1H, aromatic), 6.39 (t, 1H, aromatic), 4.43, 4.32 (d, 14 Hz, 1H), 4.16, 3.94 (d, 14.5 Hz, 1H). EI-MS [M/2] 384.02, Calc'd 384.03 (Figure C5).

4.5.4 Synthesis of O-borylated HL4 (Bpin-HL^4)

0.1 g of **H_2L^4** (0.31 mmol) was dissolved in 5 mL of THF in a vial and 44 µL of HBpin (0.31 mmol) was added and the solution was stirred at room temperature for 5 h. Then the solvent was evaporated under vacuum and the residue dissolved in C_6D_6. ^{1}H NMR (300 MHz, C_6D_6): δ

8.30 (d, 1H, N-adjacent H in Py ring), 7.40 (d, 1H, aromatic), 7.28 (d, 1H, aromatic), 7.23 (d, 1H, aromatic), 6.97 (ov mult, 2H, aromatic), 6.83 (ov mult, 2H, aromatic), 6.51 (ov mult, 2H, aromatic), 5.90 (t, 1H, NH), 4.30 (d, 2H, N-CH_2), 3.91 (s, 1H, S-CH_2), 1.00 (s, 12H, Bpin CH_3) (Figure C20). ^{11}B NMR 21.8 ppm (Figure C19). ESI-MS $[NaM]^+$ 471.18, Calc'd 471.18.

4.5.5 Catalysis protocols

A catalyst stock solution was prepared by dissolving 15 mg (0.020 mmol) of **4.1$_{Zn}$** in 4 mL of THF. Ten small vials were charged with 20 µL of the catalyst stock solution (0.7 mg, 0.001 mmol, 1 mol%). Then, THF was evaporated under vacuum and nitrile substrates (0.1 mmol: isobutyronitrile 6.9 mg or 8.9 µL, acetonitrile 4.1 mg or 5.2 µL, 2-chlorobenzonitrile 13.7 mg, 2-bromobenzonitrile 18.2 mg, 3-chlorobenzonitrile 13.7 mg, 3-bromobenzonitrile 18.2 mg, 4-fluorobenzonitrile 12.1 mg, 4-bromobenzonitrile 18.2 mg, 2-thiophenecarbonitrile 10.9 mg or 9.3 µL, 4-methoxybenzonitrile 13.3 mg) were added to the vials, and subsequently after putting a tiny magnetic stir bar in the vials, HBpin (29 µL, 0.2 mmol) was added to the vials. The vials were capped and the stir bars started stirring very gently. After 6-12 h, the reaction mixtures were dissolved in C_6D_6 and transferred to NMR tubes and a ^{1}H NMR spectrum was taken at room temperature. Concentration of the di-hydroborated products were calculated based on integrals of the characteristic product signal in the reaction mixture and the known [HBpin] as well.

4.5.6 Mechanistic studies

A small vial was charged with 4-fluorobenzonitrile (12 mg, 0.1 mmol), **4.1$_{Zn}$** (38.5 mg, 0.05 mmol) and 1 mL of C_6D_6. The vial was capped and the mixture was stirred for 2 h at room temperature and then transferred to an NMR tube and ^{19}F and ^{1}H NMR spectra were recorded (Figure C16).

A small vial was charged with **4.1$_{Zn}$** (38.5 mg, 0.05 mmol), HBpin (15 µL, 0.1 mmol) and 1 mL of C_6D_6. The vial was capped and the mixture was stirred for almost 2 h and then transferred to an NMR tube and ^{1}H and ^{11}B NMR spectra were recorded. Then 2.6 µL of acetonitrile (0.05 mmol) was added to the same NMR tube. The NMR tube was well shaken, left in the glovebox for 8 h, at room temperature. ^{1}H and ^{11}B NMR spectra were then recorded (Figure C17).

Through the same procedure, **4.1$_{Zn}$** (38.5 mg, 0.05 mmol) and 2 equiv of HBpin (15 µL, 0.1 mmol) were treated together and after 12 h, ^{1}H and ^{11}B NMR spectra were recorded for comparison (Figures C17 and C18).

To recover a zinc complex after the catalytic reaction, 15 mg (0.020 mmol) of **4.1$_{Zn}$**, acetonitrile (20.8 µL, 0.4 mmol) and HBpin (116 µL, 0.8 mmol) were added to a vial, and subsequently a magnetic stir bar was put in the vial and the vial was capped and the stir bar started stirring gently. After 12 h, any remaining acetonitrile was evaporated under vacuum and 5 mL of hexane was added. After all the product was dissolved in hexane, the mixture was filtered and the residue was collected as a very pale green-white powder and dried under vacuum. The residue showed no solubility in available solvents and a reaction run using the residue (5 mg), acetonitrile (5.2 µL, 0.1 mmol) and HBpin (29 µL, 0.2 mmol) showed no hydroboration product after 24 h. Also, addition of HCl to this residue resulted in bobbles following with the residue dissolving. Finally, the filtrate from above was evaporated and the resulting residue also showed no nitrile hydroboration activity.

4.5.7 Kinetic studies

All kinetic reactions were set up in a nitrogen-filled glovebox and performed the same way with appropriate amounts of **4.1$_{Zn}$**, 2-fluorobenzonitrile, HBpin, and N-(4-fluorobenzyl)-4,4,5,5-tetramethyl-N-(4,4,5,5-tetramethyl-1,3,2-dioxaborolan-2-yl)-1,3,2-dioxaborolan-2-amine (abbreviated as 4-F-C_6H_4)$CH_2N(Bpin)_2$) – See **Table 4.3.**

General procedure for reaction A.

Note: All employed concentrations of **4.1$_{Zn}$** in the kinetic study are calculated for a monomer form of the zinc complex (Mm: 385.79 g/mol) not the dimeric form. This consideration is only for the kinetic study (Other **4.1$_{Zn}$** concentrations in other sections are stated for the dimeric form having Mm: 771.58 g/mol).

Product isolation: A vial was charged with 7 mg of **4.1$_{Zn}$** (0.01 mmol, 1 mol%). Then, 4-fluorobenzonitrile (121 mg, 1 mmol) and HBpin (290 µL, 2 mmol) were added to the vial. After 10 h, the product (g) was extracted into 10 mL of pentane and filtered. Then, the solution was concentrated to 2 mL and kept at -30 ˚C overnight, so crystals of (4-F-C_6H_4)$CH_2N(Bpin)_2$ (*g)* were

formed (several crystals were separated for crystallography) and then filtered and dried under vacuum. Product *g* was then used in the kinetic study for reaction F (**Table 4.3**).

A catalyst stock solution was prepared by dissolving 15 mg (0.040 mM as a monomer) of **4.1$_{Zn}$** in 4 mL of THF. 10 small vials were charged with 20 µL of the catalyst stock solution (0.7 mg, 0.002 mM, 2 mol%). Then, THF was evaporated under vacuum and 4-fluorobenzonitrile (17 mg, 0.1 mM) was added to the vials and subsequently after putting a tiny magnetic stir bar in the vials, HBpin (29 µL, 0.2 mM) was added, the vials were capped and the stir bars started stirring very gently. Every 45 min (Reactions A, C, D, E and F) or 40 min (Reaction B) the reaction mixture of one of the vials was immediately dissolved in C_6D_6 and transferred to an NMR tube and ^{1}H and ^{11}B NMR spectra were taken at room temperature. The concentration of (4-F-C_6H_4)$CH_2N(Bpin)_2$ product was calculated based on integrals of the known [HBpin] and the characteristic signal of (4-F-C_6H_4)$CH_2N(Bpin)_2$. All the other 5 reactions (B-F) were carried out through the same procedure, but reaction F in which (4-F-C_6H_4)$CH_2N(Bpin)_2$ (12 mg, 0.032 mM) was added to the vials before adding HBpin. The outlier results (compared to the uniform progression of the catalytic yield vs. time) were repeated several times and for the cases in which the results of all the repetitions were close, the average was considered, otherwise the best matching one was selected.

Table 4.3. Concentrations of Reagents for Reactions A-F for VTNA*.

	[4.1$_{Zn}$]	[4-Fluorobenzonitrile]	[HBpin]	(4-F-C_6H_4)$CH_2N(Bpin)_2$
Reaction A	0.002	0.1	0.2	-
Reaction B	0.002	0.15	0.2	-
Reaction C	0.002	0.1	0.3	-
Reaction D	0.006	0.1	0.2	-
Reaction E	0.002	0.068	0.136	-
Reaction F	0.002	0.068	0.136	0.032

*All the amounts are in mM.

4.5.8 Crystallographic details

Crystallographic data for all compounds were collected from a single crystal mounted on a MiTeGen dual thickness MicroMount using Parabar oil. Data were collected on a Bruker ApexII single crystal diffractometer equipped with a graphite monochromator. The instrument was equipped with a sealed tube Mo Kα source (λ = 0.71073 Å), an ApexII CCD detector and a dry

compressed air-cooling system operating at 203 K. Raw data collection and processing were performed with the Apex3 software package from Bruker.[20] Initial unit cell parameters were determined from 36 data frames from select $\boldsymbol{\omega}$ scans. Semi-empirical absorption corrections based on equivalent reflections were applied.[21] Systematic absences in the diffraction data-set and unit-cell parameters were consistent with the assigned space group. The initial structural solutions were determined using ShelxT direct methods,[22] and refined with full-matrix least-squares procedures based on $\boldsymbol{F^2}$ using ShelXL or ShelXle.[23] Hydrogen atoms were placed geometrically and refined using a riding model. Additional crystallographic information is given in Table C1.

4.6 References

(1) (a) S. A. Lawrence, *Amines: Synthesis, properties and applications,* Cambridge University Press, **2005**; (b) Kaithal, A.; Chatterjee, B.; Gunanathan, C. Ruthenium Catalyzed Selective Hydroboration of Nitriles and Imines. *J. Org. Chem.* **2016**, *81*, 11153–11161; (c) Ghosh, P.; Wangelin, A. J. Lithium Amide-Hydroboration of Nitriles. *Org. Chem. Front.* **2020**, *7*, 960; (d) Bedi, D.; Brar, A.; Findlater, M. Transition Metal- and Solvent-free Double Hydroboration of Nitriles. *Green Chem.* **2020**, *22*, 1125–1128.

(2) (a) Suginome, M.; Uehlin, L.; Murakami, M. Aminoboranes as "Compatible" Iminium Ion Generators in Aminative C–C Bond Formations. *J. Am. Chem. Soc.* **2004**, *126*, 13196– 13197; (b) Chong, E.; Blum, S. A. Aminoboration: Addition of B–N σ Bonds across C–C π Bonds. *J. Am. Chem. Soc.* **2015**, *137*, 10144–10147; (c) Junor, G. P.; Romero, E. A.; Chen, X.; Jazzar, R.; Bertrand, G. Readily Available Primary Aminoboranes as Powerful Reagents for Aldimine Synthesis. *Angew. Chem., Int. Ed.* **2019**, *58*, 2875–2878; (d) Kitano, T.; Komuro, T.; Tobita, H. Double and Single Hydroboration of Nitriles Catalyzed by a Ruthenium–Bis(silyl)xanthene Complex: Application to One-Pot Synthesis of Diarylamines and *N*-Arylimines. *Organometallics* **2019**, *38*, 1417–1420; (e) Ghosh, C.; Kim, S.; Mena, M. R.; Kim, J.–H.; Pal, R.; Rock, C. L.; Groy, T. L.; Baik, M.–H.; Trovitch, R. J. Efficient Cobalt Catalyst for Ambient-Temperature Nitrile Dihydroboration, the Elucidation of a Chelate-Assisted Borylation Mechanism, and a New Synthetic Route to Amides. *J. Am. Chem. Soc.* **2019**, *141*, 15327–15337.

(3) Hayrapetyan, D.; Khalimon, A. Y. Catalytic Nitrile Hydroboration: A Route to N,N-Diborylamines and Uses Thereof. *Chem.-Asian J.* **2020**, *15*, 2575–2587.

(4) (a) Wu, X. F. Non-redox-metal-catalyzed Redox Reactions: Zinc Catalysts. *Chem.-Asian J.* **2012**, *7*, 2502–2509; (b) Enthaler, S.; Wu, X.-F., Eds, *Zinc Catalysis: Applications in Organic Synthesis*, Wiley-VCH, **2015**.

(5) (a) Lortie, J. L.; Dudding, T.; Gabidullin, B. M.; Nikonov, G. I. Zinc-Catalyzed Hydrosilylation and Hydroboration of N–Heterocycles. *ACS Catal.* **2017**, *7*, 8454–8459; (b) Krishnan, K. K.; Ujwaldev, S. M.; Saranya, S.; Anilkumar, G.; Beller, M. Recent Advances and Perspectives in the Synthesis of Heterocycles via Zinc Catalysis. *Adv. Synth. Catal.* **2019**, *361*, 382–404; (c) Wang, X.; Zhang, Y.; Yuan, D.; Yao, Y. Regioselective Hydroboration and Hydrosilylation of N–Heteroarenes Catalyzed by a Zinc Alkyl Complex. *Org. Lett.* **2020**, *22*, 5695–5700.

(6) (a) Sahoo, R. K.; Mahato, M.; Jana, A.; Nembenna, S. Zinc Hydride-Catalyzed Hydrofunctionalization of Ketones. *J. Org. Chem.* **2020**, *85*, 11200–11210; (b) Kumar, G. S.; Harinath, A.; Narvariya, R.; Panda, T. K. Homoleptic Zinc-Catalyzed Hydroboration of Aldehydes and Ketones in the Presence of HBpin. *Eur. J. Inorg. Chem.* **2020**, 467–474; (c) Ataie, S.; Hogeterp, S.; Ovens, J. S.; Baker, R. T. SNS ligand-assisted catalyst activation in Zn-catalysed carbonyl hydroboration. *Chem. Commun.*, **2022**, *58*, 3795–3798.

(7) Sahoo, R. K.; Sarkar, N.; Nembenna, S. Zinc Hydride Catalyzed Chemoselective Hydroboration of Isocyanates: Amide Bond Formation and C=O Bond Cleavage. *Angew. Chem. Int. Ed.*, **2021**, *60*, 11991.

(8) (a) Wang, X.; Chang, K.; Xu, X. Hydroboration of Carbon Dioxide Enabled by Molecular Zinc Dihydrides. *Dalton Trans.* **2020**, *49*, 7324–7327. (b) Shlian, D. G.; Amemiya, E.; Parkin, G. Synthesis of Bis(2-pyridylthio)methyl Zinc Hydride and Catalytic Hydrosilylation and Hydroboration of CO_2. *Chem. Commun.* **2022**, *58*, 4188–4191.

(9) (a) Mandal, S.; Mandal, S.; Geetharani, K. Zinc-Catalyzsed Hydroboration of Terminal and Internal Alkynes. *Chem.-Asian J.* **2019**, *14*, 4553–4556; (b) Procter, R. J.; Uzelac, M.; Cid, J.; Rushworth, P. J.; Ingleson, M. J. Low-Coordinate NHC-Zinc Hydride Complexes Catalyze Alkyne C–H Borylation and Hydroboration Using

Pinacolborane. *ACS Catal.* **2019**, *9*, 5760-5771; (c) Uzelac, M.; Yuan, K.; Ingleson, M. J. A Comparison of Two Zinc Hydride Catalysts for Terminal Alkyne C–H Borylation/Hydroboration and the Formation of 1,1,1-Triborylalkanes by Tandem Catalysis Using Zn–H and B–H Compounds. *Organometallics* **2020**, *39*, 1332–1338.

(10) Das, S.; Bhattacharjee, J.; Panda, T. K. An Imidazolin-2-Iminato Ligand Organozinc Complex as a Catalyst for Hydroboration of Organic Nitriles. *New J. Chem.* **2019**, *43*, 16812–16818.

(11) Wang, X.; Xu, X. Hydroboration of Nitriles and Imines by Highly Active Zinc Dihydride Catalysts. *RSC Adv.* **2021**, *11*, 1128–1133.

(12) Elsby, M. R.; Baker, R. T. Cu(I)-SNS Complexes for Outer-sphere Hydroboration and Hydrosilylation of Carbonyls. *Chem. Commun.* **2019**, *55*, 13574–13577.

(13) Elsby, M. R.; Son, M.; Oh, C.; Martin, J.; Baik, M. H.; Baker, R. T. Mechanistic Study of Metal-Ligand Cooperativity in Mn(II)-Catalyzed Hydroborations: Hemilabile SNS Ligand Enables Metal Hydride-Free Reaction Pathway. *ACS Catal.* **2021**, *11*, 9043–9051.

(14) (a) Martínez-Carrión, A.; Howlett, M. G.; Alamillo-Ferrer, C.; Clayton, A. D.; Bourne, R. A.; Codina, A.; Vidal-Ferran, A.; Adams, R. W.; Burés, J. Kinetic Treatments for Catalyst Activation and Deactivation Processes based on Variable Time Normalization Analysis. *Angew. Chem., Int. Ed.* **2019**, *58*, 10189–10193; (b) Nielsen, C. D.-T.; Burés, J. Visual Kinetic Analysis. *Chem. Sci.* **2019**, *10*, 348–353.

(15) Liu, J.; Chen, J.-Y.; Jia, M.; Ming, B.; Jia, J.; Liao, R.-Z.; Tung, C.–H.; Wang, W. Ni–O Cooperation versus Nickel(II) Hydride in Catalytic Hydroboration of N–Heteroarenes. *ACS Catal.* **2019**, *9*, 3849–3857.

(16) Y. R. Luo, *Comprehensive Handbook of Bond Energies*, CRC Press: Boca Raton, **2007**.

(17) (a) Hamilton, R. J.; Bergens, S. H. An Unexpected Possible Role of Base in Asymmetric Catalytic Hydrogenations of Ketones. Synthesis and Characterization of Several Key Catalytic Intermediates. *J. Am. Chem. Soc.* **2006**, *128*, 13700–13701; (b) van Putten, R.; Uslamin, E. A.; Garbe, M.; Liu, C.; Gonzalez-de-Castro, A.; Lutz, M.; Junge, K.; Hensen, E. J. M.; Beller, M.; Lefort, L.; Pidko, E. A. Non-Pincer-Type

Manganese Complexes as Efficient Catalysts for the Hydrogenation of Esters. *Angew. Chem., Int. Ed.* **2017**, *56*, 7531–7534.

(18) (a) Cronin, S. P.; Strain, J. M.; Mashuta, M. S.; Spurgeon, J. M.; Buchanan, R. M.; Grapperhaus, C. A. Exploiting Metal-Ligand Cooperativity to Sequester, Activate, and Reduce Atmospheric Carbon Dioxide with a Neutral Zinc Complex. *Inorg. Chem.* **2020**, *59*, 4835–4841; (b) Rauch, M.; Kar, S.; Kumar, A.; Avram, L.; Shimon, L. J. W.; Milstein, D. Metal-Ligand Cooperation Facilitates Bond Activation and Catalytic Hydrogenation with Zinc Pincer Complexes. *J. Am. Chem. Soc.* **2020**, *142*, 14513–14521.

(19) P. Chattopadhyay, Y.-H. Chiu, J.-M. Lo, C-S. Chung and T.-H. Lu, *Appl. Radiat. Isot.*, **2000**, *52*, 217.

(20) APEX Softward Suite v 2010 Bruker AXS Inc. Madison Wisconsin USA, **2010**.

(21) R. H. Blessing**,** An Empirical Correction for Absorption Anisotropy**,** *Acta Crystallogr.* **1995**, *A51*, 33–38.

(22) G. M. Sheldrick, A Short History of SHELX, *Acta Crystallogr.* **2008**, *A64*, 112–122.

(23) C. B. Hübschle, G. M. Sheldrick, B. Dittrich, *ShelXle*: a Qt graphical user interface for *SHELXL. J. Appl. Crystallogr.* **2011**, *44*, 1281–1284.

4.7 Introduction for Nitrile Hydroboration Catalyzed by NiX(NNN)

Organoboron intermediates are very important in synthetic chemistry, enabling many important transformations, such as formation of C-C[1,2] and C-N[3-5] bonds, alcohols[6-9], imines[10,11] and amines.[12-14] Hydroboration of unsaturated CC and CX bonds is one primary route for production of key organoboron intermediates.[15-22] Reduction of nitriles, for example, has received much attention due to the importance of amines as precursors for production of pharmaceutical compounds, and as components of industrial processes for production of polyesters, dyes, and agrochemicals.[23,24] The poor functional group compatibility of traditional hydroboration reagents such as diborane or alkylboranes,[25,26] led to development of less reactive catecholborane (HBcat) and pinacolborane (HBpin) which do not readily reduce aldehydes at ambient temperature.[27,28] To selectively elevate the reactivity of the latter reagents, a number of first row metal and main group complexes have been employed.[29-31] Over the past decade, Metal-Ligand Cooperation (MLC), has been shown to be particularly well-suited for catalyzed hydroboration of polar CX bonds.[29-31] In one common type of MLC, an anionic ligand X functions as a Lewis-base, converting the B–H bond into a B–X bond and a metal hydride. In this type of mechanism, the formed B–X bond either has a productive role in the catalytic cycle,[32-34] known as bifunctional catalysis, or just initiates the reaction and leaves the catalytic cycle (bifunctional catalyst activation).[35-42]

In our previous study, amido N- and phenolate O-donors were compared for activating the B–H bond of pinacolborane in Zn-catalyzed nitrile dihydroboration; the O-donor played the dominant role.[43] Herein, a series of divalent NiX(NNN) complexes, where X is Br, OPh, SPh, dimethylpyrollide, PPh_2, and Ph (**4.3$_{Ni}$-4.8$_{Ni}$** respectively, **Scheme 4.4**), are synthesized, characterized and employed as precatalysts in nitrile dihydroboration. Since five of the six X ligands include additional lone electron pairs, this allows us to assess the relative efficiency of C-, N-, O- and P-donors for B–H bond activation. We also compare our results with previously reported Ni catalysts (**Scheme 4.4**).[44]

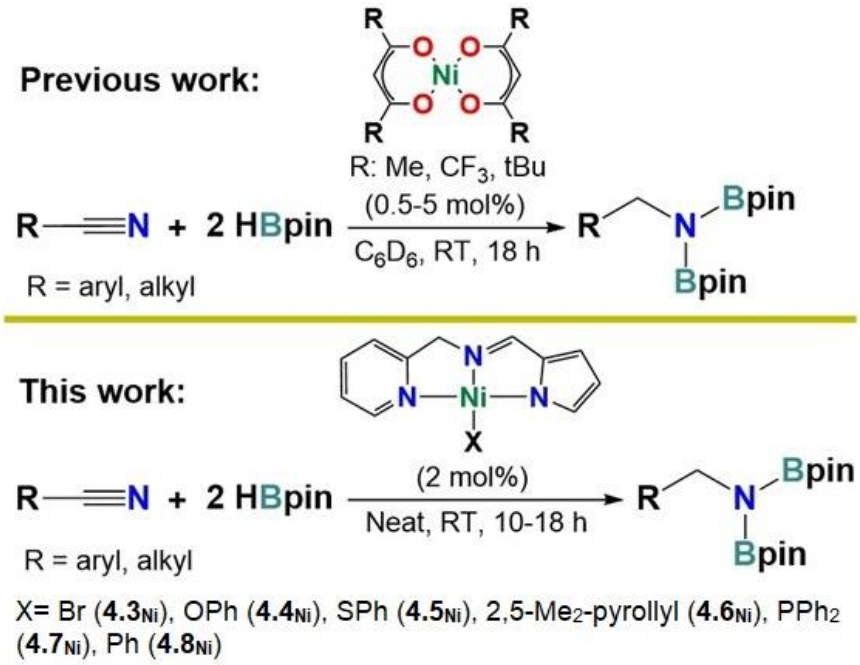

Scheme 4.5. Previous and current nickel-catalyzed nitrile hydroboration.

4.7 Results and Discussion

4.7.1 Synthesis and characterization

Treatment of $NiBr_2$(DME) with **1** equiv of **HL5** afforded $Ni^{II}Br(\kappa^3\text{-}NNS^{Me})$ (**4.2$_{Ni}$**) as a light brown solid (**Scheme 4.5**). The ^{1}H NMR spectrum of **4.2$_{Ni}$** (Fig. C27) showed a singlet at δ 2.82 for S-Me and another singlet at δ 4.39 for benzylic CH_2 adjacent to N. In addition, the 8 different aryl H resonances included a doublet at low field (δ 8.96, $^2J_{HH}$ = 5 Hz) for CH adjacent to the pyridine N. The molecular structure of **4.2$_{Ni}$**, determined by single crystal X-ray diffraction, shows a strained square planar geometry about Ni (S-Ni-N2 = 169.0, N1-Ni-N2 = 84.36 and N2-Ni-Br = 97.93°) due to the small NN bite angle and large size of Br. The Ni-N1 bond length is 0.079 Å shorter than that of Ni-N2, as expected due to the anionic nature of N1.

Stoichiometric reaction of **4.2$_{Ni}$** with HBpin afforded an insoluble black precipitate and N-borylated **Bpin-L5**, as confirmed by EI-MS (Fig. C41). In previous work with a $Zn(SNS)_2$ hydroboration precatalyst we also showed that the basic amido group binds strongly to the Bpin group, reducing the ligand's ability to coordinate the metal.[42] As a result, we turned to the less basic pyrrolyl group in **L6**.[47,51-53]

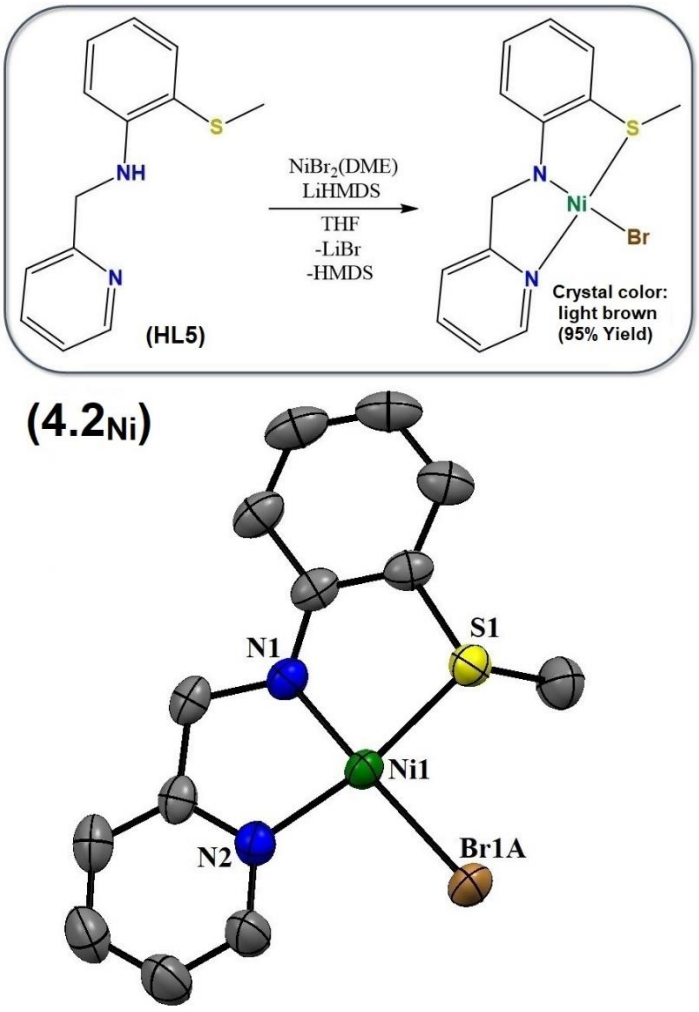

Scheme 4.6. Synthesis and molecular structures of **4.2$_{Ni}$** with 50% probability thermal ellipsoids and hydrogen atoms omitted for clarity. Selected bond distances (Å) and angles (deg) for **4.2$_{Ni}$**: Ni-S1 2.1610(5), Ni-N1 1.835(2), Ni-N2 1.914(1), Ni-Br1A 2.352(2), S1-Ni-N1 87.52(6), N1-Ni-N2 84.36(7), N2-Ni-Br1A 97.93(8), S1-Ni-Br1A 90.90(6), S1-Ni-N2 169.05(5), N1-Ni-Br1A 173.85(8).

Treatment of **HL6** with one equiv of $NiBr_2$(DME) afforded $Ni^{II}Br(\kappa^3$-NNN) (**4.3$_{Ni}$**) as a brown solid (**Scheme 4.6**). The ^{1}H NMR spectrum of **4.3$_{Ni}$** showed one singlet at δ 4.88 due to the CH_2, and 8 different aryl H resonances (Fig. C29). The molecular structure of **4.3$_{Ni}$** shows a strained square planar geometry about Ni with N1-Ni-N3 =167.0 and acute N-Ni-N angles of 83.5°.

Stoichiometric reaction of **4.3$_{Ni}$** with HBpin gave a color change to reddish brown. The ^{1}H NMR spectrum of the mixture showed a singlet resonance at δ -30.97 due to Ni–H (Fig. C43) and a ^{11}B NMR resonance at 25.8 ppm assigned to Br–Bpin (Fig. C45), showing that B–H bond activation occurs at the Ni-Br *vs.* Ni-$N_{pyrrolide}$ bond. The stability of **L6** in the presence of HBpin

then afforded the opportunity to substitute bromide with other X ligands in order to assess their efficiency for activating the B–H bond of HBpin. Indeed, reaction of **4.3$_{Ni}$** with one equiv of phenol yielded Ni^{II}(OPh)(κ^3-NNN) (**4.4$_{Ni}$**) as a red solid (**Scheme 4.7**).

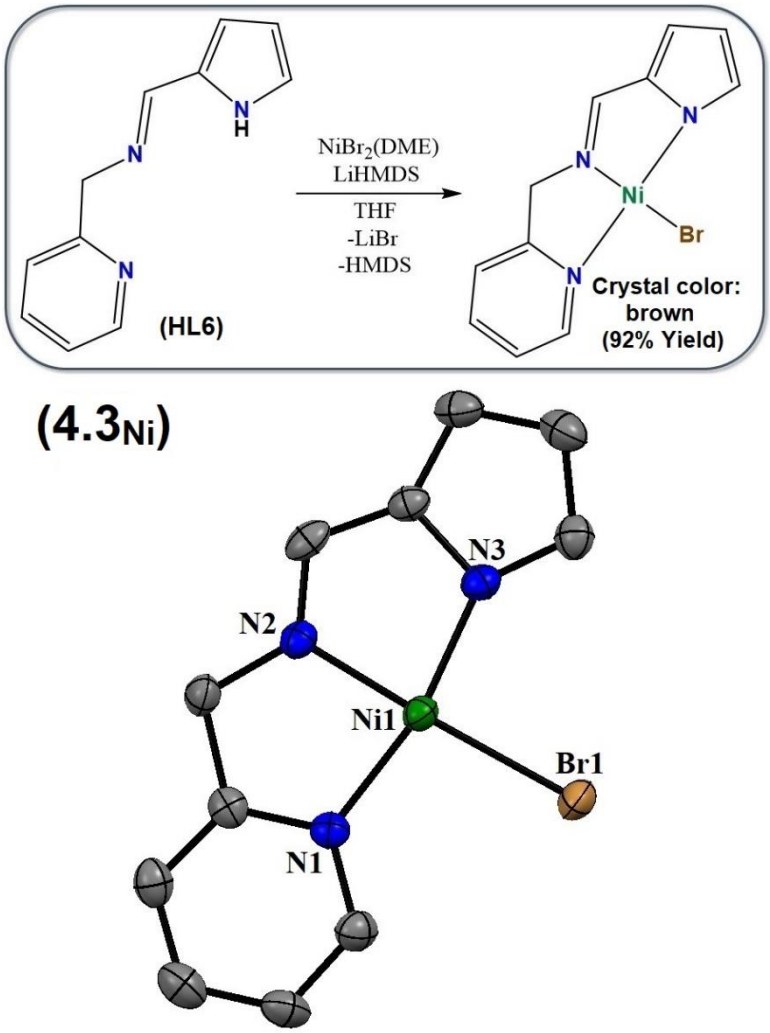

Scheme 4.7. Synthesis and molecular structures of **4.3$_{Ni}$** with 50% probability thermal ellipsoids and hydrogen atoms omitted for clarity. Selected bond distances (Å) and angles (deg) for **4.3$_{Ni}$**: Ni-N3 1.875(3), Ni-N2 1.850(2), Ni-N1 1.920(3), Ni-Br1 2.3229(4), Br1-Ni-N1 98.78(7), N1-Ni-N2 83.5(1), N2-Ni-N3 83.5(1), N3-Ni-Br1 94.14(8), Br1-Ni-N2 176.05(8), N1-Ni-N3 167.0(1).

The ^{1}H NMR spectrum of **4.4$_{Ni}$** showed one singlet at δ 4.67 due to the benzylic CH_2, and 13 different aryl H resonances (Fig. C31). The molecular structure of **4.4$_{Ni}$** shows a square planar geometry about Ni with similar distortions as in **4.3$_{Ni}$.**

Stoichiometric reaction of **4.4$_{Ni}$** with HBpin led to a color change to reddish brown and appearance of the same Ni–H resonance in the ^{1}H NMR spectrum. After solvent removal and

hexane extraction, crystals of Ph-O–Bpin (**S-P3**) were obtained and analyzed by X-ray diffraction (Fig. C60) and ^{1}H NMR spectroscopy (Fig. C46). In contrast, attempts to isolate the hexane insoluble Ni–H complex were hampered by its thermal instability.

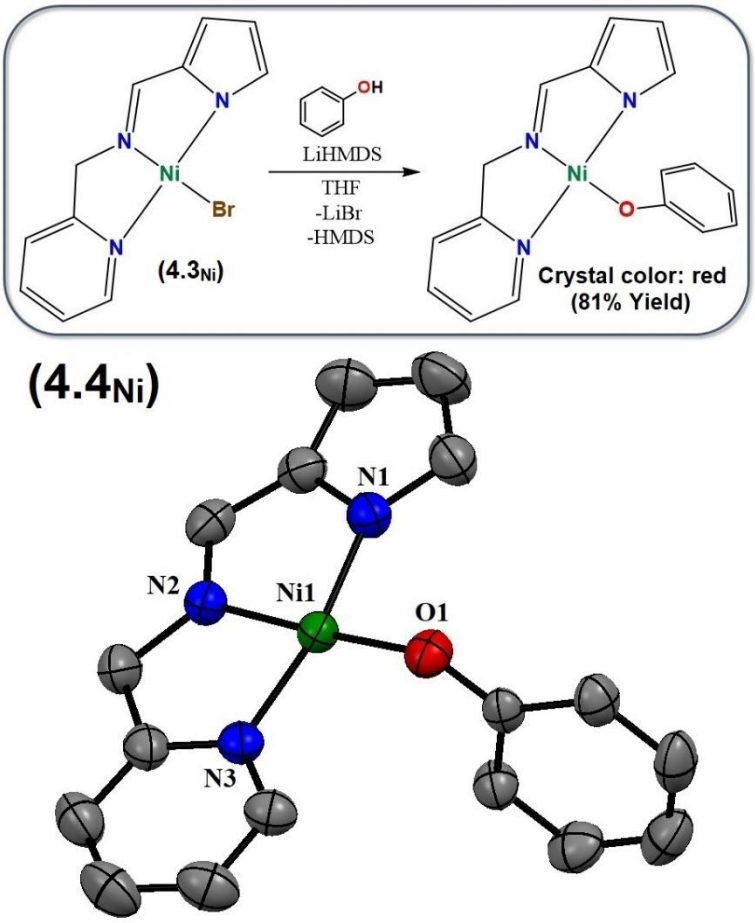

Scheme 4.8. Synthesis and molecular structures of (**4.4$_{Ni}$**) with 50% probability thermal ellipsoids and hydrogen atoms omitted for clarity. Selected bond distances (Å) and angles (deg) for (**4.4$_{Ni}$**): Ni-N3 1.881(3), Ni-N2 1.832(3), Ni-N1 1.850(3), Ni-O1 1.837(2), O1-Ni-N1 94.46(7), O1-Ni-N3 97.22(7), N2-Ni-N1 83.98(8), N3-Ni-N2 84.22(8), O1-Ni-N2 176.28(7), N1-Ni-N3 168.10(8).

Reaction of **4.3$_{Ni}$** with one equiv of thiophenol yielded Ni^{II}(SPh)(κ^3-NNN) (**4.5$_{Ni}$**) as a red solid (**Scheme 4.8**). The ^{1}H NMR spectrum of **4.5$_{Ni}$** showed a singlet at δ 4.94 due to the benzylic CH_2 and 13 different aryl H resonances (Fig. C33). The molecular structure of **4.5$_{Ni}$** showed a similar strained structure as seen for complexes **4.3$_{Ni}$** and **4.4$_{Ni}$**. Stoichiometric reaction of **4.5$_{Ni}$** with HBpin showed no color change at room temperature and no Ni–H was observed by ^{1}H NMR (Fig. C43). Even after raising the temperature to 50 ˚C, no evidence for Ni–H or PhSBpin formation was obtained.

Reaction of **4.3$_{Ni}$** with one equiv of 2,5-dimethyl- pyrrole gave Ni^{II}(2,5-Me_2-pyrrolyl))(κ^3-NNN) (**4.6$_{Ni}$**) as a navy-blue solid (**Scheme 4.9**). The ^{1}H NMR spectrum of **4.6$_{Ni}$** showed a singlet at δ 2.89 for the dimethylpyrrollide methyls, a singlet at δ 4.86 for benzylic CH_2, and 10 different aryl H resonances (Fig. C35).

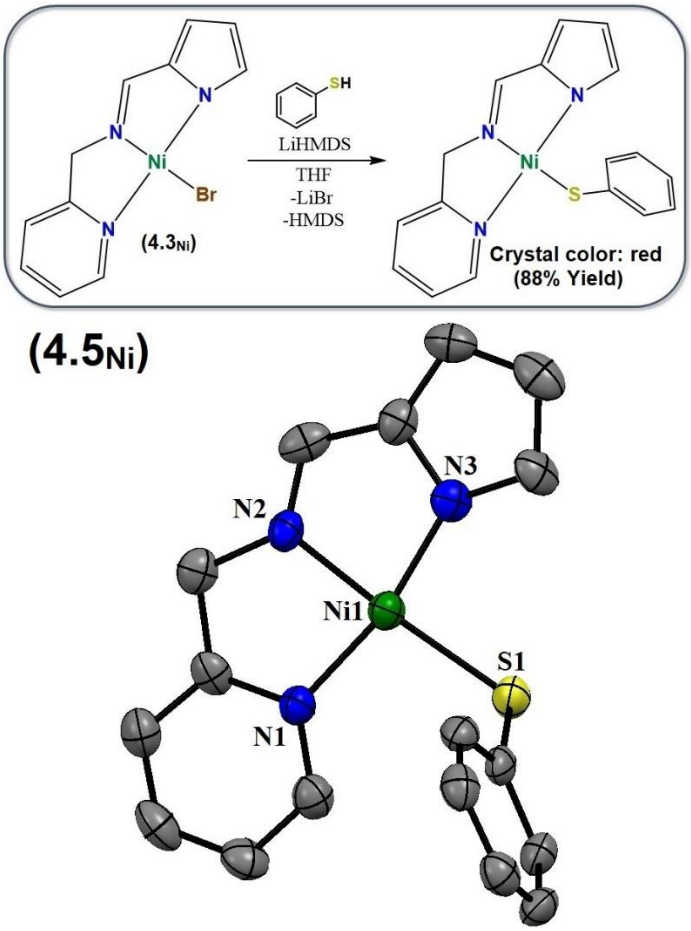

Scheme 4.9. Synthesis and molecular structures of **4.5$_{Ni}$** with 50% probability thermal ellipsoids and hydrogen atoms omitted for clarity. Selected bond distances (Å) and angles (deg) for **4.5$_{Ni}$**: Ni-S1 2.199(1), Ni-N3 1.865(4), Ni-N2 1.872(4), Ni-N1 1.915(4), S1-Ni-N1 98.8(1), S1-Ni-N3 93.9(1), N1-Ni-N2 83.8(2), N3-Ni-N2 83.3(2), S1-Ni-N2 173.9(1), N1-Ni-N3 167.2(2).

The molecular structure of **4.6$_{Ni}$** showed a slightly longer Ni-N bond length to the dimethylpyrollide (1.877Å) *vs* that to the ligand pyrollide group (1.866 Å). Interestingly, treatment of **5** with HBpin gave a reddish-brown solution with the same Ni–H observed by ^{1}H NMR (Figs. C43, C49), and 2,5-dimethyl-pyrrollide–Bpin (**S-P4**) detected by EI-MS (Fig. C47). So even though HBpin showed no propensity to add across the ligand Ni-$N_{pyrollide}$ bond in **4.5$_{Ni}$,** it readily adds across the Ni-$N_{dimethylpyrollide}$ bond in **4.6$_{Ni}$.**

Turning to a heavier X donor, complex **4.3$_{Ni}$** was treated with diphenylphosphine to give [Ni^{II}(m-PPh$_2$))(κ^2-NNN)]$_2$ (**4.7$_{Ni}$**) as a light-brown solid (**Scheme 4.10**). The unremarkable ^{1}H NMR spectrum of **4.7$_{Ni}$** showed a singlet at δ 3.98 for the benzylic CH$_2$ and 36 different aryl H resonances (Fig. C37). The molecular structure of **4.7$_{Ni}$,** however, revealed a phosphido-bridged dimer with k^2-NNN ligands due to dissociation of the pyridine donor. The large PPh$_2$ groups incur additional strain about the Ni centers (N1-Ni-P1′ = 101.0° and N2-Ni-P1 = 103.5°).

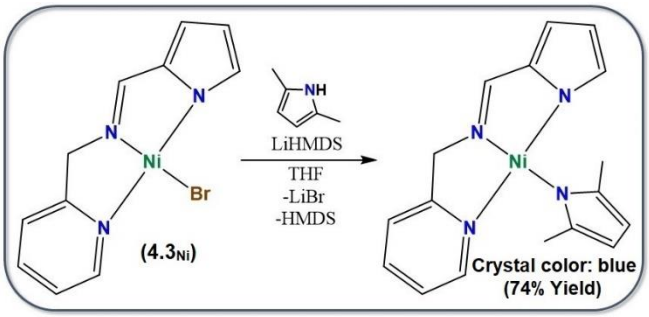

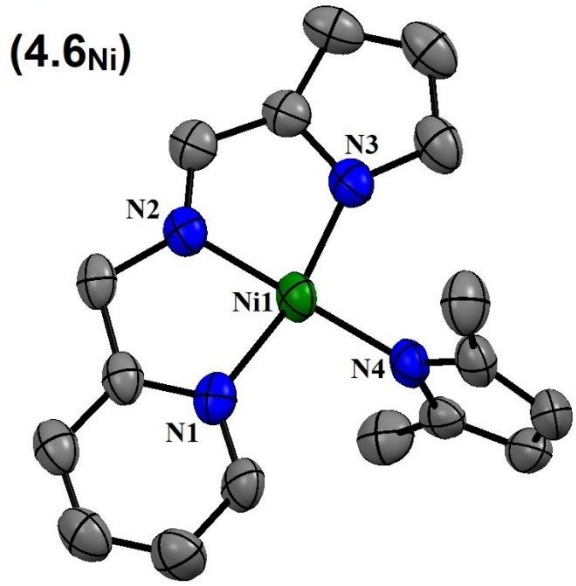

Scheme 4.10. Synthesis and molecular structures of **4.6$_{Ni}$** with 50% probability thermal ellipsoids and hydrogen atoms omitted for clarity. Selected bond distances (Å) and angles (deg) for **4.6$_{Ni}$**: Ni-N3 1.866(5), Ni-N2 1.859(5), Ni-N1 1.905(5), Ni-N4 1.877(5), N4-Ni-N1 97.4(2), N4-Ni-N3 95.4(2), N2-Ni-N1 83.7(2), N2-Ni-N3 83.6(2), N4-Ni-N2 176.4(2), N1-Ni-N3 167.2(2).

Stoichiometric reaction of **4.7$_{Ni}$** with HBpin was monitored by NMR but no evidence of Ni–H or Ph$_2$PBpin was detected, even at 50°C.

Finally, we sought to include a C-donor that did not possess an additional lone electron pair in order to compare the reactivity of complexes **4.3$_{Ni}$,4.4$_{Ni}$,4.6$_{Ni}$** with a presumed s-bond

metathesis B–H bond activation pathway. Through an alternate procedure, $NiCl(Ph)(PPh_3)_2$ was treated with one equiv of **HL6**, affording $Ni^{II}(Ph)(\kappa^3\text{-NNN})$ (**4.8$_{Ni}$**) as a dark yellow solid (**Scheme 4.11**). The ^1H NMR of **7** showed a singlet resonance at δ 4.95 for the benzylic CH_2 and 8 different aryl H resonances (Fig. C39). The molecular structure of **4.8$_{Ni}$** showed a strained square planar geometry (C1-Ni-N3 = 99.5° and C1-Ni-N1= 84.3°) showing phenyl ring deviation toward the pyrollide ring due to the larger steric hindrance of the pyridine ring.

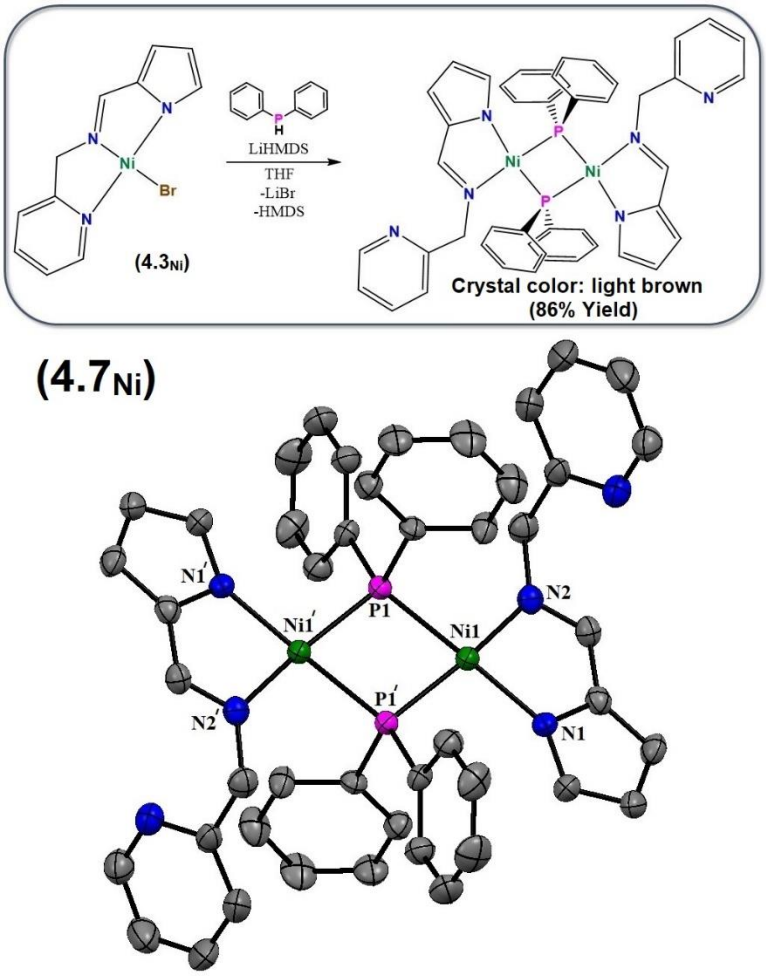

Scheme 4.11. Synthesis and molecular structures of **4.7$_{Ni}$** with 50% probability thermal ellipsoids and hydrogen atoms omitted for clarity. Selected bond distances (Å) and angles (deg) for **4.7$_{Ni}$**: Ni1-N1 1.927(4), Ni1-N2 1.985(4), Ni1-P1 2.184(1), Ni1-P1′ 2.173(1), Ni1′-P1 2.173(1), Ni1′-P1′ 2.184(1), Ni1′-N1′ 1.927(4), Ni1′-N2′ 1.985(4), N1-Ni1-N2 83.5(2), N1-Ni1-P1′ 101.0(1), N2-Ni1-P1 103.5(1), P1-Ni1-P1′ 73.33(5), P1-Ni1′-P1′ 73.33(5), P1-Ni1′-N1′ 101.0(1), P1′-Ni1′-N2′ 103.5(1), N1′-Ni1′-N2′ 83.5(2), N2-Ni1-P1′ 170.5(1), N1-Ni1-P1 169.3(1), P1-Ni1′-N2′ 170.5(1), P1′-Ni1′-N1′ 169.3(1).

Stoichiometric treatment of **4.8$_{Ni}$** with HBpin at room temperature failed to activate the B–H bond and form Ni–H (Fig. C43). Increasing the temperature to 50 ˚C, however, led to formation of Ph–Bpin (**S-P5**) as detected by EI-MS analysis (Fig. C48), but no Ni–H was observed by NMR, possibly due to its low stability at elevated temperatures.

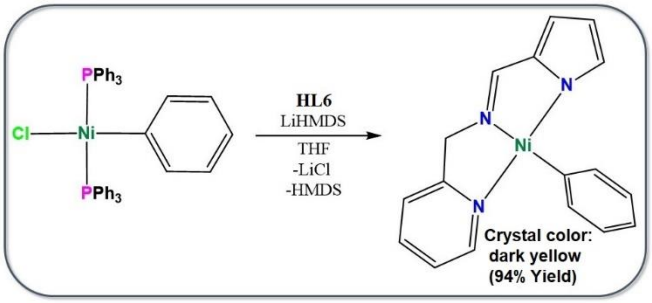

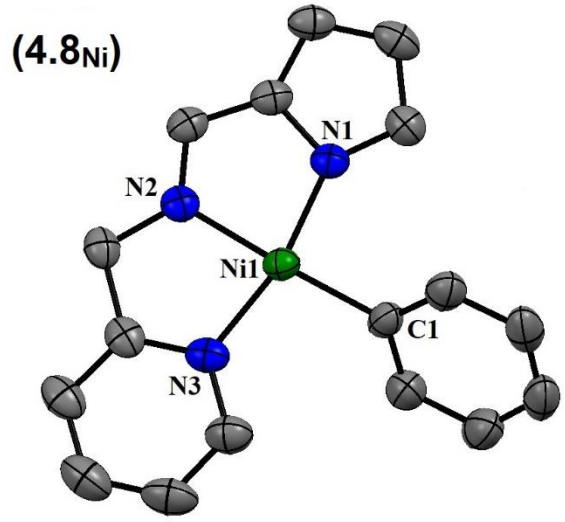

Scheme 4.12. Synthesis and molecular structures of **4.8$_{Ni}$** with 50% probability thermal ellipsoids and hydrogen atoms omitted for clarity. Selected bond distances (Å) and angles (deg) for **4.8$_{Ni}$**: Ni-N3 1.916(2), Ni-N2 1.891(2), Ni-N1 1.879(2), Ni-C1 1.893(3), C1-Ni-N1 94.3(1), C1-Ni-N3 99.5(1), N2-Ni-N3 83.06(9), N2-Ni-N1 83.18(9), C1-Ni-N2 177.3(1), N1-Ni-N3 166.22(9).

4.7.2 Hydroboration catalysis

Complexes **4.2$_{Ni}$-4.8$_{Ni}$** were assessed as precatalysts for nitrile dihydroboration (**Table 4.4**). At first, one reaction with 5 mol% of each precatalyst was carried out at room temperature without any solvent; after 15 h the reactions were analyzed by ^{1}H NMR. For precatalysts **4.3$_{Ni}$**, **4.4$_{Ni}$** and **4.6$_{Ni}$**, quantitative yields were observed (entries 2, 3 and 6), while no product was observed for precatalysts **4.5$_{Ni}$**, **4.7$_{Ni}$** and **4.8$_{Ni}$** (entries 4, 7 and 9 respectively). These preliminary results matched perfectly with **4.5$_{Ni}$**, **4.7$_{Ni}$** and **4.8$_{Ni}$** being unable to activate HBpin, as shown

above. Three more reactions were carried out with **4.5**$_{Ni}$, **4.7**$_{Ni}$ and **4.8**$_{Ni}$ under the same conditions but the temperature was increased to 50 ˚C. No products were observed for **4.5**$_{Ni}$ and **4.7**$_{Ni}$ (entries 5 and 8, respectively), but 63% yield was obtained for **4.8**$_{Ni}$ (entry 10), matching well with **4.8**$_{Ni}$ being able to activate HBpin only at higher temperature. After further optimization, it turned out that 2% loading of **4.4**$_{Ni}$ was able to catalyze the reaction in 12 h, giving quantitative yield (entry 12), while 2 mol% of **4.3**$_{Ni}$ and **4.6**$_{Ni}$ gave 89 and 92% conversion after 15 h (entries 11 and 14 respectively). Lowering the loading of **4.3**$_{Ni}$ to 1 mol% decreased the yield to 88% (entry 13).

Table 4.4. Dihydroboration of benzonitrile using **4.2**$_{Ni}$-**4.8**$_{Ni}$ as pre-catalysts

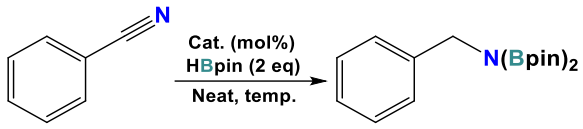

Entry	Cat. (mol%)	Time (h)	Temp. (˚C)	Yield (%)
1	**4.2**$_{Ni}$ (5)	15	RT	0
2	**4.3**$_{Ni}$ (5)	15	RT	>99
3	**4.4**$_{Ni}$ (5)	15	RT	>99
4	**4.5**$_{Ni}$ (5)	15	RT	0
5	**4.5**$_{Ni}$ (5)	15	50	0
6	**4.6**$_{Ni}$ (5)	15	RT	>99
7	**4.7**$_{Ni}$ (5)	15	RT	0
8	**4.7**$_{Ni}$ (5)	15	50	0
9	**4.8**$_{Ni}$ (5)	15	RT	0
10	**4.8**$_{Ni}$ (5)	15	50	63
11	**4.3**$_{Ni}$ (2)	15	RT	89
12	**4.4**$_{Ni}$ (2)	12	RT	>99
13	**4.4**$_{Ni}$ (1)	12	RT	88
14	**4.4**$_{Ni}$ (1)	5	50	>99
15	**4.6**$_{Ni}$ (2)	15	RT	92
16	**4.6**$_{Ni}$ (1)	5	50	>99

* Reaction conditions: benzonitrile (1 mmol, 100 µL), HBpin (2 mmol, 290 µL). Catalyst loading relative to benzonitrile. Yields were determined by ^{1}H NMR analysis based on substrates. Selectivity in all cases was 100% for the reported product.

Hydroboration of several different substrates was investigated using 2 mol% of **4.3**$_{Ni}$, **4.4**$_{Ni}$ and **4.6**$_{Ni}$ under neat condition at room temperature (**Table 4.5**). All three precatalysts catalyzed hydroboration of acetonitrile quantitatively (b) after 10 h for **4.4**$_{Ni}$ and 14 h for **4.3**$_{Ni}$ and **4.6**$_{Ni}$. Various functional groups on different positions of the phenyl ring of benzonitrile affected the

yield when compared to benzonitrile. An electron-withdrawing group in the *ortho* position (c) made no significant change since the reaction was completed after 12 h with **4.4$_{Ni}$**, and 18 h with **4.3$_{Ni}$** and **4.6$_{Ni}$.** In contrast, bulkier Br on the *ortho* position decreased efficiency (d), giving after 18 h full conversion with **4.4$_{Ni}$** and 84 and 89% yield with **4.3$_{Ni}$** and **4.6$_{Ni}$**, respectively. *Meta*–Halo substitution also reduced the catalytic efficiency with full conversion using **4.4$_{Ni}$** after 14 and 15 h for (e) and (f), respectively, whereas 91 and 82.5% yield were obtained for (e) and (f) in the presence of **4.3$_{Ni}$** and **4.6$_{Ni}$** after 18 h. Interestingly, the electronic nature of the *para* functional group significantly impacted the catalytic efficiency. While *para*-fluoro subsitution (g) led to full conversion for **4.3$_{Ni}$**, **4.4$_{Ni}$** and **4.6$_{Ni}$** in 15, 10 and 14 h respectively, both bromo and methoxy groups in this position decreased the yield for **4.3$_{Ni}$** and **4.6$_{Ni}$** after 18 h.

To find out more details about the reaction mechanism, **4.3$_{Ni}$-4.7$_{Ni}$** were treated with one equiv of 4-fluoro-benzonitrile and the reaction was monitored by ^{19}F NMR (Fig. C42). No new peaks were observed. In contrast, addition of one equiv of 4-fluoro-benzonitrile to the formed Ni–H species from **4.4$_{Ni}$** + HBpin led to disappearance of the Ni–H ^{1}H NMR resonance (Fig. C44), suggesting the next step is insertion of nitrile into Ni–H, presumably forming an imino-nickel intermediate. Using ^{19}F NMR to follow the same series of reactions (**Figure 4.3**) demonstrated that: i) After addition of 1 equiv of HBpin to **4.4$_{Ni}$**, treatment of the resulting Ni–H species with 1 equiv of 4-fluoro-benzonitrile gave only ca. 60% of imino-nickel intermediate (resonance at -120 ppm), confirming thermal instability of the Ni–H complex in the absence of substrate; ii) While subsequent addition of excess HBpin afforded the diborylamine product, using one equiv of HBpin affords both unreacted intermediate and diboryl-amine, suggesting that any monoreduced borylimine intermediate remains coordinated to nickel.

Table 4.5. Hydroboration of nitriles using **4.3**$_{Ni}$, **4.4**$_{Ni}$ and **4.6**$_{Ni}$ as pre-catalysts.

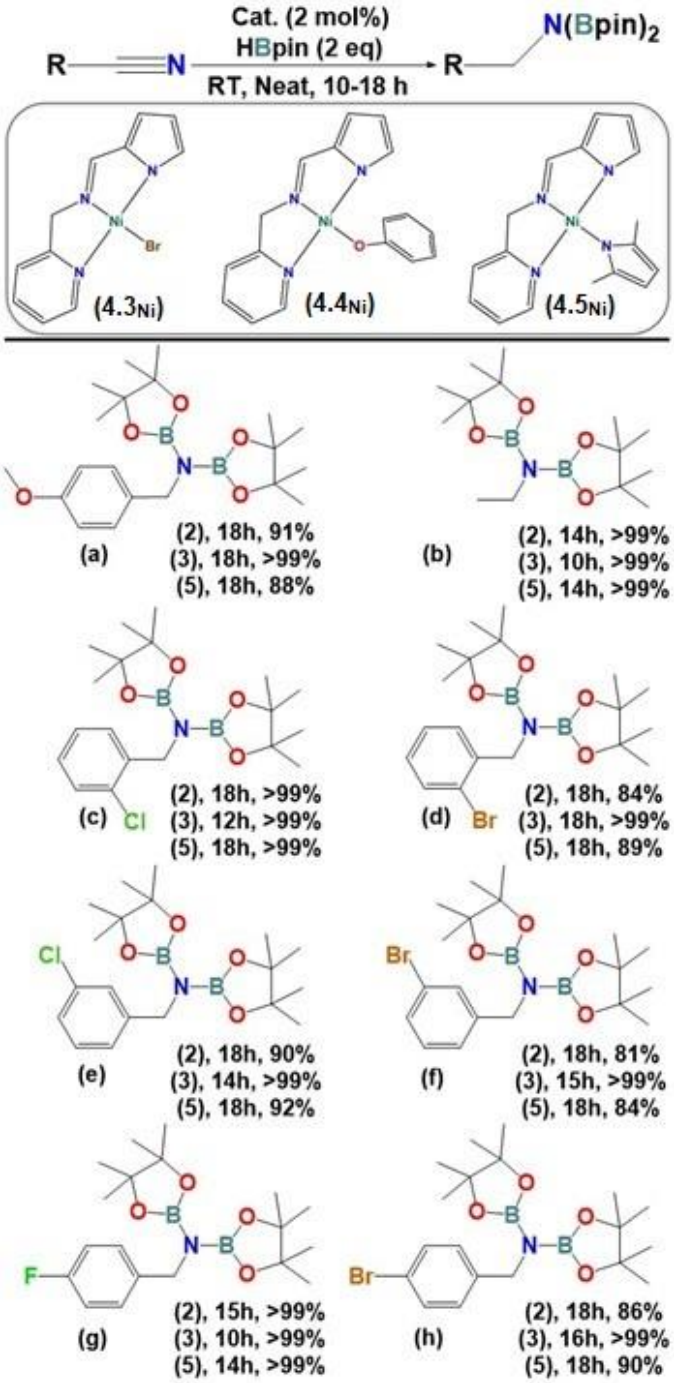

* Reaction conditions: Nitrile substrate (1 mmol), HBpin (2 mmol). Catalyst loading relative to the nitrile substrates. Yields were determined by ^{1}H NMR analysis based on substrates. Selectivity in all cases was 100% for the reported products.

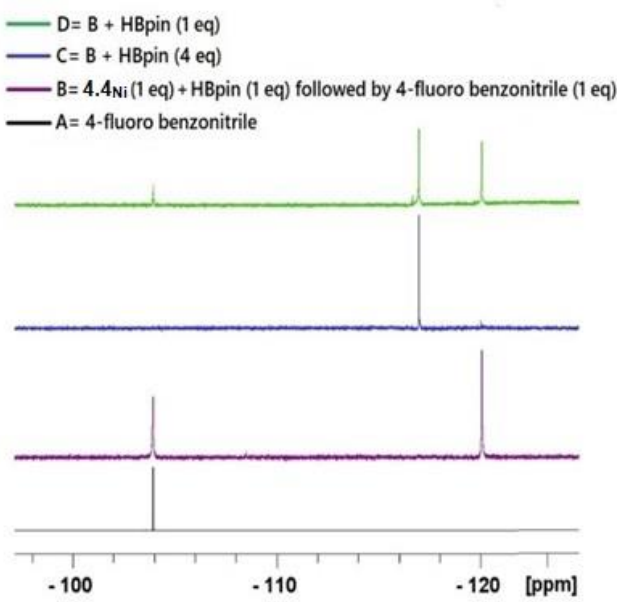

Figure 4.2. ^{19}F NMR spectra (282 MHz, C_6D_6) spectra of 4-fluoro-benzonitrile (A), stoichiometric reaction of **4.4**$_{Ni}$ with 1 equiv of HBpin and subsequently with 1 equiv of 4-fluoro-benzonitrile (B), B solution after addition of HBpin (4 eq, C), and B solution after addition of HBpin (1 eq, D).

In accord with these observations and the previous reported mechanisms for catalytic nitrile hydroborations, [10,23,35-38,48,49,54] a likely reaction pathway can be proposed for Ni- catalyzed nitrile dihydroboration (**Scheme 4.12**). First, HBpin is activated by the Ni–X bond, affording X–Bpin and NiH(NNN) (**I**). Second, the nitrile substrate coordinates to the Ni center, possibly displacing the pyridine arm of the NNN ligand as seen in the Ni-diphenylphosphide reaction.Coordination and insertion of the nitrile into Ni–H gives imino-nickel intermediate (**III**). Thereafter, HBpin coordinates to the imine nitrogen of **III** and hydride is transferred to the imine carbon, passing through intermediate (**IV**) to form borylamido intermediate (**V**). Finally, the third HBpin coordinates to N and transfers hydride to Ni through **VI**, affording diborylamine product and reforming catalyst **I**.

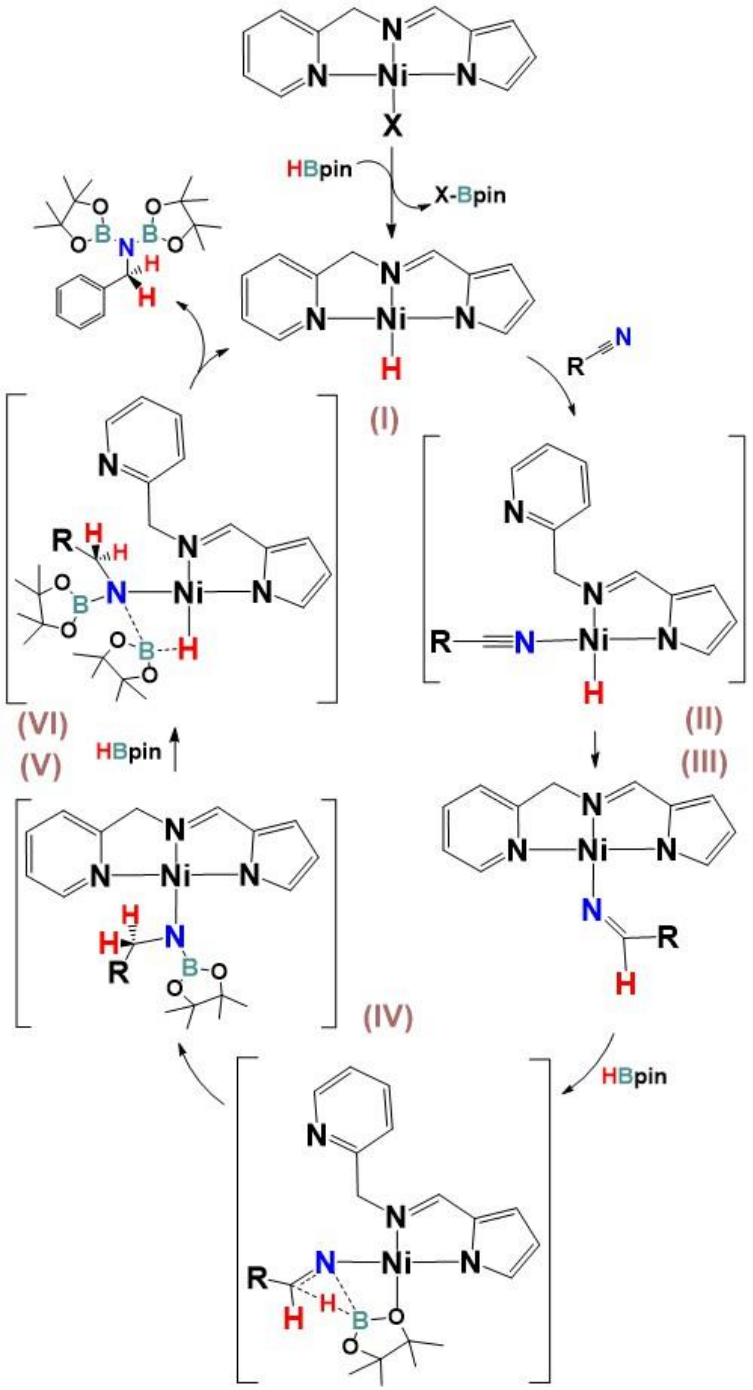

Scheme 4.13. Proposed reaction pathway for nitrile dihydroboration using HBpin and NiX(NNN) precatalysts **4.3**$_{Ni}$**, 4.4**$_{Ni}$ and **4.6**$_{Ni}$.

4.8 Conclusion

In summary, a series of divalent $Ni^{II}X$(NNN) complexes was synthesized in order to assess the different donors for pinacolborane B–H bond activation. Surprisingly, thiophenoxide complex

4.5$_{Ni}$ showed no reactivity with HBpin in spite of previous work by Tatsumi, Oestreich et al. with Ru.[55] Presumably this results from the combination of weaker bonds formed between boron and S (ca. 83 kcal/mol vs. 95 for B-N and 104 for B-O)[56] and between first row metals and H (ca. 20 kcal/mol vs. 30 for Ru–H).[57] Indeed, in our recent work on Mn-catalyzed nitrile dihydroboration we found that thiolate donors activated HBpin by simple coordination, without B–H transfer to the metal.[50] Synthesis of phosphido-bridged complex **4.7$_{Ni}$** revealed the ease of pyridine ring dissociation in the NNN ligand and the lack of reactivity of **4.7$_{Ni}$** with HBpin can also be attributed to weak B-P bonds (ca. 64 kcal/mol).[56] The work reported here also demonstrates that bifunctional B–H bond activation is more facile than the s-bond metathesis pathway presumably used by **4.8$_{Ni}$** to make PhBpin. However, given the significantly reduced activity of **4.8$_{Ni}$** vs **4.4$_{Ni}$** at 50 °C and the sustained activity of the former (Fig. C50), it would appear that **4.8$_{Ni}$** operates by a different reaction mechanism.

The correlation between Ni–H formation and dihydroboration catalytic activity suggests a conventional inner-sphere reaction pathway with nitrile insertion into Ni–H as no evidence was obtained for a bifunctional role of the NNN ligand's pyrrolide donor. However, the ligand's potential hemilability and apparent role in stabilizing the Ni–H intermediate in the presence of substrate even at 50°C provides an advantage over the previously reported Ni acac catalysts (**Scheme 4.4**).[44] Using the latter, catalysis is accompanied by formation of insoluble black solids due to irreversible formation of acac–Bpin. Finally, with all other factors being identical, we attribute the small but reproducible performance advantage of phenoxide precatalyst **4.4$_{Ni}$** over bromide **4.3$_{Ni}$** and dimethyl-pyrollide complex **4.6$_{Ni}$** to a deleterious effect of the corresponding X–Bpin complexes. Additional catalysis studies using this NNN ligand with other first row metals are in progress.

4.9 Experimental Section

4.9.1 General considerations

All experiments were performed under N_2 atmosphere, using a Schlenk line or an MBraun glovebox unless otherwise stated. THF, diethyl ether (DEE), and hexanes were dried on columns of activated alumina using a J. C. Meyer (formerly Glass Contour) solvent purification system and stored over activated 4 Å molecular sieves (heated at 180 ^{o}C for 2 d under vacuum). C_6D_6, $CDCl_3$, and dichloromethane (DCM) were purchased from Sigma Aldrich and used without drying.

Ligands 2-pyridyl-N-(2'-methylthiophenyl) methylamine (**HL5**)[45], and N-((1–H-pyrrol-2-yl)methylene)-1-(pyridin-2-yl)methanamine (**HL6**)[46], and the precursor complex *trans*-$NiCl(Ph)(PPh_3)_2$[47] were prepared according to literature procedures. Other chemicals were used as obtained commercially: 2-(methylthio)aniline (Alfa Aesar, 98%), 2-picolylamine (Sigma Aldrich, 99%), pyrrole-2-carboxaldehyde (Alfa Aesar, 99%), sodium borohydride (Sigma Aldrich, >98%), 2-pyridinecarboxaldehyde (Sigma Aldrich, 99%), lithium bis(trimethylsilyl)amide (LiHMDS, Sigma Aldrich, >99.9%), nickel dibromide(1,2-dimethoxyethane) [$NiBr_2$(DME), Sigma Aldrich, 97%], $Ni(cod)_2$ (Sigma Aldrich), pinacolborane (Alfa Aesar, 97%), phenol (Sigma Aldrich), thiophenol (Sigma Aldrich, 97%), 2,5-dimethylpyrrole (Sigma Aldrich, 98%), diphenylphosphine (Sigma Aldrich, 98%), chlorobenzene (Sigma Aldrich, 99.8%), triphenylphosphine (Sigma Aldrich, 99%). ^1H, $^{13}C\{^1H\}$, ^{19}F, and $^{31}P\{^1H\}$ NMR spectra were recorded on a 300 MHz Bruker Avance II instrument at room temperature (21−25 °C). ^{13}C and ^1H NMR spectra were referenced respectively to solvent carbons and residual protons (C_6D_6, δ 7.15; $CDCl_3$, δ 7.26). ^{19}F and $^{31}P\{^1H\}$ NMR chemical shifts were referenced to external $CFCl_3$ and H_3PO_4 both at 0 ppm. Electron impact mass spectra (EI-MS) were obtained using a Kratos Concept S1 instrument (Hres 7000−10000). X-ray diffraction data were collected on a Bruker Smart or Kappa diffractometer equipped with an ApexII CCD detector and a sealed-tube Mo K source (λ = 0.71073 Å).

4.9.2 Synthesis and characterization

4.9.2.1 Synthesis of $Ni^{II}Br(\kappa^3\text{-}NNS^{Me})$ ($\mathbf{4.2_{Ni}}$)

A 42 mL glass vial was charged with $NiBr_2$(DME) (1.339 g, 4.34 mmol) in 10 mL of THF and a solution of the **HL5** ligand (1.000 g, 4.34 mmol) and LiHMDS (726 mg, 4.34 mmol) in 20 mL of THF was added dropwise. The color changed from green to brown. After stirring overnight at room temperature, the solvent was removed under vacuum. The residue was extracted into DCM (2×20 mL) and filtered. The filtrate was evaporated under vacuum and the product was washed with hexane (3×10 mL) and DEE (3×10 mL) and dried under vacuum to give 1.516 g of **$\mathbf{4.2_{Ni}}$** as a light-brown powder (95%). Crystals of **$\mathbf{4.2_{Ni}}$** suitable for X-ray crystallography were obtained from hexane layering of a DCM solution at room temperature after 1 day. ^1H NMR (300 MHz, $CDCl_3$) δ 8.96 (d, 1H, Ar–H), 7.79 (t, 1H, Ar–H), 7.35 (d, 1H, Ar–H), 7.22 (d, 1H, Ar–H), 7.13 (mult, 2H, Ar–H), 6.39 (mult, 2H, Ar–H), 6.67 (tr, 7, 1H, Ar–H), 6.31 (d, 8,1H, Ar–H), 4.39 (s, 2H, -CH_2-), 2.82 (s, 3H, S−CH_3). $^{13}C\{^1H\}$ NMR (75 MHz, $CDCl_3$) δ 167.3, 158.9, 150.8, 137.9, 130.8, 130.6,

122.5, 120.5, 119.8, 113.5, 110.7, 58.1 (-CH_2-), 25.5 (S-CH_3). EI-MS: [M^+] 365.9344, Calcd. 365.9336 (Fig. C28).

4.9.2.2 Synthesis of $Ni^{II}Br(\kappa^3$-NNN) (4.3_{Ni})

A 42 mL glass vial was charged with $NiBr_2$(DME) (1.666 g, 5.39 mmol) in 15 mL of THF and a solution of the **HL6** ligand (1.000 g, 5.39 mmol) and LiHMDS (903 mg, 5.39 mmol) in 20 mL of THF was added dropwise. The color changed from green to brown. After stirring overnight at room temperature, the solvent was removed under vacuum. The residue was extracted into DCM (3×20 mL) and filtered. The filtrate was evaporated under vacuum and the product was washed with hexane (3×10 mL) and DEE (3×10 mL) and dried under vacuum to give 1.603 g of **4.3_{Ni}** as a brown powder (92%). Crystals of **4.3_{Ni}** suitable for X-ray crystallography were obtained from hexane layering of a DCM solution at room temperature after 1 day. ^{1}H NMR (300 MHz, $CDCl_3$) δ 8.92 (d, 1H, Ar–H), 7.77 (t, 1H, Ar–H), 7.16 (m, 3H, Ar–H), 6.90 (s, 1H, Ar–H), 6.60 (d, 1H, Ar–H), 5.98 (t, 1H, Ar–H), 4.88 (s, 2H, -CH_2-). $^{13}C\{^1H\}$ NMR (75 MHz, $CDCl_3$) δ 165.0, 160.5, 152.6, 145.2, 141.5, 138.2, 127.2, 123.0, 120.9, 118.9, 114.7, 56.9 (-CH_2-). EI-MS: 320.9387, Calcd. 320.9411 (Fig. C30).

4.9.2.3 Synthesis of $Ni^{II}(OPh)(\kappa^3$-NNN) (4.4_{Ni})

A 42 mL glass vial was charged with **4.3_{Ni}** (200 mg, 0.619 mmol) in 10 mL of THF and a solution of phenol (58 mg, 0.619 mmol) and LiHMDS (103 mg, 0.619 mmol) in 10 mL of THF was added dropwise. The color changed from brown to red. After stirring overnight at room temperature, the solvent was removed under vacuum. The residue was extracted into DCM (2×5 mL) and filtered. The filtrate was evaporated under vacuum and the product was washed with hexane (3×5 mL) and DEE (3×5 mL) and dried under vacuum to give 168 mg of **4.4_{Ni}** as a red powder (81%). Crystals of **4.4_{Ni}** suitable for X-ray crystallography were obtained from hexane layering of a DCM solution at room temperature after 3 days. ^{1}H NMR (300 MHz, $CDCl_3$) δ 7.95 (d, 1H, Ar–H), 7.79 (t, 1H, Ar–H), 7.62 (d, 2H, Ar–H), 7.18 (t, 2H, Ar–H), 7.10 (m, 3H, Ar–H), 6.57 (t, 1H, Ar–H), 6.53 (d, 1H, Ar–H), 6.10 (t, 1H, Ar–H), 5.90 (dd, 1H, Ar–H), 4.67 (s, 2H, -CH_2-). $^{13}C\{^1H\}$ NMR (75 MHz, $CDCl_3$) δ 167.1, 162.5, 158.1, 148.8, 142.3, 139.0, 138.7, 128.9, 123.1, 121.3, 120.5, 117.5, 144.6, 111.9, 57.8 (-CH_2-). EI-MS: [M^+] 335.0641, Calcd. 335.0586 (Fig. C32).

4.9.2.4 Synthesis of $Ni^{II}(SPh)(\kappa^3\text{-NNN})$ ($\mathbf{4.5_{Ni}}$)

A 42 mL glass vial was charged with **4.3$_{Ni}$** (200 mg, 0.619 mmol) in 10 mL THF and a solution of thiophenol (68 mg, 0.619 mmol) and LiHMDS (103 mg, 0.619 mmol) in 10 mL of THF was added dropwise. The color changed from brown to red. After stirring overnight at room temperature, the solvent was removed under vacuum. The residue was extracted into DCM (2×5 mL) and filtered. The filtrate was evaporated under vacuum and the product was washed with hexane (3×5 mL) and DEE (3×5 mL) and dried under vacuum to give 191 mg of **4.5$_{Ni}$** as a red powder (88%). Crystals of **4.5$_{Ni}$** suitable for X-ray crystallography were obtained from hexane layering of a DCM solution at room temperature after 1 day. ^{1}H NMR (300 MHz, $CDCl_3$) δ 8.85 (d, 1H, Ar–H), 8.15 (d, 2H, Ar–H), 7.74 (t, 1H, Ar–H), 7.38 (s, 1H, Ar–H), 7.19 (d, 1H, Ar–H), 7.08 (m, 3H, Ar–H), 6.99 (d, 1H, Ar–H), 6.70 (s, 1H, Ar–H), 6.57 (d, 1H, Ar–H), 5.93 (dd, 1H, Ar–H), 4.94 (s, 2H, -CH_2-). $^{13}C\{^1H\}$ NMR (75 MHz, $CDCl_3$) δ 164.3, 157.3, 152.0, 145.1, 143.4, 141.0, 138.6, 133.1, 127.9, 123.1, 122.3, 120.6, 118.1, 111.9, 57.9 (-CH_2-). EI-MS: [M^+] 351.0356, Calcd. 351.0340 (Fig. C34).

4.9.2.5 Synthesis of Ni^{II}(2,5-dimethylpyrrolyl)(κ^3-NNN) ($\mathbf{4.6_{Ni}}$)

A 42 mL glass vial was charged with **4.3$_{Ni}$** (200 mg, 0.619 mmol) in 10 mL of THF and a solution of 2,5-dimethylpyrrole (58 mg, 0.619 mmol) and LiHMDS (103 mg, 0.619 mmol) in 10 mL of THF was added dropwise. The color changed from brown to navy-blue. After stirring overnight at room temperature, the solvent was removed under vacuum. The residue was extracted into DCM (2×5 mL) and filtered. The filtrate was evaporated under vacuum and the product was washed with hexane (3×5 mL) and DEE (3×5 mL) and dried under vacuum to give 154 mg of **4.6$_{Ni}$** as a navy-blue powder (74%). Crystals of **4.6$_{Ni}$** suitable for X-ray crystallography were obtained from hexane layering of a DCM solution at room temperature after 3 days. ^{1}H NMR (300 MHz, $CDCl_3$) δ 7.80 (t, 1H, Ar–H), 7.31 (d, 2H, Ar–H), 7.22 (d, 1H, Ar–H), 7.12 (t, 1H, Ar–H), 6.64 (t, 1H, Ar–H), 5.97 (t, 1H, Ar–H), 5.91 (s, 2H, Ar–H), 5.86 (s, 1H, Ar–H), 4.86 (s, 2H, -CH_2-), 2.89 (s, 6H, 2(-CH_3)). $^{13}C\{^1H\}$ NMR (75 MHz, $CDCl_3$) δ 163.4, 157.9, 150.9, 142.7, 139.9, 138.6, 134.4, 123.9, 120.4, 117.9, 112.1, 106.0, 57.9 (-CH_2-), 17.4 (-CH_3). EI-MS: [M^+] 336.0373, Calcd. 336.0884 (Fig. C36).

4.9.2.6 Synthesis of $[Ni^{II}(\mu\text{-}PPh_2)(\kappa^2\text{-}NNN)]_2$ ($\mathbf{4.7_{Ni}}$)

A 42 mL glass vial was charged with $\mathbf{4.3_{Ni}}$ (200 mg, 0.619 mmol) in 10 mL of THF and a solution of diphenylphosphine (115 mg, 0.619 mmol) and LiHMDS (103 mg, 0.619 mmol) in 10 mL of THF was added dropwise. The color changed from brown to light brown. After stirring overnight at room temperature, the solvent was removed under vacuum. The residue was extracted into DCM (2×5 mL) and filtered. The filtrate was evaporated under vacuum and the product was washed with hexane (3×5 mL) and DEE (3×5 mL) and dried under vacuum to give 227 mg of $\mathbf{4.7_{Ni}}$ as a red powder (86%). Crystals of $\mathbf{4.7_{Ni}}$ suitable for X-ray crystallography were obtained from hexane layering of a DCM solution at room temperature after 1 day. ^{1}H NMR (300 MHz, $CDCl_3$) δ 8.30 (d, 2H, Ar–H), 8.05 (dd, 6H, Ar–H), 7.42 (m, 4H, Ar–H), 6.26 (t, 6H, Ar–H), 7.15 (t, 8H, Ar–H), 6.99 (m, 4H, Ar–H), 6.81 (d, 2H, Ar–H), 6.44 (d, 2H, Ar–H), 5.87 (d, 2H, Ar–H), 3.98 (s, 4H, -CH_2-). ^{13}C{^{1}H} NMR (75 MHz, $CDCl_3$) δ 164.33, 159.0, 151.4, 148.6, 141.1, 136.2, 134.9, 130.6, 129.1, 128.3, 121.7, 121.5, 116.5, 111.7, 60.7 (-CH_2-). ^{31}P{^{1}H} NMR (300 MHz, $CDCl_3$) δ -102.3. EI-MS: [$M/2^+$] 427.0731, Calcd. 427.0748 (Fig. C38).

4.9.2.7 Synthesis of $Ni^{II}(Ph)(\kappa^3\text{-}NNN)$ ($\mathbf{4.8_{Ni}}$)

A 42 mL glass vial was charged with $NiCl(Ph)(PPh_3)_2$ (200 mg, 0.287 mmol) in 10 mL of THF and a solution of **HL6** (53 mg, 0.287 mmol) and LiHMDS (48 mg, 0.287 mmol) in 10 mL of THF was added dropwise. The color changed from yellow to dark yellow. After stirring overnight at room temperature, the solvent was removed under vacuum. The residue was extracted into DCM (2×5 mL) and filtered. The filtrate was evaporated under vacuum and the product was washed with hexane (3×5 mL) and DEE (3×5 mL) and dried under vacuum to give 86 mg of $\mathbf{4.8_{Ni}}$ as a red powder (94%). Crystals of $\mathbf{4.8_{Ni}}$ suitable for X-ray crystallography were obtained from hexane layering of a DCM solution at room temperature after 1 days. ^{1}H NMR (300 MHz, $CDCl_3$) δ 7.83 (d, 2H, Ar–H), 7.72 (m, 3H, Ar–H), 7.21 (d, 1H, Ar–H), 7.10 (t, 2H, Ar–H), 7.00 (m, 2H, Ar–H), 6.60 (d, 1H, Ar–H), 5.99 (d, 2H, Ar–H), 4.95 (s, 2H, -CH_2-). ^{13}C{^{1}H} NMR (75 MHz, $CDCl_3$) δ 165.2, 159.7, 155.5, 152.4, 144.4, 139.3, 138.0, 137.5, 125.9, 123.3, 122.6, 120.9, 116.4, 111.0, 56.5 (-CH_2-). EI-MS: [M^+] 319.0621, Calcd. 319.0619 (Fig. C40).

4.9.3 Catalytic studies

Nitrile hydroboration catalysis

An 18 mL glass vial was charged with 0.02 mmol (2 mol%) of nickel complex (**4.3$_{Ni}$**: 6.4 mg, **4.4$_{Ni}$**: 6.7 mg, **4.5$_{Ni}$**: 7.0 mg, **4.6$_{Ni}$**: 6.7 mg, **4.7$_{Ni}$**: 17.1 mg, **4.8$_{Ni}$**: 6.4 mg), and 1 mmol of nitrile substrate (100 µL benzonitrile, 52 µL acetonitrile, 137 mg 2-chlorobenzonitrile, 182 mg 2-bromobenzo-nitrile, 137 mg 3-chlorobenzonitrile, 182 mg 3-bromobenzonitrile, 121 mg 4-fluorobenzo-nitrile, 182 mg 4-bromobenzonitrile, 133 mg 4-methoxybenzonitrile). After adding a stir bar to the vial, HBpin (290 µL, 2 mmol) was added, the vial capped and stirred for 10-18 h at room temperature. A portion of the resulting reaction mixture was then dissolved in C_6D_6, transferred to an NMR tube and the ^{1}H NMR spectrum recorded. All diborylamine products were characterized by comparison with their previously reported ^{1}H NMR spectra.[39,48-50] As no side-products were observed, dihydroborated product yield was calculated based on integrals compared to the starting nitrile. Similar reactions were performed with **4.5$_{Ni}$**, **4.7$_{Ni}$**, and **4.8$_{Ni}$** at 50 ºC.

4.9.4 Stoichiometric reactions

4.9.4.1 Reactions of 4.3$_{Ni}$-4.8$_{Ni}$ with nitrile

A small vial was charged with 1 equiv of 4-fluoro-benzonitrile (0.1 mmol, 12.1 mg), 1 equiv of nickel complex (0.1 mmol; **4.3$_{Ni}$**: 32.2 mg, **4.4$_{Ni}$**: 33.6 mg, **4.5$_{Ni}$**: 35.2 mg, **4.6$_{Ni}$**: 33.7 mg, **4.8$_{Ni}$**: 32.00 mg, and 0.5 equiv, 0.05 mmol of **4.7$_{Ni}$**: 42.8 mg) and 0.5 mL of C_6D_6. The solution was stirred for 2 h and then transferred to an NMR tube for analysis.

4.9.4.2 Reactions of 4.2$_{Ni}$-4.8$_{Ni}$ with HBpin

A small vial was charged with 1 equiv of nickel complex (0.1 mmol; **4.2$_{Ni}$**: 36.7 mg, **4.3$_{Ni}$**: 32.2 mg, **4.4$_{Ni}$**: 33.6 mg, **4.5$_{Ni}$**: 35.2 mg, **4.6$_{Ni}$**: 33.7 mg, **4.8$_{Ni}$**: 32.00 mg, and 0.5 equiv, 0.05 mmol of **4.7$_{Ni}$**: 42.8 mg), 0.5 mL of C_6D_6, and 1 equiv of HBpin (0.1 mmol, 14.5 µL). The solution was stirred for 30 min and then transferred to an NMR tube for analysis. After that, the solutions were transferred from the NMR tube to a vial and the solvent was evaporated under vacuum. The residue of the reaction of **4.4$_{Ni}$** was extracted into hexane and then recrystallized to grow suitable single crystal for crystallography and NMR analyses. The residue of the reactions of **4.2$_{Ni}$**, **4.5$_{Ni}$**, **4.6$_{Ni}$**, **4.7$_{Ni}$**, and **4.8$_{Ni}$** were submitted for EI-MS analysis.

In another trial, complexes **4.5**$_{Ni}$, **4.7**$_{Ni}$, and **4.8**$_{Ni}$ were treated with HBpin and heated at 50 ºC for 6 h. Only complex **4.8**$_{Ni}$ reacted, although no Ni–H was observed. Work-up as above, however, showed formation of PhBpin, cf., EI-MS spectrum in Fig. C48.

4.9.4.3 Reaction of 4.4$_{Ni}$ with HBpin, and then 4-fluoro-benzonitrile, followed by addition of HBpin

A small vial was charged with 1 equiv of **4.4**$_{Ni}$ (0.1 mmol, 33 mg), 0.5 mL of C_6D_6, and 1 equiv of HBpin (0.1 mmol, 14.5 µL). The solution immediately turned reddish brown and was then stirred for 30 min and transferred to an NMR tube for ^{1}H NMR analysis. Then a small vial charged with 1 equiv of 4-fluoro-benzonitrile (0.1 mmol, 12 mg) in 0.5 mL of C_6D_6 was injected into the NMR tube resulting in a color change to purplish brown. The NMR tube was shaken well and after 1 h ^{1}H and ^{19}F NMR analyses were carried out. To this solution, was added 4 more equiv of HBpin (0.4 mmol, 58 µL) and after almost 15 h, ^{19}F NMR analysis was carried out.

In another experiment, all the mentioned steps were carried out in the same way, but for the last step only 1 equiv of HBpin was added.

4.9.4.4 Monitoring reaction progress of benzonitrile dihydroboration using complex 4.8$_{Ni}$

6 small vials were charged with complex **4.8**$_{Ni}$ (16 mg, 5 mol%), and benzonitrile (1 mmol, 100 µL), HBpin (290 µL, 2 mmol) and a small stir bar and then were capped and heated to 50 ˚C. Every hour, to one of the vials was added 0.5 mL of C_6D_6 and the mixture transferred to an NMR tube for ^{1}H NMR analysis (Fig. C50).

4.9.5 X-ray crystallographic details (4.2$_{Ni}$-4.8$_{Ni}$ and S-P3)

Crystallographic data were collected from single crystals mounted on MiTeGen dual thickness MicroMounts using Parabar oil. Data were collected on a Bruker Smart (**4.**3$_{Ni}$, **4.**5$_{Ni}$, **4.**6$_{Ni}$, and **4.**7$_{Ni}$) or Kappa (**4.**2$_{Ni}$, **4.**4$_{Ni}$, **4.**8$_{Ni}$, and **S-P3**) ApexII single crystal diffractometer equipped with a graphite monochromator. The instrument was equipped with a sealed tube Mo K$\boldsymbol{\alpha}$ source ($\boldsymbol{\lambda} = 0.71073$ Å), an ApexII CCD detector and a dry compressed air-cooling system. All samples were cooled to 200(2) (**4.**8$_{Ni}$ and **S-P3**), 203(2) (**4.**3$_{Ni}$, **4.4**$_{Ni}$, **4.5**$_{Ni}$, **4.6**$_{Ni}$, **and 4.7**$_{Ni}$) or 293(2) (**4.2**$_{Ni}$) K during data collection. Raw data collection and processing were performed with the Apex3 software package from Bruker.[58] Initial unit cell parameters were determined from

36 data frames from select $\boldsymbol{\omega}$ scans. Semi-empirical absorption corrections based on equivalent reflections were applied.[59] Systematic absences in the diffraction data-set and unit-cell parameters were consistent with the assigned space group. The initial structural solutions were determined using ShelxT direct methods,[60] and refined with full-matrix least-squares procedures based on $\boldsymbol{F^2}$ using ShelXL or ShelXle.[61] Compound **4.2$_{Ni}$** exhibited minor positional disorder which was refined in ShelXle. Hydrogen atoms were placed geometrically and refined using a riding model. CCDC Deposition Numbers: 2155492-2155499.

4.10 References

(1) Suginome, M.; Uehlin, L.; Murakami, M. Aminoboranes as "Compatible" Iminium Ion Generators in Aminative C-C Bond Formations. *J. Am. Chem. Soc.* **2004**, *126*, 13196−13197.

(2) Chong, E.; Blum, S. A. Aminoboration: Addition of B−N σ Bonds across C−C π Bonds. *J. Am. Chem. Soc.* **2015**, *137*, 10144−10147.

(3) Junor, G. P.; Romero, E. A.; Chen, X.; Jazzar, R.; Bertrand, G. Readily Available Primary Aminoboranes as Powerful Reagents for Aldimine Synthesis. *Angew. Chem. Int. Ed.* **2019**, *58*, 2875–2878.

(4) Kitano, T.; Komuro, T.; Tobita, H. Double and Single Hydroboration of Nitriles Catalyzed by a Ruthenium−Bis(silyl)xanthene Complex: Application to One-Pot Synthesis of Diarylamines and N-Arylimines. *Organometallics* **2019**, *38*, 1417−1420.

(5) Ghosh, C.; Kim, S.; Mena, M. R.; Kim, J–H.; Pal, R.; Rock, C. L.; Groy, T. L.; Baik, M–H.; Trovitch, R. J. Efficient Cobalt Catalyst for Ambient-Temperature Nitrile Dihydroboration, the Elucidation of a Chelate-Assisted Borylation Mechanism, and a New Synthetic Route to Amides. *J. Am. Chem. Soc.* **2019**, *141*, 15327−15337.

(6) Sahoo, R. K.; Mahato, M.; Jana, A.; Nembenna, S. Zinc Hydride-Catalyzed Hydrofunctionalization of Ketones. *J. Org. Chem.* **2020**, *85*, 11200−11210.

(7) Willcox, D.; Carden, J. L.; Ruddy, A. J.; Newman, P. D.; Melen, R. L. Asymmetric Ketone Hydroboration Catalyzed by Alkali Metal Complexes Derived from BINOL Ligands. *Dalton Trans.* **2020**, *49*, 2417−2420.

(8) Vasilenko, V.; Blasius, C. K.; Wadepohl, H.; Gade, L. H. Mechanism-Based Enantiodivergence in Manganese Reduction Catalysis: A Chiral Pincer Complex for the

Highly Enantioselective Hydroboration of Ketones. *Angew. Chem. Int. Ed.* **2017**, *56*, 8393–8397.

(9) Wang, R.; Park, S. Recent Advances in Metal-Catalyzed Asymmetric Hydroboration of Ketones. *ChemCatChem* **2021**, *13*, 1898–1919.

(10) Gudun, K. A.; Slamova, A.; Hayrapetyan, D.; Khalimon, A. Y. Efficient Co-Catalyzed Double Hydroboration of Nitriles: Application to One-Pot Conversion of Nitriles to Aldimines. *Chem. - Eur. J.* **2020**, *26*, 4963–4968.

(11) Khalimon, A. Y.; Farha, P. M.; Nikonov, G. I. Imido–hydrido Complexes of Mo(IV): Catalysis and Mechanistic Aspects of Hydroboration Reactions. *Dalton Trans.* **2015**, *44*, 18945–18956.

(12) Huang, Z.; Wang, S.; Zhu, X.; Yuan, Q.; Wei, Y.; Zhou, S.; Mu, X. Well-Defined Amidate-Functionalized N–Heterocyclic Carbene-Supported Rare-Earth Metal Complexes as Catalysts for Efficient Hydroboration of Unactivated Imines and Nitriles. *Inorg. Chem.* **2018**, *57*, 15069−15078.

(13) Gautam, N.; Logdi, R. P. S.; Rajendran, N. M. Tiwari, A. K.; Mandal, S. K. Bicyclic (alkyl)(amino)carbene (BICAAC) as a Metal-free Catalyst for Reduction of Nitriles to Amines. *Chem. Commun.* **2022**, *58*, 3047–3050.

(14) Kim, H.; Kim, H. T.; Lee, J. H.; Hwang, H.; An, D. K. Lithium Bromide: An Inexpensive and Efficient Catalyst for Imine Hydroboration with Pinacolborane at Room Temperature. *RSC Adv.* **2020**, *10*, 34421−34427.

(15) Chong, C. C.; Kinjo, R. Catalytic Hydroboration of Carbonyl Derivatives, Imines, and Carbon Dioxide. *ACS Catal.* **2015**, *5*, 3238−3259.

(16) Rej, S.; Das, A.; Panda. T. K. Overview of Regioselective and Stereoselective Catalytic Hydroboration of Alkynes. *Adv. Synth. Catal.* **2021**, *363*, 4818– 4840.

(17) Collins, B. S. L.; Wilson, C. M.; Myers, E. L.; Aggarwal. V. K. Asymmetric Synthesis of Secondary and Tertiary Boronic Esters. *Angew. Chem. Int. Ed.* **2017**, *56*, 11700–11733.

(18) Obligacion, J. V.; Chirik, P. J. Earth- abundant Transition Metal Catalysts for Alkene Hydrosilylation and Hydroboration. *Nat. Rev. Chem.* **2018**, *2*, 15–34.

(19) Li, C.; Song, S.; Li, Y.; Xu, C.; Luo, Q.; Guo, Y.; Wang, X. Selective Hydroboration of Unsaturated Bonds by an Easily Accessible Heterotopic Cobalt Catalyst. *Nat. Commun.* **2021**, *12*, 3813–3820.

(20) Na´jera, C.; Beletskaya, I. P.; Yus, M. Metal-catalyzed Regiodivergent Organic Reactions. *Chem. Soc. Rev.* **2019**, *48*, 4515–4618.

(21) Bage, A. D.; Nicholson, K.; Hunt, T. A.; Langer, T.; Thomas, S. P. The Hidden Role of Boranes and Borohydrides in Hydroboration Catalysis. *ACS Catal.* **2020**, *10*, 13479–13486.

(22) Kuciński, K.; Hreczycho, G. Hydrosilylation and Hydroboration in a Sustainable Manner: From Earth-abundant Catalysts to Catalyst-free Solutions. *Green Chem.* **2020**, *22*, 5210–5224.

(23) Weetman, C.; Anker, M. D.; Arrowsmith, M.; Hill, M. S.; Kociok-Kohn, G.; Liptrot, D. J.; Mahon, M. F. Magnesium-catalysed Nitrile Hydroboration. *Chem. Sci.* **2016**, *7*, 628–641.

(24) Davit Hayrapetyan, D.; Khalimon, A. Y. Catalytic Nitrile Hydroboration: A Route to N,N-Diborylamines and Uses Thereof. *Chem.-Asian J.* **2020**, *15*, 2575–2587.

(25) Brown, H. C.; Ayyangar, N. R.; Zweifel, G. Hydroboration. XVIII. The Reaction of Diisopinocampheylborane with Representative cis-Acyclic, Cyclic, and Bicyclic Olefins. A Convenient Synthesis of Optically Active Alcohols and Olefins of High Optical Purity and Established Configuration. *J. Am. Chem. Soc.* **1964**, *86*, 397–403.

(26) Coffinet, A.; Zhang, D.; Vendier, L.; Bontemps, S.; Simonneau, A. Borane-catalysed Dinitrogen Borylation by 1,3-B–H Bond Addition. *Dalton Trans.* **2021**, ***50***, 5582–5589.

(27) Beletskaya, I.; Pelter, A. Hydroborations Catalysed by Transition Metal Complexes. *Tetrahedron* **1997**, *53*, 4957–5026.

(28) Das, A.; Rej, S.; Panda, T. K. Aluminium Complexes: Next-generation Catalysts for Selective Hydroboration. *Dalton Trans.* **2022**, *51*, 3027–3040.

(29) Elsby, M. R.; Baker, R. T. Strategies and Mechanisms of Metal–ligand Cooperativity in First-row Transition Metal Complex Catalysts. *Chem. Soc. Rev.* **2020**, *49*, 8933–8987.

(30) Khusnutdinova, J. R.; Milstein, D. Metal–Ligand Cooperation. *Angew. Chem. Int. Ed.* **2015**, *54*, 12236–12273.

(31) Fritz, M.; Schneider, S. *The Periodic Table II: Catalytic, Materials, Biological and Medical Applications*, D. M. P. Mingos, Springer, **2019**.

(32) Pang, M.; Wu, C.; Zhuang, X.; Zhang, F.; Su, M.; Tong, Q.; Tung, C–H.; Wang, W. Addition of a B−H Bond across an Amido−Cobalt Bond: Co^{II}—H Catalyzed Hydroboration of Olefins. *Organometallics* **2018**, *37*, 1462−1467.

(33) Liu, J.; Chen, J-Y.; Jia, M.; Ming, B.; Jia, J.; Liao, R-Z.; Tung, C–H.; Wang, W. Ni−O Cooperation versus Nickel(II) Hydride in Catalytic Hydroboration of N-Heteroarenes. *ACS Catal.* **2019**, *9*, 3849−3857.

(34) Elsby, M. R.; Baker, R. T. Cu(I)–SNS Complexes for Outer-sphere Hydroboration and Hydrosilylation of Carbonyls. *Chem. Commun.* **2019**, *55*, 13574–13577.

(35) Saha, S.; Eisen, M. S. Catalytic Recycling of a Th−H Bond via Single or Double Hydroboration of Inactivated Imines or Nitriles. *ACS Catal.* 2019, *9*, 5947−5956.

(36) Ding, Y.; Ma, X.; Liu, Y.; Liu, W.; Yang, Z.; Roesky, H. W. Alkylaluminum Complexes as Precatalysts in Hydroboration of Nitriles and Carbodiimides. *Organometallics* **2019**, *38*, 3092−3097.

(37) Harinath, A.; Bhattacharjee, J.; Panda, T. K. Catalytic Hydroboration of Organic Nitriles Promoted by Aluminum Complex. *Adv. Synth. Catal.* **2019**, *361*, 850–857.

(38) Das, S.; Bhattacharjee, J.; Panda, T. K. An Imidazolin-2-iminato Ligand Organozinc Complex as a Catalyst for Hydroboration of Organic Nitriles. *New J. Chem.* **2019**, *43*, 16812–16818.

(39) Wang, X.; Zhang, Y.; Yuan, D.; Yao, Y. Regioselective Hydroboration and Hydrosilylation of N-Heteroarenes Catalyzed by a Zinc Alkyl Complex. *Org. Lett.* **2020**, *22*, 5695−5700.

(40) Procter, J. R.; Uzelac, M.; Cid, J.; Rushworth, P. J.; Ingleson, M. J. Low-Coordinate NHC−Zinc Hydride Complexes Catalyze Alkyne C−H Borylation and Hydroboration Using Pinacolborane. *ACS Catal.* **2019**, 9, 5760−5771.

(41) Harinath, A.; Bhattcharjee, J.; Gorantla, K. R.; Mallik, B. S.; Panda, T. K. Hydroboration, Cyanosilylation, and Sequential Cyanosilylation and Hydroboration of

Carbonyl Compounds in the Presence of a Ti^{IV} Amido Complex as an Efficient Catalyst. *Eur. J. Org. Chem.* **2018**, *24*, 3180–3192.

(42) Ataie, S.; Hogeterp, S.; Ovens, S. O.; Baker, R. T. SNS Ligand-assisted Catalyst Activation in Zn-catalysed Carbonyl Hydroboration. *Chem. Commun.* **2022**, *58*, 3795-3798.

(43) Ataie, S.; Ovens, J. S.; Baker, R. T. A Solvent-Free Zinc (NSNO) Complex-catalysed Dihydroboration of Nitriles. *Chem. Commun.* **2022**, *58*, 8266-8269.

(44) Nakamura, G.; Nakajima, Y.; Matsumoto, K.; Srinivas, V.; Shimada, S. Nitrile Hydroboration Reactions Catalysed by Simple Nickel Salts, Bis(acetylacetonato)nickel(II) and its Derivatives. *Catal. Sci. Technol.* **2017**, *7*, 3196–3199.

(45) Chatterjee, S. K.; Roy, S.; Barman, S. K.; Maji, R. C.; Olmstead, M. M.; Patra, A. K. Shuttling of Nickel Oxidation States in N_4S_2 Coordination Geometry versus Donor Strength of Tridentate N_2S Donor Ligands. *Inorg. Chem.* **2012**, *51*, 7625−7635.

(46) Chen, Z.; Wu, J.; Chen, Y.; Li, L.; Xia, Y.; Li, Y.; Liu, W.; Lei, T.; Yang, L.; Gao, D.; Li, W. Rapid Access to Substituted Piperazines via $Ti(NMe_2)_4$-mediated C−C Bond-Making Reactions. *Organometallics* **2012**, *31*, 6005−6013.

(47) Figueira, C. A.; Lopes, P. S.; Gomes, C. S. B.; Gomes, J. C. S.; Lemos, F.; Gomes, P. T. New Phenyl–nickel Complexes of Bulky 2-Iminopyrrolyl Chelates: Synthesis, Characterization and Application as Aluminium-free Catalysts for the Production of Hyperbranched Polyethylene. *Dalton Trans.* **2018**, *47*, 15857–15872.

(48) Wang, X.; Xu, X. Hydroboration of Nitriles and Imines by Highly Active Zinc Dihydride Catalysts. *RSC Adv.* **2021**, *11*, 1128–1133.

(49) Sarkar, N.; Bera, S.; Nembenna, S. Aluminum-Catalyzed Selective Hydroboration of Nitriles and Alkynes: A Multifunctional Catalyst. *J. Org. Chem.* **2020**, *85*, 4999–5009.

(50) Elsby, M. R.; Oh, C.; Son, M.; Kim, S. Y. H.; Baik, M.–H.; Baker, R. T. Spin-state Crossover in Photo-catalyzed Nitrile Dihydroboration via Mn-thiolate Cooperation. *Chem. Sci.* **2022**, 13, 12550-12559.

(51) Stern, C.; Franceschi, F.; Solari, E.; Floriani, C.; Re, N.; Scopelliti, R. The Use of Macrocyclic and Polydentate Ligands in Ruthenium Organometallic Chemistry. *J. Organomet. Chem.* **2000**, *593–594*, 86–95.

(52) Liao, Y.; Novoa, J. J.; Arif, A.; Miller, J. S. Synthesis and Structure of an Asymmetric Copper(I) Dimer with Two-coordinate and Four-coordinate Copper(I) Sites. *Chem. Commun.* **2002**, 3008–3009.

(53) Li, R.; Moubaraki, B.; Murray, K. S.; Brooker, S. Monomeric and Dimeric Copper(II) Complexes of a Pyrrole-containing Tridentate Schiff-Base Ligand. *Eur. J. Inorg. Chem.* **2009**, *19*, 2851–2859.

(54) Liu, W.; Ding, Y.; Jin, D.; Shen, Q.; Yan, B.; Ma, X.; Yang, Z. Organic Aluminum Hydrides Catalyze Nitrile Hydroboration. *Green Chem.* **2019**, *21*, 3812–3815.

(55) Stahl, T.; Müther, K.; Ohki, Y.; Tatsumi, K.; Oestreich, M. Catalytic Generation of Borenium Ions by Cooperative B–H Bond Activation: The Elusive Direct Electrophilic Borylation of Nitrogen Heterocycles with Pinacolborane *J. Am. Chem. Soc.* **2013**, *135*, 10978– 10981.

(56) Cox, J. D.; Pilcher, G. *Thermochemistry of Organic and Organometallic Compounds*, Academic Press: London, 1970.

(57) Wang, D.; Angelici, R. J. Metal–Hydrogen Bond Dissociation Enthalpies in Series of Complexes of Eight Different Transition Metals. *J. Am. Chem. Soc.* **1996**, *118*, 5, 935–942.

(58) APEX Software Suite v 2010 Bruker AXS Inc. Madison Wisconsin USA, **2010**.

(59) Blessing, R. H. An Empirical Correction for Absorption Anisotropy**,** *Acta Crystallogr.* **1995**, *A51*, 33–38.

(60) Sheldrick, G. M. A Short History of SHELX, *Acta Crystallogr.* **2008**, *A64*, 112–122.

(61) Hübschle, C. B.; Sheldrick, G. M.; Dittrich, B. *ShelXle*: a Qt Graphical User Interface for *SHELXL. J. Appl. Crystallogr.* **2011**, *44*, 1281–1284.

CHAPTER 5

CONCLUSIONS AND FUTURE WORK

5.1 Connecting the Chapters: Key Findings and Contributions to the State of the Art

Metal-ligand cooperation is a reaction strategy that serves as a powerful tool to activate different substrates and has earned increasing interest over the last decade for its efficacy in promoting catalytic activity of economical, earth-abundant transition and main group metal complexes. In Chapter 1, the most common type of MLC is summarized, in which the X-ligand functions as a Lewis base and the metal center as a Lewis acid. Key examples of different Lewis base donor ligands were highlighted. More importantly, the mechanistic details were featured, showing that MLC can also occur in the catalyst *activation* step. Overall, we confirmed the need for deeper and more thoughtful mechanistic investigations in MLC. More interesting within the context of this dissertation was ligand design leading to MLC in the catalytic cycle.

The Baker group had previously studied the bifunctional behavior of two [SNS] pincer ligands with **L1** featuring an amido donor and **L2** a thiolate donor. In a first comparison of their performance as catalysts for carbonyl reduction, the Cu NHC thiolate complex was effective for hydroboration but not hydrosilylation, whereas the analogous amido complex catalyzed both reactions efficiently. Mechanistic studies demonstrated formation of a Cu-H, leading to the assertion of an outer-sphere mechanism in which the substrate would not need to insert into the sterically hindered Cu-H. In Chapter 2, we sought to compare the bifunctional reactivity of these two ligands with the 'redox-innocent' metal zinc. In this case, we were even able to prepare a complex with the metal bound to both amido and thiolate ligands. While all three complexes [**2.1**$_{\mathbf{Zn}}$, **2.2**$_{\mathbf{Zn}}$ and **2.4**$_{\mathbf{Zn}}$] were active carbonyl hydroboration catalysts, catalyst speciation studies showed that the amido ligand undergoes borylation-dissociation to generate the active Zn–H catalyst. While borylation of the thiolate ligand proceeded through a more complicated pathway (including an uncommon aldehyde deoxygenation), the same Zn-H active catalyst was formed, demonstrating that the ligand N- and S-donors served to *activate* the catalyst rather than participating in a bifunctional catalytic cycle.

Dissociation of the borylamido SNS ligand in Chapter 2 led us to reinvestigate the original Cu report. Indeed, we showed that this complex also undergoes ligand borylation-dissociation to

form the active catalyst, $[CuH(IPr)]_2$. **2.6$_{Cu}$** was also compared to its heavier Group 10 analogue Ag(κ^2-SNS)(IPr) (**2.7$_{Ag}$**). Interestingly, the latter complex was unable to serve as a carbonyl hydroboration catalyst.

In our next project, this MLC catalyst activation strategy was employed to prepare an especially active Zn hydride hydroboration catalyst. Using a bidentate amine-pyrollide ligand with an aryl ether side-group, a 5-coordinate Zn complex, Zn(κ^2-ONN)$_2$(DDI) (**2.12$_{Zn}$**) was prepared and used in hydroboration reactions. On treatment with excess HBpin, formation of ONN(Bpin)$_2$ gave rise to the reactive NHC-stabilized ZnH_2 catalyst that effected the rapid hydroboration of nitriles and quinoline derivatives under ambient conditions with only 0.01 and 0.05 mol% catalyst loading respectively. In our kinetic study of quinoline hydroboration, the VTNA method showed that this catalytic system does not face either catalyst deactivation or product inhibition.

The value of these contributions is derived from our detailed catalyst speciation, and how following the mechanism of the reaction gives deeper insight that then assists with the design of more efficient bifunctional ligands for more active and stable catalysts. *In situ*-generated ZnH_2(DDI) is one of the most active catalysts yet reported for carbonylation of polar bonds. The reduced steric footprint vs. conventional NHCs such as IPr presumably contributes to this catalyst's activity and the backbone chlorines likely contribute to enhanced catalyst stability.[1] However, the latter also reduce the NHC's donor power, so it would be interesting to see if the tetramethyl-substituted NHC ligand[2] affords an even more active catalyst, i.e. if activity is positively correlated with Zn-H hydricity.[3]

Early investigations indicated that mono- or bidentate Lewis base donors (especially amidos), despite being very reactive bifunctional ligands, can easily dissociate from first row metal centers upon borylation.[4] However, strongly chelating multidentate coordination can keep the borylated ligand connected.[5,6] In addition, previous reports by the Baker group showed the amido ligand (κ^3-**L1**), can tolerate an HBpin[7] or a proton[8] on the ligand N atom and retain its connectivity to the metal center. Therefore, to study the reactivity of the amido (**L1**) and thiolate (**L2**) ligands in their κ^3 form, we attempted in Chapter 3 to prepare a cobalt complex containing both amido and thiolate SNS ligands. Instead, the high basicity of the **L1** ligand led to demethylation of the **L2** ligand's thioether group, affording the Co(II) dithiolate complex, Co(κ^3-SNS)(DDI) (**3.2$_{Co}$**). This complex proved to be a selective catalyst for aldehyde hydroboration, over other functional groups such as ketones, nitriles and olefins. Our VTNA kinetic study showed that **3.2$_{Co}$** suffers from

product inhibition in the presence of aromatic (but not aliphatic) aldehydes. DFT studies not only supported these finding, but also showed that **3.2$_{Co}$** assembles the HBpin and aldehyde substrates through a bifunctional inner-sphere hydride transfer mechanism. As observed previously[9], this metal-thiolate catalytic system prefers a metal-hydride-free mechanism in hydroboration reactions.

To expand our MLC investigation to include additional donors beyond N and S, more catalytic systems needed to be investigated. In chapter 4 a dimeric Zn^{II}-[κ^4-NSNO] complex (**4.1$_{Zn}$**) was prepared in order to compare aryloxide and amido donors for B–H bond activation. **4.1$_{Zn}$** successfully catalyzed the dihydroboration of a range of aromatic and aliphatic nitriles. Mechanistic studies determined that the aryloxide donor activates the B–H bond in the first step and the mechanism then likely proceeds through an inner-sphere substrate insertion into Zn-H. As detected by our kinetic studies, at high turnovers the catalyst decomposes when Bpin also binds to the amido donor. These findings clearly highlight the necessity of a strongly chelating ligand when both amido and aryloxide donors can be borylated.

Next, a Ni-based catalytic system, $Ni^{II}X(\kappa^3$-NNN), was designed in which a series of monodentate X donors (bromide, phenoxide, thiophenoxide, 2,5-dimethylpyrrolylide, diphenylphosphide, and phenyl) was employed for a more comprehensive comparison. The Ni center was well supported by a tridentate ($N_{pyridine}N_{imine}N_{pyrollide}$) ligand. Among these complexes, only the bromide, phenoxide, and 2,5-dimethylpyrollide derivatives generated an observable Ni-H and served as catalysts for nitrile dihydroboration. Moreover, superior activity of the phenoxide derivative (*vs.* thiophenoxide or phenyl) suggested that B–H bond activation occurs at the Ni–X (*vs.* ligand Ni-$N_{pyrrolide}$) bond. In addition, **4.4$_{Ni}$** proved to be more active than **4.6$_{Ni}$**, highlighting that the basicity of the donor is not the only important factor in B–H bond activation. Both B–X and M–H bond formation energies also need to be considered, cf., the weaker bond formed between boron and S (ca. 83 kcal/mol vs. 95 for B–N and 104 for B–O)[10] and between first row metals and H (ca. 20 kcal/mol vs. 30 for Ru–H).[11]

Overall, the above findings provided us with important details on MLC both for catalyst activation and in catalytic cycles involving polar CO and CN bonds. Although we did not pursue alkyne or diene substrates, none of our catalysts were effective for hydroboration of alkene substrates such as substituted styrenes. Our ligand design for Ni catalysts enabled B-H bond activation through MLC and stabilized the active catalytic species, although these catalysts did not compete with the *in situ*-generated DDI zinc dihydride catalyst in nitrile dihydroboration. In

general, ligands with additional Lewis base capabilities have only provided rare examples of C-H bond activation,[12] whereas those with Lewis acid properties are showing significant promise.[13]

5.2 Recent Advances and Future Directions

The use of first-row transition metals in MLC over the last decade has grown this strategy as an advanced catalytic tool for functionalization of various chemical units. The modes of metal-ligand cooperativity are diverse, and the chosen method greatly depends on the desired reactivity. As shown in Chapter 1, the use of Lewis base donors for cooperative bond activation across an M–E unit has been well studied and is now the most mature type of MLC. Through this mode of MLC, activation of different bonds has been facilitated, such as H–H bond activation in (de)hydrogenation chemistry, B–H bond activation in hydroboration**,** and Si–H bond activation in hydrosilylation. Activation of stronger C-H bonds, while synthetically very useful, is still underdeveloped, with precious metal carboxylates in concerted metalation-deprotonation being the most visible example.[12]

Although extension of MLC to first-row transition metals has advanced the latter's catalysis applications, MLC has not yet been deeply studied with main group metals.[13] Furthermore, new studies show that bimetallic chemical frameworks are potentially capable of metal-metal cooperation that results in activation of stable C–H bonds.

There have been several reports of C–H bond activation through MLC utilizing either carbene[14,15] or Lewis acidic borane donors[16], although instances of well-defined catalytic functionalization are still rare. Building on borane acceptors' successful C–H bond activation, some groups have been exploring alternate Lewis acidic bifunctional donors and significant achievements have been made. The Lu group recently demonstrated a C–H bond activation facilitated through metal–metal cooperation in bimetallic complexes. In 2021 Lu et al. reported a Ni^{0}–Al^{III} complex (**5.1**) that showed cooperative activity in ortho-directed oxidative addition of a pyridine N–oxide C-H bond.[17] This C–H bond activation presumably proceeded through the pre-coordination of the oxide donor to the oxophilic Al center (**Scheme 5.1**).

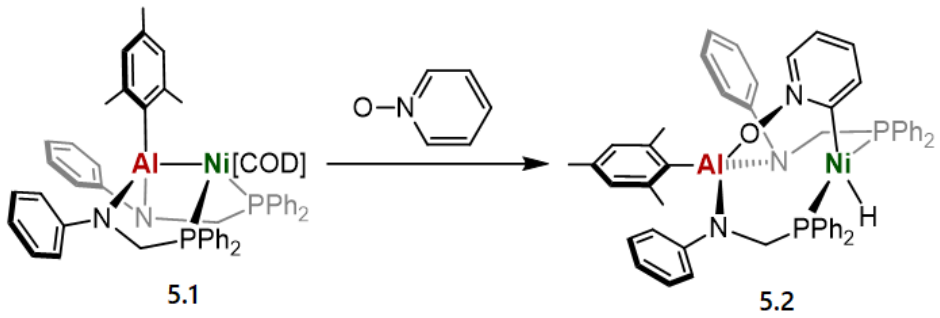

Scheme 5.1. *Ortho*-directed C–H activation of pyridine N–oxide by a cooperative Ni–Al.

The Nakao group also showed Al's donor potential for bifunctional C–H functionalization catalysis.[18] They reported the bimetallic Rh–Al complex **5.3** which catalyzed C–H silylation of pyridines at the C2 site (**Scheme 5.2**). The reaction needed 2.5 equiv. of silane reagent and also 3,3-dimethyl-1-butene as hydrogen acceptor which is common in most reported C–H silylations.[19]

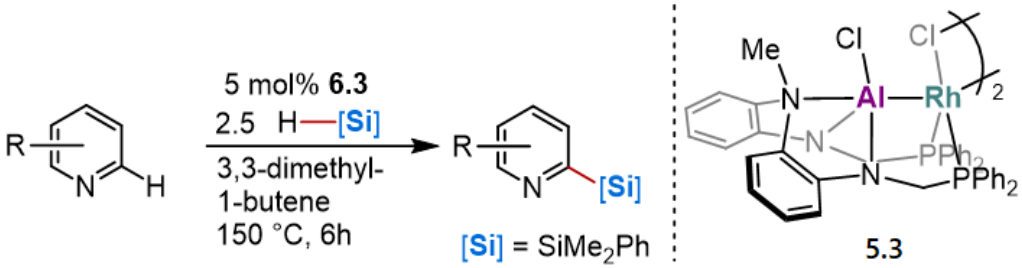

Scheme 5.2. *Ortho*-selective silylation of pyridines by a Rh–Al complex.

The selectivity for the C2 site shows the importance of the catalyst design. In the proposed reaction pathway (**Scheme 5.3**) **5.3** is initially reduced with dimethylphenylsilane and 3,3-dimethyl-1-butene to afford the active catalyst **5.4**. Then the pyridine substrate coordinates to the Al center giving **5.5**. Selective pyridine C(2)–H bond activation occurs at Rh to afford the rhodium hydride intermediate **5.6**. Subsequent alkene coordination and insertion into the Rh–H generates intermediate **5.7**. Another equiv. of silane proceeds the reaction to production of intermediate **5.8**, which affords the 2-silylpyridine product after final reductive elimination.

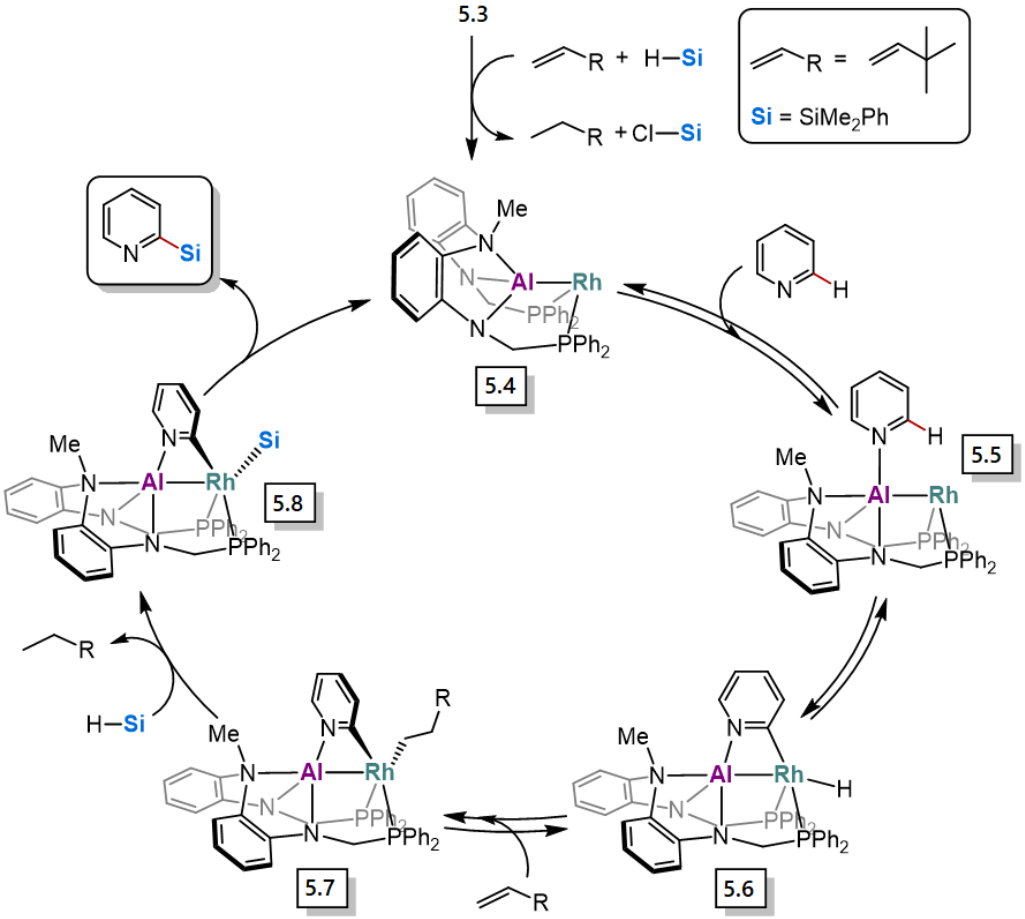

Scheme 5.3. Proposed reaction pathway for pyridine C(2)–H silylation by a Rh–Al complex.

Finally, in 2012, Lin and his co-workers demonstrated TM-aluminyl complexes can cooperatively facilitate activation of C–O bond across Au– and Cu–Al bonds (**Scheme 5.4**).[23]

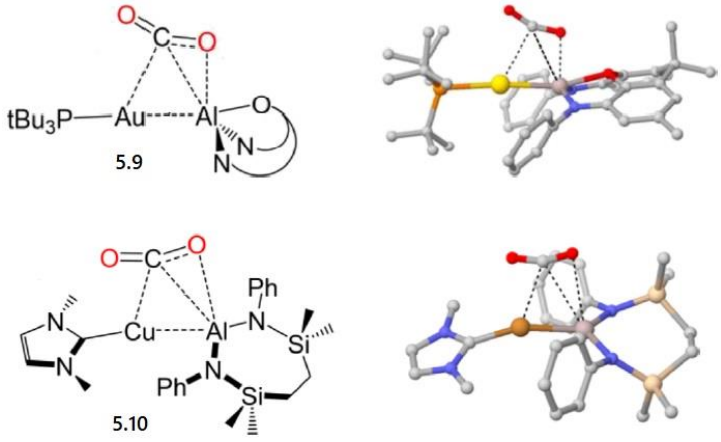

Scheme 5.4. Cooperative CO_2 activation across Au- and Cu-Al bond.

They also showed that the Cu-Al center potentially activates C=N bonds (**Scheme 5.5**).

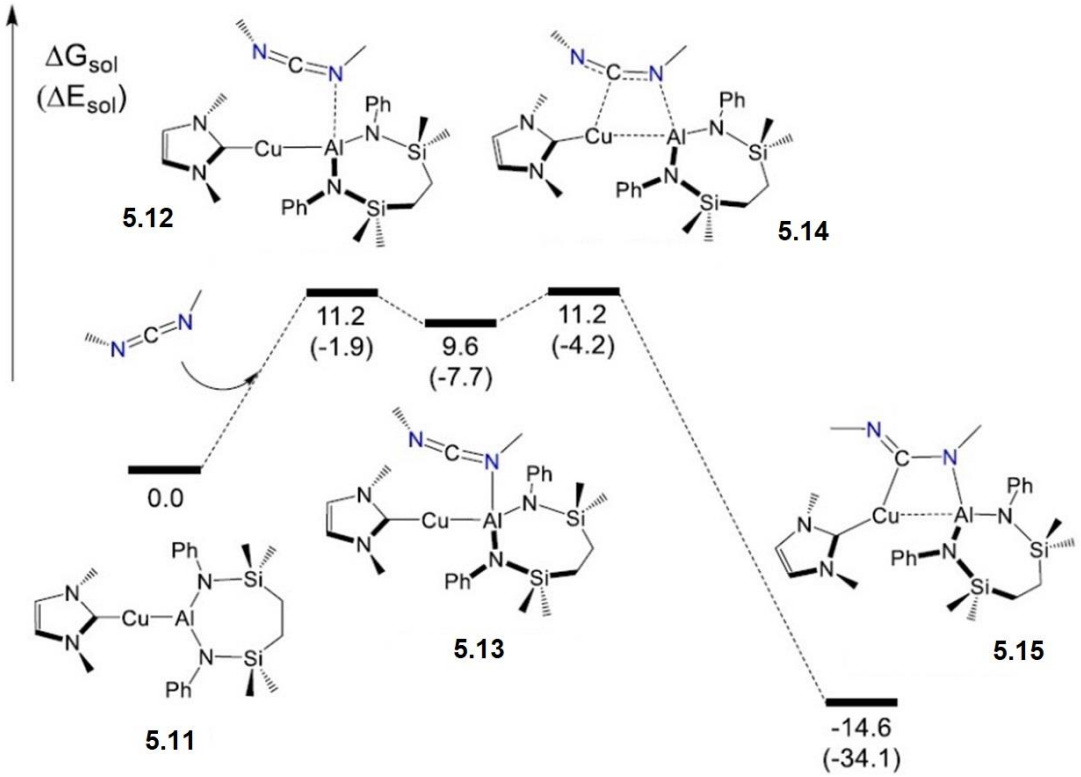

Scheme 5.5. Cooperative carbodiimide activation across Cu-Al bond.

Lin found that the reactivity of TM-Al centers with heteroallenes (including CO_2 and carbodiimides) derives from the nucleophilicity of the TM−Al σ-bond, which could be partly explainable according to the electropositive nature of the Al center that can enhance the nucleophilic role. In fact, by comparing the two classes of electropositive ligands, aluminyls and boryls,[21-23] we see that TM-B/Al nucleophilic nature may play an important role in their corresponding reactivity. These works clearly offer valuable insights that can lead to advanced design of TM-aluminyl complexes in the future and also their applications in small-molecule activations and chemical transformations.

5.3 References

(1) Froese, R. D. J.; Lombardi, C.; Pompeo, M.; Rucker, R. P.; Organ, M. G. *Acc. Chem. Res.* **2017**, *50*, 2244-2253.

(2) Arduengo, A. J., III; Dias, H. V. R.; Harlow, R. L.; Kline, M. Electronic Stabilization of Nucleophilic Carbenes. *J. Am. Chem. Soc.* **1992**, *114*, 5598-5609.

(3) Brereton, K. R.; Smith, N. E.; Hazari, N.; Miller, A. J. Thermodynamic and Kinetic Hydricity of Transition Metal Hydrides. *Chem Soc. Rev.* **2020**, *49*, 7929-7948.

(4) Baker, R. T.; Gordon, J. C.; Hamilton, C. W.; Henson, N. J.; Lin, P,-H.; Maguire, S.; Murugesu, M.; Scott, B. L.; Smythe, N. C. Iron Complex-Complex-Catalyzed Ammonia-Borane Dehydrogenation. A Potential Route Towards B-N Containing Polymer Motifs Using Earth Abundant Metal Catalysts. *J. Am. Chem. Soc.* **2012**, *134*, 5598-5609.

(5) Pang, M.; Wu, C.; Zhuang, X.; Zhang, F.; Su, M.; Tong, Q.; Tung, C.–H.; Wang, W. Addition of a B–H bond across an amido–cobalt bond: Co^{II}–H-catalyzed hydroboration of olefins. *Organometallics* **2018**, *37*, 1462-1467.

(6) Zhang, F.; Song, H.; Zhuang, X.; Tung, C.–H.; Wang, W. Iron-catalyzed 1,2-Selective Hydroboration of N–Heteroarenes. *J. Am. Chem. Soc.* **2017**, *139*, 17775-17778.

(7) Elsby, M. R.; Son, M.; Oh, C.; Martin, J.; Baik, M.–H.; Baker, R. T. Mechanistic Study of Metal–Ligand Cooperativity in Mn(II)-Catalyzed Hydroborations: Hemilabile SNS Ligand Enables Metal Hydride-Free Reaction Pathway. *ACS Catal.* **2021**, *11*, 9043–9051.

(8) Das, U. K.; Daifuku, S. L.; Iannuzzi, T. E.; Gorelsky, S. I.; Korobkov, I.; Gabidullin, B.; Neidig, M. L.; Baker, R. T. Iron(II) Complexes of a Hemilabile SNS Amido Ligand: Synthesis, Characterization, and Reactivity. *Inorg. Chem.* **2017**, *56*, 13766–13776.

(9) Elsby, M. R.; Oh, C.; Son, M.; Kim, S. Y. H.; Baik, M.–H.; Baker, R. T. Spin-state Crossover in Photo-catalyzed Nitrile Dihydroboration via Mn-thiolate Cooperation. *Chem. Sci.* **2022**, *13*, 12550-12559.

(10) Cox, J. D.; Pilcher, G. *Thermochemistry of Organic and Organometallic Compounds*, Academic Press: London, 1970.

(11) Wang, D.; Angelici, R. J. Metal–Hydrogen Bond Dissociation Enthalpies in Series of Complexes of Eight Different Transition Metals. *J. Am. Chem. Soc.* **1996**, *118*, 5, 935–942.

(12) Gorelsky, S. I.; Lapointe, D.; Fagnou, K. Analysis of the Concerted Metalation-Deprotonation Mechanism in Palladium-Catalyzed Direct Arylation Across a Broad Range of Aromatic Substrates**.** *J. Am. Chem. Soc.* **2008**, *130*, 33, 10848–10849.

(13) Greb, L.; Ebner, F.; Ginzburg, Y.; Sigmund, L. M. Element-Ligand Cooperativity with p-Block Elements. *Eur. J. Inorg. Chem.* **2020**, *32*, 3030.

(14) Comanescu, C. C.; Iluc, V. M. C–H Activation Reactions of a Nucleophilic Palladium Carbene. *Organometallics* **2015**, *34*, 4684–4692

(15) Tsang, J. Y. K.; Buschhaus, M. S. A.; Legzdins, P.; Patrick, B. O. Ortho-Selective C–H Activation of Substituted Benzenes Effected by a Tungsten Alkylidene Complex without Substituent Coordination. *Organometallics* **2006**, *25*, 4215–4225.

(16) Rudolf, G. C.; Hamilton, A.; Orpen, A. G.; Owen, G. R. A 'sting' on Grubbs' catalyst: an insight into hydride migration between boron and a transition metal. *Chem. Commun.* **2009**, 553–555.

(17) Graziano, B. J; Vollmer, M. V; Lu, C. C. Cooperative Bond Activation and Facile Intramolecular Aryl Transfer of Nickel-Aluminum Pincer-type Complexes. *Angew. Chem. Int. Ed.* **2021**, *60*, 15087-15094.

(18) Hara, N; Uemura, N; Nakao, Y. C2-Selective Silylation of Pyridines by a Rhodium-Aluminum Complex. *Chem. Commun.* **2021**, *57*, 5957-5960.

(19) Cheng, C; Hartwig, J. F. Catalytic Silylation of Unactivated C–H Bonds. *Chem Rev.* **2015**, *115*, 8946-8975.

(20) Guo, X.; Yang, T.; Zhang, Y.; Sheong, F. K.; Lin, Z. Reactivity of Unsupported Transition Metal-Aluminyl Complexes: A Nucleophilic TM-Al Bond. *Inorg. Chem.* **2022**, *61*, 10255−10262.

(21) Dang, L.; Lin, Z.; Marder, T. B. Boryl ligands and their roles in metal-catalysed borylation reactions. *Chem. Commun.* **2009**, *27*, 3987−3995.

(22) Guo, X.; Yang, T.; Sheong, F. K.; Lin, Z. Beyond the Nucleophilic Role of Metal−Boryl Complexes in Borylation Reactions. *ACS Catal*. **2021**, *11*, 5061−5068.

(23) Suzuki, A.; Guo, X.; Lin, Z.; Yamashita, M. Nucleophilic reactivity of the gold atom in a diarylborylgold(I) complex toward polar multiple bonds. *Chem. Sci*. **2021**, *12*, 917−928.

Appendices

Appendix A – Chapter 2

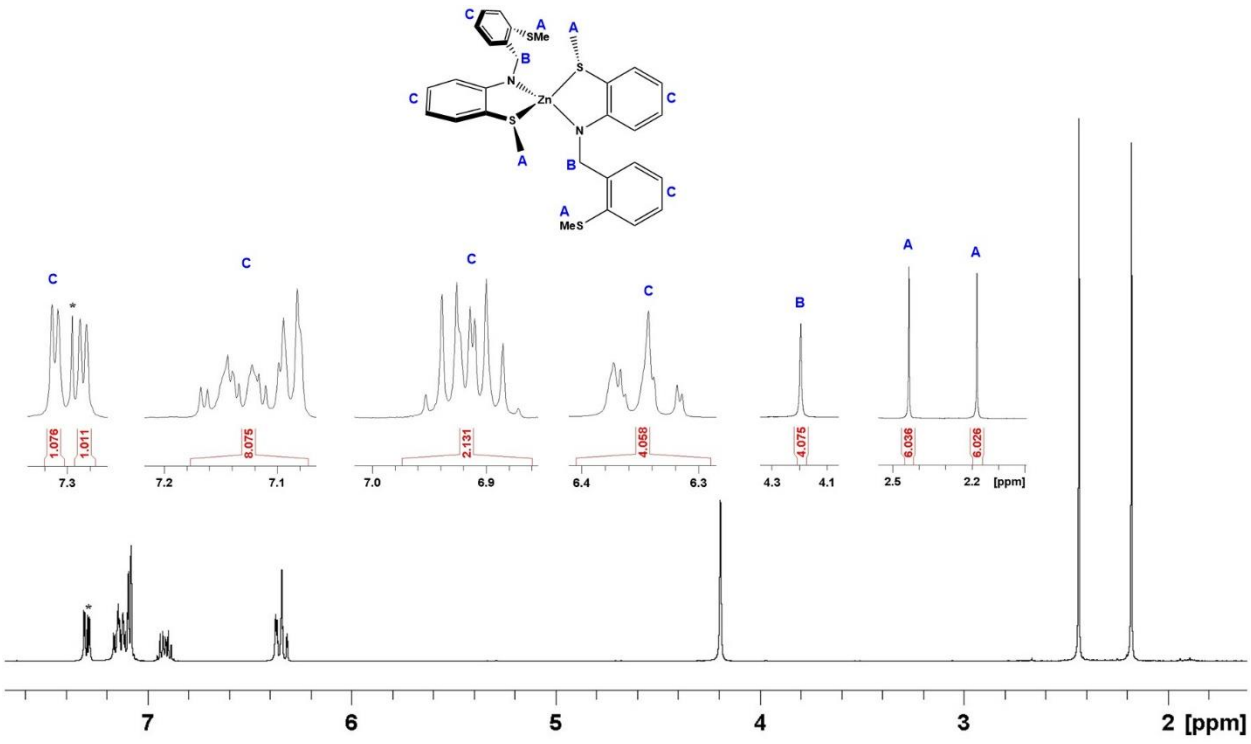

Figure A1. ^{1}H NMR spectrum of **2.1$_{Zn}$**. * indicates C_6D_6.

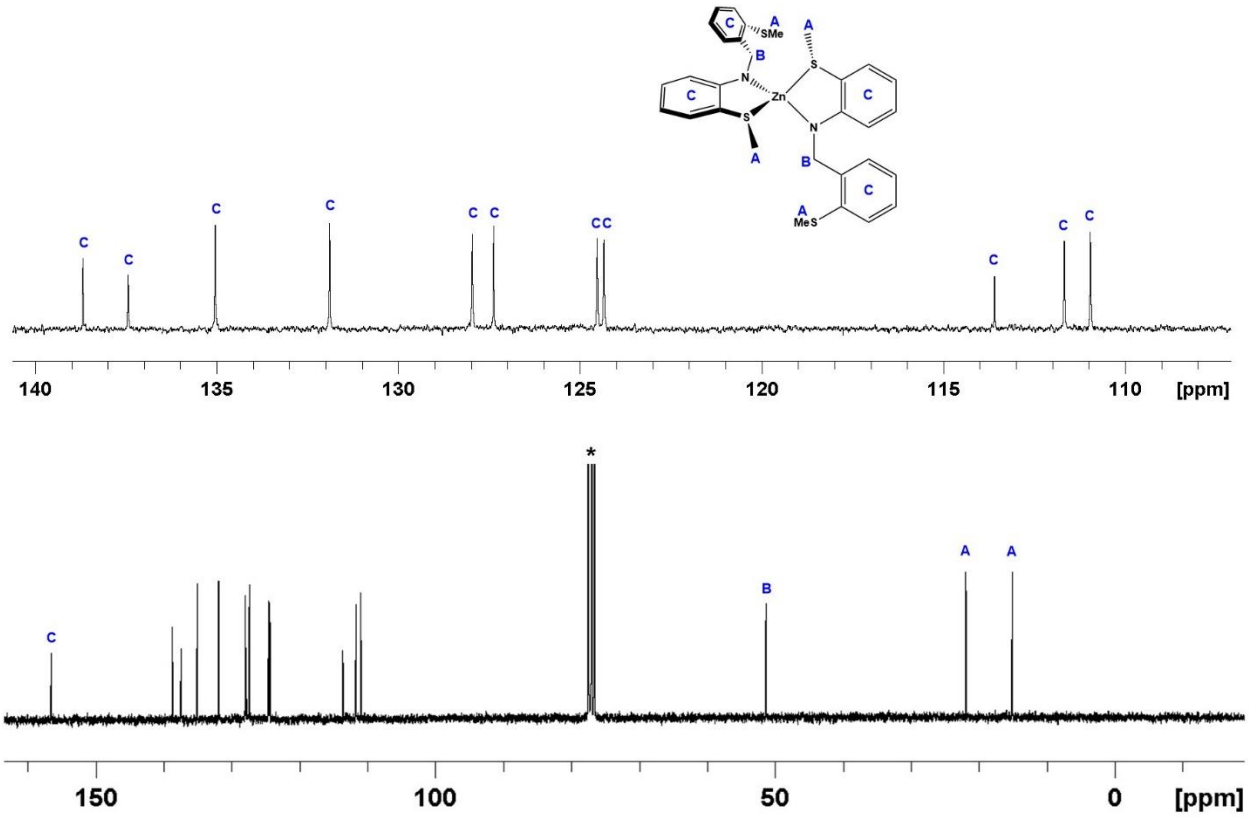

Figure A2. $^{13}C\{^{1}H\}$ NMR spectrum of **2.1$_{Zn}$**. * indicates C_6D_6.

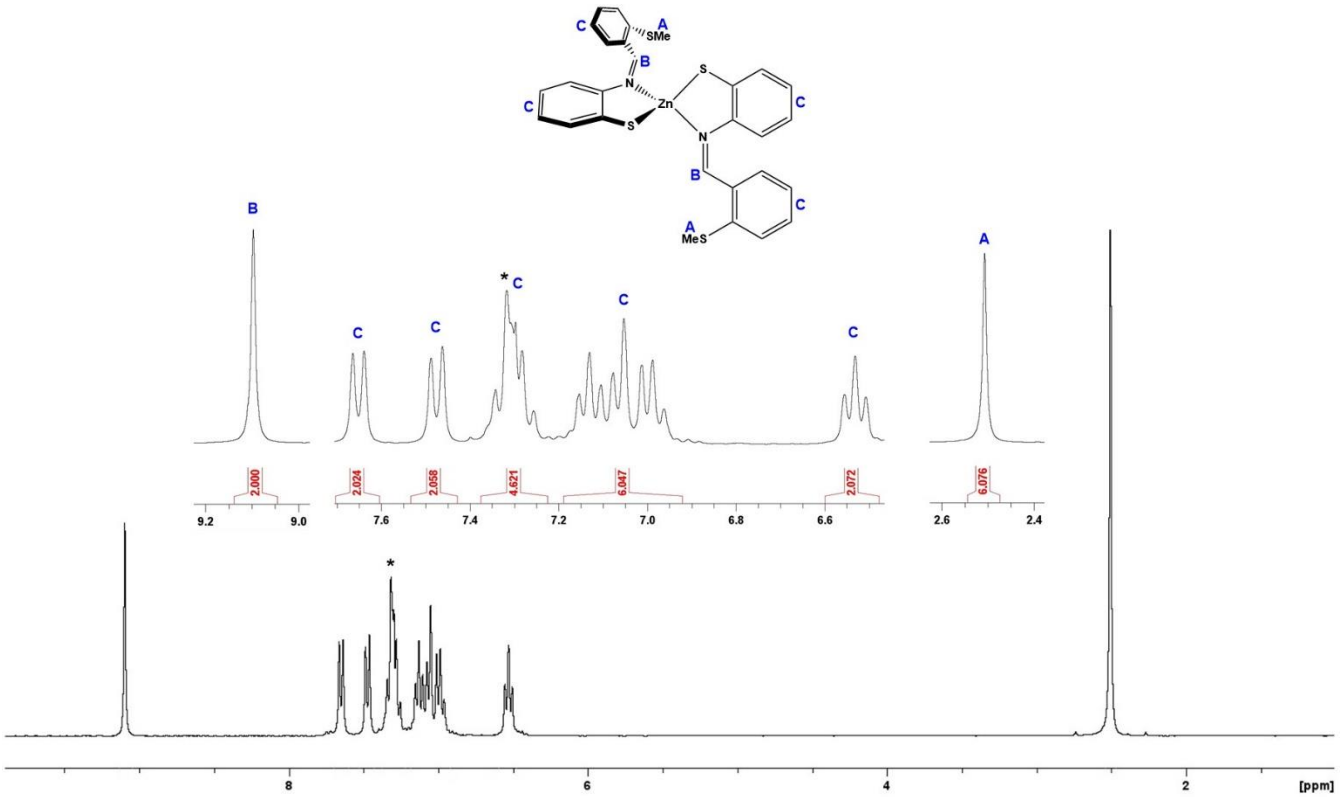

Figure A3. ^{1}H NMR spectrum of **2.2$_{Zn}$**. * indicates $CDCl_3$.

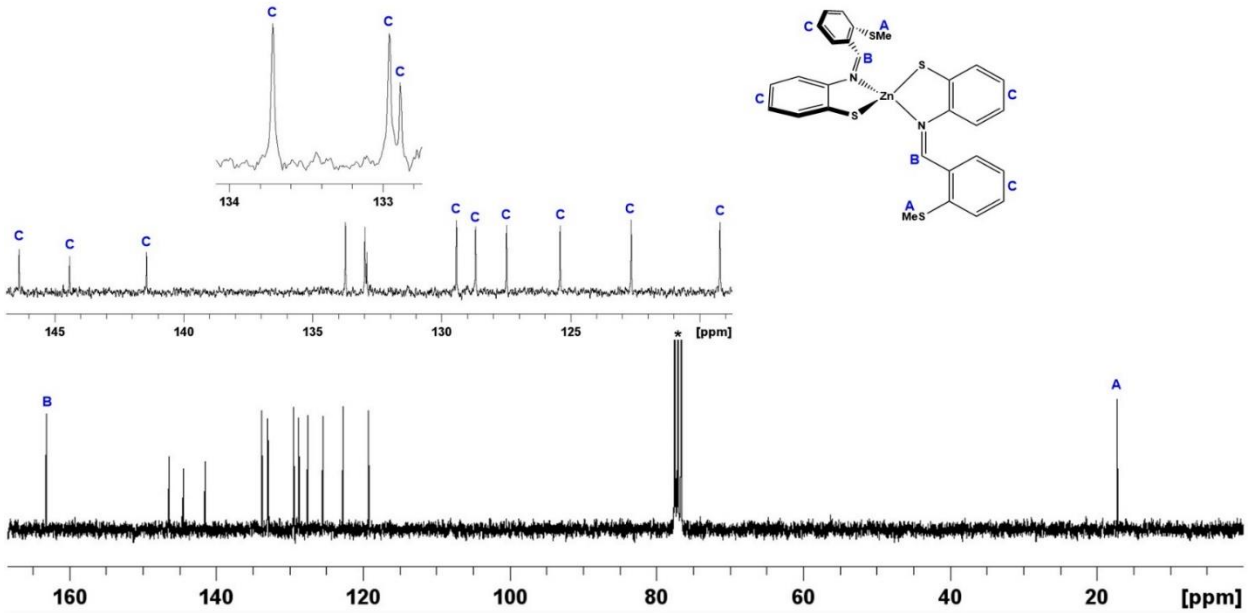

Figure A4. $^{13}C\{^{1}H\}$ NMR spectrum of **2.2$_{Zn}$**. * indicates $CDCl_3$.

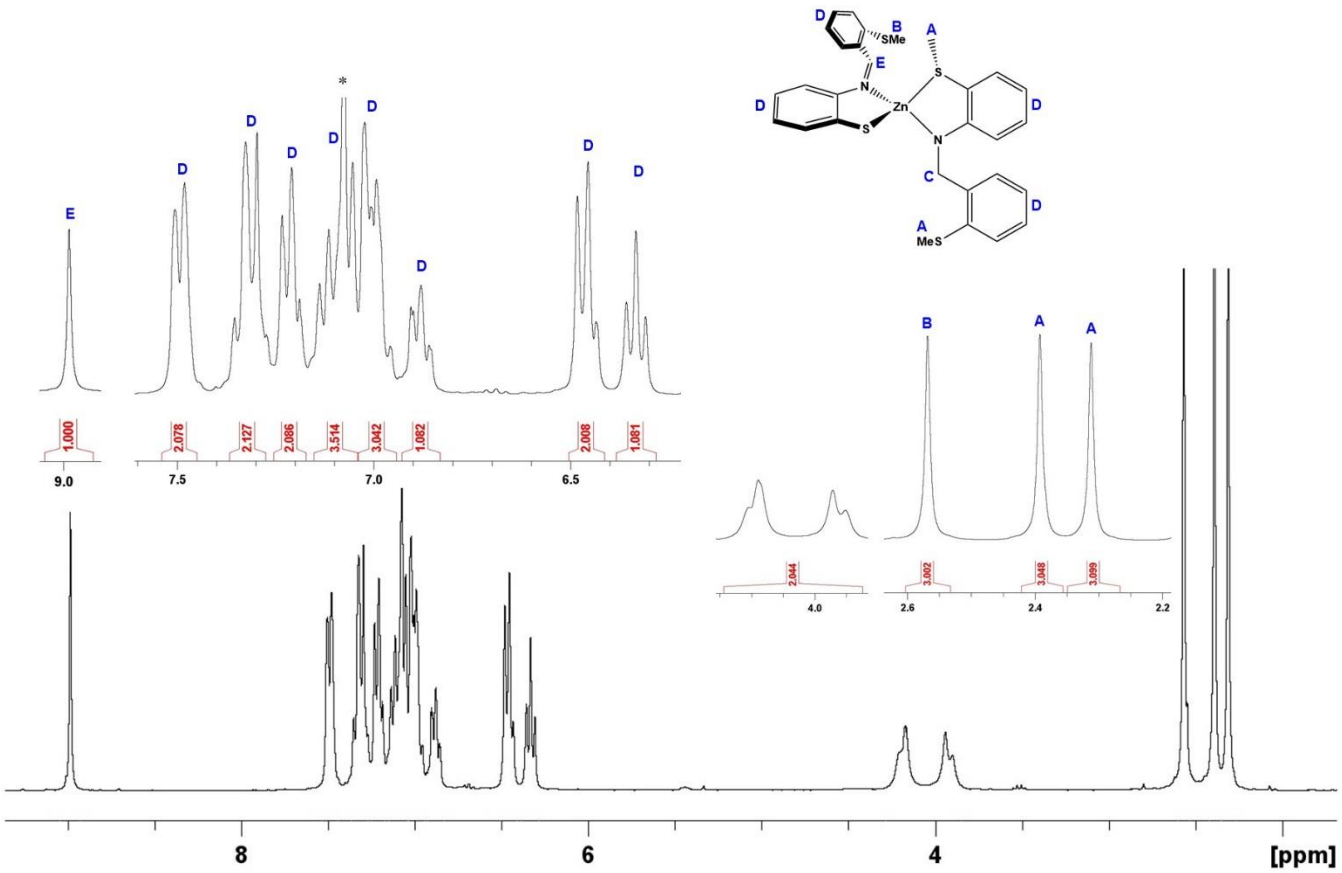

Figure A5. ^{1}H NMR spectrum of **2.4$_{Zn}$**. * indicates $CDCl_3$.

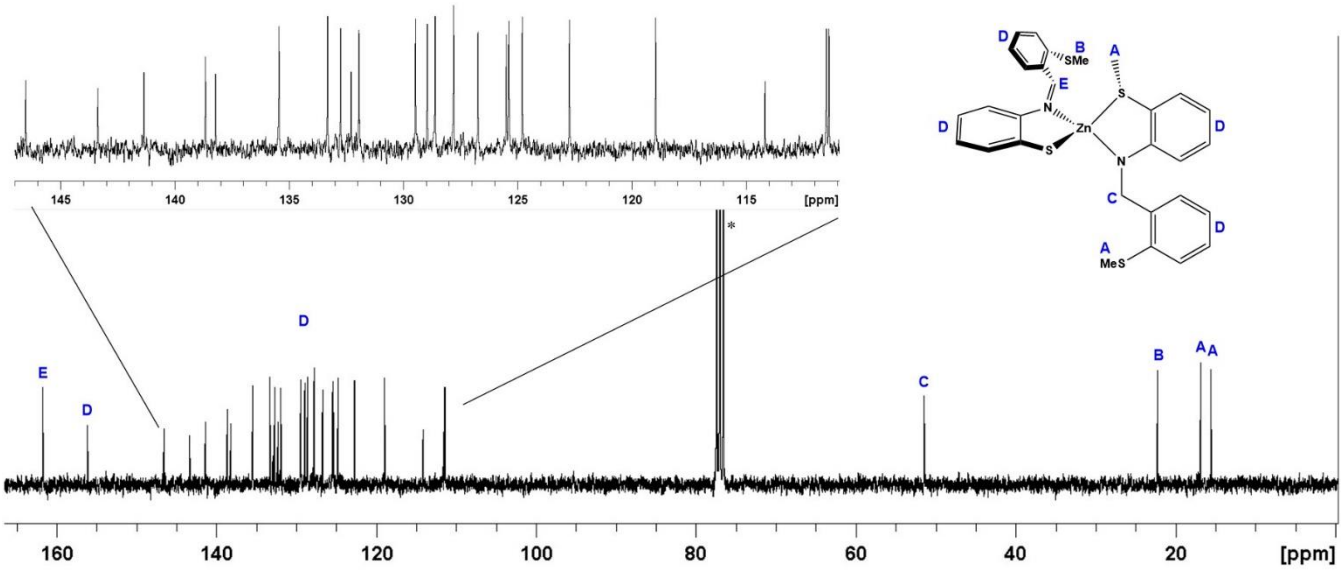

Figure A6. $^{13}C\{^{1}H\}$ NMR spectrum of **2.4$_{Zn}$**. * indicates $CDCl_3$.

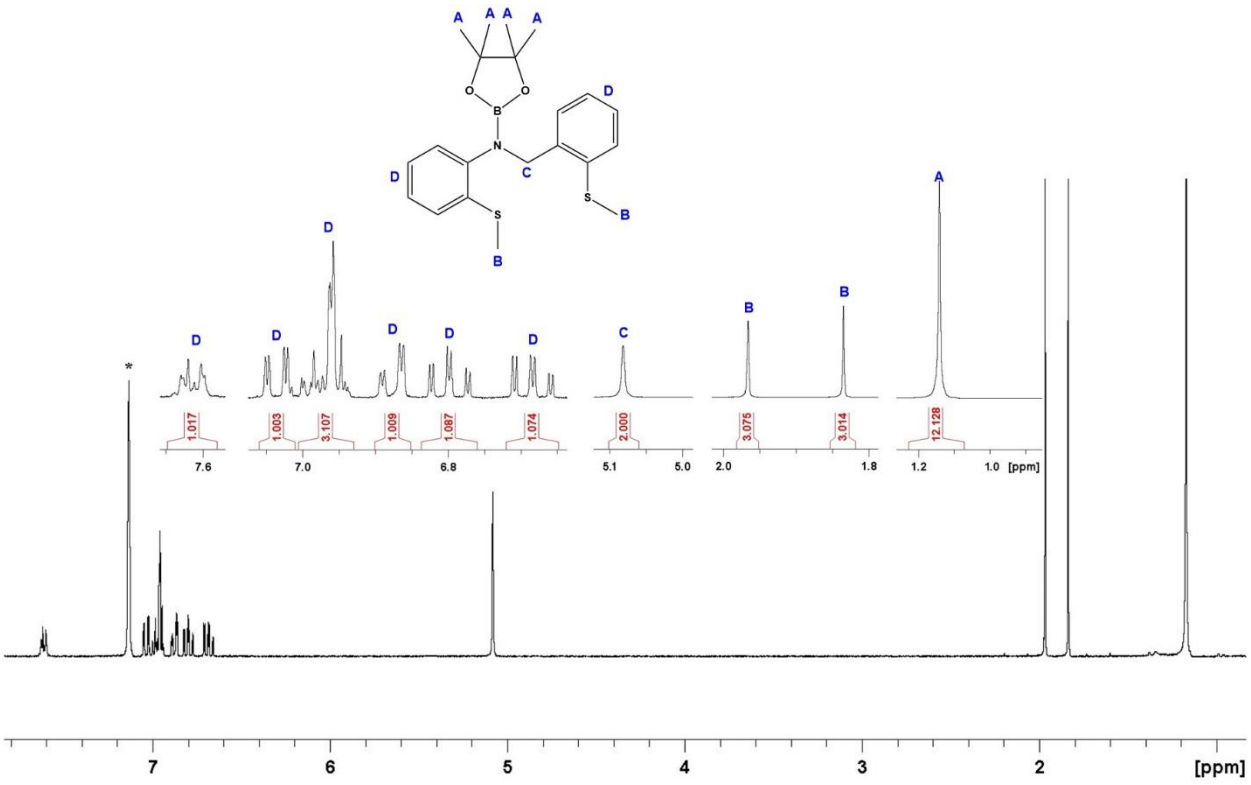

Figure A7. ^{1}H NMR spectrum of **Bpin-L1**. * indicates C_6D_6.

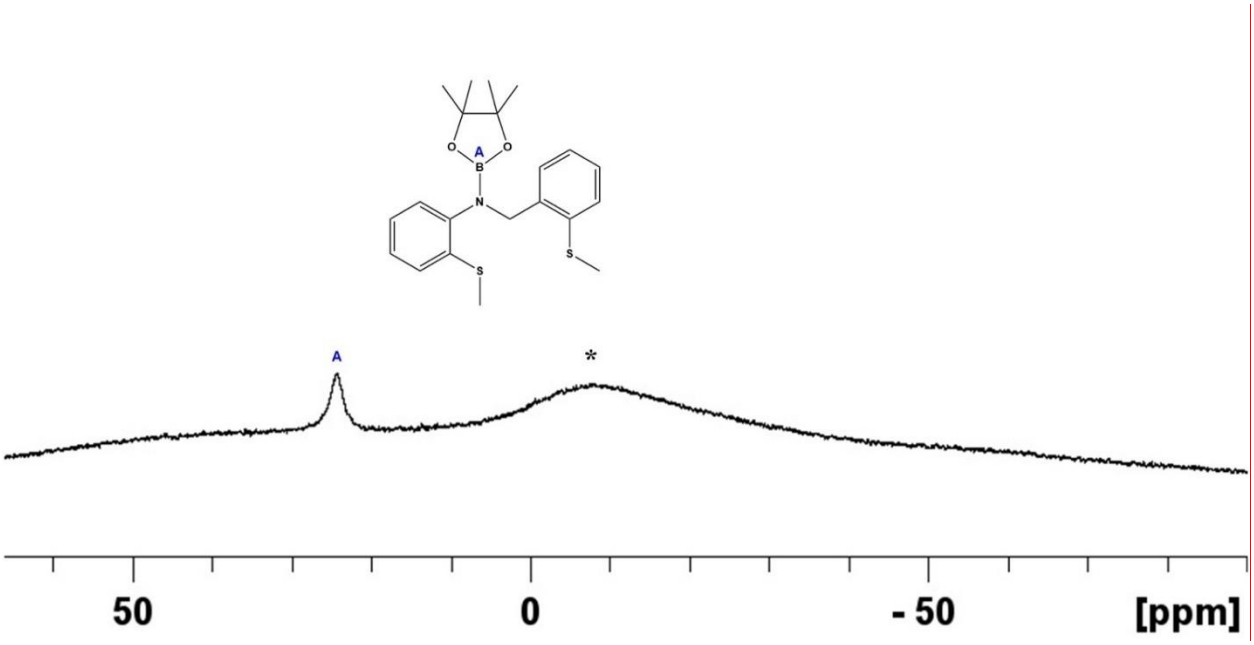

Figure A8. ^{11}B{^{1}H} NMR spectrum of **Bpin-L1**. * indicates boron in probe.

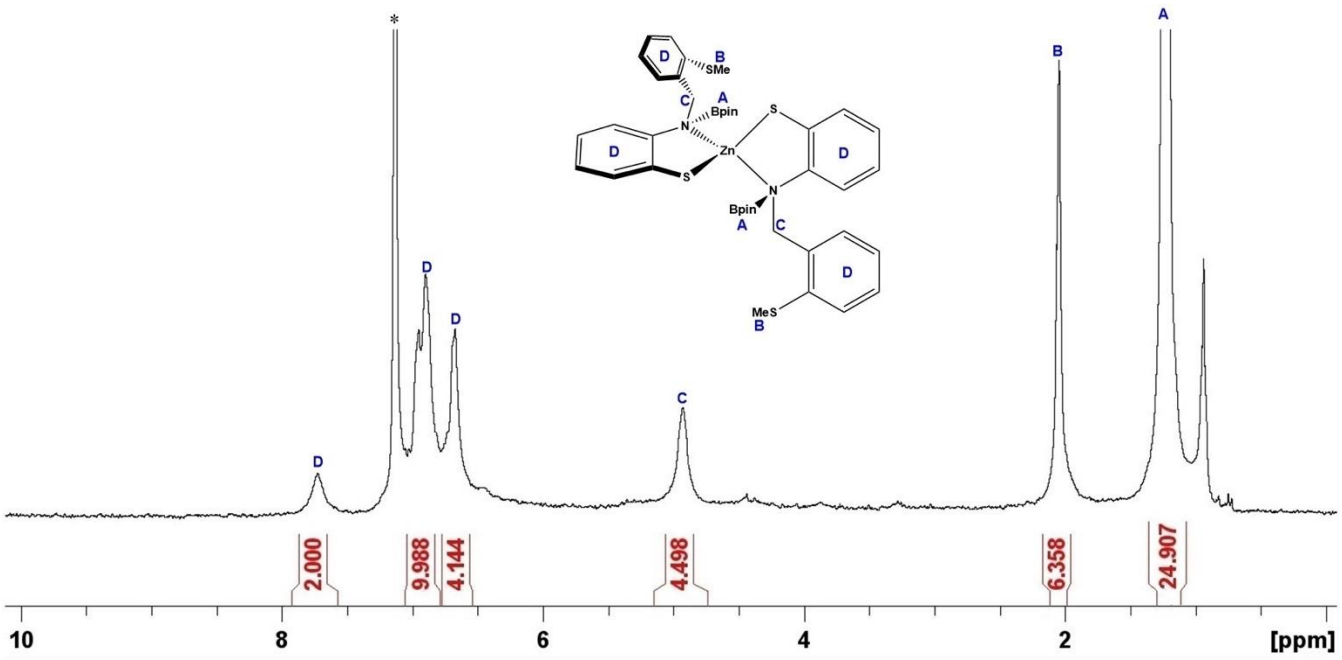

Figure A9. ^{1}H NMR spectrum of **2.3$_{Zn}$**. * indicates C_6D_6.

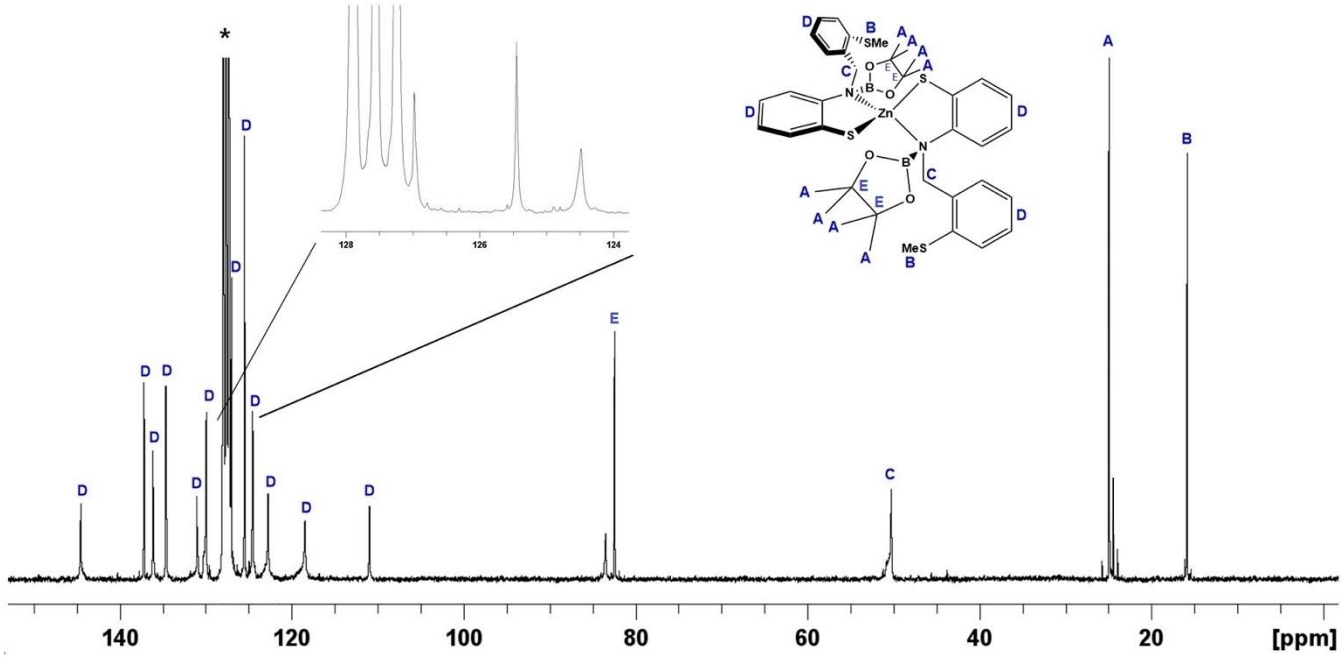

Figure A10. ^{13}C{^{1}H} NMR spectrum of **2.3$_{Zn}$**. * indicates C_6D_6.

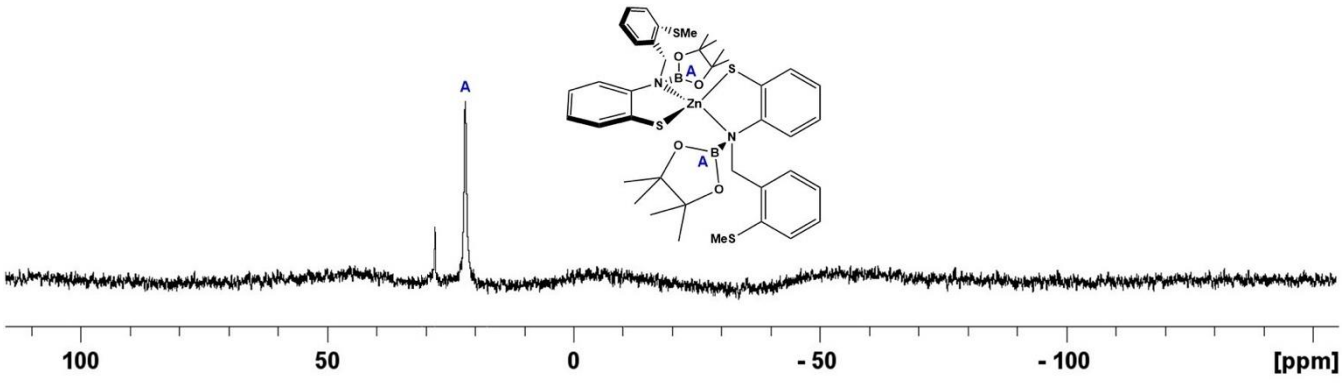

Figure A11. $^{11}B\{^{1}H\}$ NMR spectrum of **2.3$_{Zn}$**.

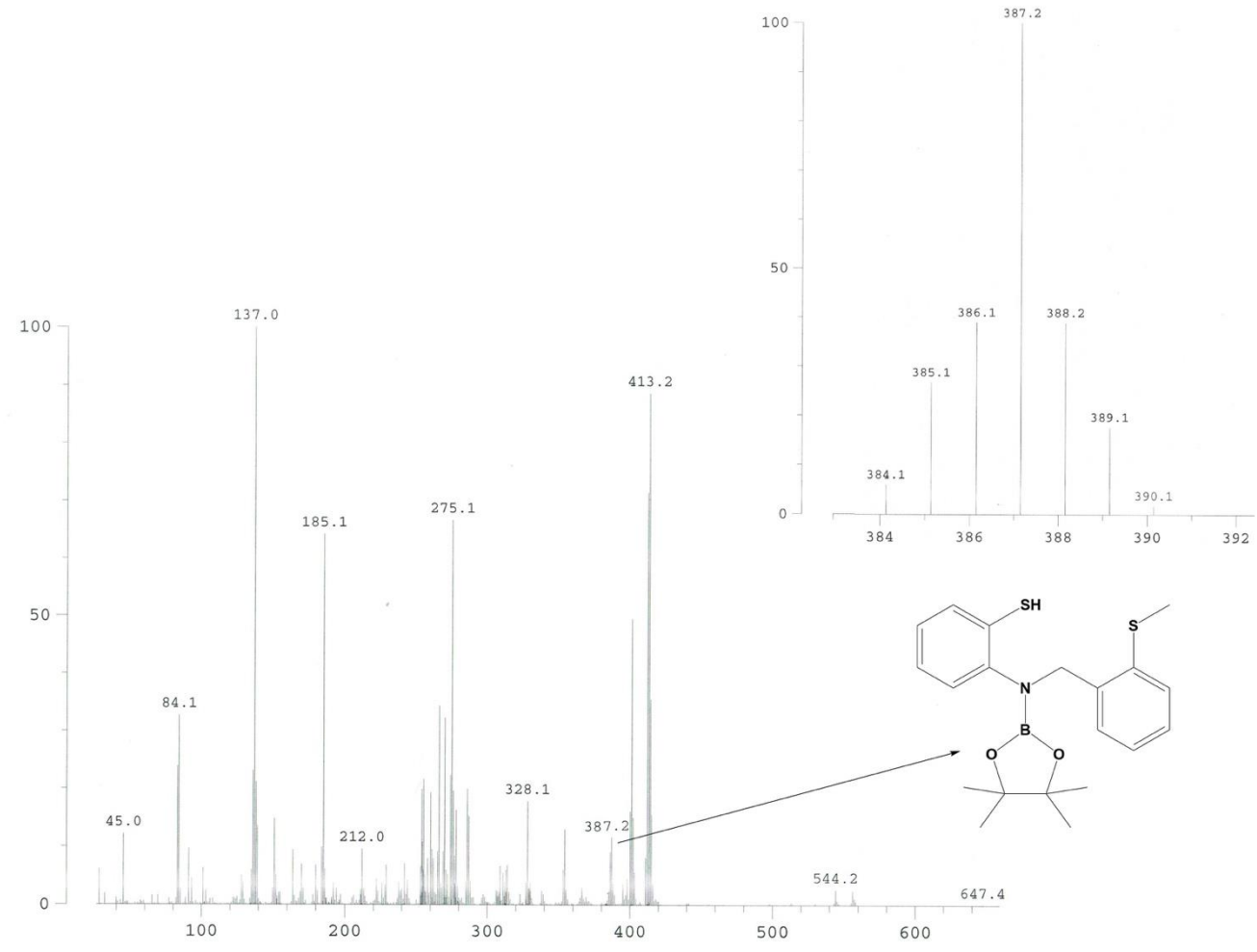

Figure A12. EI-MS spectrum of **2.3$_{Zn}$** showing [**Bpin-HL2**]$^{+}$

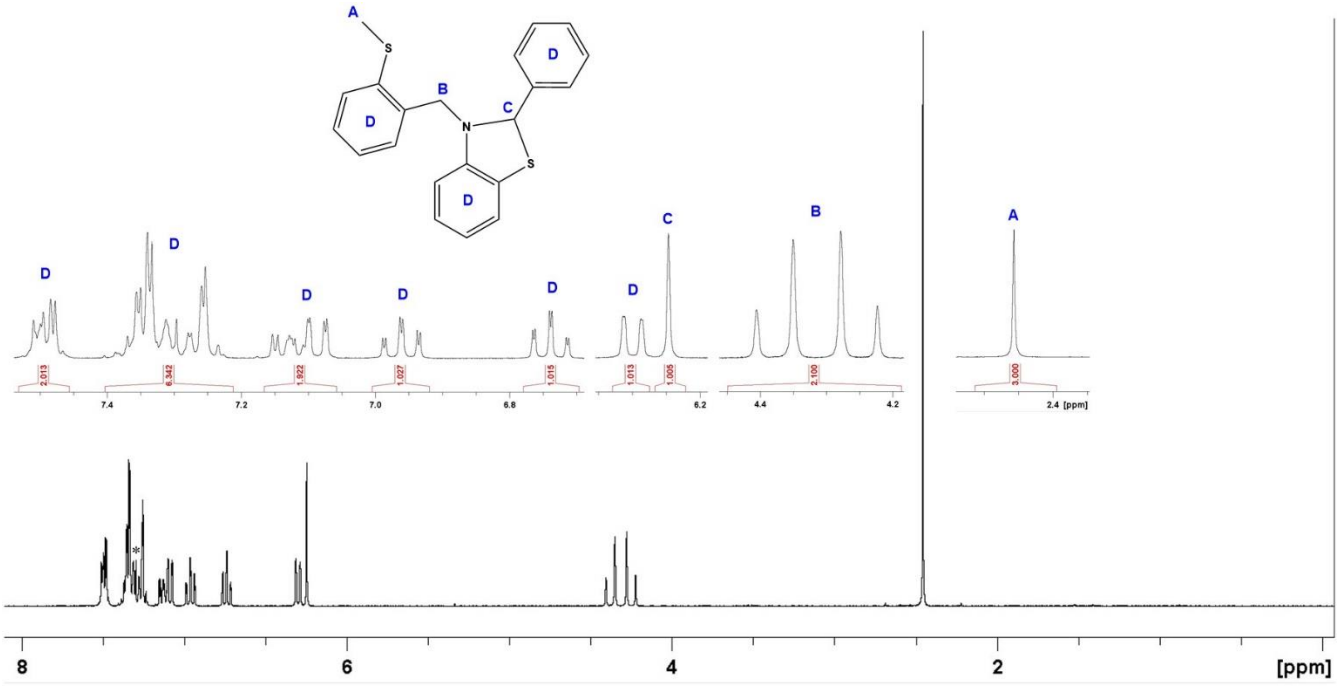

Figure A13. ^{1}H NMR spectrum of **S-P1**. * indicates $CDCl_3$.

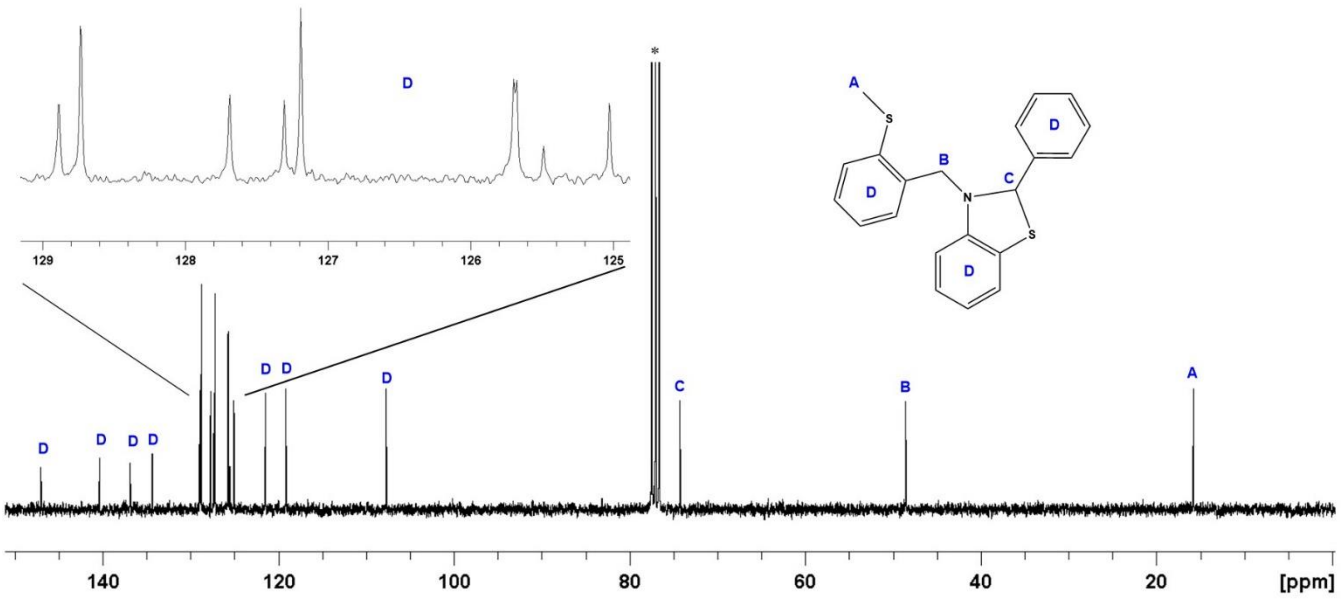

Figure A14. $^{13}C\{^{1}H\}$ NMR spectrum of **S-P1**. * indicates $CDCl_3$.

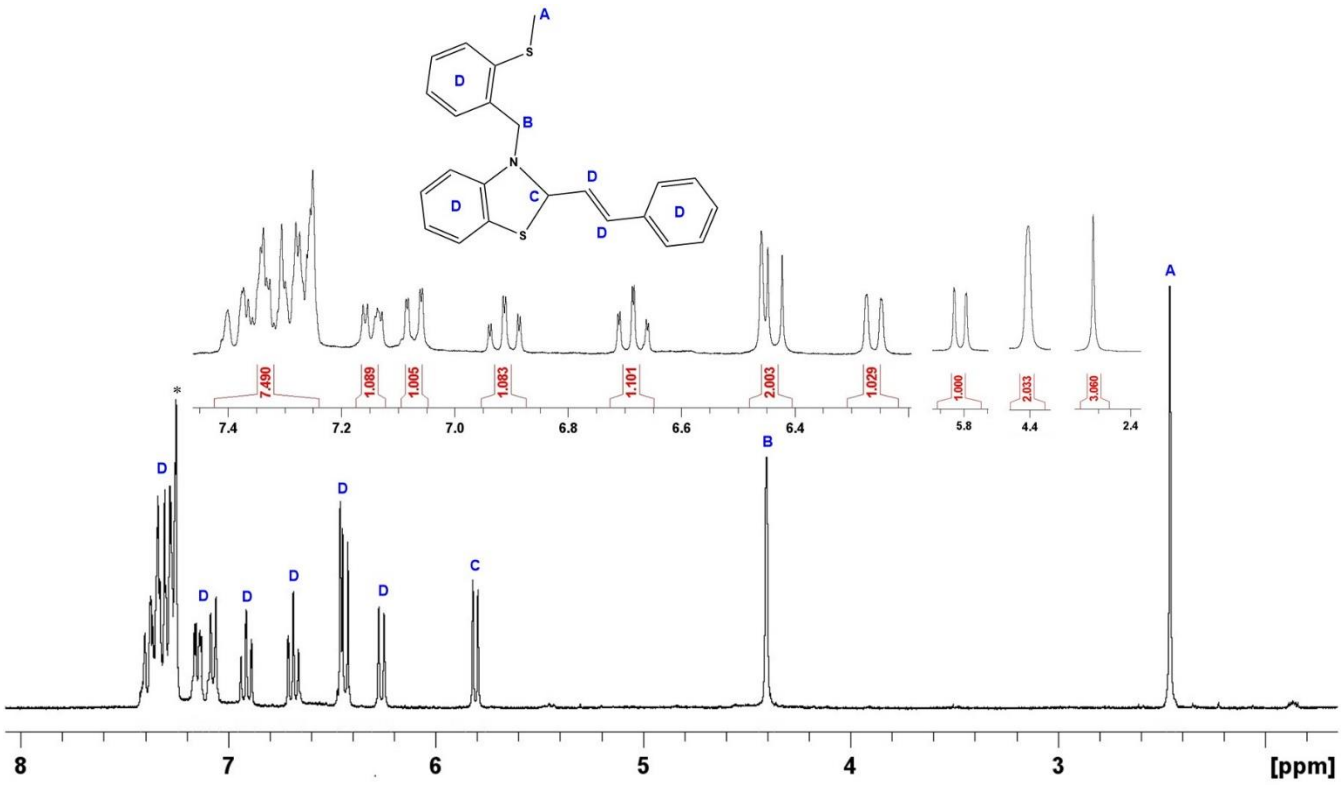

Figure A15. ^{1}H NMR spectrum of **S-P2**. * indicates $CDCl_3$.

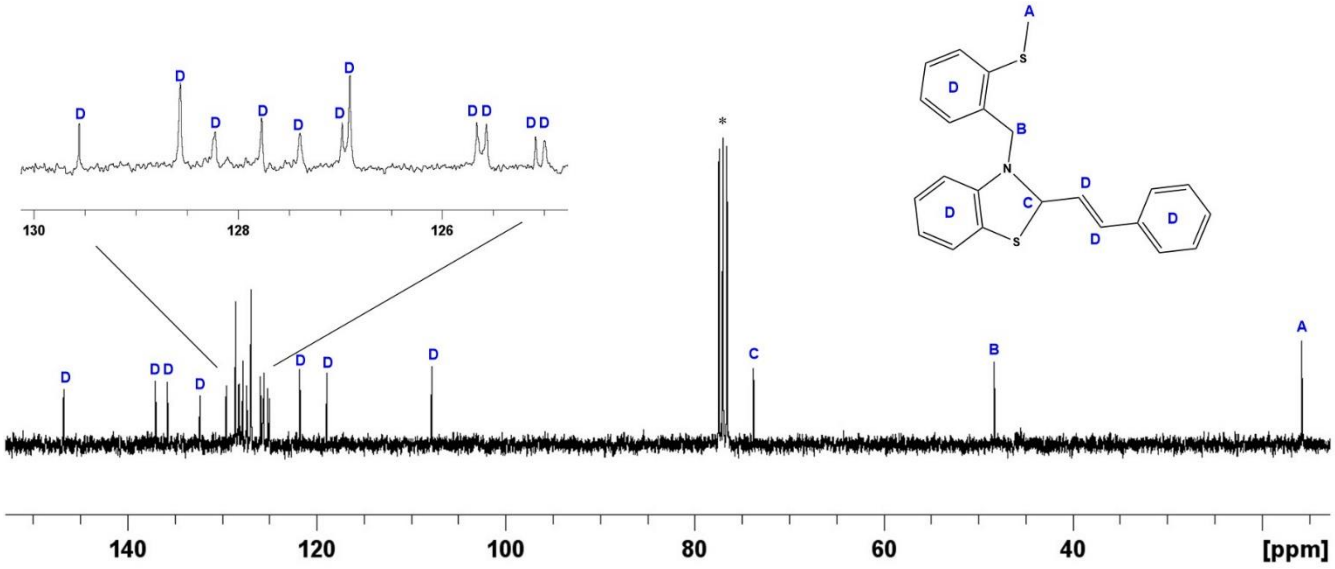

Figure A16. $^{13}C\{^{1}H\}$ NMR spectrum of **S-P2**. * indicates $CDCl_3$.

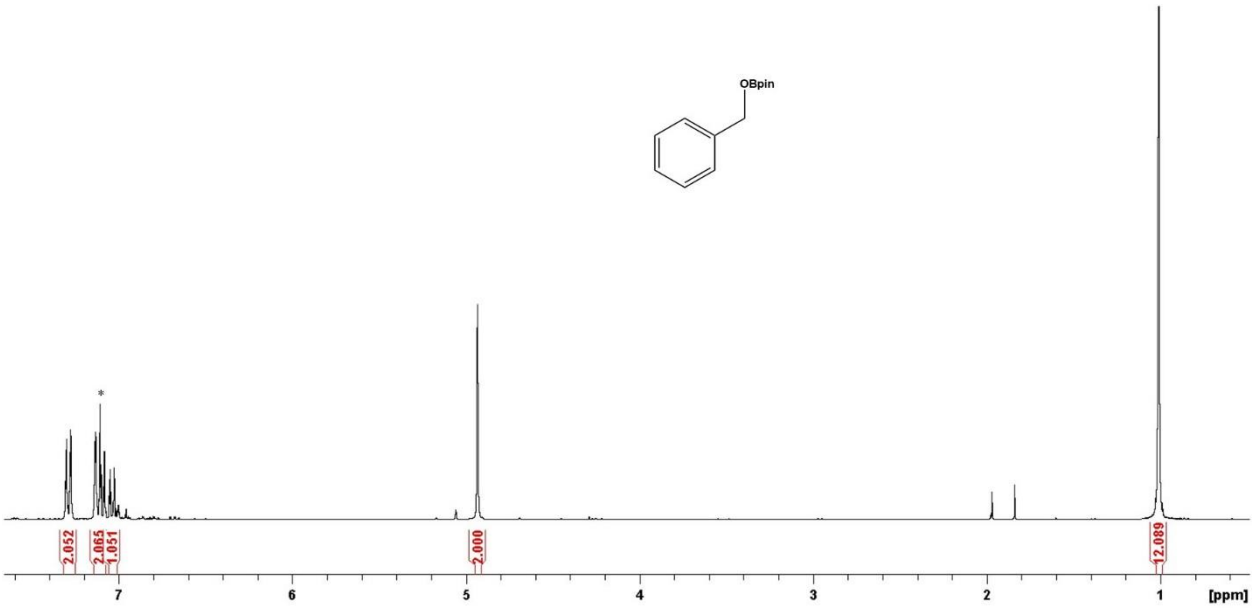

Figure A17. ^{1}H NMR spectrum of benzaldehyde hydroboration product. * indicates C_6D_6.

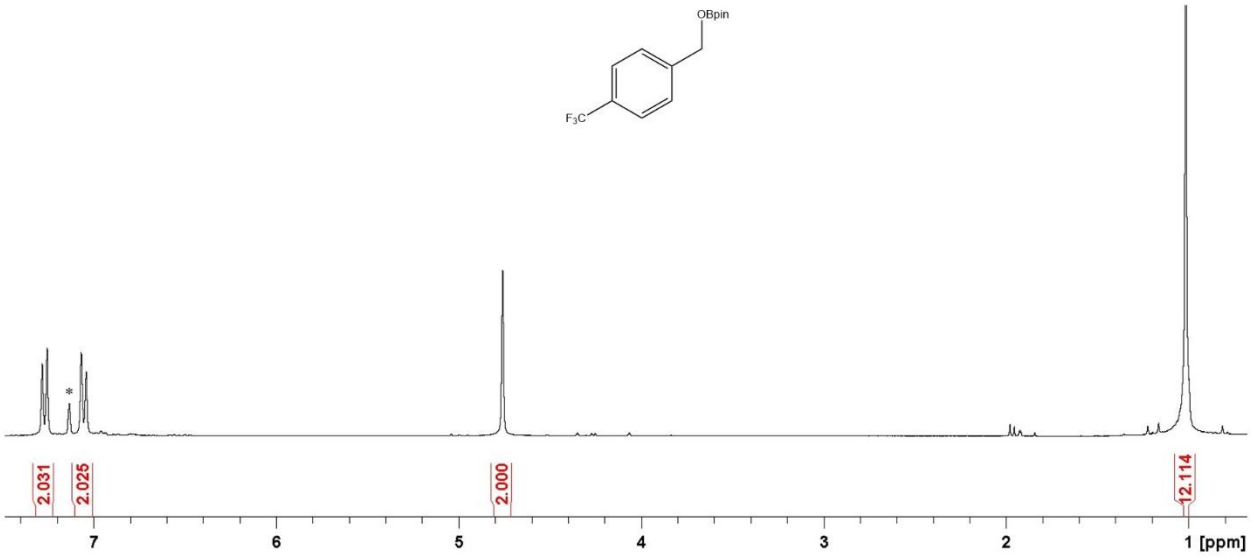

Figure A18. ^{1}H NMR spectrum of 4-trifluoromethylbenzaldehyde hydroboration product. * indicates C_6D_6.

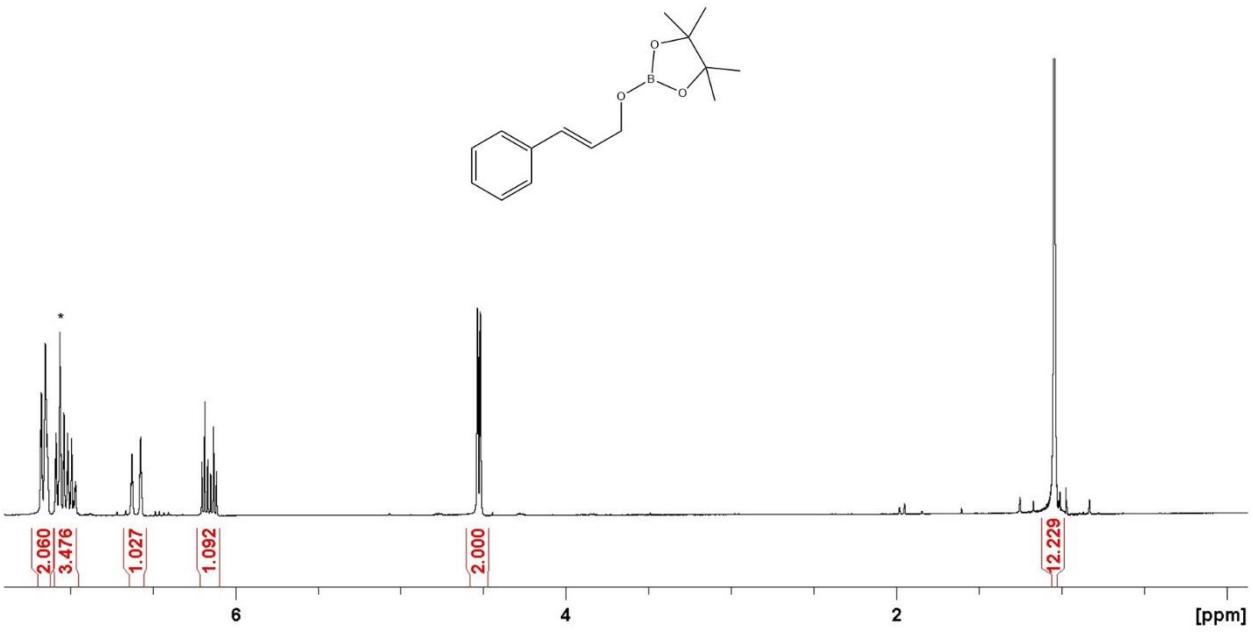

Figure A19. ^{1}H NMR spectrum of cinnamaldehyde hydroboration product. * indicates C_6D_6

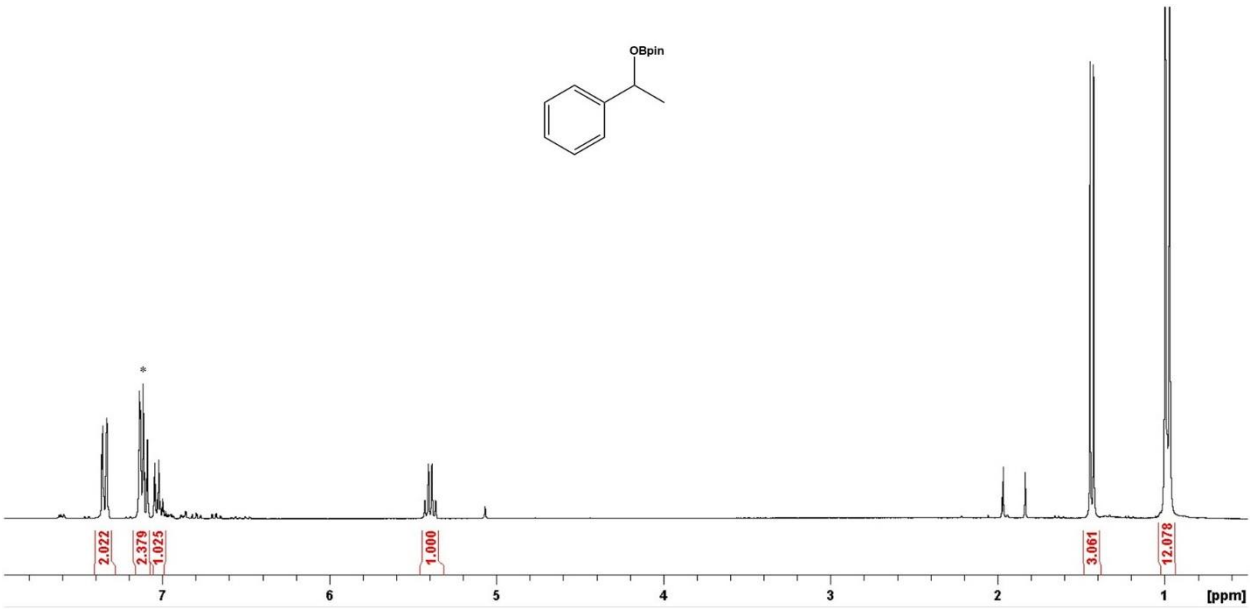

Figure A20. ^{1}H NMR spectrum of acetophenone hydroboration product. * indicates C_6D_6.

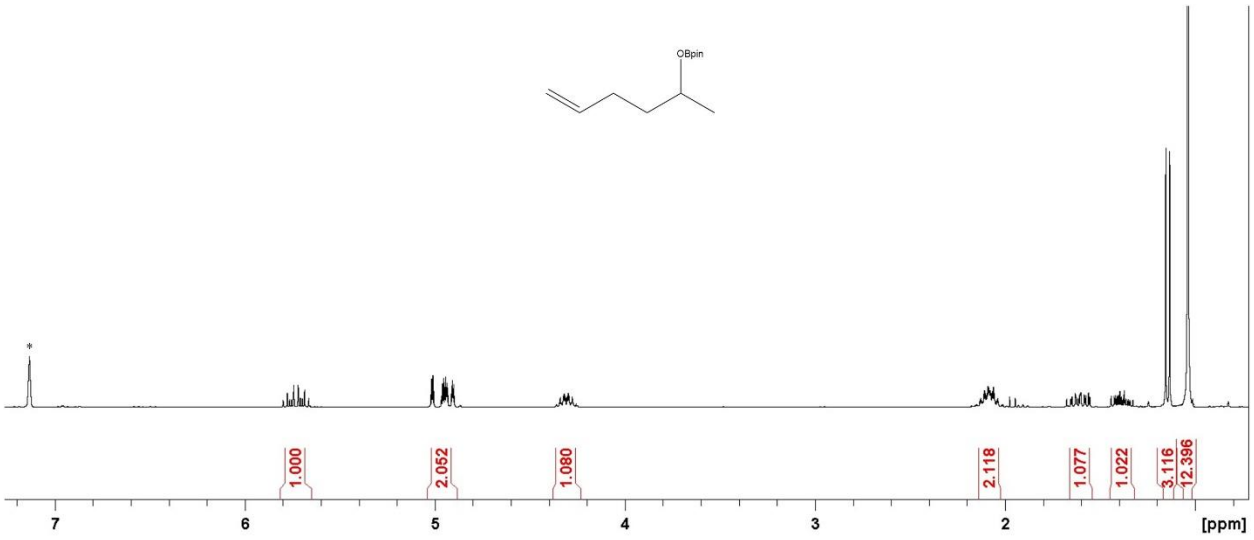

Figure A21. ^{1}H NMR spectrum of benzophenone hydroboration product. * indicates C_6D_6.

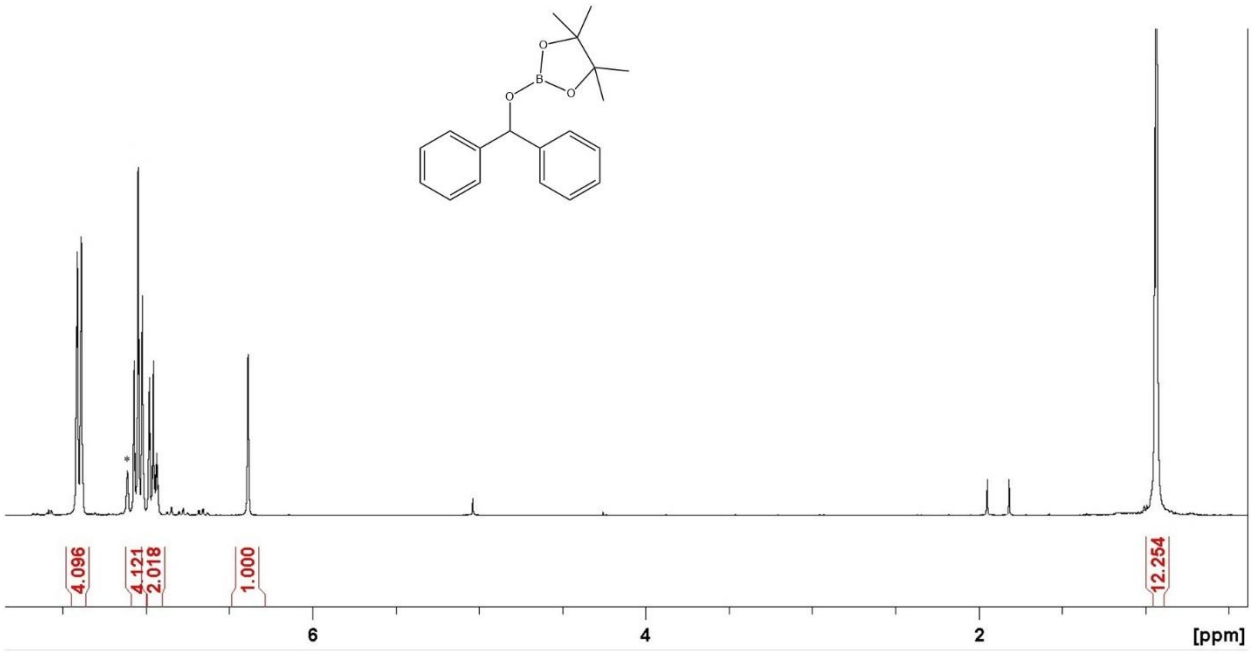

Figure A22. ^{1}H NMR spectrum of 5-hexen-2-one hydroboration product. * indicates C_6D_6.

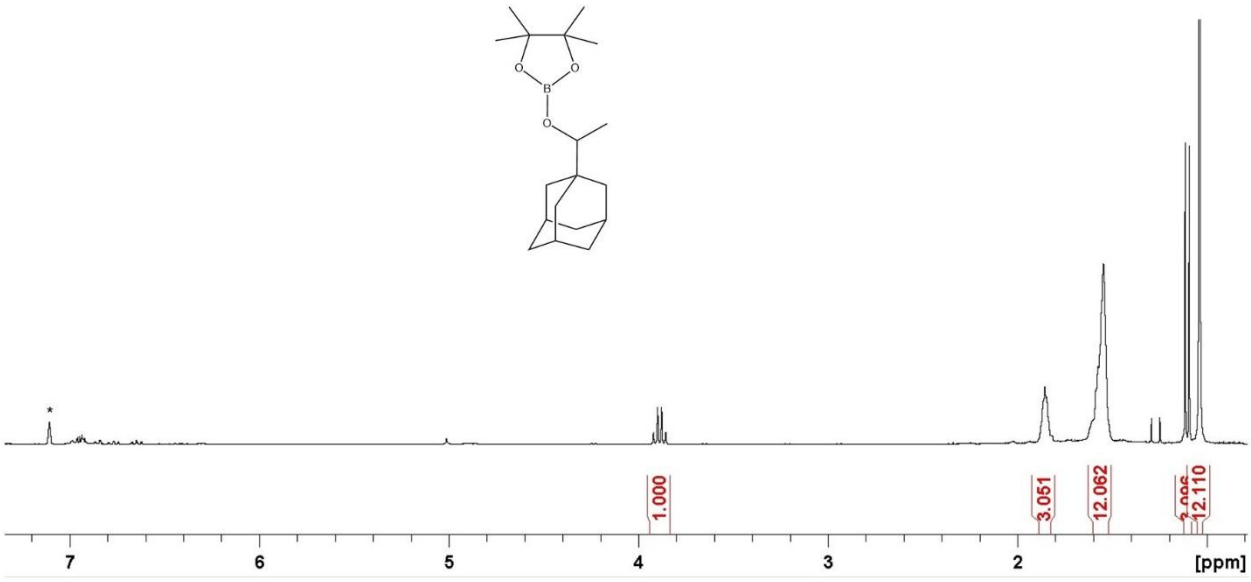

Figure A23. ^{1}H NMR spectrum of 1-adamantyl methyl ketone hydroboration product. * indicates C_6D_6.

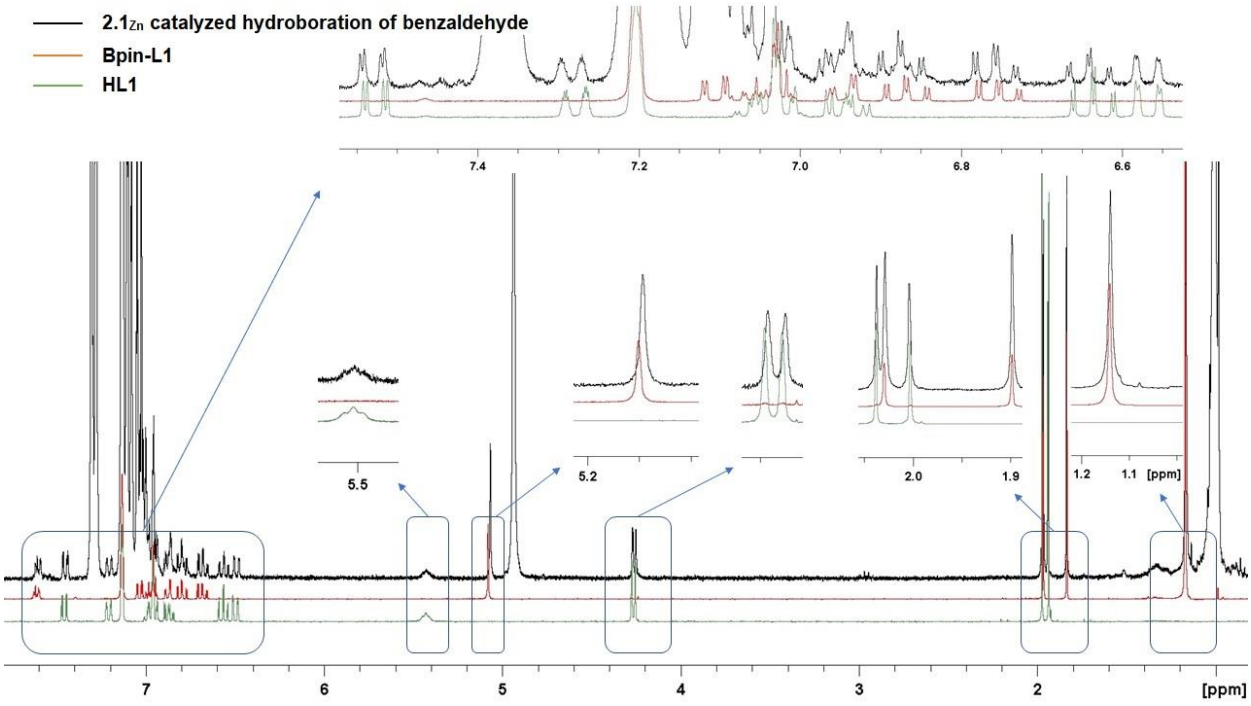

Figure A24. ^{1}H NMR spectra (C_6D_6) of **HL1**, **Bpin-L1** and **2.1$_{Zn}$** in catalyzed benzaldehyde hydroboration.

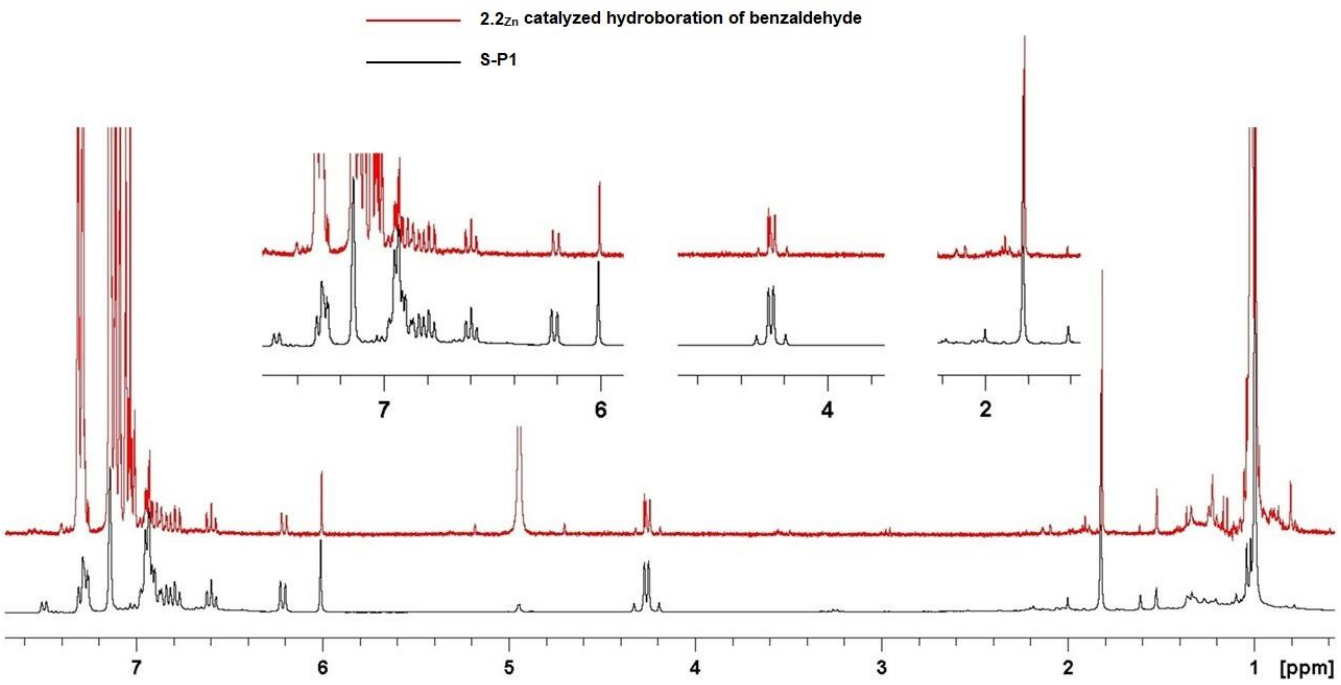

Figure A25. ^{1}H NMR spectra (C_6D_6) of **S-P1** and **2.2$_{Zn}$** in catalytic benzaldehyde hydroboration.

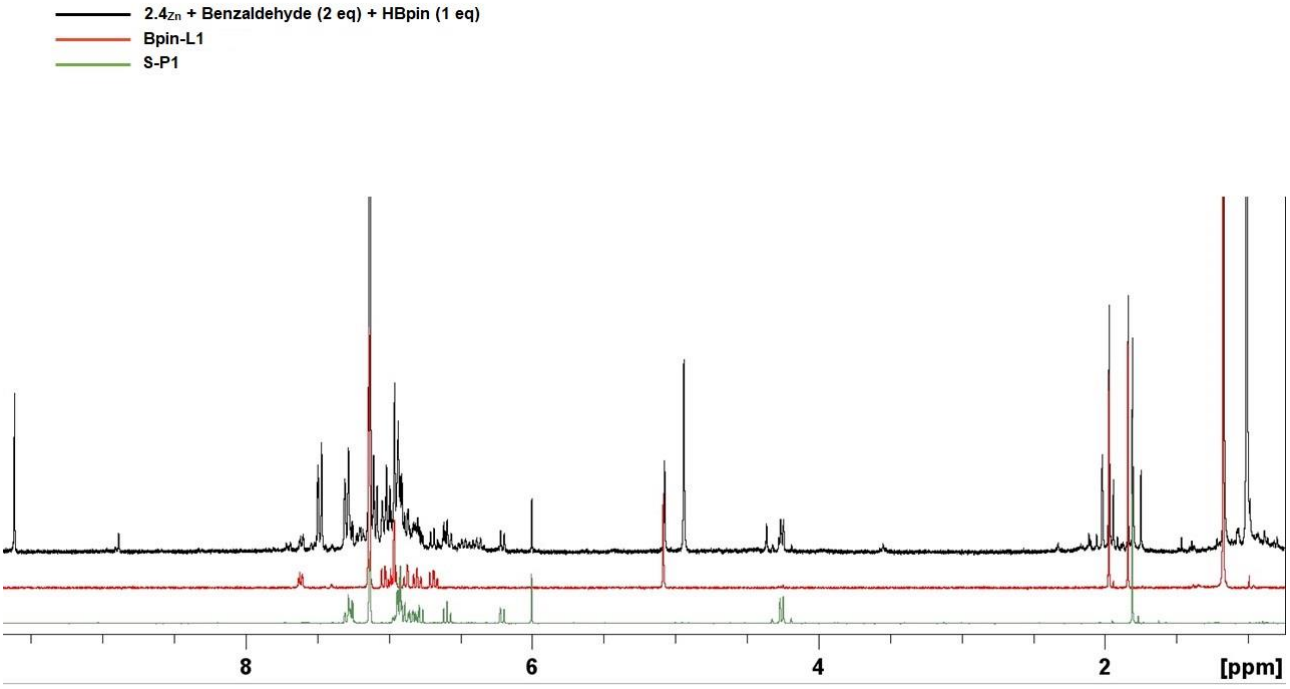

Figure A26. ^{1}H NMR spectra of **S-P1**, and **Bpin-L1**, and stoichiometric reaction of **2.4$_{Zn}$** with benzaldehyde (2eq) and HBpin (1eq) in C_6D_6.

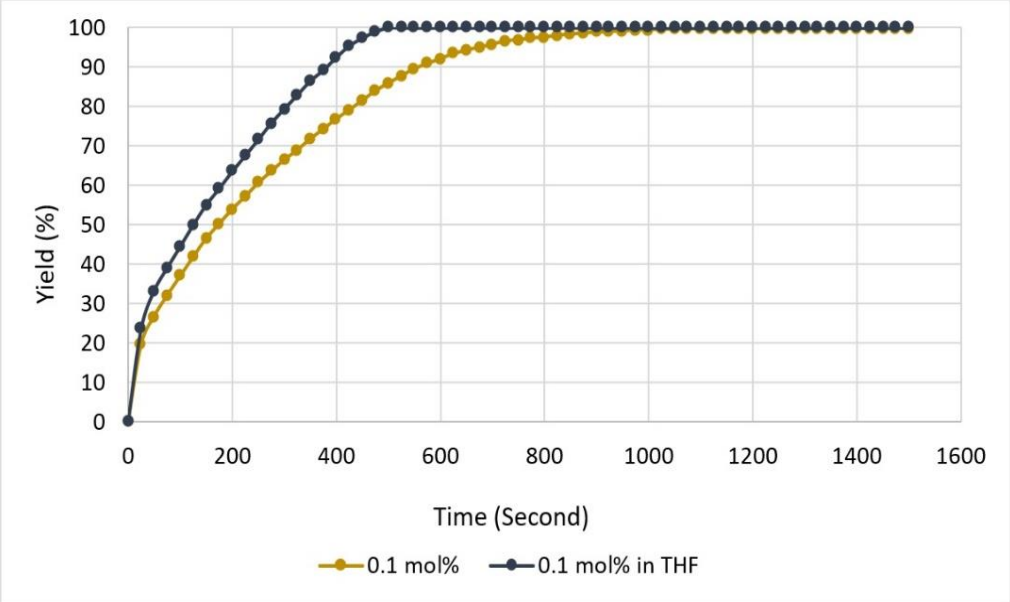

Figure A27. Profiles of acetophenone hydroboration using HBpin catalyzed by **2.4$_{Zn}$** with 0.1 mol% loading in C_6D_6 and THF.

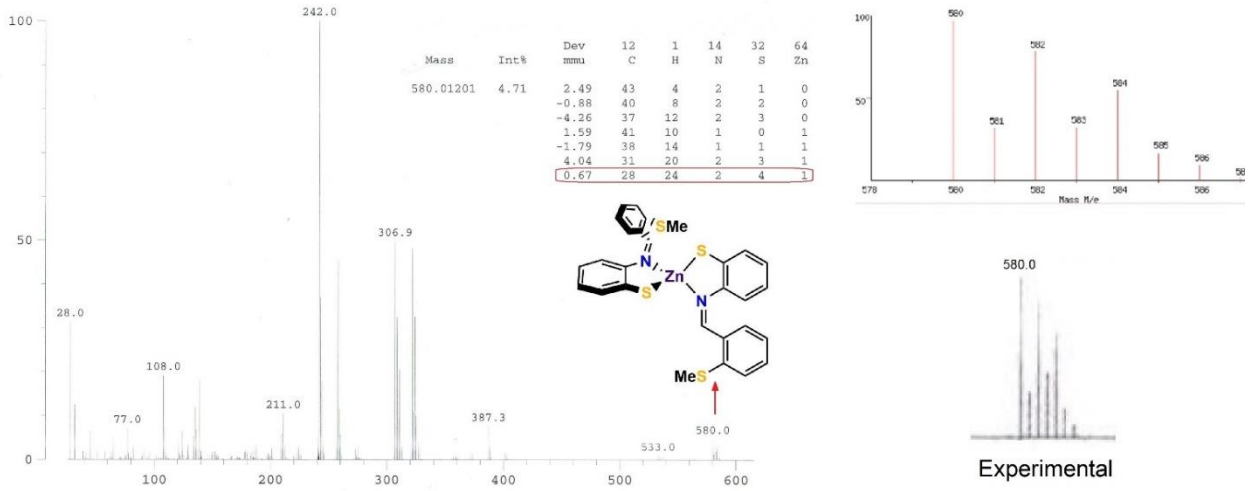

Figure A28. EI-MS spectrum of **2.2$_{Zn}$** showing [M^+].

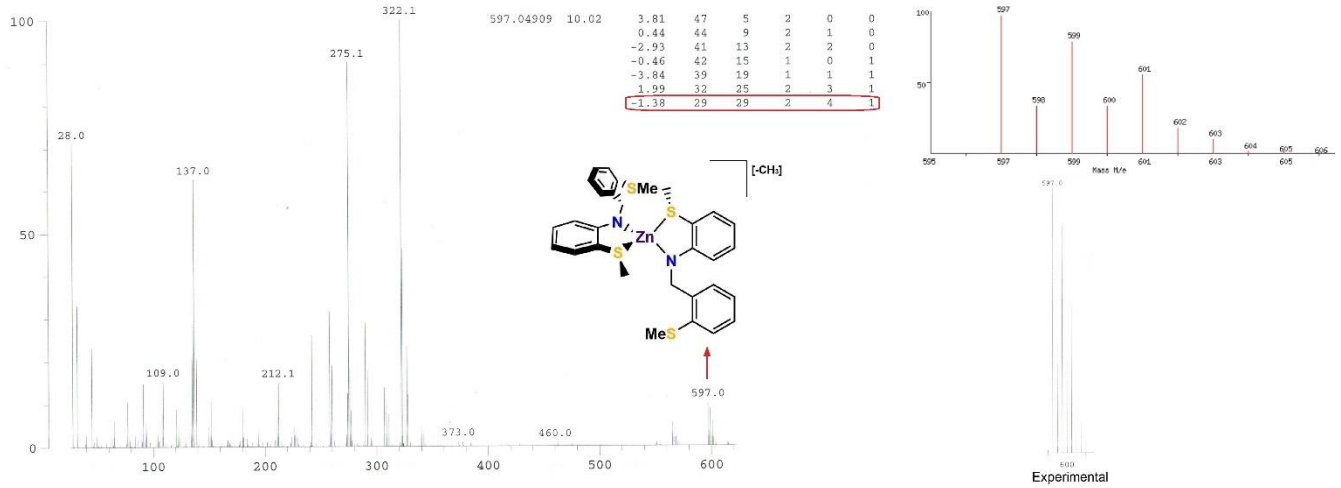

Figure A29. EI-MS spectrum of **2.1$_{Zn}$** showing $[M\text{-}CH_3]^+$.

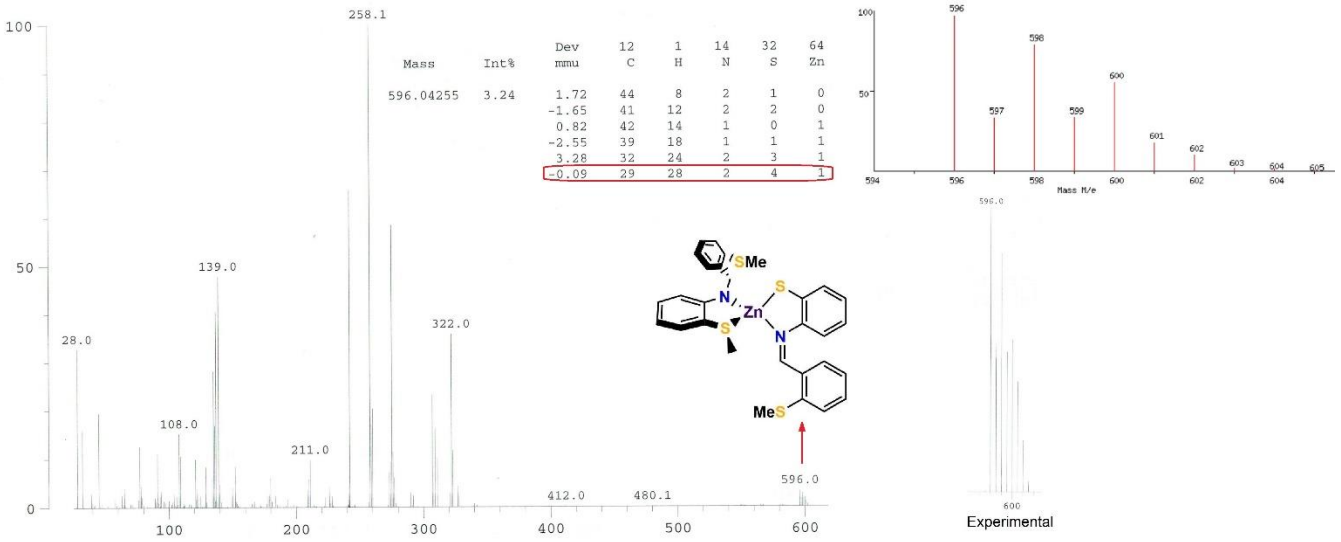

Figure A30. EI-MS spectrum of **2.4$_{Zn}$** showing $[M^+]$.

Table A1. X-ray crystallographic data collection and refinement details for **2.1_{Zn}, 2.2_{Zn}, 2.4_{Zn}, Bpin-L1 and S-P1**.

	2.1_{Zn} (S0707)	**2.2_{Zn} (S0699)**	**2.4_{Zn} (S0811)**	**Bpin-L1 (S0733)**	**S-P1 (S0927)**
empirical formula	$C_{30}H_{32}N_2S_4Zn$	$C_{28}H_{24}N_2S_4Zn$	$C_{29}H_{28}N_4S_4Zn$	$C_{21}H_{28}BNO_2S_2$	$C_{21}H_{19}NS_2$
formula weight ($g \cdot mol^{-1}$)	614.18	582.10	598.14	401.37	349.49
crystal system	orthorhombic	monoclinic	triclinic	Monoclinic	orthorhombic
space group	*P b c n*	*P* $2_1/c$	*P* $\bar{1}$	*P* $2_1/c$	*P n a* 2_1
a (A)	21.2905(10)	7.1899(7)	10.7382(9)	10.9771(4)	18.558(3)
b (A)	7.6279(4)	8.1002(8)	11.2465(11)	11.5337(4)	9.2607(14)
c (A)	17.5124(8)	44.714(4)	12.8901(12)	17.6262(6)	10.3515(16)
α (deg)	90	90	68.170(3)	90	90
β (deg)	90	94.341(3)	68.707(3)	104.460(1)	90
γ (deg)	90	90	87.560(3)	90	90
V (A^3)	2844.0(2)(7)	2596.7(4)	1338.7(2)	2160.90(13)	1779.0(5)
Z	4	4	2	4	4
T (K)	203(2)	203(2)	203(2)	203(2)	203(2)
ρ_{calcd} ($g \cdot cm^{-3}$)	1.434	1.489	1.484	1.234	1.305
μ (mm^{-1})	1.180	1.288	1.252	0.262	0.301
$2\theta_{max}$ (deg)	61.012	55.298	55.444	52.844	51.408
total/unique reflections	25606/4339	63086/6027	28566/6216	16576/4421	10688/3304
Reflections [$I_o \geq 2\sigma(I_o)$]	2853	3745	4286	3121	2681
R_1, wR_2 [$I_o \geq 2\sigma(I_o)$]	0.0408, 0.0821	0.0441, 0.685	0.0419, 0.0748	0.0502, 0.1280	0.0588, 0.1415
goodness of fit	1.022	1.005	1.005	1.055	1.034

Table A2. Bond lengths for **2.1$_{Zn}$**.

Atom	Atom	Length/Å
Zn1	S1	2.4663
Zn1	N1	1.925
Zn1	S1	2.4663
Zn1	N1	1.925
S1	C1	1.818(2)
S1	C2	1.780(2)
S2	C14	1.771(2)
S2	C15	1.789(3)
N1	C7	1.361(3)
N1	C8	1.453(3)
C2	C3	1.386(3)
C2	C7	1.422(3)
C3	C4	1.377(4)
C4	C5	1.382(4)
C5	C6	1.375(3)
C6	C7	1.423(3)
C8	C9	1.511(3)
C9	C10	1.393(3)
C9	C14	1.398(3)
C10	C11	1.376(4)
C11	C12	1.372(4)
C12	C13	1.388(4)
C13	C14	1.390(3)
S1	C1	1.818(2)
S1	C2	1.780(2)
S2	C14	1.771(2)
S2	C15	1.789(3)
N1	C7	1.361(3)
N1	C8	1.453(3)
C2	C3	1.386(3)
C2	C7	1.422(3)
C3	C4	1.377(4)
C4	C5	1.382(4)
C5	C6	1.375(3)
C6	C7	1.423(3)
C8	C9	1.511(3)
C9	C10	1.393(3)
C9	C14	1.398(3)
C10	C11	1.376(4)
C11	C12	1.372(4)
C12	C13	1.388(4)

C13	C14	1.390(3)

Table A3. Bond lengths for **2.2$_{Zn}$**.

Atom	**Atom**	**Length/Å**
Zn1	S1	2.273(1)
Zn1	S3	2.246(1)
Zn1	N1	2.085(2)
Zn1	N2	2.109(2)
S1	C14	1.755(3)
S2	C1	1.784(4)
S2	C2	1.755(3)
S3	C28	1.757(3)
S4	C15	1.798(3)
S4	C16	1.755(3)
N1	C8	1.281(4)
N1	C9	1.434(4)
N2	C22	1.284(4)
N2	C23	1.430(4)
C2	C3	1.386(5)
C2	C7	1.405(5)
C3	C4	1.369(6)
C4	C5	1.390(6)
C5	C6	1.390(5)
C6	C7	1.392(5)
C7	C8	1.462(4)
C9	C10	1.387(5)
C9	C14	1.405(4)
C10	C11	1.376(4)
C11	C12	1.385(4)
C12	C13	1.383(5)
C13	C14	1.398(4)
C16	C17	1.385(4)
C16	C21	1.417(4)
C17	C18	1.382(5)
C18	C19	1.385(5)
C19	C20	1.383(5)
C20	C21	1.381(5)
C21	C22	1.465(4)
C23	C24	1.391(4)
C23	C28	1.414(4)
C24	C25	1.382(5)

C25	C26	1.381(5)
C26	C27	1.375(5)
C27	C28	1.393(4)

Table A4. Bond lengths for **2.4$_{Zn}$.**

Atom	**Atom**	**Length/Å**
Zn1	S1	2.4793(7)
Zn1	S3	2.256(1)
Zn1	N006	1.923(3)
Zn1	N007	2.106(2)
S1	C1	1.817(3)
S1	C2	1.780(4)
S2	C14	1.771(3)
S2	C15	1.789(4)
S3	C16	1.763(3)
S4	C28	1.765(4)
S4	C29	1.790(3)
N006	C7	1.364(3)
N006	C8	1.460(3)
N007	C21	1.430(5)
N007	C22	1.287(4)
C2	C3	1.386(4)
C2	C7	1.422(4)
C3	C4	1.379(6)
C4	C5	1.391(4)
C5	C6	1.376(4)
C6	C7	1.418(5)
C8	C9	1.504(3)
C9	C10	1.390(4)
C9	C14	1.406(5)
C10	C11	1.380(5)
C11	C12	1.374(5)
C12	C13	1.381(4)
C13	C14	1.396(4)
C16	C17	1.387(6)
C16	C21	1.404(5)
C17	C18	1.383(5)
C18	C19	1.385(5)
C19	C20	1.373(6)
C20	C21	1.395(5)
C22	C23	1.453(6)
C23	C24	1.397(5)

C23	C28	1.413(4)
C24	C25	1.385(6)
C25	C26	1.384(4)
C26	C27	1.373(5)
C27	C28	1.390(6)

Table A5. Bond lengths for **Bpin-L1**.

Atom	**Atom**	**Length/Å**
S1	C14	1.763(2)
S1	C15	1.794(3)
O1	C16	1.459(4)
O1	B1	1.370(4)
N1	C7	1.436(3)
N1	C8	1.468(3)
N1	B1	1.408(4)
C2	C3	1.394(4)
C2	C7	1.398(3)
C2	S2A	1.78(1)
C3	C4	1.378(3)
C4	C5	1.375(3)
C5	C6	1.384(4)
C6	C7	1.385(3)
C8	C9	1.502(3)
C9	C10	1.414(4)
C9	C14	1.403(3)
C10	C11	1.364(4)
C11	C12	1.370(5)
C12	C13	1.383(5)
C13	C14	1.404(4)
C16	C17	1.557(5)
C16	C18	1.473(6)
C16	C19A	1.596(8)
B1	O2A	1.424(8)
O2A	C19A	1.46(1)
C1A	S2A	1.79(2)
C19A	C20A	1.54(2)
C19A	C21A	1.51(1)

Table A6. Bond lengths for **S-P1**.

Atom	**Atom**	**Length/Å**

S1	C14	1.764(6)
S1	C15	1.838(6)
S2	C1	1.789(8)
S2	C2	1.773(6)
N1	C8	1.451(7)
N1	C9	1.393(7)
N1	C15	1.480(7)
C2	C3	1.383(9)
C2	C7	1.407(8)
C3	C4	1.40(1)
C4	C5	1.350(9)
C5	C6	1.418(8)
C6	C7	1.374(8)
C7	C8	1.502(8)
C9	C10	1.391(8)
C9	C14	1.395(8)
C10	C11	1.398(8)
C11	C12	1.347(9)
C12	C13	1.40(1)
C13	C14	1.379(8)
C15	C16	1.497(8)
C16	C17	1.375(8)
C16	C21	1.387(8)
C17	C18	1.375(8)
C18	C19	1.371(9)
C19	C20	1.37(1)
C20	C21	1.381(9)

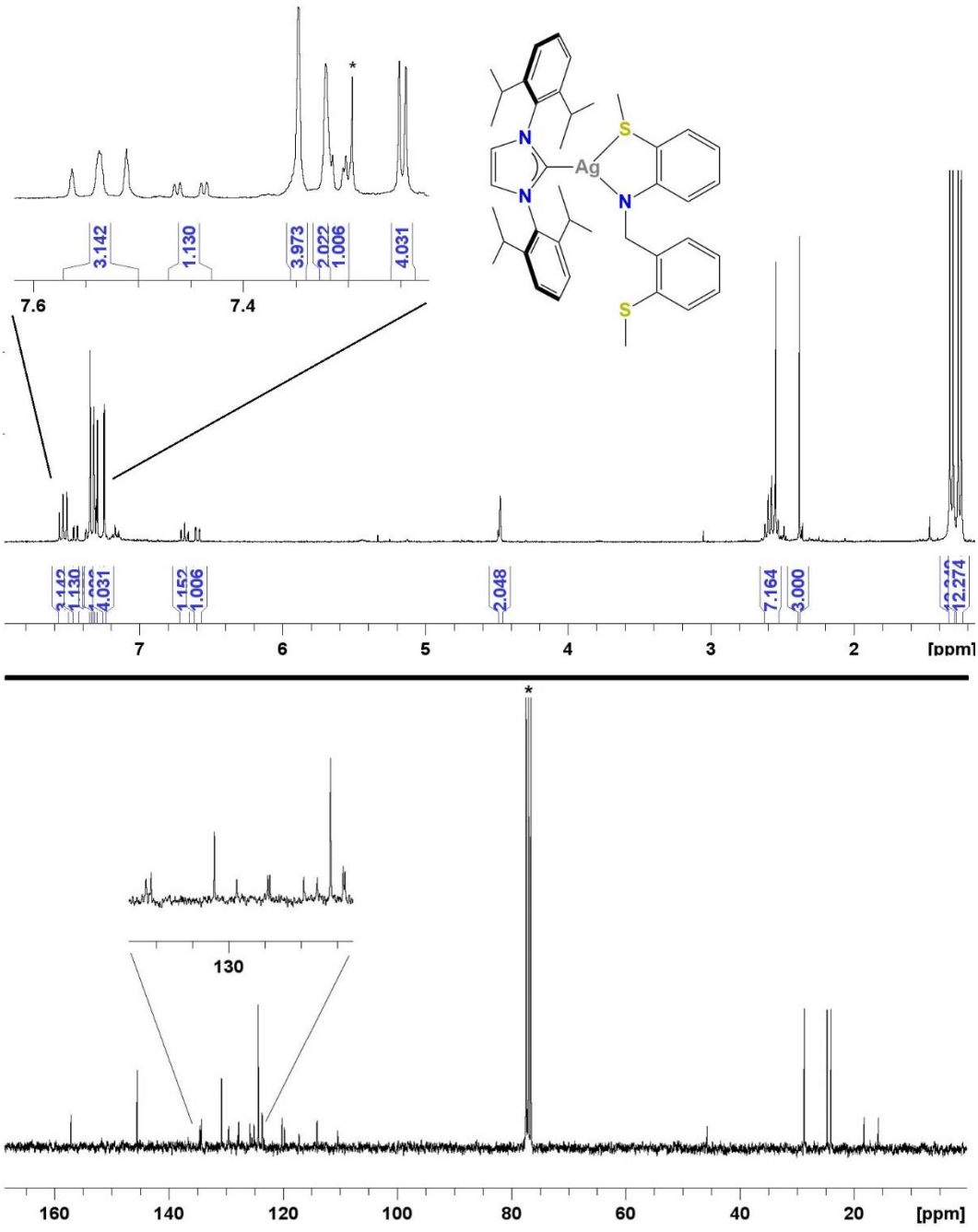

Figure A31. ^{1}H (300 MHz, $CDCl_3$ - top) and ^{13}C (75 MHz, $CDCl_3$ - bottom) NMR spectra of **2.7$_{Ag}$**. * indicates protic impurity in $CDCl_3$.

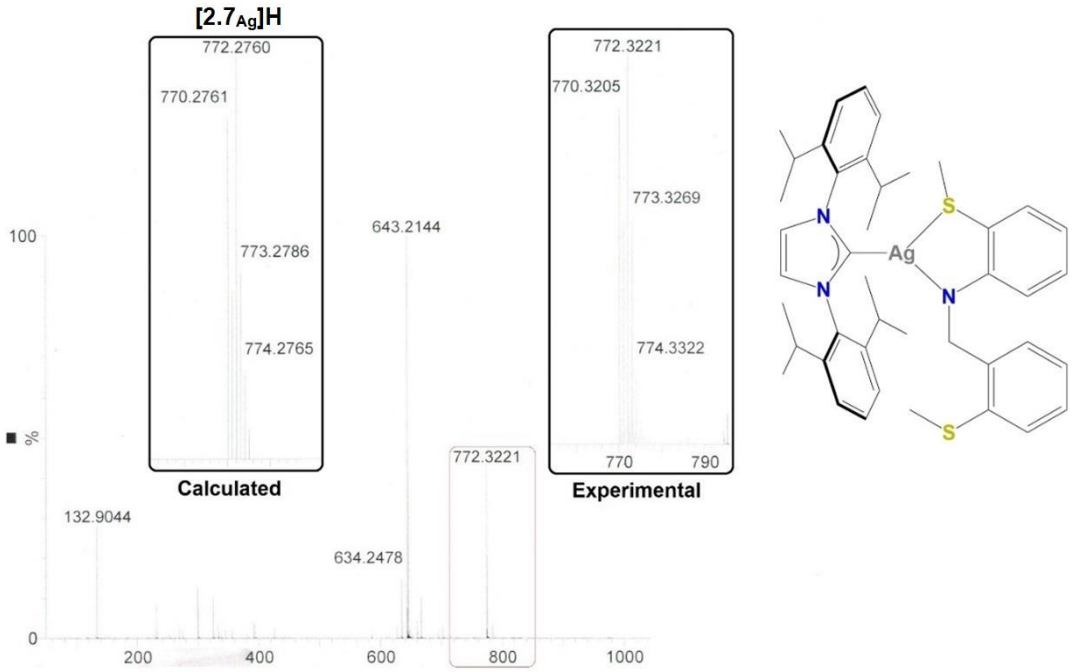

Figure A32. ESI-MS spectrum of [**2.7**$_{Ag}$ + H]$^+$.

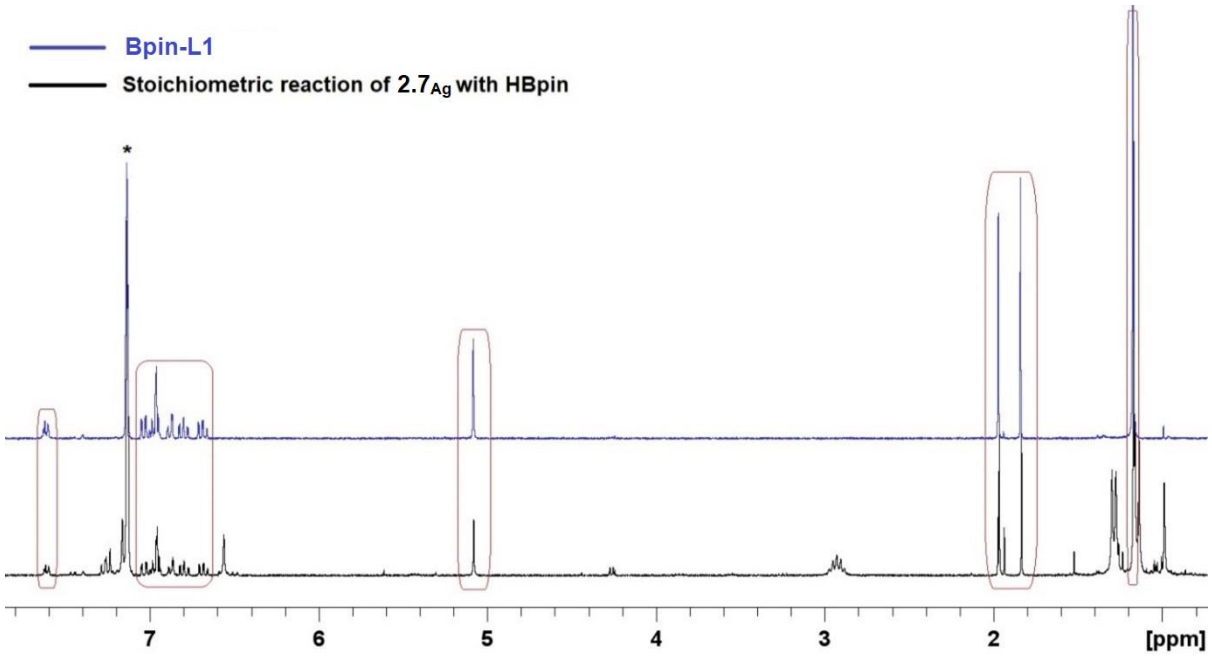

Figure A33. Stacked plot of ^{1}H NMR spectra of **Bpin-L1** and reaction mixture of stoichiometric reaction of **2.7**$_{Ag}$ with HBpin in C_6D_6. * indicates protic impurity in C_6D_6.

Table A7: X-ray crystallographic data collection and refinement details of **2.7$_{Ag}$**.

	2.7$_{Ag}$
empirical formula	$C_{42.50}H_{53}AgClN_3S_2$
formula weight (g·mol^{-1})	813.32
crystal system	monoclininc
space group	*P* 2$_1$/*c*
a (A)	16.9305(4)
b (A)	12.5740(3)
c (A)	19.3854(5)
α (deg)	90
β (deg)	98.888(1)
γ (deg)	90
V (A^3)	4077.29(17)
Z	4
T (K)	200
p_{calcd}(g·cm^{-3})	1.325
μ(mm^{-1})	0.695
$2\theta_{max}$ (deg)	50.054
total/unique reflections	24912/7185
Reflections [$I_o \geq 2\sigma(I_o)$]	6173
R_1, wR_2 [$I_o \geq 2\sigma(I_o)$]	0.0276, 0.0651
goodness of fit	1.066
CCDC number	2201240

Table A8. Bond lengths for **2.7$_{Ag}$**.

Atom1	**Atom2**	**Length**
Cl2	Cl3	0.926(5)
Cl3	Cl2	0.926(5)
C1A	H1AA	0.989
C1A	H1AB	0.991
C1A	C1A	1.64(1)
C1A	H1AA	0.989
C1A	H1AB	0.991
Ag1	S1	2.8032(8)
Ag1	N1	2.105(2)
Ag1	C1	2.070(2)
S1	C2	1.787(4)
S1	C3	1.769(3)
S2	C15	1.768(2)
S2	C16	1.784(3)

N1	C4	1.347(3)
N1	C9	1.451(3)
N2	C1	1.352(3)
N2	C18	1.383(3)
N2	C31	1.447(3)
N3	C1	1.351(3)
N3	C17	1.391(3)
N3	C19	1.446(3)
C2	H2A	0.981
C2	H2B	0.98
C2	H2C	0.979
C3	C4	1.427(3)
C3	C8	1.388(3)
C4	C5	1.423(3)
C5	H5	0.95
C5	C6	1.376(3)
C6	H6	0.95
C6	C7	1.379(4)
C7	H7	0.95
C7	C8	1.378(4)
C8	H8	0.95
C9	H9A	0.99
C9	H9B	0.99
C9	C10	1.519(3)
C10	C11	1.373(3)
C10	C15	1.403(3)
C11	H11	0.95
C11	C12	1.384(4)
C12	H12	0.95
C12	C13	1.371(4)
C13	H13	0.95
C13	C14	1.376(4)
C14	H14	0.95
C14	C15	1.389(3)
C16	H16A	0.979
C16	H16B	0.98
C16	H16C	0.98
C17	H17	0.95
C17	C18	1.340(3)
C18	H18	0.95
C19	C20	1.388(3)
C19	C24	1.397(3)
C20	C21	1.396(3)
C20	C28	1.514(3)
C21	H21	0.95

C21	C22	1.377(4)
C22	H22	0.95
C22	C23	1.367(4)
C23	H23	0.95
C23	C24	1.395(4)
C24	C26	1.511(3)
C25	H25A	0.98
C25	H25B	0.98
C25	H25C	0.981
C25	C26	1.524(4)
C26	H26	1
C26	C27	1.527(4)
C27	H27A	0.98
C27	H27B	0.98
C27	H27C	0.98
C28	H28	1
C28	C29	1.524(4)
C28	C30	1.529(4)
C29	H29A	0.98
C29	H29B	0.98
C29	H29C	0.98
C30	H30A	0.98
C30	H30B	0.98
C30	H30C	0.98
C31	C32	1.391(3)
C31	C36	1.398(3)
C32	C33	1.390(3)
C32	C37	1.516(3)
C33	H33	0.95
C33	C34	1.373(3)
C34	H34	0.95
C34	C35	1.367(4)
C35	H35	0.95
C35	C36	1.391(4)
C36	C40	1.513(4)
C37	H37	1
C37	C38	1.529(3)
C37	C39	1.524(3)
C38	H38A	0.98
C38	H38B	0.98
C38	H38C	0.98
C39	H39A	0.981
C39	H39B	0.98
C39	H39C	0.98
C40	H40	1

C40	C41	1.527(5)
C40	C42	1.528(4)
C41	H41A	0.98
C41	H41B	0.98
C41	H41C	0.979
C42	H42A	0.98
C42	H42B	0.98
C42	H42C	0.98

Table A9. All angles for **2.7$_{Ag}$**.

Atom1	**Atom2**	**Atom3**	**Angle**
H1AA	C1A	H1AB	110
H1AA	C1A	C1A	125.1
H1AB	C1A	C1A	124.4
C1A	C1A	H1AA	125.1
C1A	C1A	H1AB	124.4
H1AA	C1A	H1AB	110
S1	Ag1	N1	75.83(5)
S1	Ag1	C1	126.07(6)
N1	Ag1	C1	158.10(8)
Ag1	S1	C2	94.3(1)
Ag1	S1	C3	93.79(8)
C2	S1	C3	102.0(2)
C15	S2	C16	104.1(1)
Ag1	N1	C4	127.6(1)
Ag1	N1	C9	114.9(1)
C4	N1	C9	117.5(2)
C1	N2	C18	111.5(2)
C1	N2	C31	122.0(2)
C18	N2	C31	126.5(2)
C1	N3	C17	111.1(2)
C1	N3	C19	123.8(2)
C17	N3	C19	125.1(2)
Ag1	C1	N2	124.6(1)
Ag1	C1	N3	131.2(1)
N2	C1	N3	104.2(2)
S1	C2	H2A	109.4
S1	C2	H2B	109.5
S1	C2	H2C	109.5
H2A	C2	H2B	109.4
H2A	C2	H2C	109.5
H2B	C2	H2C	109.5
S1	C3	C4	120.8(2)

S1	C3	C8	118.0(2)
C4	C3	C8	121.2(2)
N1	C4	C3	121.7(2)
N1	C4	C5	123.6(2)
C3	C4	C5	114.8(2)
C4	C5	H5	118.7
C4	C5	C6	122.6(2)
H5	C5	C6	118.7
C5	C6	H6	119.5
C5	C6	C7	121.1(2)
H6	C6	C7	119.5
C6	C7	H7	120.8
C6	C7	C8	118.4(2)
H7	C7	C8	120.8
C3	C8	C7	121.8(2)
C3	C8	H8	119.1
C7	C8	H8	119.1
N1	C9	H9A	108.3
N1	C9	H9B	108.3
N1	C9	C10	115.9(2)
H9A	C9	H9B	107.4
H9A	C9	C10	108.3
H9B	C9	C10	108.3
C9	C10	C11	121.7(2)
C9	C10	C15	119.4(2)
C11	C10	C15	118.8(2)
C10	C11	H11	119.4
C10	C11	C12	121.3(2)
H11	C11	C12	119.4
C11	C12	H12	120.2
C11	C12	C13	119.5(2)
H12	C12	C13	120.3
C12	C13	H13	119.6
C12	C13	C14	120.7(3)
H13	C13	C14	119.7
C13	C14	H14	120.1
C13	C14	C15	119.9(2)
H14	C14	C15	120.1
S2	C15	C10	116.7(2)
S2	C15	C14	123.5(2)
C10	C15	C14	119.8(2)
S2	C16	H16A	109.5
S2	C16	H16B	109.4
S2	C16	H16C	109.5
H16A	C16	H16B	109.5

H16A	C16	H16C	109.5
H16B	C16	H16C	109.4
N3	C17	H17	126.7
N3	C17	C18	106.6(2)
H17	C17	C18	126.7
N2	C18	C17	106.6(2)
N2	C18	H18	126.7
C17	C18	H18	126.7
N3	C19	C20	118.6(2)
N3	C19	C24	118.2(2)
C20	C19	C24	123.2(2)
C19	C20	C21	117.3(2)
C19	C20	C28	123.1(2)
C21	C20	C28	119.6(2)
C20	C21	H21	119.6
C20	C21	C22	120.8(2)
H21	C21	C22	119.6
C21	C22	H22	119.8
C21	C22	C23	120.5(3)
H22	C22	C23	119.8
C22	C23	H23	119.3
C22	C23	C24	121.5(2)
H23	C23	C24	119.2
C19	C24	C23	116.7(2)
C19	C24	C26	121.9(2)
C23	C24	C26	121.3(2)
H25A	C25	H25B	109.5
H25A	C25	H25C	109.5
H25A	C25	C26	109.5
H25B	C25	H25C	109.4
H25B	C25	C26	109.5
H25C	C25	C26	109.4
C24	C26	C25	113.6(2)
C24	C26	H26	107.6
C24	C26	C27	110.2(2)
C25	C26	H26	107.6
C25	C26	C27	109.9(2)
H26	C26	C27	107.6
C26	C27	H27A	109.5
C26	C27	H27B	109.5
C26	C27	H27C	109.5
H27A	C27	H27B	109.5
H27A	C27	H27C	109.5
H27B	C27	H27C	109.5
C20	C28	H28	107.6

C20	C28	C29	111.7(2)
C20	C28	C30	111.0(2)
H28	C28	C29	107.6
H28	C28	C30	107.6
C29	C28	C30	111.2(2)
C28	C29	H29A	109.5
C28	C29	H29B	109.5
C28	C29	H29C	109.5
H29A	C29	H29B	109.5
H29A	C29	H29C	109.5
H29B	C29	H29C	109.5
C28	C30	H30A	109.5
C28	C30	H30B	109.5
C28	C30	H30C	109.5
H30A	C30	H30B	109.5
H30A	C30	H30C	109.4
H30B	C30	H30C	109.5
N2	C31	C32	118.8(2)
N2	C31	C36	118.2(2)
C32	C31	C36	122.9(2)
C31	C32	C33	117.2(2)
C31	C32	C37	122.3(2)
C33	C32	C37	120.5(2)
C32	C33	H33	119.5
C32	C33	C34	121.0(2)
H33	C33	C34	119.5
C33	C34	H34	119.7
C33	C34	C35	120.6(2)
H34	C34	C35	119.7
C34	C35	H35	119.3
C34	C35	C36	121.3(2)
H35	C35	C36	119.3
C31	C36	C35	116.9(2)
C31	C36	C40	123.0(2)
C35	C36	C40	120.1(2)
C32	C37	H37	107.7
C32	C37	C38	110.8(2)
C32	C37	C39	113.2(2)
H37	C37	C38	107.7
H37	C37	C39	107.7
C38	C37	C39	109.5(2)
C37	C38	H38A	109.5
C37	C38	H38B	109.5
C37	C38	H38C	109.5
H38A	C38	H38B	109.5

H38A	C38	H38C	109.5
H38B	C38	H38C	109.5
C37	C39	H39A	109.5
C37	C39	H39B	109.5
C37	C39	H39C	109.5
H39A	C39	H39B	109.5
H39A	C39	H39C	109.4
H39B	C39	H39C	109.5
C36	C40	H40	107.9
C36	C40	C41	111.6(2)
C36	C40	C42	111.0(2)
H40	C40	C41	107.9
H40	C40	C42	107.9
C41	C40	C42	110.3(2)
C40	C41	H41A	109.5
C40	C41	H41B	109.4
C40	C41	H41C	109.5
H41A	C41	H41B	109.5
H41A	C41	H41C	109.5
H41B	C41	H41C	109.5
C40	C42	H42A	109.4
C40	C42	H42B	109.5
C40	C42	H42C	109.5
H42A	C42	H42B	109.5
H42A	C42	H42C	109.5
H42B	C42	H42C	109.5

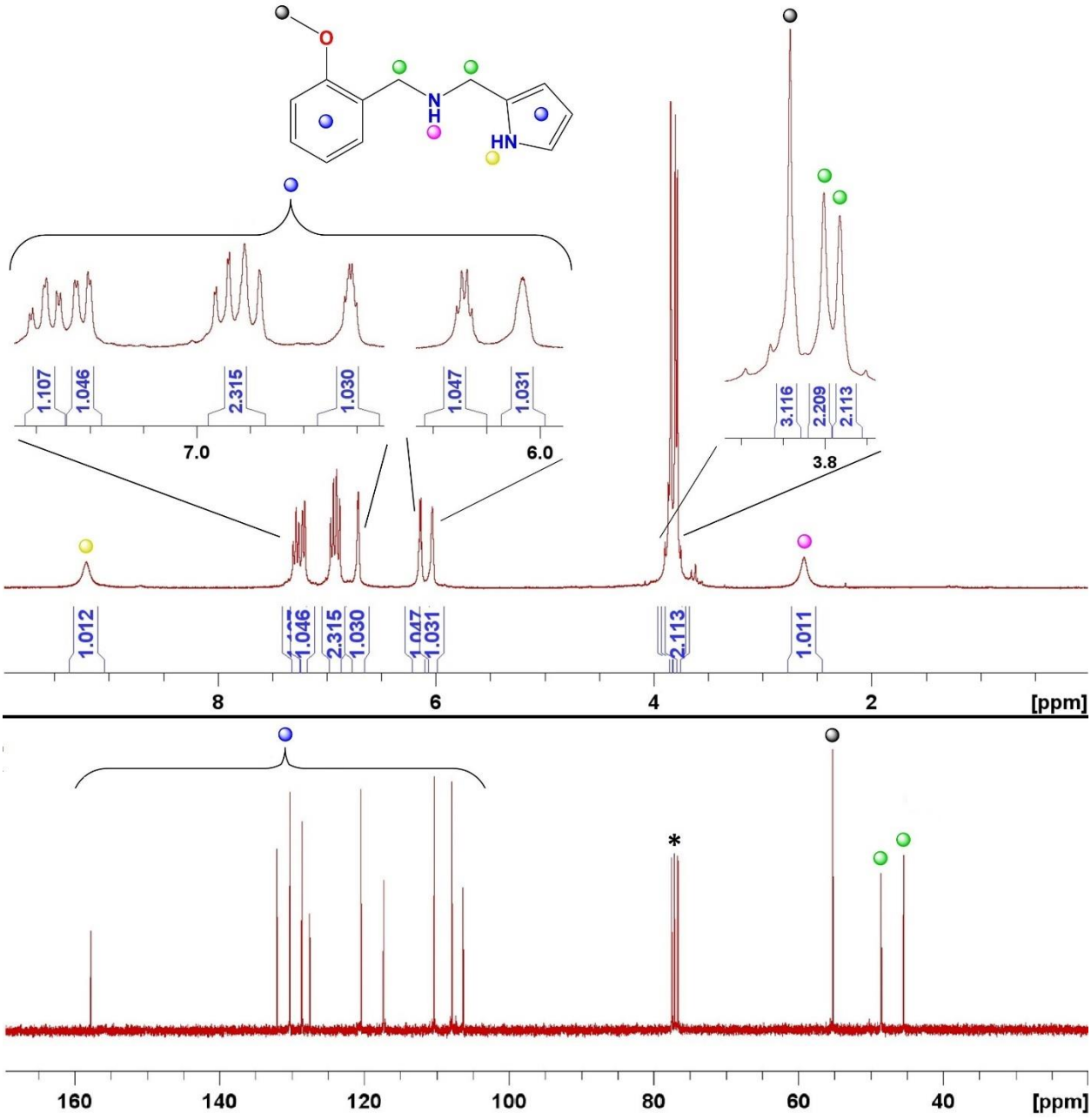

Figure A34. ^{1}H NMR (top, 300 MHz, $CDCl_3$) and $^{13}C\{^{1}H\}$ NMR spectra (bottom, 75 MHz, $CDCl_3$) of (**H_2L3**). * indicates protic impurity in $CDCl_3$.

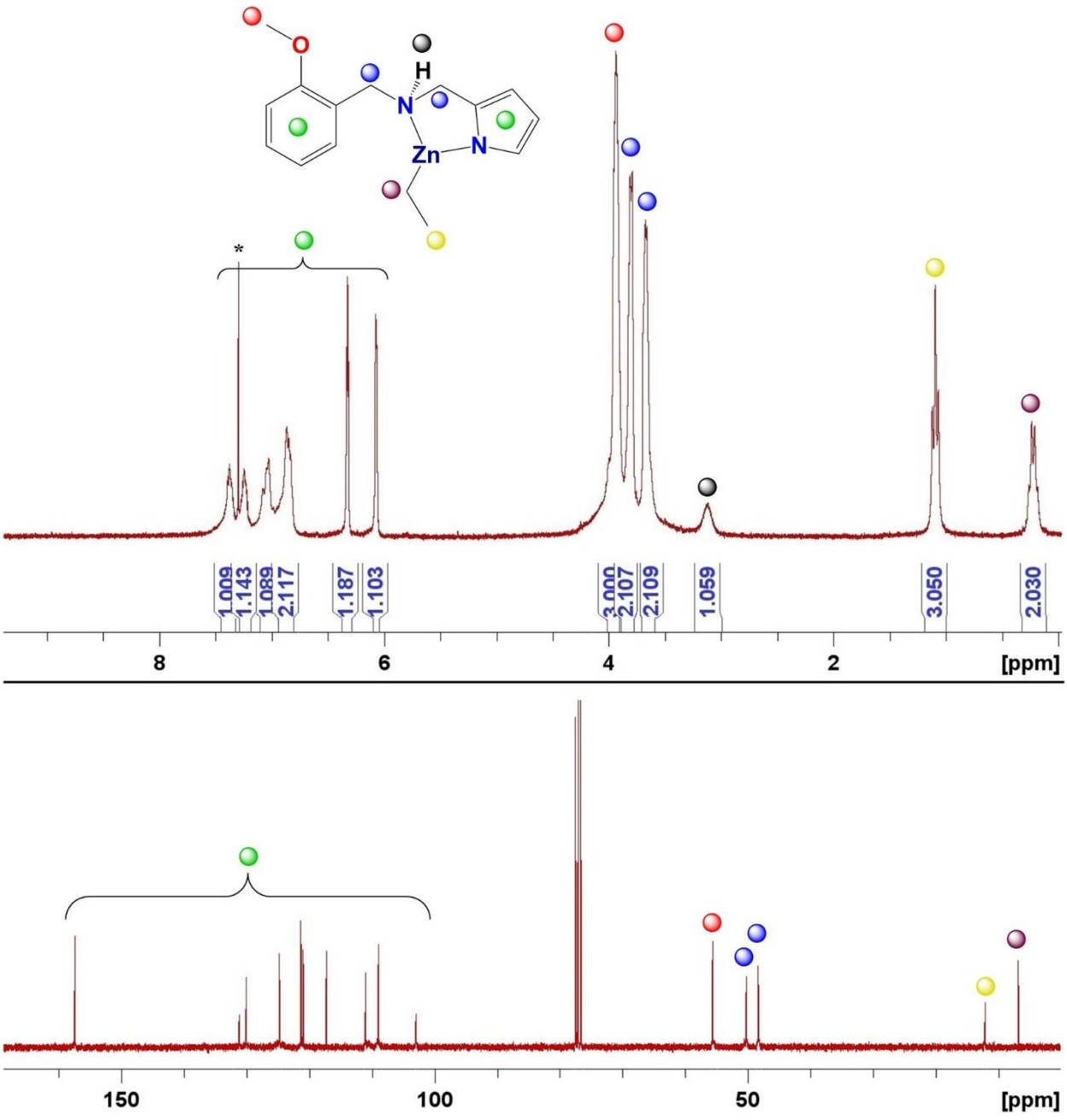

Figure A35. ^{1}H NMR (top, 300 MHz, $CDCl_3$) and $^{13}C\{^{1}H\}$ NMR spectra (bottom, 75 MHz, $CDCl_3$) of **2.8$_{Zn}$**. * indicates protic impurity in $CDCl_3$.

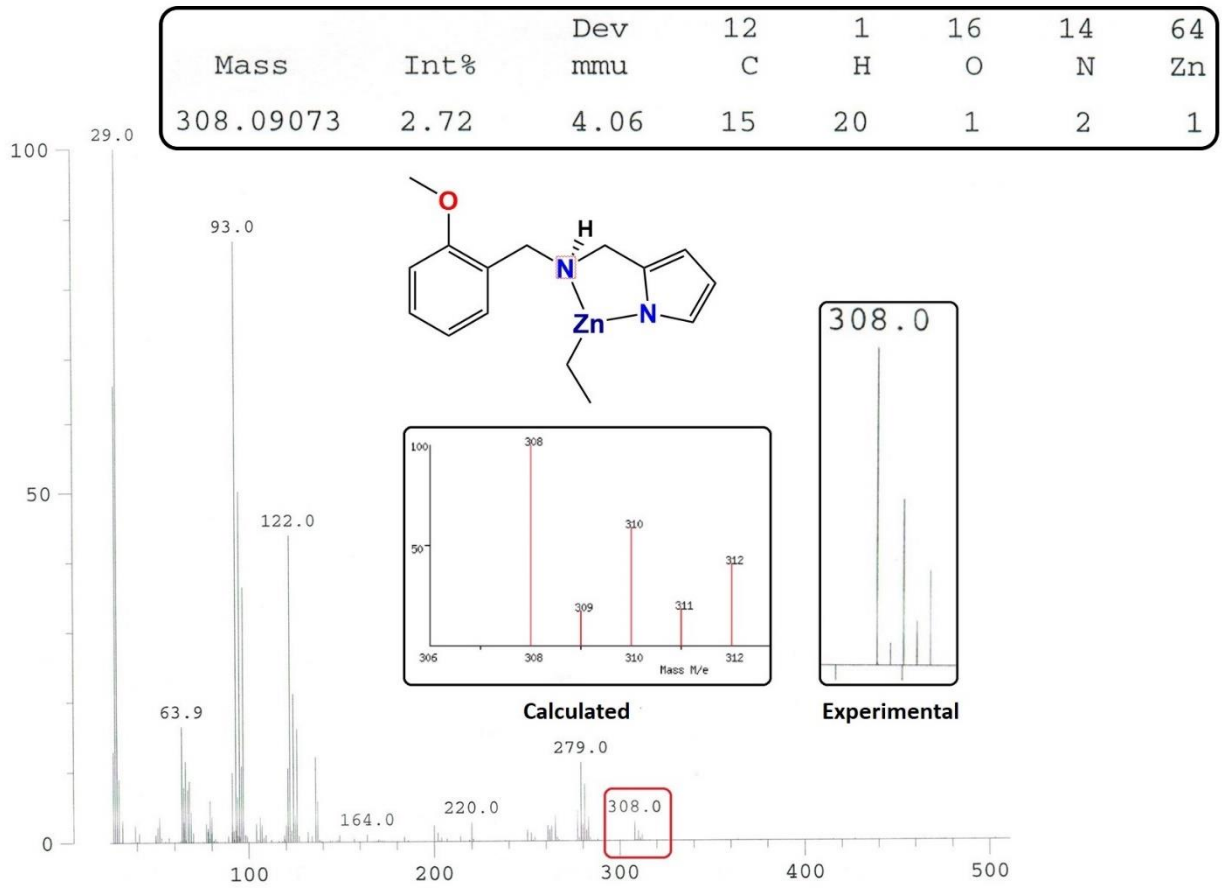

Figure A36. EI-MS spectrum of **2.8$_{Zn}$** showing [M$^+$].

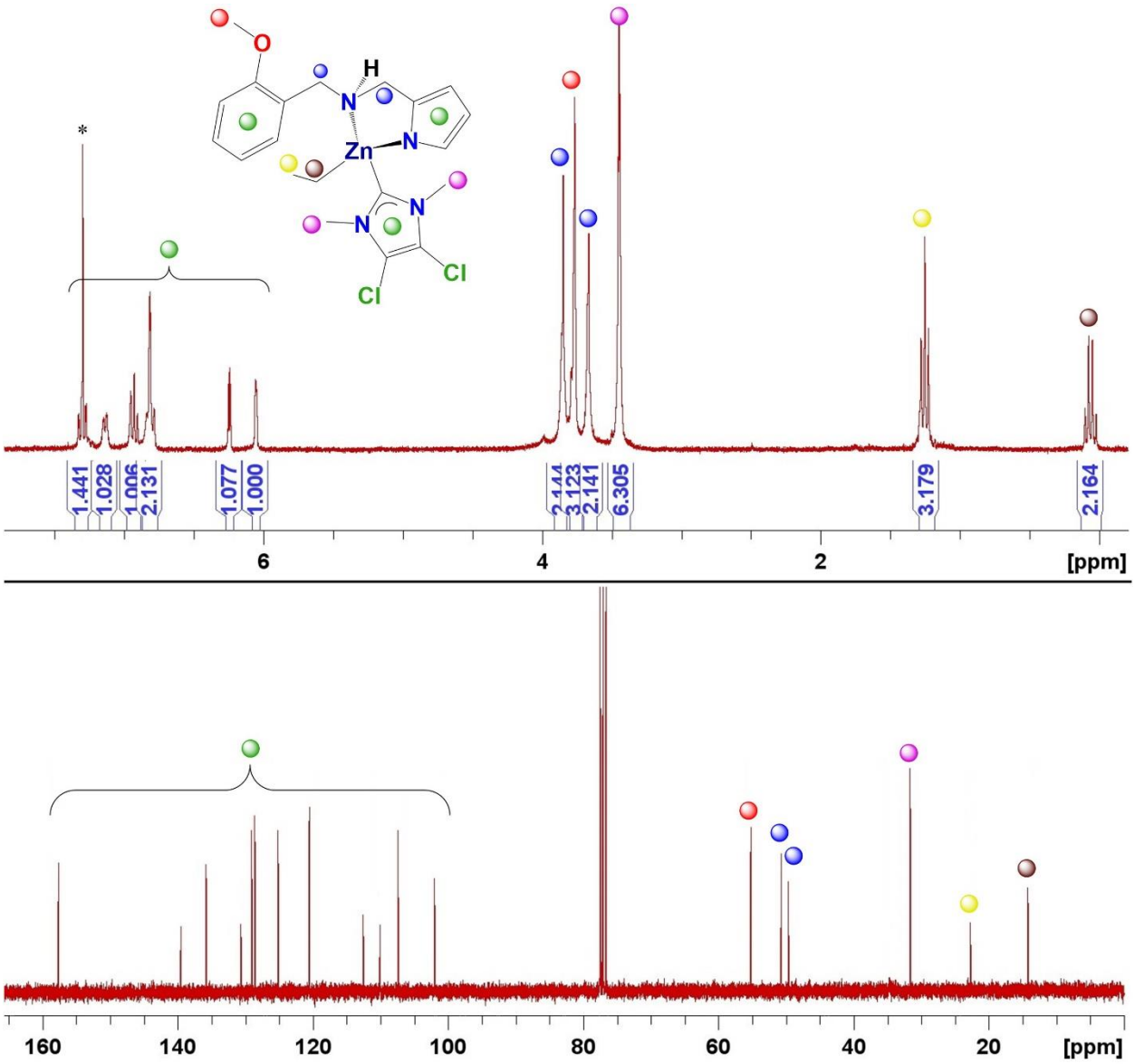

Figure A37. ^{1}H NMR (top, 300 MHz, $CDCl_3$) and $^{13}C\{^{1}H\}$ NMR spectra (bottom, 75 MHz, $CDCl_3$) of **2.9$_{Zn}$**. * indicates protic impurity in $CDCl_3$.

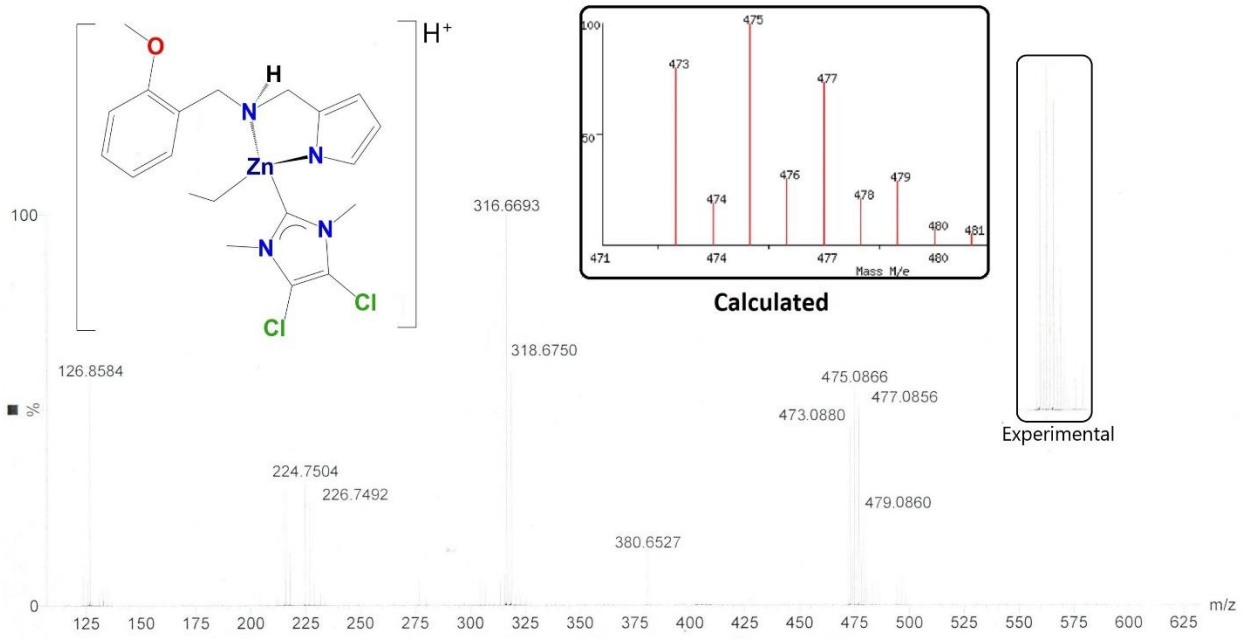

Figure A38. EI-MS spectrum of **2.9$_{Zn}$** showing $[M + H]^+$.

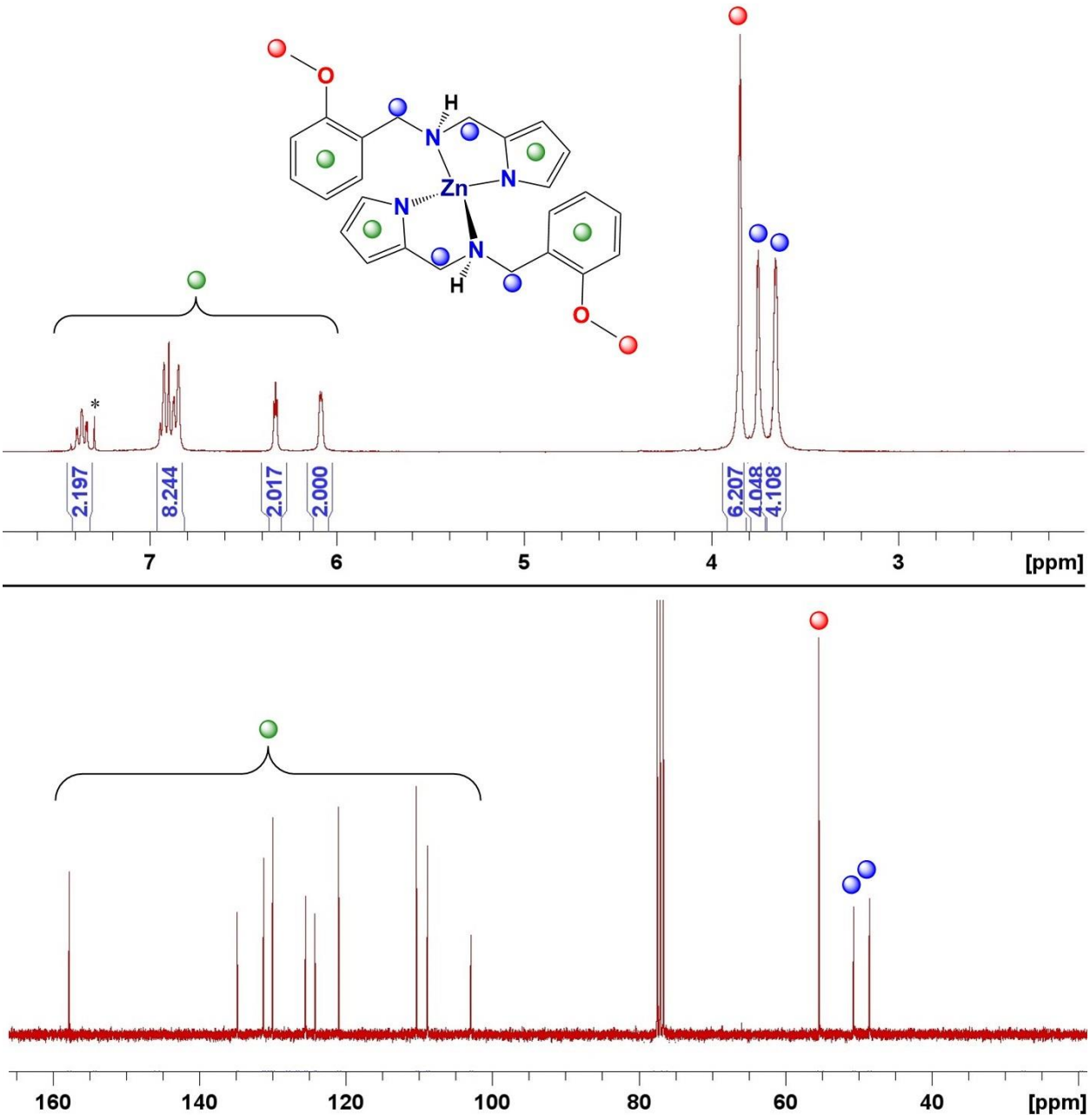

Figure A39. ^{1}H NMR (top, 300 MHz, $CDCl_3$) and $^{13}C\{^{1}H\}$ NMR spectra (bottom, 75 MHz, $CDCl_3$) of **2.10$_{Zn}$**. * indicates protic impurity in $CDCl_3$.

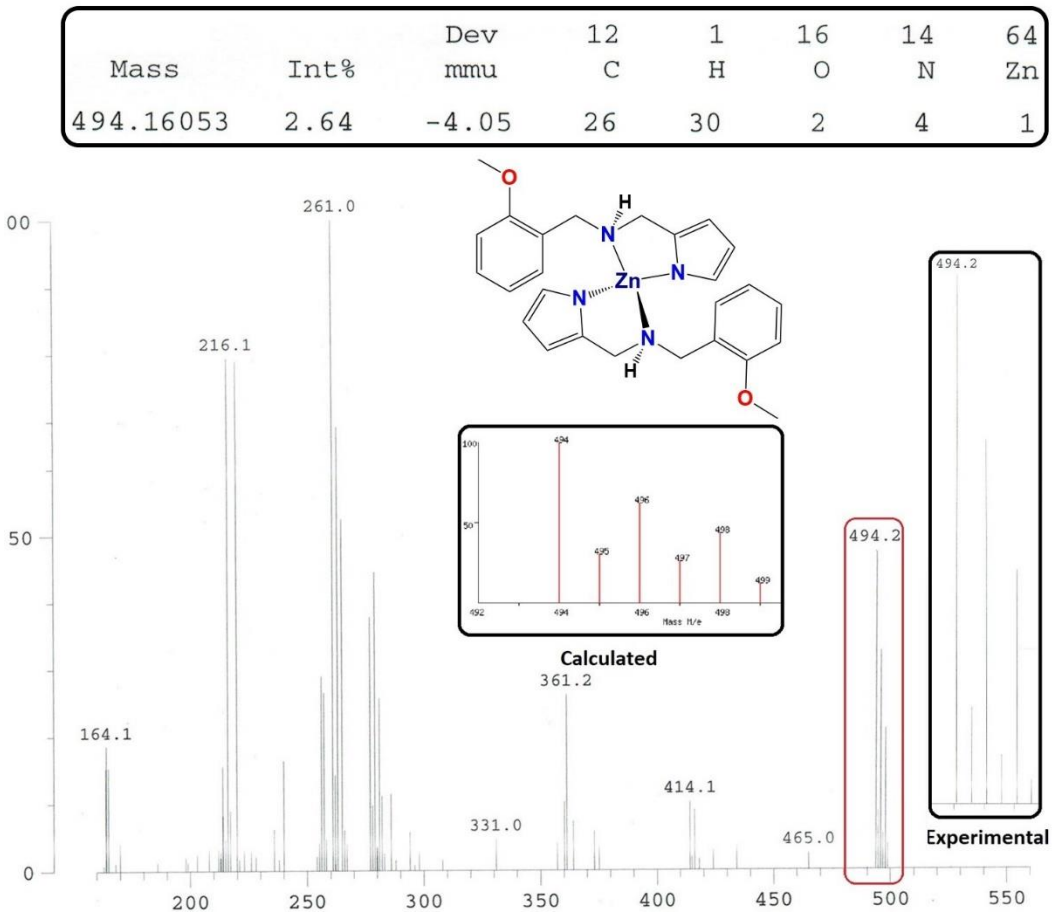

Figure A40. EI-MS spectrum of **2.8$_{Zn}$** showing [M$^+$].

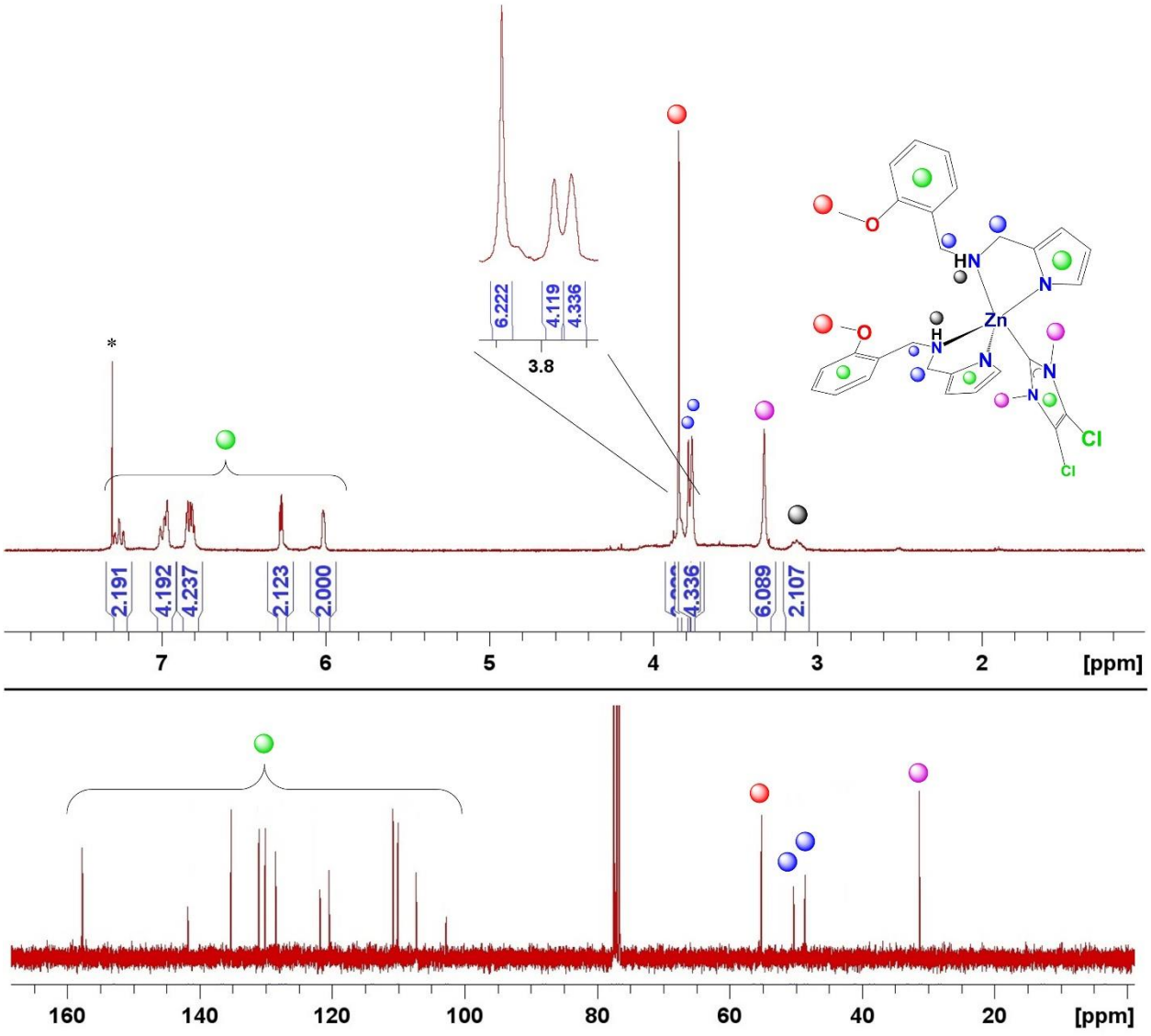

Figure A41. ^{1}H NMR (top, 300 MHz, $CDCl_3$) and $^{13}C\{^{1}H\}$ NMR spectra (bottom, 75 MHz, $CDCl_3$) of **2.11$_{Zn}$**. * indicates protic impurity in $CDCl_3$.

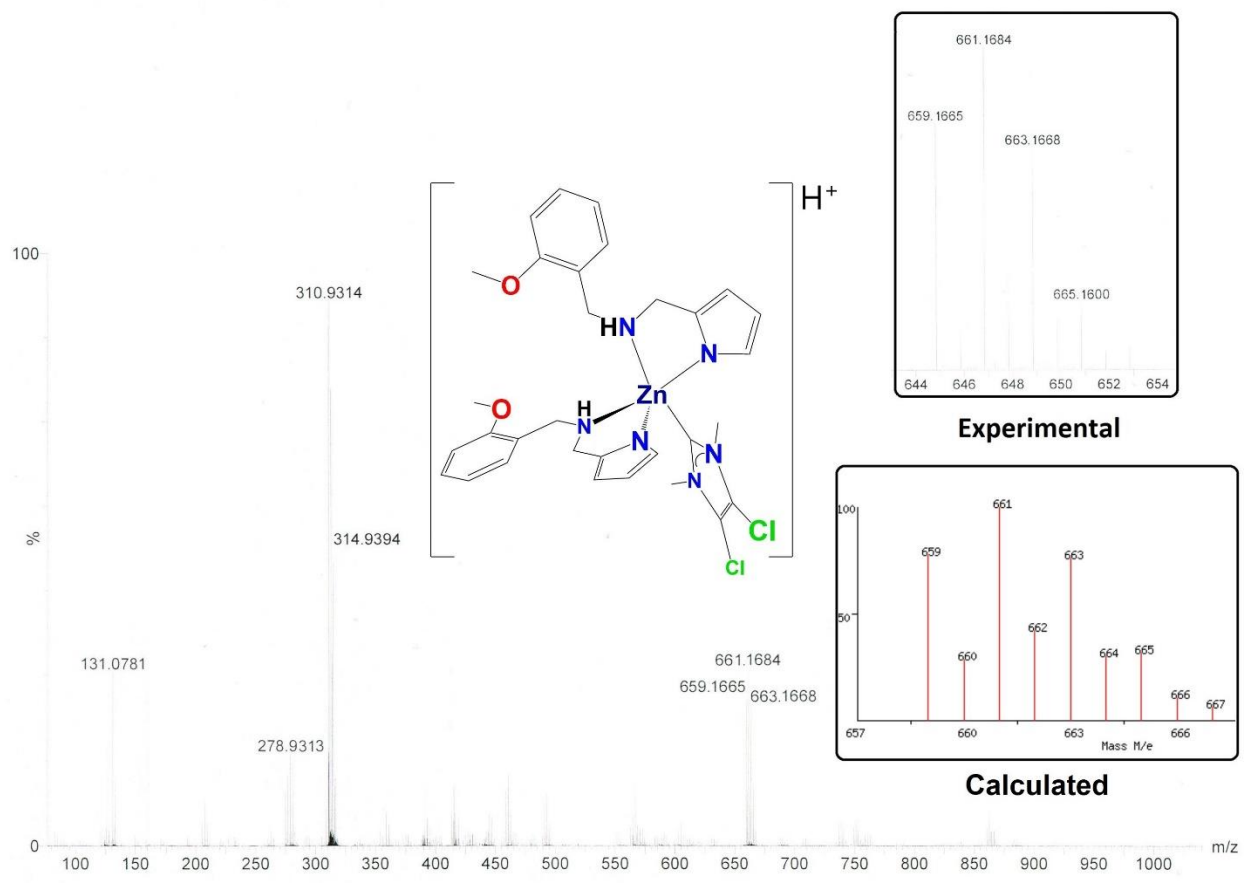

Figure A42. ESI-MS spectrum of **2.11$_{Zn}$** showing $[M+H]^+$.

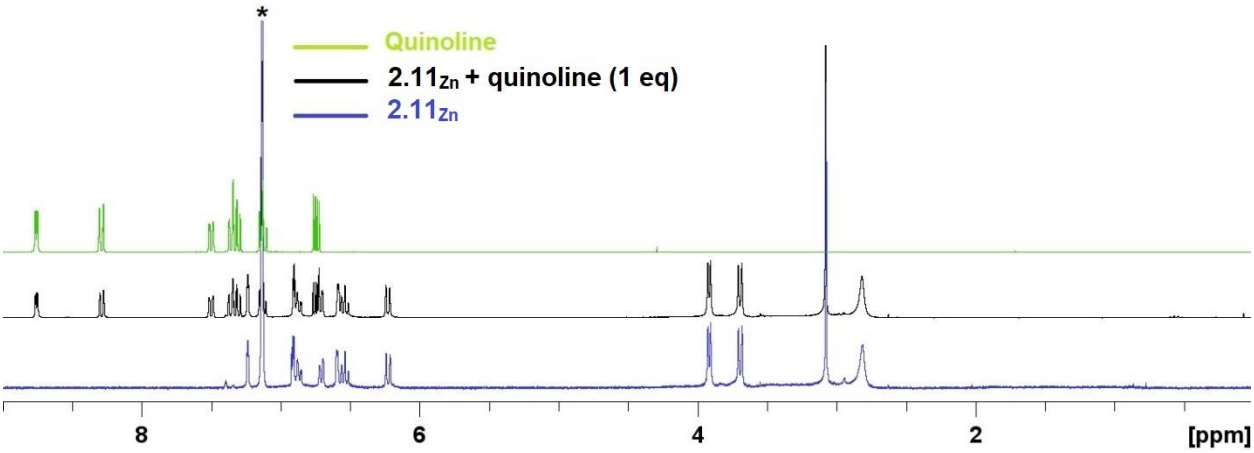

Figure A43. Stock plot of ^{1}H NMR (300 MHz, C_6D_6) spectra showing quinoline (green), stoichiometric reaction of **2.11$_{Zn}$** with quinoline (black), and **2.11$_{Zn}$** (blue). * indicates protic impurity in C_6D_6.

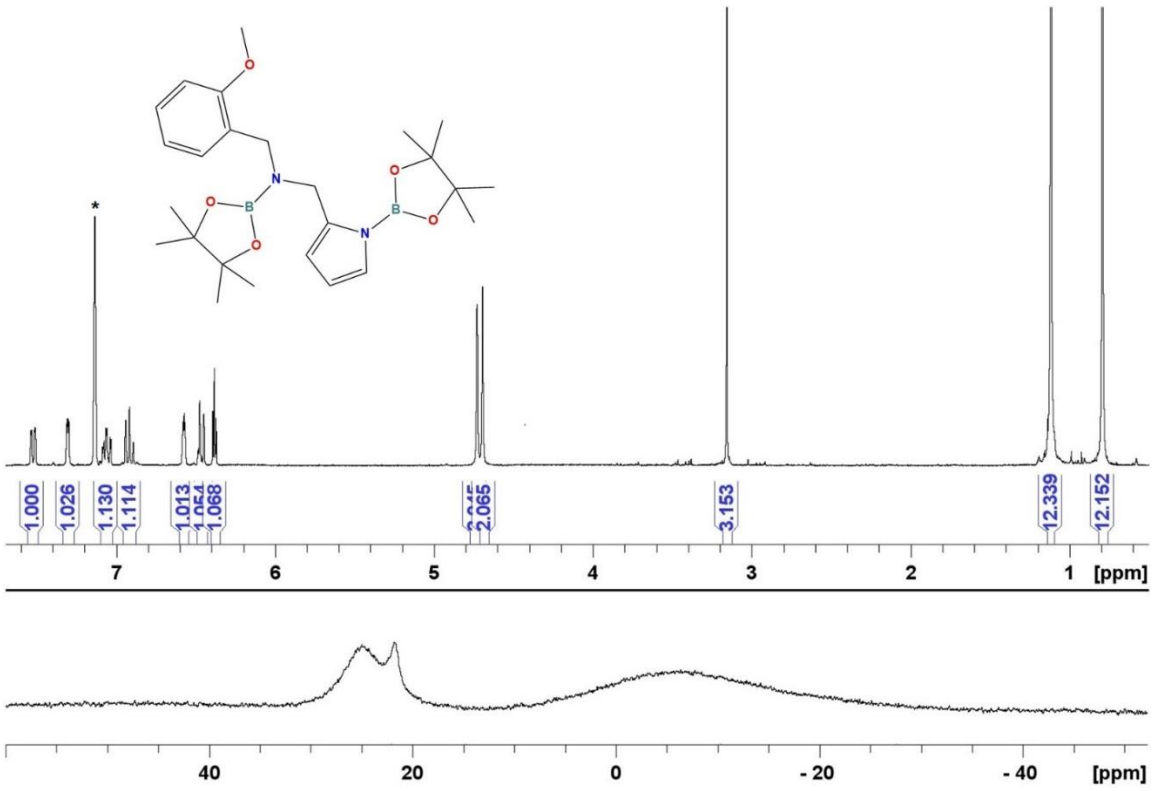

Figure A44. ^{1}H (300 MHz, C_6D_6 - top) and ^{11}B (96 MHz - bottom) NMR spectra of **$(Bpin)_2$-L3**. * indicates protic impurity in C_6D_6.

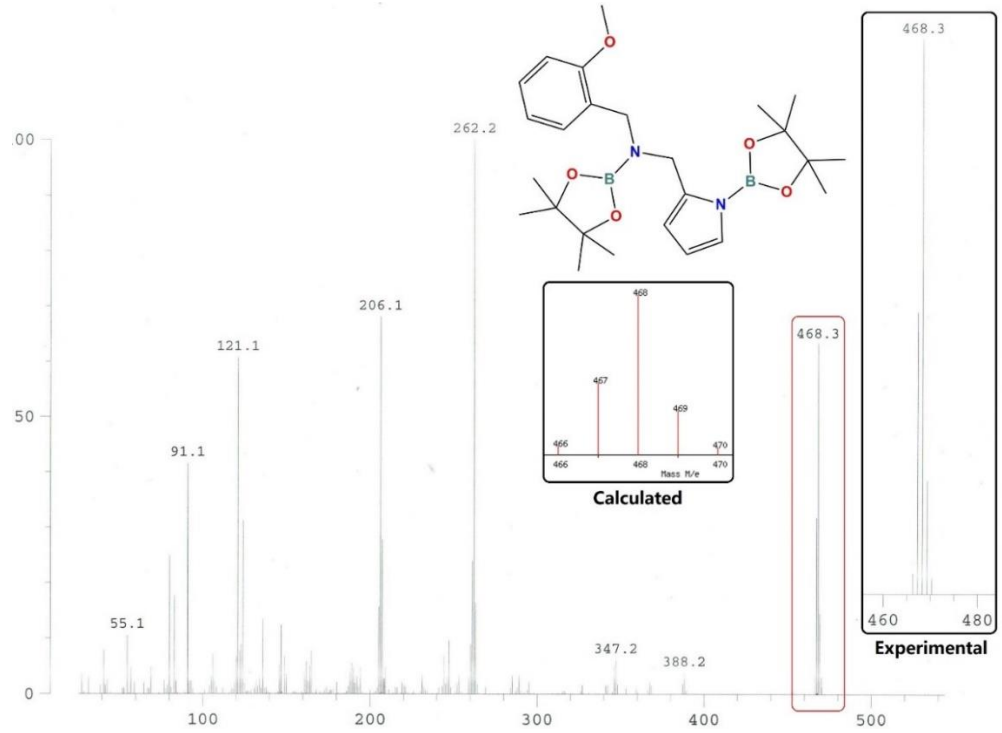

Figure A45. EI-MS spectrum of **$(Bpin)_2$-L3** [M^+].

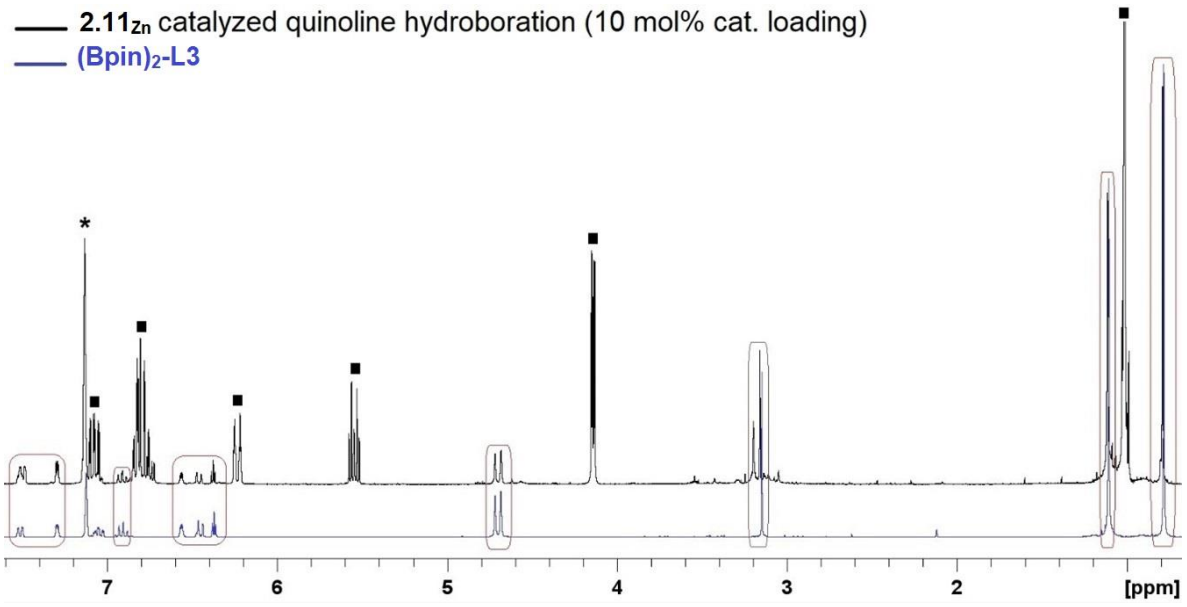

Figure A46. Stock plot of ^{1}H NMR (300 MHz, C_6D_6) spectra showing **(Bpin)$_2$-L3** (blue), and **2.11$_{Zn}$** catalyzed quinoline hydroboration reaction (black). * indicates protic impurity in C_6D_6.

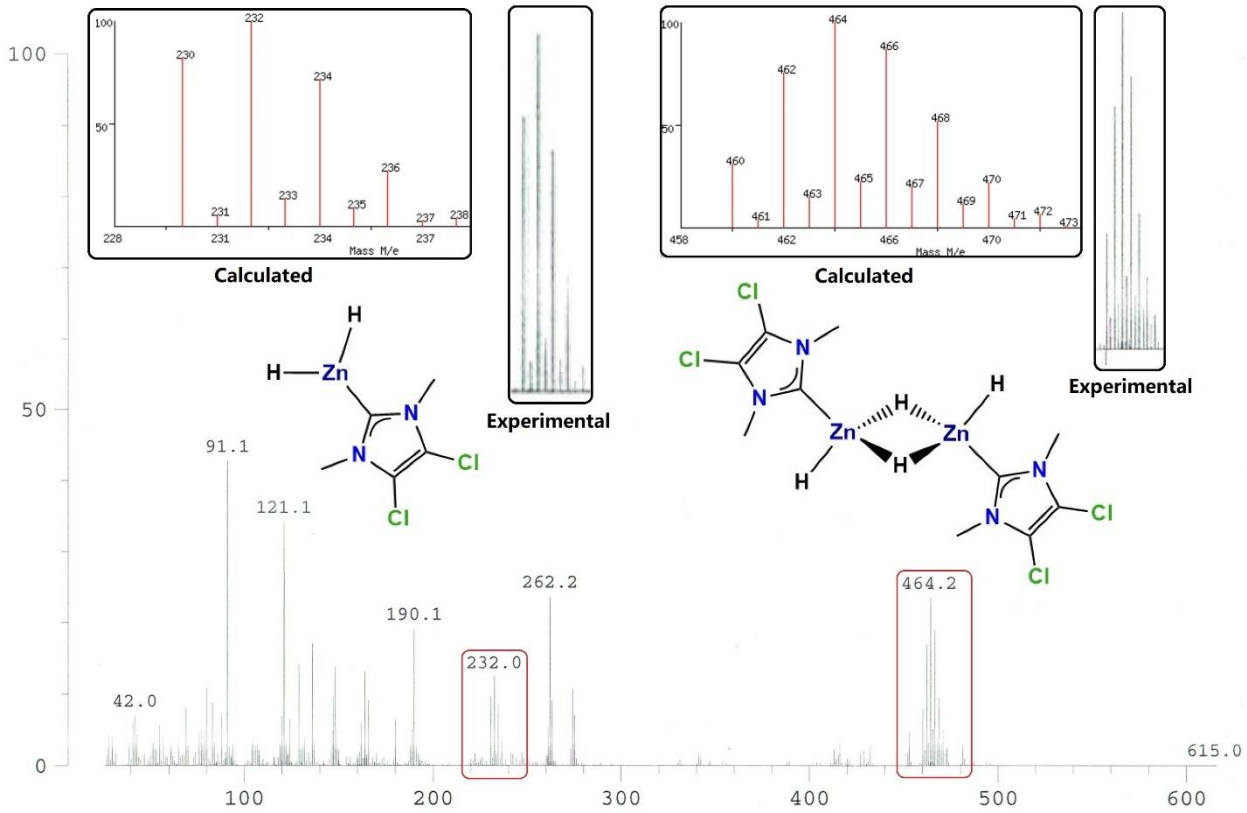

Figure A47. EI-MS spectrum of **2.12$_{Zn}$** [M^{+}].

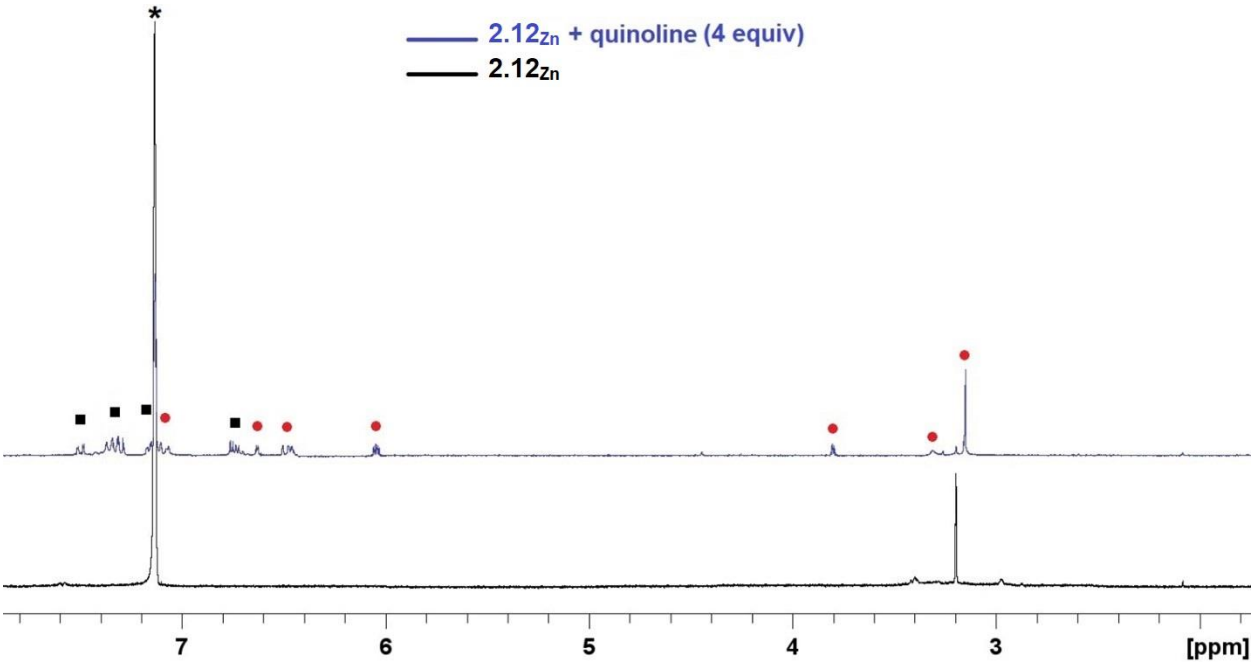

Figure A48. Stock plot of ^{1}H NMR (300 MHz, C_6D_6) spectra showing reaction of **2.12$_{Zn}$** with quinoline with ratio 1:4 (blue), and **2.12$_{Zn}$** (black). ■ indicates free quinoline, ● indicates product of the reaction and * indicates protic impurity in C_6D_6.

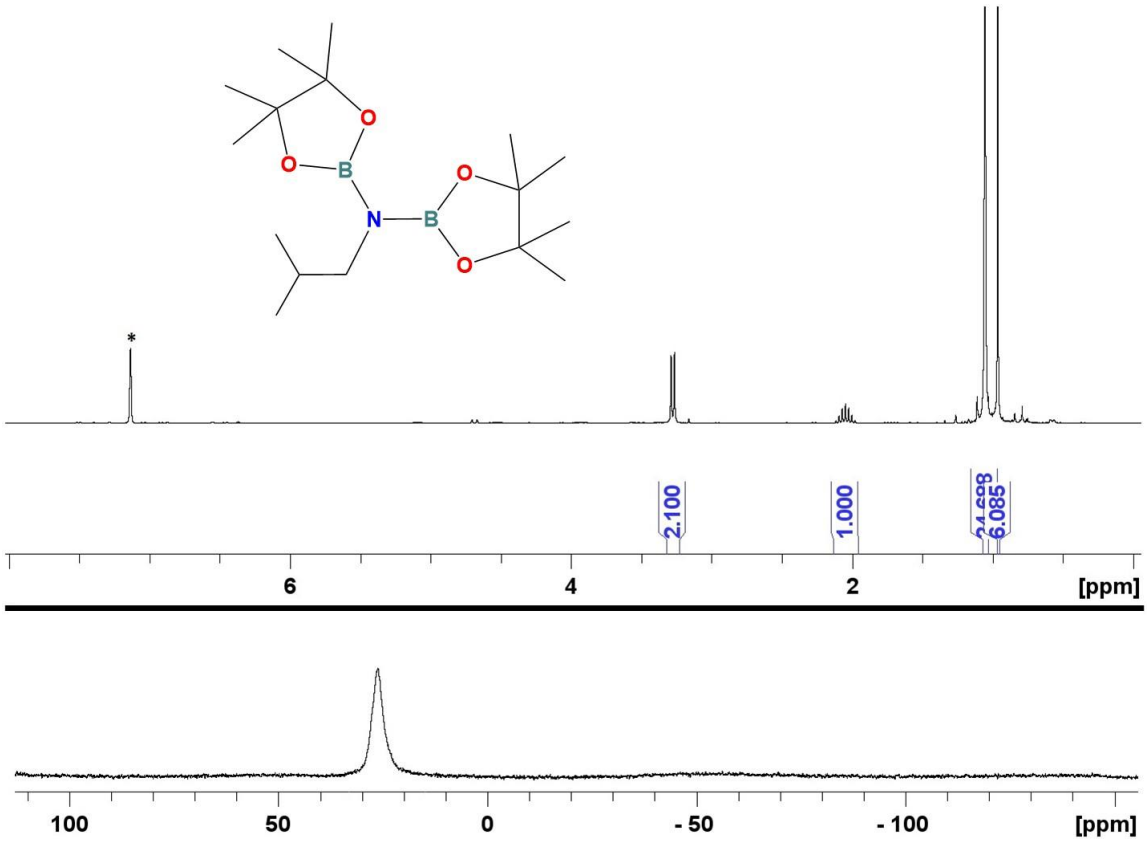

Figure A49. ^{1}H (300 MHz, C_6D_6 - top) and ^{11}B (96 MHz - bottom) NMR spectra of isobutyronitrile hydroboration product. * indicates protic impurity in C_6D_6.

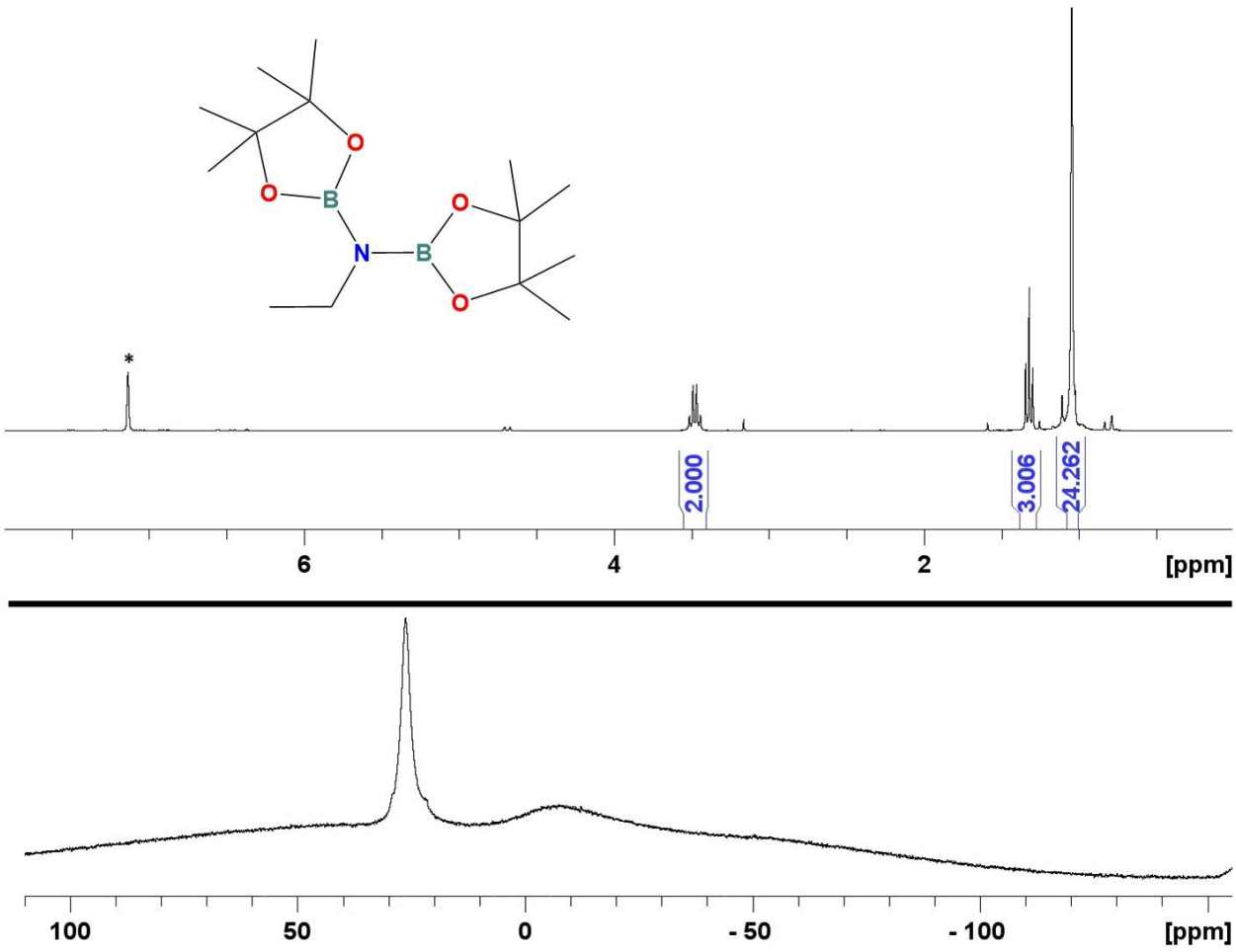

Figure A50. ^{1}H (300 MHz, C_6D_6 - top) and ^{11}B (96 MHz - bottom) NMR spectra of acetonitrile hydroboration product. * indicates protic impurity in C_6D_6.

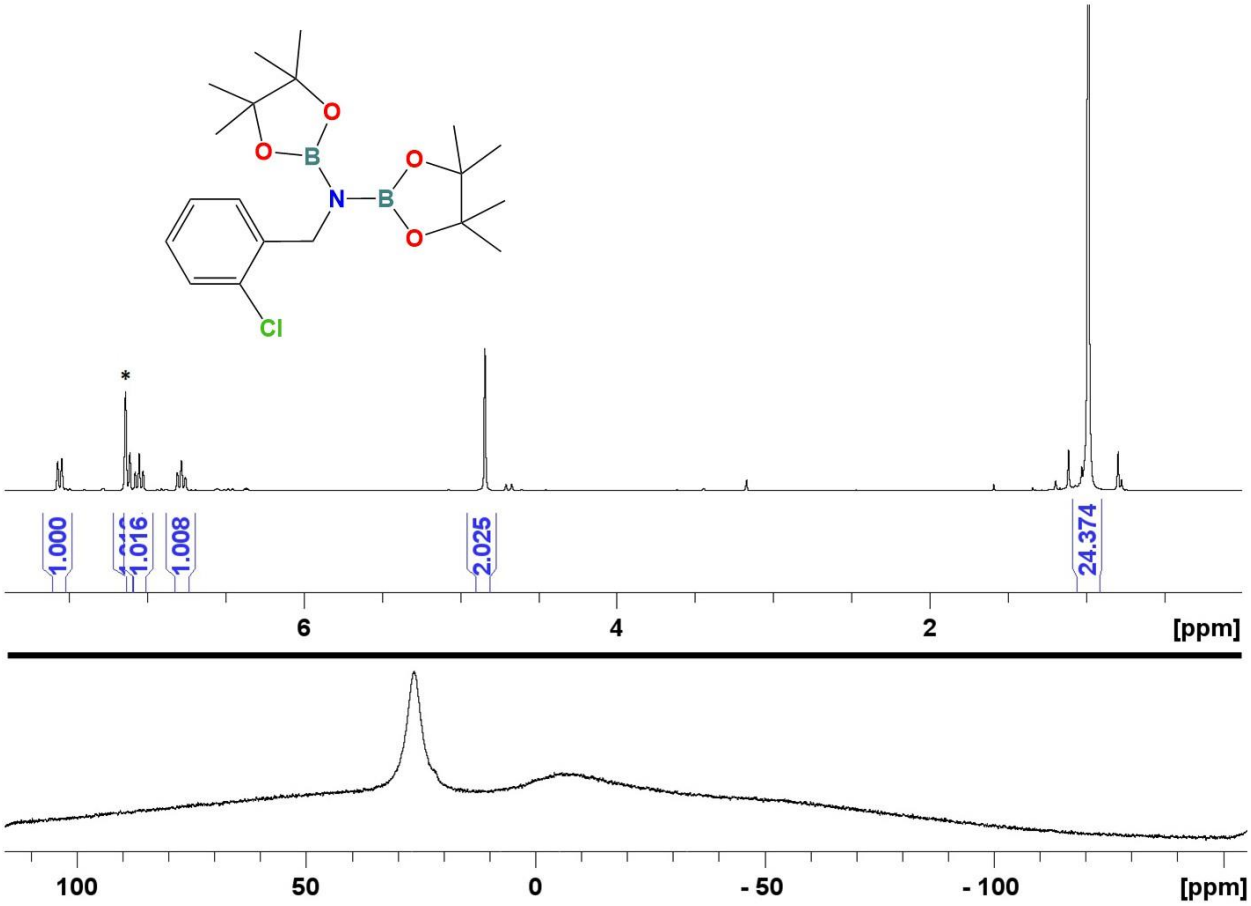

Figure A51. ^{1}H (300 MHz, C_6D_6 - top) and ^{11}B (96 MHz - bottom) NMR spectra of 2-chloro-benzonitrile hydroboration product. * indicates protic impurity in C_6D_6.

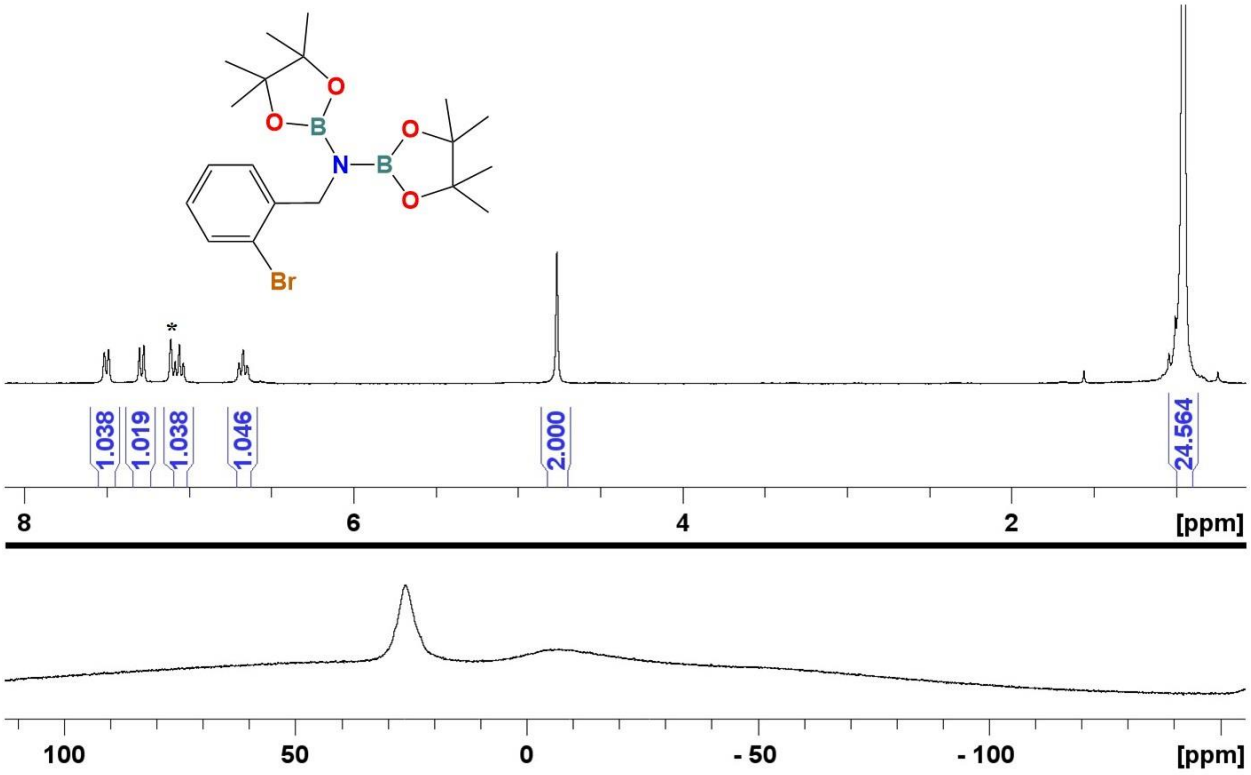

Figure A52. ^{1}H (300 MHz, C_6D_6 - top) and ^{11}B (96 MHz - bottom) NMR spectra of 2-bromo-benzonitrile hydroboration product. * indicates protic impurity in C_6D_6.

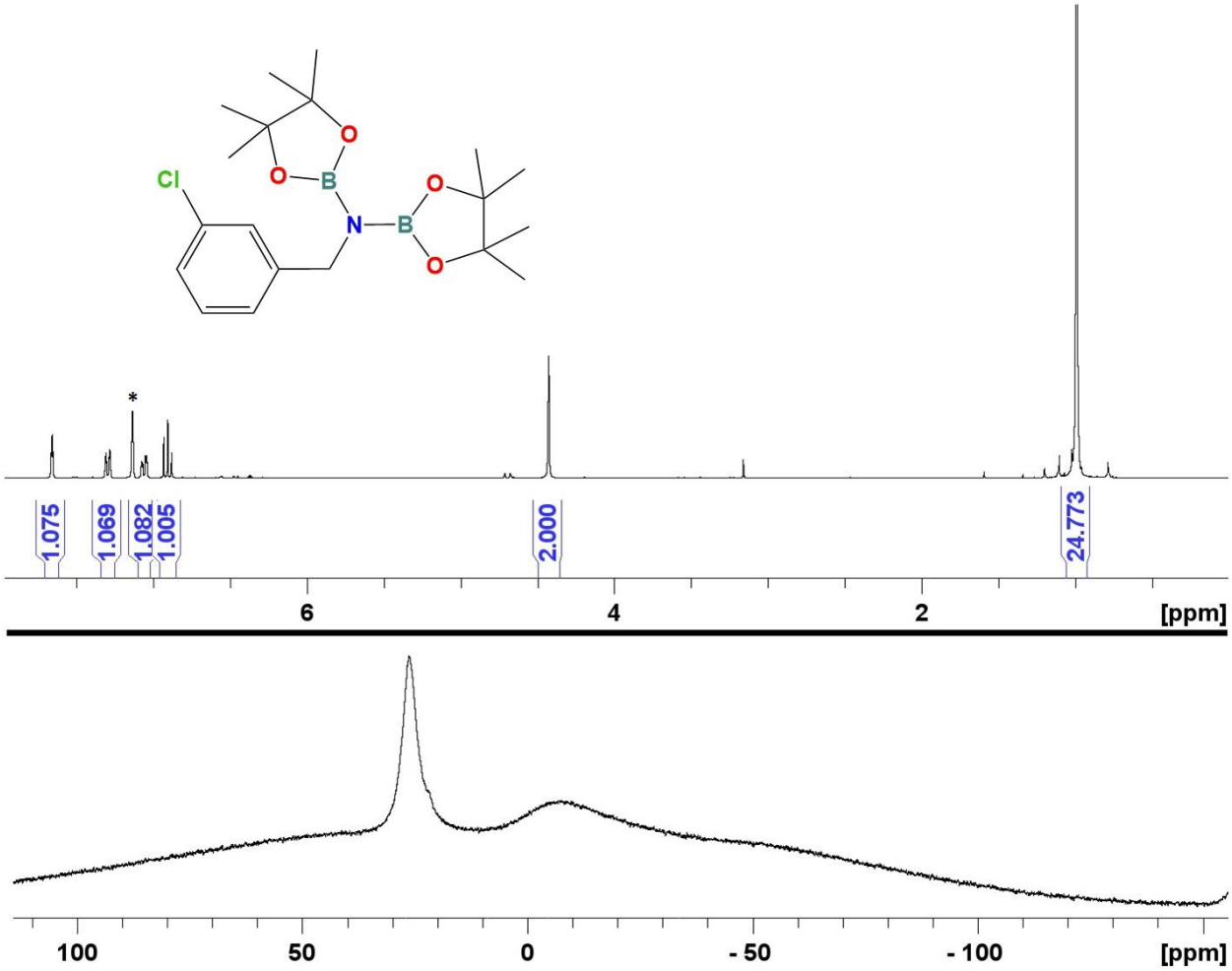

Figure A53. ^{1}H (300 MHz, C_6D_6 - top) and ^{11}B (96 MHz - bottom) NMR spectra of 3-chloro-benzonitrile hydroboration product. * indicates protic impurity in C_6D_6.

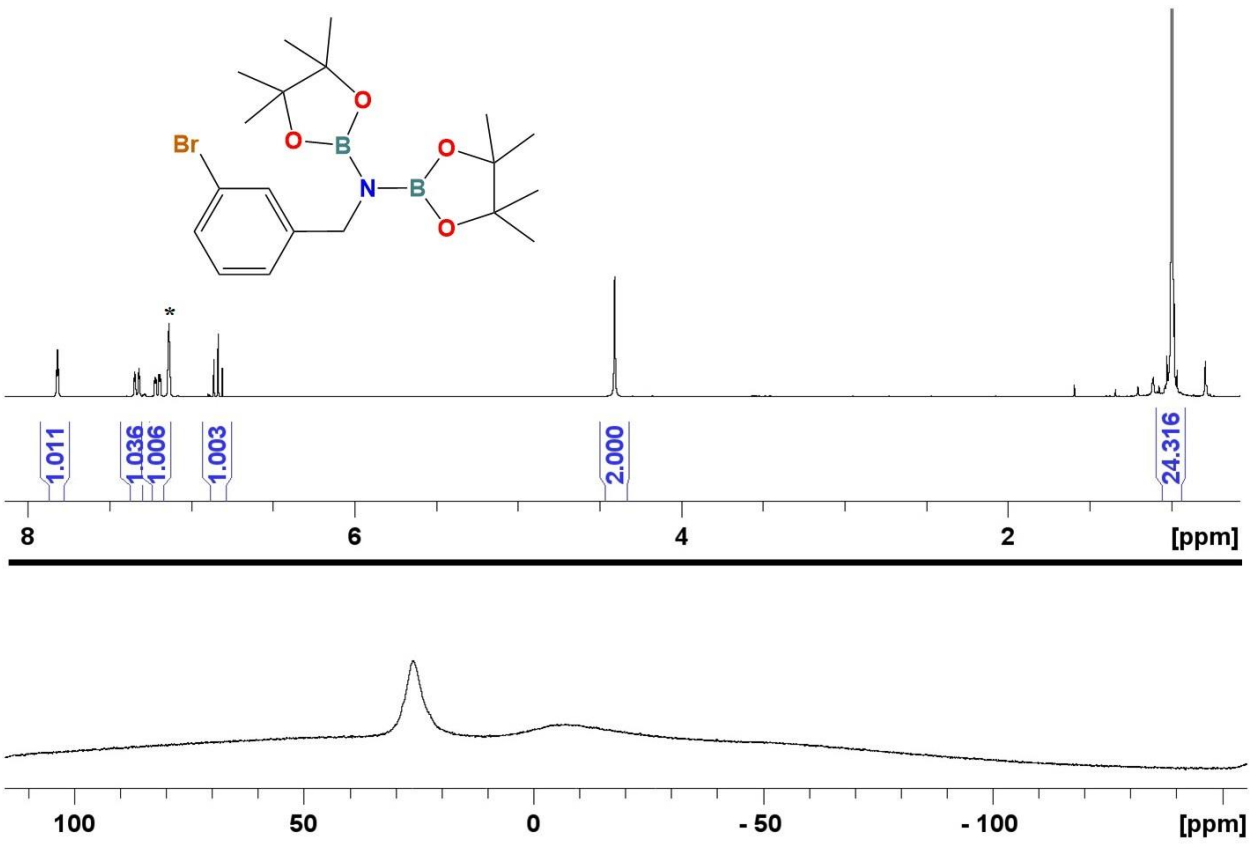

Figure A54. ^{1}H (300 MHz, C_6D_6 - top) and ^{11}B (96 MHz - bottom) NMR spectra of 3-bromo-benzonitrile hydroboration product. * indicates protic impurity in C_6D_6.

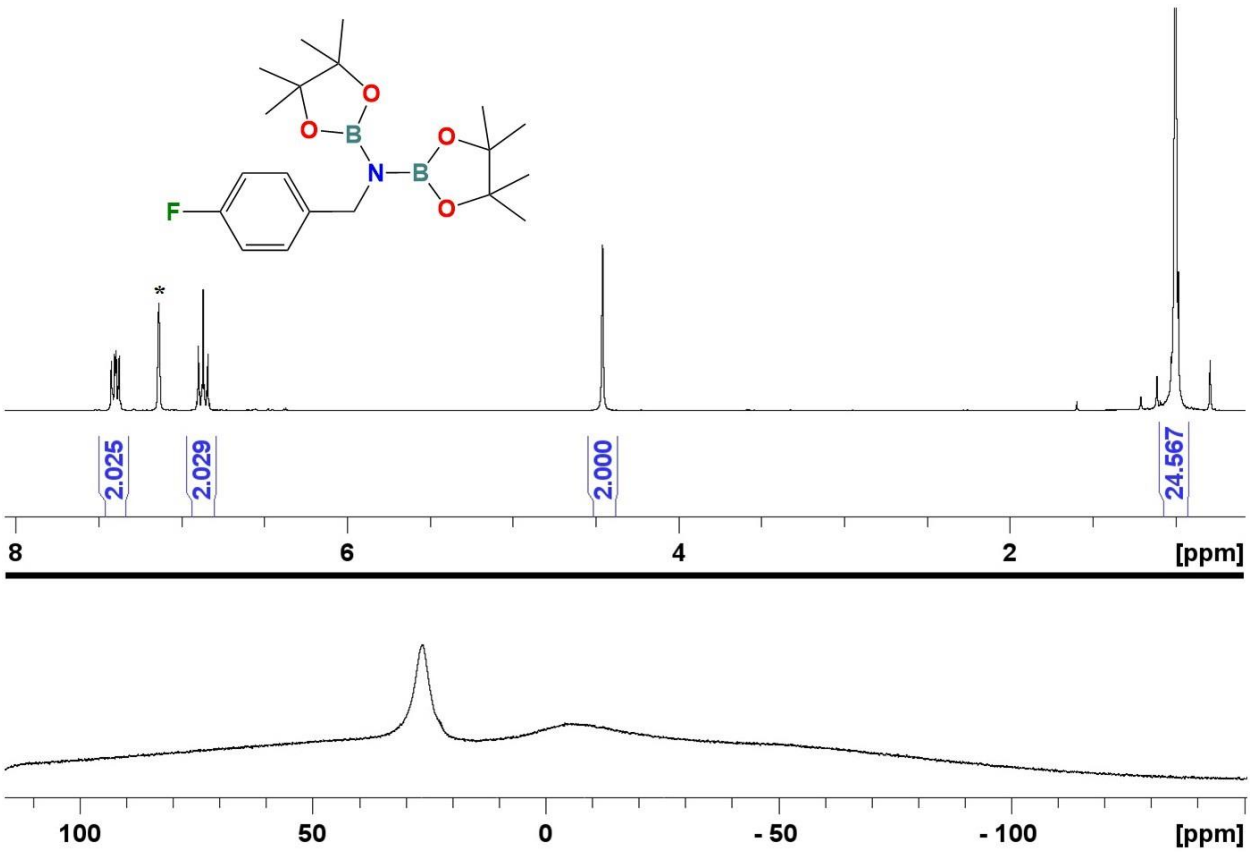

Figure A55. ^{1}H (300 MHz, C_6D_6 - top) and ^{11}B (96 MHz - bottom) NMR spectra of 4-fluoro-benzonitrile hydroboration product. * indicates protic impurity in C_6D_6.

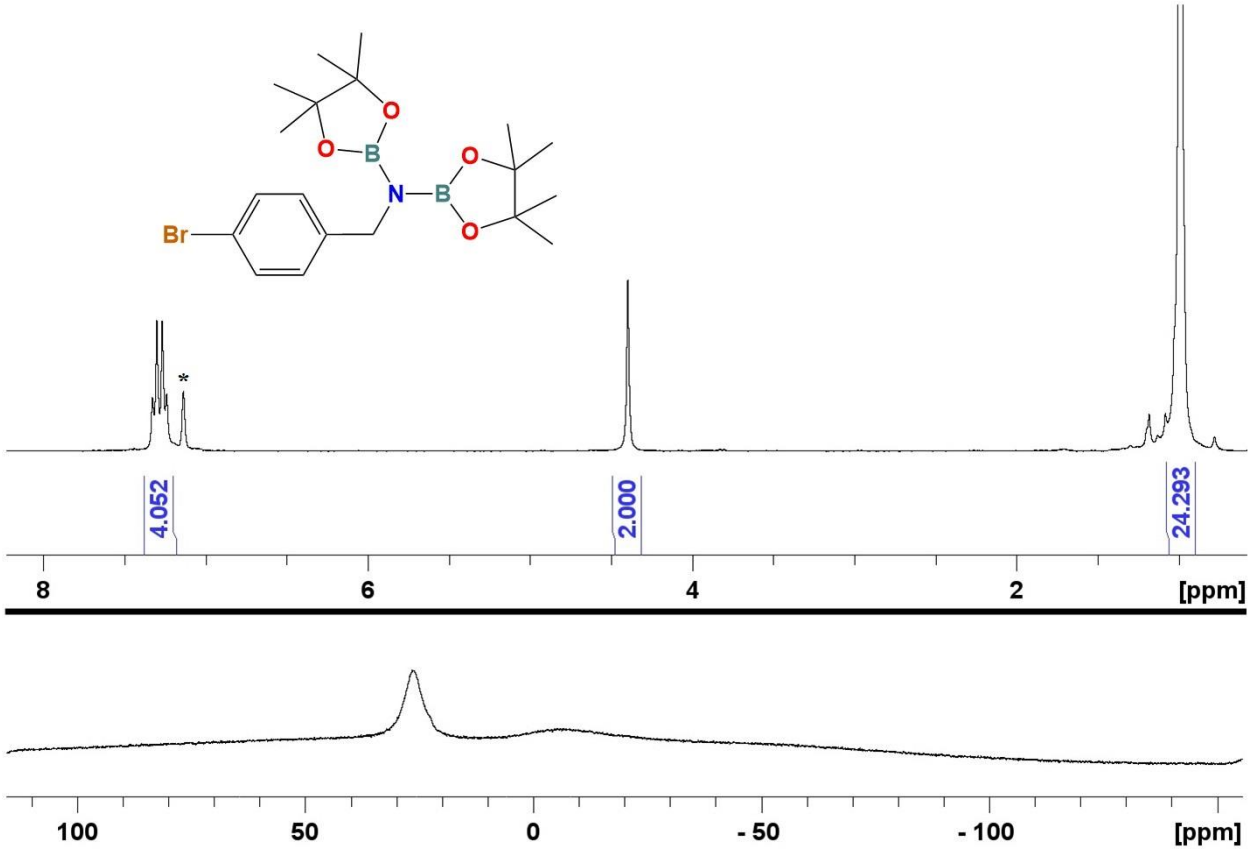

Figure A56. ^{1}H (300 MHz, C_6D_6 - top) and ^{11}B (96 MHz - bottom) NMR spectra of 4-bromo-benzonitrile hydroboration product. * indicates protic impurity in C_6D_6.

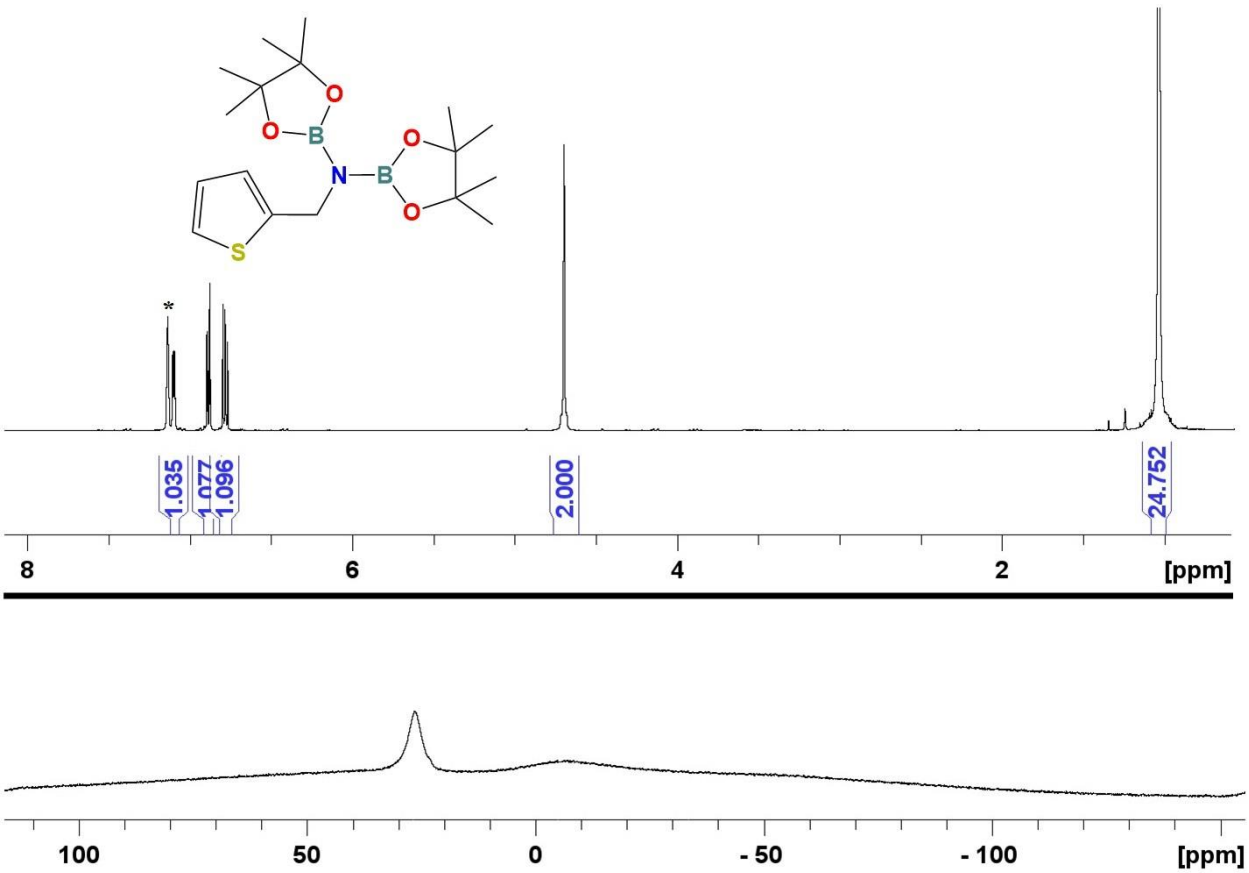

Figure A57. ^{1}H (300 MHz, C_6D_6 - top) and ^{11}B (96 MHz - bottom) NMR spectra of 2-cyano-thiophene hydroboration product. * indicates protic impurity in C_6D_6.

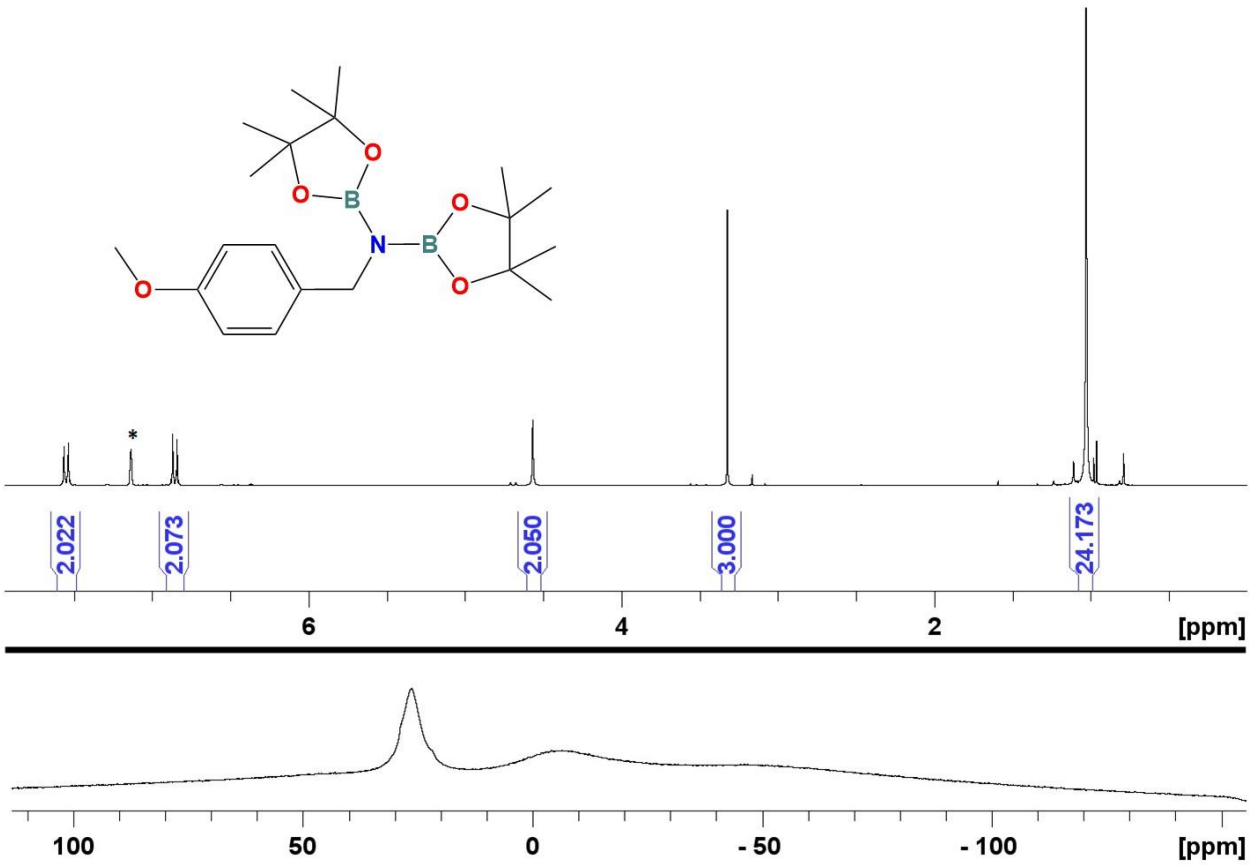

Figure A58. ^{1}H (300 MHz, C_6D_6 - top) and ^{11}B (96 MHz - bottom) NMR spectra of 4-methoxy-benzonitrile hydroboration product. * indicates protic impurity in C_6D_6.

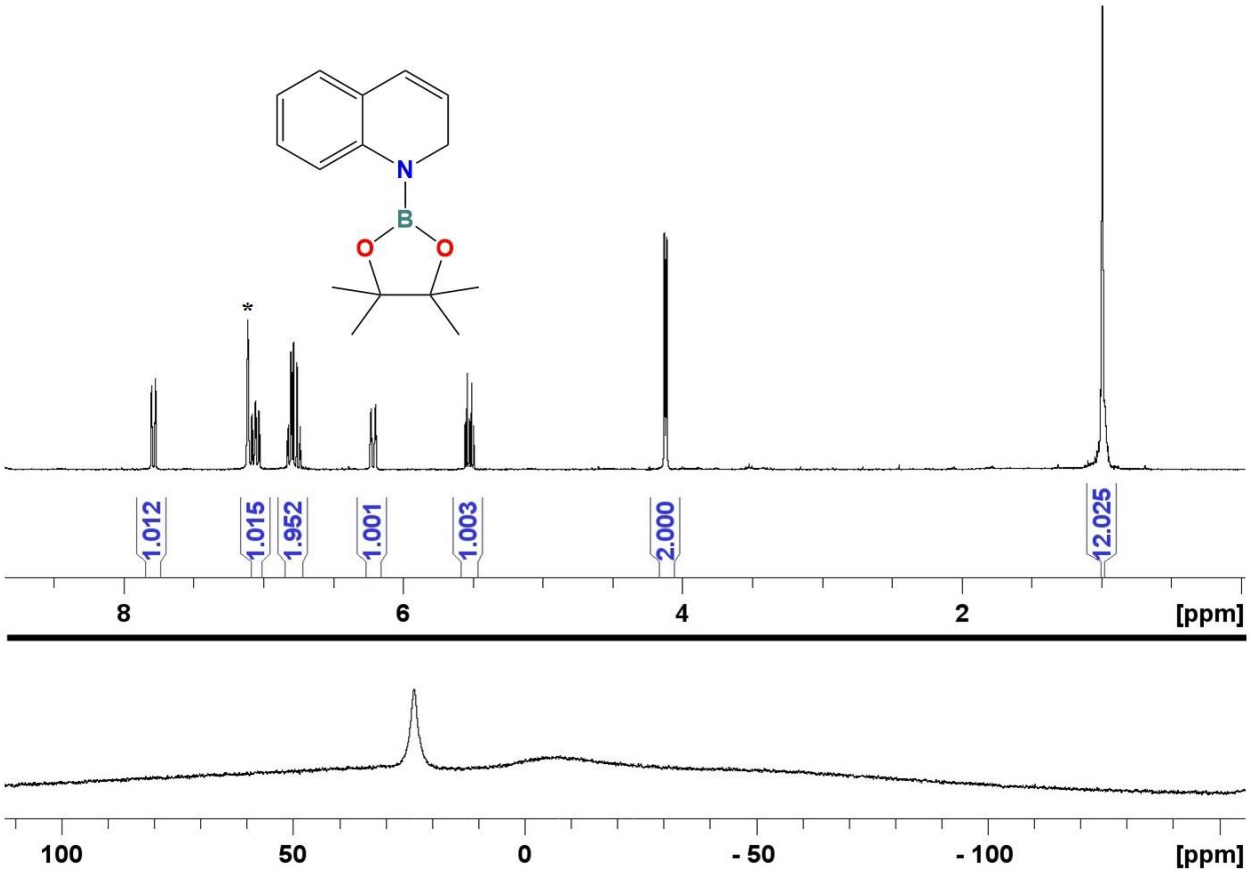

Figure A59. ^{1}H (300 MHz, C_6D_6 - top) and ^{11}B (96 MHz - bottom) NMR spectra of quinoline hydroboration product. * indicates protic impurity in C_6D_6.

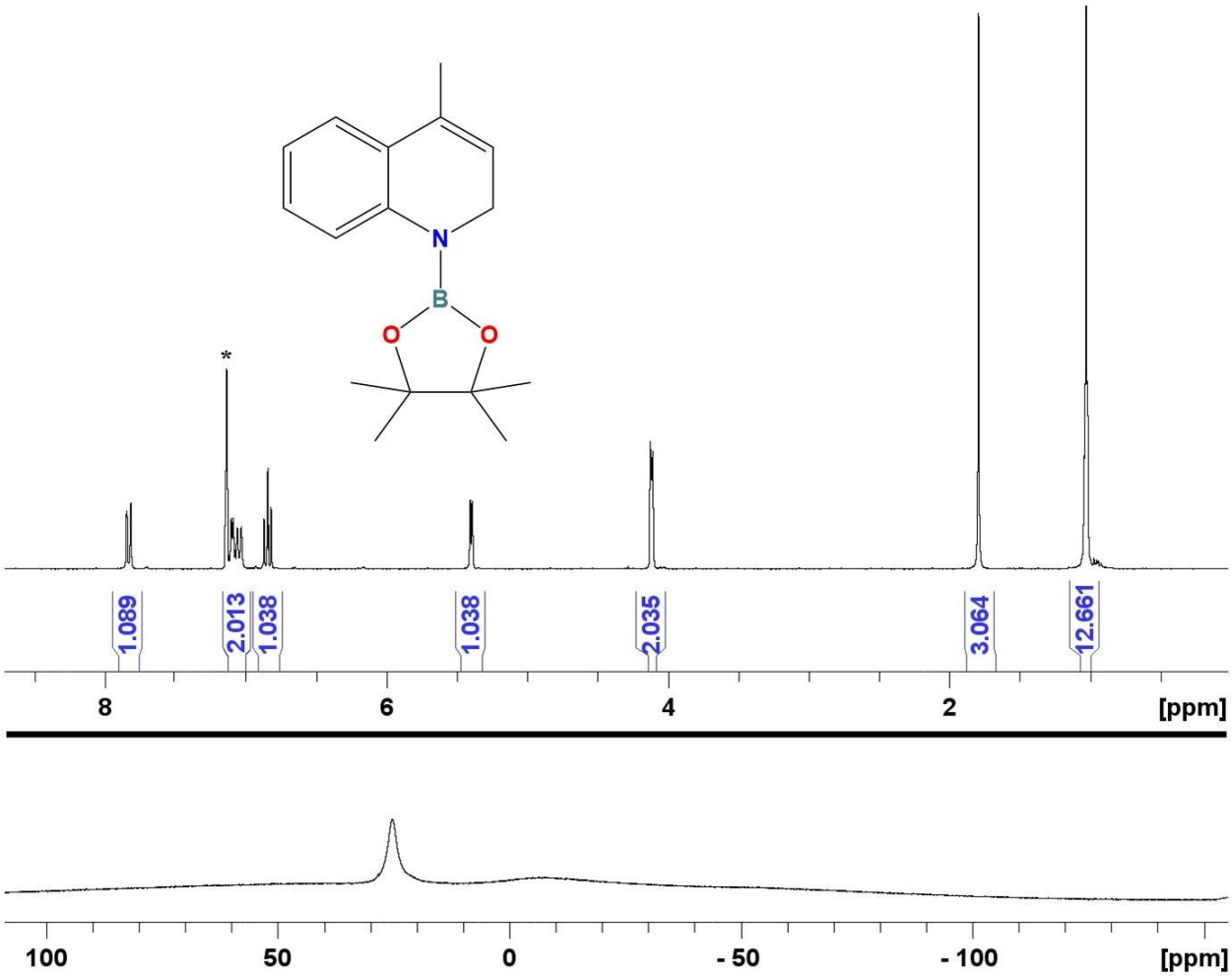

Figure A60. ^{1}H (300 MHz, C_6D_6 - top) and ^{11}B (96 MHz - bottom) NMR spectra of 4-methyl-quinoline hydroboration product. * indicates protic impurity in C_6D_6.

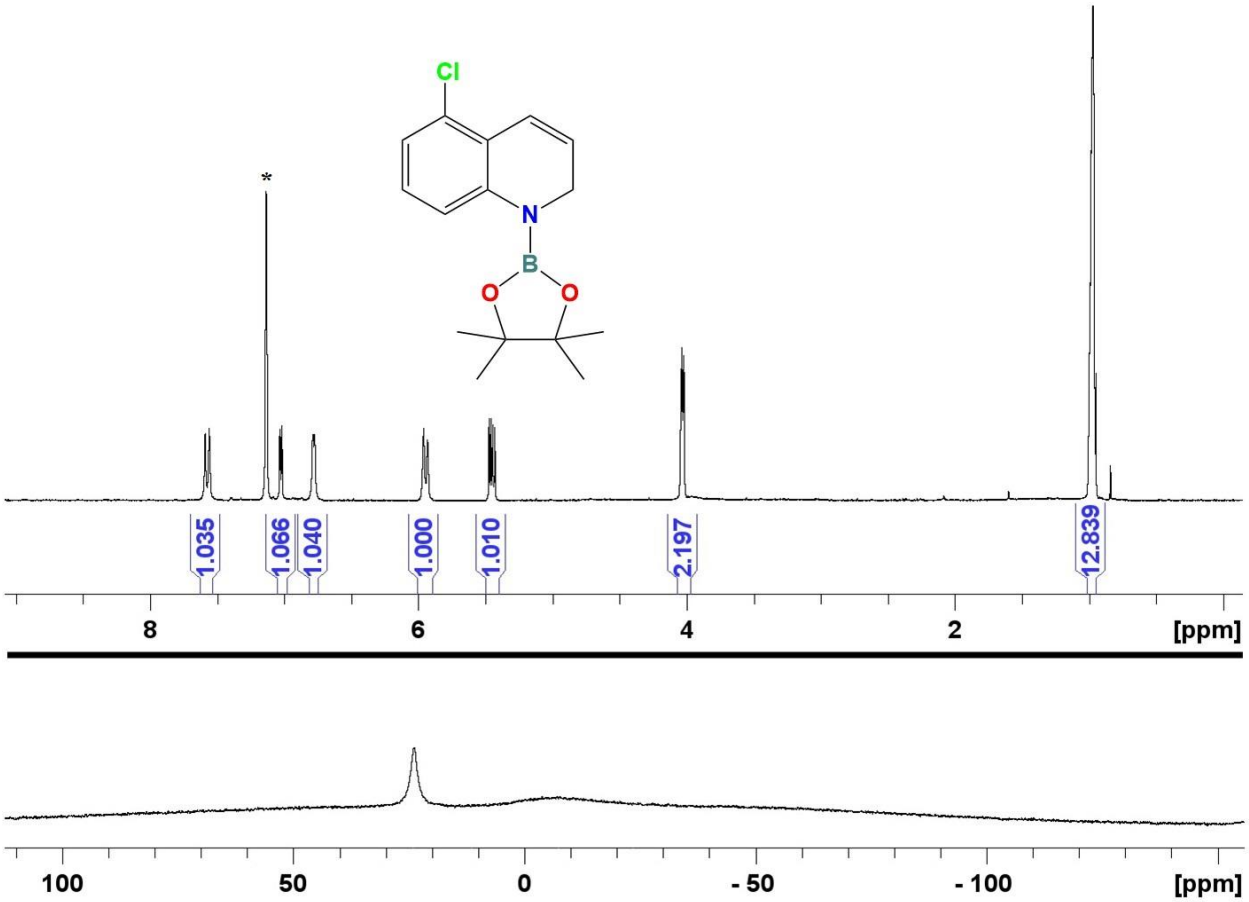

Figure A61. ^{1}H (300 MHz, C_6D_6 - top) and ^{11}B (96 MHz - bottom) NMR spectra of 6-chloro-quinoline hydroboration product. * indicates protic impurity in C_6D_6.

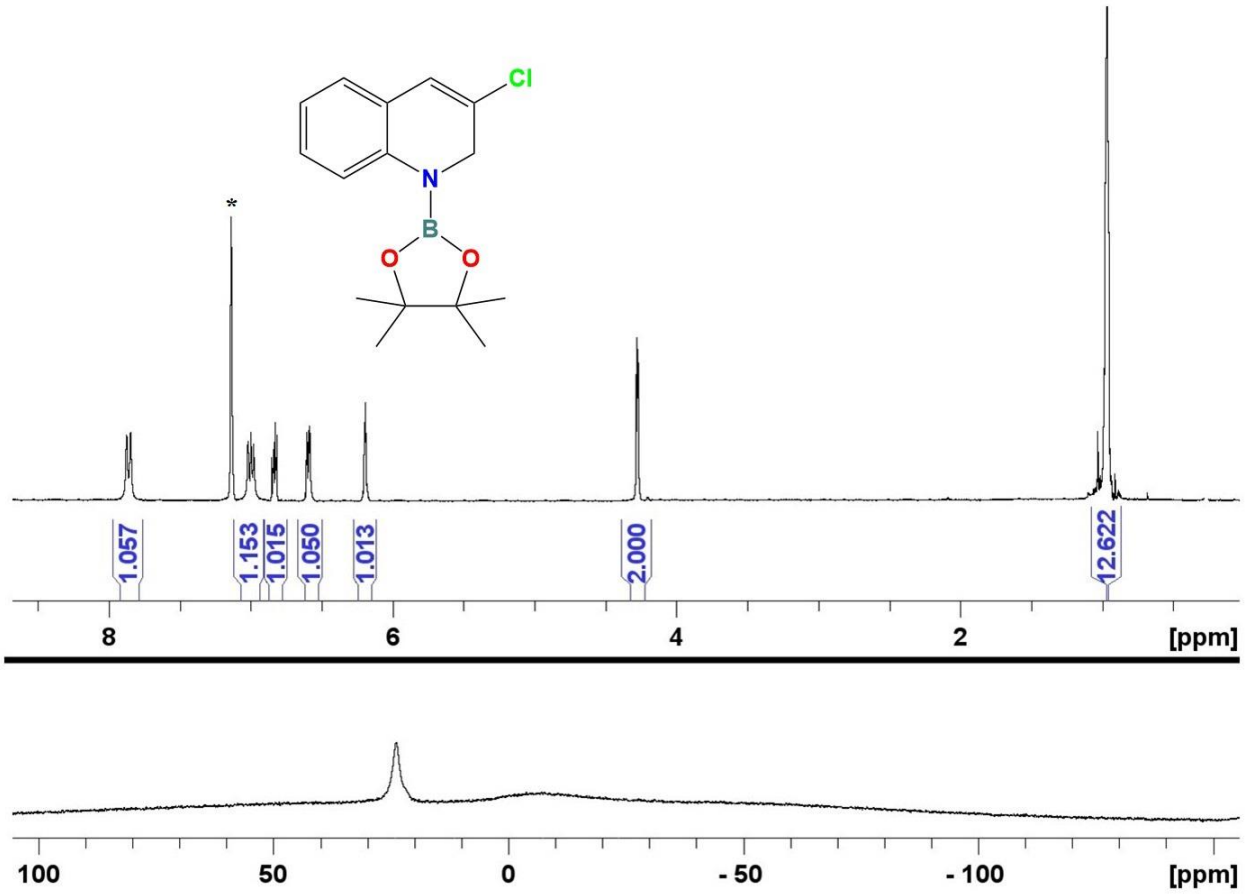

Figure A62. ^{1}H (300 MHz, C_6D_6 - top) and ^{11}B (96 MHz - bottom) NMR spectra of 3-chloro-quinoline hydroboration product. * indicates protic impurity in C_6D_6.

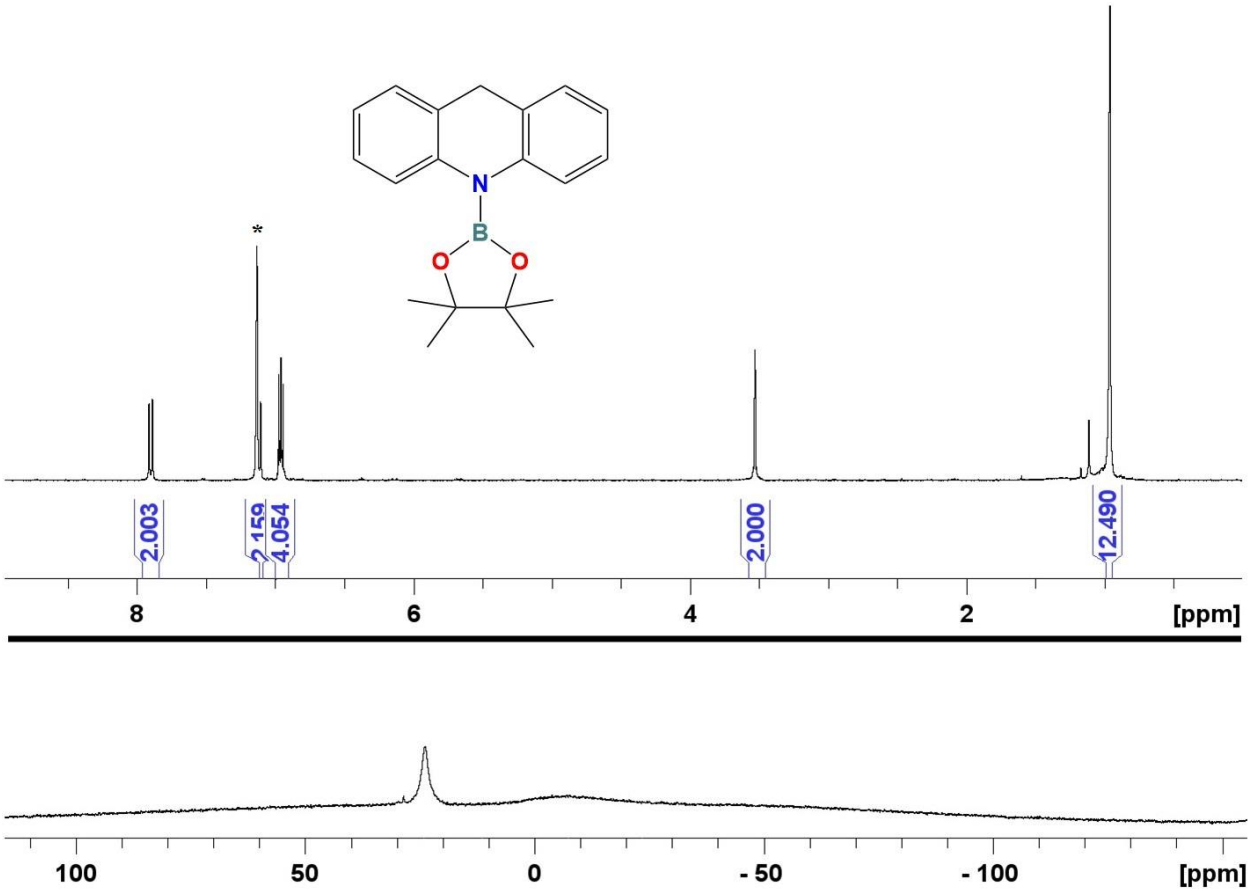

Figure A63. ^{1}H (300 MHz, C_6D_6 - top) and ^{11}B (96 MHz - bottom) NMR spectra of acridine hydroboration product. * indicates protic impurity in C_6D_6.

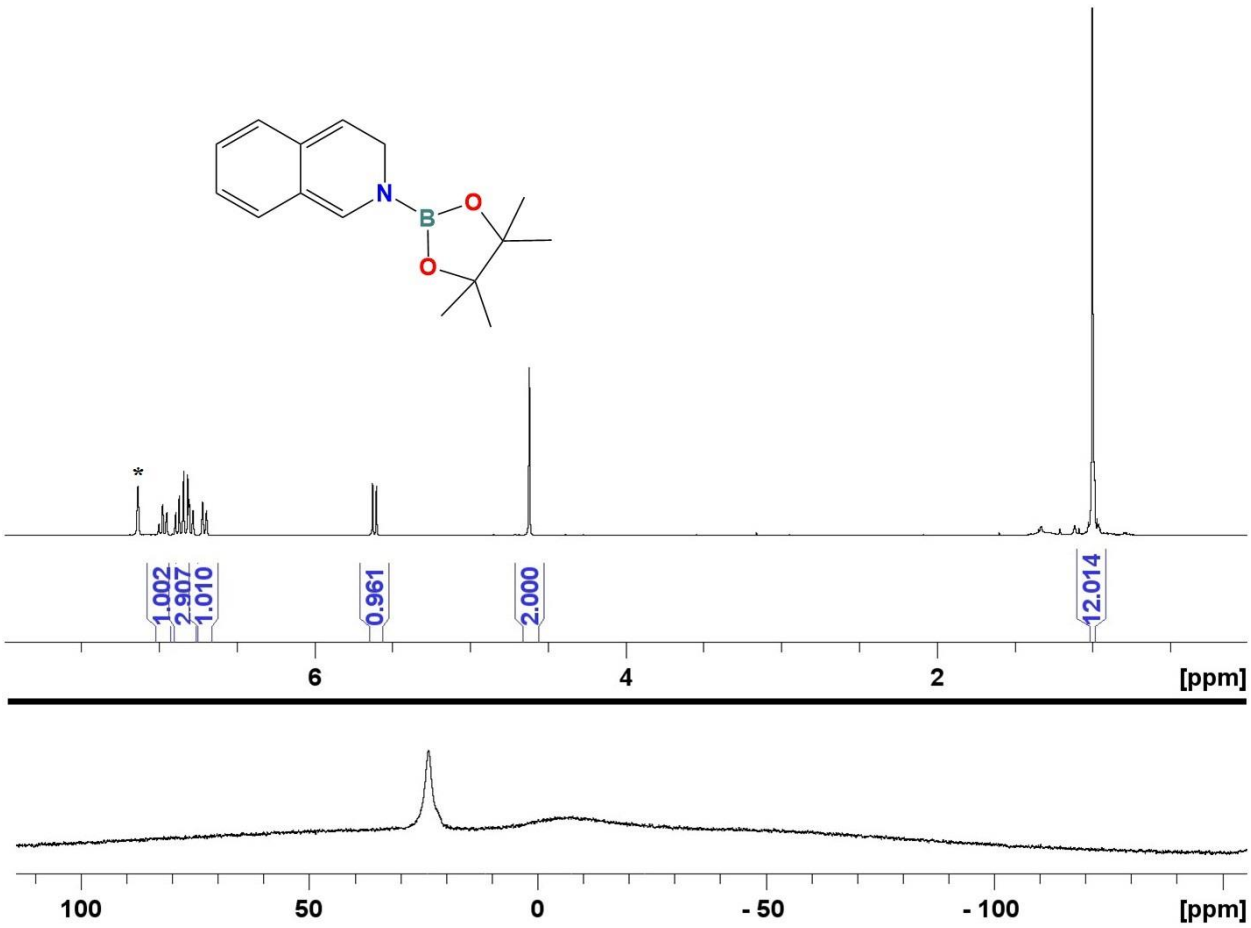

Figure A64. ^{1}H (300 MHz, C_6D_6 - top) and ^{11}B (96 MHz - bottom) NMR spectra of iso-quinoline hydroboration product. * indicates protic impurity in C_6D_6.

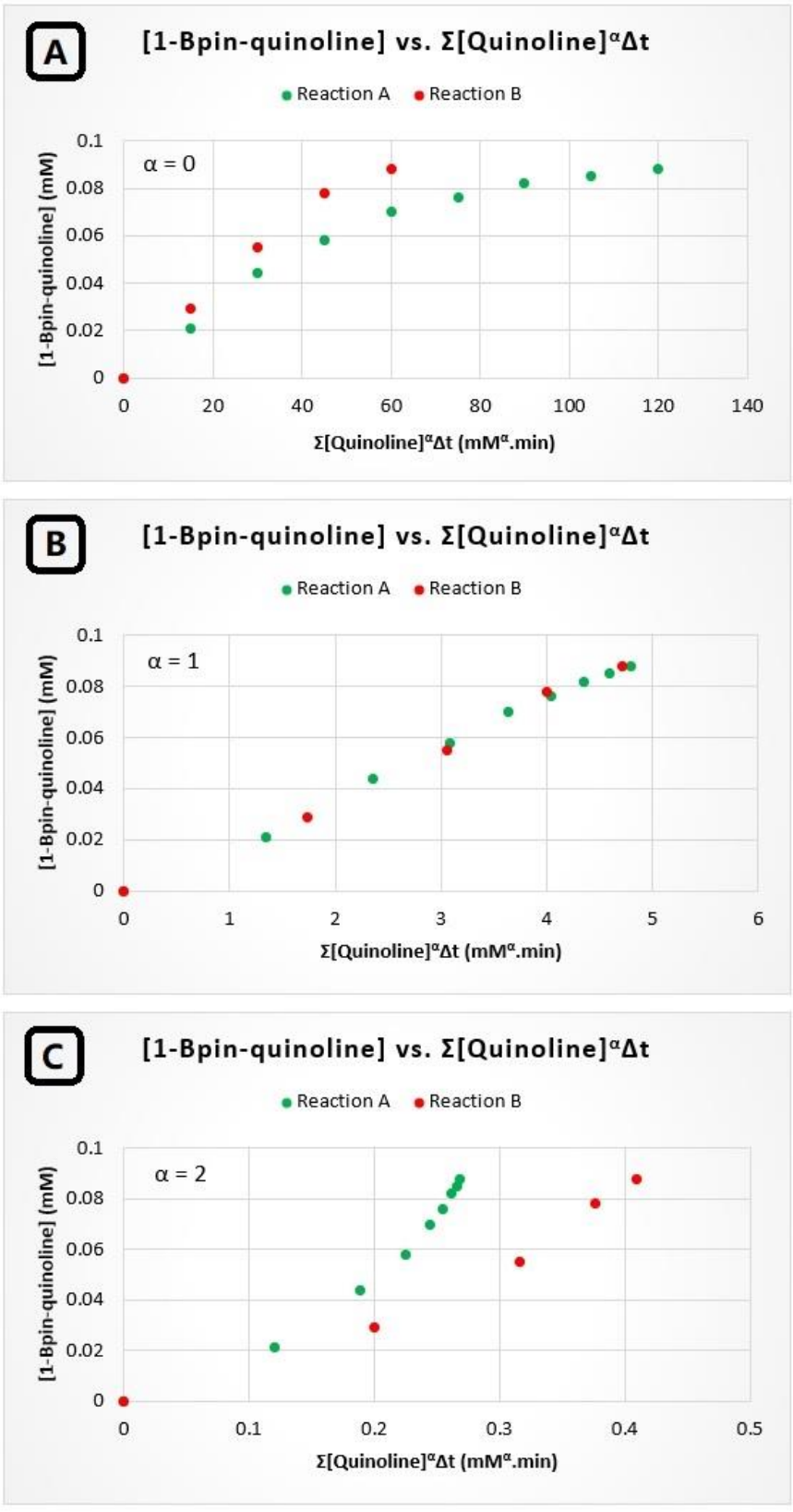

Figure A65. VTNA of rate order of [Quinoline].

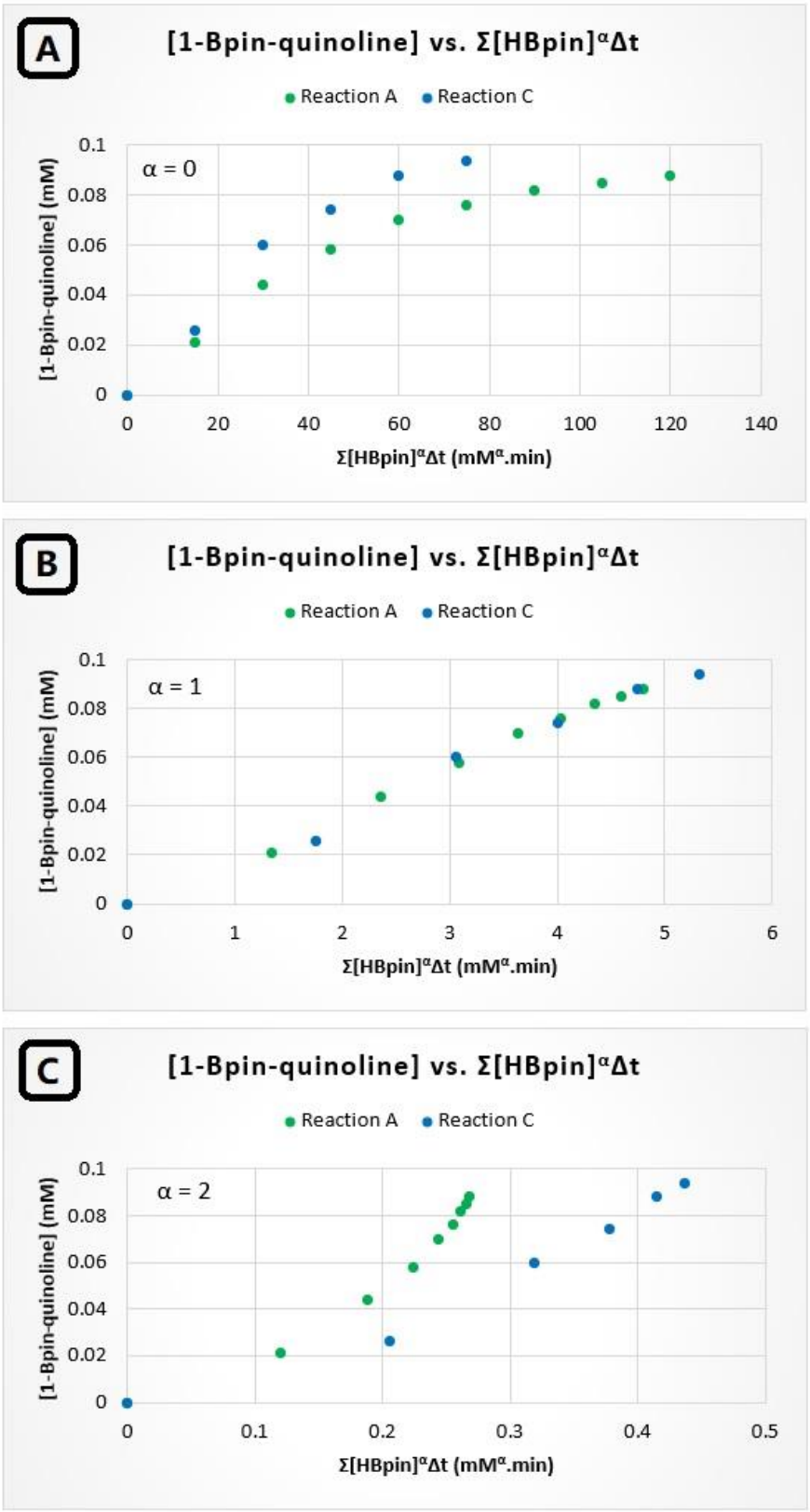

Figure A66. VTNA of rate order of [HBpin].

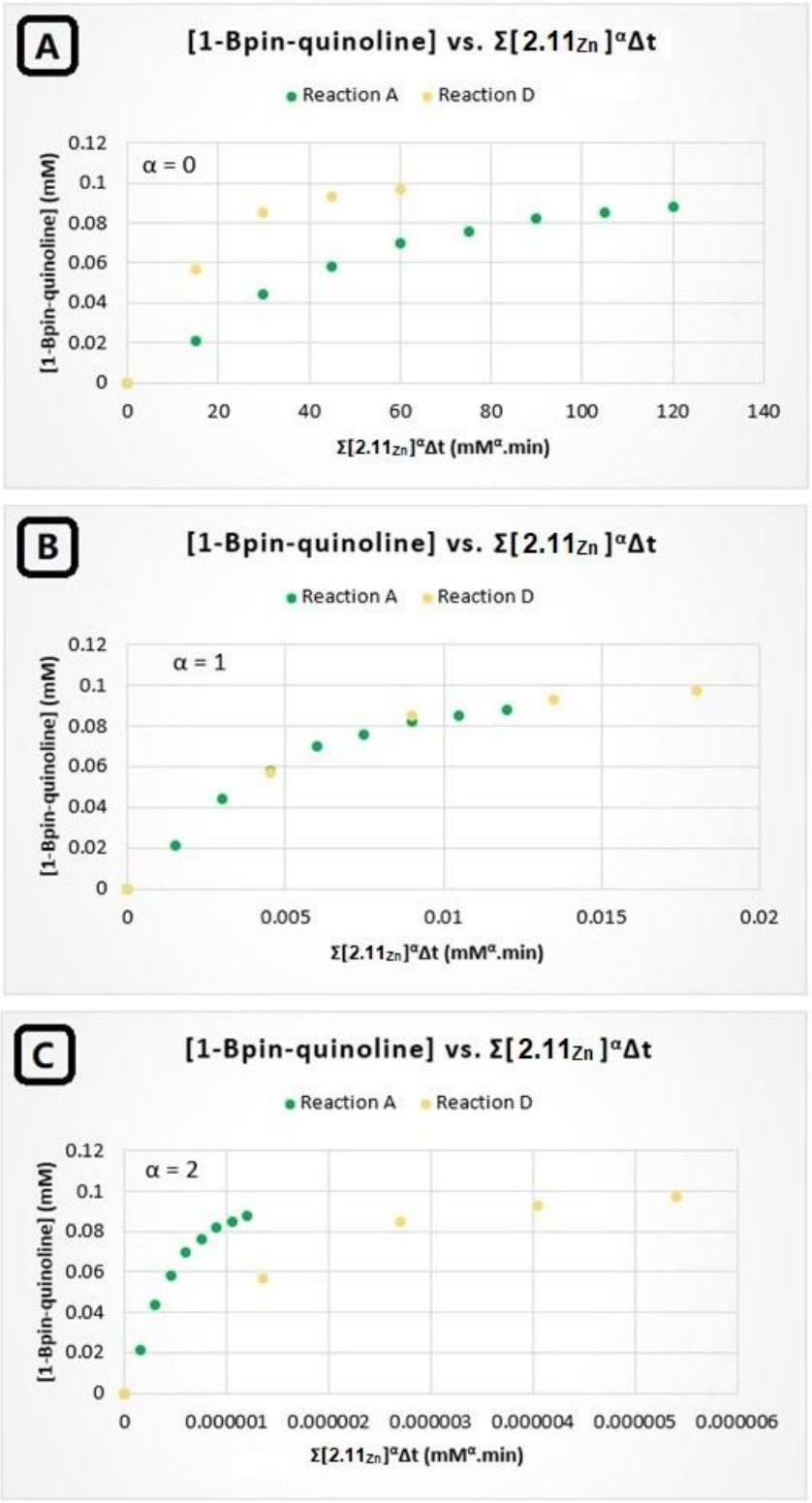

Figure A67. VTNA of rate order of [**2.11$_{Zn}$**].

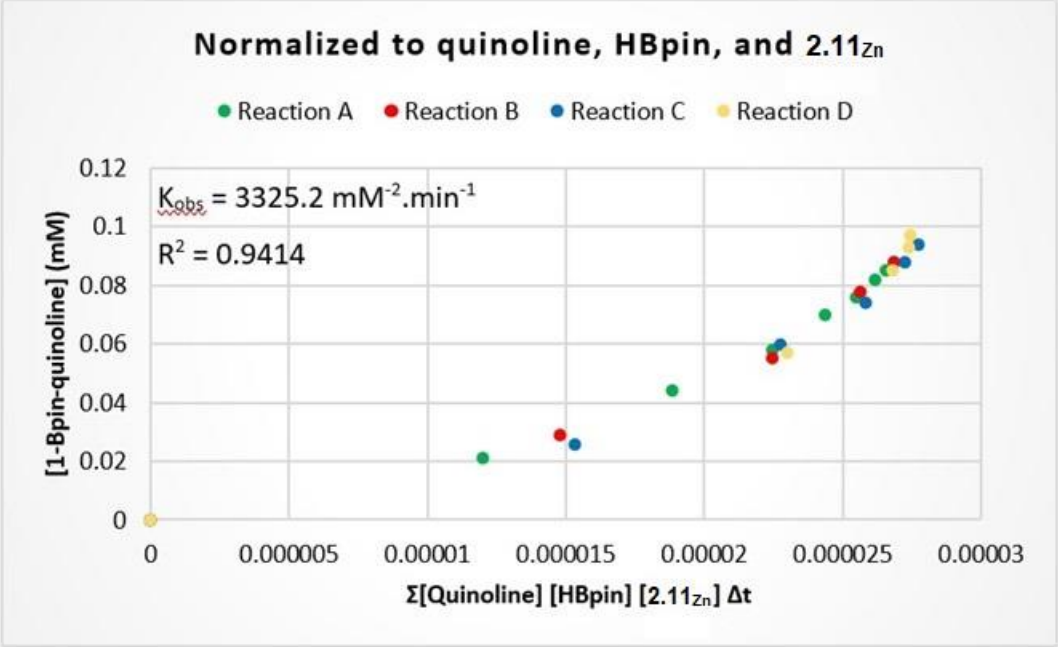

Figure A68. VTNA of [1–Bpin-quinoline] vs. Σ [quinoline][HBpin][**2.11$_{Zn}$**] Δt to give k_{obs}.

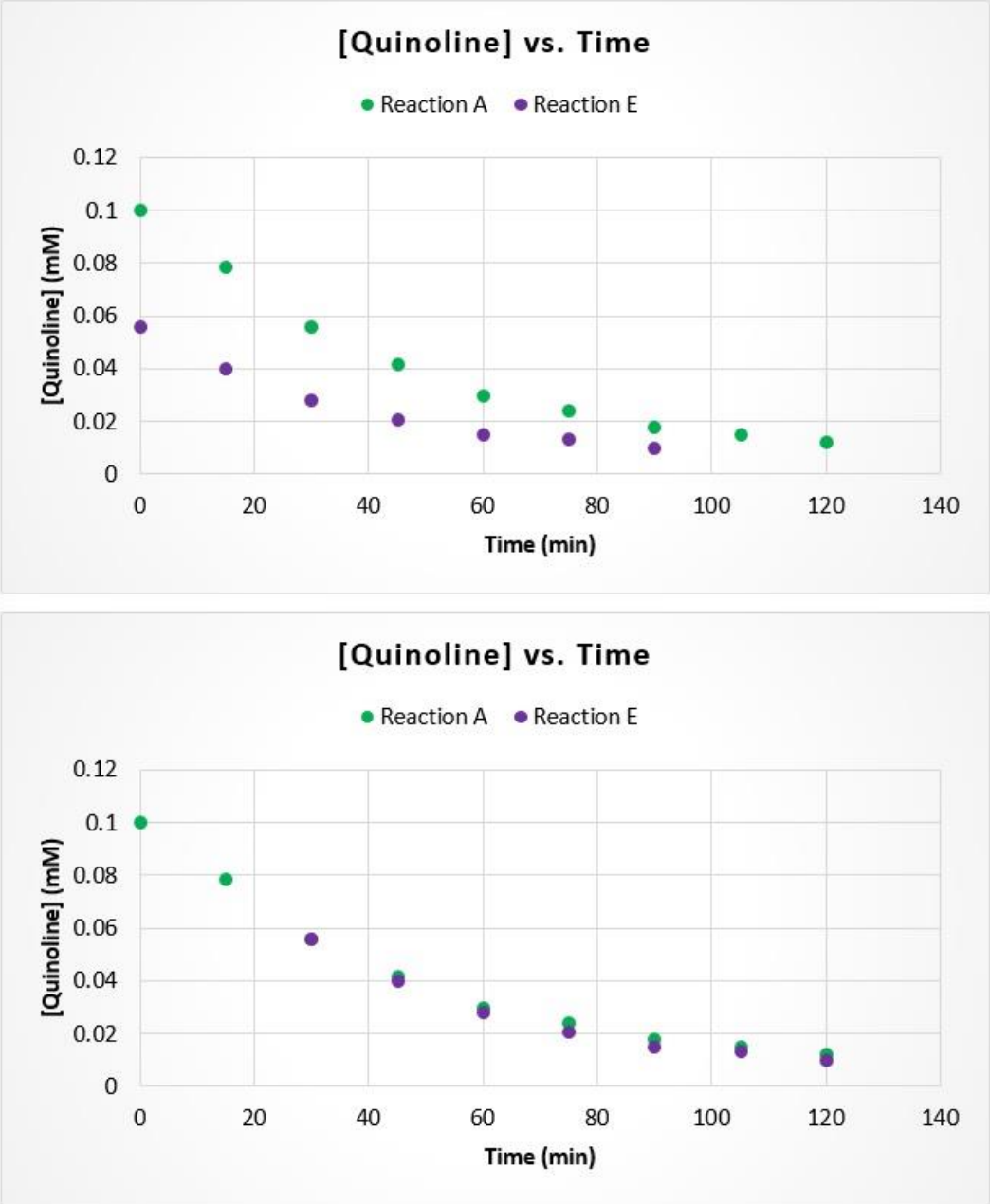

Figure A69. VTNA of [quinoline] vs. time to find out if the catalytic system suffers either product inhibition or catalyst deactivation. Top: before time adjustment. Bottom: after time adjustment.

Table A10. Data collection and refinement metrics for **H_2L3** and complexes **2.8_{Zn}-2.11_{Zn}.**

	H_2L3	**2.8_{Zn}**	**2.9_{Zn}**	**2.10_{Zn}**	**2.11_{Zn}**
empirical formula	$C_{13}H_{16}N_2O$	$C_{15}H_{20}N_2OZn$	$C_{20}H_{26}Cl_2N_4OZn$	$C_{26}H_{30}N_4O_2Zn$	$C_{31}H_{36}Cl_2N_6O_2Zn$
formula weight ($g \cdot mol^{-1}$)	216.28	309.70	474.72	495.91	660.93
crystal system	Orthorhombic	Triclinic	Monoclinic	Triclinic	Monoclinic
space group	*Pna 2₁*	$P\bar{1}$	$P\,2_1/n$	$P\bar{1}$	$P\,2_1/n$
a (A)	12.1012(5)	11.1033(5)	7.4008(3)	10.6633(11)	9.8318(4)
b (A)	7.6551(3)	11.5670(5)	16.3380(6)	10.7873(11)	25.6044(11)
c (A)	25.5457(12)	13.3255(6)	18.3165(7)	11.6049(12)	12.4012(6)
α (deg)	90	89.530(1)	90	66.418(3)	90
β (deg)	90	65.995(1)	99.385(3)	82.864(3)	90.869(1)
γ (deg)	90	73.581(1)	90	82.468(3)	90
V (A^3)	2366.45(17)	1488.47(12)	2185.08(15)	1209.1(2)	3121.5(2)
Z	8	4	4	2	4
T (K)	203(2)	293(2)	203(2)	208(2)	200(2)
ρ_{calcd} ($g \cdot cm^{-3}$)	1.214	1.382	1.443	1.362	1.406
μ (mm^{-1})	0.078	1.644	1.386	1.046	0.997
$2\theta_{max}$ (deg)	50.048	50.046	54.622	50.044	50.05
total/unique reflections	7300/2608	19140/5170	26412/4862	12079/4268	16568/5459
Reflections [$I_o \geq 2\sigma(I_o)$]	2300	4382	4219	3377	5028
R_1, wR_2 [$I_o \geq 2\sigma(I_o)$]	0.0400, 0.0910	0.0355, 0.0764	0.0530, 0.1267	0.0550, 0.1476	0.0362, 0.0815
goodness of fit	1.085	1.114	1.195	1.069	1.089
CCDC number	2190706	2190707	2190709	2190708	2190710

Table A11. Bond lengths for **H_2L3**.

Atom1	Atom2	Length (Å)
O1	C12	1.363(4)
O1	C13	1.429(5)
N1	C1	1.366(5)
N1	C4	1.372(4)
N1	H5	0.96(5)
N2	C5	1.470(4)
N2	C6	1.478(5)
N2	H6	0.90(5)
C1	H1	0.94
C1	C2	1.350(6)
C2	H2	0.94
C2	C3	1.406(6)
C3	H3	0.94
C3	C4	1.371(6)
C4	C5	1.484(6)
C5	H5A	0.98
C5	H5B	0.98
C6	H6A	0.98
C6	H6B	0.98
C6	C7	1.504(5)
C7	C8	1.385(5)
C7	C12	1.407(5)
C8	H8	0.94
C8	C9	1.395(6)
C9	H9	0.94
C9	C10	1.375(6)
C10	H10	0.94
C10	C11	1.375(5)
C11	H11	0.94
C11	C12	1.385(5)
C13	H13A	0.97
C13	H13B	0.97
C13	H13C	0.97
O2	C25	1.376(4)
O2	C26	1.423(6)
N3	C14	1.372(5)
N3	C17	1.361(5)
N3	H4	0.94(5)
N4	C18	1.477(5)
N4	C19	1.474(5)
N4	H7	0.90(5)
C14	H14	0.94

C14	C15	1.361(6)
C15	H15	0.94
C15	C16	1.412(6)
C16	H16	0.94
C16	C17	1.369(6)
C17	C18	1.482(6)
C18	H18A	0.98
C18	H18B	0.98
C19	H19A	0.98
C19	H19B	0.98
C19	C20	1.512(5)
C20	C21	1.382(5)
C20	C25	1.394(5)
C21	H21	0.94
C21	C22	1.382(6)
C22	H22	0.94
C22	C23	1.379(6)
C23	H23	0.94
C23	C24	1.375(5)
C24	H24	0.94
C24	C25	1.379(5)
C26	H26A	0.97
C26	H26B	0.971
C26	H26C	0.97

Table A12. All angles for **H_2L3**.

Atom1	**Atom2**	**Atom3**	**Angle (deg)**
C12	O1	C13	117.4(3)
C1	N1	C4	109.1(3)
C1	N1	H5	125(3)
C4	N1	H5	126(3)
C5	N2	C6	110.3(3)
C5	N2	H6	110(3)
C6	N2	H6	106(3)
N1	C1	H1	125.7
N1	C1	C2	108.5(3)
H1	C1	C2	125.7
C1	C2	H2	126.3
C1	C2	C3	107.5(4)
H2	C2	C3	126.3
C2	C3	H3	126.1
C2	C3	C4	107.8(3)
H3	C3	C4	126.1

N1	C4	C3	107.1(3)
N1	C4	C5	122.7(3)
C3	C4	C5	130.1(3)
N2	C5	C4	113.1(3)
N2	C5	H5A	108.9
N2	C5	H5B	109
C4	C5	H5A	109
C4	C5	H5B	109
H5A	C5	H5B	107.8
N2	C6	H6A	108.5
N2	C6	H6B	108.5
N2	C6	C7	115.0(3)
H6A	C6	H6B	107.5
H6A	C6	C7	108.5
H6B	C6	C7	108.5
C6	C7	C8	122.6(3)
C6	C7	C12	118.8(3)
C8	C7	C12	118.6(3)
C7	C8	H8	119.8
C7	C8	C9	120.5(4)
H8	C8	C9	119.8
C8	C9	H9	120.2
C8	C9	C10	119.6(4)
H9	C9	C10	120.2
C9	C10	H10	119.3
C9	C10	C11	121.4(4)
H10	C10	C11	119.3
C10	C11	H11	120.4
C10	C11	C12	119.2(4)
H11	C11	C12	120.4
O1	C12	C7	113.9(3)
O1	C12	C11	125.3(3)
C7	C12	C11	120.8(3)
O1	C13	H13A	109.5
O1	C13	H13B	109.5
O1	C13	H13C	109.5
H13A	C13	H13B	109.5
H13A	C13	H13C	109.5
H13B	C13	H13C	109.4
C25	O2	C26	117.5(3)
C14	N3	C17	109.6(3)
C14	N3	H4	123(3)
C17	N3	H4	127(3)
C18	N4	C19	111.1(3)
C18	N4	H7	107(3)

C19	N4	H7	111(3)
N3	C14	H14	126.1
N3	C14	C15	107.9(3)
H14	C14	C15	126
C14	C15	H15	126.4
C14	C15	C16	107.2(4)
H15	C15	C16	126.4
C15	C16	H16	126.1
C15	C16	C17	107.8(3)
H16	C16	C17	126.1
N3	C17	C16	107.5(3)
N3	C17	C18	123.5(3)
C16	C17	C18	129.0(4)
N4	C18	C17	113.2(3)
N4	C18	H18A	108.9
N4	C18	H18B	109
C17	C18	H18A	108.9
C17	C18	H18B	108.9
H18A	C18	H18B	107.8
N4	C19	H19A	108.5
N4	C19	H19B	108.5
N4	C19	C20	115.0(3)
H19A	C19	H19B	107.5
H19A	C19	C20	108.5
H19B	C19	C20	108.5
C19	C20	C21	122.1(3)
C19	C20	C25	119.6(3)
C21	C20	C25	118.3(3)
C20	C21	H21	119.5
C20	C21	C22	121.0(4)
H21	C21	C22	119.5
C21	C22	H22	120.2
C21	C22	C23	119.6(4)
H22	C22	C23	120.2
C22	C23	H23	119.7
C22	C23	C24	120.6(4)
H23	C23	C24	119.7
C23	C24	H24	120.3
C23	C24	C25	119.4(4)
H24	C24	C25	120.3
O2	C25	C20	114.6(3)
O2	C25	C24	124.3(3)
C20	C25	C24	121.1(3)
O2	C26	H26A	109.5
O2	C26	H26B	109.4

O2	C26	H26C	109.5
H26A	C26	H26B	109.4
H26A	C26	H26C	109.5
H26B	C26	H26C	109.4

Table A13. Bond lengths for **2.8$_{Zn}$**.

Atom1	**Atom2**	**Length (Å)**
Zn1	N1	1.975(2)
Zn1	N2	2.191(3)
Zn1	C1	1.973(4)
O1	C16	1.369(4)
O1	C17	1.430(5)
N1	C5	1.364(5)
N1	C8	1.368(4)
N2	C9	1.475(3)
N2	C10	1.485(6)
N2	H1	0.83(6)
C1	H1A	0.98
C1	H1B	0.98
C1	C2	1.523(4)
C2	H2A	0.97
C2	H2B	0.97
C2	H2C	0.97
C5	H5	0.94
C5	C6	1.376(4)
C6	H6	0.94
C6	C7	1.405(6)
C7	H7	0.94
C7	C8	1.374(3)
C8	C9	1.493(5)
C9	H9A	0.98
C9	H9B	0.98
C10	H10A	0.979
C10	H10B	0.98
C10	C11	1.496(4)
C11	C12	1.379(4)
C11	C16	1.398(5)
C12	H12	0.94
C12	C13	1.384(4)
C13	H13	0.94
C13	C14	1.366(6)
C14	H14	0.94
C14	C15	1.385(6)

C15	H15	0.94
C15	C16	1.386(4)
C17	H17A	0.97
C17	H17B	0.97
C17	H17C	0.97
Zn2	N3	1.964(2)
Zn2	N4	2.146(3)
Zn2	C3	1.965(4)
O2	C29	1.374(4)
O2	C30	1.421(5)
N3	C18	1.367(4)
N3	C21	1.357(5)
N4	C22	1.488(4)
N4	C23	1.478(4)
N4	H2	0.88(6)
C3	H3A	0.98
C3	H3B	0.98
C3	C4	1.491(8)
C4	H4A	0.97
C4	H4B	0.97
C4	H4C	0.97
C18	H18	0.941
C18	C19	1.362(6)
C19	H19	0.94
C19	C20	1.409(7)
C20	H20	0.94
C20	C21	1.389(5)
C21	C22	1.497(5)
C22	H22A	0.981
C22	H22B	0.979
C23	H23A	0.98
C23	H23B	0.98
C23	C24	1.506(6)
C24	C25	1.384(4)
C24	C29	1.390(5)
C25	H25	0.94
C25	C26	1.394(6)
C26	H26	0.94
C26	C27	1.368(7)
C27	H27	0.94
C27	C28	1.384(5)
C28	H28	0.94
C28	C29	1.389(6)
C30	H30A	0.97
C30	H30B	0.97

C30	H30C	0.97

Table A14. All angles for **2.8$_{Zn}$**.

Atom1	Atom2	Atom3	Angle (deg)
N1	Zn1	N2	81.3(1)
N1	Zn1	C1	138.3(1)
N2	Zn1	C1	119.3(1)
C16	O1	C17	118.1(3)
Zn1	N1	C5	137.0(2)
Zn1	N1	C8	115.6(2)
C5	N1	C8	106.3(2)
Zn1	N2	C9	106.6(2)
Zn1	N2	C10	119.7(2)
Zn1	N2	H1	100(4)
C9	N2	C10	112.3(3)
C9	N2	H1	108(4)
C10	N2	H1	108(4)
Zn1	C1	H1A	107.8
Zn1	C1	H1B	107.8
Zn1	C1	C2	118.1(3)
H1A	C1	H1B	107.1
H1A	C1	C2	107.8
H1B	C1	C2	107.8
C1	C2	H2A	109.5
C1	C2	H2B	109.4
C1	C2	H2C	109.5
H2A	C2	H2B	109.5
H2A	C2	H2C	109.5
H2B	C2	H2C	109.5
N1	C5	H5	124.9
N1	C5	C6	110.2(3)
H5	C5	C6	124.9
C5	C6	H6	126.7
C5	C6	C7	106.7(3)
H6	C6	C7	126.6
C6	C7	H7	126.9
C6	C7	C8	106.4(3)
H7	C7	C8	126.8
N1	C8	C7	110.4(3)
N1	C8	C9	117.7(2)
C7	C8	C9	131.8(3)
N2	C9	C8	109.8(3)
N2	C9	H9A	109.7

N2	C9	H9B	109.8
C8	C9	H9A	109.7
C8	C9	H9B	109.7
H9A	C9	H9B	108.2
N2	C10	H10A	109.6
N2	C10	H10B	109.5
N2	C10	C11	110.2(3)
H10A	C10	H10B	108.2
H10A	C10	C11	109.6
H10B	C10	C11	109.6
C10	C11	C12	121.7(3)
C10	C11	C16	119.5(3)
C12	C11	C16	118.8(3)
C11	C12	H12	119.4
C11	C12	C13	121.1(4)
H12	C12	C13	119.4
C12	C13	H13	120.4
C12	C13	C14	119.2(4)
H13	C13	C14	120.4
C13	C14	H14	119.3
C13	C14	C15	121.5(4)
H14	C14	C15	119.2
C14	C15	H15	120.6
C14	C15	C16	118.8(4)
H15	C15	C16	120.6
O1	C16	C11	114.6(3)
O1	C16	C15	124.8(3)
C11	C16	C15	120.5(3)
O1	C17	H17A	109.5
O1	C17	H17B	109.4
O1	C17	H17C	109.4
H17A	C17	H17B	109.5
H17A	C17	H17C	109.5
H17B	C17	H17C	109.5
N3	Zn2	N4	83.6(1)
N3	Zn2	C3	145.2(2)
N4	Zn2	C3	122.4(1)
C29	O2	C30	118.1(3)
Zn2	N3	C18	134.6(2)
Zn2	N3	C21	113.5(2)
C18	N3	C21	107.6(3)
Zn2	N4	C22	106.6(2)
Zn2	N4	C23	117.6(2)
Zn2	N4	H2	102(4)
C22	N4	C23	113.4(3)

C22	N4	H2	109(4)
C23	N4	H2	107(4)
Zn2	C3	H3A	107.7
Zn2	C3	H3B	107.7
Zn2	C3	C4	118.2(3)
H3A	C3	H3B	107.1
H3A	C3	C4	107.8
H3B	C3	C4	107.8
C3	C4	H4A	109.5
C3	C4	H4B	109.5
C3	C4	H4C	109.5
H4A	C4	H4B	109.5
H4A	C4	H4C	109.5
H4B	C4	H4C	109.4
N3	C18	H18	125.1
N3	C18	C19	109.7(3)
H18	C18	C19	125.2
C18	C19	H19	126.4
C18	C19	C20	107.2(4)
H19	C19	C20	126.4
C19	C20	H20	126.9
C19	C20	C21	106.1(3)
H20	C20	C21	126.9
N3	C21	C20	109.3(3)
N3	C21	C22	118.0(3)
C20	C21	C22	132.7(3)
N4	C22	C21	109.5(3)
N4	C22	H22A	109.8
N4	C22	H22B	109.8
C21	C22	H22A	109.8
C21	C22	H22B	109.8
H22A	C22	H22B	108.2
N4	C23	H23A	108.7
N4	C23	H23B	108.6
N4	C23	C24	114.3(3)
H23A	C23	H23B	107.6
H23A	C23	C24	108.7
H23B	C23	C24	108.7
C23	C24	C25	121.4(3)
C23	C24	C29	120.5(3)
C25	C24	C29	118.1(3)
C24	C25	H25	119.4
C24	C25	C26	121.3(3)
H25	C25	C26	119.3
C25	C26	H26	120.4

C25	C26	C27	119.3(4)
H26	C26	C27	120.3
C26	C27	H27	119.5
C26	C27	C28	120.9(4)
H27	C27	C28	119.5
C27	C28	H28	120.5
C27	C28	C29	119.0(4)
H28	C28	C29	120.5
O2	C29	C24	114.5(3)
O2	C29	C28	124.2(3)
C24	C29	C28	121.3(3)
O2	C30	H30A	109.5
O2	C30	H30B	109.5
O2	C30	H30C	109.5
H30A	C30	H30B	109.5
H30A	C30	H30C	109.4
H30B	C30	H30C	109.5

Table A15. Bond lengths for **2.9$_{Zn}$**.

Atom1	**Atom2**	**Length (Å)**
Zn1	N1	2.019(3)
Zn1	N2	2.212(3)
Zn1	C1	2.049(4)
Zn1	C3	2.098(4)
Cl1	C6	1.688(4)
Cl2	C7	1.684(4)
O1	C19	1.371(6)
O1	C20	1.422(6)
N1	C8	1.362(5)
N1	C11	1.358(5)
N2	C12	1.474(5)
N2	C13	1.479(5)
N2	H1	0.79(7)
N3	C3	1.353(5)
N3	C4	1.464(4)
N3	C6	1.365(5)
N4	C3	1.360(5)
N4	C5	1.467(5)
N4	C7	1.377(5)
C1	H1A	0.98
C1	H1B	0.98
C1	C2	1.373(9)
C2	H2A	0.97

C2	H2B	0.969
C2	H2C	0.97
C4	H4A	0.97
C4	H4B	0.969
C4	H4C	0.971
C5	H5A	0.97
C5	H5B	0.97
C5	H5C	0.969
C6	C7	1.348(5)
C8	H8	0.94
C8	C9	1.372(7)
C9	H9	0.94
C9	C10	1.401(6)
C10	H10	0.94
C10	C11	1.378(5)
C11	C12	1.494(5)
C12	H12A	0.98
C12	H12B	0.98
C13	H13A	0.98
C13	H13B	0.98
C13	C14	1.506(6)
C14	C15	1.384(7)
C14	C19	1.392(5)
C15	H15	0.94
C15	C16	1.385(8)
C16	H16	0.94
C16	C17	1.365(8)
C17	H17	0.939
C17	C18	1.374(7)
C18	H18	0.94
C18	C19	1.390(6)
C20	H20A	0.969
C20	H20B	0.97
C20	H20C	0.97

Table A16. All angles for **2.9$_{Zn}$**.

Atom1	**Atom2**	**Atom3**	**Angle (deg)**
N1	Zn1	N2	81.1(1)
N1	Zn1	C1	119.4(2)
N1	Zn1	C3	107.2(1)
N2	Zn1	C1	117.4(1)
N2	Zn1	C3	95.4(1)
C1	Zn1	C3	125.5(2)

C19	O1	C20	118.0(4)
Zn1	N1	C8	134.7(3)
Zn1	N1	C11	113.7(2)
C8	N1	C11	106.2(3)
Zn1	N2	C12	105.4(2)
Zn1	N2	C13	121.0(2)
Zn1	N2	H1	103(5)
C12	N2	C13	112.5(3)
C12	N2	H1	109(5)
C13	N2	H1	106(5)
C3	N3	C4	124.2(3)
C3	N3	C6	111.9(3)
C4	N3	C6	123.8(3)
C3	N4	C5	125.7(3)
C3	N4	C7	111.3(3)
C5	N4	C7	123.0(3)
Zn1	C1	H1A	108.4
Zn1	C1	H1B	108.4
Zn1	C1	C2	115.4(4)
H1A	C1	H1B	107.5
H1A	C1	C2	108.4
H1B	C1	C2	108.4
C1	C2	H2A	109.5
C1	C2	H2B	109.5
C1	C2	H2C	109.4
H2A	C2	H2B	109.5
H2A	C2	H2C	109.4
H2B	C2	H2C	109.5
Zn1	C3	N3	125.8(3)
Zn1	C3	N4	130.4(3)
N3	C3	N4	103.6(3)
N3	C4	H4A	109.5
N3	C4	H4B	109.5
N3	C4	H4C	109.5
H4A	C4	H4B	109.5
H4A	C4	H4C	109.4
H4B	C4	H4C	109.5
N4	C5	H5A	109.4
N4	C5	H5B	109.4
N4	C5	H5C	109.5
H5A	C5	H5B	109.4
H5A	C5	H5C	109.5
H5B	C5	H5C	109.5
Cl1	C6	N3	124.1(3)
Cl1	C6	C7	129.2(3)

N3	C6	C7	106.8(3)
Cl2	C7	N4	123.3(3)
Cl2	C7	C6	130.3(3)
N4	C7	C6	106.4(3)
N1	C8	H8	124.8
N1	C8	C9	110.3(4)
H8	C8	C9	124.9
C8	C9	H9	126.6
C8	C9	C10	106.8(4)
H9	C9	C10	126.6
C9	C10	H10	127
C9	C10	C11	106.0(3)
H10	C10	C11	127
N1	C11	C10	110.7(3)
N1	C11	C12	117.3(3)
C10	C11	C12	132.0(3)
N2	C12	C11	108.9(3)
N2	C12	H12A	110
N2	C12	H12B	109.9
C11	C12	H12A	109.9
C11	C12	H12B	109.9
H12A	C12	H12B	108.3
N2	C13	H13A	109.4
N2	C13	H13B	109.4
N2	C13	C14	111.0(3)
H13A	C13	H13B	108
H13A	C13	C14	109.5
H13B	C13	C14	109.4
C13	C14	C15	120.8(4)
C13	C14	C19	120.8(4)
C15	C14	C19	118.4(4)
C14	C15	H15	119.3
C14	C15	C16	121.3(4)
H15	C15	C16	119.4
C15	C16	H16	120.3
C15	C16	C17	119.3(5)
H16	C16	C17	120.4
C16	C17	H17	119.5
C16	C17	C18	121.0(5)
H17	C17	C18	119.5
C17	C18	H18	120.2
C17	C18	C19	119.7(4)
H18	C18	C19	120.1
O1	C19	C14	115.6(4)
O1	C19	C18	124.1(4)

C14	C19	C18	120.3(4)
O1	C20	H20A	109.5
O1	C20	H20B	109.4
O1	C20	H20C	109.5
H20A	C20	H20B	109.5
H20A	C20	H20C	109.5
H20B	C20	H20C	109.4

Table A17. Bond lengths for **2.10$_{Zn}$**.

Atom1	**Atom2**	**Length (Å)**
Zn1	N1	1.934(5)
Zn1	N3	1.949(3)
Zn1	N2A	2.11(2)
Zn1	N4A	2.055(6)
N1	C1	1.362(8)
N1	C4	1.365(6)
N3	C14	1.358(6)
N3	C17	1.349(6)
C1	H1	0.94
C1	C2	1.359(9)
C2	H2	0.941
C2	C3	1.420(7)
C3	H3	0.94
C3	C4	1.386(8)
C4	C5	1.489(7)
C5	H5AA	0.98
C5	H5AB	0.98
C5	N2A	1.50(2)
C14	H14	0.94
C14	C15	1.391(8)
C15	H15	0.94
C15	C16	1.390(7)
C16	H16	0.939
C16	C17	1.385(7)
C17	C18	1.498(5)
C18	H18A	0.98
C18	H18B	0.98
C18	N4A	1.479(8)
O1A	C12A	1.37(1)
O1A	C13A	1.43(1)
N2A	H2A	0.99
N2A	C6A	1.50(3)
C6A	H6AA	0.98

C6A	H6AB	0.98
C6A	C7A	1.50(1)
C7A	C8A	1.37(1)
C7A	C12A	1.401(7)
C8A	H8A	0.939
C8A	C9A	1.41(1)
C9A	H9A	0.94
C9A	C10A	1.38(1)
C10A	H10A	0.94
C10A	C11A	1.36(1)
C11A	H11A	0.94
C11A	C12A	1.40(1)
C13A	H13A	0.97
C13A	H13B	0.97
C13A	H13C	0.97
O2A	C25A	1.412(9)
O2A	C26A	1.42(2)
N4A	H4A	0.991
N4A	C19A	1.504(9)
C19A	H19A	0.98
C19A	H19B	0.98
C19A	C20A	1.52(1)
C20A	C21A	1.32(1)
C20A	C25A	1.37(1)
C21A	H21A	0.94
C21A	C22A	1.39(2)
C22A	H22A	0.94
C22A	C23A	1.35(2)
C23A	H23A	0.94
C23A	C24A	1.39(1)
C24A	H24A	0.94
C24A	C25A	1.40(1)
C26A	H26A	0.97
C26A	H26B	0.97
C26A	H26C	0.97

Table A18. All angles for **2.10$_{Zn}$**.

Atom1	**Atom2**	**Atom3**	**Angle (deg)**
N1	Zn1	N3	137.7(2)
N1	Zn1	N2A	83.5(6)
N1	Zn1	N4A	117.7(2)
N3	Zn1	N2A	111.2(6)
N3	Zn1	N4A	86.4(2)

N2A	Zn1	N4A	125.9(6)
Zn1	N1	C1	139.9(4)
Zn1	N1	C4	112.2(3)
C1	N1	C4	106.2(4)
Zn1	N3	C14	139.3(3)
Zn1	N3	C17	112.8(3)
C14	N3	C17	107.4(4)
N1	C1	H1	124.3
N1	C1	C2	111.2(5)
H1	C1	C2	124.5
C1	C2	H2	126.7
C1	C2	C3	106.6(5)
H2	C2	C3	126.7
C2	C3	H3	127.2
C2	C3	C4	105.6(4)
H3	C3	C4	127.1
N1	C4	C3	110.4(4)
N1	C4	C5	117.6(4)
C3	C4	C5	132.0(4)
C4	C5	H5AA	110.4
C4	C5	H5AB	110.4
C4	C5	N2A	106.3(8)
H5AA	C5	H5AB	108.7
H5AA	C5	N2A	110.5
H5AB	C5	N2A	110.4
N3	C14	H14	125.2
N3	C14	C15	109.5(5)
H14	C14	C15	125.3
C14	C15	H15	126.8
C14	C15	C16	106.5(5)
H15	C15	C16	126.7
C15	C16	H16	126.7
C15	C16	C17	106.6(4)
H16	C16	C17	126.7
N3	C17	C16	110.0(4)
N3	C17	C18	119.1(4)
C16	C17	C18	130.9(4)
C17	C18	H18A	108.9
C17	C18	H18B	109
C17	C18	N4A	113.2(4)
H18A	C18	H18B	107.7
H18A	C18	N4A	108.9
H18B	C18	N4A	108.9
C12A	O1A	C13A	117.3(9)
Zn1	N2A	C5	102(1)

Zn1	N2A	H2A	108
Zn1	N2A	C6A	114(1)
C5	N2A	H2A	109
C5	N2A	C6A	114(1)
H2A	N2A	C6A	108
N2A	C6A	H6AA	109
N2A	C6A	H6AB	109
N2A	C6A	C7A	113(1)
H6AA	C6A	H6AB	107.7
H6AA	C6A	C7A	108.9
H6AB	C6A	C7A	108.9
C6A	C7A	C8A	122.6(7)
C6A	C7A	C12A	118.8(6)
C8A	C7A	C12A	118.5(6)
C7A	C8A	H8A	119.5
C7A	C8A	C9A	120.9(7)
H8A	C8A	C9A	119.6
C8A	C9A	H9A	121
C8A	C9A	C10A	118.5(9)
H9A	C9A	C10A	121
C9A	C10A	H10A	119
C9A	C10A	C11A	122(1)
H10A	C10A	C11A	119
C10A	C11A	H11A	120.2
C10A	C11A	C12A	119.6(8)
H11A	C11A	C12A	120.2
O1A	C12A	C7A	115.9(6)
O1A	C12A	C11A	123.5(7)
C7A	C12A	C11A	120.6(6)
O1A	C13A	H13A	110
O1A	C13A	H13B	109
O1A	C13A	H13C	109
H13A	C13A	H13B	109
H13A	C13A	H13C	110
H13B	C13A	H13C	109
C25A	O2A	C26A	115.0(8)
Zn1	N4A	C18	107.9(4)
Zn1	N4A	H4A	106.3
Zn1	N4A	C19A	117.0(5)
C18	N4A	H4A	106.3
C18	N4A	C19A	112.3(6)
H4A	N4A	C19A	106.3
N4A	C19A	H19A	108.7
N4A	C19A	H19B	108.7
N4A	C19A	C20A	114.4(7)

H19A	C19A	H19B	107.6
H19A	C19A	C20A	108.7
H19B	C19A	C20A	108.6
C19A	C20A	C21A	124.8(7)
C19A	C20A	C25A	119.2(7)
C21A	C20A	C25A	116.0(7)
C20A	C21A	H21A	117.4
C20A	C21A	C22A	125(1)
H21A	C21A	C22A	118
C21A	C22A	H22A	122
C21A	C22A	C23A	117(1)
H22A	C22A	C23A	122
C22A	C23A	H23A	119
C22A	C23A	C24A	123(1)
H23A	C23A	C24A	119
C23A	C24A	H24A	122
C23A	C24A	C25A	115.8(9)
H24A	C24A	C25A	122
O2A	C25A	C20A	115.3(6)
O2A	C25A	C24A	121.2(7)
C20A	C25A	C24A	123.5(7)
O2A	C26A	H26A	109
O2A	C26A	H26B	109
O2A	C26A	H26C	109
H26A	C26A	H26B	109
H26A	C26A	H26C	109
H26B	C26A	H26C	109

Table A19. Bond lengths for **2.11$_{Zn}$**.

Atom1	**Atom2**	**Length (Å)**
Zn1	N1	2.003(2)
Zn1	N2	2.329(2)
Zn1	N3	1.975(2)
Zn1	N4	2.540(2)
Zn1	C1	2.061(2)
Cl1	C4	1.696(2)
Cl2	C5	1.697(2)
O1	C17	1.373(4)
O1	C18	1.429(4)
O2	C30	1.366(3)
O2	C31	1.431(4)
N1	C6	1.366(3)
N1	C9	1.356(3)

N2	C10	1.475(3)
N2	C11	1.483(3)
N2	H1	0.92(5)
N3	C19	1.355(3)
N3	C22	1.360(3)
N4	C23	1.484(3)
N4	C24	1.462(3)
N4	H2	0.89(5)
N5	C1	1.351(3)
N5	C3	1.462(3)
N5	C5	1.382(3)
N6	C1	1.358(3)
N6	C2	1.463(3)
N6	C4	1.383(3)
C2	H2A	0.98
C2	H2B	0.98
C2	H2C	0.98
C3	H3A	0.98
C3	H3B	0.98
C3	H3C	0.98
C4	C5	1.336(4)
C6	H6	0.95
C6	C7	1.372(4)
C7	H7	0.95
C7	C8	1.402(4)
C8	H8	0.95
C8	C9	1.374(3)
C9	C10	1.491(3)
C10	H10A	0.99
C10	H10B	0.99
C11	H11A	0.99
C11	H11B	0.99
C11	C12	1.509(4)
C12	C13	1.390(4)
C12	C17	1.395(4)
C13	H13	0.95
C13	C14	1.378(4)
C14	H14	0.95
C14	C15	1.369(6)
C15	H15	0.95
C15	C16	1.382(6)
C16	H16	0.95
C16	C17	1.395(5)
C18	H18A	0.979
C18	H18B	0.98

C18	H18C	0.98
C19	H19	0.95
C19	C20	1.376(4)
C20	H20	0.95
C20	C21	1.405(4)
C21	H21	0.95
C21	C22	1.373(4)
C22	C23	1.500(3)
C23	H23A	0.99
C23	H23B	0.99
C24	H24A	0.99
C24	H24B	0.99
C24	C25	1.506(3)
C25	C26	1.383(3)
C25	C30	1.410(4)
C26	H26	0.95
C26	C27	1.394(4)
C27	H27	0.95
C27	C28	1.378(4)
C28	H28	0.95
C28	C29	1.378(5)
C29	H29	0.95
C29	C30	1.383(4)
C31	H31A	0.98
C31	H31B	0.98
C31	H31C	0.98

Table A20. All angles for **2.11$_{Zn}$**.

Atom1	**Atom2**	**Atom3**	**Angle (deg)**
N1	Zn1	N2	78.76(7)
N1	Zn1	N3	123.81(8)
N1	Zn1	N4	88.81(7)
N1	Zn1	C1	123.14(8)
N2	Zn1	N3	96.89(8)
N2	Zn1	N4	160.22(7)
N2	Zn1	C1	100.94(8)
N3	Zn1	N4	77.22(7)
N3	Zn1	C1	112.75(8)
N4	Zn1	C1	98.73(8)
C17	O1	C18	118.1(2)
C30	O2	C31	117.6(3)
Zn1	N1	C6	135.8(2)
Zn1	N1	C9	116.9(1)

C6	N1	C9	106.2(2)
Zn1	N2	C10	104.2(1)
Zn1	N2	C11	125.3(1)
Zn1	N2	H1	98(3)
C10	N2	C11	111.5(2)
C10	N2	H1	112(3)
C11	N2	H1	104(3)
Zn1	N3	C19	131.8(2)
Zn1	N3	C22	119.2(2)
C19	N3	C22	106.8(2)
Zn1	N4	C23	96.7(1)
Zn1	N4	C24	116.8(1)
Zn1	N4	H2	111(3)
C23	N4	C24	111.5(2)
C23	N4	H2	111(3)
C24	N4	H2	110(3)
C1	N5	C3	124.9(2)
C1	N5	C5	110.9(2)
C3	N5	C5	124.1(2)
C1	N6	C2	125.9(2)
C1	N6	C4	110.4(2)
C2	N6	C4	123.6(2)
Zn1	C1	N5	125.7(2)
Zn1	C1	N6	129.3(2)
N5	C1	N6	104.7(2)
N6	C2	H2A	109.5
N6	C2	H2B	109.5
N6	C2	H2C	109.4
H2A	C2	H2B	109.5
H2A	C2	H2C	109.5
H2B	C2	H2C	109.5
N5	C3	H3A	109.4
N5	C3	H3B	109.4
N5	C3	H3C	109.4
H3A	C3	H3B	109.5
H3A	C3	H3C	109.5
H3B	C3	H3C	109.5
Cl1	C4	N6	123.8(2)
Cl1	C4	C5	129.0(2)
N6	C4	C5	107.2(2)
Cl2	C5	N5	123.3(2)
Cl2	C5	C4	129.8(2)
N5	C5	C4	106.8(2)
N1	C6	H6	124.8
N1	C6	C7	110.5(2)

H6	C6	C7	124.8
C6	C7	H7	126.8
C6	C7	C8	106.3(2)
H7	C7	C8	126.8
C7	C8	H8	126.8
C7	C8	C9	106.4(2)
H8	C8	C9	126.8
N1	C9	C8	110.6(2)
N1	C9	C10	119.5(2)
C8	C9	C10	129.9(2)
N2	C10	C9	109.8(2)
N2	C10	H10A	109.7
N2	C10	H10B	109.7
C9	C10	H10A	109.7
C9	C10	H10B	109.7
H10A	C10	H10B	108.2
N2	C11	H11A	108.5
N2	C11	H11B	108.6
N2	C11	C12	114.9(2)
H11A	C11	H11B	107.5
H11A	C11	C12	108.6
H11B	C11	C12	108.6
C11	C12	C13	120.8(2)
C11	C12	C17	120.9(2)
C13	C12	C17	118.3(2)
C12	C13	H13	119.2
C12	C13	C14	121.6(3)
H13	C13	C14	119.2
C13	C14	H14	120.4
C13	C14	C15	119.3(3)
H14	C14	C15	120.3
C14	C15	H15	119.5
C14	C15	C16	121.1(4)
H15	C15	C16	119.4
C15	C16	H16	120.4
C15	C16	C17	119.3(3)
H16	C16	C17	120.3
O1	C17	C12	114.8(2)
O1	C17	C16	124.8(3)
C12	C17	C16	120.4(3)
O1	C18	H18A	109.5
O1	C18	H18B	109.4
O1	C18	H18C	109.5
H18A	C18	H18B	109.5
H18A	C18	H18C	109.5

H18B	C18	H18C	109.4
N3	C19	H19	124.7
N3	C19	C20	110.6(2)
H19	C19	C20	124.7
C19	C20	H20	127.1
C19	C20	C21	105.8(2)
H20	C20	C21	127.1
C20	C21	H21	126.5
C20	C21	C22	106.9(2)
H21	C21	C22	126.6
N3	C22	C21	109.9(2)
N3	C22	C23	118.1(2)
C21	C22	C23	132.0(2)
N4	C23	C22	110.7(2)
N4	C23	H23A	109.5
N4	C23	H23B	109.5
C22	C23	H23A	109.5
C22	C23	H23B	109.5
H23A	C23	H23B	108.1
N4	C24	H24A	108.9
N4	C24	H24B	108.9
N4	C24	C25	113.3(2)
H24A	C24	H24B	107.7
H24A	C24	C25	108.9
H24B	C24	C25	108.9
C24	C25	C26	124.1(2)
C24	C25	C30	118.0(2)
C26	C25	C30	117.9(2)
C25	C26	H26	119.2
C25	C26	C27	121.5(3)
H26	C26	C27	119.3
C26	C27	H27	120.2
C26	C27	C28	119.6(3)
H27	C27	C28	120.2
C27	C28	H28	120
C27	C28	C29	120.0(3)
H28	C28	C29	120
C28	C29	H29	119.7
C28	C29	C30	120.6(3)
H29	C29	C30	119.7
O2	C30	C25	114.8(2)
O2	C30	C29	124.8(3)
C25	C30	C29	120.4(3)
O2	C31	H31A	109.4
O2	C31	H31B	109.4

O2	C31	H31C	109.5
H31A	C31	H31B	109.5
H31A	C31	H31C	109.5
H31B	C31	H31C	109.5

Appendix B – Chapter 3

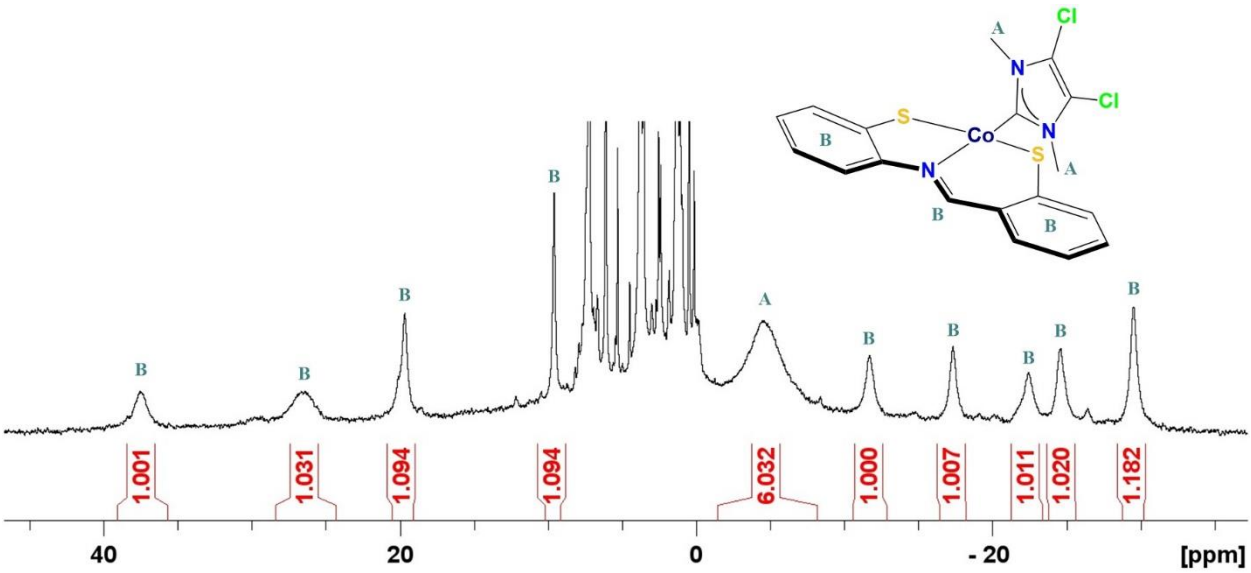

Figure B1. ^{1}H NMR spectrum (300 MHz, $CDCl_3$) of **3.2$_{Co}$**.

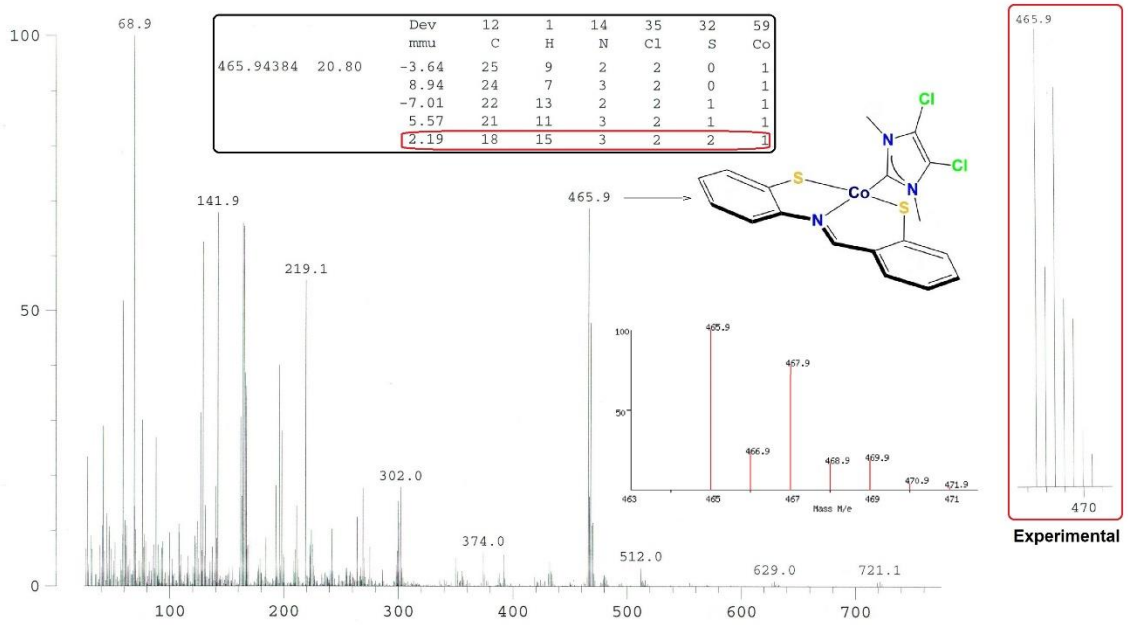

Figure B2. EI-MS spectrum of **3.2**$_{Co}$ $[M]^+$.

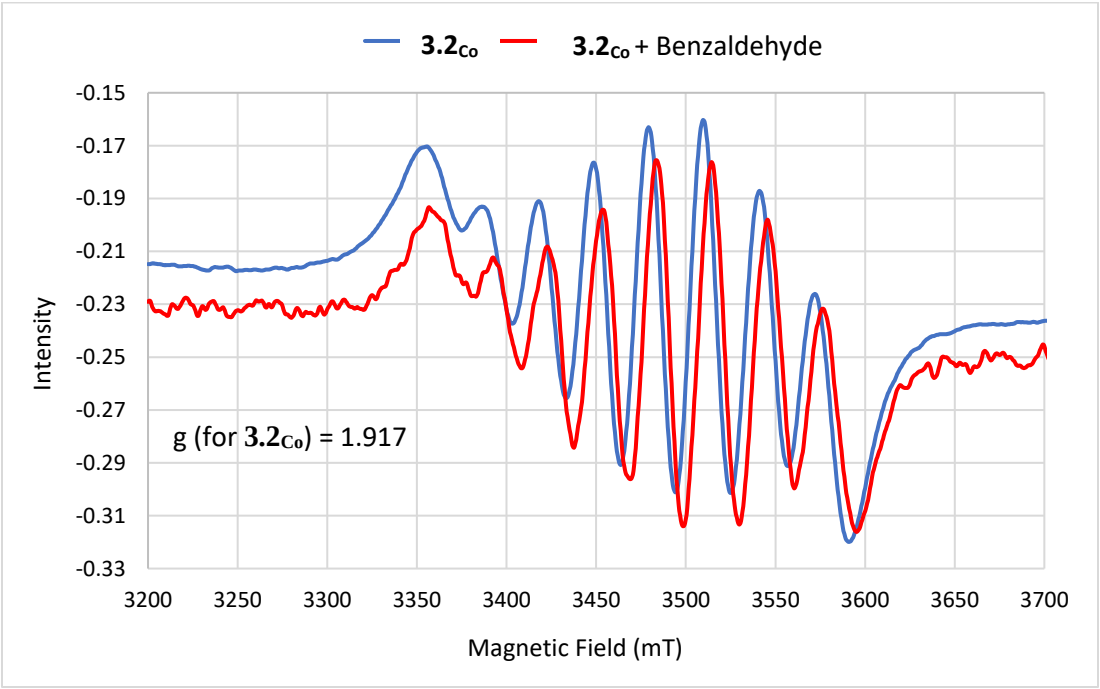

Figure B3. EPR spectra of **3.2**$_{Co}$ (blue) and mixture of **3.2**$_{Co}$ and benzaldehyde (red).

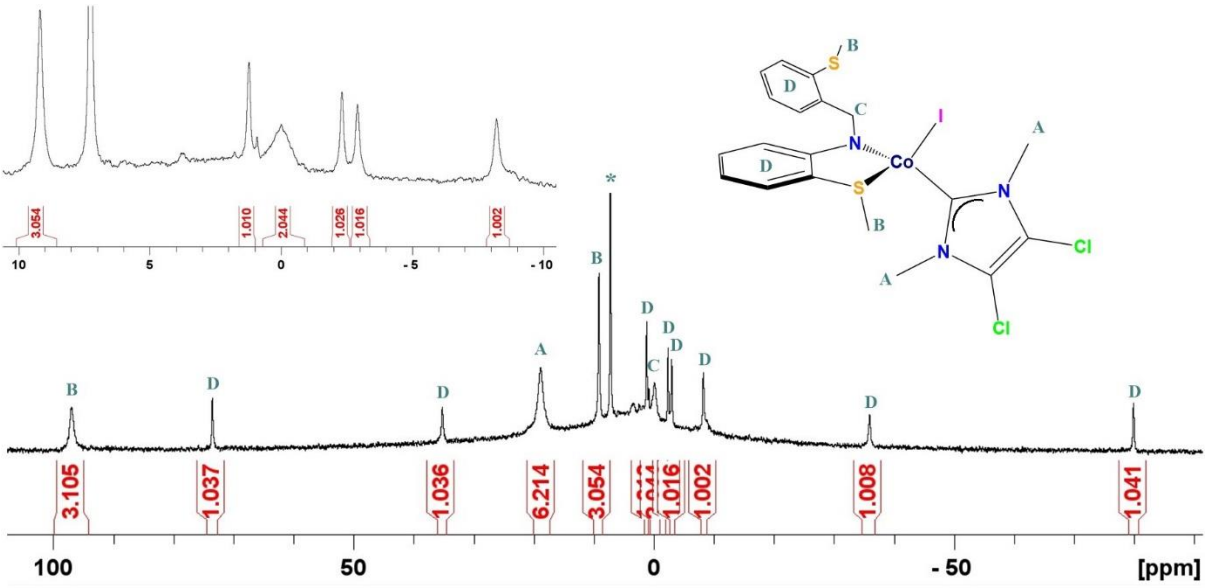

Figure B4. ^{1}H NMR spectrum (300 MHz, $CDCl_3$) of $\mathbf{3.3_{Co}}$. * indicates protic impurity in $CDCl_3$.

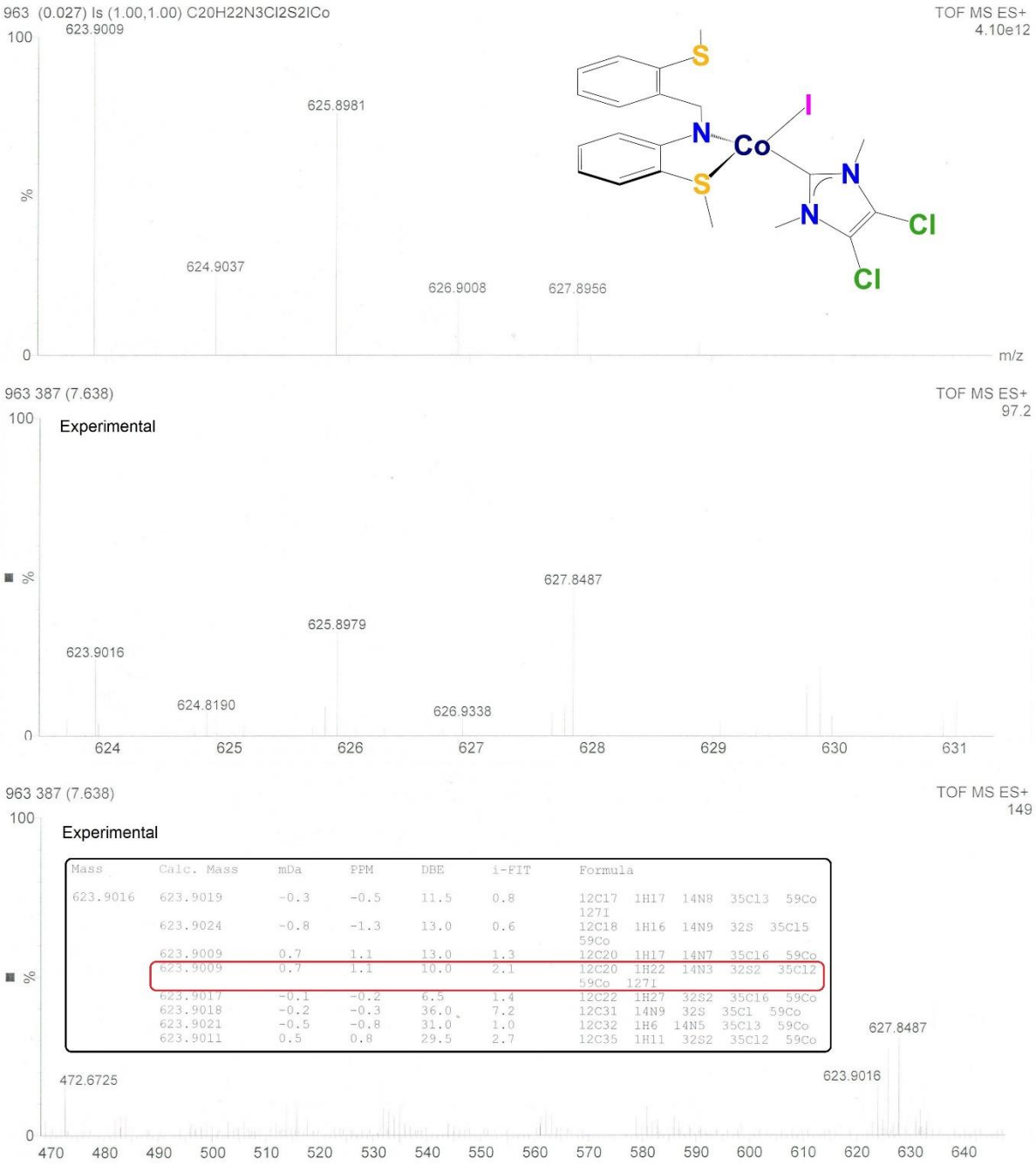

Figure B5. ESI-MS spectrum of **3.3$_{Co}$** $[M]^+$.

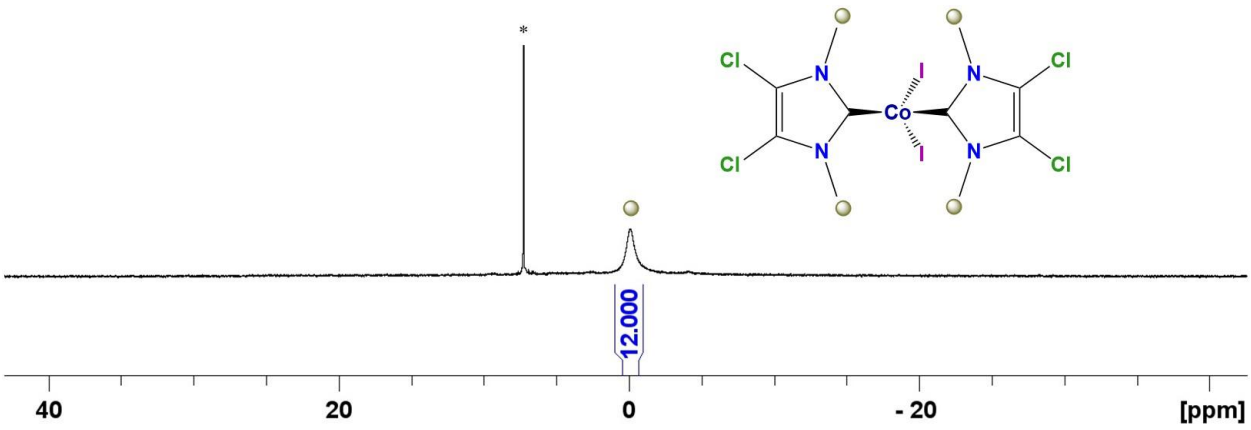

Figure B6. ^{1}H NMR spectrum (300 MHz, $CDCl_3$) of **3.4$_{Co}$**. * indicates protic impurity in $CDCl_3$.

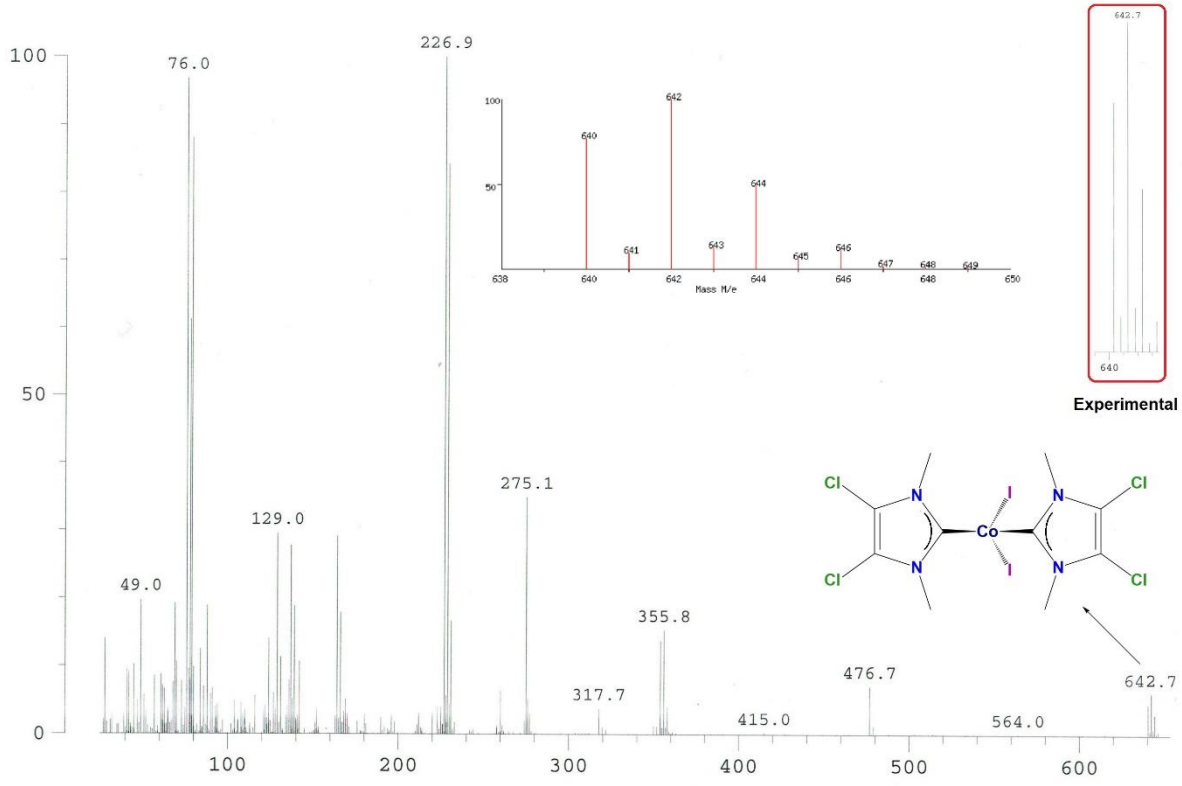

Figure B7. EI-MS spectrum of **3.4$_{Co}$** $[M]^{+}$.

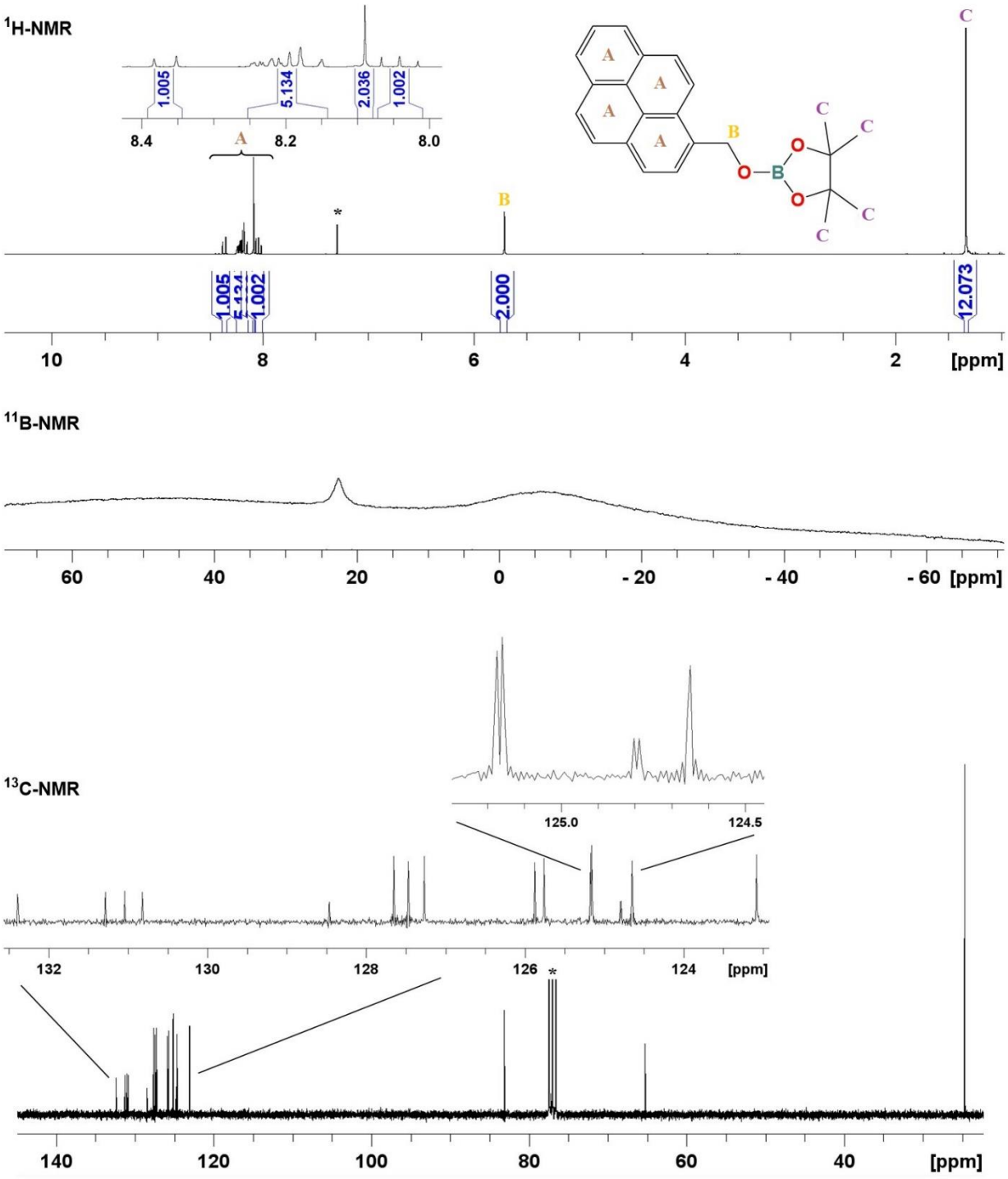

Figure B8. ^{1}H (300 MHz, $CDCl_3$), ^{11}B (96 MHz), and ^{13}C (75 MHz) NMR spectra of 4,4,5,5-tetramethyl-2-(pyren-1-ylmethoxy)-1,3,2-dioxaborolane. * indicates protic impurity in $CDCl_3$.

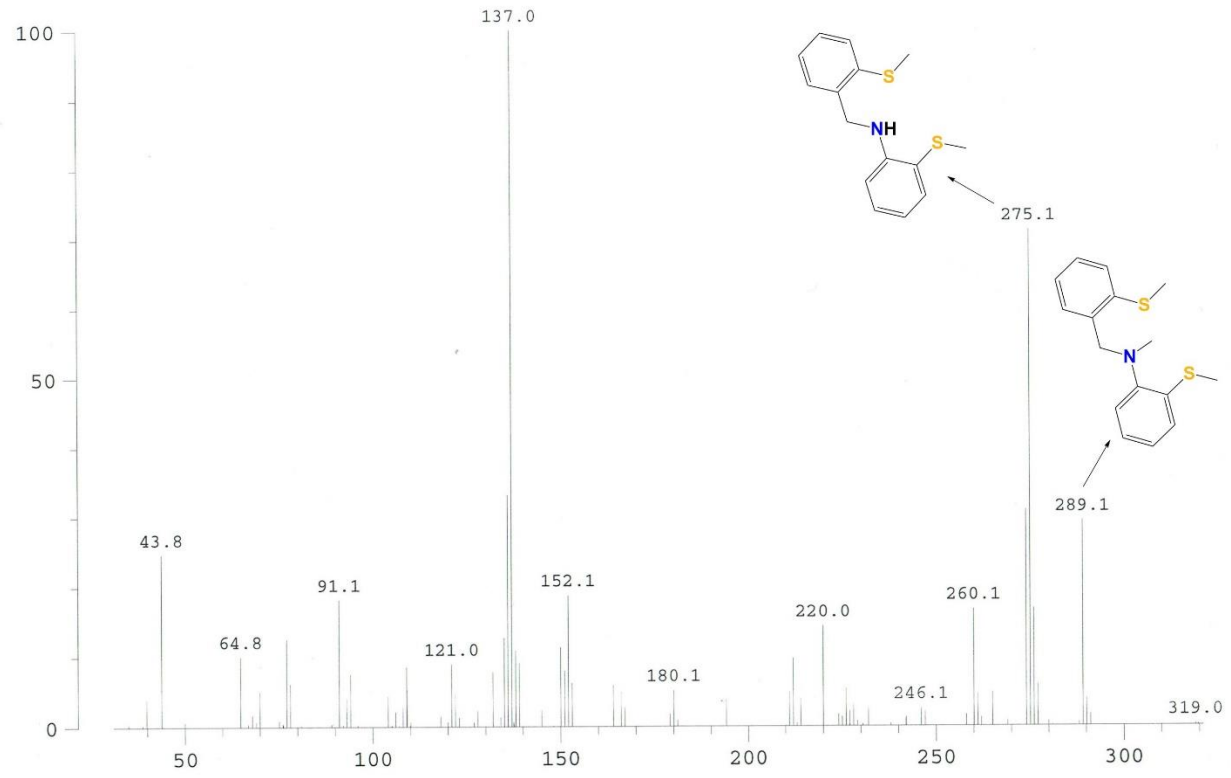

Figure B9. EI-MS spectrum of the filtrate portion of the workup process of synthetic reaction of **3.2$_{Co}$**.

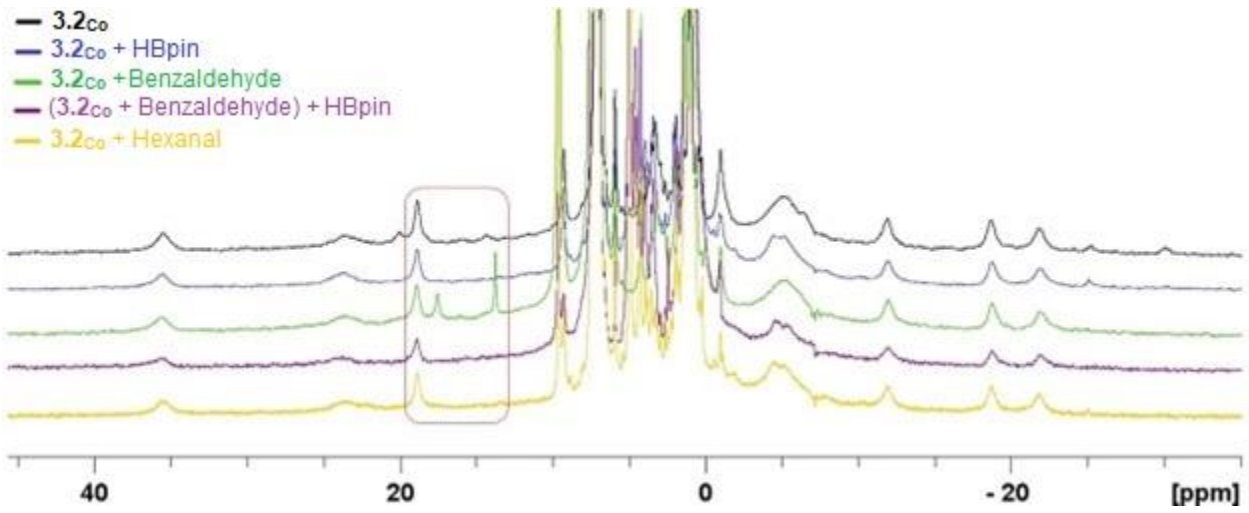

Figure B10. Stacked plot of ^{1}H NMR spectra (300 MHz, C_6D_6) of **3.2$_{Co}$** (black), stoichiometric reactions of **3.2$_{Co}$** with HBpin (blue), **3.2$_{Co}$** with benzaldehyde (green), **3.2$_{Co}$** with benzaldehyde and subsequently HBpin (purple), and **3.2$_{Co}$** with Hexanal.

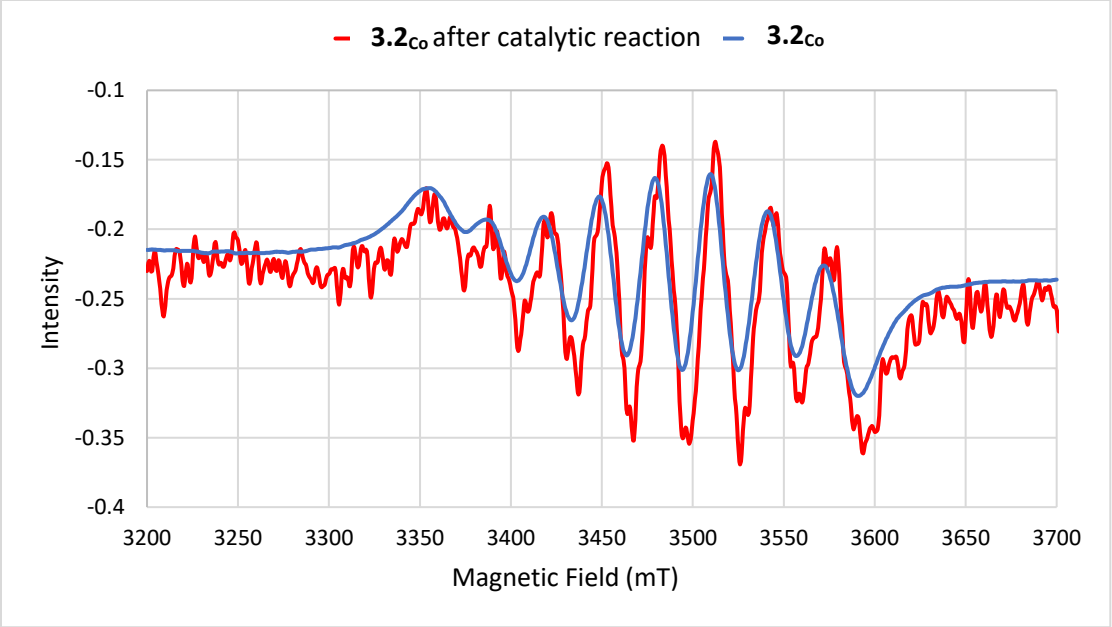

Figure B11. Stacked plot of EPR spectra of **3.2$_{Co}$** (in blue) and recovered **3.2$_{Co}$** (in red).

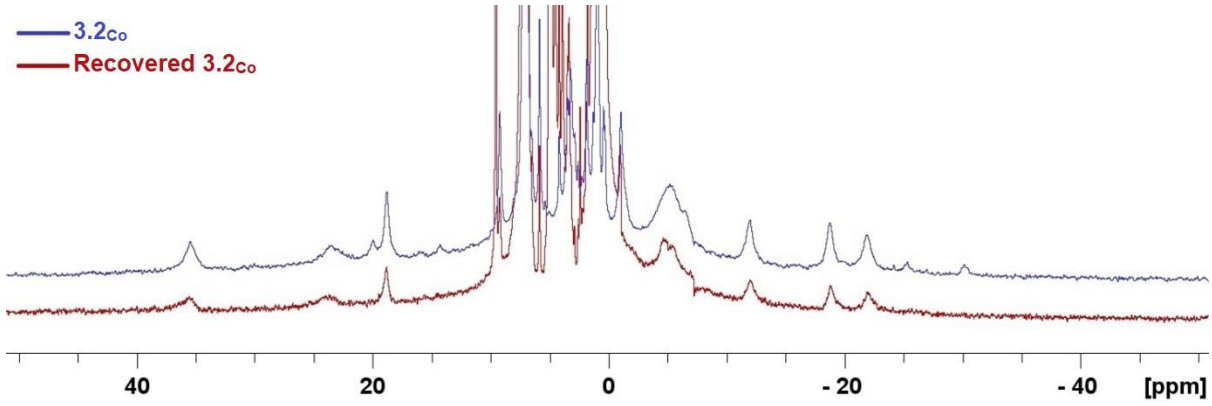

Figure B12. Stacked plot of ^{1}H NMR spectra (300 MHz, C_6D_6) of **3.2$_{Co}$** (blue) and recovered **3.2$_{Co}$** (red).

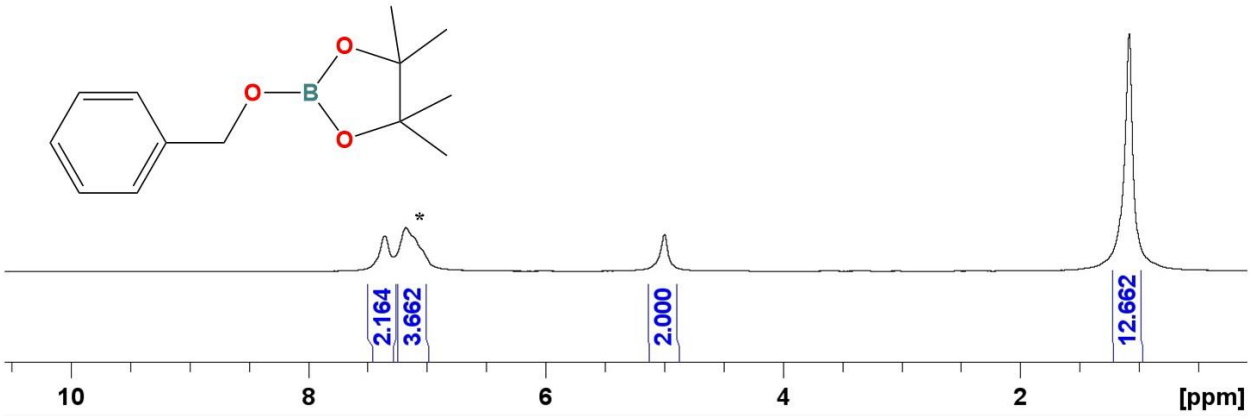

Figure B13. ^{1}H NMR spectrum (300 MHz, C_6D_6) of hydroborated benzaldehyde. * indicates protic impurity in C_6D_6.

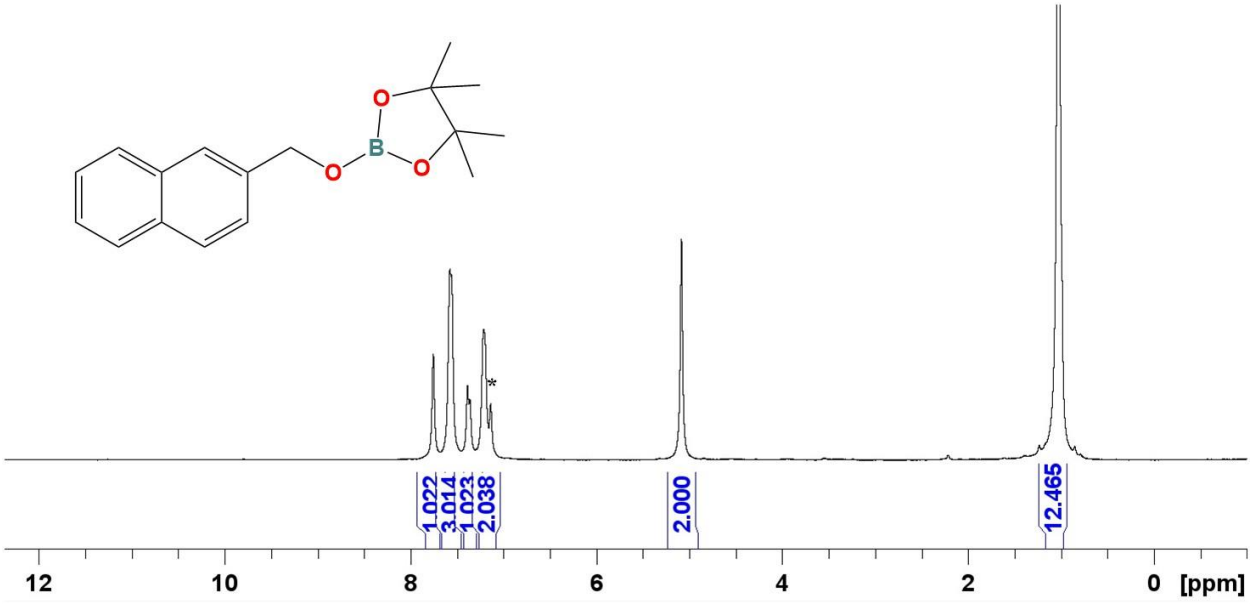

Figure B14. ^{1}H NMR spectrum (300 MHz, C_6D_6) of hydroborated 2-naphthaldehyde. * indicates protic impurity in C_6D_6.

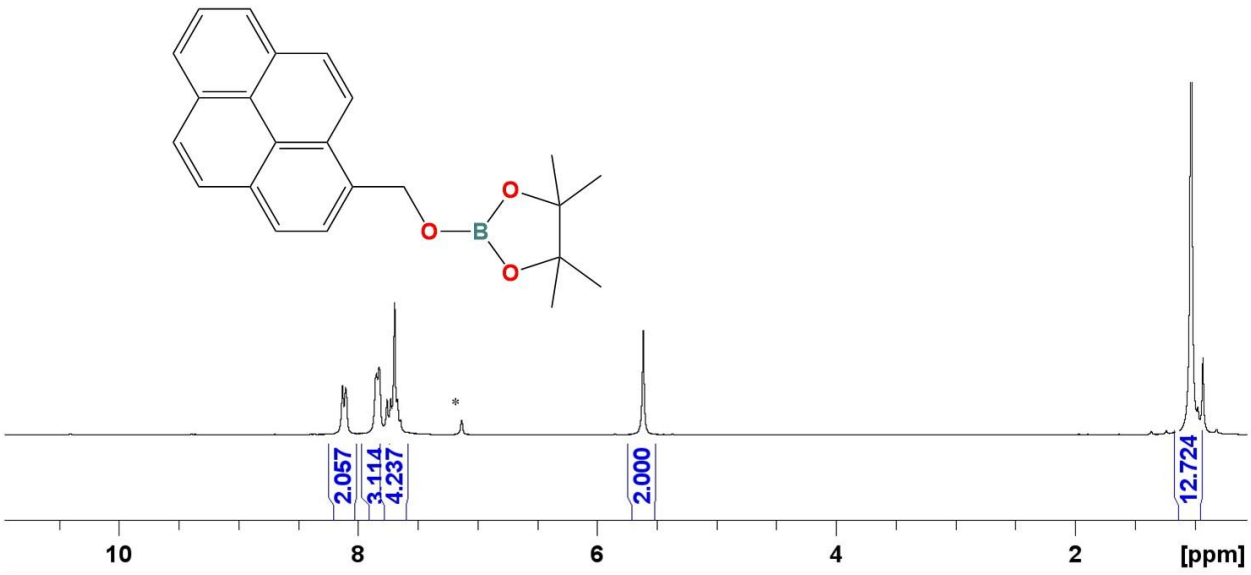

Figure B15. ^{1}H NMR spectrum (300 MHz, C_6D_6) of hydroborated 1-pyrenecarboxaldehyde. * indicates protic impurity in C_6D_6.

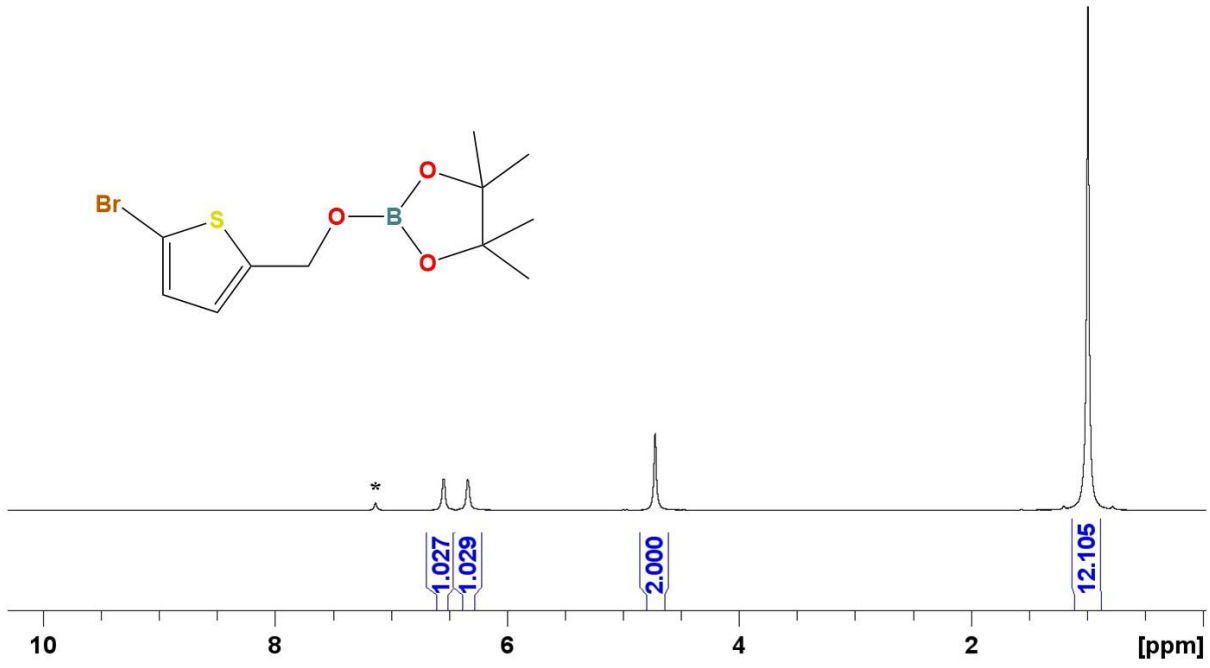

Figure B16. ^{1}H NMR spectrum (300 MHz, C_6D_6) of hydroborated 5-bromo-2-thiophenecarboxaldehyde. * indicates protic impurity in C_6D_6.

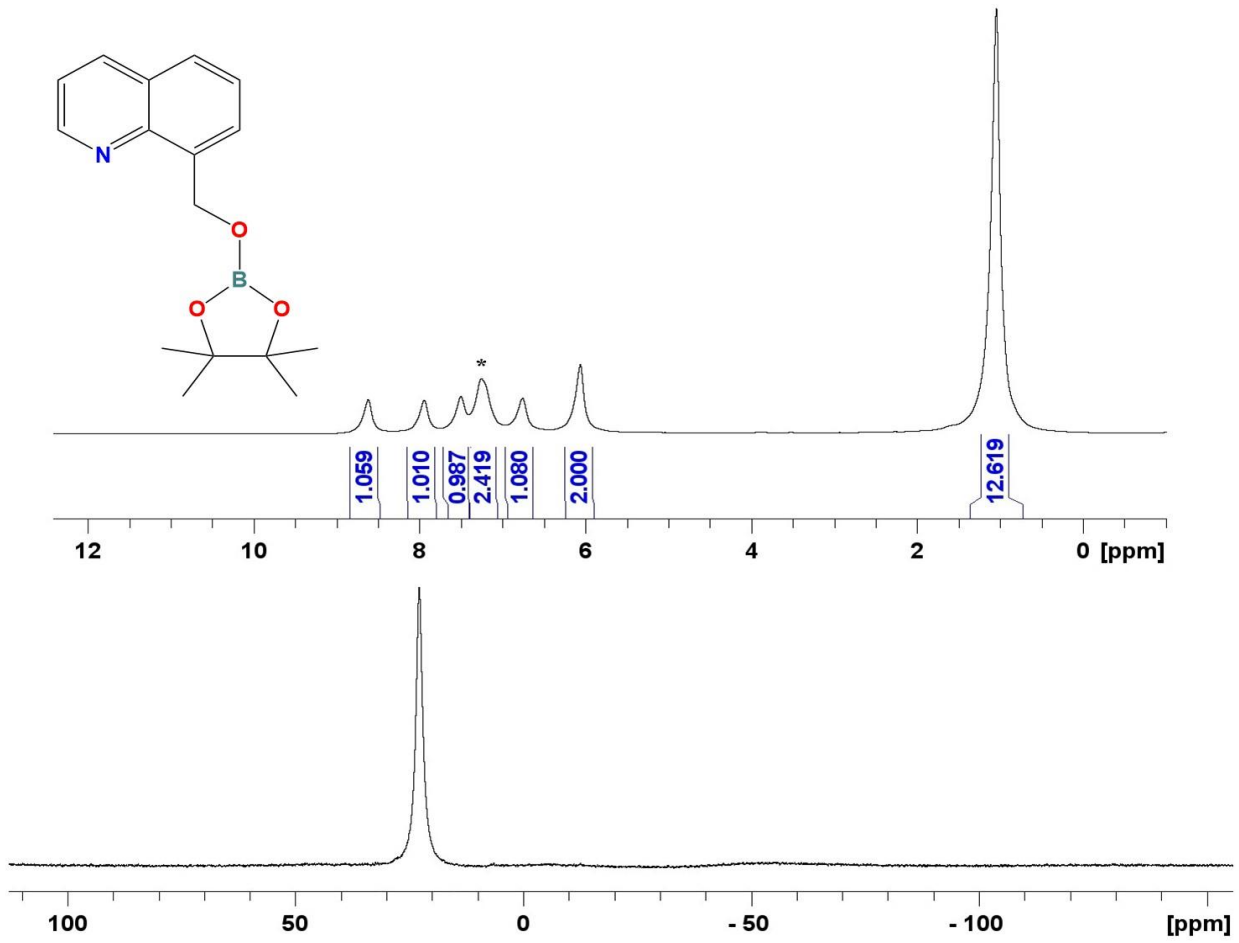

Figure B17. ^{1}H (300 MHz, C_6D_6) and ^{11}B (96 MHz) NMR spectra of hydroborated quinoline-8-carboxaldehyde. * indicates protic impurity in C_6D_6.

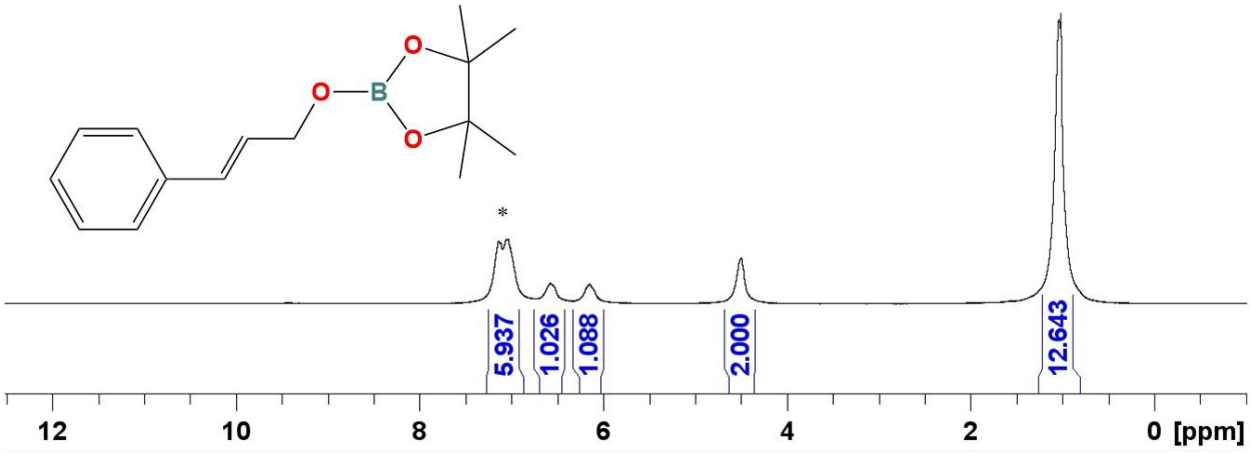

Figure B18. ^{1}H NMR spectrum (300 MHz, C_6D_6) of hydroborated cinnamaldehyde. * indicates protic impurity in C_6D_6.

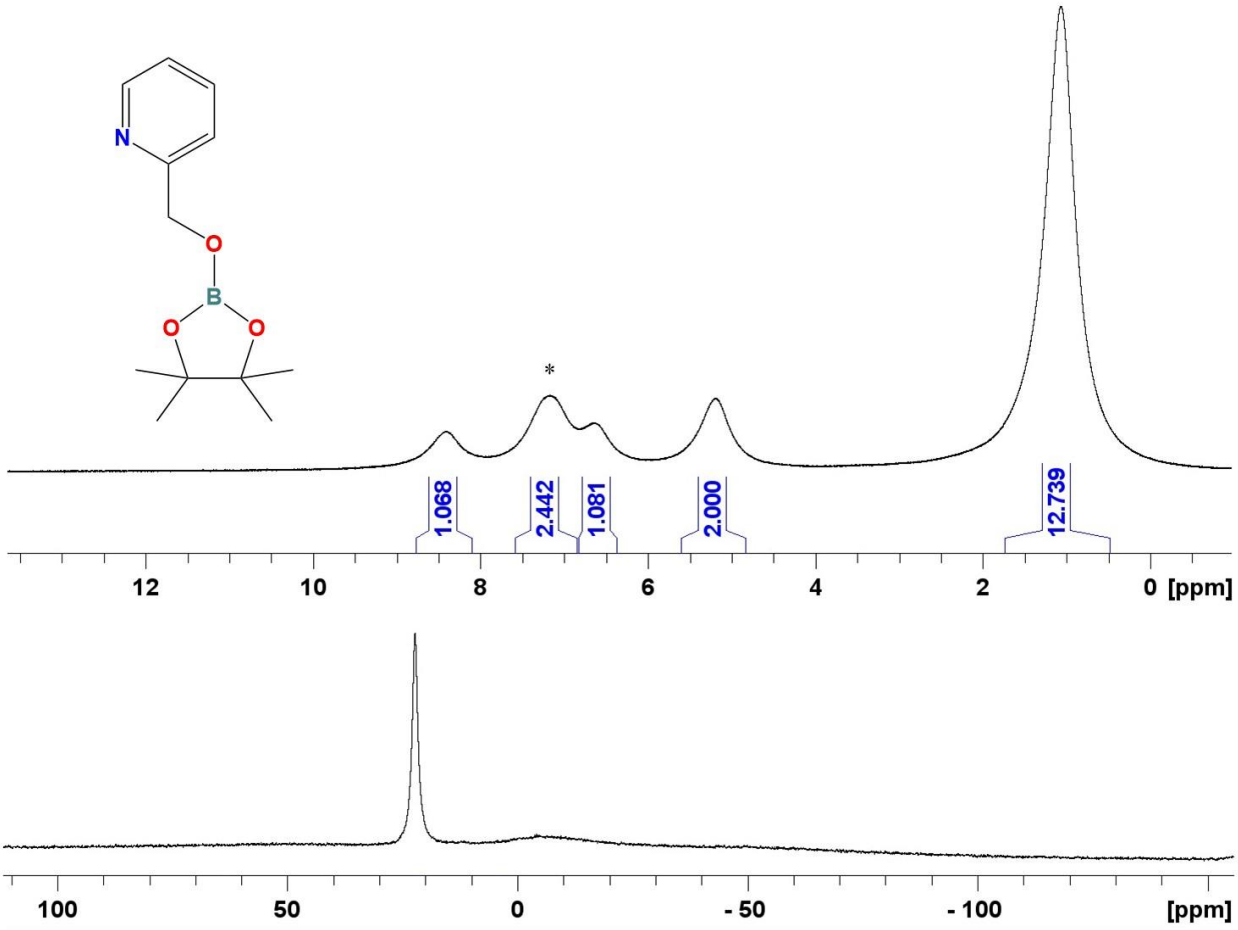

Figure B19. ^{1}H (300 MHz, C_6D_6) and ^{11}B (96 MHz) NMR spectra of hydroborated pyridine-2-carboxaldehyde. * indicates protic impurity in C_6D_6.

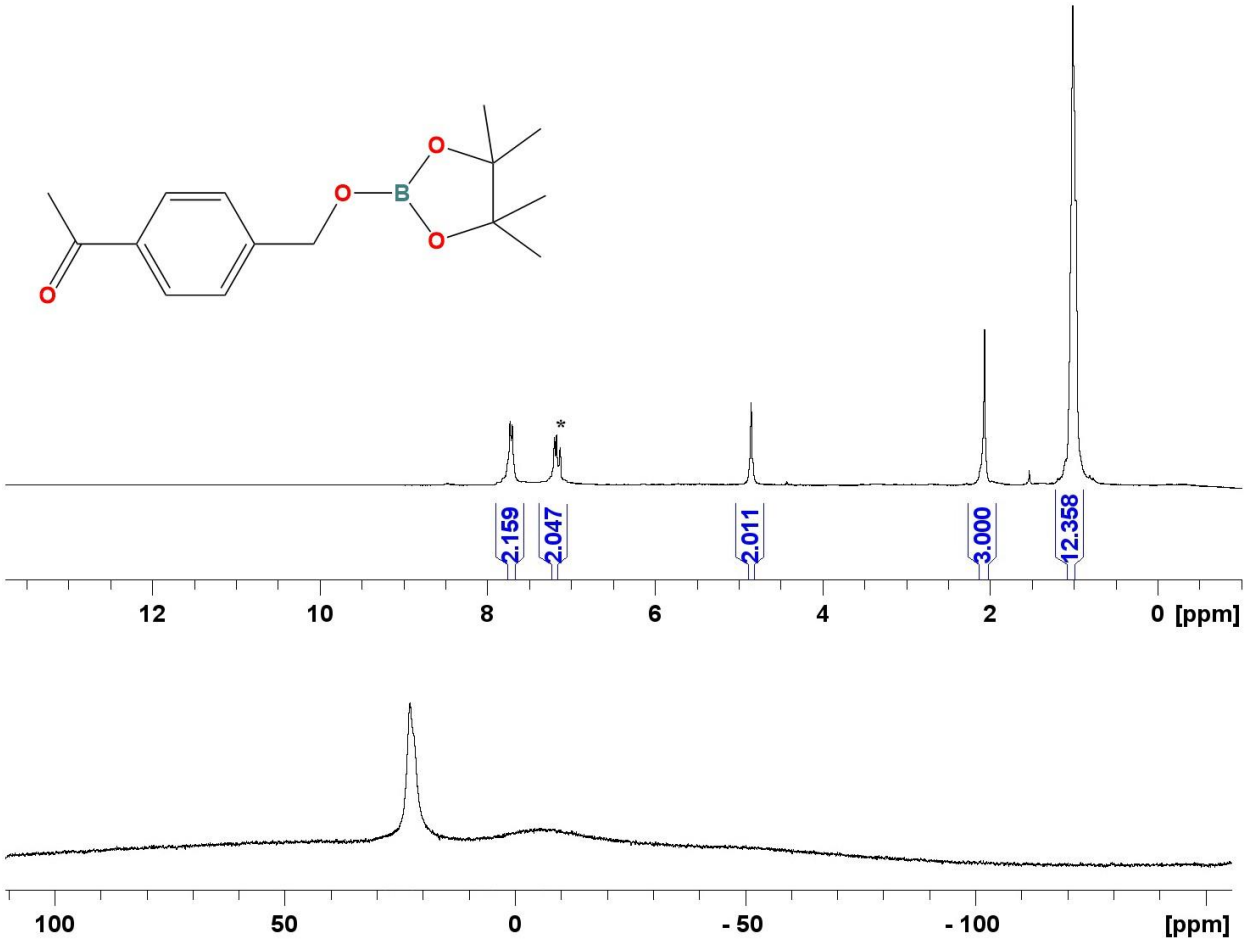

Figure B20. ^{1}H (300 MHz, C_6D_6) and ^{11}B (96 MHz) NMR spectra of hydroborated 4-acetylbenzaldehyde. * indicates protic impurity in C_6D_6.

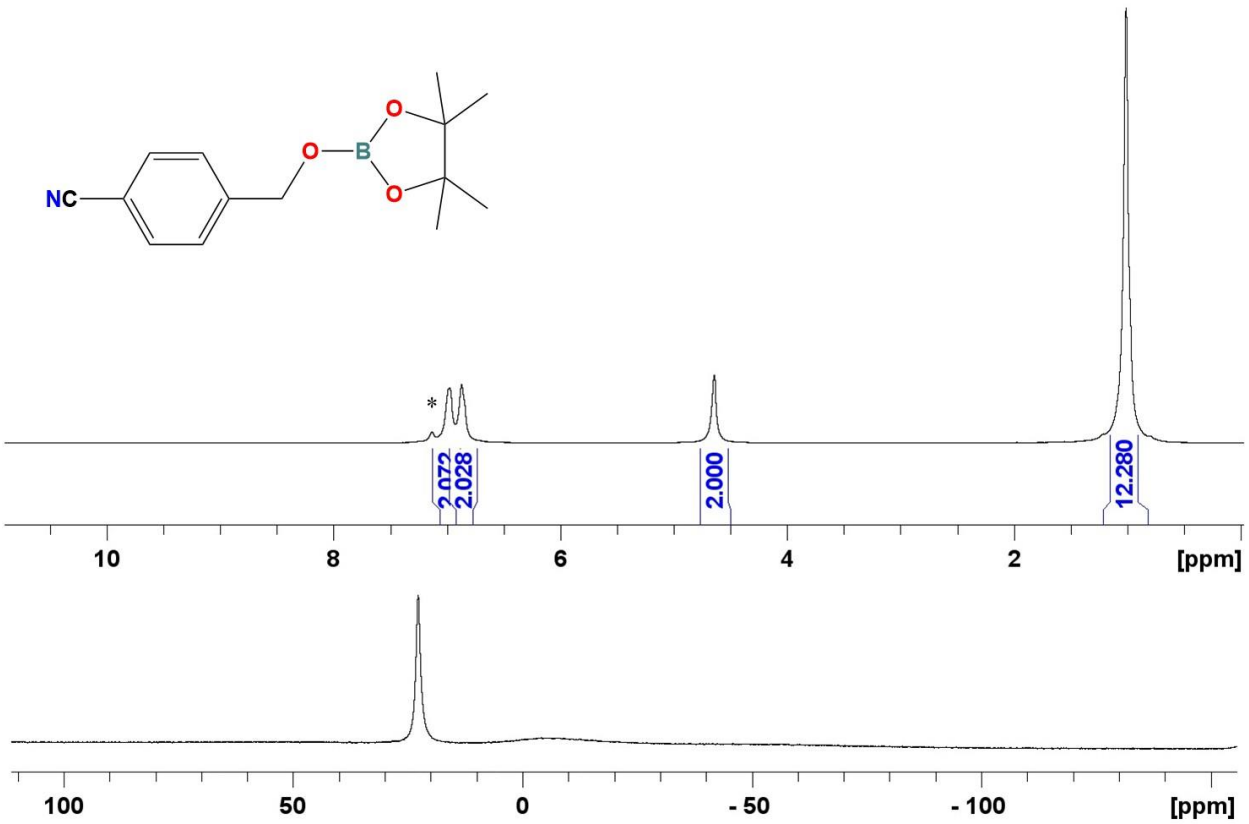

Figure B21. ^{1}H (300 MHz, C_6D_6) and ^{11}B (96 MHz) NMR spectra of hydroborated 4-cyanobenzaldehyde. * indicates protic impurity in C_6D_6.

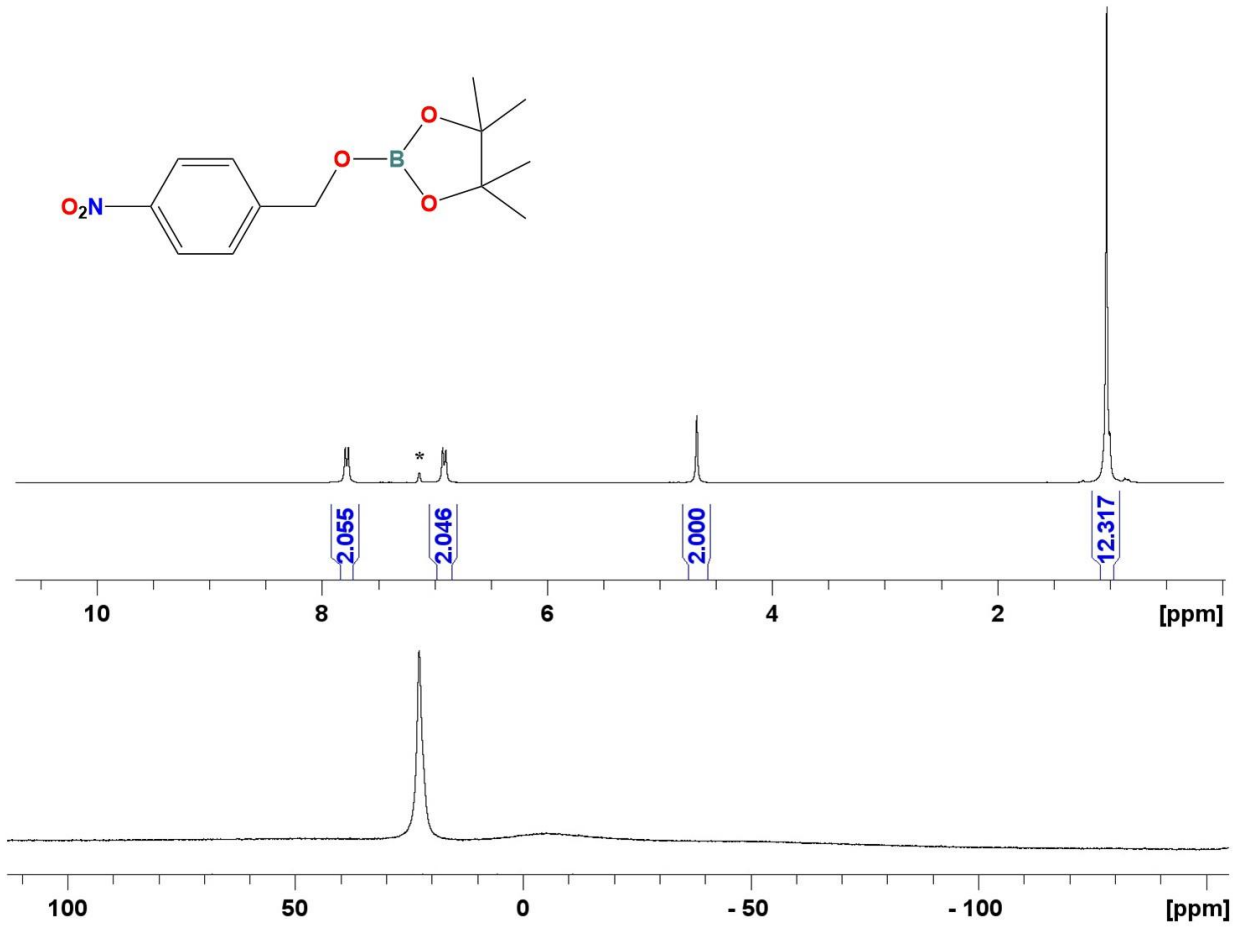

Figure B22. ^{1}H (300 MHz, C_6D_6) and ^{11}B (96 MHz) NMR spectra of hydroborated 4-nitrobenzaldehyde. * indicates protic impurity in C_6D_6.

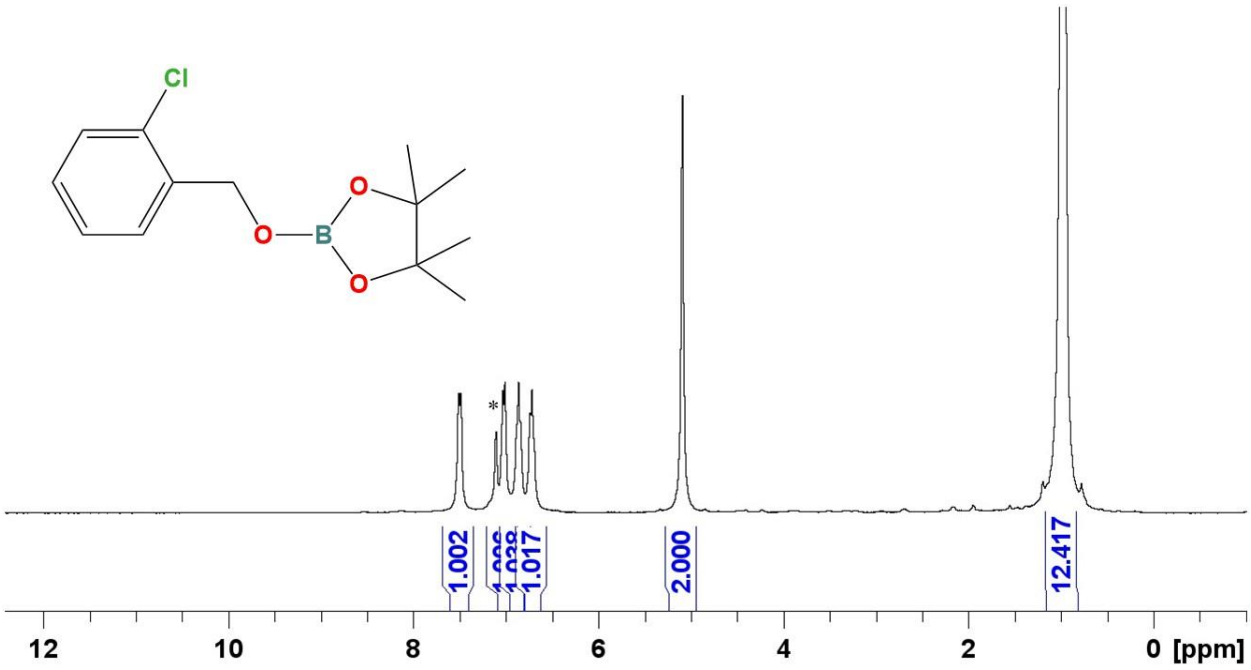

Figure B23. ^{1}H NMR spectrum (300 MHz, C_6D_6) of hydroborated 2-chlorobenzaldehyde. * indicates protic impurity in C_6D_6.

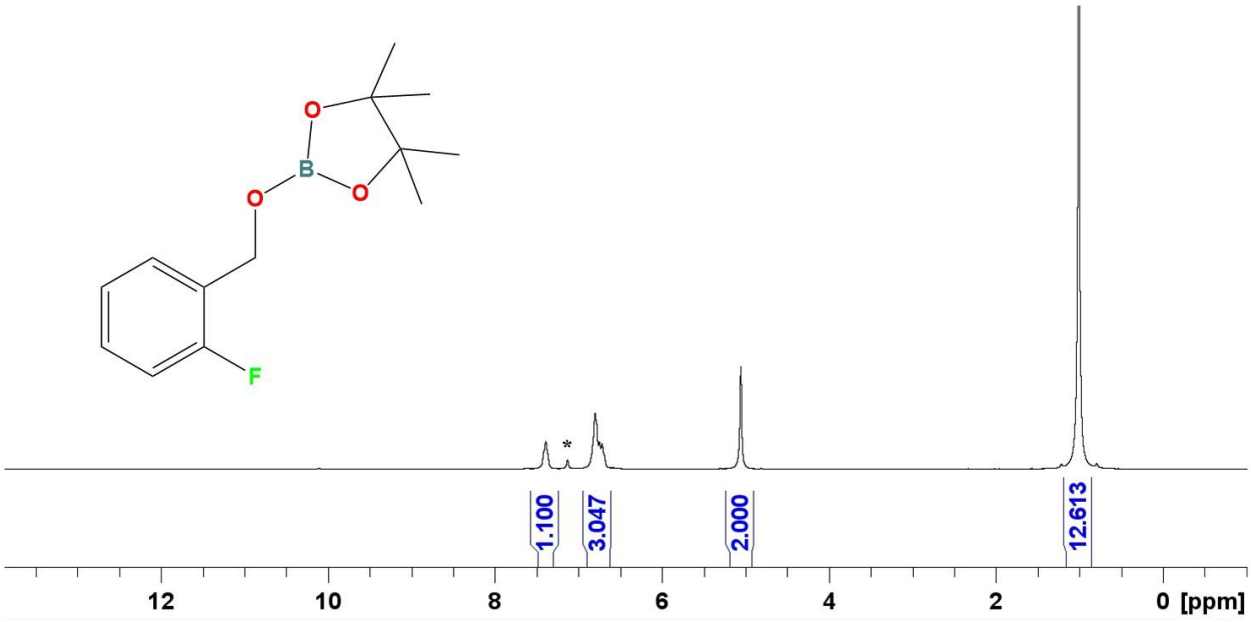

Figure B24. ^{1}H NMR spectrum (300 MHz, C_6D_6) of hydroborated 2-fluorobenzaldehyde. * indicates protic impurity in C_6D_6.

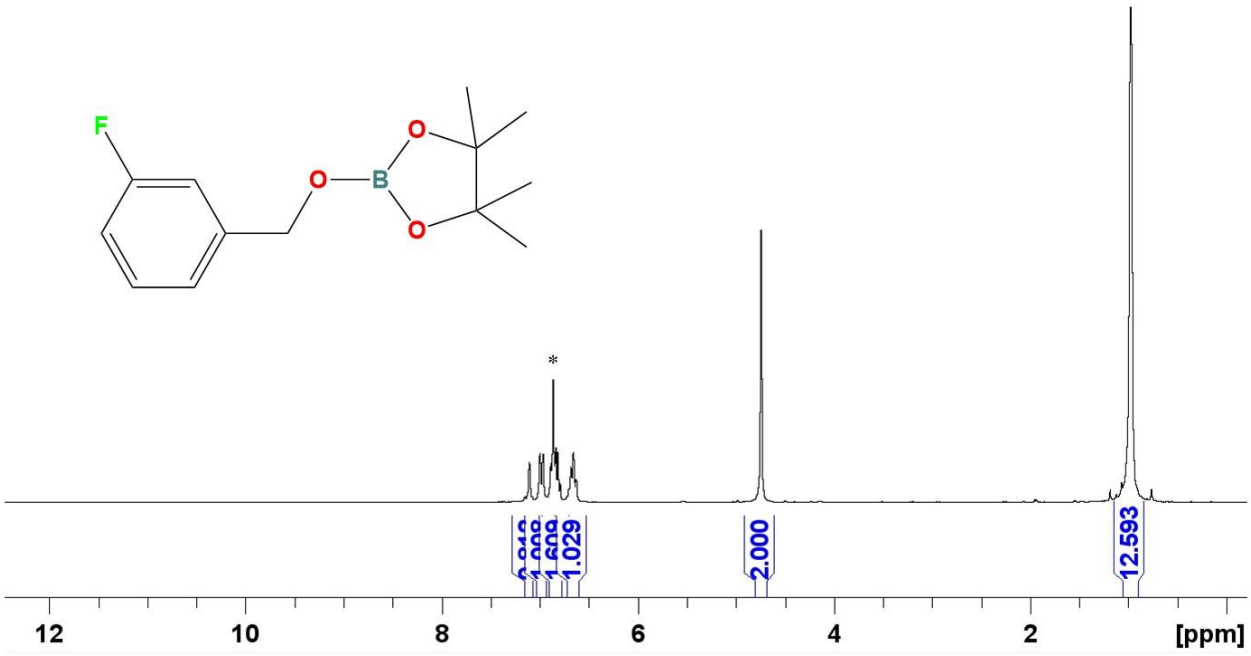

Figure B25. ^{1}H NMR spectrum (300 MHz, C_6D_6) of hydroborated 3-fluorobenzaldehyde. * indicates protic impurity in C_6D_6.

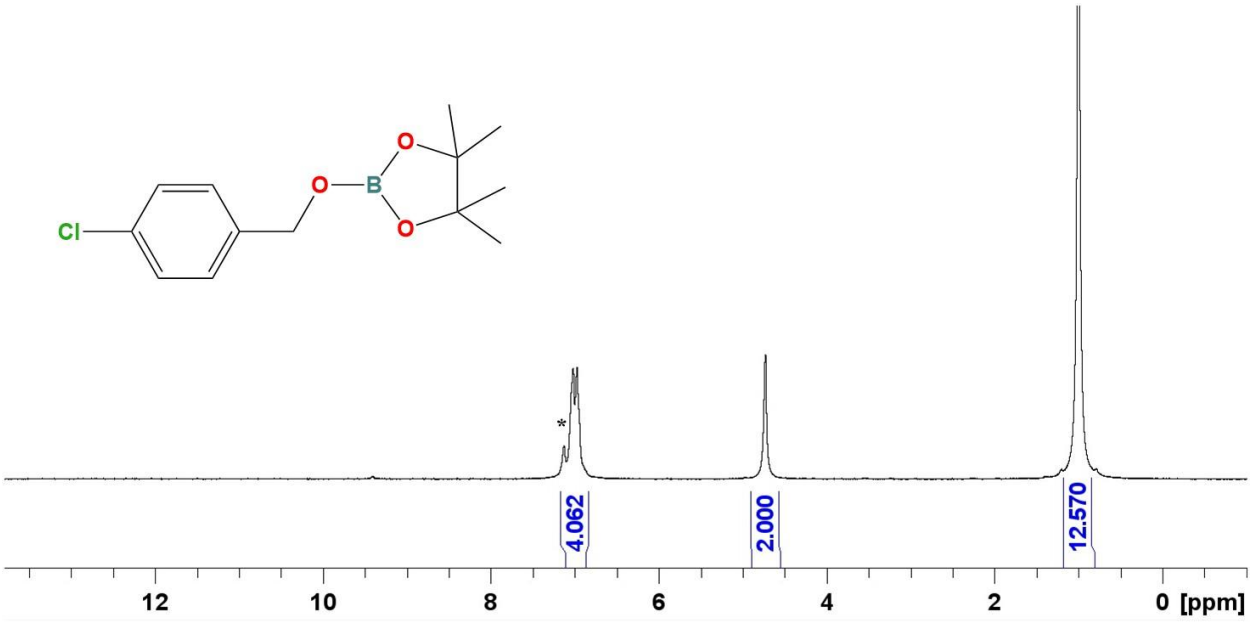

Figure B26. ^{1}H NMR spectrum (300 MHz, C_6D_6) of hydroborated 4-chlorobenzaldehyde. * indicates protic impurity in C_6D_6.

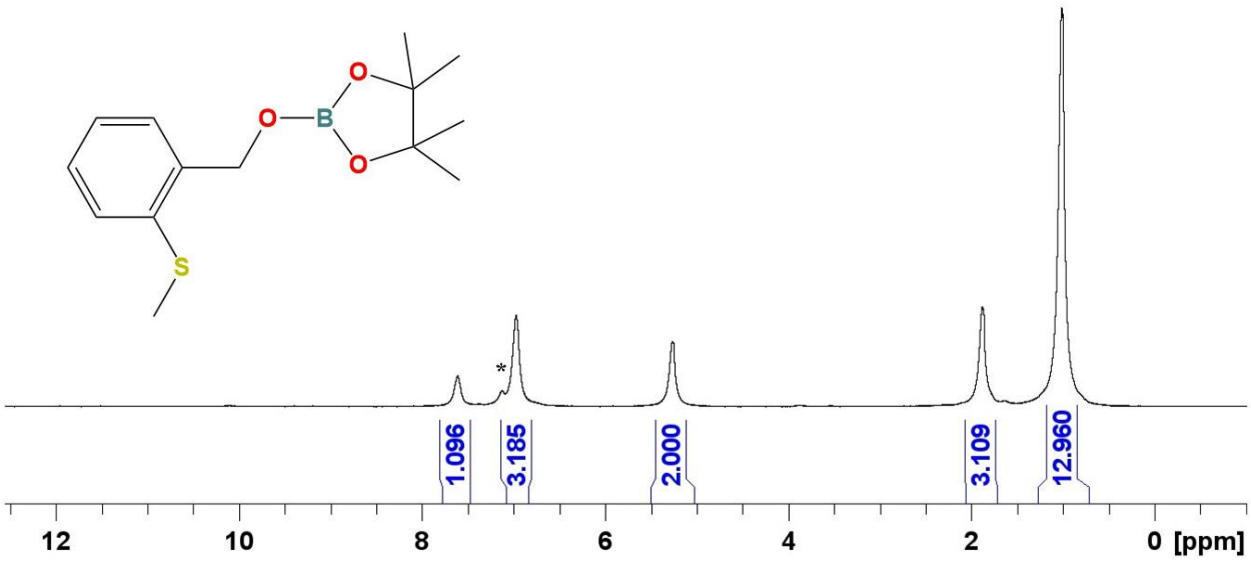

Figure B27. ^{1}H NMR spectrum (300 MHz, C_6D_6) of hydroborated 2-(methylthio)-benzaldehyde. * indicates protic impurity in C_6D_6.

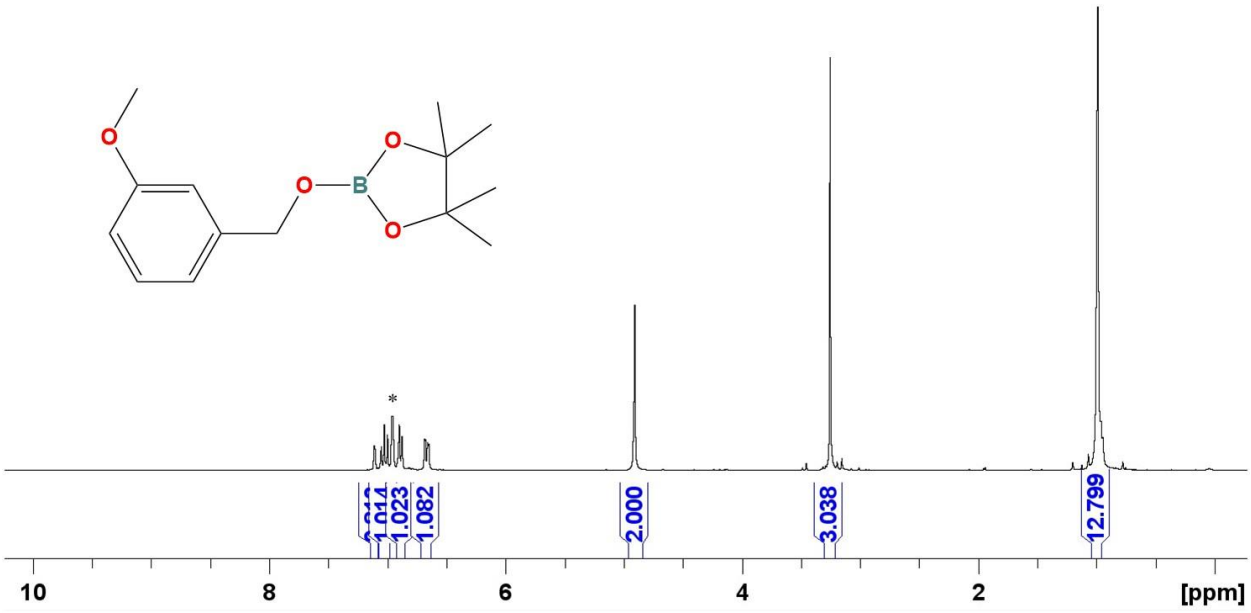

Figure B28. ^{1}H NMR spectrum (300 MHz, C_6D_6) of hydroborated 3-methoxybenzaldehyde. * indicates protic impurity in C_6D_6.

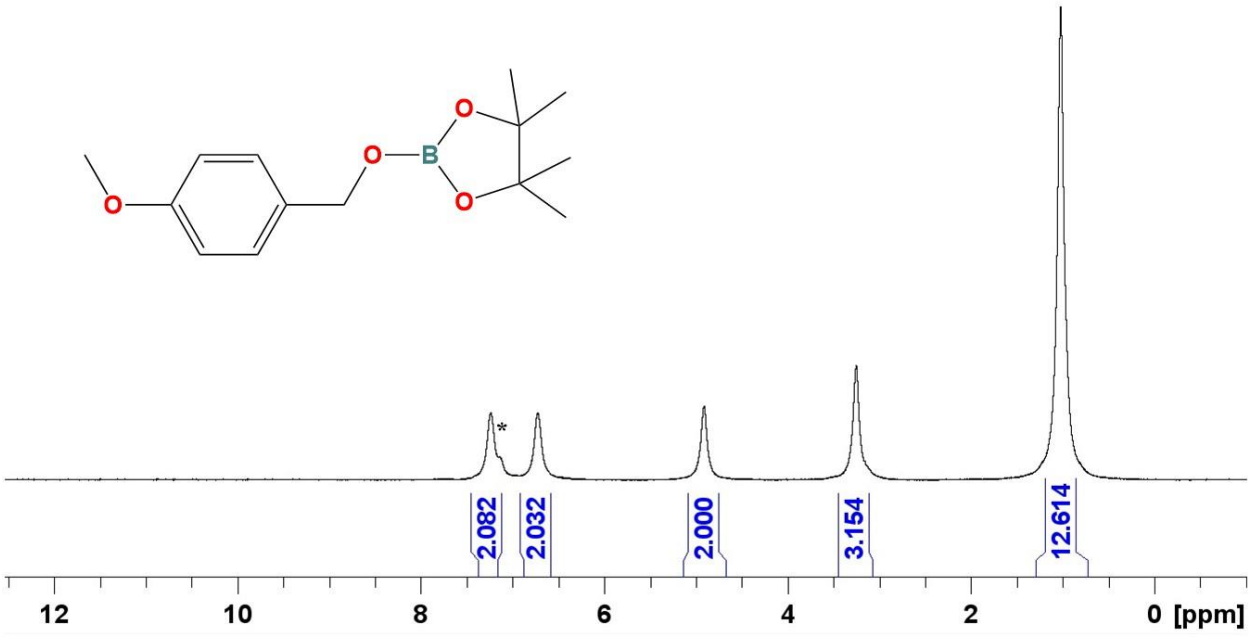

Figure B29. ^{1}H NMR spectrum (300 MHz, C_6D_6) of hydroborated 4-methoxybenzaldehyde. * indicates protic impurity in C_6D_6.

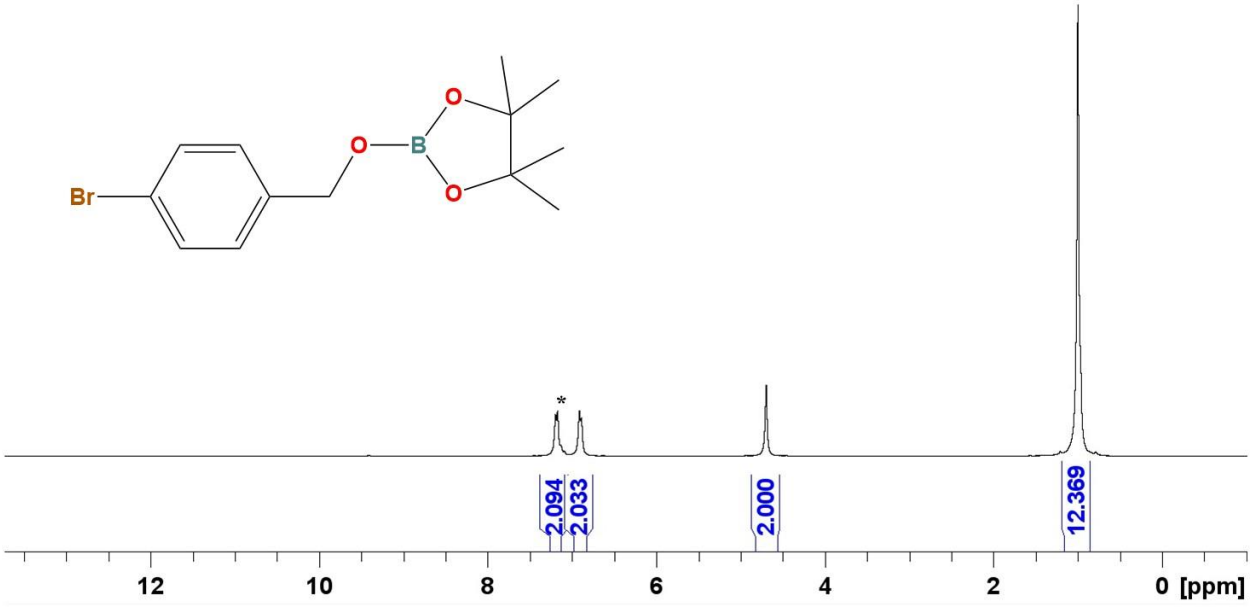

Figure B30. ^{1}H NMR spectrum (300 MHz, C_6D_6) of hydroborated 4-bromobenzaldehyde. * indicates protic impurity in C_6D_6.

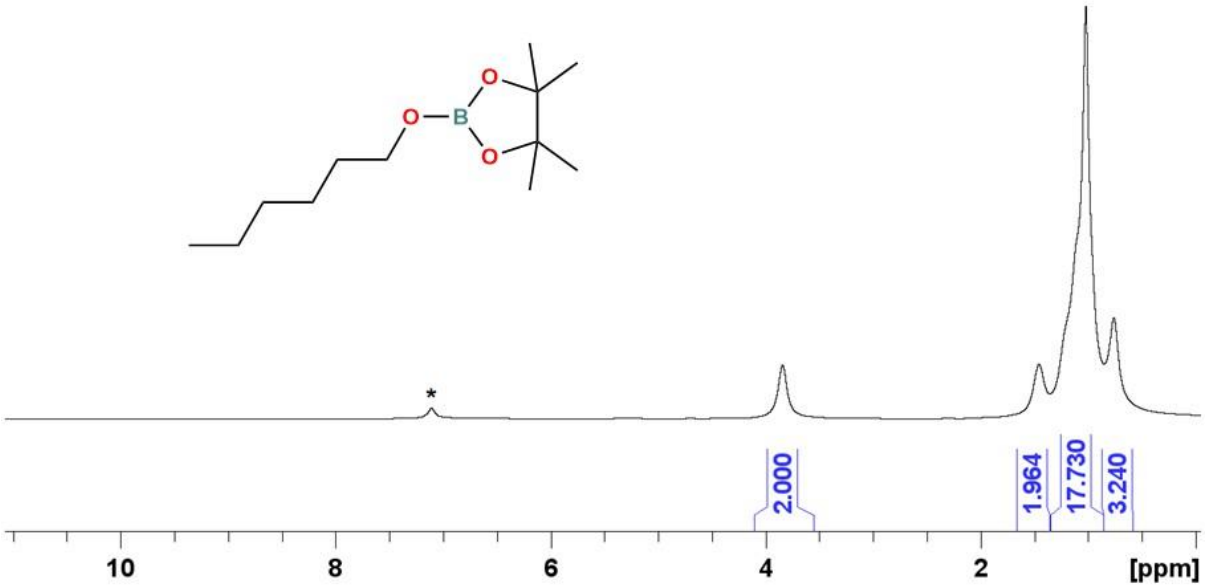

Figure B31. ^{1}H NMR spectrum (300 MHz, C_6D_6) of hydroborated Hexanal. * indicates protic impurity in C_6D_6.

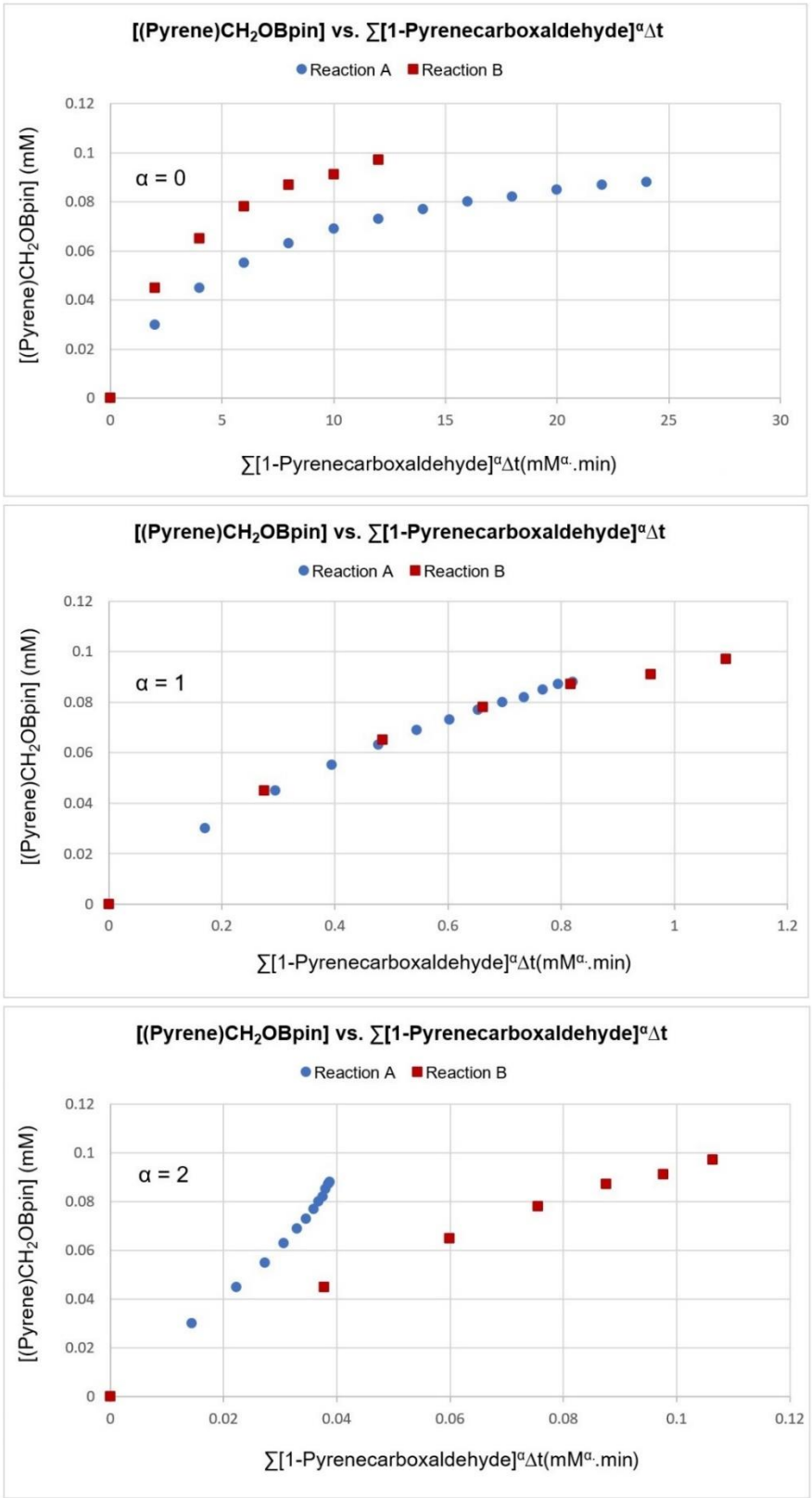

Figure B32. VTNA of rate order of [1-pyrenecarboxaldehyde].

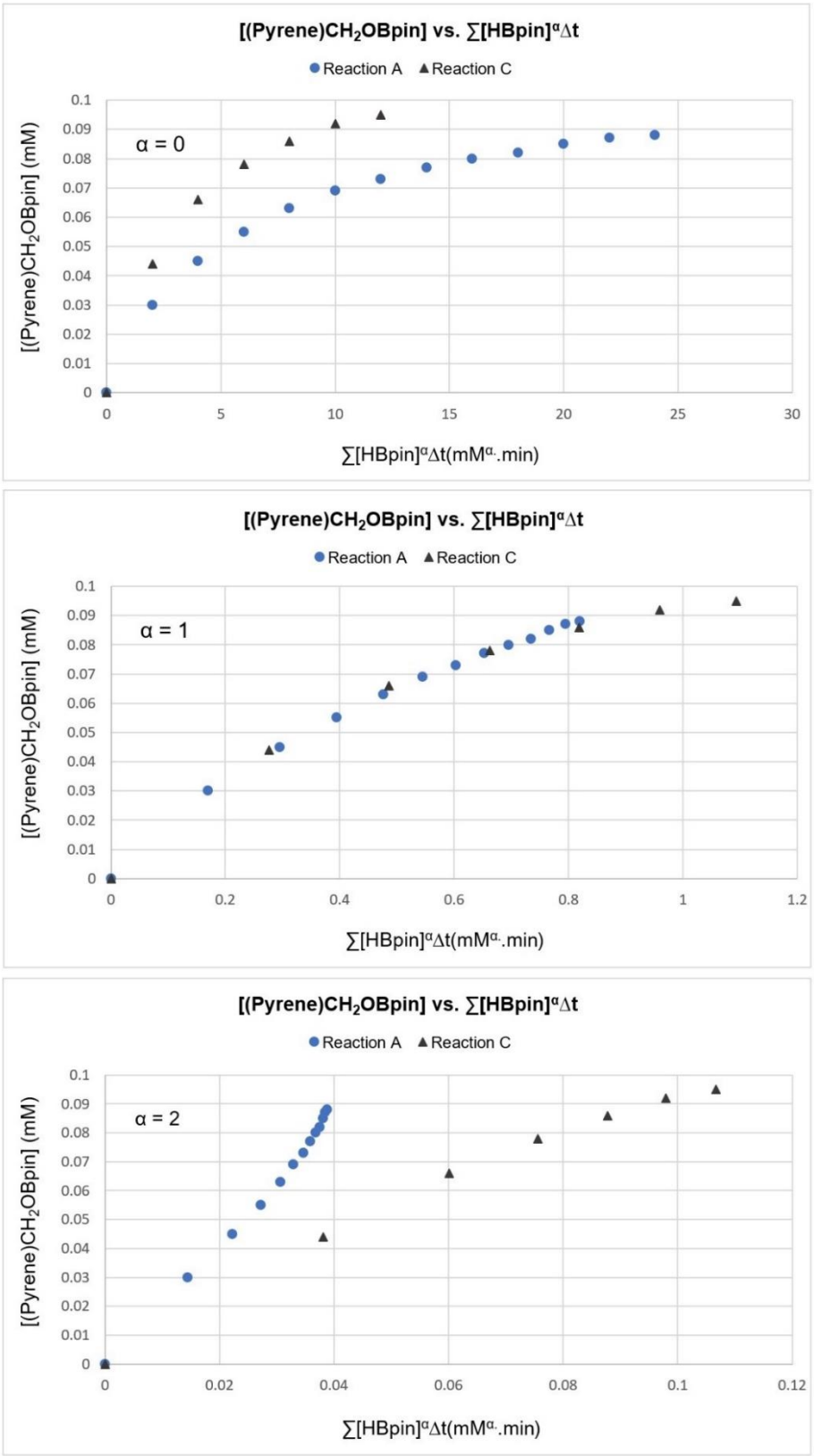

Figure B33. VTNA of rate order of [HBpin].

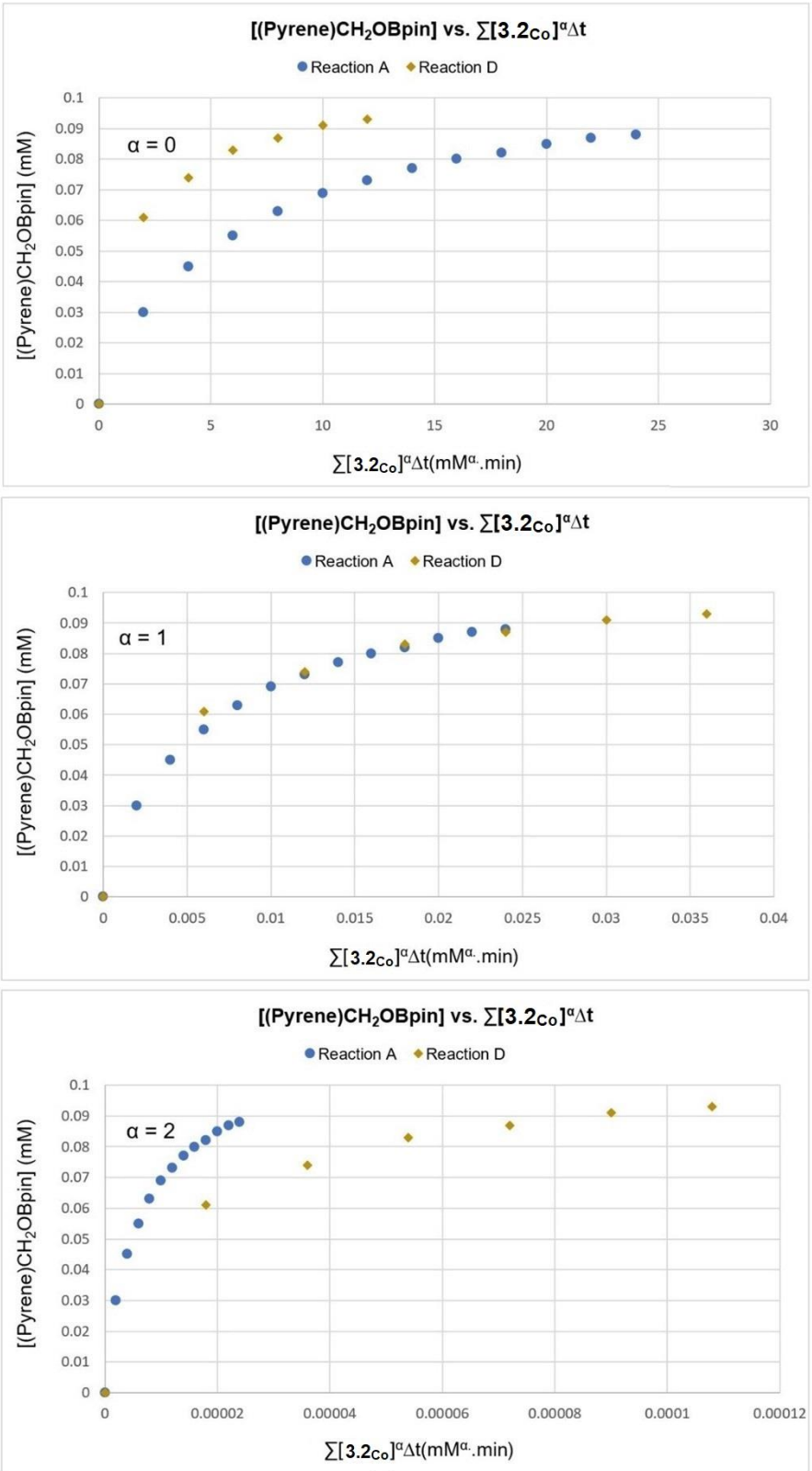

Figure B34. VTNA of rate order of [**3.2$_{Co}$**].

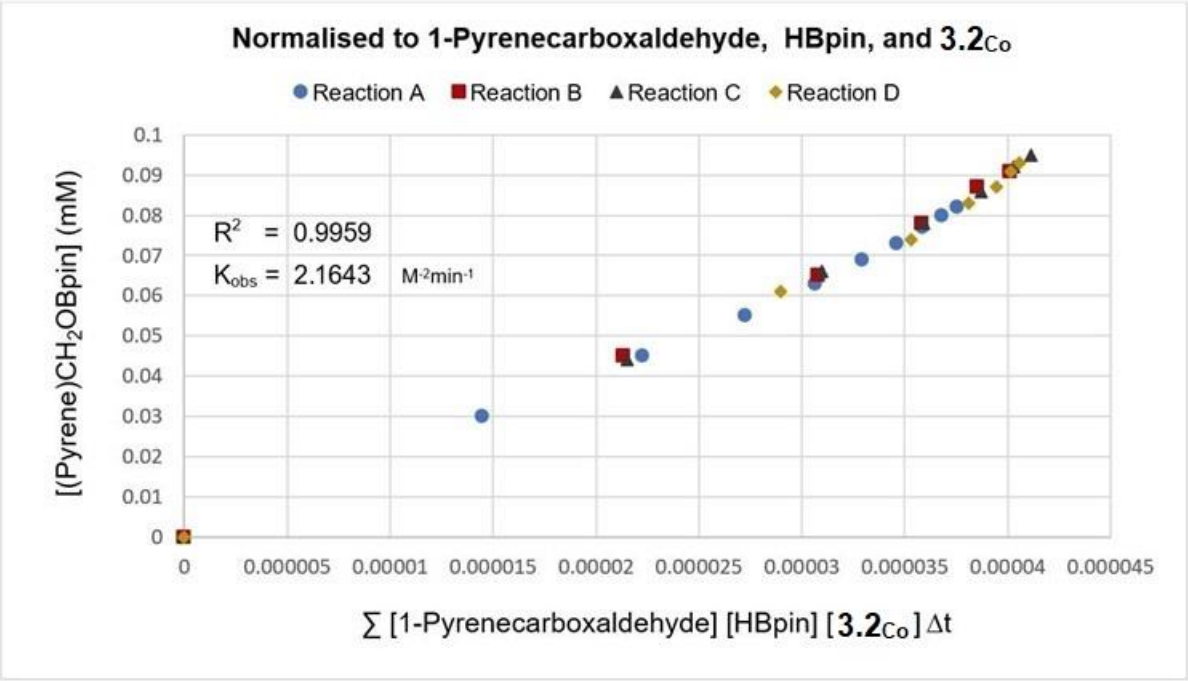

Figure B35. VTNA of [(pyrene)CH_2OBpin] vs. Σ [1-pyrenecarboxaldehyde][HBpin][**3.2**$_{Co}$] Δt to give k_{obs}.

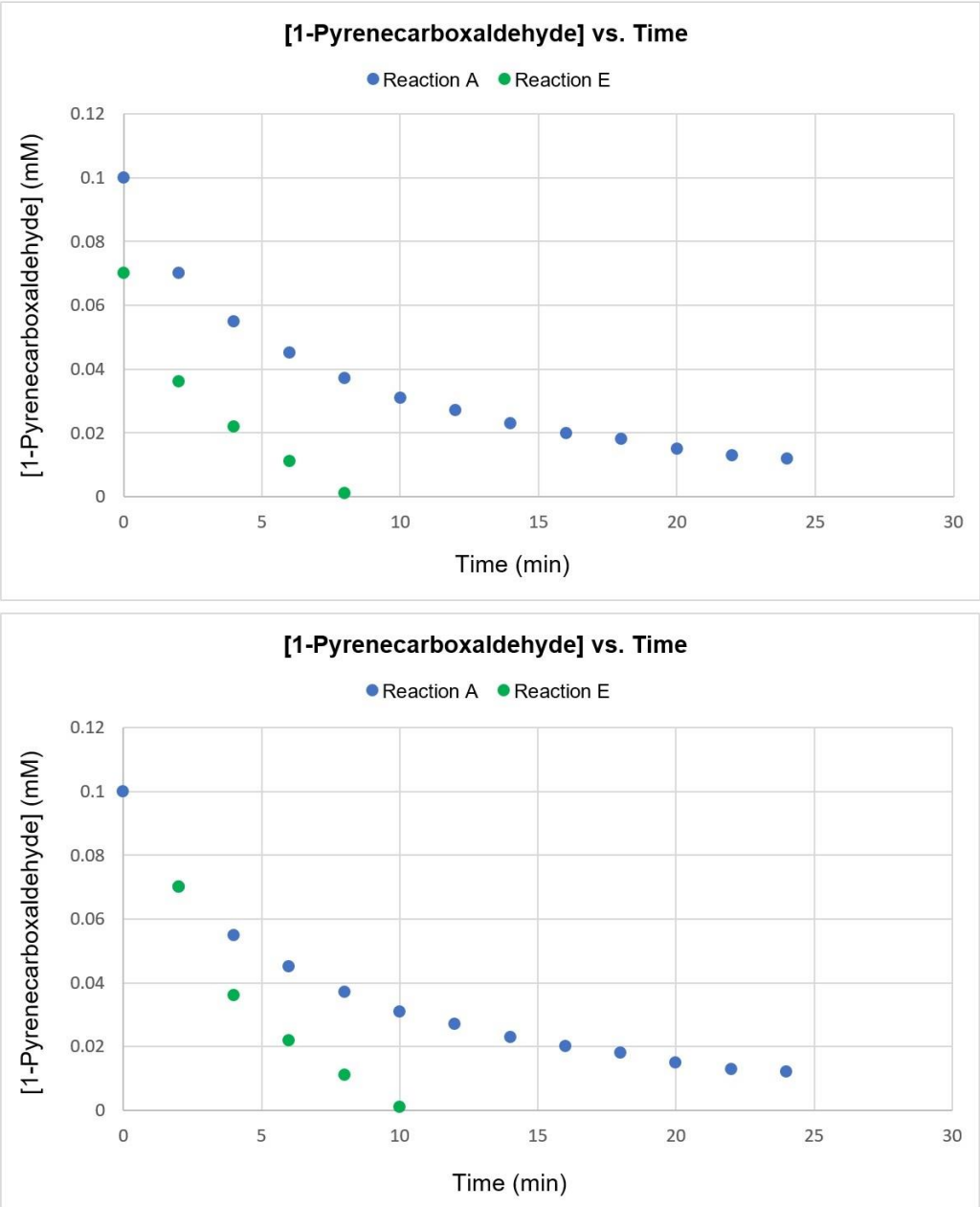

Figure B36. VTNA of [1-pyrenecarboxaldehyde] vs. time to find out if the catalytic system suffers either product inhibition or catalyst deactivation. Top: before time adjustment. Bottom: after time adjustment.

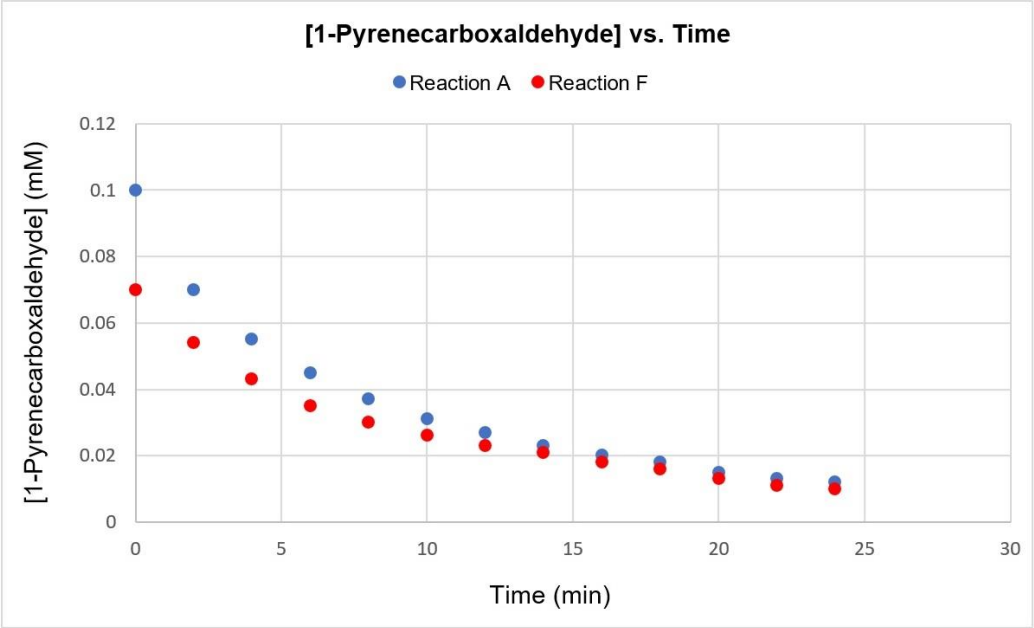

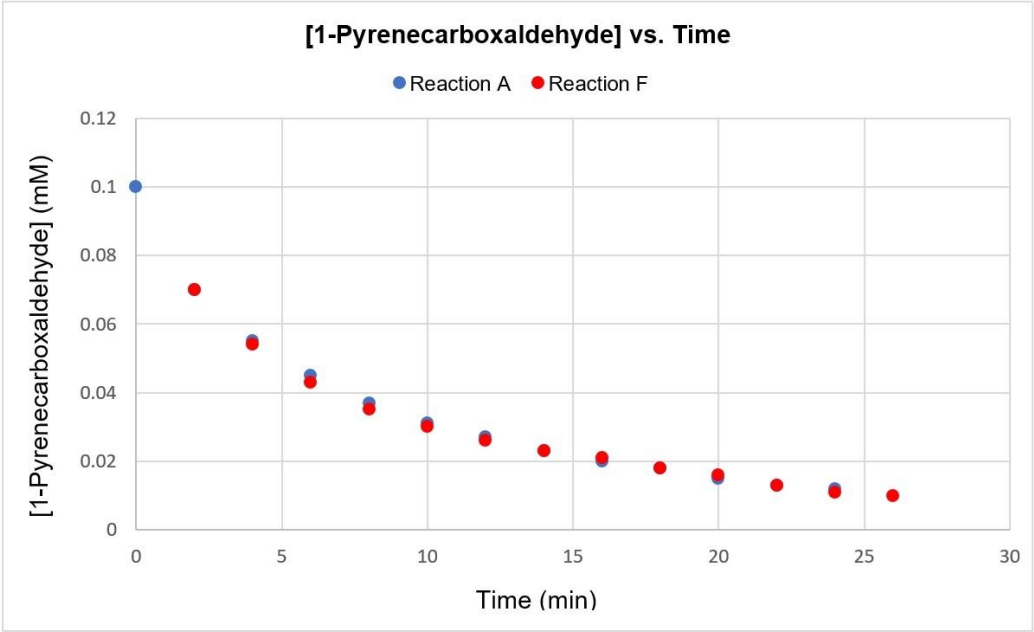

Figure B37. VTNA of [1-Pyrenecarboxaldehyde] vs. time to find out if the catalytic system suffers product inhibition. Top: before time adjustment. Bottom: after time adjustment.

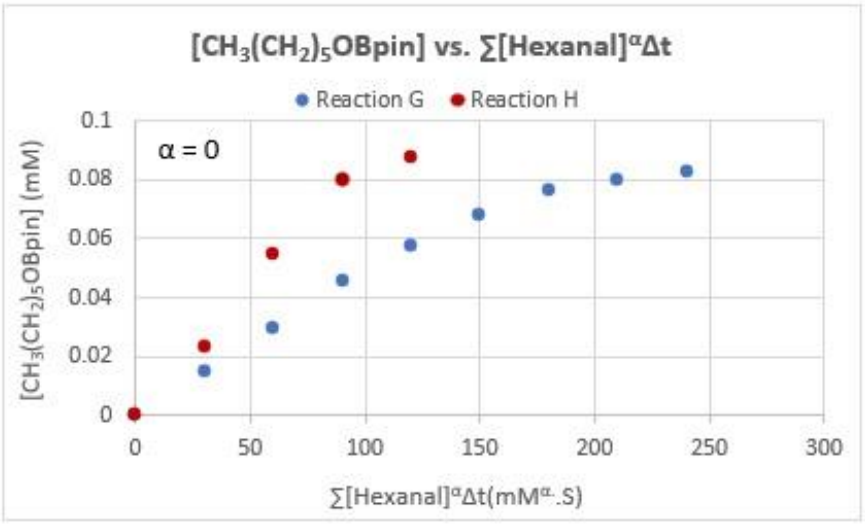

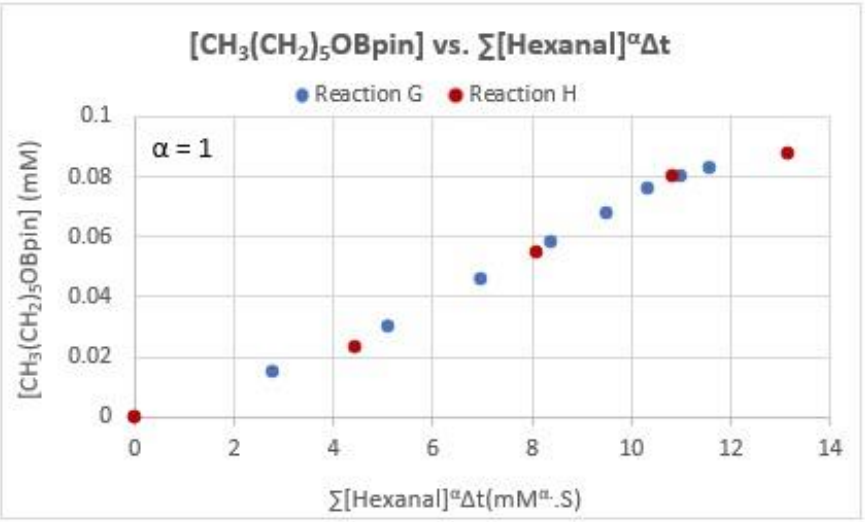

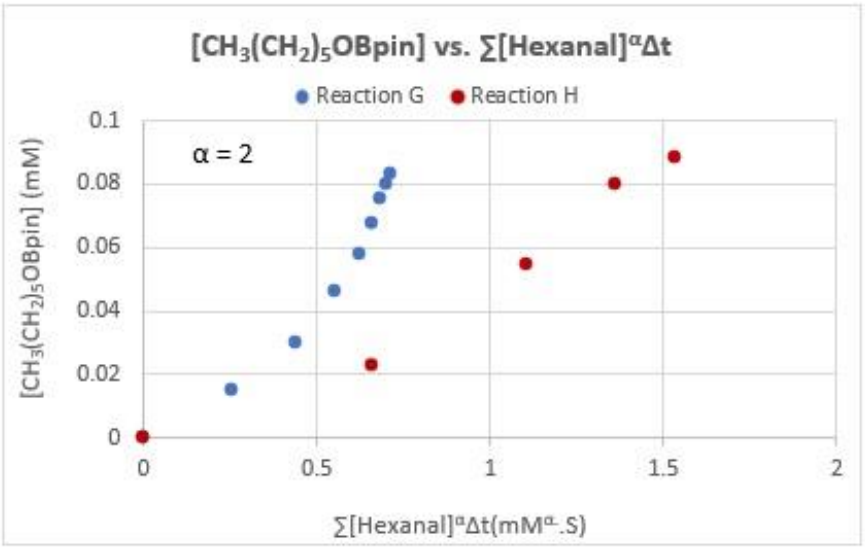

Figure B38. VTNA of rate order of [Hexanal].

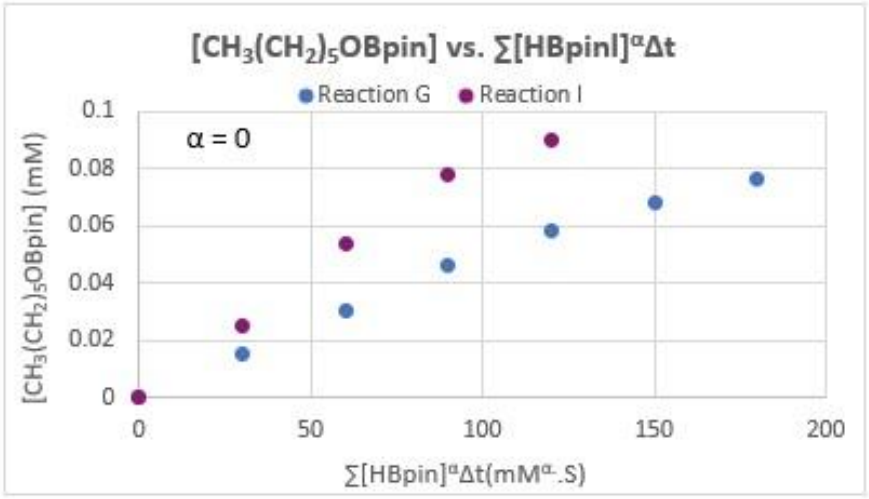

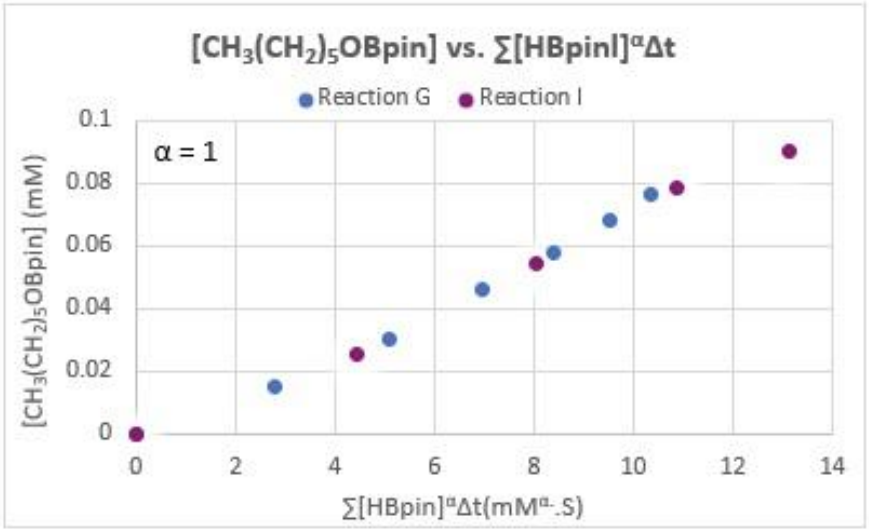

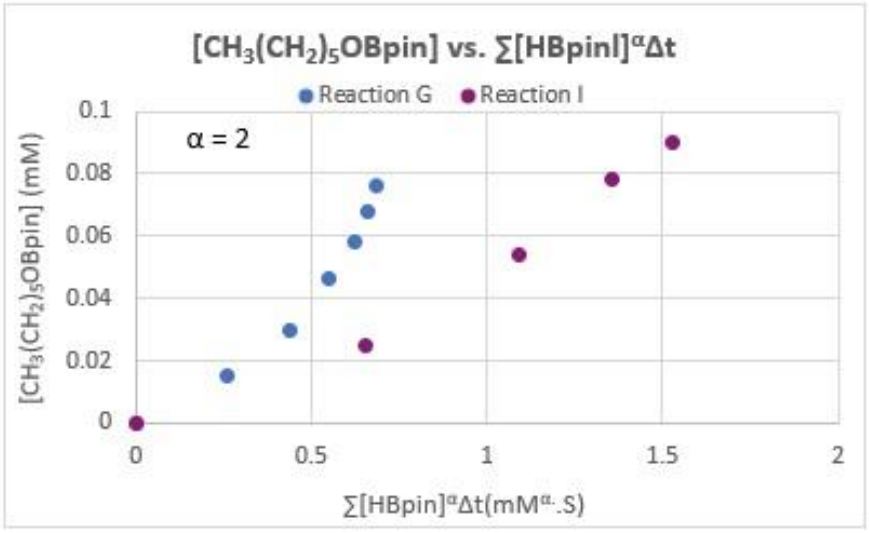

Figure B39. VTNA of rate order of [HBpin].

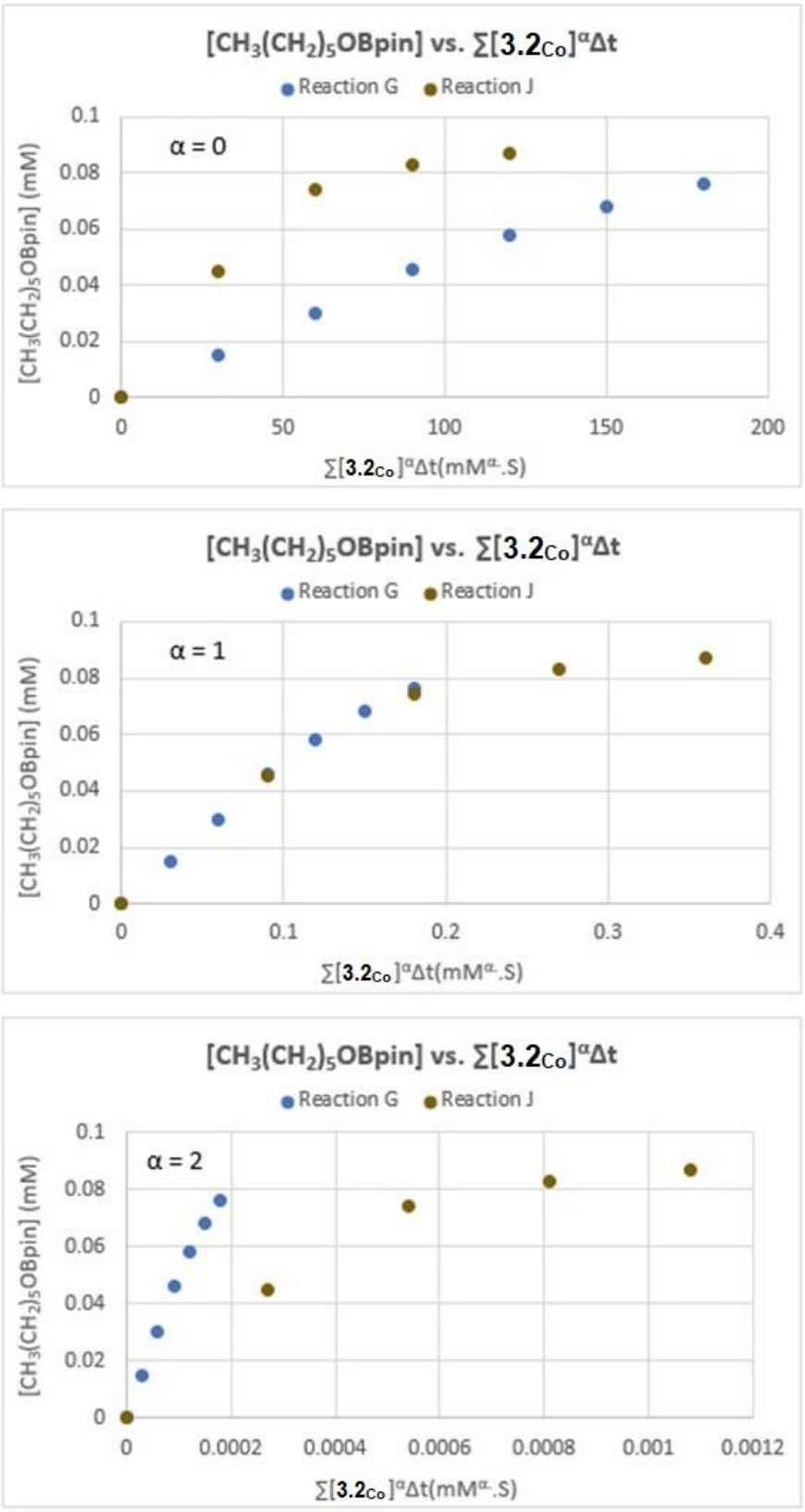

Figure B40. VTNA of rate order of [$\mathbf{3.2_{Co}}$].

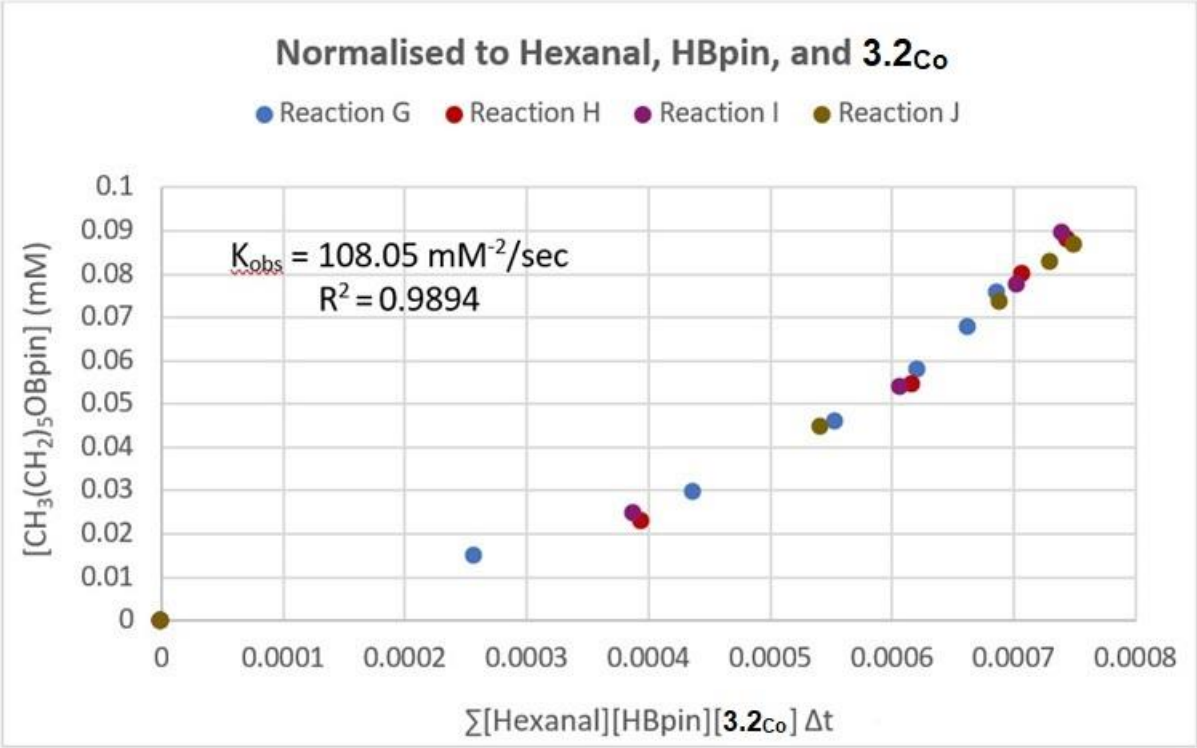

Figure B41. VTNA of $[CH_3(CH_2)_5OBpin]$ vs. Σ [Hexanal][HBpin][**3.2**$_{Co}$] Δt to give k_{obs}.

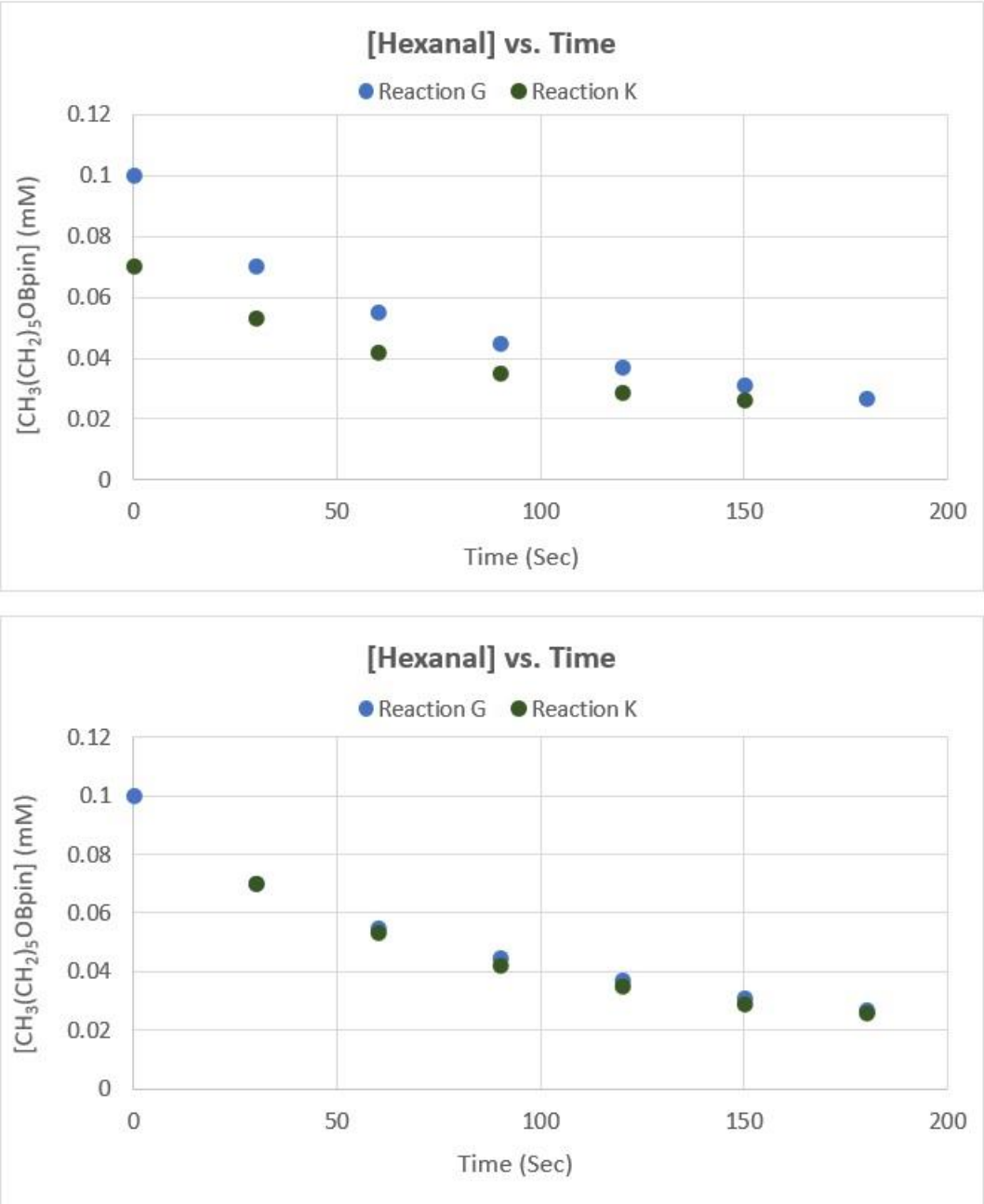

Figure B42. VTNA of [Hexanal] vs. time to find out if the catalytic system suffers either product inhibition or catalyst deactivation. Top: before time adjustment. Bottom: after time adjustment.

Table B1. Data collection and refinement metrics for **3.2$_{Co}$**, **3.4$_{Co}$**and **C.**

	3.2$_{Co}$ (S0933)	**3.4$_{Co}$** (S0907)	**C** (S1040)
empirical formula	$C_{18}H_{15}Cl_2CoN_3S_2$	$C_{10}H_{12}Cl_4CoI_2N_4$	$C_{23}H_{23}B_3O_3$
formula weight ($g \cdot mol^{-1}$)	467.28	642.77	358.22
crystal system	Monoclinic	Monoclinic	Monoclinic
space group	*P* $2_1/n$	*P* $2_1/c$	*P* $2_1/c$
a (A)	9.9944(6)	8.3466(4)	10.027(6)
b (A)	14.7779(10)	18.4430(9)	11.235(6)
c (A)	13.3704(8)	25.5300(11)	17.190(10)
α (deg)	90	90	90
β (deg)	106.754(2)	97.492(2)	92.096(19)
γ (deg)	90	90	90
V (A^3)	1890.9(2)	3896.4(3)	1935.2(19)
Z	4	8	4
T (K)	203(2)	203(2)	293(2)
ρ_{calcd} ($g \cdot cm^{-3}$)	1.641	2.191	1.230
μ (mm^{-1})	1.418	4.596	0.079
$2\theta_{max}$ (deg)	52.764	56.93	50.048
total/unique reflections	13977/3820	60226/9770	11007/3413
Reflections [$I_o \geq 2\sigma(I_o)$]	2395	6611	1564
R_1, wR_2 [$I_o \geq 2\sigma(I_o)$]	0.0399, 0.0724	0.0405, 0.0842	0.0558, 0.1337
goodness of fit	1.011	1.020	0.940
CCDC number	2162426	2162428	2162427

Table B2. Bond lengths for **3.2$_{Co}$.**

Atom1	Atom2	Length
Cl1	C5	1.693(3)
Cl2	C4	1.696(3)
N1	C1	1.458(3)
N1	C2	1.355(4)
N1	C5	1.378(3)
N2	C2	1.359(3)
N2	C3	1.451(4)
N2	C4	1.381(4)
C1	H1A	0.97
C1	H1B	0.97
C1	H1C	0.97
C2	Co1A	1.891(5)
C3	H3A	0.969
C3	H3B	0.97
C3	H3C	0.97
C4	C5	1.337(4)
C6	C7	1.404(4)
C6	C11	1.392(4)
C6	S1A	1.720(9)
C7	H7	0.94
C7	C8	1.367(6)
C8	H8	0.94
C8	C9	1.367(5)
C9	H9	0.94
C9	C10	1.366(5)
C10	H10	0.94
C10	C11	1.399(6)
C11	C12A	1.437(7)
C13	C14	1.389(5)
C13	C18	1.387(5)
C13	N3A	1.512(5)
C14	H14	0.94
C14	C15	1.367(4)
C15	H15	0.94
C15	C16	1.369(5)
C16	H16	0.94
C16	C17	1.370(4)
C17	H17	0.94
C17	C18	1.383(4)
C18	S2A	1.811(4)
Co1A	S1A	2.160(8)
Co1A	N3A	1.921(6)

Co1A	S2A	2.166(6)
N3A	C12A	1.301(9)
C12A	H12A	0.94

Table B3. Bond lengths for **3.4$_{Co}$.**

Atom1	Atom2	Length
I1	Co1	2.5917(7)
I2	Co1	2.5988(8)
Co1	C3	2.056(4)
Co1	C8	2.049(4)
Cl1	C2	1.699(6)
Cl2	C4	1.690(6)
Cl3	C7	1.702(4)
Cl4	C9	1.692(5)
N1	C1	1.454(8)
N1	C2	1.380(7)
N1	C3	1.365(6)
N2	C3	1.362(6)
N2	C4	1.390(7)
N2	C5	1.451(9)
N3	C6	1.453(6)
N3	C7	1.379(6)
N3	C8	1.357(6)
N4	C8	1.360(6)
N4	C9	1.380(6)
N4	C10	1.461(7)
C1	H1A	0.969
C1	H1B	0.971
C1	H1C	0.969
C2	C4	1.326(8)
C5	H5A	0.97
C5	H5B	0.97
C5	H5C	0.969
C6	H6A	0.971
C6	H6B	0.97
C6	H6C	0.969
C7	C9	1.339(7)
C10	H10A	0.97
C10	H10B	0.969
C10	H10C	0.971
I3	Co2	2.5936(9)
I4	Co2	2.5995(8)

Co2	C13	2.054(5)
Co2	C18	2.051(5)
Cl5	C12	1.696(5)
Cl6	C14	1.692(6)
Cl7	C17	1.699(5)
Cl8	C19	1.703(5)
N5	C11	1.453(6)
N5	C12	1.382(7)
N5	C13	1.364(6)
N6	C13	1.356(6)
N6	C14	1.375(7)
N6	C15	1.466(7)
N7	C16	1.443(7)
N7	C17	1.376(6)
N7	C18	1.365(7)
N8	C18	1.358(7)
N8	C19	1.377(6)
N8	C20	1.473(7)
C11	H11A	0.969
C11	H11B	0.97
C11	H11C	0.97
C12	C14	1.332(7)
C15	H15A	0.971
C15	H15B	0.969
C15	H15C	0.97
C16	H16A	0.969
C16	H16B	0.97
C16	H16C	0.97
C17	C19	1.322(7)
C20	H20A	0.97
C20	H20B	0.97
C20	H20C	0.97

Table B4. Bond lengths for **C**

Atom1	Atom2	Length
O1	C00J	1.437(4)
O1	B1	1.338(4)
O2	B1	1.349(4)
O2	C5A	1.46(1)
O3	B1	1.364(4)
O3	C6A	1.46(2)
C00A	H00A	0.93
C00A	C007	1.343(5)
C00A	C008	1.430(5)

C00B	C00H	1.430(5)
C00B	C00L	1.376(5)
C00B	C005	1.422(4)
C00C	C00E	1.423(5)
C00C	C00M	1.397(6)
C00C	C006	1.420(4)
C00D	H00D	0.93
C00D	C00L	1.388(5)
C00D	C009	1.385(5)
C00E	H00E	0.93
C00E	C00H	1.336(6)
C00H	H00H	0.93
C00J	H00B	0.97
C00J	H00C	0.971
C00J	C009	1.497(5)
C00K	H00K	0.93
C00K	C00N	1.372(5)
C00K	C008	1.391(5)
C00L	H00L	0.93
C00M	H00M	0.93
C00M	C00N	1.361(6)
C00N	H00N	0.93
C004	C005	1.422(3)
C004	C007	1.432(4)
C004	C009	1.401(4)
C005	C006	1.416(4)
C006	C008	1.405(4)
C007	H007	0.93
C1A	H1AA	0.96
C1A	H1AB	0.96
C1A	H1AC	0.96
C1A	C6A	1.51(1)
C2A	H2AA	0.96
C2A	H2AB	0.96
C2A	H2AC	0.96
C2A	C6A	1.49(2)
C3A	H3AA	0.961
C3A	H3AB	0.959
C3A	H3AC	0.96
C3A	C5A	1.55(1)
C4A	H4AA	0.96
C4A	H4AB	0.96
C4A	H4AC	0.959
C4A	C5A	1.49(1)
C5A	C6A	1.55(2)

3.2_{Co}

total energy (SCF+XDM) -3.959275815966E+03

Thermal correction to Gibbs Free Energy=0.243701

Cl	5.13761	-0.33071	1.71989
C	3.80753	-0.10957	0.66544
N	2.48925	-0.32991	1.03806
C	3.78757	0.29386	-0.63314
C	2.04966	-0.77303	2.35717
C	1.65064	-0.06671	0.00179
Cl	5.08605	0.71357	-1.66639
N	2.45746	0.31455	-1.02746
H	0.97701	-0.95571	2.29692
H	2.25488	0.00487	3.10259
H	2.56344	-1.69818	2.62833
Co	-0.25741	-0.20690	-0.00058
C	1.97985	0.68829	-2.35499
S	-0.01205	-2.32283	-0.57207
N	-2.19212	-0.46004	-0.00281
S	-0.24277	1.95889	0.40006
H	0.89550	0.58495	-2.35037
H	2.41269	0.02439	-3.10747
H	2.24955	1.72477	-2.57181
C	-1.69578	-2.80712	-0.35066
C	-3.01893	1.89380	-0.03690
C	-3.10728	0.46197	-0.14874
C	-1.84874	2.63800	0.27168
C	-2.64522	-1.82268	-0.01919
H	-4.11800	0.11589	-0.36191
C	-2.09611	-4.14686	-0.43860
C	-4.24774	2.58533	-0.19756
C	-1.97258	4.03315	0.44587
C	-3.95025	-2.21066	0.32157
H	-1.35962	-4.89706	-0.71206
C	-3.40773	-4.51634	-0.15130
H	-5.13701	2.00764	-0.43942
C	-4.34242	3.95461	-0.04320
C	-3.18808	4.68110	0.29098
H	-1.07995	4.60102	0.69173
C	-4.33222	-3.54828	0.24937
H	-4.66659	-1.47998	0.68258
H	-3.70045	-5.56106	-0.21039
H	-5.29555	4.45837	-0.17088
H	-3.24240	5.75838	0.42435
H	-5.34364	-3.83293	0.52389

benzaldehyde
total energy (SCF+XDM) -3.456994589618E+02
Thermal correction to Gibbs Free Energy=0.082711

C	-1.04796	-0.36184	0.00000
C	-0.76079	-1.72256	0.00000
C	0.57010	-2.15787	0.00000
C	1.61634	-1.23240	0.00000
C	1.33037	0.13166	0.00000
C	0.00000	0.57260	0.00000
C	-0.27916	2.02292	0.00000
O	-1.39134	2.52448	0.00000
H	-1.56871	-2.44871	0.00000
H	0.79038	-3.22196	0.00000
H	2.64737	-1.57403	0.00000
H	2.13646	0.86225	0.00000
H	0.62305	2.67162	0.00000
H	-2.07124	0.00001	0.00000

HBpin
total energy (SCF+XDM) -4.120369179696E+02
Thermal correction to Gibbs Free Energy=0.162253

C	0.00000	1.96399	-0.47725
C	-0.55291	0.56290	-0.19242
C	-1.76132	0.28296	-1.08066
C	0.55291	-0.56290	-0.19242
C	0.00000	-1.96399	-0.47725
C	1.76132	-0.28296	-1.08066
O	0.99571	-0.56763	1.20152
B	0.00000	0.00000	1.94884
O	-0.99571	0.56763	1.20152
H	-1.46191	0.21523	-2.13290
H	-2.48228	1.10072	-0.98493
H	-2.26424	-0.64479	-0.79990
H	0.30733	2.06869	-1.52302
H	0.85818	2.19351	0.16188
H	-0.78136	2.70173	-0.27185
H	1.46191	-0.21523	-2.13290
H	2.48228	-1.10072	-0.98493
H	2.26424	0.64479	-0.79990
H	-0.30733	-2.06869	-1.52302
H	-0.85818	-2.19351	0.16188
H	0.78136	-2.70173	-0.27185
H	0.00000	0.00000	3.13697

TS, catalyst-free reaction
total energy (SCF+XDM) -7.576891616150E+02

Thermal correction to Gibbs Free Energy=0.260258

C	-2.68951	0.70827	-0.71212
C	-3.88833	1.40387	-0.60537
C	-4.95265	0.85598	0.12060
C	-4.82517	-0.38849	0.74642
C	-3.62755	-1.08896	0.64532
C	-2.56067	-0.54534	-0.08865
C	-1.31473	-1.29356	-0.20746
O	-0.39424	-0.97293	-1.05090
H	-3.99818	2.37376	-1.08090
H	-5.88719	1.40437	0.20179
H	-5.65600	-0.80459	1.30802
H	-3.51118	-2.05638	1.12774
H	-1.30186	-2.29244	0.25123
H	-1.84145	1.11021	-1.25644
C	3.03463	-0.72692	-1.58581
C	2.82923	-0.51985	-0.07765
C	4.07270	-0.96738	0.68639
C	2.31851	0.92930	0.27622
C	2.51899	1.28480	1.75662
C	2.87902	2.03998	-0.60959
O	0.89729	0.82749	0.02987
B	0.56116	-0.54193	0.20305
O	1.71547	-1.34378	0.34387
H	4.92537	-0.31451	0.46411
H	4.34005	-1.98665	0.38864
H	3.90103	-0.96573	1.76514
H	3.91801	-0.19134	-1.95179
H	2.16253	-0.39398	-2.15564
H	3.17641	-1.79517	-1.77739
H	3.96986	2.10312	-0.51597
H	2.45664	3.00295	-0.30367
H	2.62531	1.87842	-1.65957
H	3.57465	1.45437	1.99644
H	2.13802	0.49212	2.40780
H	1.96479	2.20284	1.97657
H	-0.27758	-0.74818	1.14637

product

total energy (SCF+XDM) -7.578020831774E+02

Thermal correction to Gibbs Free Energy=0.264998

C	1.14270	1.90644	0.57417
C	1.86133	0.87569	-0.30500
C	2.65125	1.57630	-1.40555
C	2.67343	-0.19349	0.52532
C	3.75918	-0.89853	-0.29681
C	3.25496	0.31944	1.83912

O	1.65633	-1.18863	0.82844
B	0.67376	-1.05849	-0.12622
O	0.82746	0.05855	-0.92471
H	3.48457	2.14808	-0.98132
H	1.99807	2.27484	-1.93829
H	3.04934	0.86452	-2.13201
H	1.84966	2.60503	1.03387
H	0.56590	1.42179	1.36789
H	0.44546	2.47751	-0.04603
H	3.97747	1.12350	1.65714
H	3.77544	-0.49541	2.35198
H	2.47462	0.69305	2.50551
H	4.59893	-0.22990	-0.51373
H	3.36144	-1.27492	-1.24466
H	4.13615	-1.75206	0.27449
C	-1.44461	-1.66744	-1.11789
H	-1.94554	-2.62651	-1.27696
H	-1.08195	-1.30038	-2.08376
H	-4.77363	1.91793	1.17375
C	-4.10620	1.19716	0.70894
C	-3.35949	1.55657	-0.41369
H	-3.44228	2.55879	-0.82576
C	-2.50144	0.62898	-1.00819
H	-1.90833	0.91049	-1.87402
C	-2.38585	-0.66585	-0.49156
C	-3.14174	-1.01907	0.63428
H	-3.05295	-2.02290	1.04234
C	-3.99418	-0.09342	1.23382
H	-4.57527	-0.37840	2.10678
O	-0.32903	-1.96482	-0.25723

3.2$_{Co}$-benzaldehyde, 5-membered ring

total energy (SCF+XDM) -4.305001957451E+03

Thermal correction to Gibbs Free Energy=0.342410

Cl	-6.16753	-0.63035	-1.00575
C	-4.66007	-0.26175	-0.28225
N	-3.43805	-0.50350	-0.89165
C	-4.39156	0.29351	0.92974
C	-3.26231	-1.08246	-2.21937
C	-2.41650	-0.10312	-0.08443
Cl	-5.47065	0.80968	2.15398
N	-3.01148	0.38287	1.03720
H	-2.19583	-1.25534	-2.36092
H	-3.63356	-0.39407	-2.98340
H	-3.79694	-2.03291	-2.28367
Co	-0.54848	-0.20172	-0.50409
C	-2.29768	0.93106	2.18901

S	-0.56755	-2.30008	0.19806
N	1.33119	-0.41211	-0.97247
S	-0.72327	1.93853	-0.98928
H	-1.22930	0.82612	2.01606
H	-2.57401	0.37968	3.09078
H	-2.54471	1.98848	2.30999
C	1.01905	-2.75115	-0.43017
C	2.08239	1.95432	-1.16610
C	2.23309	0.52887	-1.07115
C	0.85100	2.66144	-1.21237
C	1.80987	-1.76090	-1.04336
H	3.27271	0.20717	-1.09752
C	1.49245	-4.06928	-0.37464
C	3.29666	2.68035	-1.27953
C	0.89359	4.05882	-1.41072
C	2.99447	-2.13015	-1.69696
H	0.88670	-4.82339	0.11992
C	2.70256	-4.41569	-0.97248
H	4.23152	2.12799	-1.23124
C	3.31513	4.05028	-1.45029
C	2.09414	4.74137	-1.52405
H	-0.04708	4.59995	-1.45418
C	3.44343	-3.44839	-1.65718
H	3.55999	-1.39706	-2.26250
H	3.04883	-5.44496	-0.93467
H	4.25755	4.58280	-1.53391
H	2.08662	5.81910	-1.66461
H	4.35907	-3.72014	-2.17421
O	0.86549	0.70960	3.09849
C	1.50260	-0.23716	2.65823
H	1.03463	-1.23680	2.58312
C	2.90115	-0.15645	2.18966
C	3.54582	-1.32176	1.75351
H	3.00963	-2.26681	1.75711
C	4.86169	-1.26208	1.29565
H	5.35480	-2.16426	0.94721
C	5.53319	-0.03755	1.27606
C	4.89243	1.12957	1.71320
H	5.41993	2.07901	1.69326
H	6.55925	0.01064	0.92059
C	3.57980	1.07267	2.16847
H	3.05755	1.96352	2.50233

3.2$_{Co}$-benzaldehyde, 6-membered ring
total energy (SCF+XDM) -4.305001209311E+03
Thermal correction to Gibbs Free Energy=0.341465

Cl	-5.51227	0.04489	2.18407

C	-4.36690	-0.13735	0.92509
N	-3.03258	0.22264	1.04505
C	-4.53217	-0.63419	-0.32979
C	-2.43549	0.82391	2.23595
C	-2.36387	-0.04289	-0.10959
Cl	-5.94140	-1.24509	-1.08651
N	-3.29507	-0.56915	-0.95311
H	-1.38973	1.04120	2.02782
H	-2.50600	0.13028	3.07781
H	-2.95588	1.75313	2.47947
Co	-0.51616	0.28230	-0.50316
C	-3.02935	-0.98124	-2.32763
S	-1.08466	2.36967	-0.92896
N	1.32927	0.72962	-0.95263
S	-0.21391	-1.88190	-0.17448
H	-1.98088	-0.77152	-2.53416
H	-3.66402	-0.41502	-3.01407
H	-3.21799	-2.05148	-2.44201
C	0.55118	3.02020	-1.04615
C	2.33845	-1.52393	-1.29654
C	2.26298	-0.08751	-1.35727
C	1.36347	-2.38885	-0.73278
C	1.63907	2.12941	-0.99389
H	3.15461	0.36579	-1.78805
C	0.79516	4.39665	-1.14005
C	3.54861	-2.08025	-1.78132
C	1.66768	-3.76403	-0.63921
C	2.94695	2.63578	-0.94417
H	-0.05030	5.07648	-1.19336
C	2.09789	4.88880	-1.13493
H	4.28734	-1.40914	-2.21292
C	3.81775	-3.43333	-1.70046
C	2.86501	-4.27985	-1.11177
H	0.92609	-4.42474	-0.19911
C	3.17626	4.00765	-1.01978
H	3.78920	1.96783	-0.80265
H	2.27084	5.95995	-1.19317
H	4.75337	-3.83234	-2.08015
H	3.05844	-5.34651	-1.03217
H	4.19320	4.38586	-0.97016
C	3.53822	0.78055	2.03280
C	4.84497	0.52519	1.62930
C	5.27808	-0.79460	1.44782
C	4.40531	-1.86148	1.67007
C	3.09493	-1.60781	2.07066
C	2.65714	-0.28953	2.25369

C	1.26730	-0.04563	2.68501
O	0.79803	1.05531	2.93486
H	5.53153	1.35000	1.45857
H	6.29972	-0.98899	1.13209
H	4.73866	-2.88283	1.51620
H	2.40190	-2.42848	2.23430
H	0.64169	-0.95462	2.78011
H	3.17647	1.79403	2.17295

3.2$_{Co}$-benzaldehyde–HBpin, 5-membered ring
total energy (SCF+XDM) -4.717053798639E+03
Thermal correction to Gibbs Free Energy=0.519356

Cl	-4.53569	-3.04761	1.78581
C	-3.21148	-2.45542	0.87348
N	-2.06571	-1.92174	1.44309
C	-3.04598	-2.39121	-0.47468
C	-1.81233	-1.81753	2.87536
C	-1.19077	-1.53439	0.47219
Cl	-4.10988	-2.87850	-1.72214
N	-1.80286	-1.82820	-0.70401
H	-0.89700	-1.24080	3.00404
H	-1.69228	-2.81308	3.31161
H	-2.64055	-1.29721	3.36219
Co	0.55585	-0.79190	0.76412
C	-1.24394	-1.57241	-2.02955
S	-0.38665	1.17730	1.12624
N	2.29295	0.01868	1.13169
S	1.29259	-2.80525	0.25857
H	-0.30115	-1.04285	-1.91437
H	-1.94196	-0.95692	-2.59863
H	-1.06606	-2.52027	-2.54349
C	1.04414	1.99992	1.74625
C	3.85713	-1.65927	0.16187
C	3.46142	-0.39440	0.71498
C	3.01742	-2.79237	-0.01015
C	2.26601	1.30106	1.77048
H	4.28627	0.31101	0.79859
C	0.99034	3.30659	2.25103
C	5.23186	-1.76409	-0.17541
C	3.60439	-3.99028	-0.47385
C	3.37297	1.87062	2.41646
H	0.05038	3.84907	2.20136
C	2.11415	3.88988	2.83304
H	5.85970	-0.88576	-0.04970
C	5.77952	-2.93934	-0.64961
C	4.95121	-4.06552	-0.79049
H	2.96554	-4.85960	-0.59921

C	3.30124	3.15991	2.93950
H	4.28982	1.30319	2.53648
H	2.05362	4.89822	3.23346
H	6.83408	-2.99386	-0.90197
H	5.36411	-5.00207	-1.15620
H	4.16550	3.58472	3.44166
C	-5.16680	3.46351	-2.04212
C	-4.31978	3.03227	-0.83929
C	-4.55175	3.97962	0.33455
C	-4.45024	1.49508	-0.49142
C	-4.17991	1.17482	0.98222
C	-5.75457	0.83879	-0.93650
O	-3.35885	0.90227	-1.26336
B	-2.47446	1.90295	-1.57258
O	-2.92553	3.15296	-1.25319
H	-5.57624	3.88855	0.71347
H	-4.40233	5.01213	0.00372
H	-3.85603	3.78238	1.15296
H	-6.23622	3.44960	-1.80681
H	-4.99228	2.81607	-2.90697
H	-4.88861	4.48359	-2.32352
H	-6.61143	1.28723	-0.42078
H	-5.72925	-0.22675	-0.68790
H	-5.90838	0.92905	-2.01401
H	-4.97429	1.56786	1.62561
H	-3.21957	1.57680	1.31456
H	-4.14980	0.08872	1.10466
H	-1.44351	1.70230	-2.12134
O	1.34371	0.33108	-2.91133
C	1.64425	1.25078	-2.16357
H	0.85675	1.81443	-1.62949
C	3.02989	1.68673	-1.89336
C	3.24997	2.78148	-1.04686
H	2.40266	3.29426	-0.59987
C	4.55150	3.19471	-0.76368
H	4.71959	4.03518	-0.09745
C	5.63234	2.51501	-1.32956
C	5.41602	1.42210	-2.17969
H	6.26157	0.89793	-2.61629
H	6.64748	2.83595	-1.11051
C	4.11915	1.00680	-2.46144
H	3.92464	0.15622	-3.10685

3.2$_{Co}$-benzaldehyde–HBpin, 6-membered ring
total energy (SCF+XDM) -4.717053383819E+03
Thermal correction to Gibbs Free Energy=0.520019

Cl	4.19837	-2.80743	1.86570

C	3.04171	-2.51223	0.63939
N	1.77669	-1.99997	0.88002
C	3.14764	-2.69291	-0.70464
C	1.25289	-1.63967	2.19641
C	1.09875	-1.84471	-0.28769
Cl	4.46314	-3.28506	-1.62757
N	1.94809	-2.27750	-1.26076
H	0.16844	-1.56065	2.12559
H	1.69054	-0.69068	2.51579
H	1.50373	-2.42550	2.91146
Co	-0.68543	-1.19380	-0.54088
C	1.62815	-2.30512	-2.68367
S	-1.35616	-3.27269	-0.27319
N	-2.54374	-0.65854	-0.81351
S	0.24408	0.75534	-0.96589
H	0.60204	-1.95626	-2.79291
H	1.71385	-3.32551	-3.06543
H	2.30300	-1.64387	-3.23332
C	-3.08554	-2.93638	-0.19335
C	-2.29550	1.63168	-1.76848
C	-2.97482	0.40745	-1.43252
C	-0.93108	1.92677	-1.51184
C	-3.53356	-1.62412	-0.43135
H	-4.02864	0.41984	-1.70679
C	-4.01403	-3.92909	0.14620
C	-3.12125	2.64633	-2.31432
C	-0.47248	3.24191	-1.73938
C	-4.88835	-1.31134	-0.23904
H	-3.65947	-4.94129	0.31791
C	-5.36367	-3.61935	0.29069
H	-4.16363	2.41069	-2.51516
C	-2.64645	3.92032	-2.56342
C	-1.30999	4.22041	-2.25464
H	0.56052	3.47537	-1.49955
C	-5.79981	-2.30379	0.11300
H	-5.23299	-0.28651	-0.31703
H	-6.06994	-4.39707	0.56823
H	-3.30228	4.68000	-2.97777
H	-0.92322	5.22209	-2.42353
H	-6.84310	-2.04410	0.26730
C	4.03795	0.86757	-0.73869
C	4.17703	1.74466	0.50912
C	5.51780	1.47485	1.18745
C	3.85152	3.27214	0.25033
C	4.58512	4.22730	1.19832
C	4.02421	3.73023	-1.19538

O	2.43386	3.36600	0.58996
B	2.11452	2.27303	1.34788
O	3.11662	1.34507	1.43522
H	6.34859	1.79713	0.54941
H	5.62355	0.39973	1.36421
H	5.59785	1.98425	2.15012
H	4.81839	1.09649	-1.47220
H	3.05881	0.98861	-1.20849
H	4.14589	-0.17984	-0.44511
H	5.06906	3.63691	-1.51266
H	3.73759	4.78327	-1.28008
H	3.39887	3.15140	-1.87870
H	5.65923	4.25681	0.98746
H	4.44373	3.93932	2.24448
H	4.18045	5.23564	1.06896
H	1.09427	2.17571	1.94502
O	-1.89877	-0.62316	2.93032
C	-1.70515	0.46177	2.40136
H	-0.67489	0.79910	2.18000
C	-2.76146	1.41477	2.01151
C	-2.39138	2.66179	1.48984
H	-1.33838	2.90202	1.37383
C	-3.36976	3.57998	1.11265
H	-3.08121	4.54036	0.69749
C	-4.71875	3.24816	1.25197
C	-5.09288	2.00303	1.77412
H	-6.14517	1.75466	1.88316
H	-5.48402	3.96028	0.95427
C	-4.11838	1.08672	2.15670
H	-4.38140	0.11309	2.55719

3.2$_{Co}$-benzaldehyde–HBpin TS, 5-membered ring
total energy (SCF+XDM) -4.717016850788E+03
Thermal correction to Gibbs Free Energy=0.528659

Cl	-4.74701	-2.84611	1.82555
C	-3.45903	-2.38343	0.79457
N	-2.18624	-2.07338	1.24476
C	-3.43717	-2.24286	-0.55683
C	-1.76312	-2.13353	2.63945
C	-1.38000	-1.71732	0.19859
Cl	-4.69876	-2.47839	-1.69092
N	-2.15602	-1.85098	-0.90771
H	-0.67480	-2.08352	2.66300
H	-2.08731	-3.07951	3.07887
H	-2.18086	-1.29687	3.20556
Co	0.43717	-1.07276	0.45366
C	-1.72815	-1.61370	-2.28475

S	-0.45436	0.80445	1.36189
N	2.21481	-0.37920	0.99985
S	1.06246	-3.16106	0.05142
H	-0.69805	-1.25708	-2.25018
H	-2.36619	-0.84659	-2.72864
H	-1.80699	-2.54482	-2.85237
C	1.06181	1.59501	1.84323
C	3.66831	-2.11411	-0.04503
C	3.35221	-0.85680	0.57153
C	2.77503	-3.20500	-0.24377
C	2.25981	0.87606	1.68626
H	4.22844	-0.22429	0.69196
C	1.04730	2.86780	2.41950
C	5.03456	-2.27053	-0.40464
C	3.31157	-4.41500	-0.74401
C	3.43168	1.44013	2.22454
H	0.10464	3.40061	2.49017
C	2.23014	3.43812	2.87923
H	5.70517	-1.42732	-0.25382
C	5.52636	-3.44999	-0.92357
C	4.64798	-4.53715	-1.08167
H	2.63533	-5.25309	-0.88515
C	3.41725	2.70649	2.79890
H	4.36526	0.89031	2.21574
H	2.22184	4.42970	3.32190
H	6.57372	-3.54031	-1.19440
H	5.01601	-5.47960	-1.47907
H	4.34062	3.11817	3.19612
C	-2.22489	4.16256	-1.90646
C	-2.61560	3.58458	-0.53905
C	-3.35095	4.63690	0.28622
C	-3.34737	2.19491	-0.64856
C	-4.12044	1.81874	0.62387
C	-4.24269	2.03002	-1.87393
O	-2.23636	1.27464	-0.76853
B	-1.12546	1.88282	-0.14815
O	-1.39275	3.23237	0.15784
H	-4.32146	4.87827	-0.16322
H	-2.75739	5.55614	0.32410
H	-3.51450	4.29790	1.31169
H	-3.09907	4.52055	-2.46101
H	-1.70689	3.41889	-2.52016
H	-1.54734	5.00845	-1.75272
H	-5.05891	2.76185	-1.86560
H	-4.68771	1.02910	-1.87190
H	-3.67736	2.14714	-2.80134

H	-5.02592	2.42309	0.74560
H	-3.49837	1.93874	1.51619
H	-4.41709	0.76667	0.55581
H	-0.05642	1.74421	-0.94358
O	0.78955	-0.17653	-1.54339
C	0.77186	1.07433	-1.81849
H	0.17945	1.38493	-2.70323
C	2.03737	1.88452	-1.62403
C	2.01860	3.24255	-1.28799
H	1.06840	3.73853	-1.10906
C	3.21301	3.94601	-1.13586
H	3.18862	4.99532	-0.85411
C	4.43735	3.30263	-1.33396
C	4.46036	1.95168	-1.68614
H	5.40956	1.44785	-1.85264
H	5.36749	3.85214	-1.21486
C	3.26555	1.24410	-1.82758
H	3.26654	0.19180	-2.09237

3.2$_{Co}$-benzaldehyde–HBpin TS, 6-membered ring
total energy (SCF+XDM) -4.717014844341E+03
Thermal correction to Gibbs Free Energy=0.529945

Cl	-4.98880	-2.04926	-1.53870
C	-3.66055	-1.89474	-0.46826
N	-2.35597	-1.70536	-0.89018
C	-3.64429	-1.92279	0.88993
C	-1.95926	-1.63338	-2.29417
C	-1.52447	-1.58522	0.17664
Cl	-4.93875	-2.12492	1.99458
N	-2.32457	-1.74926	1.27381
H	-0.89293	-1.40821	-2.32340
H	-2.51676	-0.83022	-2.78175
H	-2.17549	-2.58852	-2.78016
Co	0.38900	-1.27462	0.28663
C	-1.85280	-1.79839	2.65374
S	0.59879	-3.48705	0.07082
N	2.33538	-1.19263	0.62476
S	-0.11187	0.74442	1.22835
H	-0.77171	-1.93150	2.63415
H	-2.30788	-2.65165	3.16139
H	-2.10208	-0.87419	3.18119
C	2.34480	-3.49702	-0.12015
C	2.62436	1.02593	1.75705
C	3.00537	-0.29300	1.27734
C	1.34687	1.62904	1.72209
C	3.07177	-2.31597	0.13131
H	4.05208	-0.51426	1.48189

C	3.03633	-4.64036	-0.55226
C	3.70105	1.78988	2.26372
C	1.18583	2.94655	2.17159
C	4.44909	-2.27321	-0.14360
H	2.47405	-5.55199	-0.73271
C	4.40783	-4.60136	-0.77840
H	4.68804	1.33605	2.29177
C	3.53851	3.09683	2.69481
C	2.27020	3.68095	2.64146
H	0.20075	3.39577	2.12554
C	5.11575	-3.40875	-0.59223
H	4.99706	-1.34132	-0.05412
H	4.92221	-5.49165	-1.13020
H	4.39055	3.65721	3.06755
H	2.12188	4.70495	2.97252
H	6.17688	-3.35694	-0.81733
C	-3.78202	2.09858	0.79243
C	-3.09708	2.31865	-0.56387
C	-4.11137	2.16839	-1.69456
C	-2.23492	3.63386	-0.61373
C	-1.91684	4.08727	-2.04522
C	-2.79033	4.80146	0.19689
O	-0.99112	3.20538	0.00016
B	-0.87550	1.82293	-0.24142
O	-2.08936	1.28928	-0.71418
H	-4.85194	2.97627	-1.66678
H	-4.64516	1.21832	-1.58688
H	-3.62443	2.17393	-2.67243
H	-4.60693	2.80152	0.95120
H	-3.07079	2.20219	1.61773
H	-4.18865	1.08249	0.82009
H	-3.77089	5.10983	-0.18431
H	-2.11309	5.65839	0.12074
H	-2.89206	4.54296	1.25343
H	-2.80018	4.49717	-2.54652
H	-1.52930	3.26058	-2.64869
H	-1.15164	4.86911	-2.00722
H	0.08517	1.54748	-1.15051
O	0.72625	-0.45050	-1.71012
C	0.84365	0.79617	-1.99221
H	0.31020	1.15219	-2.89710
C	2.18298	1.47241	-1.77781
C	2.29549	2.83925	-1.49967
H	1.39752	3.44122	-1.38901
C	3.55041	3.41924	-1.31651
H	3.62659	4.47700	-1.07925

C	4.70572	2.64104	-1.42667
C	4.59823	1.28041	-1.72216
H	5.49358	0.67166	-1.82298
H	5.68355	3.09410	-1.28528
C	3.34175	0.69706	-1.89265
H	3.24171	-0.36181	-2.10617

3.2$_{Co}$-product, 5-membered ring
total energy (SCF+XDM) -4.717113279069E+03
Thermal correction to Gibbs Free Energy=0.529957

Cl	4.01256	-2.86356	-2.05472
C	2.93479	-2.60198	-0.74950
N	1.74412	-1.90358	-0.86207
C	3.04605	-2.99165	0.54809
C	1.21501	-1.35872	-2.10968
C	1.11286	-1.84309	0.34136
Cl	4.29658	-3.87061	1.32116
N	1.91727	-2.52628	1.20493
H	0.47387	-0.60613	-1.85665
H	0.75624	-2.15814	-2.69755
H	2.02108	-0.88111	-2.66455
Co	-0.53724	-0.94520	0.74291
C	1.60612	-2.78947	2.60690
S	0.61838	0.48964	1.97260
N	-2.15352	0.06914	1.16447
S	-1.50479	-2.66606	-0.22929
H	0.62618	-2.36199	2.81198
H	2.35010	-2.31948	3.25463
H	1.58856	-3.86818	2.78315
C	-0.65888	1.68565	2.17788
C	-3.96074	-1.51307	0.49580
C	-3.38975	-0.34528	1.11139
C	-3.24592	-2.54074	-0.17379
C	-1.94669	1.38630	1.69582
H	-4.13986	0.29902	1.56714
C	-0.40829	2.94710	2.73602
C	-5.37787	-1.56937	0.52183
C	-3.98531	-3.55698	-0.81706
C	-2.92973	2.38720	1.69170
H	0.58543	3.16529	3.11485
C	-1.40499	3.91932	2.77076
H	-5.91553	-0.77812	1.03896
C	-6.08207	-2.57902	-0.10484
C	-5.37097	-3.57942	-0.78718
H	-3.43857	-4.33852	-1.33682
C	-2.66381	3.64408	2.23035
H	-3.88736	2.21539	1.21436

H	-1.19107	4.89807	3.19144
H	-7.16719	-2.59446	-0.07439
H	-5.90564	-4.38010	-1.29159
H	-3.43269	4.41071	2.20629
C	3.29187	3.17039	1.35233
C	3.35018	3.19284	-0.17803
C	4.15371	4.40295	-0.64962
C	3.79215	1.80760	-0.82214
C	4.52770	1.95694	-2.15890
C	4.57921	0.89087	0.11303
O	2.52785	1.15922	-1.11587
B	1.54092	2.11572	-1.07478
O	1.98217	3.34877	-0.65324
H	5.20495	4.31232	-0.35334
H	3.74849	5.30836	-0.18708
H	4.10521	4.52766	-1.73363
H	4.29402	3.09950	1.78883
H	2.68652	2.33593	1.71427
H	2.83269	4.10171	1.69900
H	5.52584	1.35324	0.41469
H	4.81067	-0.04532	-0.40562
H	4.00225	0.64880	1.00817
H	5.51703	2.40800	-2.02985
H	3.95546	2.56825	-2.86360
H	4.65882	0.96479	-2.60260
H	-0.75783	3.21115	-0.32097
C	-2.29087	0.94393	-2.06277
C	-3.57059	0.46194	-2.35079
C	-4.67185	1.31521	-2.29763
C	-4.48503	2.66018	-1.96290
C	-3.20735	3.13851	-1.67764
C	-2.09782	2.28336	-1.71763
C	-0.74158	2.84226	-1.35299
O	0.27303	1.84572	-1.48472
H	-3.70269	-0.58636	-2.60212
H	-5.66725	0.93768	-2.51518
H	-5.33517	3.33669	-1.92574
H	-3.06976	4.18377	-1.40809
H	-0.49752	3.69411	-2.00134
H	-1.44373	0.27157	-2.08579

3.2$_{Co}$-product, 6-membered ring
total energy (SCF+XDM) -4.717113087156E+03
Thermal correction to Gibbs Free Energy=0.529781

Cl	-3.82090	-3.14145	-1.75626
C	-2.65915	-2.78609	-0.55078
N	-1.47556	-2.11197	-0.80178

C	-2.68558	-3.05690	0.78188
C	-1.05132	-1.62403	-2.11126
C	-0.76758	-1.94907	0.34734
Cl	-3.88425	-3.85178	1.71121
N	-1.51886	-2.53671	1.32033
H	-0.01871	-1.29543	-2.00913
H	-1.68450	-0.78896	-2.41533
H	-1.10512	-2.43799	-2.83787
Co	0.94845	-1.11860	0.55406
C	-1.12644	-2.63654	2.72225
S	1.81328	-3.05268	-0.03096
N	2.75766	-0.38727	0.72977
S	-0.16858	0.60107	1.35600
H	-0.15719	-2.15063	2.82448
H	-1.04823	-3.68740	3.01258
H	-1.85934	-2.12894	3.35419
C	3.49702	-2.53722	-0.11454
C	2.31101	1.81752	1.81947
C	3.10226	0.71320	1.34110
C	0.89509	1.90563	1.80915
C	3.82637	-1.21620	0.24011
H	4.16606	0.86996	1.50435
C	4.50015	-3.40652	-0.56698
C	3.05962	2.93102	2.27938
C	0.29512	3.12092	2.20708
C	5.14699	-0.77356	0.05773
H	4.22934	-4.42629	-0.82533
C	5.81320	-2.96816	-0.70173
H	4.14428	2.85301	2.29237
C	2.45464	4.10753	2.67827
C	1.05413	4.20133	2.62967
H	-0.78726	3.19544	2.16631
C	6.13370	-1.64149	-0.40051
H	5.41251	0.26309	0.22613
H	6.57915	-3.64993	-1.06120
H	3.05397	4.94709	3.01694
H	0.55853	5.12183	2.92703
H	7.14673	-1.27472	-0.53853
C	-3.95009	0.45539	0.70320
C	-4.09644	1.36081	-0.52438
C	-5.40941	1.05952	-1.24218
C	-3.84648	2.89060	-0.20402
C	-4.53321	3.83926	-1.19360
C	-4.15996	3.30673	1.23015
O	-2.41422	3.03137	-0.41678
B	-2.01970	1.99381	-1.23454

O	-3.00161	1.04585	-1.43226
H	-6.26715	1.33295	-0.61705
H	-5.47056	-0.01357	-1.45041
H	-5.48401	1.59226	-2.19268
H	-4.76406	0.61960	1.41743
H	-2.99448	0.61746	1.20848
H	-3.99113	-0.58791	0.37893
H	-5.22286	3.16339	1.45571
H	-3.92614	4.36815	1.36149
H	-3.56948	2.73632	1.95060
H	-5.62087	3.83597	-1.06716
H	-4.30372	3.56975	-2.22939
H	-4.16906	4.85648	-1.01997
H	0.08673	3.28769	-0.59764
C	1.77738	1.14080	-2.50172
C	3.07529	0.68228	-2.73397
C	4.17179	1.44279	-2.32721
C	3.96217	2.65895	-1.67220
C	2.66449	3.11084	-1.43297
C	1.56077	2.35916	-1.85226
C	0.17284	2.90775	-1.62005
O	-0.81882	1.90829	-1.85861
H	3.22963	-0.27361	-3.22678
H	5.18040	1.08356	-2.50884
H	4.80947	3.25662	-1.34515
H	2.50783	4.05035	-0.90743
H	-0.01558	3.74911	-2.30170
H	0.92189	0.55906	-2.82234

3.2$_{Co}$ - quartet state

total energy (SCF+XDM) -3.959271826126E+03

Thermal correction to Gibbs Free Energy=0.240773

Cl	-3.68968	-2.50514	1.97176
C	-3.05940	-1.37249	0.85336
N	-1.70683	-1.15347	0.65553
C	-3.72009	-0.52922	0.01230
C	-0.63790	-1.87421	1.34331
C	-1.50551	-0.20154	-0.29856
Cl	-5.40412	-0.31696	-0.20846
N	-2.75451	0.18291	-0.68076
H	0.29690	-1.35315	1.15020
H	-0.56506	-2.89632	0.96358
H	-0.83896	-1.88901	2.41673
Co	0.32478	0.33858	-1.06735
C	-3.04016	1.19435	-1.69846
S	0.42042	2.50739	-1.81374
N	1.69692	0.83930	0.29922

S	1.27308	-1.55185	-1.86007
H	-2.10973	1.72208	-1.91379
H	-3.77818	1.90127	-1.31321
H	-3.42842	0.71764	-2.60278
C	0.89968	3.06538	-0.19490
C	3.13196	-1.17217	0.28612
C	2.76238	0.18286	0.63837
C	2.55657	-1.98692	-0.73925
C	1.51363	2.18184	0.72802
H	3.49084	0.69773	1.27133
C	0.70342	4.39706	0.20359
C	4.21445	-1.68901	1.04518
C	3.09094	-3.28631	-0.91003
C	1.87724	2.62269	2.00670
H	0.24294	5.08644	-0.49791
C	1.08475	4.83492	1.47008
H	4.65604	-1.04899	1.80579
C	4.70856	-2.96475	0.85913
C	4.13136	-3.77030	-0.13451
H	2.66090	-3.91016	-1.68772
C	1.66592	3.94750	2.38072
H	2.29724	1.91641	2.71795
H	0.91463	5.87028	1.75303
H	5.53116	-3.33177	1.46496
H	4.50524	-4.77599	-0.30786
H	1.93802	4.27953	3.37826

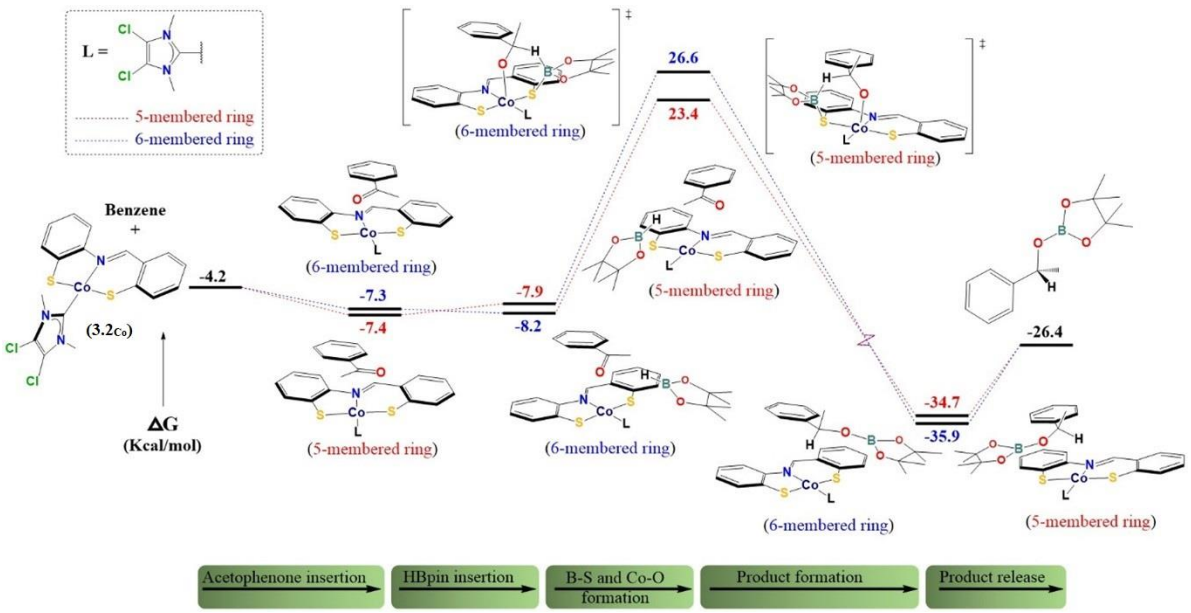

Figure B43. DFT calculated energy profile of **3.2$_{Co}$**-catalyzed acetophenone hydroboration through 5- and 6-membered metallocycles.

acetophenone
total energy (SCF+XDM) -3.850384612810E+02
Thermal correction to Gibbs Free Energy=0.108696

C	0.58051	-1.22417	0.00000
C	1.96891	-1.13651	0.00000
C	2.59121	0.11592	0.00000
C	1.81927	1.27909	-0.00000
C	0.42757	1.19196	-0.00000
C	-0.20534	-0.06048	-0.00000
C	-1.69559	-0.20290	-0.00000
O	-2.22020	-1.31059	-0.00000
H	2.56929	-2.04196	0.00000
H	3.67572	0.18425	0.00000
H	2.30024	2.25315	-0.00000
H	-0.16113	2.10366	-0.00000
C	-2.55343	1.05038	0.00000
H	0.07852	-2.18592	-0.00000
H	-3.60484	0.75897	0.00000
H	-2.34748	1.66640	-0.88336
H	-2.34747	1.66640	0.88337

product
total energy (SCF+XDM) -7.578020831774E+02
Thermal correction to Gibbs Free Energy=0.264998

C	-1.30078	-2.04323	0.01365
C	-1.96473	-0.79359	-0.57709

C	-2.73026	-1.14924	-1.84738
C	-2.78102	0.04289	0.48528
C	-3.81357	0.98194	-0.14949
C	-3.42549	-0.78081	1.59575
O	-1.74917	0.88361	1.07527
B	-0.73125	0.97199	0.15376
O	-0.88939	0.12464	-0.92440
H	-3.59057	-1.78812	-1.61665
H	-2.07373	-1.69868	-2.52953
H	-3.08645	-0.25680	-2.36659
H	-2.03815	-2.81679	0.25270
H	-0.73779	-1.80445	0.92134
H	-0.59678	-2.44939	-0.71865
H	-4.16507	-1.47755	1.18417
H	-3.93946	-0.11316	2.29439
H	-2.68253	-1.35013	2.15839
H	-4.66102	0.42724	-0.56595
H	-3.36797	1.58518	-0.94686
H	-4.19094	1.66303	0.61921
C	1.48329	1.66995	-0.51826
C	2.33533	2.92103	-0.32275
H	1.16166	1.60764	-1.56486
H	4.19442	-2.84417	0.73214
C	3.64819	-1.93881	0.48143
C	3.43041	-1.59807	-0.85442
H	3.80336	-2.23891	-1.64902
C	2.72109	-0.43878	-1.17312
H	2.53624	-0.18498	-2.21434
C	2.23003	0.39589	-0.16466
C	2.45364	0.04849	1.17445
H	2.06352	0.68547	1.96321
C	3.15496	-1.11342	1.49511
H	3.31794	-1.37487	2.53739
O	0.31603	1.82281	0.31515
H	3.23016	2.87291	-0.95217
H	2.65119	3.00773	0.72200
H	1.76201	3.81504	-0.58841

3.2$_{Co}$-acetophenone, 5-membered ring
total energy (SCF+XDM) -4.344342677571E+03
Thermal correction to Gibbs Free Energy=0.368945

Cl	-5.92004	0.06874	-1.47032
C	-4.43480	0.10285	-0.61910
N	-3.19665	0.15383	-1.24175
C	-4.20122	0.09293	0.72084
C	-2.98331	0.18449	-2.68455
C	-2.19964	0.17790	-0.31447

Cl	-5.31332	0.03191	2.02013
N	-2.82607	0.14332	0.89097
H	-1.90786	0.14762	-2.85540
H	-3.39675	1.10436	-3.10656
H	-3.45590	-0.68382	-3.14971
Co	-0.31734	0.22632	-0.67790
C	-2.13718	0.13393	2.18005
S	-0.40066	-1.96534	-0.88812
N	1.57936	0.17625	-1.14667
S	-0.47690	2.37971	-0.25761
H	-1.08052	0.30052	1.98359
H	-2.26055	-0.83158	2.67279
H	-2.52708	0.93761	2.80886
C	1.23100	-2.19518	-1.50963
C	2.31515	2.48198	-0.52901
C	2.46696	1.11060	-0.93518
C	1.09123	3.14651	-0.25525
C	2.07303	-1.07531	-1.65084
H	3.50786	0.83827	-1.08835
C	1.69533	-3.46158	-1.89463
C	3.52734	3.21408	-0.43311
C	1.13632	4.51885	0.07588
C	3.31664	-1.23364	-2.28217
H	1.03991	-4.31904	-1.76833
C	2.95830	-3.61623	-2.46003
H	4.46015	2.69566	-0.64334
C	3.55083	4.55182	-0.09190
C	2.33477	5.20877	0.16008
H	0.19875	5.02799	0.27952
C	3.76206	-2.49370	-2.67449
H	3.94043	-0.37409	-2.50192
H	3.29984	-4.60198	-2.76378
H	4.49289	5.08745	-0.02645
H	2.33008	6.26265	0.42575
H	4.72661	-2.59253	-3.16378
O	-0.12415	-2.08155	3.21463
C	0.82846	-2.45572	2.53716
C	0.89686	-3.87973	2.02488
C	1.96515	-1.52590	2.24611
C	3.09544	-1.93299	1.52348
H	3.15221	-2.93376	1.11019
C	4.15820	-1.05195	1.32259
H	5.02924	-1.38038	0.76295
C	4.09594	0.24569	1.83223
C	2.96488	0.66688	2.53981
H	2.91023	1.68098	2.92452

H	4.92360	0.93270	1.67696
C	1.91042	-0.21487	2.74781
H	1.03380	0.08785	3.31003
H	1.73592	-4.41120	2.49162
H	1.04651	-3.90147	0.94165
H	-0.03515	-4.38954	2.27331

3.2$_{Co}$-acetophenone, 6-membered ring
total energy (SCF+XDM) -4.344341863389E+03
Thermal correction to Gibbs Free Energy=0.368368

Cl	-5.35574	-0.23754	1.99010
C	-4.22205	-0.06749	0.71939
N	-2.87483	0.18985	0.92215
C	-4.41172	-0.14732	-0.62512
C	-2.23648	0.35382	2.22727
C	-2.22103	0.26017	-0.26752
Cl	-5.84829	-0.43634	-1.51096
N	-3.17519	0.05864	-1.21803
H	-1.23761	0.74857	2.04997
H	-2.15887	-0.60567	2.74033
H	-2.81079	1.06561	2.82423
Co	-0.35149	0.57254	-0.55978
C	-2.92903	0.07573	-2.65619
S	-0.78468	2.71869	-0.34452
N	1.52775	1.00990	-0.87550
S	-0.22745	-1.60230	-0.90636
H	-1.87648	0.31263	-2.80431
H	-3.55215	0.83860	-3.12977
H	-3.14724	-0.90452	-3.08697
C	0.88355	3.28911	-0.36239
C	2.42103	-1.16223	-1.72456
C	2.42622	0.24905	-1.43875
C	1.35516	-2.06615	-1.47559
C	1.91804	2.36182	-0.58586
H	3.35990	0.72781	-1.72762
C	1.20027	4.63230	-0.11462
C	3.64042	-1.66905	-2.24118
C	1.57470	-3.43953	-1.72318
C	3.25218	2.78534	-0.47304
H	0.39096	5.33949	0.04285
C	2.52602	5.04944	-0.04760
H	4.44885	-0.96778	-2.43501
C	3.83337	-3.01630	-2.48103
C	2.78462	-3.90967	-2.21076
H	0.75786	-4.13109	-1.53612
C	3.55571	4.11881	-0.21282
H	4.06531	2.07255	-0.54456

H	2.75665	6.09144	0.15651
H	4.78027	-3.37612	-2.87158
H	2.91370	-4.97347	-2.39256
H	4.59401	4.42460	-0.12267
C	2.01368	-0.03767	2.65205
C	3.11865	0.77570	2.42860
C	4.25831	0.24876	1.81117
C	4.27957	-1.08584	1.40495
C	3.16696	-1.89912	1.62151
C	2.02749	-1.38521	2.25610
C	0.83362	-2.23527	2.55605
O	-0.10936	-1.78246	3.19809
H	3.09523	1.81920	2.72743
H	5.12655	0.88154	1.64704
H	5.15836	-1.49612	0.91581
H	3.19288	-2.93171	1.29100
C	0.82289	-3.67734	2.09153
H	1.12577	0.34980	3.13942
H	1.61131	-4.24672	2.59983
H	1.00307	-3.74628	1.01483
H	-0.14669	-4.11766	2.32917

3.2$_{Co}$-acetophenone–HBpin, 5-membered ring
total energy (SCF+XDM)
Thermal correction to Gibbs Free Energy=0.545465

Cl	3.92115	-3.57841	-1.34259
C	2.61610	-2.83619	-0.51832
N	1.57547	-2.18400	-1.16171
C	2.38975	-2.71919	0.81617
C	1.38783	-2.11093	-2.60550
C	0.70415	-1.67096	-0.24993
Cl	3.33322	-3.26475	2.13266
N	1.21112	-2.00660	0.96431
H	0.60310	-1.37904	-2.79614
H	1.08911	-3.08679	-2.99868
H	2.31338	-1.78617	-3.08483
Co	-0.89789	-0.69424	-0.65409
C	0.58811	-1.67367	2.24298
S	0.34230	1.11967	-0.79029
N	-2.45702	0.36860	-1.16921
S	-1.92947	-2.60397	-0.29686
H	-0.33037	-1.13255	2.02914
H	1.24842	-1.03651	2.83173
H	0.35709	-2.59196	2.78848
C	-0.88807	2.19507	-1.44485
C	-4.33232	-1.19108	-0.63297
C	-3.71364	0.05230	-1.00644

C	-3.66324	-2.41077	-0.35023
C	-2.18813	1.69519	-1.65028
H	-4.44130	0.84105	-1.17859
C	-0.59224	3.52005	-1.79623
C	-5.75052	-1.16103	-0.58278
C	-4.44688	-3.54905	-0.05709
C	-3.12785	2.49668	-2.31675
H	0.40955	3.89858	-1.61173
C	-1.55399	4.32856	-2.39654
H	-6.25359	-0.22114	-0.79867
C	-6.49730	-2.28157	-0.27772
C	-5.83038	-3.49052	-0.01724
H	-3.93441	-4.48321	0.15376
C	-2.81861	3.80580	-2.67899
H	-4.10152	2.10171	-2.58571
H	-1.30804	5.35002	-2.67375
H	-7.58129	-2.22984	-0.24642
H	-6.39898	-4.38574	0.22061
H	-3.56000	4.40774	-3.19630
C	5.98570	2.58998	0.95480
C	4.79194	2.27819	0.04517
C	4.66622	3.34310	-1.04144
C	4.76402	0.78400	-0.48004
C	4.07420	0.61897	-1.83827
C	6.11853	0.07926	-0.49570
O	3.91920	0.11348	0.50490
B	3.21430	1.07379	1.18068
O	3.60378	2.35088	0.88762
H	5.51799	3.30297	-1.73011
H	4.65065	4.33453	-0.57788
H	3.74480	3.22268	-1.61546
H	6.92722	2.59849	0.39561
H	6.06965	1.86204	1.76743
H	5.84112	3.57804	1.40211
H	6.80390	0.56723	-1.19819
H	5.98256	-0.95794	-0.81795
H	6.58202	0.06579	0.49302
H	4.64971	1.09564	-2.63884
H	3.06171	1.03170	-1.82988
H	4.00267	-0.44908	-2.06441
H	2.37640	0.81964	1.97725
O	-0.09278	1.19208	3.42444
C	-0.58689	2.06776	2.72061
C	0.22845	3.27173	2.29843
C	-2.02085	1.97604	2.29674
C	-2.64102	2.97988	1.53989

H	-2.07322	3.83684	1.19518
C	-3.99487	2.88445	1.21723
H	-4.46369	3.66903	0.63056
C	-4.73749	1.78150	1.64097
C	-4.12318	0.76543	2.38125
H	-4.69737	-0.10021	2.69809
H	-5.79352	1.70852	1.39399
C	-2.77545	0.86474	2.70786
H	-2.28540	0.09470	3.29383
H	1.24303	3.17159	2.68495
H	-0.22122	4.19571	2.68243
H	0.27062	3.34429	1.20730

3.2$_{Co}$-acetophenone–HBpin, 6-membered ring
total energy (SCF+XDM) -4.756394791763E+03
Thermal correction to Gibbs Free Energy=0.545186

Cl	3.57077	-2.97413	2.33914
C	2.53256	-2.65133	1.02079
N	1.29520	-2.04255	1.15329
C	2.71508	-2.88959	-0.30451
C	0.69127	-1.63224	2.41832
C	0.70990	-1.88683	-0.06202
Cl	4.04880	-3.59670	-1.11410
N	1.58615	-2.41839	-0.95792
H	-0.29481	-1.23124	2.19547
H	1.29061	-0.85482	2.89260
H	0.59887	-2.49757	3.07931
Co	-0.97564	-1.06861	-0.47603
C	1.35566	-2.48487	-2.39594
S	-1.87923	-3.06021	-0.29908
N	-2.71794	-0.34070	-0.99525
S	0.19665	0.78055	-0.64580
H	0.34147	-2.13178	-2.57987
H	1.45207	-3.51751	-2.73997
H	2.07026	-1.84880	-2.92423
C	-3.55184	-2.57915	-0.57802
C	-2.11105	1.98762	-1.67228
C	-2.94424	0.81838	-1.55264
C	-0.76473	2.10629	-1.24158
C	-3.83842	-1.23373	-0.87648
H	-3.93388	0.97341	-1.97700
C	-4.60042	-3.50449	-0.47037
C	-2.75653	3.13051	-2.20877
C	-0.14020	3.37075	-1.32093
C	-5.18060	-0.83333	-0.98864
H	-4.36062	-4.54082	-0.25031
C	-5.92310	-3.10262	-0.62277

H	-3.78613	3.03150	-2.54513
C	-2.12702	4.35859	-2.28893
C	-0.80541	4.47656	-1.82910
H	0.88589	3.45794	-0.97486
C	-6.21390	-1.75811	-0.87114
H	-5.43870	0.20949	-1.12911
H	-6.72556	-3.82903	-0.52780
H	-2.64928	5.21849	-2.69711
H	-0.29550	5.43539	-1.87614
H	-7.24385	-1.42405	-0.95691
C	3.85335	0.47547	-1.88650
C	4.55275	0.95211	-0.60907
C	5.98851	0.43337	-0.57875
C	4.39502	2.50352	-0.33713
C	5.55264	3.10878	0.46490
C	4.11847	3.34794	-1.57841
O	3.22057	2.56563	0.52683
B	3.01949	1.31613	1.05160
O	3.83526	0.35662	0.51458
H	6.58191	0.88015	-1.38476
H	5.98343	-0.65183	-0.72172
H	6.47778	0.64430	0.37449
H	4.34025	0.87719	-2.78145
H	2.79695	0.75697	-1.89510
H	3.91511	-0.61586	-1.92947
H	4.96104	3.30221	-2.27787
H	3.97999	4.39325	-1.28399
H	3.21612	3.01814	-2.09799
H	6.47568	3.14371	-0.12326
H	5.74414	2.54045	1.38011
H	5.28804	4.13082	0.75262
H	2.26166	1.09510	1.93398
O	-0.34085	1.10227	3.52090
C	-0.82919	1.98917	2.82727
C	-0.03312	3.23501	2.49881
C	-2.23158	1.86840	2.31844
C	-2.86281	2.90780	1.62122
H	-2.32395	3.82033	1.39044
C	-4.19116	2.77803	1.21475
H	-4.67215	3.59299	0.68122
C	-4.89445	1.60507	1.49061
C	-4.26573	0.55303	2.16527
H	-4.80613	-0.36825	2.36022
H	-5.93029	1.50431	1.17818
C	-2.94554	0.68700	2.57947
H	-2.44675	-0.11282	3.11578

H	-0.52382	4.12539	2.91093
H	0.04900	3.37297	1.41613
H	0.96602	3.14291	2.92549

3.2$_{Co}$-acetophenone–HBpin TS, 5-membered ring
total energy (SCF+XDM) -4.756355613594E+03
Thermal correction to Gibbs Free Energy=0.556400

Cl	-4.74683	-2.85513	1.89909
C	-3.44976	-2.42831	0.86330
N	-2.18944	-2.07251	1.31518
C	-3.40991	-2.35764	-0.49302
C	-1.78232	-2.07471	2.71582
C	-1.37293	-1.75564	0.26337
Cl	-4.65079	-2.67407	-1.63083
N	-2.13094	-1.95956	-0.84525
H	-0.69577	-1.99917	2.74926
H	-2.09078	-3.01234	3.18381
H	-2.22553	-1.22958	3.24900
Co	0.43476	-1.08025	0.49587
C	-1.66961	-1.81944	-2.22488
S	-0.46271	0.80052	1.40173
N	2.20642	-0.37385	1.05140
S	1.08609	-3.17198	0.14475
H	-0.67126	-1.37857	-2.18905
H	-2.34840	-1.15284	-2.76195
H	-1.65764	-2.80254	-2.70386
C	1.04612	1.59179	1.90862
C	3.67133	-2.08106	-0.01581
C	3.34699	-0.83024	0.60933
C	2.79269	-3.18839	-0.18782
C	2.24258	0.86832	1.75795
H	4.21466	-0.18505	0.72471
C	1.02549	2.85082	2.51209
C	5.03129	-2.21457	-0.40535
C	3.34020	-4.39234	-0.69066
C	3.40667	1.41537	2.32860
H	0.08349	3.38493	2.58243
C	2.20361	3.40674	3.00201
H	5.68878	-1.35776	-0.27545
C	5.53221	-3.38817	-0.92939
C	4.67050	-4.49218	-1.05913
H	2.67650	-5.24370	-0.81048
C	3.38822	2.67088	2.92660
H	4.33616	0.85855	2.32463
H	2.19202	4.38839	3.46617
H	6.57428	-3.46120	-1.22482
H	5.04633	-5.43058	-1.45893

H	4.30636	3.07004	3.34802
C	-2.24434	4.20057	-1.83135
C	-2.62120	3.59350	-0.47518
C	-3.33173	4.63735	0.38307
C	-3.37397	2.21175	-0.59629
C	-4.19191	1.85457	0.65257
C	-4.23055	2.05058	-1.84895
O	-2.27929	1.26119	-0.66717
B	-1.17740	1.86035	-0.04824
O	-1.38964	3.21842	0.20390
H	-4.30520	4.89909	-0.04787
H	-2.72600	5.54808	0.42868
H	-3.48514	4.28173	1.40431
H	-3.12519	4.58382	-2.35770
H	-1.74770	3.47054	-2.47441
H	-1.55457	5.03428	-1.66648
H	-5.03922	2.79034	-1.86872
H	-4.68419	1.05380	-1.85589
H	-3.63583	2.15852	-2.75866
H	-5.08291	2.48386	0.75052
H	-3.59221	1.95499	1.56263
H	-4.51475	0.81123	0.57353
H	-0.06790	1.68326	-0.96669
O	0.71352	-0.21721	-1.45019
C	0.71386	1.05886	-1.74554
C	0.09634	1.40347	-3.11067
C	2.02427	1.80930	-1.50177
C	2.06813	3.12198	-1.02206
H	1.14292	3.63008	-0.76322
C	3.29117	3.76929	-0.84021
H	3.31177	4.78243	-0.44722
C	4.48450	3.11506	-1.15302
C	4.44616	1.80953	-1.64902
H	5.37055	1.29574	-1.90317
H	5.43726	3.61899	-1.01205
C	3.22287	1.15948	-1.81896
H	3.18006	0.13790	-2.18362
H	0.11322	2.48014	-3.30888
H	-0.93377	1.03862	-3.15773
H	0.68269	0.90159	-3.88926

3.2$_{Co}$-acetophenone–HBpin TS, 6-membered ring
total energy (SCF+XDM) -4.756353646576E+03
Thermal correction to Gibbs Free Energy=0.558012

Cl	-4.95354	-2.17908	-1.49734
C	-3.63619	-1.97405	-0.42139

N	-2.32966	-1.78649	-0.83794
C	-3.63260	-1.95138	0.93686
C	-1.90895	-1.80267	-2.23675
C	-1.50900	-1.61772	0.23121
Cl	-4.93674	-2.11990	2.03633
N	-2.31827	-1.75096	1.32658
H	-0.85791	-1.51141	-2.26376
H	-2.50577	-1.07963	-2.79813
H	-2.05733	-2.80516	-2.64763
Co	0.39944	-1.28531	0.32879
C	-1.85858	-1.76485	2.71145
S	0.62596	-3.50506	0.17971
N	2.34506	-1.18591	0.66879
S	-0.10578	0.73018	1.29221
H	-0.77655	-1.89095	2.70369
H	-2.31261	-2.60985	3.23376
H	-2.11923	-0.83148	3.21674
C	2.36861	-3.49933	-0.04406
C	2.62498	1.02799	1.81487
C	3.01272	-0.28548	1.32112
C	1.34559	1.62692	1.79115
C	3.08581	-2.30633	0.17663
H	4.06157	-0.50171	1.52036
C	3.06670	-4.64017	-0.47138
C	3.69737	1.79096	2.32994
C	1.17590	2.93475	2.26240
C	4.45752	-2.25008	-0.12032
H	2.51314	-5.56142	-0.62845
C	4.43380	-4.58720	-0.72220
H	4.68715	1.34309	2.34856
C	3.52842	3.09109	2.78038
C	2.25738	3.66909	2.74016
H	0.18747	3.37765	2.22877
C	5.13030	-3.38392	-0.56482
H	4.99309	-1.30932	-0.05285
H	4.95302	-5.47617	-1.07033
H	4.37861	3.65047	3.15883
H	2.10401	4.68674	3.08801
H	6.18681	-3.32284	-0.80870
C	-3.84784	2.04938	0.86514
C	-3.13110	2.28212	-0.47203
C	-4.11384	2.12437	-1.62880
C	-2.27745	3.60714	-0.49763
C	-1.97998	4.10982	-1.91493
C	-2.83227	4.74619	0.35404
O	-1.02016	3.17560	0.09539

B	-0.92022	1.79580	-0.10924
O	-2.11497	1.25327	-0.59359
H	-4.86704	2.92066	-1.61419
H	-4.63446	1.16527	-1.53916
H	-3.60357	2.14361	-2.59434
H	-4.67514	2.75200	1.01120
H	-3.15669	2.14378	1.70861
H	-4.25559	1.03364	0.87322
H	-3.81902	5.05786	-0.00769
H	-2.16194	5.60965	0.29380
H	-2.92040	4.45806	1.40398
H	-2.87377	4.53252	-2.38621
H	-1.59808	3.30959	-2.55309
H	-1.21894	4.89466	-1.85991
H	0.06726	1.50369	-1.12413
O	0.67478	-0.46032	-1.61275
C	0.78562	0.80950	-1.90882
C	0.18386	1.20749	-3.26585
C	2.15371	1.44677	-1.66535
C	2.30257	2.78548	-1.28715
H	1.42037	3.39558	-1.11156
C	3.57273	3.33100	-1.09721
H	3.67390	4.36650	-0.78304
C	4.70992	2.54604	-1.30036
C	4.56727	1.21340	-1.69434
H	5.44769	0.59843	-1.86571
H	5.69992	2.97070	-1.15488
C	3.29561	0.66581	-1.87127
H	3.17010	-0.37474	-2.15239
H	0.27629	2.28131	-3.45796
H	-0.87051	0.91814	-3.30536
H	0.72340	0.66865	-4.05348

3.2$_{Co}$-product, 5-membered ring
total energy (SCF+XDM) -4.756448784118E+03
Thermal correction to Gibbs Free Energy=0.556940

Cl	4.01256	-2.86356	-2.05472
C	2.93479	-2.60198	-0.74950
N	1.74412	-1.90358	-0.86207
C	3.04605	-2.99165	0.54809
C	1.21501	-1.35872	-2.10968
C	1.11286	-1.84309	0.34136
Cl	4.29658	-3.87061	1.32116
N	1.91727	-2.52628	1.20493
H	0.47387	-0.60613	-1.85665
H	0.75624	-2.15814	-2.69755
H	2.02108	-0.88111	-2.66455

Co	-0.53724	-0.94520	0.74291
C	1.60612	-2.78947	2.60690
S	0.61838	0.48964	1.97260
N	-2.15352	0.06914	1.16447
S	-1.50479	-2.66606	-0.22929
H	0.62618	-2.36199	2.81198
H	2.35010	-2.31948	3.25463
H	1.58856	-3.86818	2.78315
C	-0.65888	1.68565	2.17788
C	-3.96074	-1.51307	0.49580
C	-3.38975	-0.34528	1.11139
C	-3.24592	-2.54074	-0.17379
C	-1.94669	1.38630	1.69582
H	-4.13986	0.29902	1.56714
C	-0.40829	2.94710	2.73602
C	-5.37787	-1.56937	0.52183
C	-3.98531	-3.55698	-0.81706
C	-2.92973	2.38720	1.69170
H	0.58543	3.16529	3.11485
C	-1.40499	3.91932	2.77076
H	-5.91553	-0.77812	1.03896
C	-6.08207	-2.57902	-0.10484
C	-5.37097	-3.57942	-0.78718
H	-3.43857	-4.33852	-1.33682
C	-2.66381	3.64408	2.23035
H	-3.88736	2.21539	1.21436
H	-1.19107	4.89807	3.19144
H	-7.16719	-2.59446	-0.07439
H	-5.90564	-4.38010	-1.29159
H	-3.43269	4.41071	2.20629
C	3.29187	3.17039	1.35233
C	3.35018	3.19284	-0.17803
C	4.15371	4.40295	-0.64962
C	3.79215	1.80760	-0.82214
C	4.52770	1.95694	-2.15890
C	4.57921	0.89087	0.11303
O	2.52785	1.15922	-1.11587
B	1.54092	2.11572	-1.07478
O	1.98217	3.34877	-0.65324
H	5.20495	4.31232	-0.35334
H	3.74849	5.30836	-0.18708
H	4.10521	4.52766	-1.73363
H	4.29402	3.09950	1.78883
H	2.68652	2.33593	1.71427
H	2.83269	4.10171	1.69900
H	5.52584	1.35324	0.41469

H	4.81067	-0.04532	-0.40562
H	4.00225	0.64880	1.00817
H	5.51703	2.40800	-2.02985
H	3.95546	2.56825	-2.86360
H	4.65882	0.96479	-2.60260
H	-0.75783	3.21115	-0.32097
C	-2.29087	0.94393	-2.06277
C	-3.57059	0.46194	-2.35079
C	-4.67185	1.31521	-2.29763
C	-4.48503	2.66018	-1.96290
C	-3.20735	3.13851	-1.67764
C	-2.09782	2.28336	-1.71763
C	-0.74158	2.84226	-1.35299
O	0.27303	1.84572	-1.48472
H	-3.70269	-0.58636	-2.60212
H	-5.66725	0.93768	-2.51518
H	-5.33517	3.33669	-1.92574
H	-3.06976	4.18377	-1.40809
H	-0.49752	3.69411	-2.00134
H	-1.44373	0.27157	-2.08579

3.2$_{Co}$-product, 6-membered ring
total energy (SCF+XDM) -4.756449931861E+03
Thermal correction to Gibbs Free Energy=0.556251

Cl	-3.63069	-3.25387	-1.88021
C	-2.48272	-2.92238	-0.65531
N	-1.33720	-2.17218	-0.86223
C	-2.48737	-3.28426	0.65587
C	-0.94329	-1.57828	-2.13637
C	-0.63062	-2.05395	0.29254
Cl	-3.63910	-4.19943	1.53261
N	-1.34557	-2.74242	1.22572
H	0.03678	-1.12832	-1.98985
H	-1.66498	-0.81142	-2.42160
H	-0.88041	-2.35794	-2.89950
Co	1.04731	-1.16352	0.54905
C	-0.94293	-2.90866	2.61811
S	1.99697	-3.03267	-0.11626
N	2.82203	-0.37386	0.78656
S	-0.14554	0.48084	1.39454
H	-0.00752	-2.36725	2.75291
H	-0.79378	-3.96860	2.83952
H	-1.70615	-2.49353	3.28101
C	3.65732	-2.44241	-0.16326
C	2.27943	1.74873	1.98659
C	3.11722	0.69415	1.47651
C	0.86291	1.80019	1.92401

C	3.92694	-1.12865	0.26203
H	4.17165	0.86883	1.68072
C	4.70027	-3.24049	-0.65468
C	2.97917	2.86077	2.52054
C	0.21526	2.98545	2.33687
C	5.22606	-0.61688	0.10930
H	4.47709	-4.25645	-0.96783
C	5.99266	-2.73658	-0.75948
H	4.06419	2.80926	2.57670
C	2.32706	4.00630	2.93631
C	0.92804	4.06819	2.82906
H	-0.86607	3.03442	2.25303
C	6.25261	-1.41439	-0.38841
H	5.44247	0.42075	0.33449
H	6.78952	-3.36345	-1.15033
H	2.88941	4.84676	3.33149
H	0.39692	4.96532	3.13638
H	7.24838	-0.99584	-0.50267
C	-3.92928	0.12626	0.89979
C	-4.18227	1.08484	-0.26864
C	-5.51755	0.75697	-0.93192
C	-3.98595	2.60705	0.11898
C	-4.77337	3.56940	-0.77830
C	-4.23478	2.93373	1.58866
O	-2.57741	2.83037	-0.16522
B	-2.18150	1.85688	-1.05954
O	-3.12613	0.86919	-1.24736
H	-6.35155	0.95611	-0.24921
H	-5.54044	-0.30580	-1.19374
H	-5.66840	1.33288	-1.84755
H	-4.71021	0.21442	1.66273
H	-2.95635	0.30828	1.36337
H	-3.94070	-0.89967	0.52201
H	-5.27476	2.72617	1.86532
H	-4.04410	3.99760	1.76332
H	-3.57695	2.35792	2.24349
H	-5.85064	3.50423	-0.59315
H	-4.59120	3.36597	-1.83833
H	-4.44960	4.59373	-0.56940
H	-0.12206	3.23933	-0.50413
C	1.55428	1.26294	-2.63765
C	2.84926	0.80717	-2.88752
C	3.94372	1.44669	-2.30347
C	3.73249	2.53838	-1.45911
C	2.43595	2.98394	-1.19970
C	1.33524	2.35295	-1.78894

C	-0.05389	2.90566	-1.54467
O	-1.02170	1.86448	-1.76032
H	3.00445	-0.04965	-3.53755
H	4.95019	1.08726	-2.49491
H	4.57719	3.04165	-0.99486
H	2.27776	3.82163	-0.52448
C	-0.36650	4.08319	-2.47344
H	0.70261	0.77583	-3.09860
H	-0.33587	3.75758	-3.51872
H	0.37164	4.88108	-2.33887
H	-1.36005	4.48773	-2.25418

Appendix C – Chapter 4

II. Spectroscopic Data

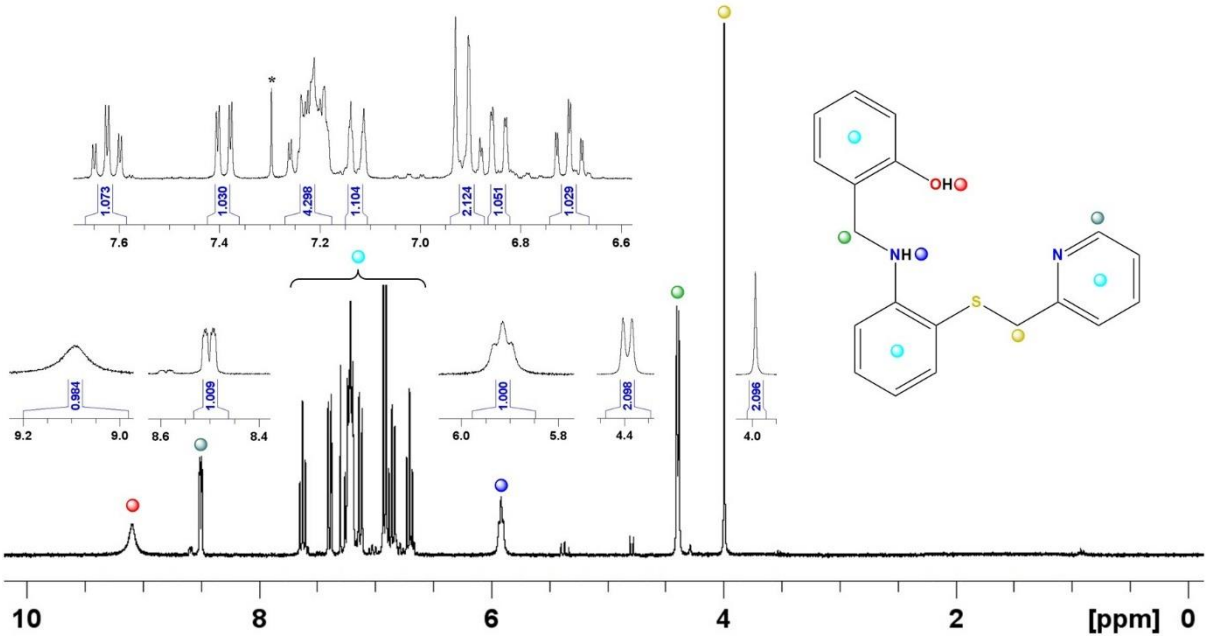

Figure C1. ^{1}H NMR spectrum of **H_2L4**. * indicates protic impurity in $CDCl_3$.

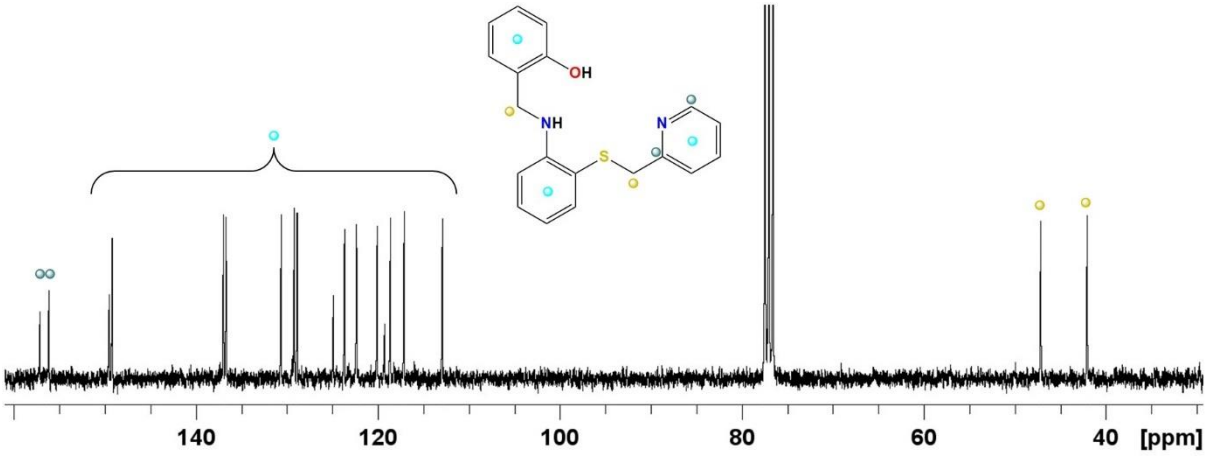

Figure C2. ^{13}C NMR spectrum of **H_2L4**. * indicates protic impurity in $CDCl_3$.

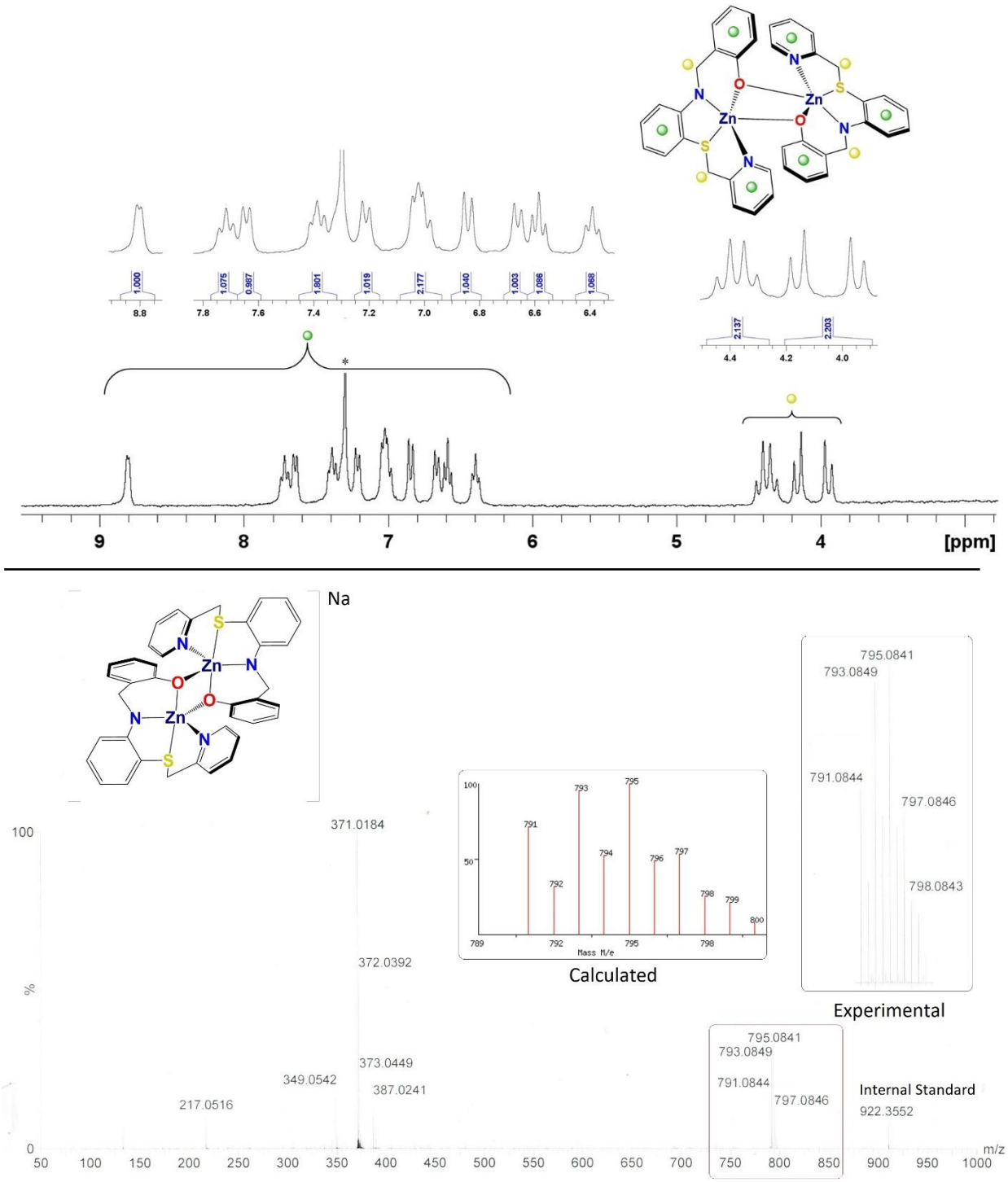

Figure C3. ^{1}H NMR spectrum of **4.1$_{Zn}$**. * indicates protic impurity in $CDCl_3$ (top). ESI-MS spectrum of **4.1$_{Zn}$** (bottom).

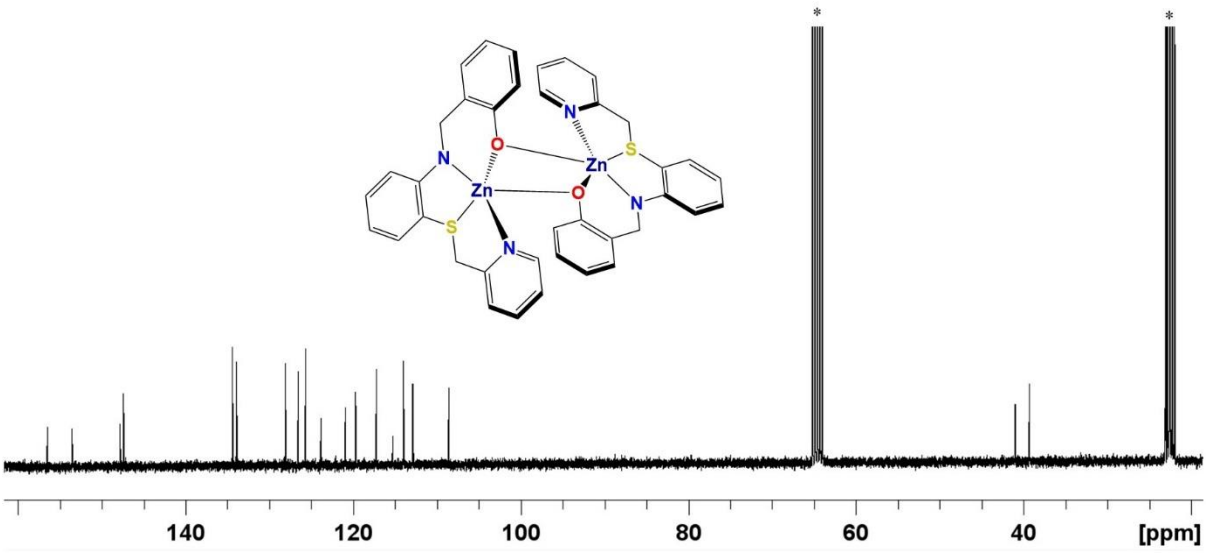

Figure C4. ^{13}C NMR spectrum of $\mathbf{4.1_{Zn}}$. * indicates protic impurity in THF-d_8.

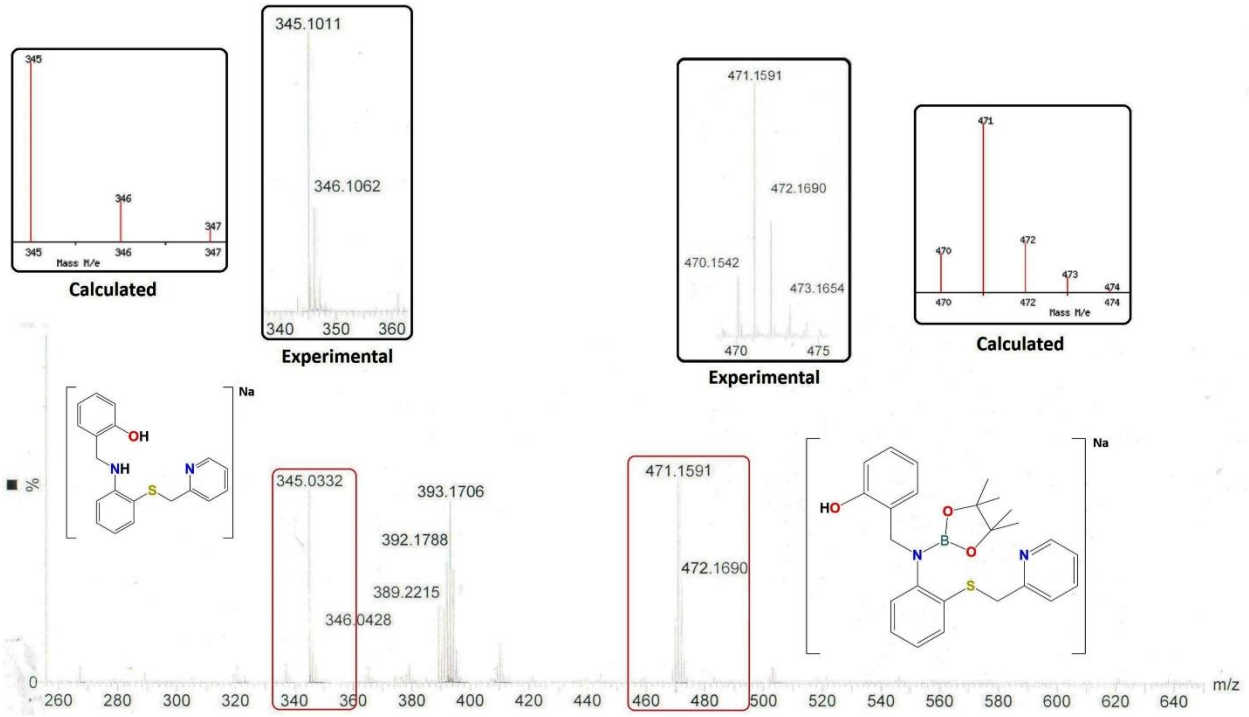

Figure C5. ESI-MS spectrum of the evaporated filterate of the stoichiometric reaction mixture of $\mathbf{4.1_{Zn}}$ and HBpin.

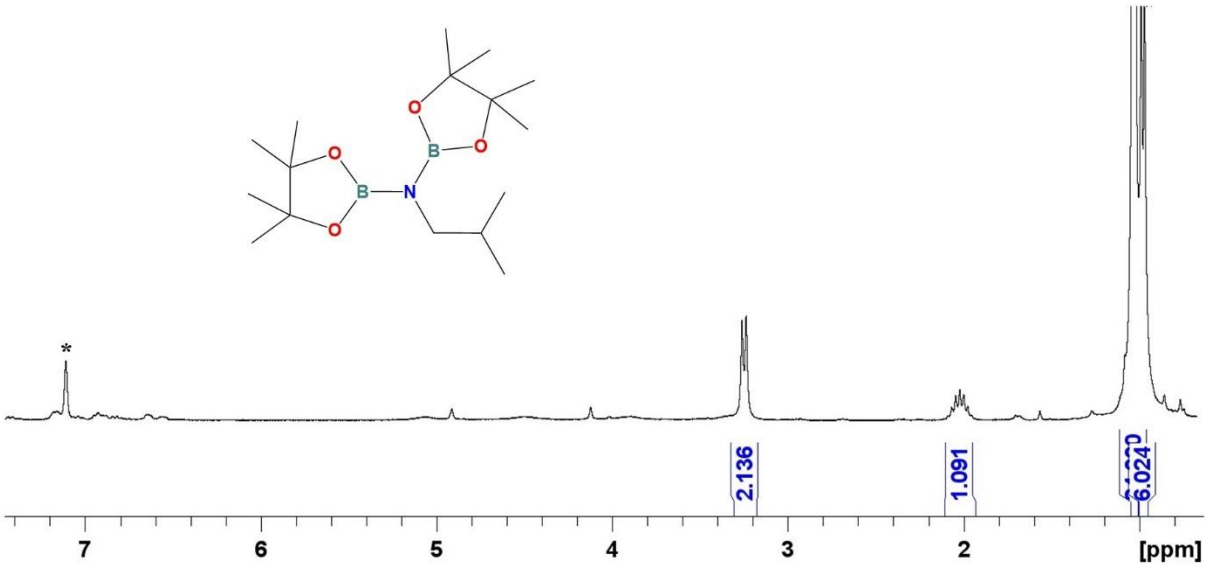

Figure C6. ^{1}H NMR spectrum of isobutyronitrile hydroboration product. * indicates protic impurity in C_6D_6.

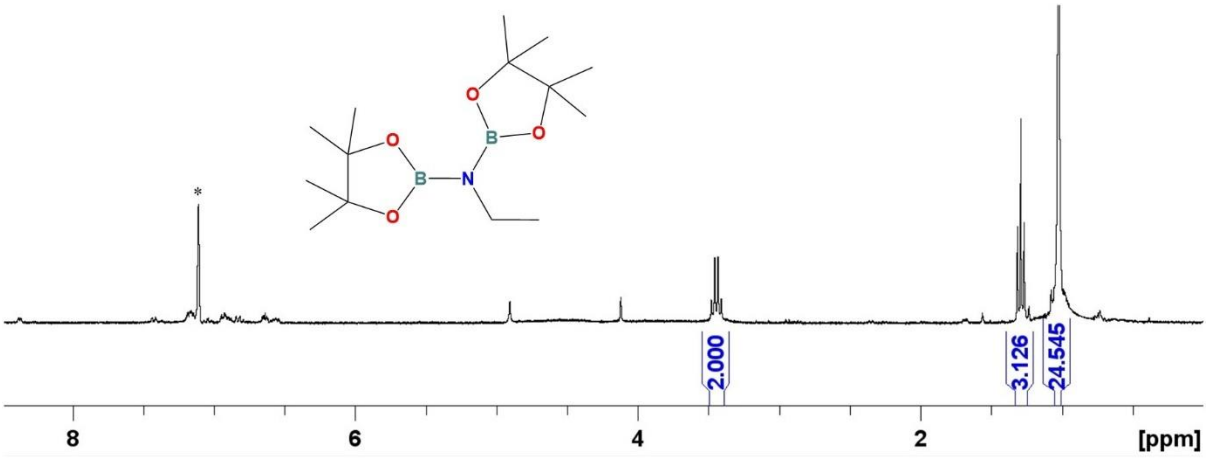

Figure C7. ^{1}H NMR spectrum of acetonitrile hydroboration product. * indicates protic impurity in C_6D_6.

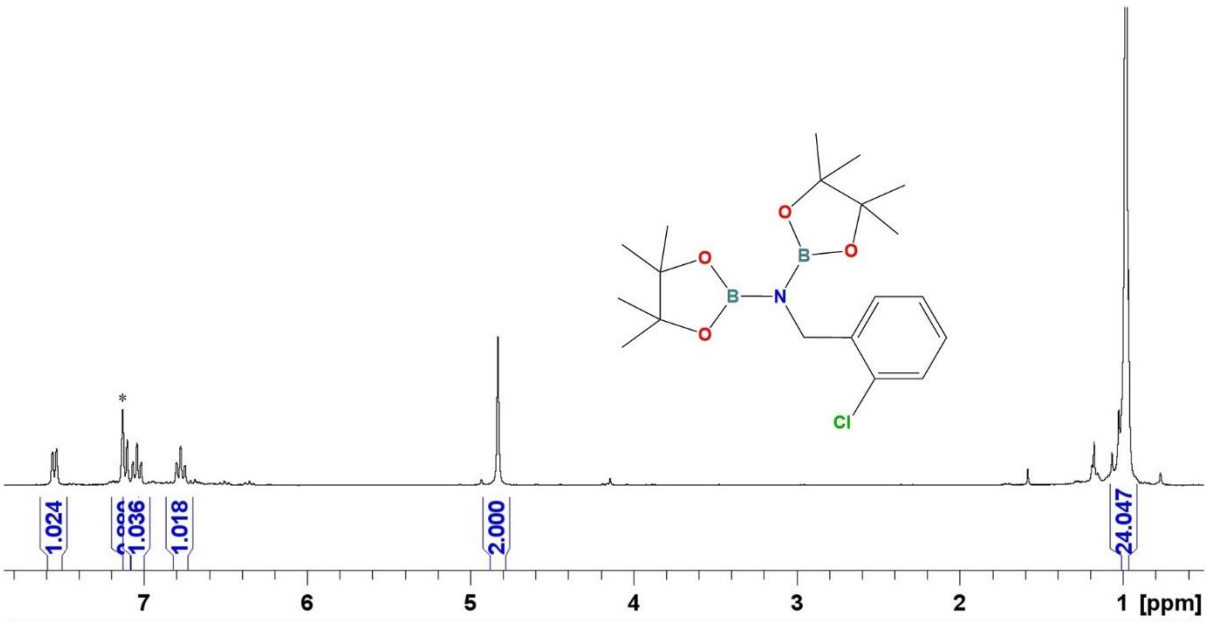

Figure C8. ^{1}H NMR spectrum of 2-chloro-benzonitrile hydroboration product. * indicates protic impurity in C_6D_6.

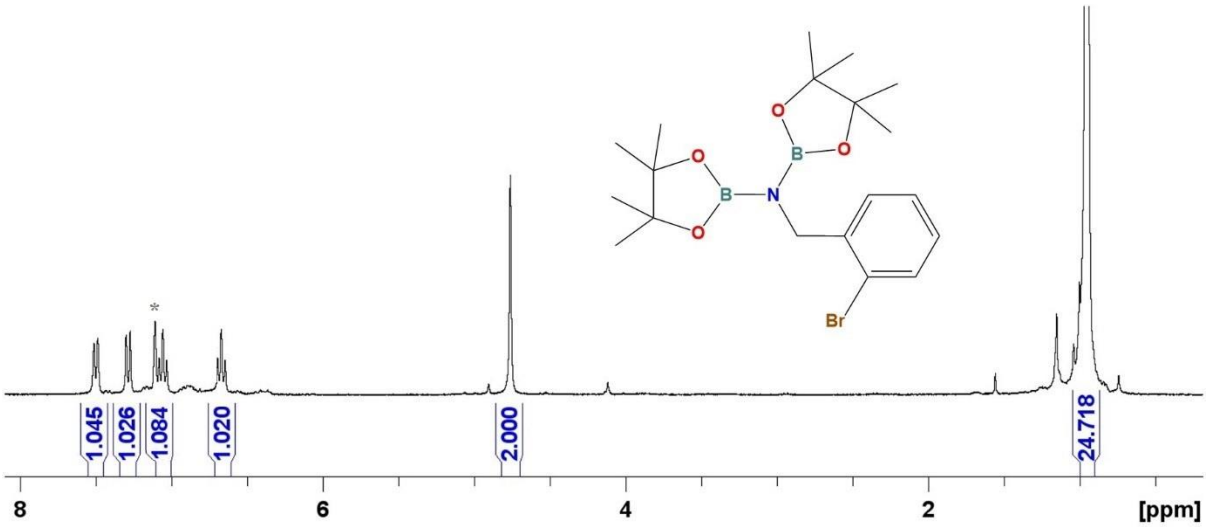

Figure C9. ^{1}H NMR spectrum of 2-bromo-benzonitrile hydroboration product. * indicates protic impurity in C_6D_6.

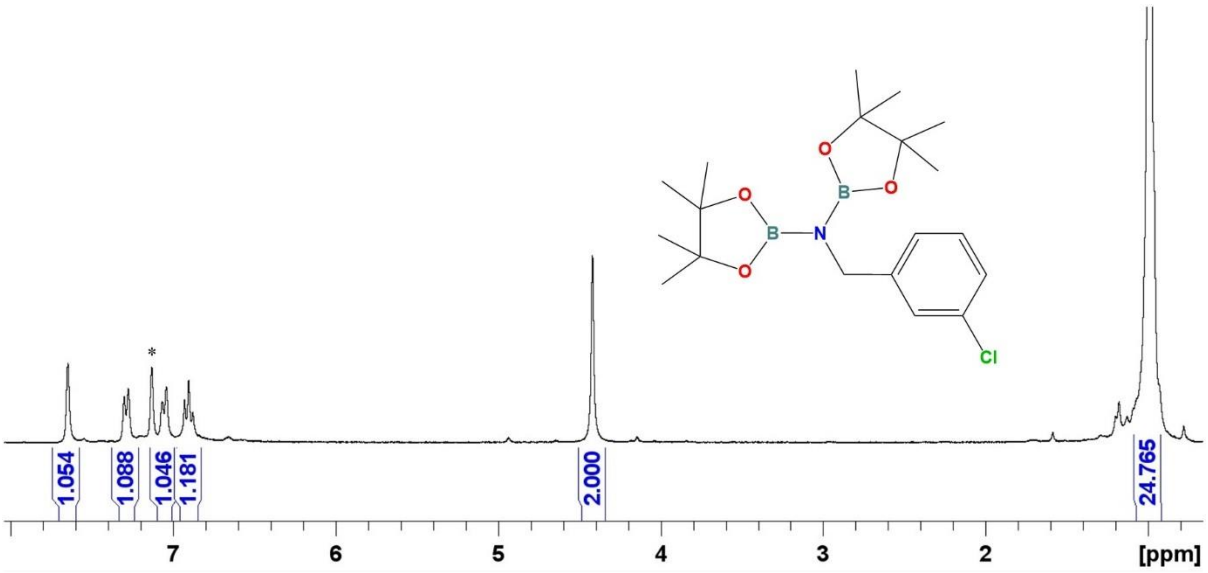

Figure C10. ^{1}H NMR spectrum of 3-chloro-benzonitrile hydroboration product. * indicates protic impurity in C_6D_6.

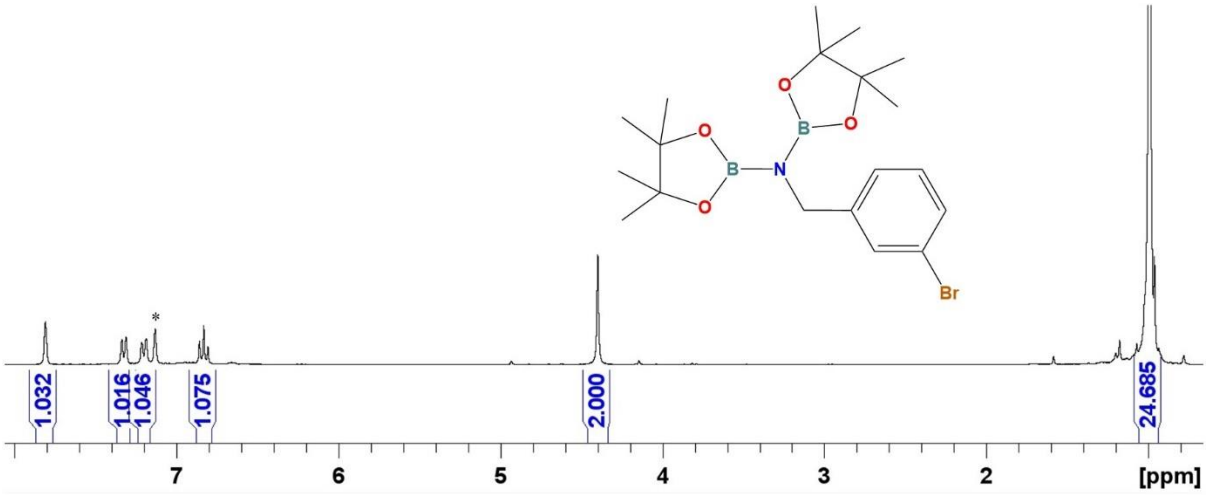

Figure C11. ^{1}H NMR spectrum of 3-bromo-benzonitrile hydroboration product. * indicates protic impurity in C_6D_6.

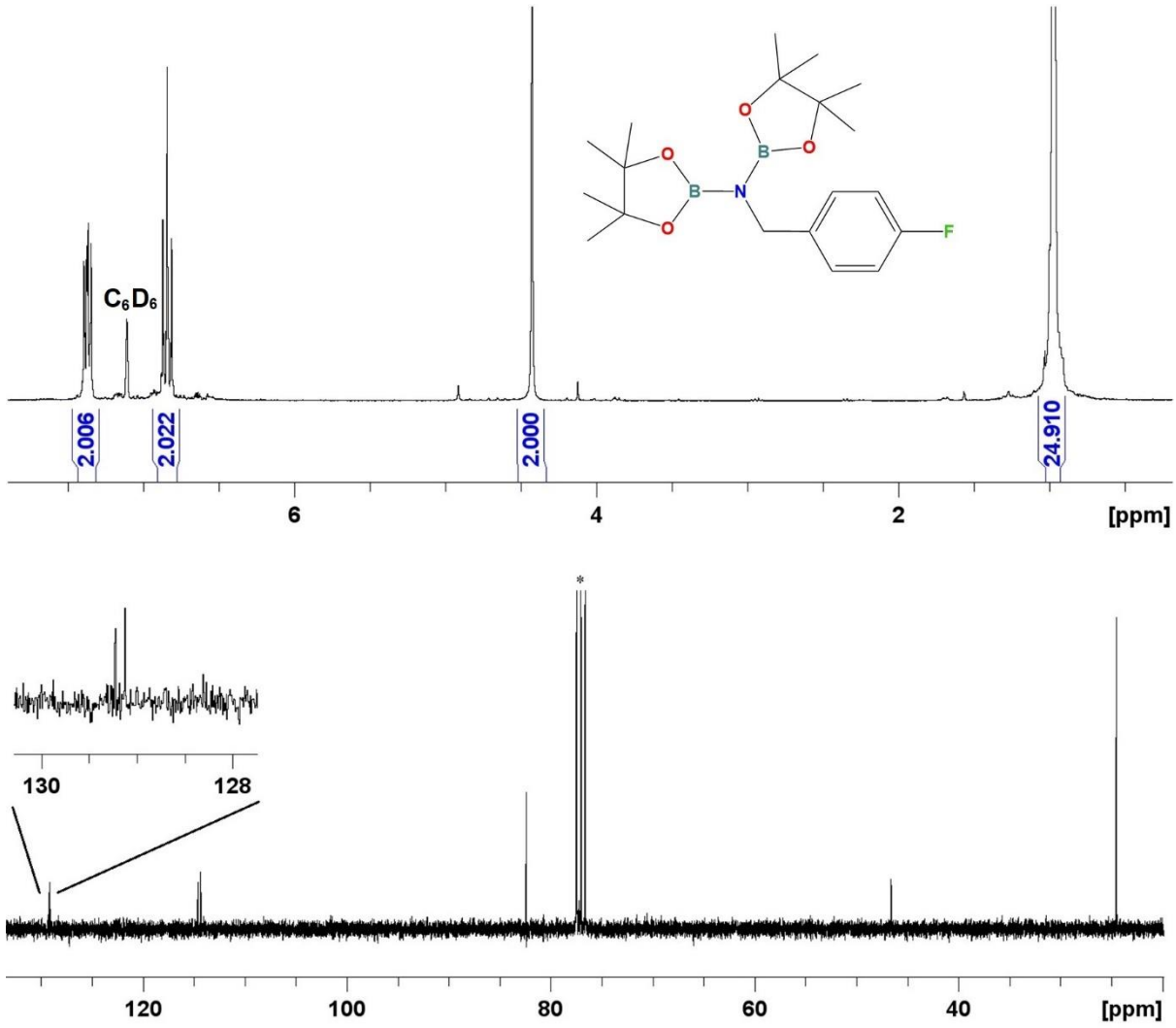

Figure C12. ^{1}H and ^{13}C NMR spectra of 4-fluoro-benzonitrile hydroboration product. * indicates protic impurity in $CDCl_3$.

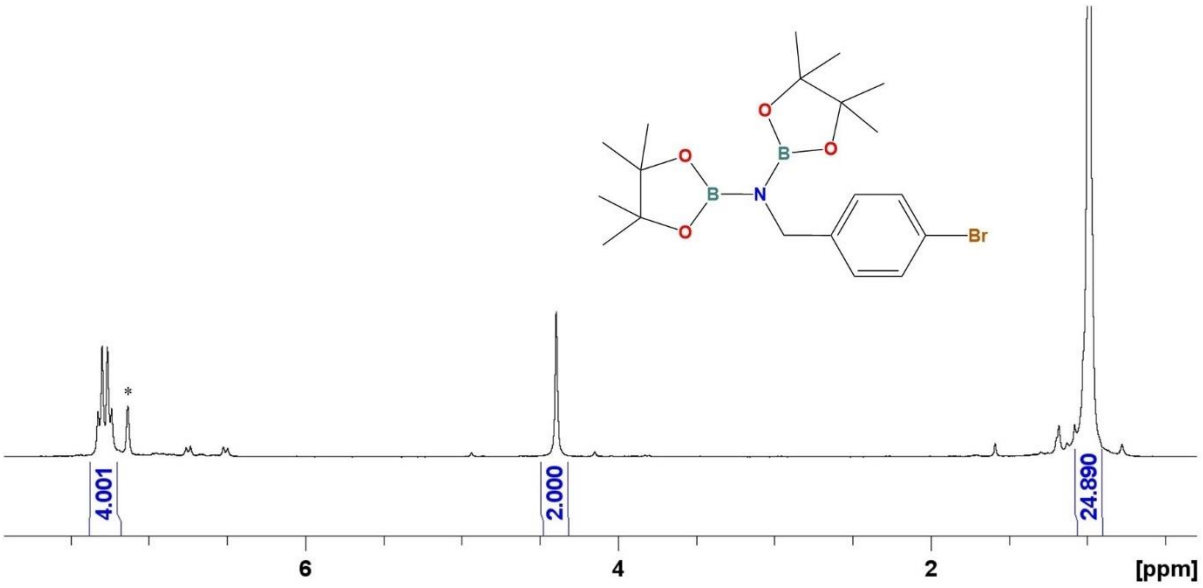

Figure C13. ^{1}H NMR spectrum of 4-bromo-benzonitrile hydroboration product. * indicates protic impurity in C_6D_6.

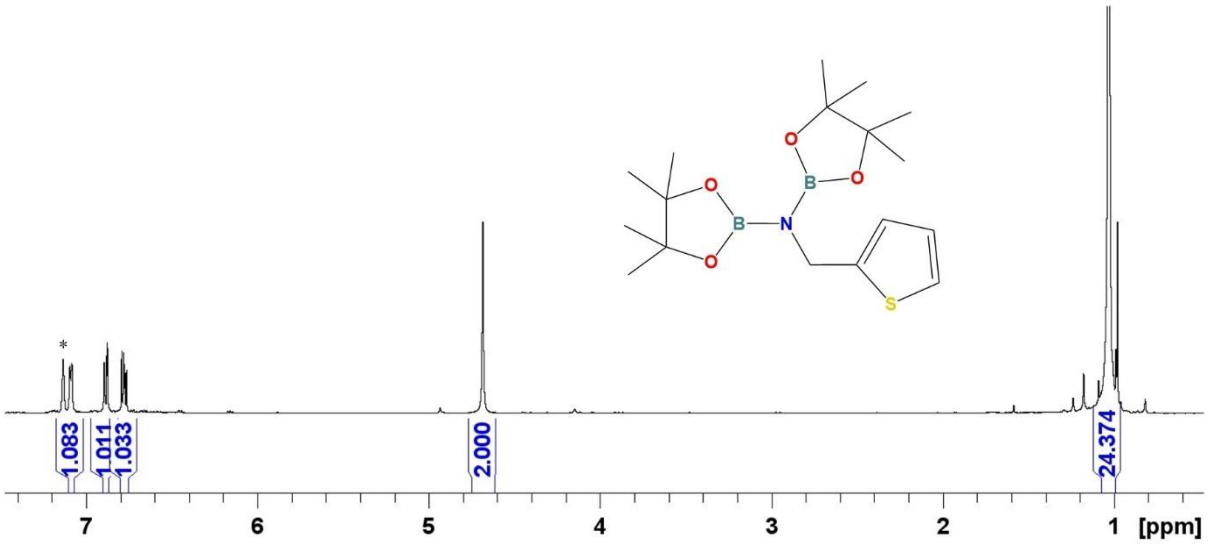

Figure C14. ^{1}H NMR spectrum of 2-cyano-thiophene hydroboration product. * indicates protic impurity in C_6D_6.

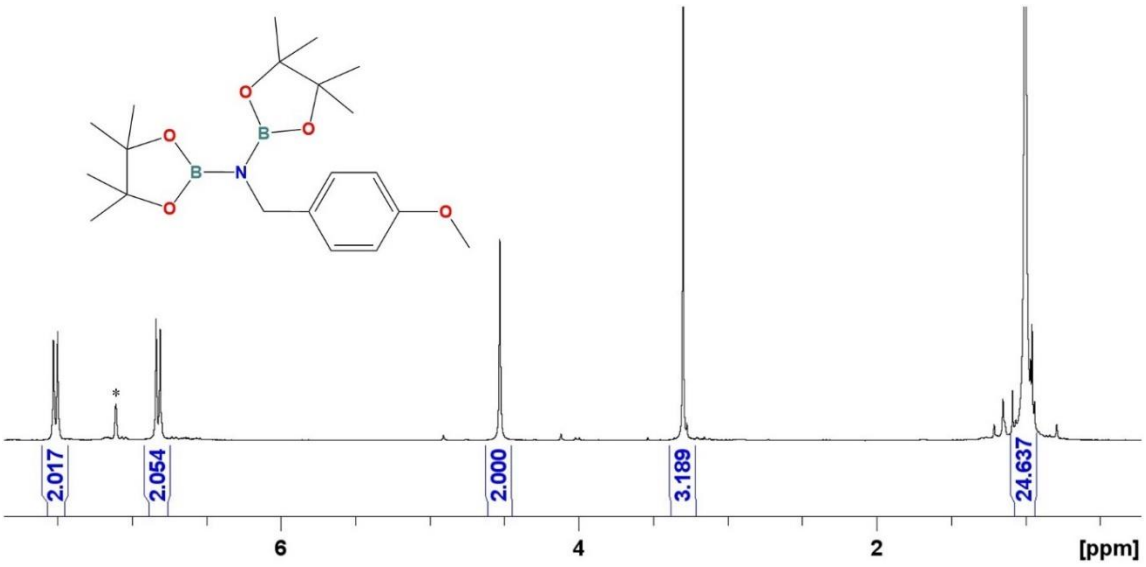

Figure C15. ^{1}H NMR spectrum of 4-methoxy-benzonitrile hydroboration product. * indicates protic impurity in C_6D_6.

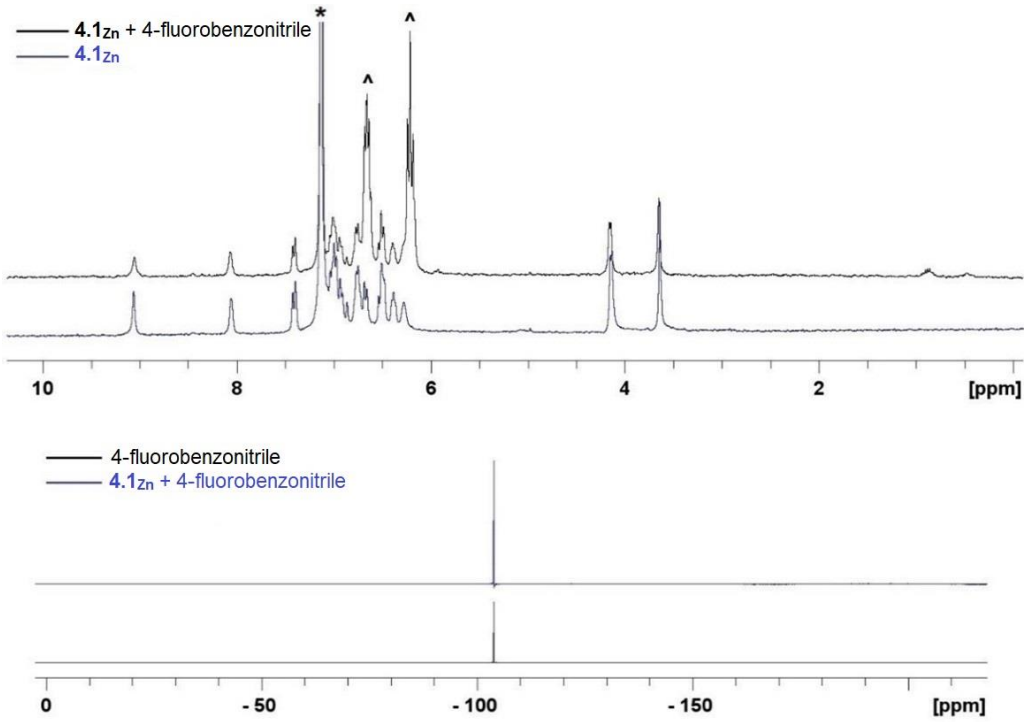

Figure C16. Stacked plot of ^{1}H NMR (top) and ^{19}F NMR (bottom) spectra of **4.1$_{Zn}$** in C_6D_6 (black) and reaction of **4.1$_{Zn}$** dimer with two equiv of 4-fluorobenzonitrile (blue). * Indicates C_6D_6 and ^ indicates 4-fluorobenzonitrile.

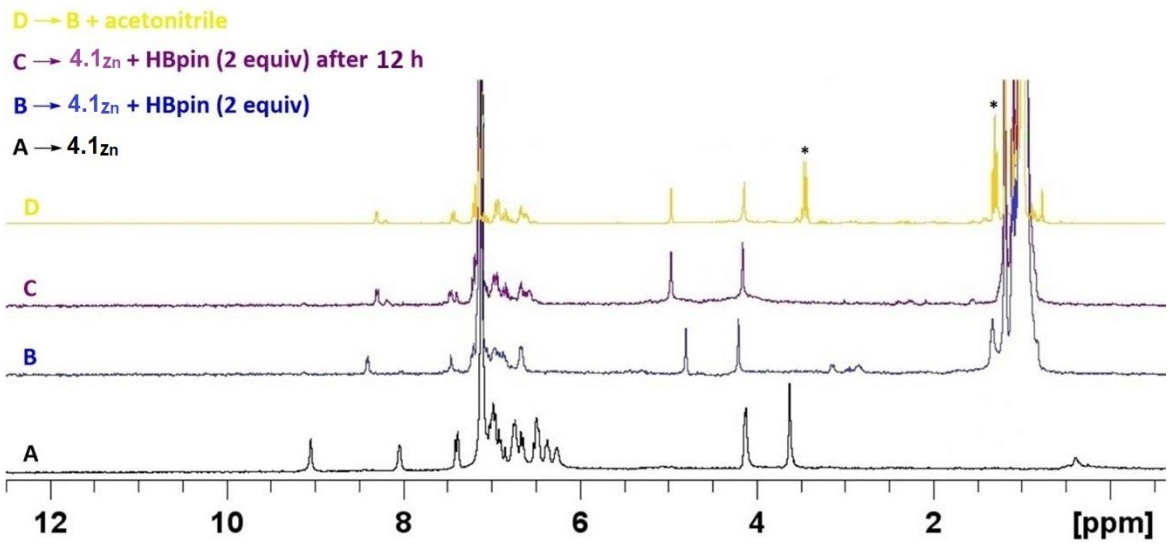

Figure C17. Stacked plot of $^{1}H\{^{11}B\}$ NMR spectra (in C_6D_6) of **4.1$_{Zn}$** (**A**), reaction of **4.1$_{Zn}$** dimer with two equiv of HBpin (**B**), B after 12 h (**C**), and subsequent addition of one equiv of acetonitrile to B (**D**).* indicates diborylamine product of acetonitrile hydroboration.

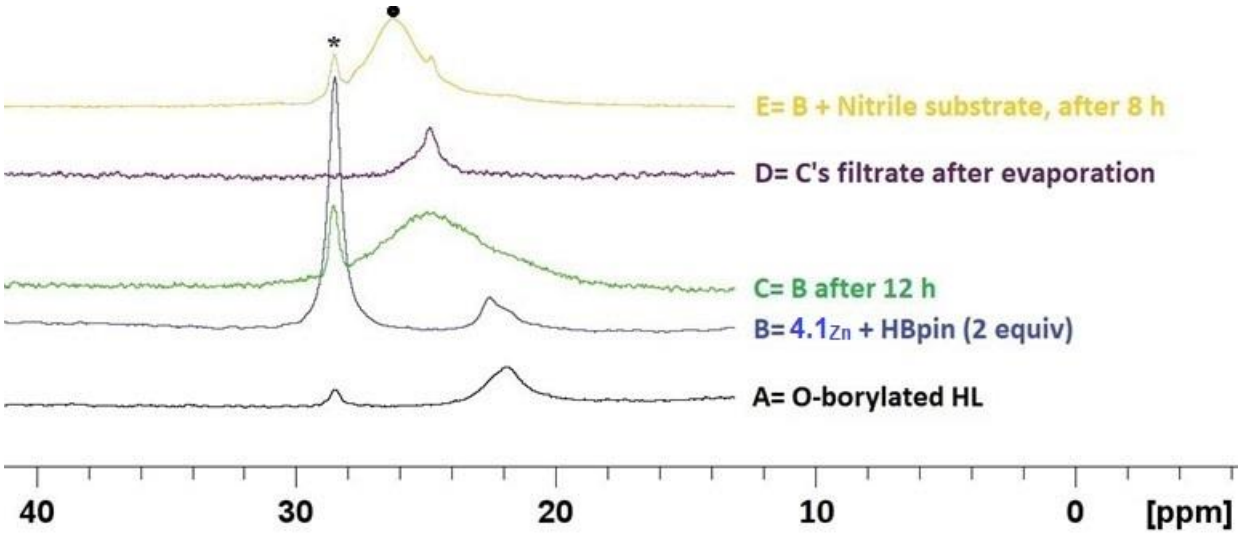

Figure C18. $^{11}B\{^{1}H\}$ NMR spectra (in C_6D_6) of O-borylated HL (**A**), stoichiometric reaction of **4.1$_{Zn}$** dimer with 2 equiv of HBpin (**B**), **B** after 12 h (**C**), **C**'s filtrate after evaporation (**D**), and subsequent reaction of **B** with acetonitrile (**E**). * indicates HBpin and ● indicates product of acetonitrile hydroboration.

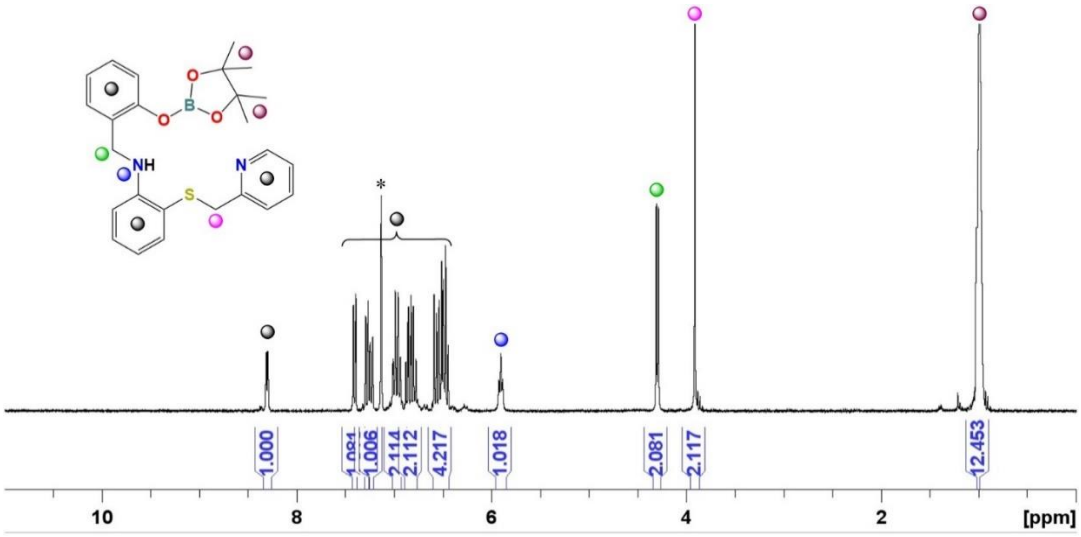

Figure C19. ^{1}H NMR spectrum of O-borylated HL (**Bpin-HL4**). * indicates protic impurity in C_6D_6.

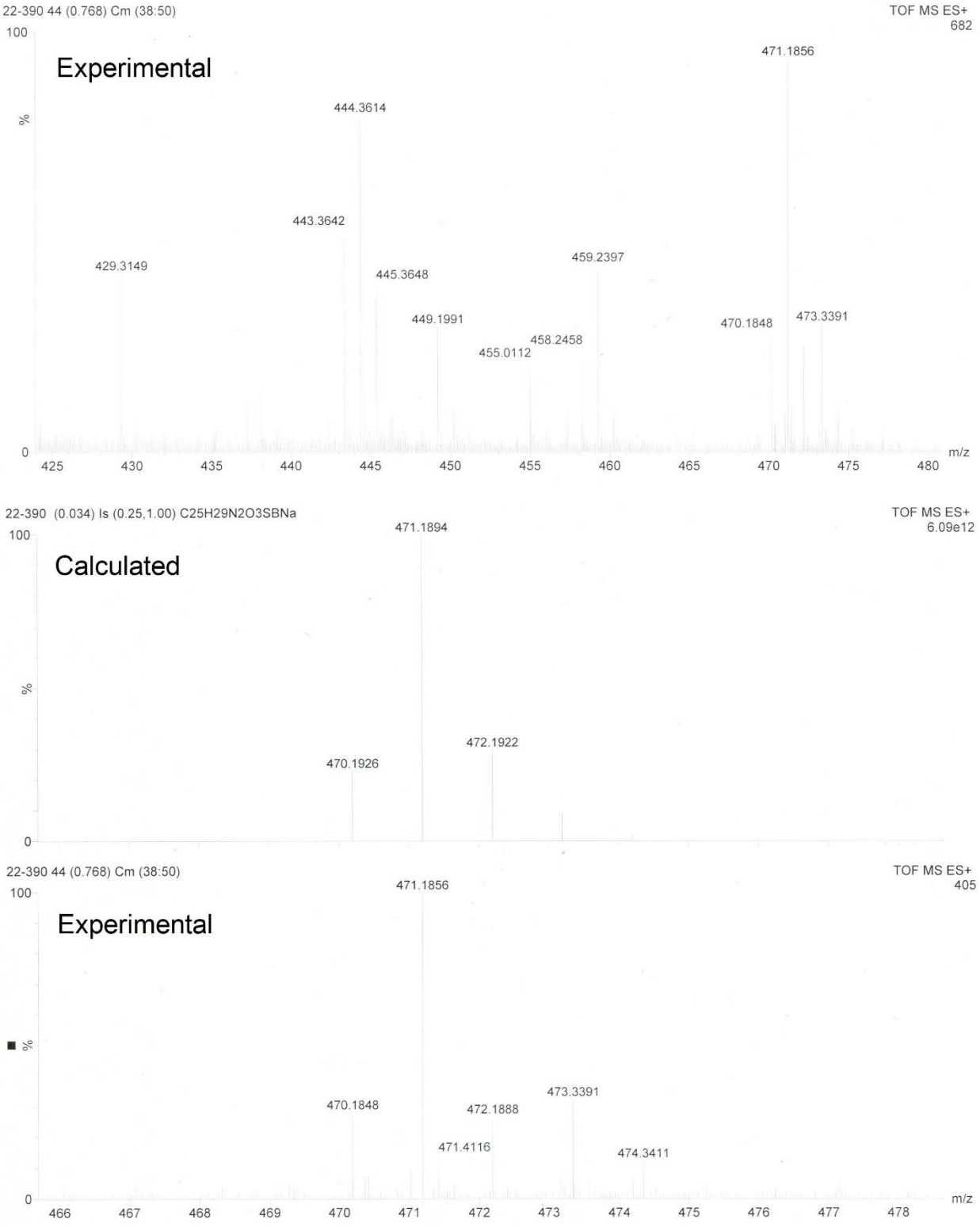

Figure C20. ESI-MS spectrum of O-borylated HL4 (**Bpin-HL4**) $[NaM]^+$.

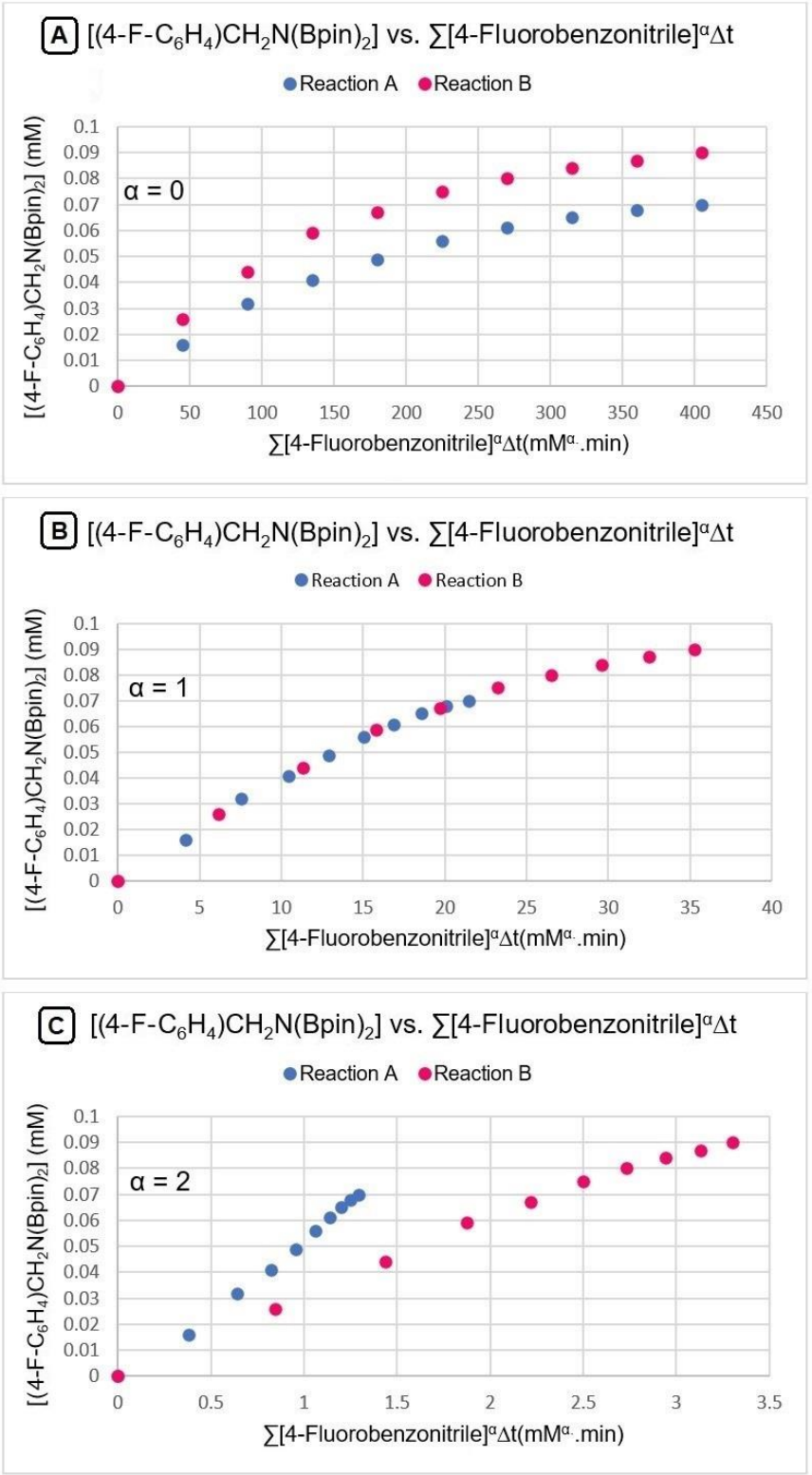

Figure C21. VTNA of rate order of [4-Fluorobenzonitrile].

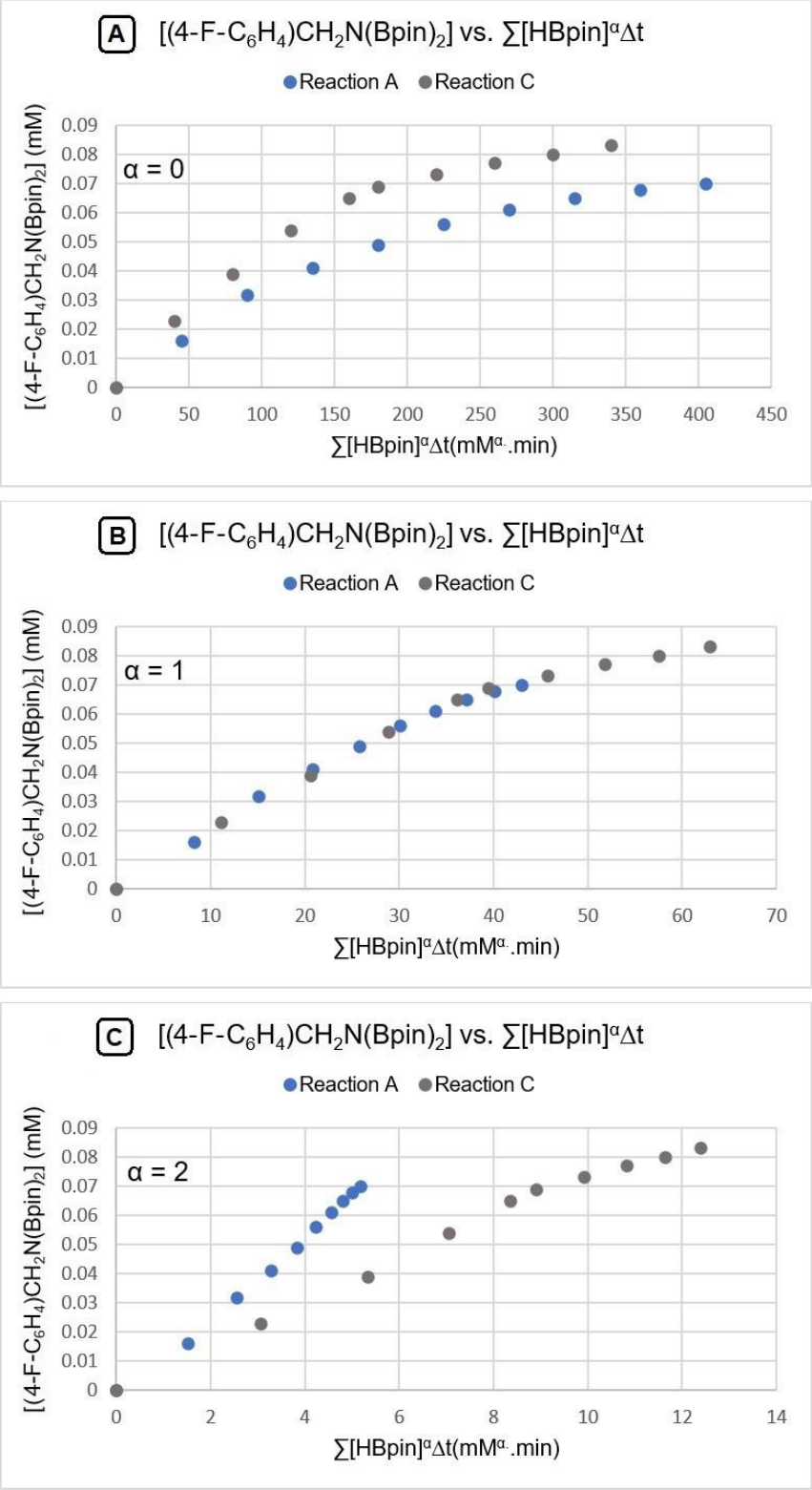

Figure C22. VTNA of rate order of [HBpin].

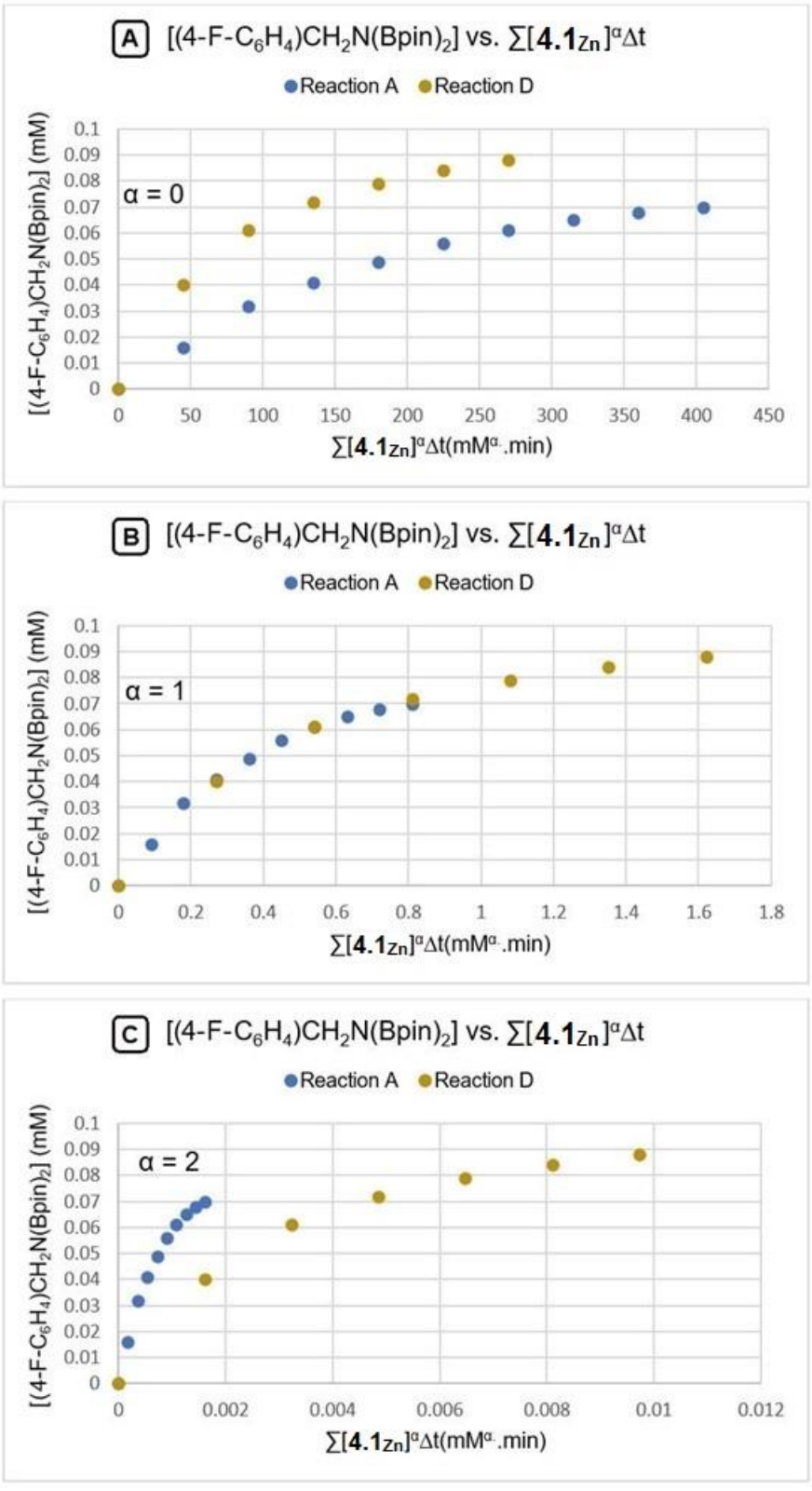

Figure C23. VTNA of rate order of [**4.1**$_{Zn}$].

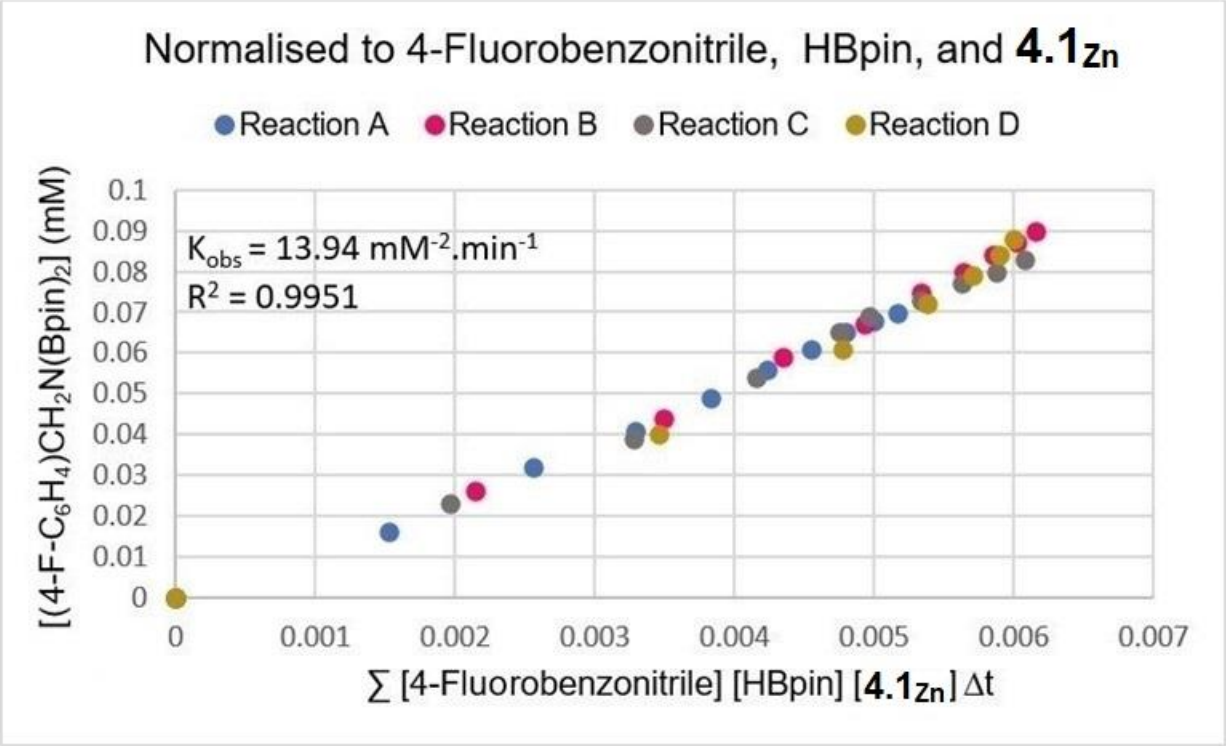

Figure C24. VTNA of $(4\text{-F-}C_6H_4)CH_2N(Bpin)_2$ vs. Σ [4-Fluorobenzonitrile][HBpin][**4.1$_{Zn}$**] Δt to give k_{obs}.

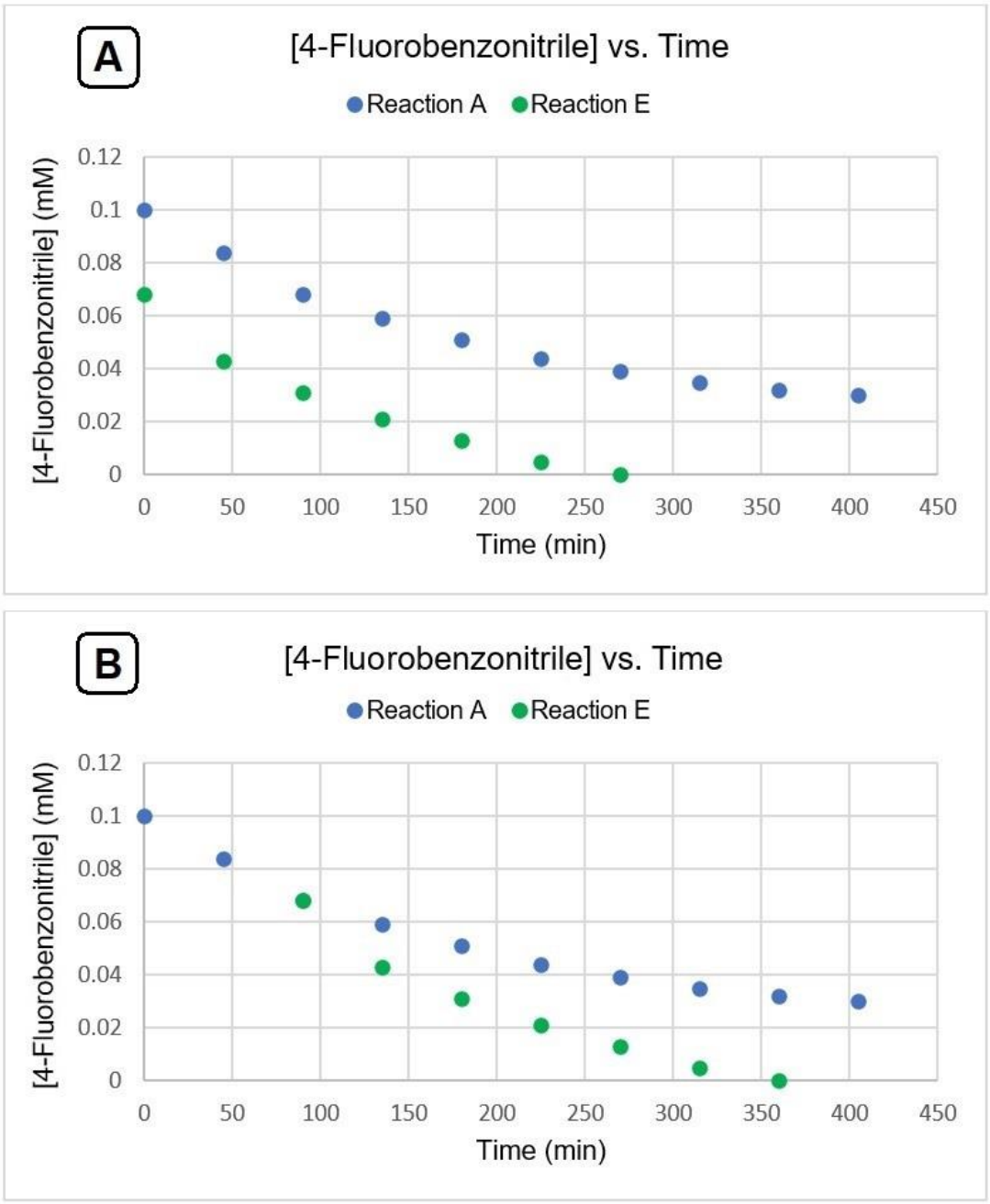

Figure C25. VTNA of [4-Fluorobenzonitrile] vs. Time to find out if the catalytic system suffers either product inhibition or catalyst deactivation. Top: before time adjustment. Bottom: after time adjustment.

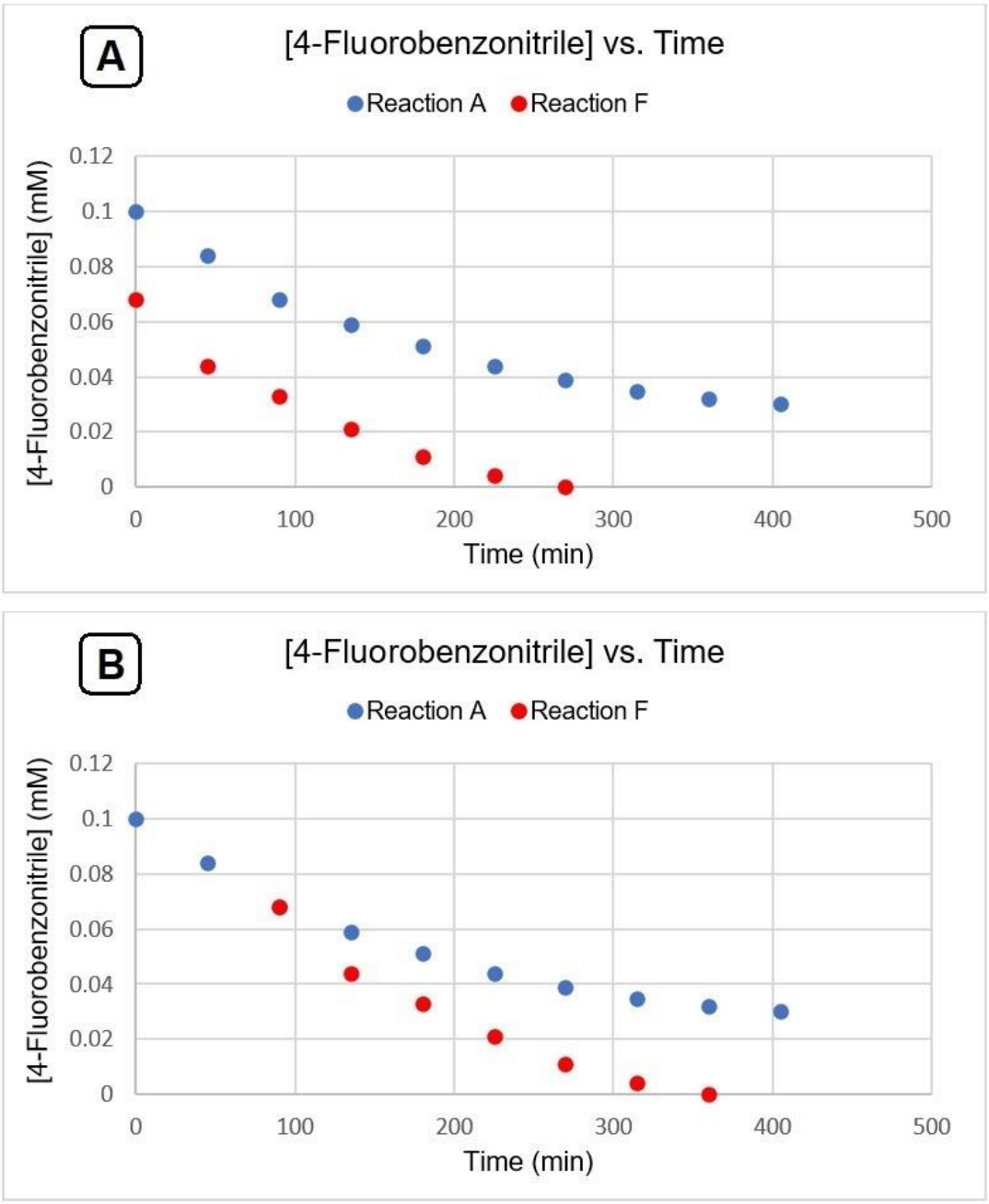

Figure C26. VTNA of [4-Fluorobenzonitrile] vs. Time to find out if the catalytic system suffers product inhibition. Top: before time adjustment. Bottom: after time adjustment.

Table C1: X-ray crystallographic data collection and refinement details for **g**, **H_2L4** and **4.1$_{Zn}$**..

	g (K0991)	**H_2L4 (S0769)**	**4.1$_{Zn}$ (K0572)**
empirical formula	$C_{19}H_{30}B_2FNO_4$	$C_{19}H_{18}N_2OS$	$C_{54}H_{64}N_4O_6S_2Zn_2$
formula weight ($g \cdot mol^{-1}$)	377.06	322.41	1059.95
crystal system	triclinic	monoclininc	triclinic
space group	$P\,\bar{1}$	$P\,2_1/n$	$P\,\bar{1}$
a (A)	6.5967(4)	8.4071(19)	9.9532(13)
b (A)	12.0859(6)	17.688(4)	10.9777(14)
c (A)	14.3335(7)	11.345(2)	12.1123(16)
α (deg)	105.426(1)	90	88.174(2)
β (deg)	97.881(1)	103.767(7)	83.185(2)
γ (deg)	103.322(1)	90	80.990(2)
V (A^3)	1047.7(1)	1638.6(6)	1297.7(3)
Z	2	4	1
T (K)	203(2)	203(2)	203(2)
ρ_{calcd} ($g \cdot cm^{-3}$)	1.195	1.307	1.356
μ (mm^{-1})	0.086	0.203	1.057
$2\theta_{max}$ (deg)	50.042	50.484	50.484
total/unique reflections	15994/3664	12506/3740	31432/8030
Reflections [$I_o \geq 2\sigma(I_o)$]	2901	2679	5376
R_1, wR_2 [$I_o \geq 2\sigma(I_o)$]	0.0391, 0.1000	0.0418, 0.0844	0.0487, 0.1327
goodness of fit	1.036	1.015	1.014
CCDC number	2128270	2129544	2129545

Table C2. Bond lengths for product ***g***.

Atom1	Atom2	Length/Å
F1	C17	1.365(2)
O1	C2	1.458(2)
O1	B1	1.371(2)
O2	B1	1.366(2)
O2	C1A	1.444(3)
O3	C7	1.466(2)
O3	B2	1.371(2)
O4	C8	1.457(2)
O4	B2	1.375(2)
N1	C13	1.478(2)
N1	B1	1.423(2)
N1	B2	1.429(2)
C2	C1A	1.643(5)
C2	C3A	1.338(6)
C2	C4A	1.655(7)
C6	H6A	0.97
C6	H6B	0.97
C6	H6C	0.97
C6	C1A	1.404(5)
C7	C8	1.550(2)
C7	C11	1.522(2)
C7	C12	1.515(2)
C8	C9	1.520(2)
C8	C10	1.516(2)
C9	H9A	0.97
C9	H9B	0.97
C9	H9C	0.97
C10	H10A	0.97
C10	H10B	0.97
C10	H10C	0.97
C11	H11A	0.97
C11	H11B	0.97
C11	H11C	0.97
C12	H12A	0.97
C12	H12B	0.97
C12	H12C	0.97
C13	H13A	0.98
C13	H13B	0.98
C13	C14	1.511(2)
C14	C15	1.385(2)
C14	C19	1.382(3)
C15	H15	0.94

C15	C16	1.387(2)
C16	H16	0.94
C16	C17	1.355(3)
C17	C18	1.364(3)
C18	H18	0.94
C18	C19	1.385(3)
C19	H19	0.94
C1A	C5A	1.501(8)
C3A	H3A1	0.97
C3A	H3A2	0.97
C3A	H3A3	0.97
C4A	H4AA	0.97
C4A	H4AB	0.97
C4A	H4AC	0.97
C5A	H5AA	0.97
C5A	H5AB	0.97
C5A	H5AC	0.97

Table C3. Bond lengths for **H_2L4**.

Atom1	**Atom2**	**Length/Å**
S1	C6	1.827(2)
S1	C7	1.774(2)
O1	H1A	0.83
O1	C19	1.358(2)
N1	C1	1.335(3)
N1	C5	1.336(2)
N2	H2A	0.87
N2	C12	1.360(2)
N2	C13	1.446(2)
C1	H1	0.94
C1	C2	1.371(3)
C2	H2	0.94
C2	C3	1.362(3)
C3	H3	0.94
C3	C4	1.381(3)
C4	H4	0.94
C4	C5	1.380(2)
C5	C6	1.498(3)
C6	H6A	0.98
C6	H6AB	0.98
C7	C8	1.382(3)
C7	C12	1.409(2)
C8	H8	0.94

C8	C9	1.375(3)
C9	H9	0.94
C9	C10	1.379(3)
C10	H10	0.94
C10	C11	1.374(3)
C11	H11	0.94
C11	C12	1.399(3)
C13	H13A	0.98
C13	H13B	0.98
C13	C14	1.507(2)
C14	C15	1.383(2)
C14	C19	1.401(2)
C15	H15	0.94
C15	C16	1.389(3)
C16	H16	0.94
C16	C17	1.381(3)
C17	H17	0.94
C17	C18	1.380(2)
C18	H18	0.94
C18	C19	1.384(3)

Table C4. Bond lengths for **4.1$_{Zn}$.**

Atom1	**Atom2**	**Length/Å**
Zn1	S1	2.5784(8)
Zn1	N1	1.940(2)
Zn1	O1	2.059(2)
Zn1	N2	2.056(2)
Zn1	O1	1.964(2)
C1	O1	1.342(3)
C1	C2	1.404(3)
C1	C6	1.391(3)
S1	C13	1.764(3)
S1	C14	1.844(3)
N1	C8	1.359(3)
N1	C7	1.468(3)
O1	Zn1	1.964(2)
C2	H2	0.94
C2	C3	1.377(5)
N2	C15	1.342(4)
N2	C19	1.338(4)
C6	C5	1.397(4)
C6	C7	1.516(3)
C5	H5	0.94

C5	C4	1.395(5)
C4	H4	0.94
C4	C3	1.353(5)
C3	H3	0.94
C9	H9	0.94
C9	C8	1.409(4)
C9	C10	1.390(5)
C8	C13	1.432(4)
C7	H7A	0.98
C7	H7AB	0.98
C10	H10	0.94
C10	C11	1.383(6)
C11	H11	0.94
C11	C12	1.368(6)
C12	H12	0.94
C12	C13	1.392(4)
C14	H14A	0.98
C14	H14B	0.98
C14	C15	1.495(4)
C15	C16	1.387(4)
C16	H16	0.94
C16	C17	1.373(5)
C17	H17	0.939
C17	C18	1.374(5)
C18	H18	0.94
C18	C19	1.380(4)
C19	H19	0.94
Zn1	S1	2.5784(8)
Zn1	N1	1.940(2)
Zn1	O1	2.059(2)
Zn1	N2	2.056(2)
C1	O1	1.342(3)
C1	C2	1.404(3)
C1	C6	1.391(3)
S1	C13	1.764(3)
S1	C14	1.844(3)
N1	C8	1.359(3)
N1	C7	1.468(3)
C2	H2	0.94
C2	C3	1.377(5)
N2	C15	1.342(4)
N2	C19	1.338(4)
C6	C5	1.397(4)
C6	C7	1.516(3)
C5	H5	0.94

C5	C4	1.395(5)
C4	H4	0.94
C4	C3	1.353(5)
C3	H3	0.94
C9	H9	0.94
C9	C8	1.409(4)
C9	C10	1.390(5)
C8	C13	1.432(4)
C7	H7A	0.98
C7	H7AB	0.98
C10	H10	0.94
C10	C11	1.383(6)
C11	H11	0.94
C11	C12	1.368(6)
C12	H12	0.94
C12	C13	1.392(4)
C14	H14A	0.98
C14	H14B	0.98
C14	C15	1.495(4)
C15	C16	1.387(4)
C16	H16	0.94
C16	C17	1.373(5)
C17	H17	0.939
C17	C18	1.374(5)
C18	H18	0.94
C18	C19	1.380(4)
C19	H19	0.94
O1_1	C1_1	1.48(1)
O1_1	C4_1	1.45(1)
C1_1	H1A_1	0.98
C1_1	H1AB_1	0.98
C1_1	C2_1	1.39(1)
C2_1	H2A_1	0.98
C2_1	H2B_1	0.98
C2_1	C3_1	1.34(1)
C3_1	H3A_1	0.979
C3_1	H3B_1	0.98
C3_1	C4_1	1.40(1)
C4_1	H4A_1	0.98
C4_1	H4AB_1	0.98
O1_3	C1_3	1.48(1)
O1_3	C4_3	1.45(2)
C1_3	H1A_3	0.98
C1_3	H1AB_3	0.98
C1_3	C2_3	1.38(1)

C2_3	H2A_3	0.98
C2_3	H2B_3	0.98
C2_3	C3_3	1.34(2)
C3_3	H3A_3	0.98
C3_3	H3B_3	0.98
C3_3	C4_3	1.40(1)
C4_3	H4A_3	0.98
C4_3	H4AB_3	0.98

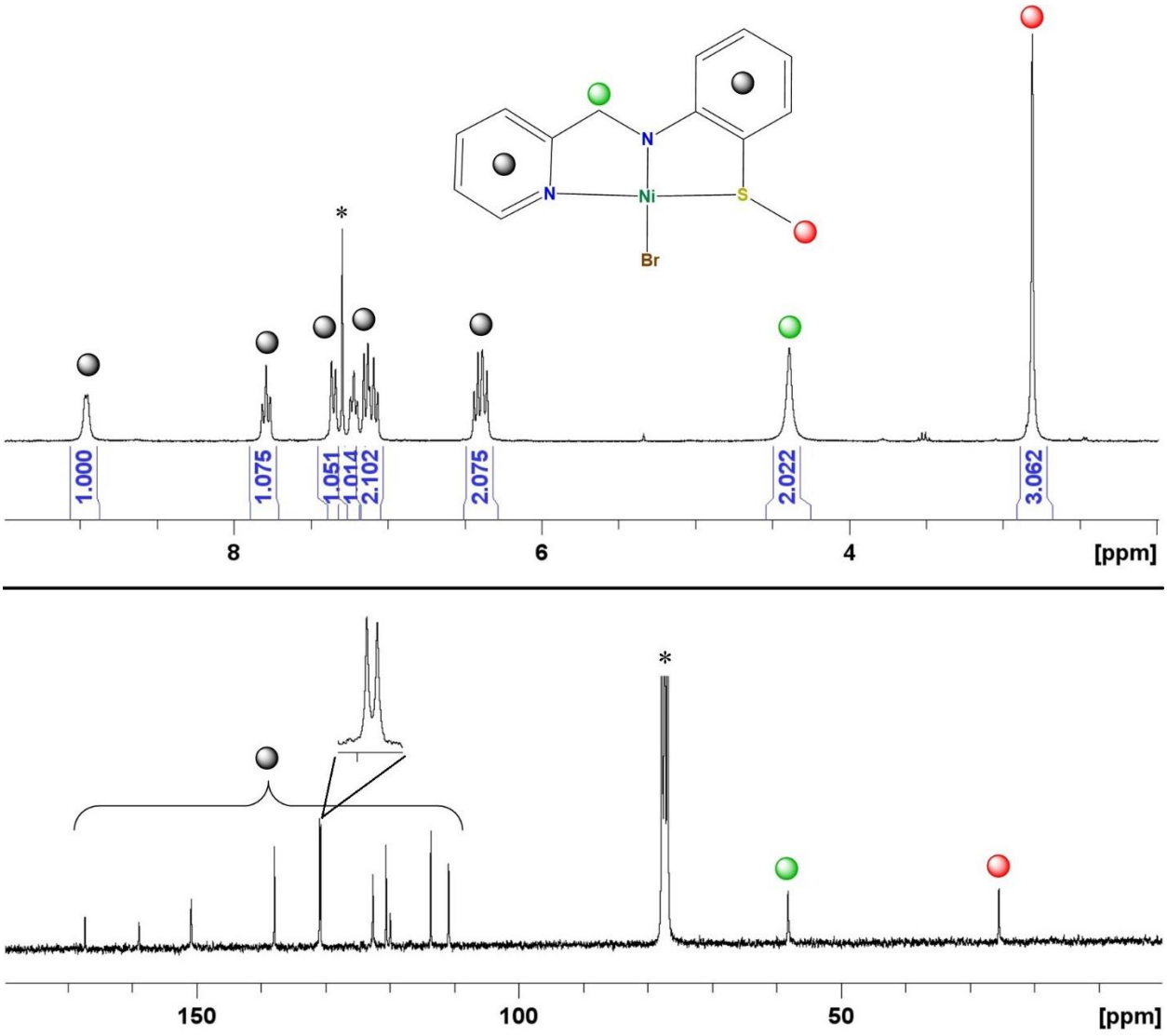

Figure C27. ^{1}H NMR (top, 300 MHz, $CDCl_3$) and $^{13}C\{^{1}H\}$ NMR spectra (bottom, 75 MHz, $CDCl_3$) of **4.2$_{Ni}$**. * indicates protic impurity in or ^{13}C resonance of $CDCl_3$.

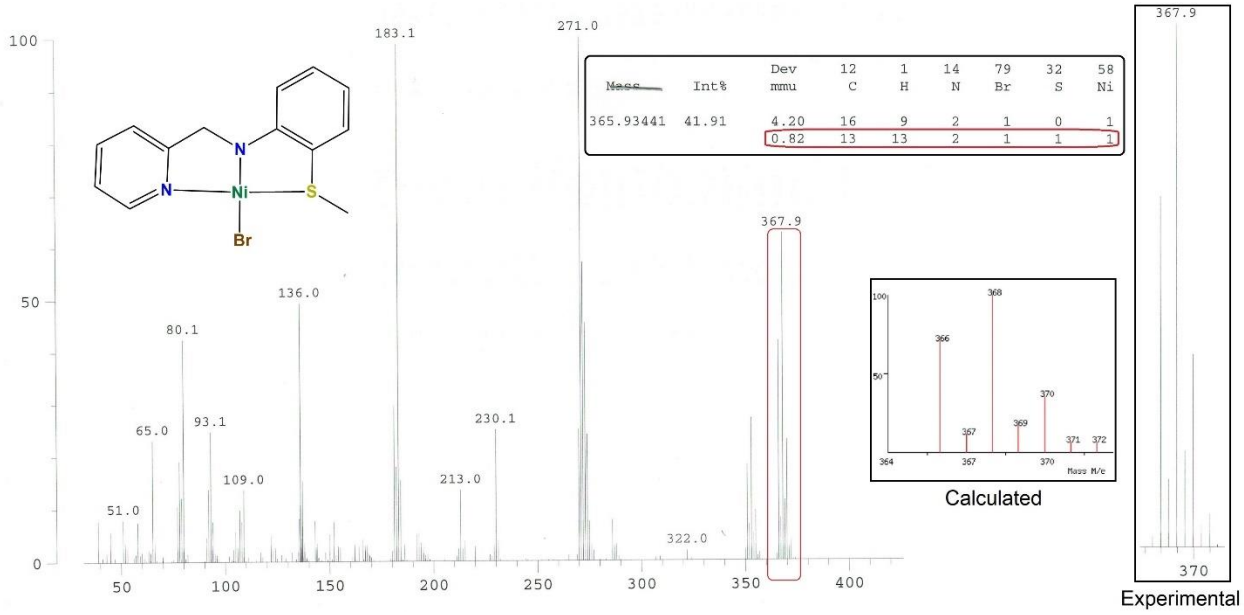

Figure C28. EI-mass spectrum of **4.2$_{Ni}$** showing [M$^+$].

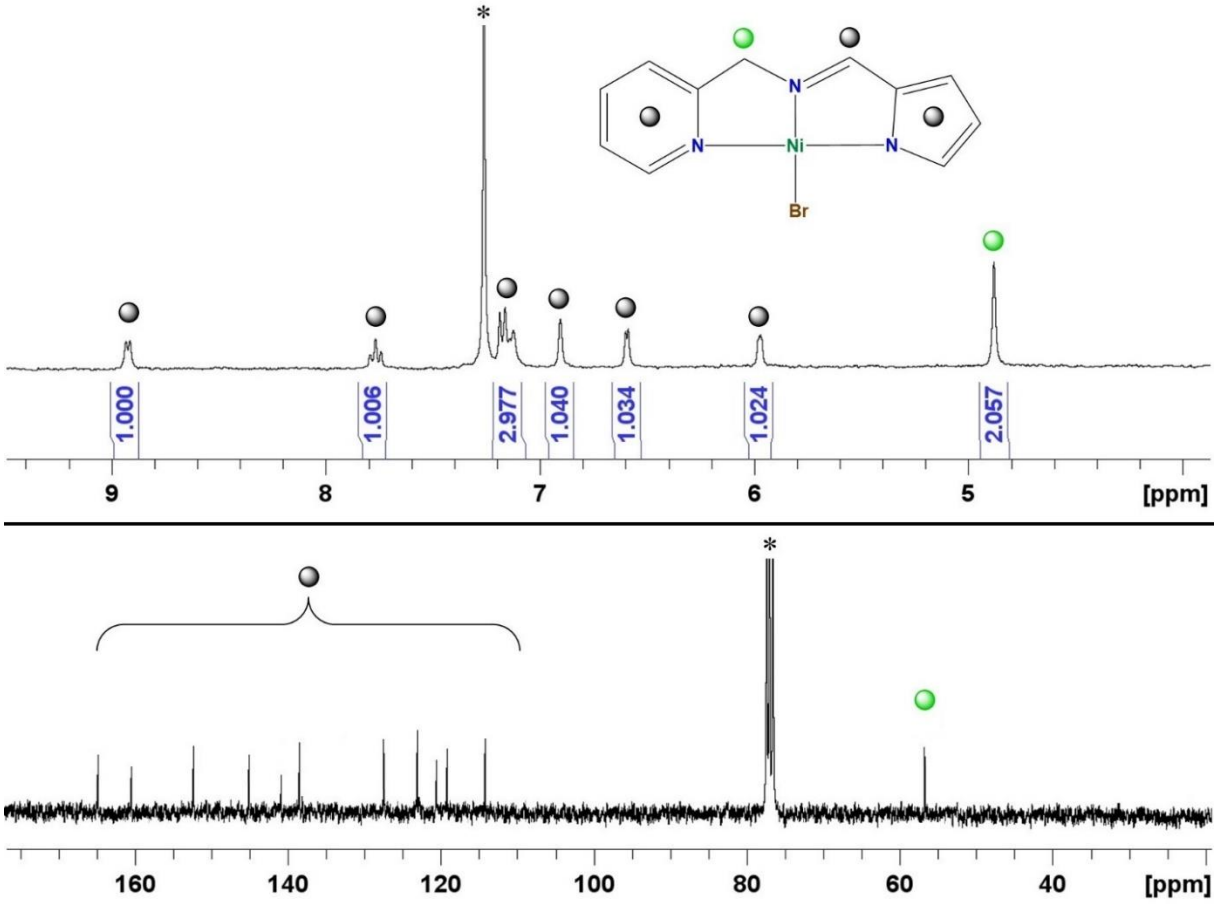

Figure C29. ^{1}H NMR (top, 300 MHz, $CDCl_3$) and $^{13}C\{^1H\}$ NMR spectra (bottom, 75 MHz, $CDCl_3$) of **4.3$_{Ni}$**. * indicates protic impurity in or ^{13}C resonance of $CDCl_3$.

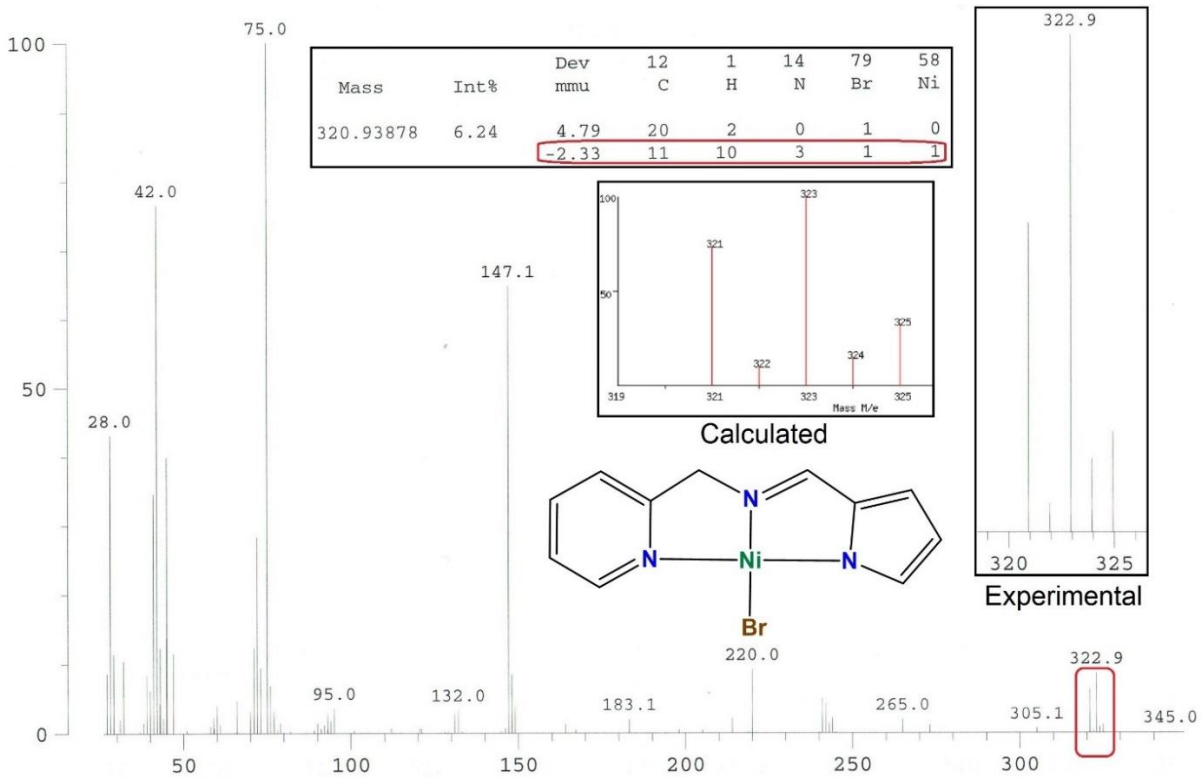

Figure C30. EI-mass spectrum of **4.3**$_{Ni}$ showing [M^+].

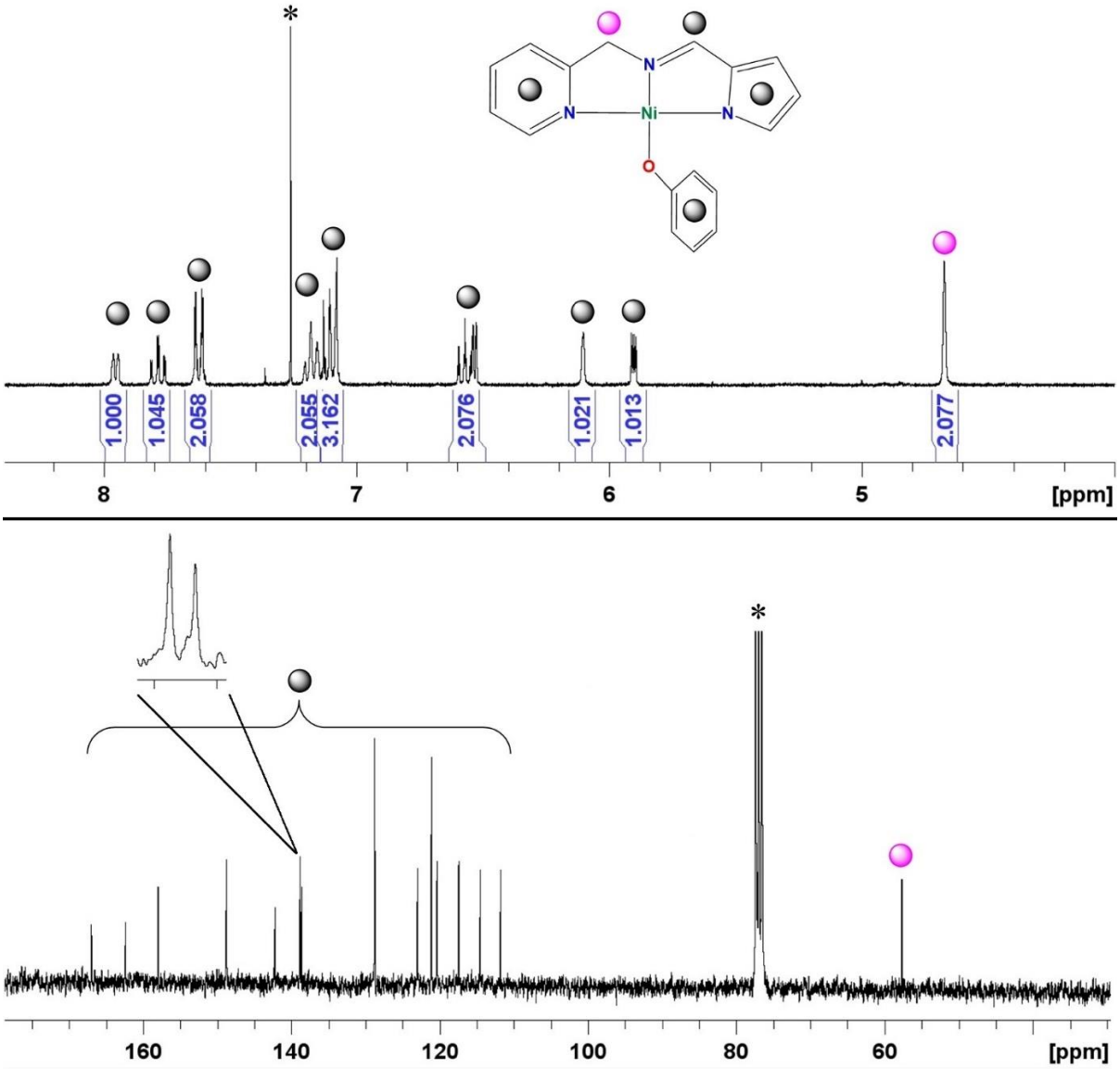

Figure C31. ^{1}H NMR (top, 300 MHz, $CDCl_3$) and $^{13}C\{^{1}H\}$ NMR spectra (bottom, 75 MHz, $CDCl_3$) of **4.4**$_{Ni}$. * indicates protic impurity in or ^{13}C resonance of $CDCl_3$.

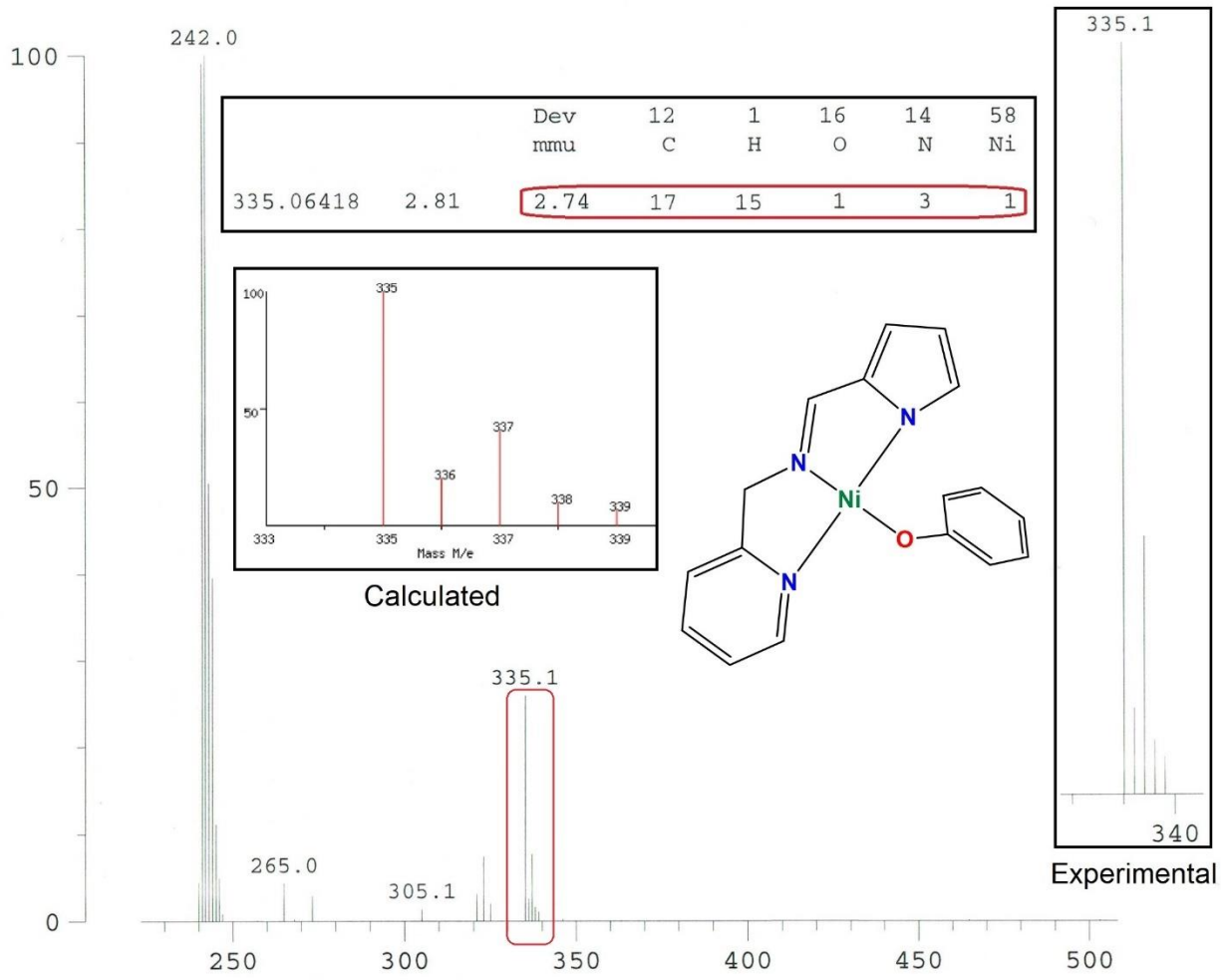

Figure C32. EI-mass spectrum of **4.4$_{Ni}$** showing [M^{+}].

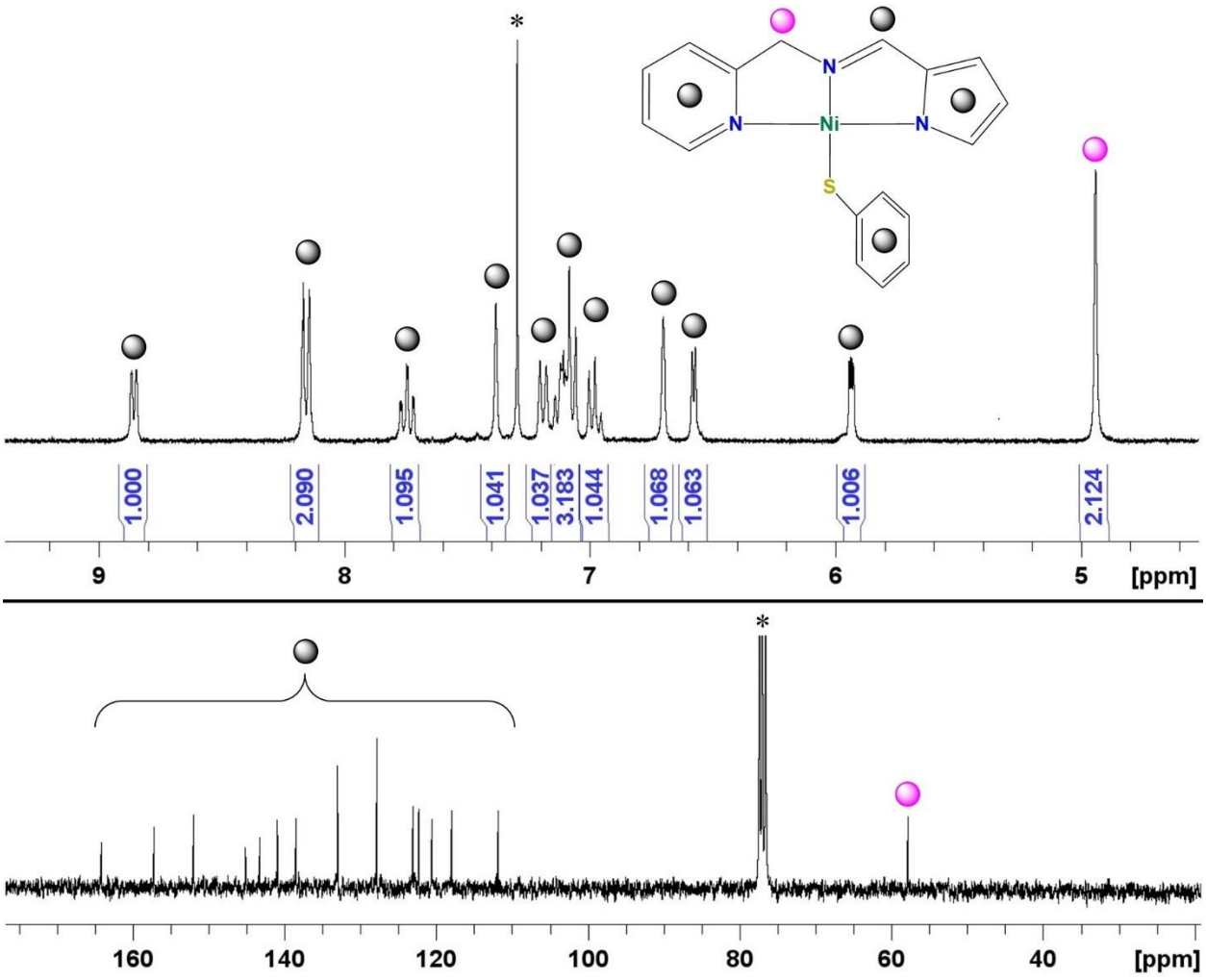

Figure C33. ^{1}H NMR (top, 300 MHz, $CDCl_3$) and $^{13}C\{^{1}H\}$ NMR spectra (bottom, 75 MHz, $CDCl_3$) of **4.5$_{Ni}$**. * indicates protic impurity in or ^{13}C resonance of $CDCl_3$.

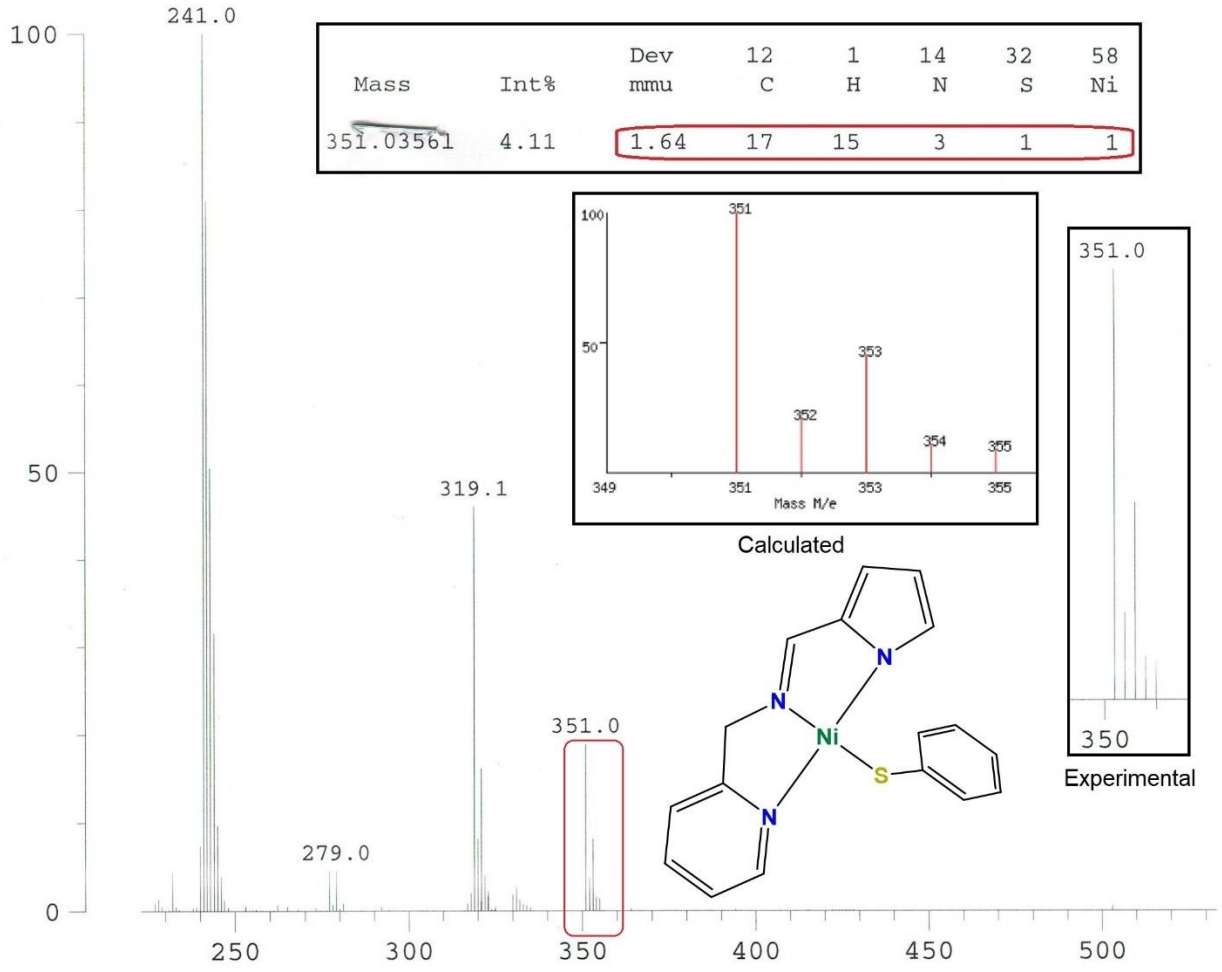

Figure C34. EI-mass spectrum of **4.5$_{Ni}$** showing [M^{+}].

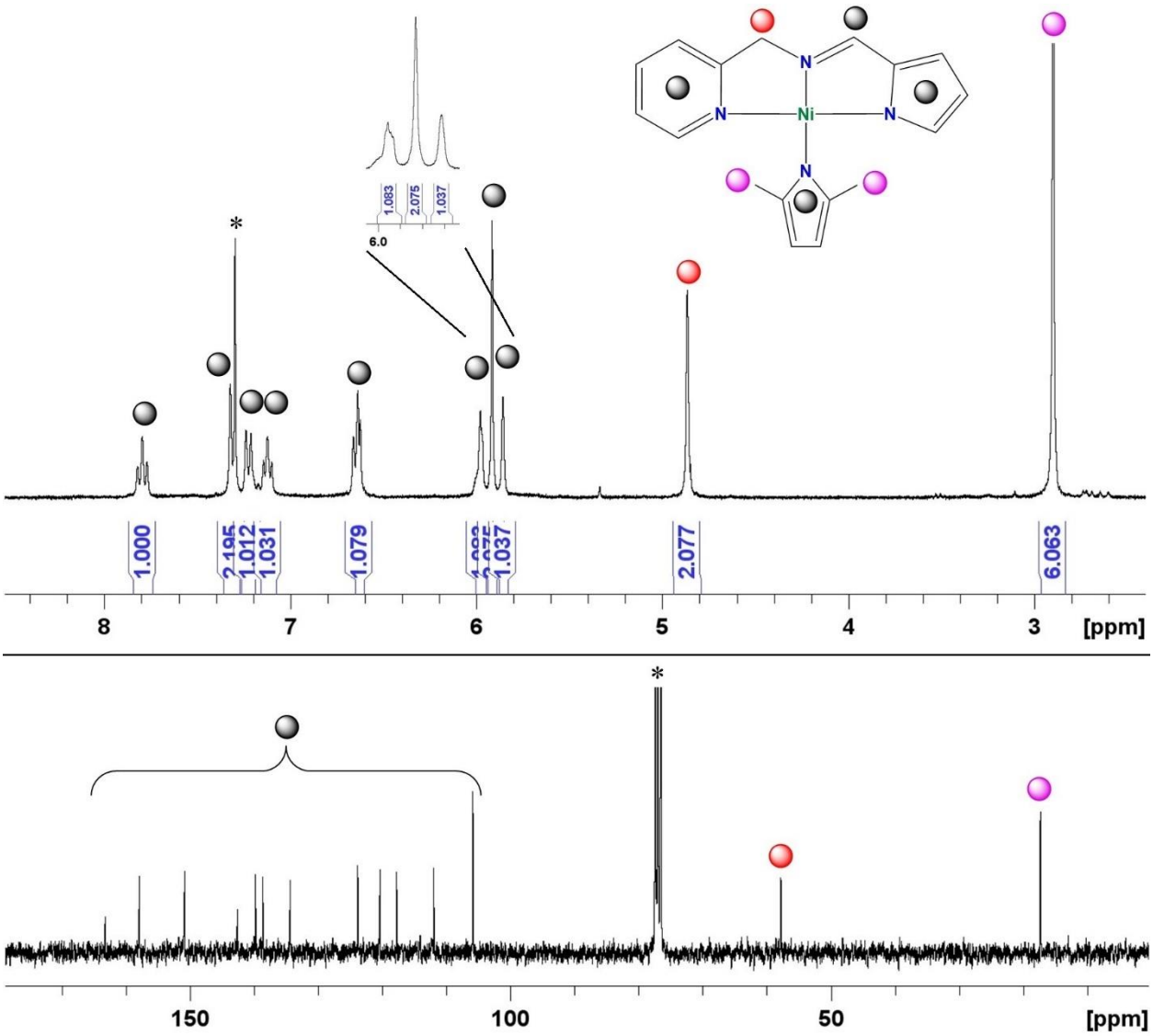

Figure C35. ^{1}H NMR (top, 300 MHz, $CDCl_3$) and $^{13}C\{^{1}H\}$ NMR spectra (bottom, 75 MHz, $CDCl_3$) of **4.6$_{Ni}$**. * indicates protic impurity in or ^{13}C resonance of $CDCl_3$.

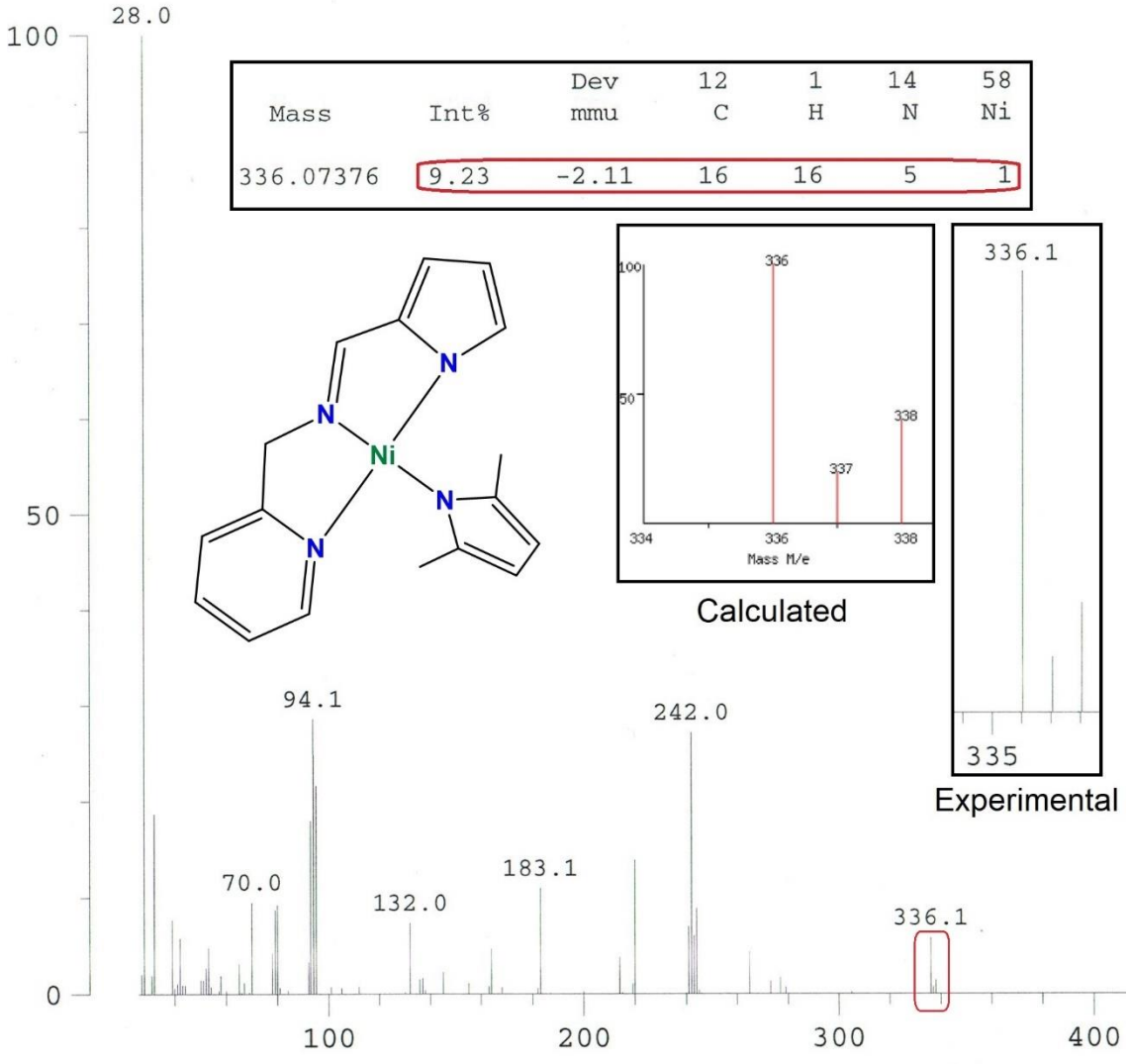

Figure C36. EI-mass spectrum of **4.6**$_{Ni}$ showing [M^+].

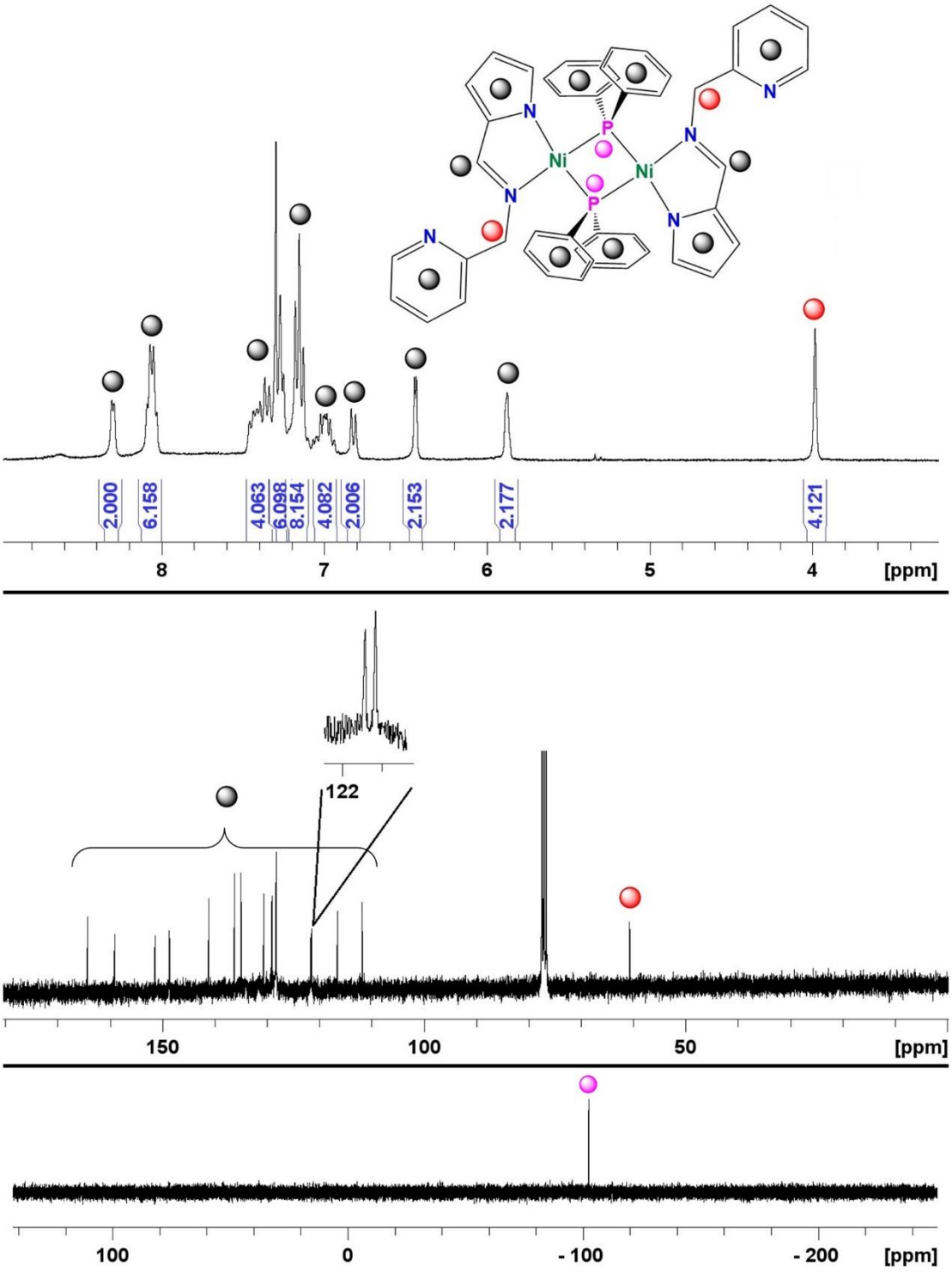

Figure C37. ^{1}H NMR (top, 300 MHz, $CDCl_3$), $^{13}C\{^{1}H\}$ NMR (middle, 75 MHz, $CDCl_3$) and $^{31}P\{^{1}H\}$ (bottom, 121 MHz, $CDCl_3$) NMR spectra of **4.7**$_{Ni}$. * indicates protic impurity in or ^{13}C resonance of $CDCl_3$.

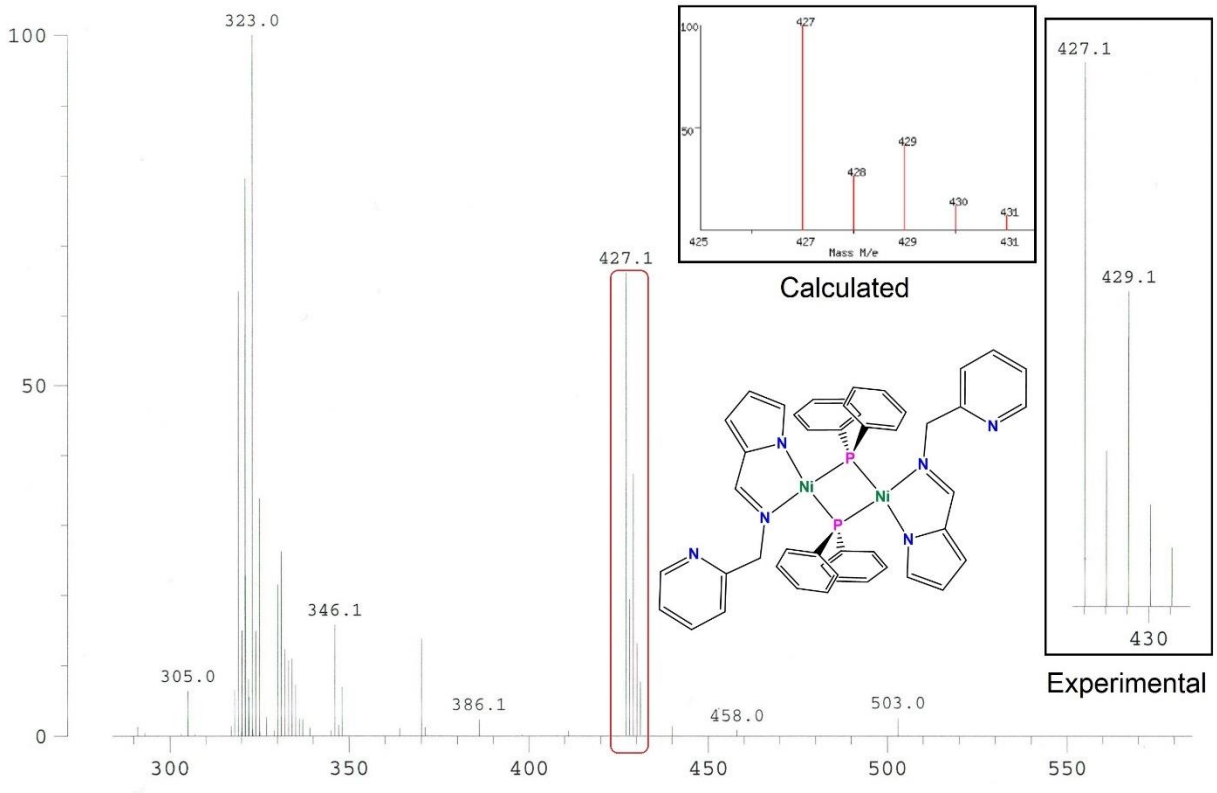

Figure C38. EI-mass spectrum of **4.7**$_{Ni}$ showing [(M/2)$^{+}$].

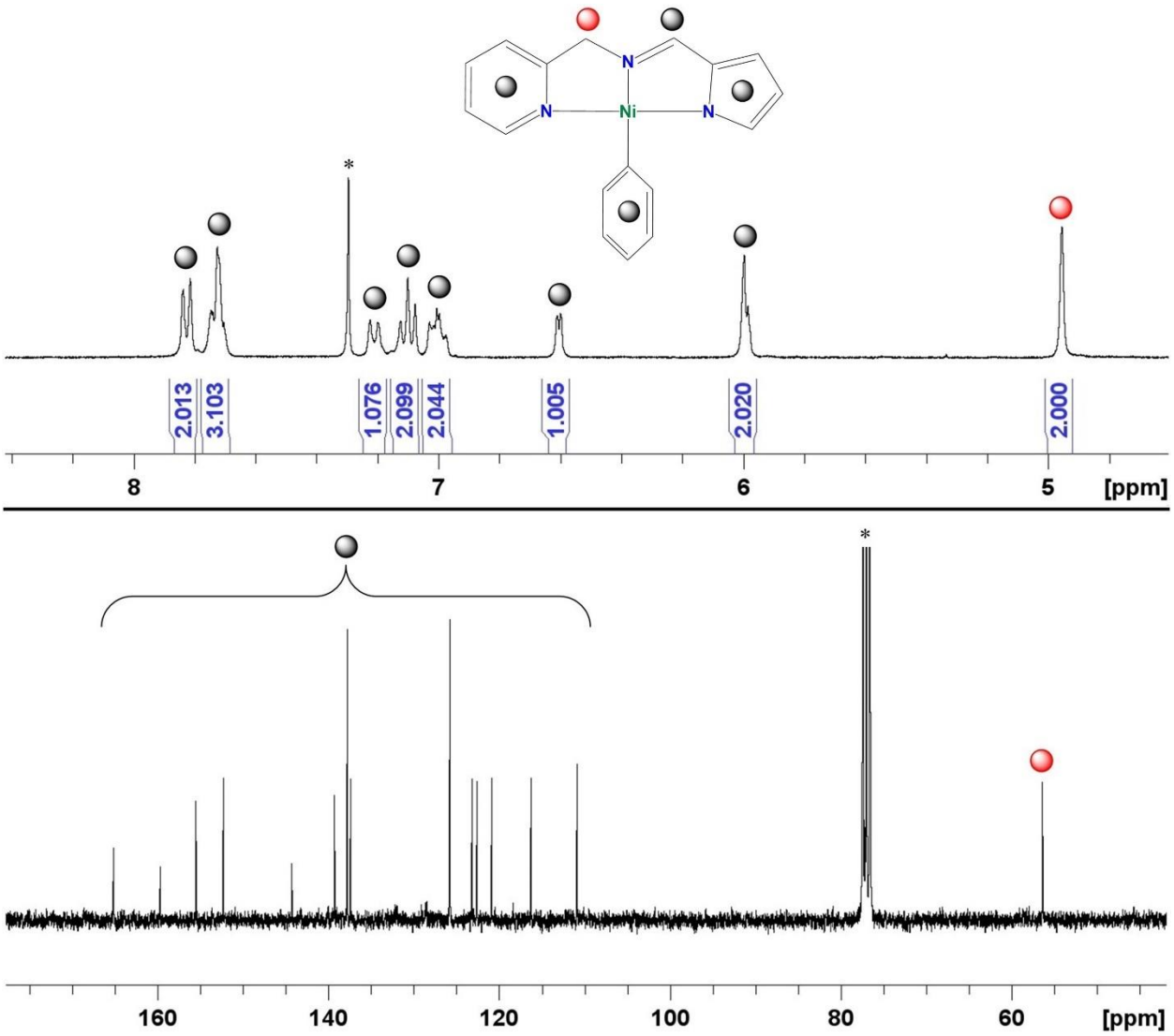

Figure C39. ^{1}H NMR (top, 300 MHz, $CDCl_3$) and $^{13}C\{^{1}H\}$ NMR spectra (bottom, 75 MHz, $CDCl_3$) of **4.8$_{Ni}$**. * indicates protic impurity in or ^{13}C resonance of $CDCl_3$.

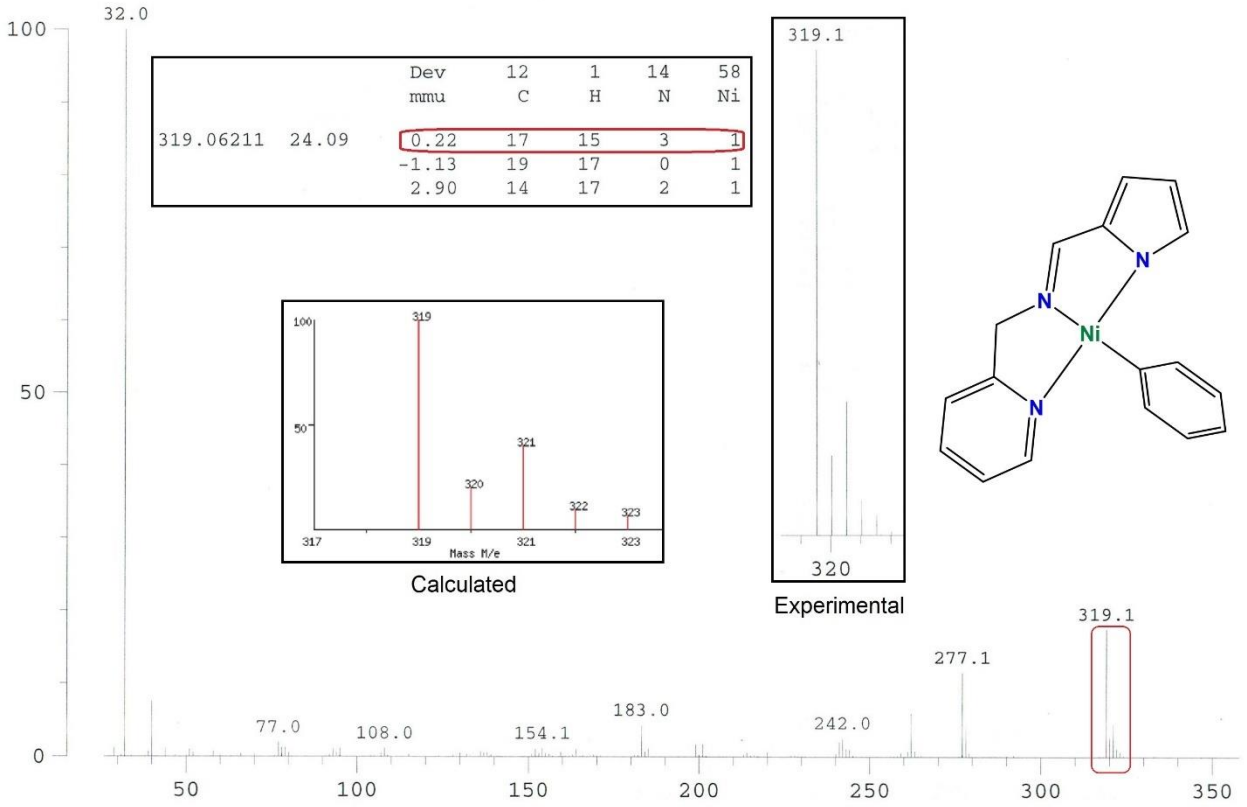

Figure C40. EI-mass spectrum of **4.8$_{Ni}$** showing [M^{+}].

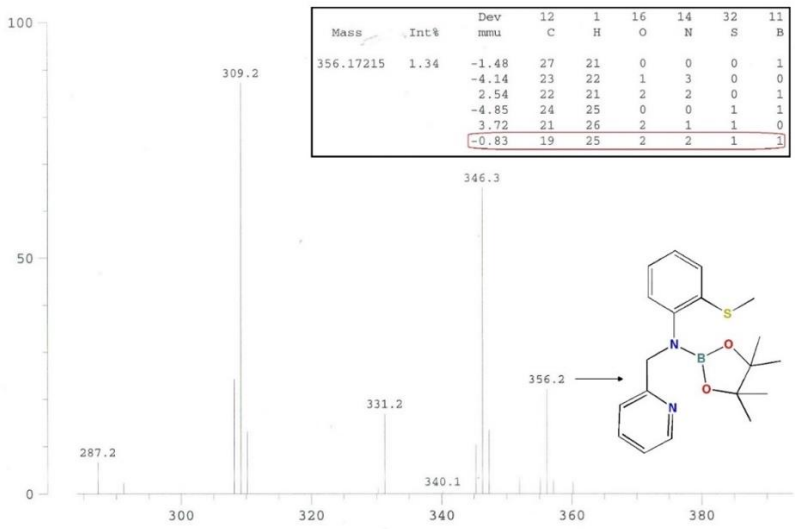

Figure C41. EI-mass spectrum of stoichiometric reaction of **4.2$_{Ni}$** with pinacolborane showing **Bpin-L5** [M^+]. (Calculated: $C_{19}H_{25}N_2BSO_2$ = 365.1729).

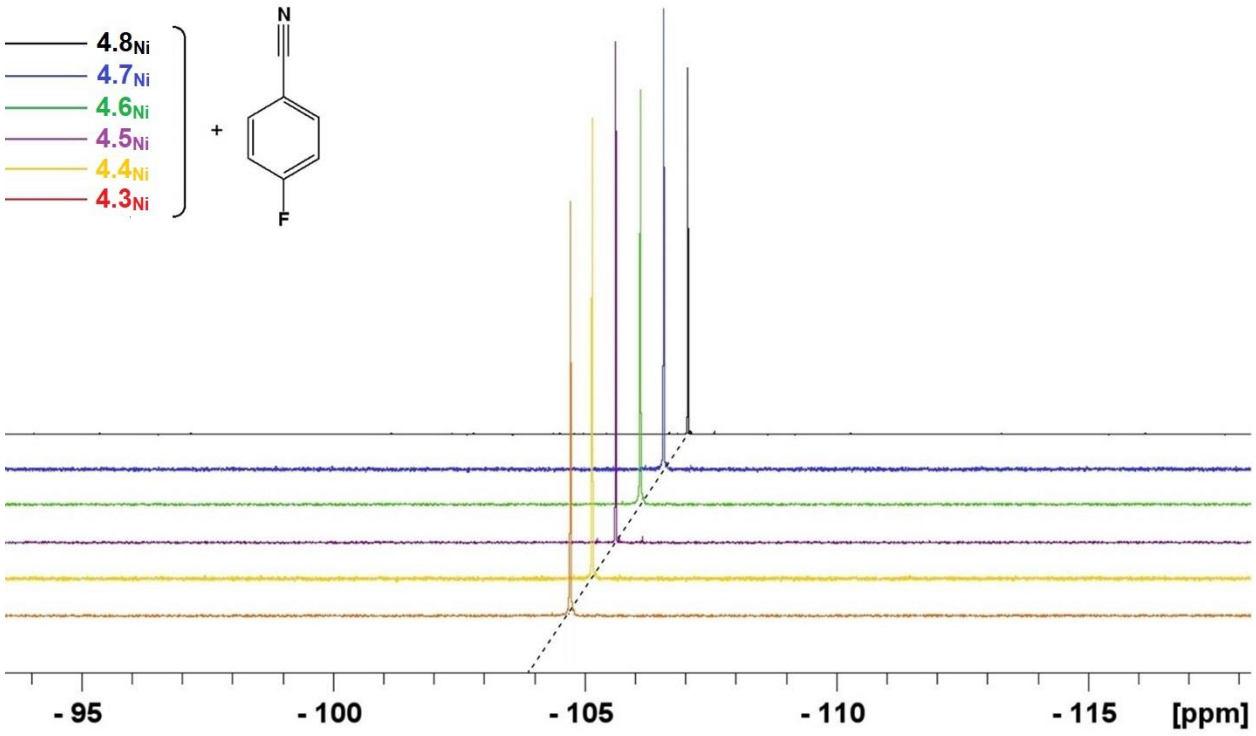

Figure C42. ^{19}F NMR (282 MHz, C_6D_6) spectra of stoichiometric reactions of **4.3$_{Ni}$**, **4.4$_{Ni}$**, **4.5$_{Ni}$**, **4.6$_{Ni}$**, **4.7$_{Ni}$**, and **4.8$_{Ni}$** with 4-fluoro-benzonitrile.

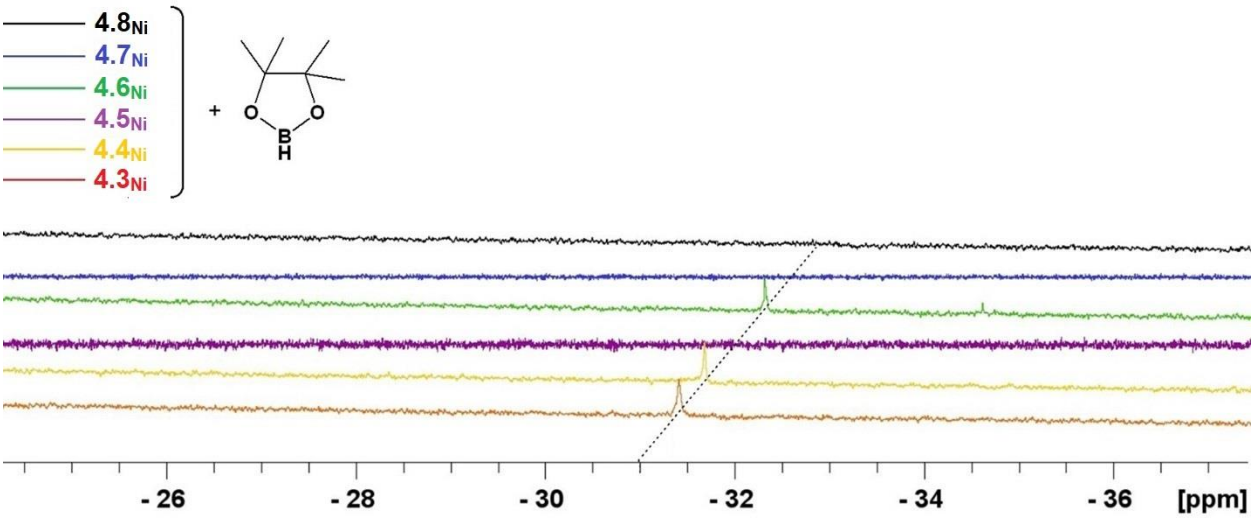

Figure C43. ^{1}H NMR (300 MHz, C_6D_6) spectra of stoichiometric reactions of pinacolborane with **4.3$_{Ni}$**, **4.4$_{Ni}$**, **4.5$_{Ni}$**, **4.6$_{Ni}$** and **4.7$_{Ni}$** at room temperature after 30 min.

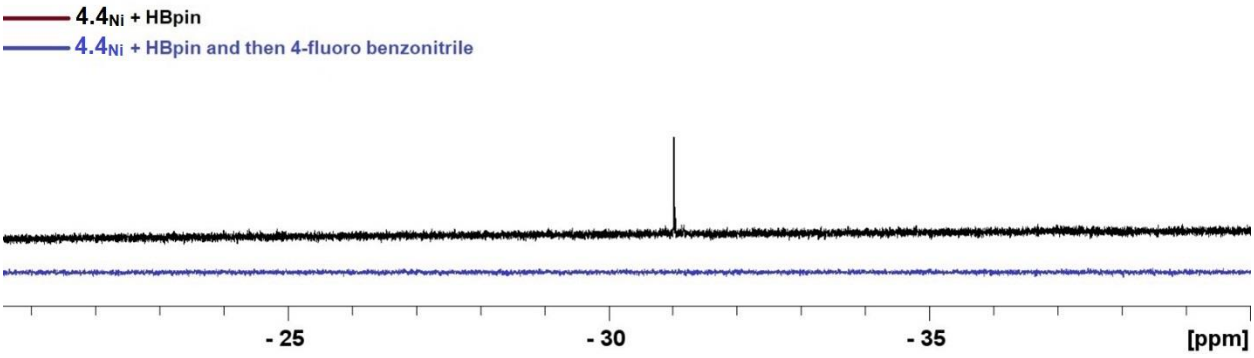

Figure C44. ^{1}H NMR (300 MHz, C_6D_6) spectra of stoichiometric reactions of **4.4$_{Ni}$** with pinacolborane, and then 4-fluoro-benzonitrile.

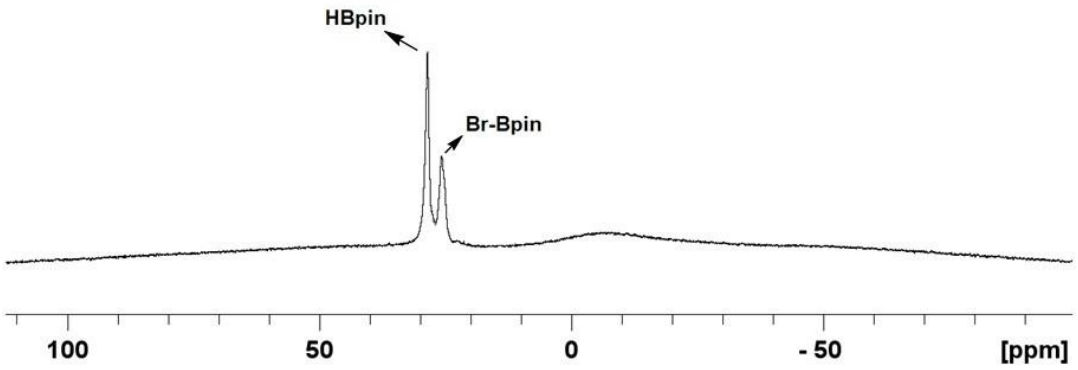

Figure C45. ^{11}B{^{1}H} NMR (96 MHz, C_6D_6) spectrum of stoichiometric reaction of **4.4$_{Ni}$** with pinacolborane.

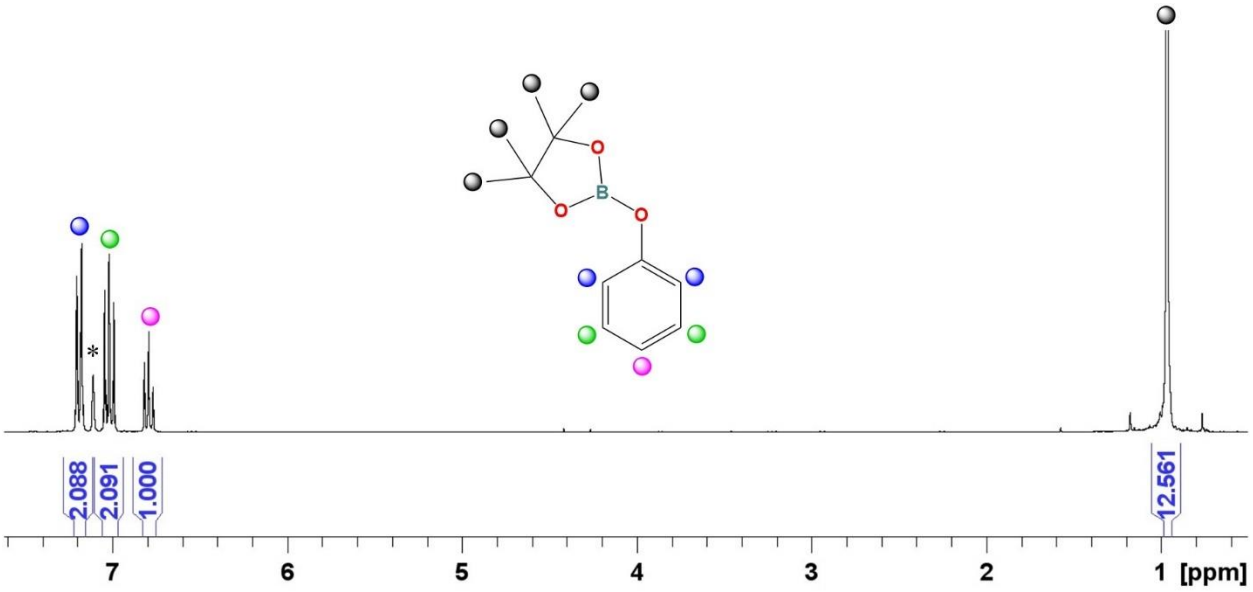

Figure C46. ^{1}H NMR (300 MHz, C_6D_6) spectrum of **S-P3**. * indicates protic impurity in C_6D_6.

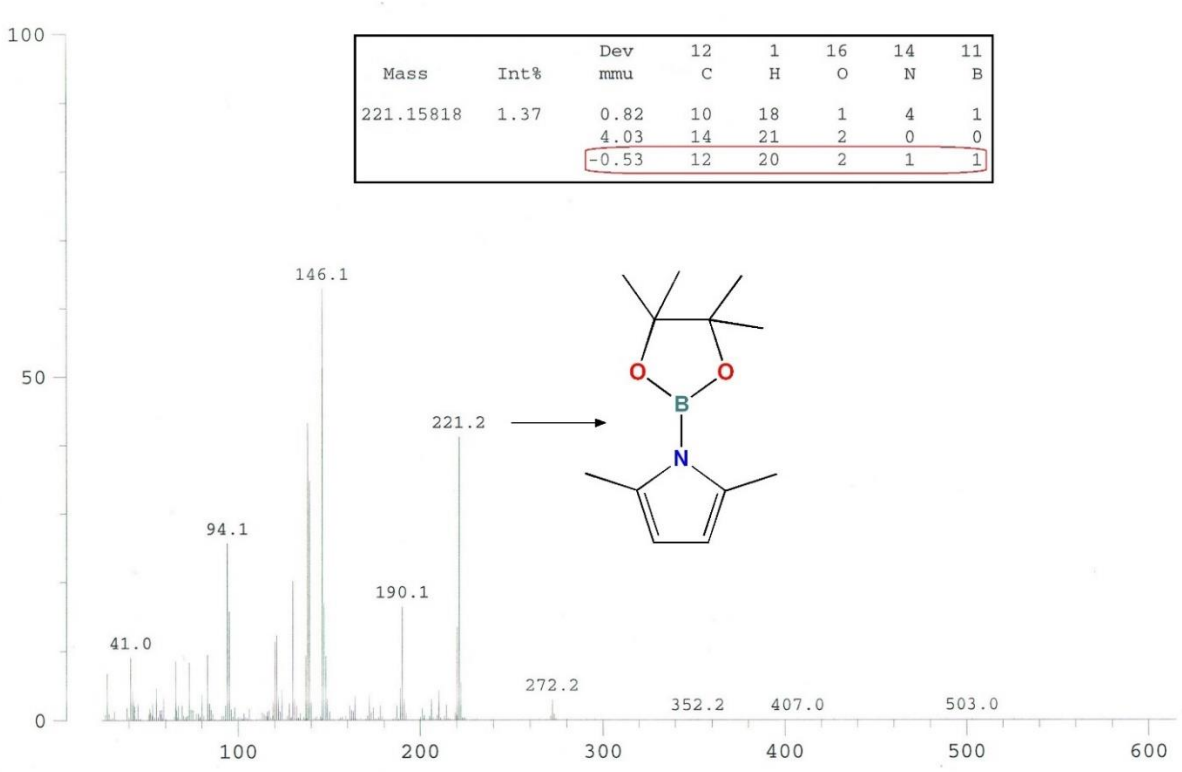

Figure C47. EI-mass spectrum of stoichiometric reaction of **4.6$_{Ni}$** with pinacolborane showing N-borylated 2,5-dimethylpyrrole (**S-P4**) [M^+]. (Calculated: $C_{12}H_{20}NBO_2$ = 221.1587).

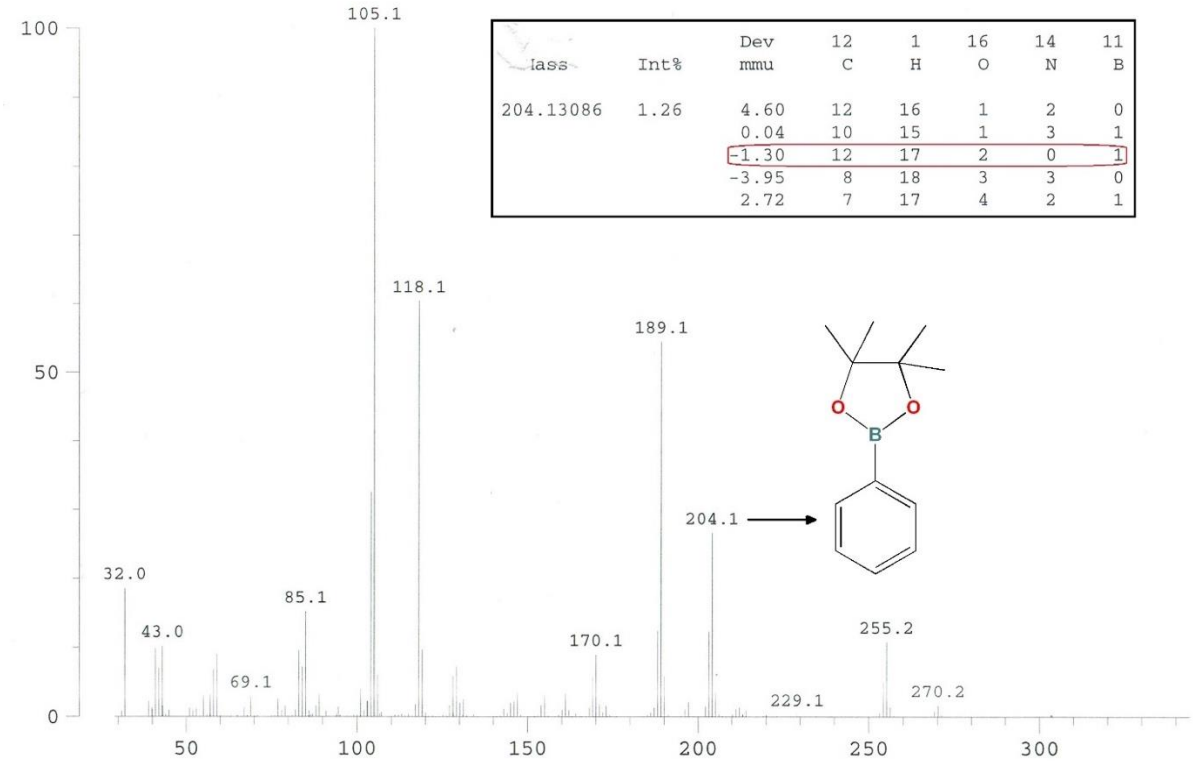

Figure C48. EI-mass spectrum of stoichiometric reaction of **4.8$_{Ni}$** with pinacolborane at 50 ºC, showing Ph–Bpin (**S-P5**) [M^+]. (Calculated: $C_{12}H_{17}BO_2$ = 204.1321).

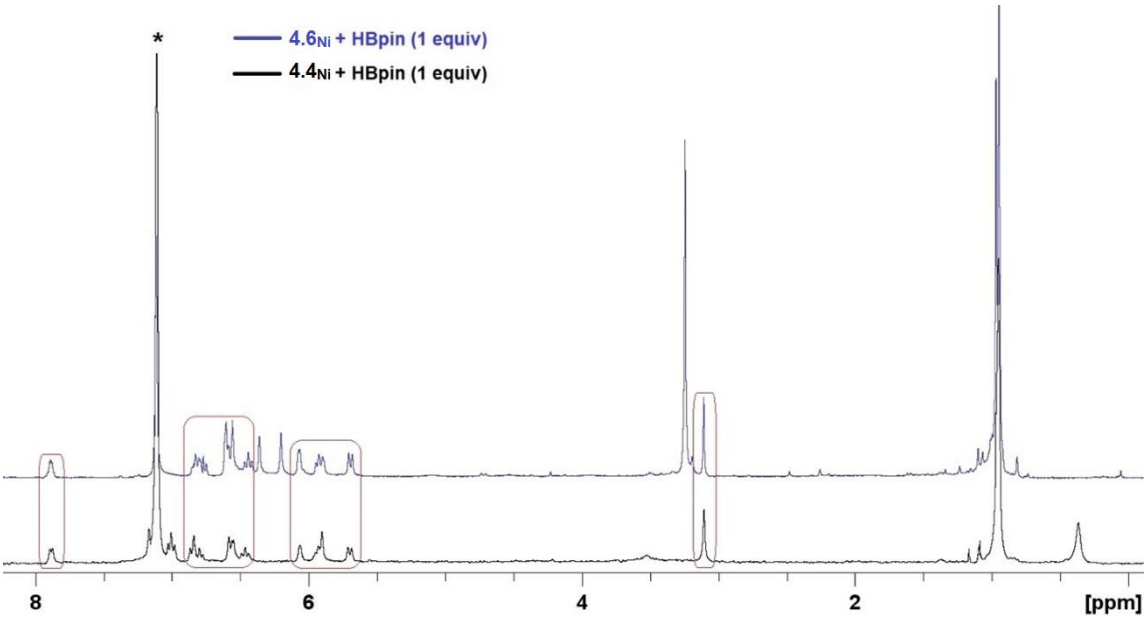

Figure C49. $^1H\{^{11}B\}$ NMR spectra (300 MHz, C_6D_6) of stoichiometric reactions of **4.4$_{Ni}$** and **4.6$_{Ni}$** with pinacolborane. * indicates protic impurity in C_6D_6.

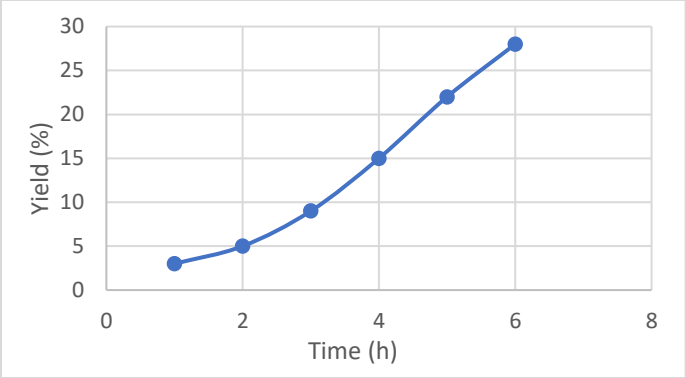

Figure C50. Reaction profile of **4.8**$_{Ni}$-catalyzed benzonitrile dihydroboration at 50 ˚C.

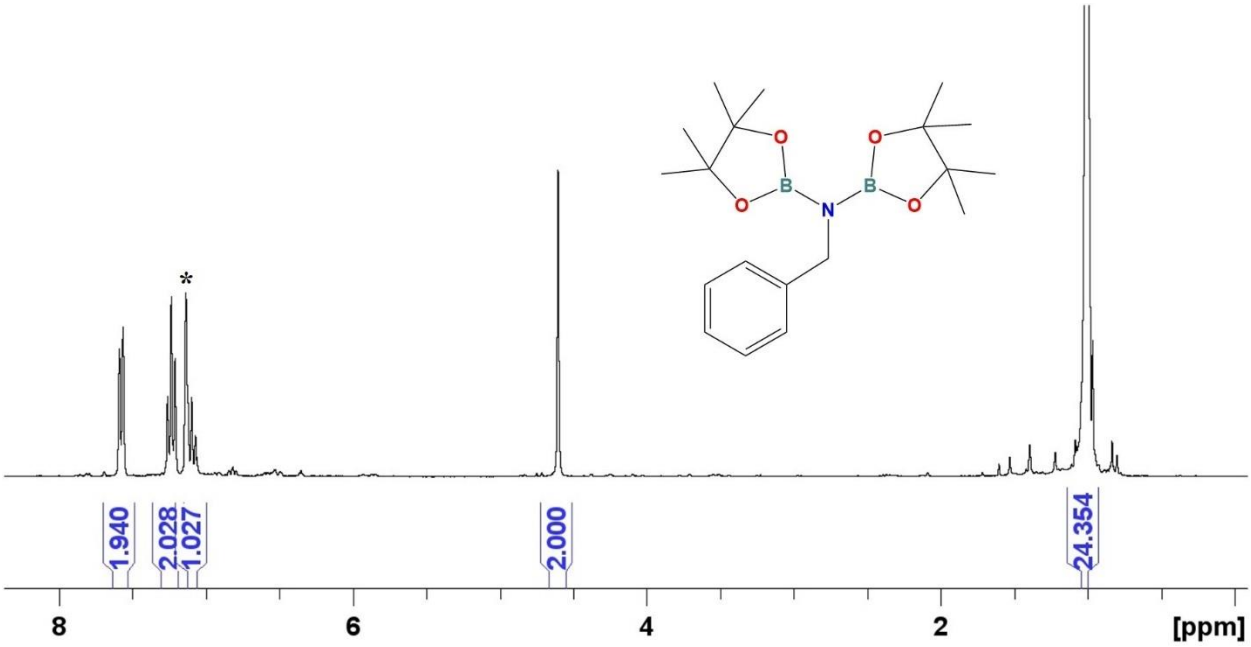

Figure C51. ^{1}H NMR (300 MHz, C_6D_6) spectrum of benzonitrile hydroboration product. * indicates protic impurity in C_6D_6. Chemical shifts matched with literature values.

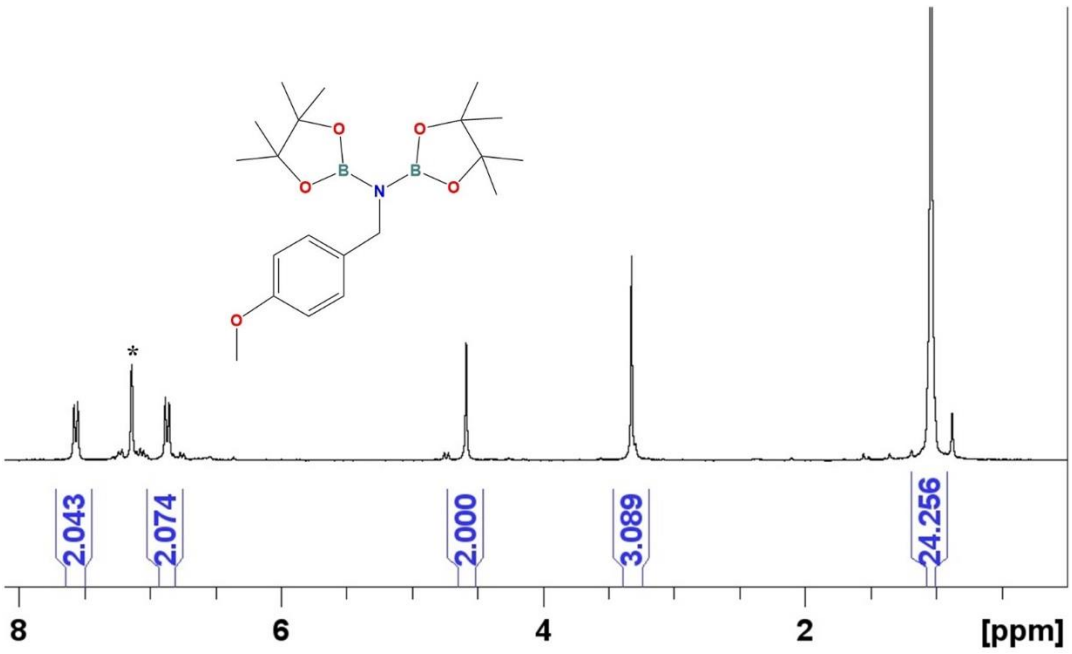

Figure C52. ^{1}H NMR (300 MHz, C_6D_6) spectrum of 4-methoxy-benzonitrile hydroboration product. * indicates protic impurity in C_6D_6. Chemical shifts matched with literature values.

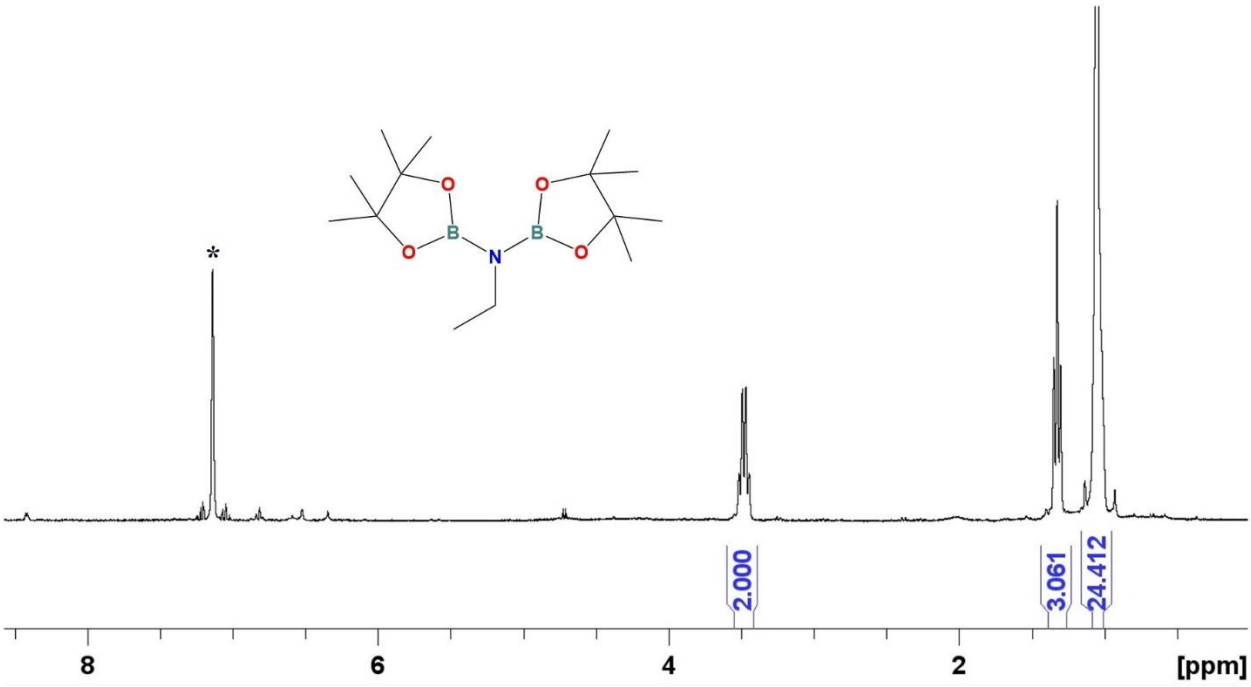

Figure C53. ^{1}H NMR (300 MHz, C_6D_6) spectrum of acetonitrile hydroboration product. * indicates protic impurity in C_6D_6. Chemical shifts matched with literature values.

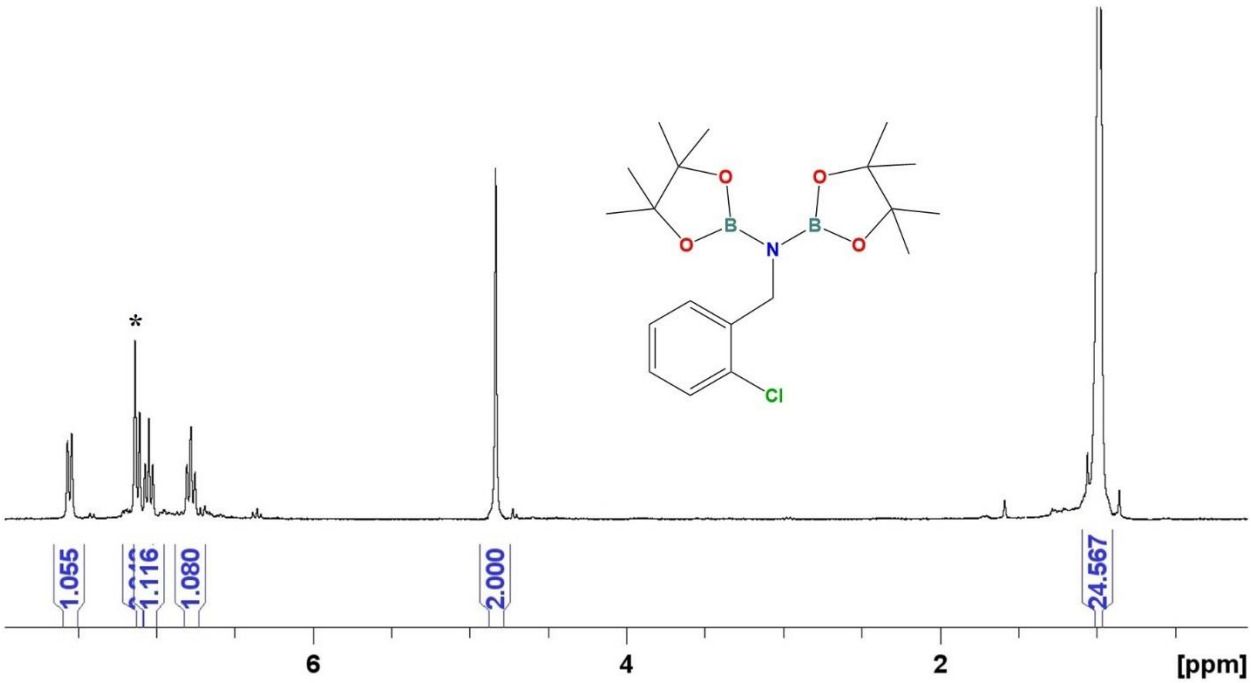

Figure C54. ^{1}H NMR (300 MHz, C_6D_6) spectrum of 2-chloro-benzonitrile hydroboration product. * indicates protic impurity in C_6D_6. Chemical shifts matched with literature values.

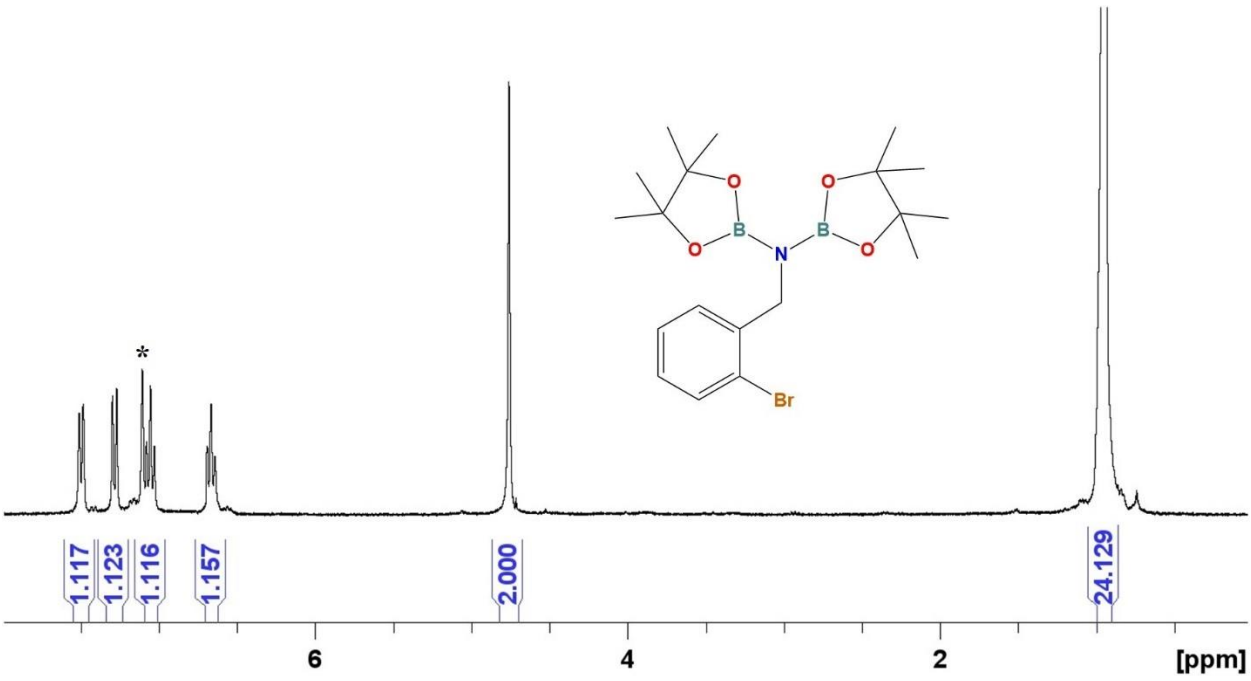

Figure C55. ^{1}H NMR (300 MHz, C_6D_6) spectrum of 2-bromo-benzonitrile hydroboration product. * indicates protic impurity in C_6D_6. Chemical shifts matched with literature values.

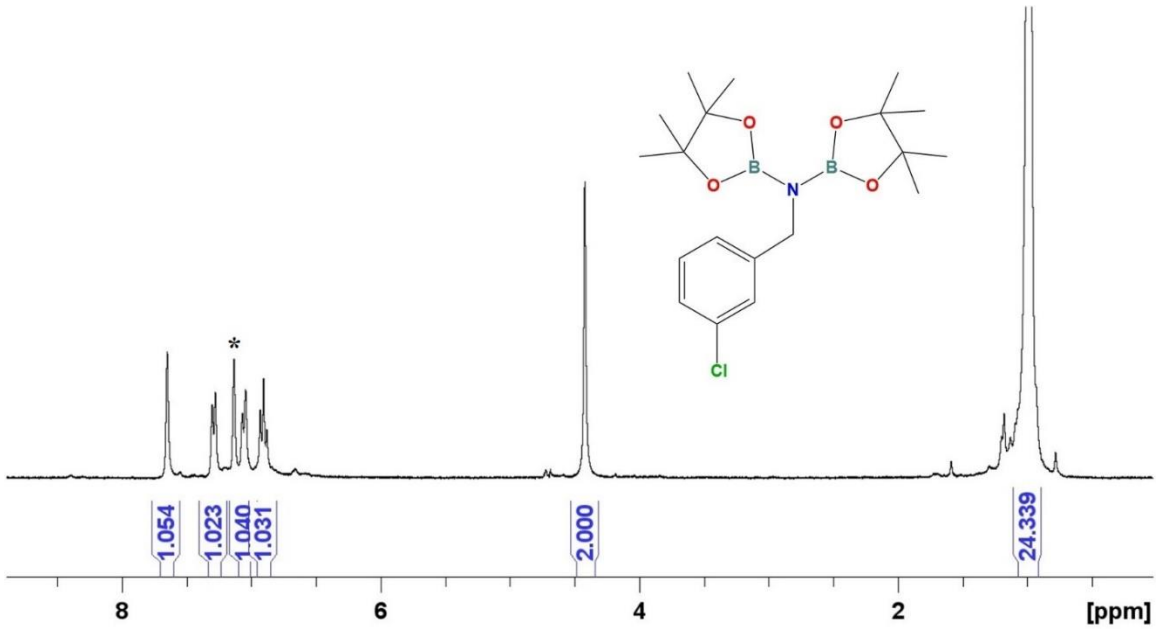

Figure C56. ^{1}H NMR (300 MHz, C_6D_6) spectrum of 3-chloro-benzonitrile hydroboration product. * indicates protic impurity in C_6D_6. Chemical shifts matched with literature values.

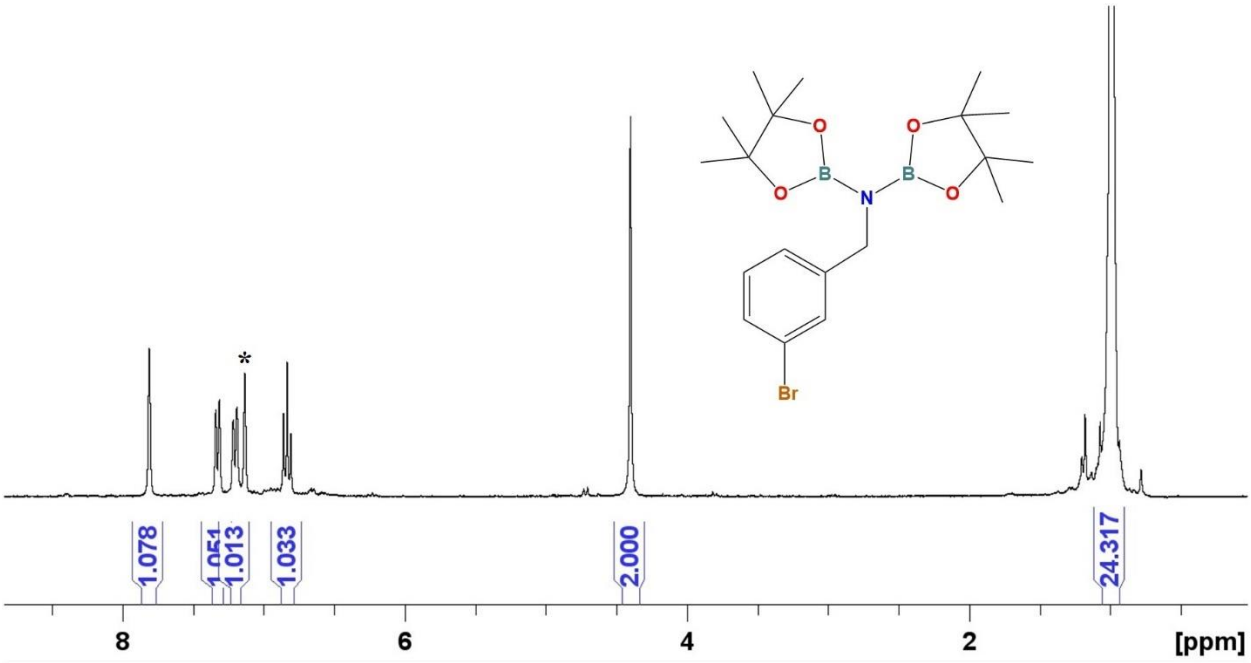

Figure C57. ^{1}H NMR (300 MHz, C_6D_6) spectrum of 3-bromo-benzonitrile hydroboration product. * indicates protic impurity in C_6D_6. Chemical shifts matched with literature values.

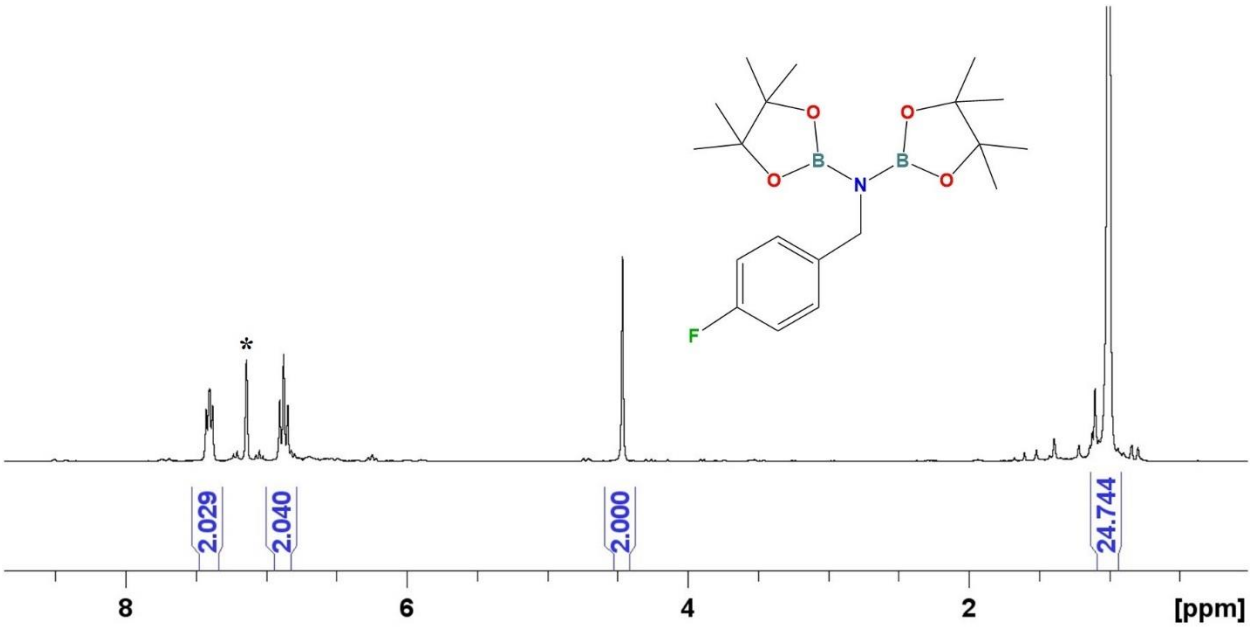

Figure C58. ^{1}H NMR (300 MHz, C_6D_6) spectrum of 4-fluoro-benzonitrile hydroboration product. * indicates protic impurity in C_6D_6. Chemical shifts matched with literature values.

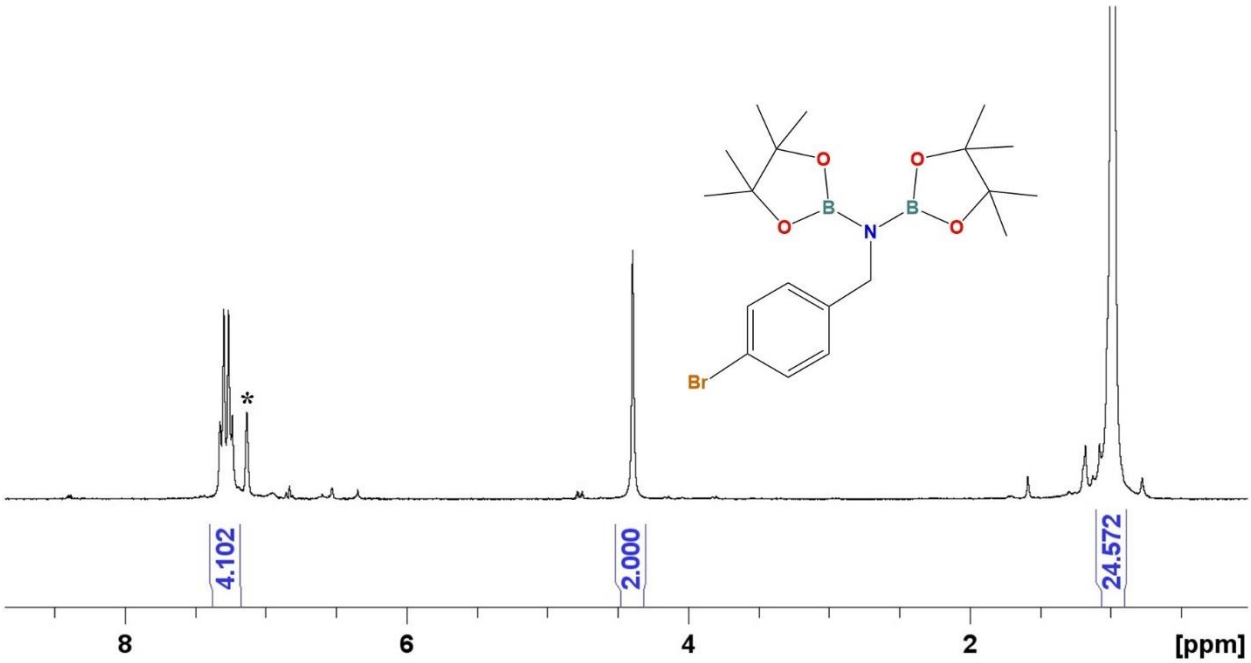

Figure C59. ^{1}H NMR (300 MHz, C_6D_6) spectrum of 4-bromo-benzonitrile hydroboration product. * indicates protic impurity in C_6D_6. Chemical shifts matched with literature values.

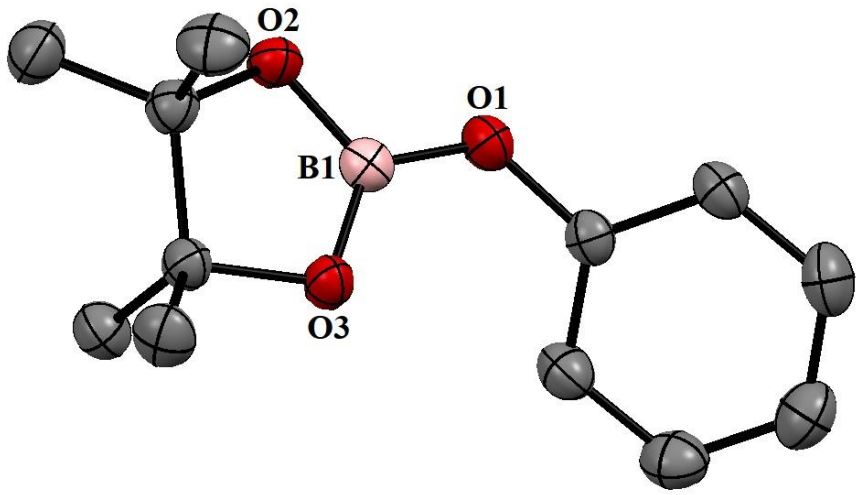

Figure C60. Molecular structure of **S-P3** with 50% probability thermal ellipsoids and hydrogen atoms omitted for clarity.

Table C5. Data collection and refinement metrics for complexes **4.2_{Ni}-4.5_{Ni}.**

	4.2_{Ni}	**4.3_{Ni}**	**4.4_{Ni}**	**4.5_{Ni}**
empirical formula	$C_{13}H_{13}BrN_2NiS$	$C_{11}H_{10}BrN_3Ni$	$C_{17}H_{15}N_3NiO$	$C_{17}H_{15}N_3NiS$
formula weight ($g \cdot mol^{-1}$)	367.93	322.84	336.03	352.09
crystal system	Triclinic	Monoclinic	Monoclinic	Monoclinic
space group	$P\,\bar{1}$	$P\,2_1/c$	$P\,2_1/n$	$P\,2_1/c$
a (A)	7.5250(3)	7.3811(5)	9.214(13)	10.3659(10)
b (A)	8.9184(3)	8.1534(5)	11.288(16)	10.4859(11)
c (A)	11.0649(3)	18.4811(12)	14.213(19)	13.7324(14)
α (deg)	112.9840(10)	90	90	90
β (deg)	90.1810(10)	94.171(2)	94.81(2)	94.595(3)
γ (deg)	95.6140(10)	90	90	90
V (A^3)	679.65(4)	1109.27(12)	1473(3)	1487.9(3)
Z	2	4	4	4
T (K)	293(2)	203(2)	203(2)	203(2)
ρ_{calcd} ($g \cdot cm^{-3}$)	1.798	1.933	1.515	1.572
μ (mm^{-1})	4.502	5.323	1.321	1.443
$2\theta_{max}$ (deg)	50.05	55.058	53.162	50.036
total/unique reflections	7451/2391	9332/2549	16248/3061	10050/2638
Reflections [$I_o \geq 2\sigma(I_o)$]	2199	1877	2337	1526
R_1, wR_2 [$I_o \geq 2\sigma(I_o)$]	0.0189, 0.0517	0.0346, 0.0590	0.0293, 0.0652	0.0481, 0.0691
goodness of fit	1.090	1.023	1.015	0.987
CCDC number	2155496	2155498	2155495	2155494

Table C6. Data collection and refinement metrics for complexes **4.6_{Ni}-4.8_{Ni} and S-P3.**

	4.6_{Ni}	**4.7_{Ni}**	**4.8_{Ni}**	**S-P3**
empirical formula	$C_{17}H_{18}N_4Ni$	$C_{23}H_{20}N_3NiP$	$C_{17}H_{15}N_3Ni$	$C_{12}H_7F_{12}BO_3$
formula weight ($g \cdot mol^{-1}$)	337.06	428.10	320.03	220.06
crystal system	Monoclinic	Monoclinic	Monoclinic	Triclinic
space group	$P\ 2_1/n$	$P\ 2_1/n$	$P\ 2_1/n$	$P\ \bar{1}$
a (A)	8.664(2)	12.6767(6)	11.5760(5)	7.7162(14)
b (A)	10.080(3)	10.8270(6)	6.9204(3)	8.2131(15)
c (A)	18.037(5)	14.8883(7)	17.7451(7)	9.8584(18)
α (deg)	90	90	90	82.347(4)
β (deg)	98.080(8)	103.974(2)	97.717(2)	83.715(3)
γ (deg)	90	90	90	76.098(4)
V (A^3)	1559.6(7)	1982.95(17)	1408.70(10)	599.11(19)
Z	4	4	4	2
T (K)	203(2)	203(2)	200(2)	200(2)
ρ_{calcd} ($g \cdot cm^{-3}$)	1.435	1.434	1.509	1.220
μ (mm^{-1})	1.245	1.072	1.373	0.084
$2\theta_{max}$ (deg)	50.054	52.84	50.056	56.778
total/unique reflections	10264/2731	41878/4071	9142/2481	8154/2952
Reflections [$I_o \geq 2\sigma(I_o)$]	1275	2849	2293	2411
R_1, wR_2 [$I_o \geq 2\sigma(I_o)$]	0.0632, 0.1080	0.0586, 0.0996	0.0341, 0.0909	0.0758, 0.2003
goodness of fit	0.971	1.096	1.030	1.094
CCDC number	2155493	2155499	2155497	2155492

Table C7. Bond lengths for **4.2$_{Ni}$**.

Atom1	Atom2	Length
Ni1	S1	2.1610(5)
Ni1	N1	1.835(2)
Ni1	N2	1.914(1)
Ni1	Br1A	2.352(2)
S1	C12	1.772(3)
S1	C13	1.801(3)
N1	C6	1.446(2)
N1	C7	1.364(3)
N2	C1	1.356(3)
N2	C5	1.343(3)
C1	H1	0.93
C1	C2	1.361(3)
C2	H2	0.93
C2	C3	1.368(5)
C3	H3	0.93
C3	C4	1.372(5)
C4	H4	0.93
C4	C5	1.386(3)
C5	C6	1.488(3)
C6	H6A	0.97
C6	H6B	0.97
C7	C8	1.410(4)
C7	C12	1.405(3)
C8	H8	0.93
C8	C9	1.379(3)
C9	H9	0.93
C9	C10	1.373(5)
C10	H10	0.93
C10	C11	1.387(5)
C11	H11	0.93
C11	C12	1.384(3)
C13	H13A	0.96
C13	H13B	0.96
C13	H13C	0.96

Table C8. Bond lengths for **4.3$_{Ni}$**.

Atom1	Atom2	Length
Br1	Ni1	2.3229(4)
Ni1	N1	1.920(3)
Ni1	N2	1.850(2)
Ni1	N3	1.875(3)
N1	C1	1.354(4)
N1	C5	1.357(4)
N2	C6	1.445(4)
N2	C7	1.296(4)
N3	C8	1.387(3)
N3	C11	1.351(4)
C1	H1	0.94
C1	C2	1.369(5)
C2	H2	0.94
C2	C3	1.376(5)
C3	H3	0.941
C3	C4	1.385(5)
C4	H4	0.94
C4	C5	1.380(5)
C5	C6	1.498(4)
C6	H6A	0.98
C6	H6AB	0.98
C7	H7	0.94
C7	C8	1.399(5)
C8	C9	1.392(5)
C9	H9	0.94
C9	C10	1.390(5)
C10	H10	0.941
C10	C11	1.392(5)
C11	H11	0.94

Table C9. Bond lengths for **4.4$_{Ni}$**.

Atom1	Atom2	Length
Ni1	O1	1.837(2)
Ni1	N1	1.850(3)
Ni1	N2	1.832(3)
Ni1	N3	1.881(3)
O1	C12	1.297(3)
N1	C1	1.331(4)
N1	C4	1.369(3)
N2	C5	1.283(3)
N2	C6	1.437(4)
N3	C7	1.343(3)
N3	C11	1.334(3)
C1	H1	0.93
C1	C2	1.382(4)
C2	H2	0.93
C2	C3	1.374(5)
C3	H3	0.93
C3	C4	1.381(4)
C4	C5	1.403(3)
C5	H5	0.93
C6	H6A	0.97
C6	H6AB	0.97
C6	C7	1.479(3)
C7	C8	1.368(4)
C8	H8	0.93
C8	C9	1.363(4)
C9	H9	0.93
C9	C10	1.369(4)
C10	H10	0.93
C10	C11	1.356(4)
C11	H11	0.93
C12	C13	1.386(3)
C12	C17	1.395(3)
C13	H13	0.93
C13	C14	1.358(4)
C14	H14	0.93
C14	C15	1.368(4)
C15	H15	0.93
C15	C16	1.371(4)
C16	H16	0.93
C16	C17	1.375(4)
C17	H17	0.93

Table C10. Bond lengths for **4.5$_{Ni}$**.

Atom1	Atom2	Length
Ni1	S1	2.199(1)
Ni1	N1	1.915(4)
Ni1	N2	1.872(4)
Ni1	N3	1.865(4)
S1	C12	1.761(4)
N1	C1	1.345(7)
N1	C5	1.357(6)
N2	C6	1.446(5)
N2	C7	1.300(7)
N3	C8	1.384(7)
N3	C11	1.347(6)
C1	H1	0.94
C1	C2	1.387(7)
C2	H2	0.94
C2	C3	1.368(7)
C3	H3	0.94
C3	C4	1.370(7)
C4	H4	0.94
C4	C5	1.383(7)
C5	C6	1.492(7)
C6	H6A	0.98
C6	H6AB	0.981
C7	H7	0.94
C7	C8	1.416(7)
C8	C9	1.392(7)
C9	H9	0.94
C9	C10	1.398(7)
C10	H10	0.94
C10	C11	1.389(7)
C11	H11	0.939
C12	C13	1.392(7)
C12	C17	1.396(6)
C13	H13	0.94
C13	C14	1.376(7)
C14	H14	0.941
C14	C15	1.379(7)
C15	H15	0.94
C15	C16	1.369(8)
C16	H16	0.939
C16	C17	1.389(7)
C17	H17	0.94

Table C11. Bond lengths for **4.6$_{Ni}$**.

Atom1	Atom2	Length
Ni1	N1	1.905(5)
Ni1	N2	1.859(5)
Ni1	N3	1.866(5)
Ni1	N4	1.877(5)
N1	C1	1.355(9)
N1	C5	1.351(9)
N2	C6	1.466(7)
N2	C7	1.295(8)
N3	C8	1.385(9)
N3	C11	1.363(8)
N4	C13	1.365(9)
N4	C16	1.382(8)
C1	H1	0.94
C1	C2	1.386(9)
C2	H2	0.94
C2	C3	1.37(1)
C3	H3	0.94
C3	C4	1.36(1)
C4	H4	0.94
C4	C5	1.400(9)
C5	C6	1.485(9)
C6	H6A	0.98
C6	H6AB	0.98
C7	H7	0.94
C7	C8	1.418(8)
C8	C9	1.391(9)
C9	H9	0.94
C9	C10	1.40(1)
C10	H10	0.94
C10	C11	1.39(1)
C11	H11	0.94
C12	H12A	0.97
C12	H12B	0.969
C12	H12C	0.97
C12	C13	1.49(1)
C13	C14	1.39(1)
C14	H14	0.94
C14	C15	1.40(1)
C15	H15	0.94
C15	C16	1.36(1)
C16	C17	1.48(1)
C17	H17A	0.969

C17	H17B	0.97
C17	H17C	0.97

Table C12. Bond lengths for **4.7$_{Ni}$**.

Atom1	Atom2	Length
Ni1	P1	2.173(1)
Ni1	N1	1.927(4)
Ni1	N2	1.985(4)
Ni1	P1	2.184(1)
P1	C12	1.825(4)
P1	C18	1.828(5)
P1	Ni1	2.184(1)
N1	C1	1.361(5)
N1	C4	1.379(6)
N2	C5	1.287(6)
N2	C6	1.465(6)
N3	C7	1.345(7)
N3	C11	1.333(8)
C1	H1	0.94
C1	C2	1.388(7)
C2	H2	0.94
C2	C3	1.381(7)
C3	H3	0.94
C3	C4	1.392(6)
C4	C5	1.419(6)
C5	H5	0.939
C6	H6A	0.98
C6	H6B	0.98
C6	C7	1.532(8)
C7	C8	1.388(7)
C8	H8	0.939
C8	C9	1.39(1)
C9	H9	0.94
C9	C10	1.37(1)
C10	H10	0.94
C10	C11	1.385(8)
C11	H11	0.94
C12	C13	1.388(7)
C12	C17	1.388(6)
C13	H13	0.94
C13	C14	1.386(7)
C14	H14	0.94
C14	C15	1.392(8)

C15	H15	0.94
C15	C16	1.366(8)
C16	H16	0.939
C16	C17	1.374(7)
C17	H17	0.94
C18	C19	1.386(6)
C18	C23	1.392(7)
C19	H19	0.94
C19	C20	1.384(8)
C20	H20	0.94
C20	C21	1.394(9)
C21	H21	0.941
C21	C22	1.376(8)
C22	H22	0.94
C22	C23	1.387(7)
C23	H23	0.94
Ni1	P1	2.173(1)
Ni1	N1	1.927(4)
Ni1	N2	1.985(4)
P1	C12	1.825(4)
P1	C18	1.828(5)
N1	C1	1.361(5)
N1	C4	1.379(6)
N2	C5	1.287(6)
N2	C6	1.465(6)
N3	C7	1.345(7)
N3	C11	1.333(8)
C1	H1	0.94
C1	C2	1.388(7)
C2	H2	0.94
C2	C3	1.381(7)
C3	H3	0.94
C3	C4	1.392(6)
C4	C5	1.419(6)
C5	H5	0.939
C6	H6A	0.98
C6	H6B	0.98
C6	C7	1.532(8)
C7	C8	1.388(7)
C8	H8	0.939
C8	C9	1.39(1)
C9	H9	0.94
C9	C10	1.37(1)
C10	H10	0.94
C10	C11	1.385(8)

C11	H11	0.94
C12	C13	1.388(7)
C12	C17	1.388(6)
C13	H13	0.94
C13	C14	1.386(7)
C14	H14	0.94
C14	C15	1.392(8)
C15	H15	0.94
C15	C16	1.366(8)
C16	H16	0.939
C16	C17	1.374(7)
C17	H17	0.94
C18	C19	1.386(6)
C18	C23	1.392(7)
C19	H19	0.94
C19	C20	1.384(8)
C20	H20	0.94
C20	C21	1.394(9)
C21	H21	0.941
C21	C22	1.376(8)
C22	H22	0.94
C22	C23	1.387(7)
C23	H23	0.94

Table C13. Bond lengths for **4.8$_{Ni}$**.

Atom1	Atom2	Length
Ni1	N1	1.879(2)
Ni1	N2	1.891(2)
Ni1	N3	1.916(2)
Ni1	C1	1.893(3)
N1	C7	1.350(3)
N1	C10	1.381(3)
N2	C11	1.288(3)
N2	C12	1.449(3)
N3	C13	1.349(4)
N3	C17	1.353(4)
C1	C2	1.380(4)
C1	C6	1.416(4)
C2	H2	0.95
C2	C3	1.401(4)
C3	H3	0.95
C3	C4	1.365(5)
C4	H4	0.95

C4	C5	1.384(6)
C5	H5	0.95
C5	C6	1.376(4)
C6	H6	0.95
C7	H7	0.95
C7	C8	1.389(4)
C8	H8	0.95
C8	C9	1.387(4)
C9	H9	0.95
C9	C10	1.383(3)
C10	C11	1.421(4)
C11	H11	0.95
C12	H12A	0.99
C12	H12B	0.99
C12	C13	1.495(4)
C13	C14	1.385(3)
C14	H14	0.95
C14	C15	1.365(5)
C15	H15	0.95
C15	C16	1.368(5)
C16	H16	0.951
C16	C17	1.383(5)
C17	H17	0.95

Table C14. Bond lengths for **S-P3**.

Atom1	Atom2	Length
O1	C1	1.386(4)
O1	B1	1.365(4)
O2	C7	1.468(4)
O2	B1	1.363(4)
O3	C8	1.469(4)
O3	B1	1.369(4)
C1	C2	1.388(5)
C1	C6	1.382(5)
C2	H2	0.95
C2	C3	1.383(5)
C3	H3	0.95
C3	C4	1.390(6)
C4	H4	0.95
C4	C5	1.386(5)
C5	H5	0.95
C5	C6	1.390(5)
C6	H6	0.95

C7	C8	1.562(5)
C7	C9	1.523(4)
C7	C10	1.520(4)
C8	C11	1.523(4)
C8	C12	1.515(4)
C9	H9A	0.98
C9	H9B	0.98
C9	H9C	0.98
C10	H10A	0.98
C10	H10B	0.98
C10	H10C	0.98
C11	H11A	0.98
C11	H11B	0.98
C11	H11C	0.98
C12	H12A	0.98
C12	H12B	0.98
C12	H12C	0.98